

**Modeling, Control and Safety for
Probe-and-Drogue Autonomous Aerial
Refueling**

Symbols

ΔF_0	=	Bow wave disturbance force
$\Delta \mathbf{p}_{\text{dr}}^e$	=	Drogue position offsets from equilibrium position
$\Delta \mathbf{p}_{\text{dr/pr}}$	=	Position error between drogue and probe
$\Delta \mathbf{p}_{\text{dr/pr}}(T)$	=	Terminal position error
$\Delta R_{\text{dr/pr}}$	=	Radial error between hose and drogue
F_T	=	Tanker joint frame
$\mathbf{F}_r, \mathbf{F}_{\text{hd}}$	=	Disturbance forces on receiver and hose-drogue
\mathbf{F}_{bow}	=	Disturbance force from bow wave effect
$\mathbf{p}_{\text{dr}}(t), \mathbf{p}_{\text{pr}}(t)$	=	Current positions of drogue and probe
$\mathbf{p}_{\text{dr}}(T), \mathbf{p}_{\text{pr}}(T)$	=	Terminal positions of drogue and probe
$\mathbf{p}_{\text{dr}}^{e0}$	=	Drogue initial equilibrium position
\mathbb{R}, \mathbb{R}_+	=	Real number set and positive real number set
R_C	=	Threshold radius for a successful docking attempt
T	=	Terminal time of a docking attempt
$\hat{\mathbf{u}}_{\text{pr}}$	=	Reference trajectory for autopilot

Table 0.1: Nomenclature

Symbol	Type	Denotation
c_h	scalar	latitudinal correlation coefficient
c_v	scalar	longitudinal correlation coefficient
k	scalar	recursive step
N	scalar	the number of the chosen grid points
$p_q^k(q)$	scalar	the transition probability from the grid point q to itself in the k -th step
$p_{q'}^k(q)$	scalar	the probability of transition from the grid point q to the grid point q' in the k -th step
$P^{(k)}(q)$	scalar	the probability transited to the grid point q in the k -th step
P_j	scalar	the probabilities of docking success which are obtained by stochastic approximation method
$P_{MC,j}$	scalar	the probabilities of docking success which are obtained by Monte Carlo method
q	scalar	a specific grid point
r	scalar	the correlation coefficient of the probabilities of docking success obtained by stochastic approximation method and Monte Carlo method
t_f	scalar	the end time of the docking phase
Δt	scalar	time step
V_t	scalar	tanker speed

Continued on next page

Table 0.1 – Continued from previous page

Symbol	Type	Denotation
V_r	scalar	receiver speed
Δx	scalar	the longitudinal distance between receiver and tanker
Δy	scalar	the lateral distance between receiver and tanker
Δh	scalar	the vertical distance between receiver and tanker
γ_r	scalar	the flight path angle of receiver
φ_r	scalar	the azimuth angle of receiver
$\Delta\gamma$	scalar	the flight path angle of receiver relative to tanker
$\Delta\varphi$	scalar	the azimuth angle of receiver relative to tanker
σ_i	scalar	the element of diagonal matrix Γ
$\bar{\sigma}$	scalar	the max value among $\sigma_i (i = 1, 2, 3)$
σ_h	scalar	the variation of lateral stochastic perturbation
σ_v	scalar	the variation of longitudinal stochastic perturbation
δ	scalar	grid size
λ	scalar	positive constant related to time step
η_i	scalar	relative parameter, where $i = 1, 2, 3$
\mathcal{D}	set	target set
\mathcal{X}	set	state constraint set
\mathcal{L}	set	state space
\mathcal{Q}	set	set of grids
\mathcal{Q}_0	set	interior grids of the state space
$\partial\mathcal{Q}_{\mathcal{L}}$	set	boundary grids of the state space
$\partial\mathcal{Q}_{\mathcal{X}}$	set	boundary grids of the state constraint set
$\partial\mathcal{Q}_{\mathcal{D}}$	set	boundary grids of the target set
\mathcal{N}_q	set	adjacent grids of the specific grid point q
$\tilde{\mathbf{x}}_{r/t}$	vector	the position of receiver relative to tanker
\mathbf{x}_1	vector	the position of the tip of probe
\mathbf{y}_1	vector	the position of the center of drogue
$\alpha(\tilde{\mathbf{x}}_{r/t}, t)$	function	the drift term of the stochastic differential equation
$\beta(\tilde{\mathbf{x}}_{r/t})$	function	the diffusion term of the stochastic differential equation
$\mathbf{a}_1(t)$	function	kinematic equation of the probe
$\mathbf{a}_2(t)$	function	kinematic equation of the drogue
$\mathbf{f}(\mathbf{x}, t)$	function	affine transformation in \mathbf{x}
$\mathbf{u}(t)$	function	the kinematic states of the tip of the probe with respect to the center of the drogue
$\mathbf{z}(t)$	function	Gaussian process

Continued on next page

Table 0.1 – Continued from previous page

Symbol	Type	Denotation
$\rho(\mathbf{x})$	function	the spatial correlation function
$\mathbf{B}(\mathbf{x}_0, t)$	function	standard Brownian motion for a specific position \mathbf{x}_0
$\mathbf{B}(\mathbf{x}, t)$	function	stochastic perturbation of current state \mathbf{x}
$\mathbf{W}(t)$	function	a standard 3D Brownian motion
\mathbf{I}_3	matrix	the 3-by-3identity matrix
Γ	matrix	variance of the random perturbation

\mathbb{R}^n	n -dimensional Euclidean space.
\mathbb{R}	set of real numbers.
\mathbb{R}_+	set of positive real numbers.
\mathbb{N}	set of nonnegative integers.
$\mathbf{x}_1 \oplus \mathbf{x}_2$	direct sum of \mathbf{x}_1 and \mathbf{x}_2 .
ω_{cg}	gain crossover frequency.
ω_{cp}	phase crossover frequency.
γ_{\max}	\mathcal{L}_2 gain margin of a closed-loop system.
τ_{\max}	\mathcal{L}_2 time-delay margin of a closed-loop system.
\mathcal{L} and \mathcal{L}^{-1}	Laplace transform and the inverse Laplace transform.
\mathcal{Z} and \mathcal{Z}^{-1}	Z-transform and the inverse Z-transform.
$\mathcal{L}_{\infty}[a, b]$	$\mathcal{L}_{\infty}[a, b] \triangleq \{\mathbf{f} \sup_{t \in [a, b]} \ \mathbf{f}(t)\ < \infty\}.$
$\mathcal{L}_1[a, b]$	$\mathcal{L}_1[a, b] \triangleq \left\{ \mathbf{f} \sup_{t \in [a, b]} \left(\int_a^b \ \mathbf{f}(t)\ dt \right) < \infty \right\}.$
$\ \mathbf{u}\ _{\mathcal{L}_2}$	norm of a piecewise continuous, square-integrable function $\mathbf{u}(t) \in \mathbb{R}^n$, and $\ \mathbf{u}\ _{\mathcal{L}_2} \triangleq \sqrt{\int_0^\infty \mathbf{u}^T(t) \mathbf{u}(t) dt} < \infty$.
\mathcal{L}_2^n	$\mathcal{L}_2^n \triangleq \{\mathbf{u} \ \mathbf{u}\ _{\mathcal{L}_2} < \infty\}$, \mathbf{u} is a piecewise continuous, square-integrable function $\mathbf{u}(t) \in \mathbb{R}^n$.
\mathbf{u}_{σ}	a truncation of \mathbf{u} defined by $\mathbf{u}_{\sigma}(t) \triangleq \begin{cases} \mathbf{u}(t) & 0 \leq t \leq \sigma \\ 0 & \text{otherwise.} \end{cases}$
\mathcal{L}_{2e}^n	$\mathcal{L}_{2e}^n \triangleq \{\mathbf{u} \mathbf{u}_{\sigma} \in \mathcal{L}_2^n, \forall \sigma < \infty\}.$
$\underline{\sigma}(\mathbf{C}), \bar{\sigma}(\mathbf{C})$	maximum singular value and the minimum singular of matrix $\mathbf{C} \in \mathbb{C}^{n \times n}$.
$\lambda(\mathcal{A}), \lambda_{\max}(\mathcal{A}), \lambda_{\min}(\mathcal{A})$	eigenvalue, maximum eigenvalue and the minimum eigenvalue of the operator \mathcal{A} .
$\rho(\mathcal{A})$	spectral radius of the operator \mathcal{A} . In particular, for matrices, $\rho(\mathbf{A}) = \max \{ \lambda(\mathbf{A}) \}, \mathbf{A} \in \mathbb{R}^{n \times n}$.
$\ \mathbf{H}\ _{\infty}$	\mathcal{H}_{∞} norm of a transfer function matrix \mathbf{H} ,
	$\ \mathbf{H}\ _{\infty} \triangleq \sup_{\omega} \bar{\sigma}(\mathbf{H}(j\omega)).$
$ s $	modulus of a complex number s is defined as $ s \triangleq \sqrt{a^2 + b^2}$, where $s = a + ib, a, b \in \mathbb{R}$.
$\mathbf{A} \geq \mathbf{0}, \mathbf{A} > \mathbf{0}$	$\mathbf{A} \in \mathbb{R}^{n \times n}$ is a positive semidefinite or positive definite matrix.
$\text{adj}(\mathbf{A})$	adjoint matrix of matrix \mathbf{A} .

\bar{s}	conjugate of the complex number $s = a + ib$ is $\bar{s} \triangleq a - ib$.
\mathbf{C}^*	conjugate transpose is formally defined by $(\mathbf{C}^*)_{ij} \triangleq (\bar{\mathbf{C}})_{ji}$, $\mathbf{C} \in \mathbb{C}^{n \times m}$.
$C([a, b], \mathbb{R}^n)$	space of continuous n -dimension function vector on $[a, b]$.
$C_{PT}^m([0, \infty), \mathbb{R}^n)$	space of m th-order continuously differentiable functions $\mathbf{f} : [0, \infty) \rightarrow \mathbb{R}^n$ which are T -periodic, i.e. $\mathbf{f}(t + T) = \mathbf{f}(t)$.
$\ \mathbf{x}_t\ _{[a, b]}$	$\ \mathbf{x}_t\ _{[a, b]} \triangleq \sup_{\theta \in [a, b]} \ \mathbf{x}(t + \theta)\ $, where $\mathbf{x}_t \triangleq \mathbf{x}_t(\theta) = \mathbf{x}(t + \theta)$, $\theta \in [a, b]$.
$\mathcal{B}(\delta)$	$\mathcal{B}(\delta) \triangleq \{\xi \in \mathbb{R} \mid \ \xi\ \leq \delta\}$, $\delta > 0$; the notation $x(t) \rightarrow \mathcal{B}(\delta)$ means $\min_{y \in \mathcal{B}(\delta)} x(t) - y \rightarrow 0$.
\mathcal{K}	a continuous function $\alpha : [0, a] \rightarrow [0, \infty)$ is said to belong to class \mathcal{K} if it is strictly increasing and $\alpha(0) = 0$.
\mathcal{K}_∞	a continuous function α is said to belong to class \mathcal{K}_∞ if $a = \infty$ and $\alpha(r) \rightarrow \infty$ as $r \rightarrow \infty$.
\mathcal{KL}	a continuous function $\beta : [0, a] \times [0, \infty) \rightarrow [0, \infty)$ is said to belong to class \mathcal{KL} if, for each fixed s , the mapping $\beta(r, s)$ belongs to \mathcal{K} with respect to r and, for each fixed r , the mapping $\beta(r, s)$ is decreasing with respect with s and $\beta(r, s) \rightarrow 0$ as $s \rightarrow \infty$.
$\ \mathbf{f}\ _a$	$\ \mathbf{f}\ _a \triangleq \limsup_{t \rightarrow \infty} \ \mathbf{f}(t)\ $, where $\mathbf{f} \in \mathcal{L}_\infty[0, \infty)$.
$ \cdot $	modulus of a complex number.
$O(\mathbf{x})^n$	a function $\delta(\mathbf{x})$ is said to be $O(\mathbf{x})^n$ if $\lim_{\ \mathbf{x}\ \rightarrow 0} \frac{\ \delta(\mathbf{x})\ }{\ \mathbf{x}\ ^n}$ exists and is nonzero. In particular, a function $\delta(\mathbf{x})$, said to be $O(\mathbf{x})^0$ or $O(1)$, implies $\lim_{\ \mathbf{x}\ \rightarrow 0} \ \delta(\mathbf{x})\ $ exists and is nonzero.
\circ	function composition, $\mathbf{f}_1 \circ \mathbf{f}_2 : \mathbb{R}^n \rightarrow \mathbb{R}^m$ implies that $(\mathbf{f}_1 \circ \mathbf{f}_2)(\mathbf{x}) = \mathbf{f}_1(\mathbf{f}_2(\mathbf{x}))$, $\forall \mathbf{x} \in \mathbb{R}^n$, where $\mathbf{f}_1 : \mathbb{R}^p \rightarrow \mathbb{R}^m$, $\mathbf{f}_2 : \mathbb{R}^n \rightarrow \mathbb{R}^p$.
\mathcal{G}	a linear operator: $\mathcal{L}_2[0, T] \mapsto \mathcal{L}_2[0, T]$, defined as $\mathcal{G}u = \int_0^t \mathbf{c}^T e^{\mathbf{A}(t-\tau)} \mathbf{b} u(\tau) d\tau$.
\mathcal{H}	a linear operator: $\mathcal{L}_2[0, T] \mapsto \mathcal{L}_2[0, T]$.
\mathcal{G}^*	an adjoint operator: $\mathcal{L}_2[0, T] \mapsto \mathcal{L}_2[0, T]$, calculated as $\mathcal{G}_l^* u = \int_t^T \mathbf{b}^T e^{-\mathbf{A}_l^T(t-\tau)} \mathbf{c} u(\tau) d\tau$, defined by $\langle \mathbf{y}, \mathcal{G}\mathbf{u} \rangle = \langle \mathcal{G}^*\mathbf{y}, \mathbf{u} \rangle$.
$\ \boldsymbol{\alpha}\ _{[t_1, t_2]}$	$\ \boldsymbol{\alpha}\ _{[t_1, t_2]} = \sup_{t \in [t_1, t_2]} \ \boldsymbol{\alpha}(t)\ _2$, where $\boldsymbol{\alpha}$ is a function vector defined on $[t_1, t_2]$.
$\ \boldsymbol{\alpha}\ _{\mathcal{L}_2}$	$\ \boldsymbol{\alpha}\ _{\mathcal{L}_2} = \sqrt{\int_0^T \boldsymbol{\alpha}^T(t) \boldsymbol{\alpha}(t) dt}$, where $\boldsymbol{\alpha}$ is a function vector defined on $[0, T]$.
$\langle \boldsymbol{\alpha}_1, \boldsymbol{\alpha}_2 \rangle_{\mathcal{L}_2}$	$\langle \boldsymbol{\alpha}_1, \boldsymbol{\alpha}_2 \rangle_{\mathcal{L}_2} = \int_0^T \boldsymbol{\alpha}_1^T(t) \boldsymbol{\alpha}_2(t) dt$, where $\boldsymbol{\alpha}_1, \boldsymbol{\alpha}_2$ are function vectors defined on $[0, T]$.
$\ \boldsymbol{\alpha}\ _2$	$\ \boldsymbol{\alpha}\ _2 = \sqrt{\boldsymbol{\alpha}^T \boldsymbol{\alpha}}$, where $\boldsymbol{\alpha}$ is a vector.
$\ \mathcal{G}\ $	$\ \mathcal{G}\ = \sup_{\ \mathbf{x}\ _{\mathcal{L}_2} \leq 1} \ \mathcal{G}\mathbf{x}\ _{\mathcal{L}_2}$, where \mathbf{x} is a function defined on $[0, T]$.



Acronyms

2D Two-dimensional

3D Three-dimensional

4D Four-dimensional

JLC Jacobian-linearization-based control

FLC Feedback-linearization-based control

SCLC State-compensation-based control

SM Stability margin

MIMO Multiple-input multiple-output

SISO Single-input single-output

LTI Linear time-variant

GM Gain margin

PM Phase margin

LQR Linear quadratic regulator

ASD Additive state decomposition

ASDB Additive-state-decomposition-based

ISS Input to state stability

TORA Translational oscillator with a rotational actuator

ILC Iterative learning control

RC Repetitive control

NMP Non-minimum phase

BTT Back-to-turn

UAVs Unmanned aerial vehicles

STT Skid-to-turn

EM-RAAT Extended medium range air-to-air technology

LQG Linear-quadratic-gaussian

PID Proportional-integral-derivative

PI Proportional-Integral

AR Aerial refueling

PDR Probe-droge refueling

AAR Autonomous aerial refueling

ILC Iterative learning control

NZSP Nonzero setpoint

ADRC Active disturbance rejection control

NATO North Atlantic Treaty Organisation

SIL Software-in-the-loop

MEMS Micro-electro-mechanical system



Chapter 1 Introduction

This chapter is from our published survey paper [1]. By refueling aircraft while in flight, aerial refueling is an efficient technique to extend their endurance and range. Autonomous Aerial Refueling (AAR) is anticipated to be used to complete aerial refueling for unmanned aircraft. There are three aerial refueling methods: the probe-and-drogue method, the flying-boom method, and the boom-drogue-adapter method. The paper considers the Probe-and-Drogue Refueling (PDR) approach since its control task is the most challenging. PDR is divided into four phases, with the refueling phase being the most crucial: the rendezvous phase, joining phase, refueling phase, and reform phase. The controller design faces the most significant challenge during the docking control of the refueling phase since it calls for a high level of safety, precision, and efficiency. As a result, the modeling and control issues encountered during the refueling phase are typical and difficult. The fundamental idea of AAR is presented in the chapter initially, after which the characteristics and requirements of AAR are outlined. The development of modeling and control techniques for the AAR's refueling phase is then systematically reviewed. Besides, potential future work for high safety, precision, and efficiency requirements is examined and suggested. Finally, the objective, chapter introduction, and book structure are given. An excellent survey about modeling, sensors, control strategies, simulation, and testing can be found in [2], which pays much attention to the practical side of AAR. In 2014, a Chinese survey [3] on PDR modeling and control was released.

1.1 Basic concept and significance of AAR

In Aerial Refueling (AR), also known as air-to-air refueling, in-flight refueling, or simply air refueling, one air-craft, referred to as the tanker, refuels one or more other aircraft, referred to as the receivers, while they are in the air. AR is frequently employed in the military field to extend endurance, range, and resolve the conflict between payload and takeoff distance. AR is also used in the civil field to increase the effectiveness of long-haul flights and boost the civil aviation's emergency response capabilities. Unmanned aerial vehicles (UAVs) have difficulty performing AR, which is primarily carried out by the receiver pilot in manned aircraft. Realizing autonomous aerial refueling is important for both reducing the pilots' pressure of performing AR and achieving the AR of UAVs while maintaining a high enough level of safety, precision, and efficiency.

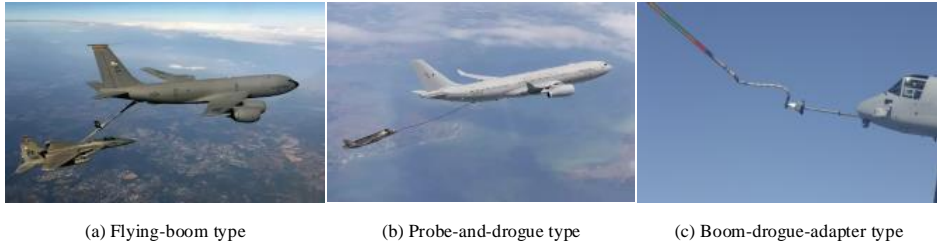


Figure 1.1: Three kinds of aerial refueling systems

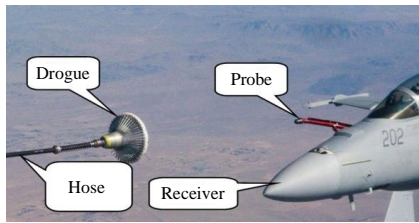


Figure 1.2: Probe-and-drogue aerial refueling apparatus

1.1.1 Classification

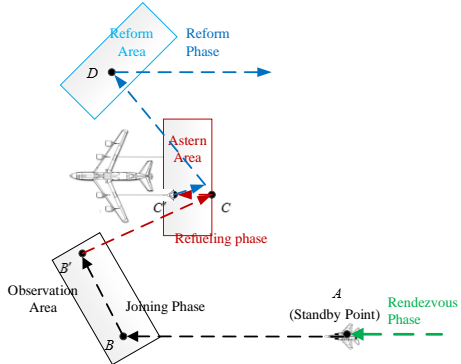
Aerial refueling systems that are now in use include the flying-boom type (Figure 1.1 (a)), the probe-and-drogue type (Figure 1.1 (b)), and the boom-drogue-adapter type (Figure 1.1 (c)). The three aerial refueling systems will be detailed in the following.

A tanker with a flying boom is often modified by a civil aircraft or a large transport aircraft. The flying boom is supervised and controlled by a human operator from a station near the rear of the tanker aircraft. The flying boom is often equipped with a V-tail, which can be used to control it. The refueling process is controlled cooperatively by the receiver and the flying boom. The receiver first flies to the flying boom working area and then keeps relatively stationary with the tanker. Then, the operator in the station at the rear of the tanker controls the attitude of the flying boom, extends the flying boom to approach the receiver slowly and insert it into the fuel tank at the back of the receiver fuselage.

The probe-and-drogue refueling equipment (shown in Figure 1.2) is simple and compact. A hose-drogue pod can be added to any aircraft with enough payload capacity, including fighters, large transport aircraft, and UAVs. The pod releases a hose with a drogue at the end, in which the hose length should match the tanker length for safety considerations. For manned aircraft, the probe is typically placed to the side of the cockpit for clear pilots' visibility, but for unmanned aerial vehicles, it is generally placed in front of the receiver nose. The tanker frequently maintains level flight while moving forward during the preparation phase of refueling and releases a hose in the refueling region. The receiver then moves towards the tanker and places its probe into the drogue. The aerial docking operation is finished once the mechanical self-locking mechanism on the drogue locks the drogue and the probe together. The receiver must then maintain its position in relation to the tanker until refueling is complete.

Table 1.1: Performance of three types of aerial refueling systems

Refueling type	Tanker modification	Oil rate	Safety	Influence by disturbances	Docking difficulty
Flying-boom	++	++	+	+	+
Probe-and-drogue	+	+	+++	+++	+++
Boom-drogue-adapter	++	+	++	++	++

**Figure 1.3:** Aerial refueling phase

The boom-drogue-adapter aerial refueling uses a hose installed at the end of a flying boom. On the one hand, it is designed to keep the flexible connection between the receiver and the tanker after docking in order to improve the safety in the fuel transferring process. On the other hand, it is designed to solve the shortcoming that the rigid flying boom cannot refuel helicopters. Since the end of the adapter is a hose, the refueling process is similar to that of the probe-and-drogue aerial refueling.

The three different types of aerial refueling systems' primary performance is displayed in Table 1.1. It can be seen from Table 1.1 that the boom-drogue-adapter type has most of the features of the flying-boom refueling and is slightly compromised towards the probe-and-drogue type. Because of its flexible connection and lightweight equipment, the PDR has a wide range of applications despite its challenging docking. By mounting multiple refueling pods on a receiver, PDR can also support aerial refueling for helicopters. The United States Navy and the air forces of many countries favor the probe-and-drogue refueling method due to its adaptability to various aircraft and refueling rates. In contrast, airborne early warning aircraft and some fighters use the flying-boom refueling method. When refueling numerous aircraft, PDR is favored if small aircraft predominate in the refueling process because small aircraft have lower oil transfer rate requirements, and PDR can accomplish multi-point refueling. If large aircraft outnumber small aircraft, flying-boom refueling may be chosen instead. As a result, from the implementation perspective, one refueling method cannot replace another. The PDR is primarily considered in this book.

1.1.2 Aerial refueling phase

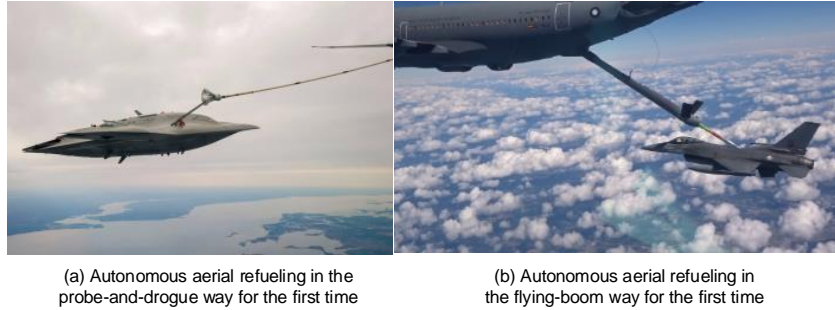
Aerial refueling consists of four phases: rendezvous phase, joining phase, refueling phase and reform phase. The details are as follows:

- (i) Rendezvous phase (to A shown in Figure.1.3): The process of the rendezvous between the tanker and the receiver flying from different directions to the designated area. For a single receiver, it waits at point A (as shown in Figure. 1.3) for the next instruction.
- (ii) Joining phase ($A \rightarrow B \rightarrow B'$ shown in Figure.1.3): The process of the receiver entering the observation area, completing the formation with the tanker and other receivers. As shown in Figure.1.3, for multiple receivers, they will be in a staggered queue in the observation area and move from B to B' one by one.
- (iii) Refueling phase ($B' \rightarrow C \rightarrow C'$ shown in Figure.1.3): The process of the receiver from the observation area to the astern area. After a successful capture, the receiver and the tanker keep relatively stationary to transfer the fuel. There are two main subphases, namely docking subphase and fuel transferring subphase, where the former is especially important and challenging.
- (iv) Reform phase ($C' \rightarrow D$ shown in Figure.1.3): After completing the fuel transferring, the probe in the receiver and the drogue are separated, and then the receiver leaves the astern area and enters the reform area.

1.1.3 AAR

With the development of aerial refueling technology and the increasing requirements of aerial refueling from modern flight missions, aerial refueling urgently needs to be autonomous to expand its scope of application and meanwhile be implemented with high precision, high safety, and high efficiency. The importance and difficulties of AAR were comprehensively discussed in [4]. AAR refers to automating manned or unmanned aerial refueling. Under a specific autonomous authority, the receiver automatically processes sensor data and creates relevant trajectory commands for its guidance and control system to implement AAR.

On April 22, 2015, Northrop Grumman Corporation and the U.S. Navy successfully demonstrated full probe-and-drogue AAR with an X-47B UAV for the first time in history that a UAV has been refueled in-flight (as shown in Figure.1.4 (a)). Before it, two small UAVs flying in leader-follower formation performed airborne docking by the University of Sydney. A complete navigation, guidance and control solution was given in [5]. On May 09, 2017, Airbus Defense and Space successfully demonstrated AAR contacts between a fighter aircraft and a tanker's flying boom for the first time in the world (as shown in Figure.1.4 (b)). Airbus has disclosed that the testing for a new function that would enable the A330-200 Multi Role Tanker Transport (MRTT) to achieve AAR for UAVs will begin in 2023.

**Figure 1.4:** AAR for the first time

1.1.4 The significance of AAR

Aerial refueling is widely used in the military field, such as the endurance of fighters and the take-off with a heavy load of carrier-based aircraft. Besides, the technology is being actively promoted to the civil field to reduce fuel load and improve the economy of civil aviation [6].

For military fields, the meaning of aerial refueling is significant.

(i) Increasing the range. The operational radius is one of the most important indicators to measure the combat capability of the fighter and even the air force. After a single aerial refueling, the bomber's operational radius can be increased by 25%-30%, the fighter's operational radius can be increased by 30%-40%, and the range of the transport aircraft can be doubled.

(ii) Prolonging the endurance. Patrol aircraft, early warning aircraft, reconnaissance aircraft, and other special duty aircraft often need to stay in the air for a long time. The use of aerial refueling can prolong the endurance and avoid the delay and inconvenience caused by the landing for the refueling.

(iii) Solving the contradiction between payload and take-off distance. The short-distance runway, such as that for an aircraft carrier and a plateau airport, may not meet the requirement of full-payload takeoff. Therefore, the aircraft can take off with a part of the fuel and then be refueled by a tanker in the air.

For civilian areas, the benefits of aerial refueling are in the following.

(i) Making long-distance flights more efficient. Avoid landing and taking off at midway airports for fuel supply and make long-distance flights more efficient.

(ii) Improving the emergency response capability of civil aviation. Refuel civil aviation in case of emergency and increase endurance.

The main purpose of AAR is to extend the aerial refueling technology to the UAV field, and it can also be used to assist docking operation to reduce the burden of pilots. The docking phase of aerial refueling is a high-precision and high-risk maneuvering flight phase. The improper operation will not only lead to the docking failure, but also even lead to serious flight accidents caused by the damage to the trailing hose and drogue. Therefore, it is necessary to standardize the automatic operation procedure to ensure the safe and efficient operation of aerial refueling. For

UAVs, payload and endurance are important problems for UAV development. In the “Unmanned Aircraft Systems Roadmap 2005-2030” published by the US Air Force in 2005 [7], AAR is regarded as an important way to solve these problems, and the technology was expected to be realized for UAVs in 2015-2020.

1.1.5 The significance of docking phase of probe-and-drogue AAR

AAR mainly emphasizes the autonomy of the receiver, namely getting rid of or minimizing human participation of the whole process from the rendezvous phase to the reform phase. From this point of view, it is more general to study the autonomous docking. First of all, the docking control problem of the probe-and-drogue refueling is more representative. The flying boom is rigid, which is hardly disturbed by the airflow. By contrast, the hose with a drogue is flexible, which is easy to be disturbed by the airflow. Thus, probe-and-drogue AAR faces more difficult docking problems. Secondly, although the flying-boom refueling requires less on receivers and is easier to achieve aerial refueling for manned aerial vehicles, the advantages of the flying-boom refueling are not obvious for the development of the UAV-to-UAV aerial refueling. Probe-and-drogue AAR only needs to control the receiver to achieve the UAV-to-UAV aerial refueling, while the flying-boom refueling needs the tanker to cooperate, i.e., it also needs to design the autonomous control for the flying boom to achieve the UAV-to-UAV aerial refueling.

Among the four phases of aerial refueling, the refueling phase, especially the docking subphase, is the most difficult phase, which is representative and challenging. It requires the highest accuracy, safety, and efficiency, and the key to the success of aerial refueling is to solve the control problem of this phase. In addition, the control problem of the refueling phase covers position keeping and trajectory tracking, which is also a problem that needs to be solved in all phases.

1.2 Characteristics and problems of the docking control of probe-and-drogue AAR

Before introducing modeling and control, it is necessary to understand the characteristics and requirements of the docking control of probe-and-drogue AAR, which will help to understand the current modeling and control methods better.

1.2.1 Characteristic analysis of probe-and-drogue AAR

1.2.1.1 Uncertainty

(i) The uncertainty of the motion of the receiver caused by the tanker vortex and wind turbulence. Aerial refueling is a close formation flying mission. The tanker in front generates a vortex, which affects the flight performance of the receiver behind. The vortex of the tanker can



be divided into three types: the wake vortex (also known as the wingtip vortex), the engine jet and the turbulent flow in the boundary layer, wherein the wake vortex has the greatest influence on the receiver. The wake vortex is formed by the airflow from the bottom of the tanker wingtip. Before forming, the vortex is similar to downwash flow, and after forming, it becomes two downward and backward spiral flows pulled by the wingtip. Besides the tanker vortex, the receiver will also be affected by atmospheric turbulence and wind gust.

(ii) The uncertainty of the drogue motion. Wind gust and tanker wake vortex may cause the drogue to drift, which makes docking position very uncertain. Another important influence is brought by the receiver. In high-speed flight, the drogue is affected by the airflow change near the receiver nose, which is called the bow wave effect [8], [9] or forebody (aerodynamic) effect [10], [11]. When approaching the receiver nose, the drogue will be pushed away from the original position. This disturbance is evident when the probe is on the side of the receiver's central symmetrical plane, which is a widely-used configuration as shown in Figure 1.5 (a). At present, some reported UAVs with aerial refueling capability adopt the "on the nose" configuration as shown in Figure 1.5 (b). When the probe is "on the side", the drogue will pass the nose, so the bow wave effect is very serious. In contrast, the effect of the bow wave effect of the receiver with the probe "on the nose" configuration is not as obvious as that of the probe on the side. This is because the drogue will not pass the nose for docking.

(iii) The uncertainty in the dynamic model of the receiver. As for the accurate docking requirements, the flight control model of the receiver with parameters generated by the wind tunnel has some uncertainties which cannot be ignored. In the process of refueling, the mass of the receiver will increase with the increase of the amount of fuel. Meanwhile, the mass of the tanker will decrease. What is more, for both the tanker and the receiver, their positions of the center of mass will change during refueling. It should be noticed that a larger mass proportion will increase for the receiver because it is often lighter than the tanker. As a result, uncertainty in the dynamic model of the receiver will be correspondingly greater. In addition, because of the highly accurate docking requirement, some uncertainties on the control actuator cannot be ignored as well, such as throttle thrust accuracy. All of these will lead to uncertainty in the dynamic model of the receiver.

(iv) The uncertainty of initial states. Before docking, the receiver has to complete the formation with the tanker. They both keep a constant speed and fixed altitude. The receiver at a position close to the tanker keeps relatively stationary with the tanker. Then, the receiver will take this position as the initial position to start the docking task. However, due to various uncertain factors, the receiver itself cannot accurately stay at this position but floats in a small range.



(a) Probe on the side



(b) Probe on the nose

Figure 1.5: Probe positions

1.2.1.2 Slower dynamic

During the docking process, the flow field of the receiver may push the drogue away as the receiver approaches the tanker. Because the mass and the volume of the drogue are smaller than that of the receiver, it is easy to be disturbed by disturbances and then swings fast. The swing frequency is so high that the dynamic response of the receiver is hard to track. Not only that, but the receiver also needs to change attitude indirectly to change the direction of velocity. These lead the receiver has a slower dynamic. In the experimental paper [10] provided by the National Aeronautics and Space Administration (NASA), the author explained that in the actual aerial refueling experiments, the velocity changes of the receiver's probe in the vertical direction and lateral direction obviously lagged behind the drogue. This problem makes it difficult for receivers to capture a fast-moving drogue by only using conventional feedback methods. In order to solve this problem, some studies focused on increasing the damping of drogue motion to slow down the drogue dynamic, such as adding an active stability control device [12].

1.2.1.3 Nonminimum Phase [13]

For a fixed-wing aircraft with the conventional configuration, the aerodynamic focus is designed behind the center of gravity in order to make the aircraft have good static stability. If the aircraft wants to move in one direction, it must be put a force in the opposite direction to adjust its attitude, so its flight trajectory will move in the opposite direction for a short period before starting to move in the desired direction. This causes the nonminimum phase system to adjust for a long time, making it unable to track changing trajectories rapidly. Thus, trajectory tracking becomes more difficult due to the nonminimum phase property of the receiver. Mathematically, the nonminimum phase property for linear systems means that the transfer function has unstable zeroes, i.e., zeroes with positive real parts, which means that the inverse transfer function are unstable. Moreover, a given non-minimum phase system will have a greater phase contribution than the minimum phase system with the equivalent magnitude response. For an aircraft with the

Table 1.2: Requirements in the docking process

Requirements	High Safety	High Precision (Position error $\leq 0.2/0.25/0.3\text{m}$; Velocity error: 1–1.5m/s)	High Efficiency
Justifications	Receiver flies close to the tanker; Probe collides with the drogue	Drogue radius is 0.305m; Too low relative speed cannot hit the valve open; Too high relative speed will damage the drogue.	Receiver becomes vulnerable to attacks and anti-reconnaissance capability decreases during AR; To save time for the primary mission

configuration shown in [14], since the positive real part of the zero of the longitudinal channel transfer function is very large, the unstable zero can be ignored in most cases. However, it cannot be ignored in the docking control as the requirement of the control accuracy is very high.

1.2.2 Requirements in the docking process

In the refueling phase, the docking procedure is difficult and demands a high level of safety, precision, and efficiency. Table 1.2 lists the three requirements along with the justifications for the requirements' necessity.

1.2.2.1 High Safety

In an actual aerial refueling process, the most important thing is to reduce the risk and ensure flight safety, after which the success of docking can be considered. With the traditional flight knowledge, it is dangerous for aircraft to collide with an object, e.g. a bird, in the air. When refueling in the air, the receiver pilot needs to control the aircraft to make the receiver's probe collide with the drogue within the prescribed range of relative velocity for docking. In this process, risk detection and risk control are needed to reduce risk consequences and the frequency of their occurrence. To be specific, the receiver should first avoid colliding with the tanker in the air. Furthermore, the apparatus (hose, drogue, probe or other refueling equipment) damage should be avoided, which requires that the capture speed control should be reasonable in the docking process, and the offset distance of the drogue should be strictly controlled in the docking process. Once the relative velocity and the docking error between the drogue and the probe exceed reasonable thresholds (specified safety range requirements), the receiver is required to return to a safe place to adjust and evaluate whether to continue docking or not to ensure the safety of the docking.

1.2.2.2 High Accuracy

The docking control accuracy of probe-and-drogue aerial refueling methods needs to be within the centimeter level [15], which is a quite high accuracy requirement for actual aircraft control system due to aircraft maneuverability limitation and atmospheric disturbances. This requires that the navigation and control accuracy reaches the centimeter level or higher. Moreover,



the drogue-and-probe refueling also needs to limit the capture speed within a very small range, such as 1–1.5m/s [2]. This kind of speed can cause the probe to hit the fuel transferring valve in the drogue open. Too small speed cannot hit the valve open, and too high speed will damage the drogue.

1.2.2.3 High Efficiency

In the aerial refueling process, especially in the docking and fuel transferring phase, the receiver's concealment and anti-reconnaissance capability will decrease greatly. Once be discovered, it will become the enemy's key target, so the aerial refueling must be completed within a short time. This is particularly necessary in the enemy-occupied airspace. In addition, for both military and civilian fields, aerial refueling as an auxiliary mission aims to achieve the main task better, so it also needs a more efficient implementation on the basis of safety.

1.3 Progress in Modeling of PDR

There are two purposes of mathematical modeling for the PDR system: one is for high-fidelity analysis of the aerial refueling system through virtual flight simulations with computers, and the other is for the controller design. Generally, the former tends to establish a very elaborate model to include all the kinematics and dynamics of the PDR system, while the latter is based on a simplified model, which is often obtained by simplifying the former model to some degree. The modeling of PDR systems consists of mathematical descriptions of the kinematics and dynamics of aircraft, refueling equipment (hose, drogue, probe), and wind disturbances.

1.3.1 Aircraft modeling

Tanker modeling and receiver modeling are both a part of aircraft modeling. In the PDR, the receiver moves to carry out a refueling procedure while the tanker simply flies level and forward. As a result, studies are mainly concentrated on receiver modeling.

In most studies, the tanker model is frequently regarded as a mass point model [16]. In addition, a rigid model with six degrees of freedom (DOF) is created in order to build a controller for the tanker. A strict-feedback version of a non-affine nonlinear tanker model was taken into consideration in Ref. [17].

Linear models with small-angle perturbations are typically used for receiver modeling[18]. High model precision is necessary for aerial refueling, and it is also necessary to characterize the model's dynamic properties under the wake vortex. The receiver model in Ref.[19] was modified for this reason. The docking model of a tailless UAV was put forth in Ref.[20]. The receiver modeling with varying mass was examined in Refs.[21] [22]. Ref.[23] took into account the modeling of the time-varying uncertain inertia. For the ease of the latter nonlinear controller

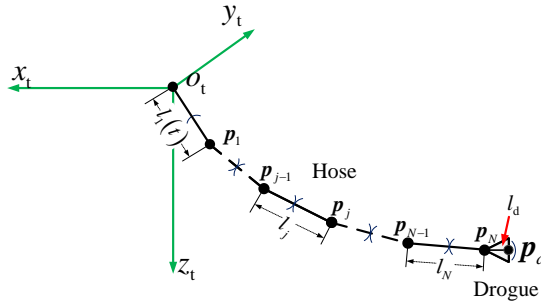


Figure 1.6: Link-connected hose model (l_* indicates the link length, p_* indicates the position of each joint).

design, nonlinear receiver models were also taken into consideration in the previous couple of years and frequently converted to an affine nonlinear form [24].

1.3.2 Refueling apparatus modeling

The primary components of PDR equipment are a hose, a drogue, and a Hose-Drum Unit (HDU). The flexible hose causes the drogue not to be fixed in the position under the tanker coordinate system. Studying the basic dynamics of the drogue is helpful to do the simulation and design the docking control law.

The cornerstone of PDR equipment modeling is hose modeling. Since the hose is flexible, the lumped parameter technique and the finite-segment strategy are frequently used to create a link-connected model[25] [26]. Figure 1.6 illustrates the breakdown of a hose into a number of lumped-mass, rigid cylindrical links joined by frictionless ball-and-socket joints. Each link is subject to aerodynamic and gravitational loads brought by the tanker wake, disturbances in the atmosphere, etc. The link masses and all external forces are lumped at the connecting joints. The coordinate system in Figure 1.6 is anchored to the tanker. In Ref.[27], simulations demonstrated a reasonable agreement between the model's features and the published flight test data. A basic pendulum-based hose model was also researched in Refs. [28, 29].

Ref.[30] performed a dynamic study of the KC-10 tanker's hose but neglected to account for two important elements: restoring force between two rigid links and variable length. Ref.[31] investigated the attitude model of the hose-drogue system while taking into account restoring force by combining CFD and multi-rigid body dynamics. After that, the hose-drogue system's movement rule was examined. This force was added to the hose model in Ref.[32]. To prevent harm to the equipment, the model can be used to evaluate the Hose Whip Phenomenon (HWP) [11]. By adjusting the hose length to keep the hose tension, the HDU hose reel control device can prevent HWP. In Ref.[33], a modeling approach for the variable-length hose was proposed. In Ref. [34], a dynamic variable-length hose-drogue model with the restoring force resulting from bending was examined. An integrated drogue model was suggested in Ref. [35] to explain the drogue behavior under wind disturbances while taking the impact of the HDU controller into consideration. Additionally, system identification was used to create a reduced lower-order

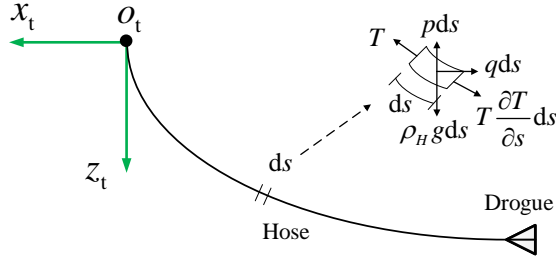


Figure 1.7: Continuum model established on the analysis of [38] (T is the hose tension, p and q are the hose drag and lift per unit length, ρ_H is the hose mass per unit length).

drogue dynamic model that aided in constructing the docking controller.

The core of the lumped-mass finite-segment technique is rigid link kinematics, which did not take into account the hose's elasticity and damping. The elastodynamic hose model was created using the finite element method (FEM) [36], which is based on the mechanics of materials. A three-node, nonlinear curved beam element was used to model the hose in the Lagrangian framework [37], and the dynamic analysis of the established model regarding cable tension, tow point disturbance, and vortex wake was also investigated.

The hose was discretized in the study mentioned above to model the hose-drogue assembly. As shown in Figure 1.7, some research, in contrast, established continuum models based on the analysis of infinitesimals. The hose is considered as an infinite dimensional distributed parameter system, and the dynamic equation is built using partial differential equations. Ref. [38] suggested a precise hose-drogue model that took into account the hose bending effect, the downwash angle, and the phase lag between the hose motion and its unsteady aerodynamic forces in order to study the flutter-type aeroelastic instability of the hose-drogue system. Ref. [39] used partial differential equations to model the flexible hose as an infinite dimensional distributed parameter system to prevent spillover effects caused by truncated hose models.

A full hose-drogue assembly model is produced after the hose model is established and the aerodynamic model of the drogue is combined. Ref. [40] extracted a second-order transfer function model to characterize drogue dynamics under the bow wave effect by parameter identification of the higher-order link-connected system in order to create a lower-order dynamic model suitable to the latter docking controller design.

1.3.3 Wind disturbance modeling

During the refueling process, the trailing hose-drogue and the receiver are subject to various disturbances caused by the airflow, thus increasing the difficulty of control. The main wind disturbances can be classified into three categories: (i) the bow wave effect from the receiver, (ii) the turbulence and wind gust in the atmosphere, and (iii) the wake vortex caused by the tanker. The receiver is affected by the last two disturbances, while the hose-drogue system is affected by three disturbances.

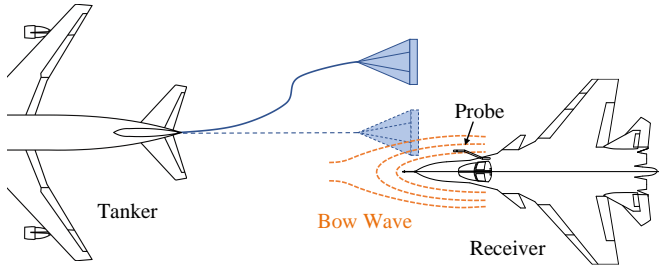


Figure 1.8: Bow wave effect [9]

1.3.3.1 Bow wave effect.

One of the greatest issues for PDR is the disturbance of the drogue brought on by the bow wave of the receiver, which has received a lot of focus in the past ten years[41]. The bow wave effect or forebody (aerodynamic) effect as shown in Figure 1.8 occurs during aerial refueling because the aircraft frequently travel at high speed, creating a powerful airflow at the receiver nose [10, 11]. As the receiver reaches the tanker, the airflow will disturb the drogue’s motion. This kind of disturbance is more obvious when the probe is side-mounted on the aircraft forebody, which is widely used in manned aircraft for pilots to better observe the relative position of the probe and the drogue, but it still exists for the probe “on the nose” although it has less influence. In reality, a docking failure is frequently caused by this disturbance. According to NASA experimental data from 2004[42], [43], as the receiver gets closer to the drogue, it typically produces a location offset of 30.5–36.6 centimeters from the desired position. Because of the light weight of the drogue, it moved very fast in the docking process, caused overshooting, and then swang back. If the receiver was forced to connect with the drogue, then the receiver may have a significant overshoot and cause the probe to break [11]. Therefore, in order to finish docking, it is essential to anticipate the drogue offset. Based on their previous experience, pilots frequently predict the drogue offset. Similarly, it is expected that the receiver autopilot will anticipate the drogue offset to finish AAR. In other words, it is important to examine the relationship between the force acting on the drogue and its relative location and speed with respect to the receiver nose.

Since the bow wave is very complicated, it is challenging to develop an extremely precise dynamic model. A lot of computer simulation data and flight experiment data are needed, which will use up a lot of material and human resources. It is also essential to think about what kind of model to construct. The current modeling techniques are split into offline and online methods depending on whether real-time data processing is used. The acquired models are divided into dynamic and static models depending on whether the model is dynamic.

i) Offline dynamic model. If the probe of the receiver is on the side of the nose, it is necessary to consider the influence of the nose on the drogue in the modeling and establish the dynamic model. In Ref. [8], Cart3D analyses were used to study the bow wave of a C-141 receiver behind a KC-135 tanker, and an analytical approach based on stream functions was suggested. The resulting nonuniform flow field was then roughly modeled using components

of uniform velocity components. Based on the stream function technique, Ref.[44] developed an analytical bow wave model for PDR that took the receiver nose and cockpit into account. The analytical model is applicable to the latter controller design and real-time simulations. Ref. [40] used training data from CFD models to create a nonlinear bow wave model for PDR using nonlinear regression.

ii) Offline static model. Current modeling techniques typically focus on the entire dynamic AAR process. However, for docking control, the trajectory of the drogue to the steady-state value is less important than the ultimate steady-state drift value of the drogue produced by the bow wave. In this way, a simple static model can be built, and the parameter identification becomes much simpler. As a consequence, a straightforward static model can be created, such as lookup tables based on CFD analysis or qualitative static findings from trials. According to the aerial refueling experiments conducted by NASA using F/A-18 fighter aircraft, two conclusions can be drawn. First, the steady position of drogue has a functional relationship with the tanker's altitude and velocity; secondly, the drogue drift offset when it is disturbed by the receiver has some certain rules, where the drogue offset is that of the drogue from its steady-state position. That is to say, although the airflow environment is complex, the steady law of drogue motion can still be described by modeling. Further, NASA conducted research on the correlation between the drogue offset under disturbances and the receiver location. The receiver shifted in the perpendicular plane during NASA's trial[43]. The drogue's greatest steady-state deviation while being affected by the bow wave was approximately 0.368m. Reference [12] gave similar conclusions by modeling and simulation. The basic drogue dynamic was given in [26].

iii) Online model. In practice, the pilot's operation follows “aligning → docking → gaining experience → returning to the initial docking position → realigning...”. The iterative process is carried out in the aerial docking. In actual flight, online identification corresponding to “gain experience” can also be considered for autonomous docking in the air. The online identification mentioned here is performed after one docking trial, which can use all the data from the last docking trial. The resulting model can be used for the next trial. Compared with real-time identification at each sensor sampling period, the identification here can use more sampling data and has sufficient calculation time. There aren't many findings for the online bow wave model. In order to provide online static models, some learning-based strategies have been attempted. To guarantee the precision of the docking control, Ref. [45] proposed the deep learning technique to model the bow wave and predict the location of the drogue in real-time. Additionally, the drogue offset was predicted online in Refs.[29, 41].

1.3.3.2 Atmospheric turbulence and wind gust

Nearly all aircraft must contend with atmospheric turbulence and wind gusts, and related models are very rich. Corresponding models are very rich. At present, the Dryden turbulence model proposed by NASA is widely used in the study of the aerial refueling [46]. The realization is

that the band-limited white noise passes through specific forming filters to obtain the longitudinal, lateral and vertical velocities of the atmospheric turbulence flow field and their angular velocities. There are two widely accepted models: the model with MIL-HDBK-1797 standard [47] and the model with MIL-F-8785C standard [48].

1.3.3.3 Wake vortex caused by the tanker

The wake vortex caused by the tanker received the most attention by researchers among the three kinds of disturbances. When the relative distance is short, large aircraft create a powerful wake vortex at the wingtips that progressively diffuses backward and leaves a strong aerodynamic interference to the aircraft behind, as shown in Figure 1.9 . Due to the closer relative distance between a tanker and a receiver during aerial refueling compared with typical formation flight, the wake vortex's impact is more severe[49]. In 2004, the computer result was contrasted with the wind tunnel experimental result in order to assess the viability of wake vortex modeling[50]. Although there was a good agreement between the two findings, drag and peak lift were not well congruent. As a result, from 2004 to 2008, the modeling of wake vortices was thoroughly studied[51] [52] and represented by a more cohesive mathematical model that divided the wake vortex's action into equivalent wind components and wind gradient components along three-axis directions. The wake vortex velocity was determined by the combination of the two components. Rankine Vortex, Lamb-Oseen Vortex, and Hallock-Burnham Vortex are the three most frequently used vortex models at present[53], with Hallock-Burnham Vortex being used in aerial refueling the most.

A horseshoe vortex model was established in Ref.[54] using the lifting line theory. Ref.[55] investigated tanker wake effects through ANSYS. It was observed that wingtip vortices of the tanker wing and horizontal tail dominate the tanker wake effects on the receiver. Ref.[56] developed a lower-order analytic response surface model based on three-dimensional tricubic interpolation to incorporate an aerodynamic interference module into the simulation of an aircraft. In this model, the complex wake effects were described by an increase in the aerodynamic coefficient. Additionally, actual flight data was used to verify the model. Based on the CFD technique[57], a numerical study of the flow field of an embarked aircraft being refueled by a buddy aircraft was produced. In order to simulate the aerodynamic interplay from the tanker to the receiver, the hose, and the drogue, Reynolds-Averaged Navier Stokes CFD calculations were carried out in Ref.[16]. Ref.[58] established an inviscid-flow-based model to estimate the aerodynamic interaction between a tanker and a much smaller receiver.

1.3.4 Modeling and validation methods

There are generally four kinds of modeling methods: first principles modeling methods (mechanism modelling method), computational fluid dynamics (CFD) modeling methods, wind tunnel modeling methods, and real experimental modeling methods. The first principles modeling

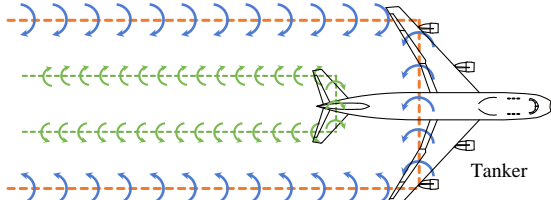


Figure 1.9: Wake-vortex effect [54]

method can give a unified model well, but model parameters are uncertain or too many, which need to be determined by identification or measurement. The CFD method is commonly used in aerodynamics modeling and simulation, although the amount of calculation is huge. It is economical to conduct numerical experiments on the fluid dynamic problems of the aerial refueling docking phase to get data. Through the data, the parameters in the model established by the first principles can be corrected or be fitted. For example, the CFD method is used in the analysis of bow wave models in [8]. Compared with the former two methods, the wind tunnel modeling method has a higher authenticity but a higher cost, which can be further used to improve the existing models. Due to the limitation of experimental conditions, the wind tunnel experiments in the present study only aim at some special parts of aerial refuelings, such as the aerodynamic characteristics of the drogue [59]. The modeling methods above can be used for the modeling of the receiver, the modeling of the trailing hose and drogue, and the modeling of the bow wave effect on the drogue. As for the docking process of aerial refueling, existing real experimental modelings from the open research and academic publications were generally used to verify or carry out some simple model modeling, such as the wake vortex model and the maximum drogue offset under the bow wave.

1.4 Progress in Control of PDR

The primary control challenge during the refueling phase is docking the probe into the drogue and maintaining the relative position. The goal of docking control is to effectively guide the probe to successfully catch the drogue by having the receiver approach the drogue along a specific trajectory. Figure 1.10 illustrates how docking controllers are typically composed of three terms: the command generator term, the tracking control term, and the stabilizing control term. The purpose of the command generator is to ensure the smoothness of the tracking reference and further ensure the control performance. The purpose of the tracking control term is to design a feedforward to turn the tracking problem into a stabilizing control problem, thus solving the nonminimum phase problem. The purpose of stabilizing control is to suppress some uncertainties and disturbances. Additionally, the station-keeping control must be finished both before and after docking. It could be viewed as a special case of tracking control. Along with receiver control, anti-HWP control (HDU control) and drogue stabilization and control (control from the control surfaces of the drogue) are also attractive. Without taking into account the

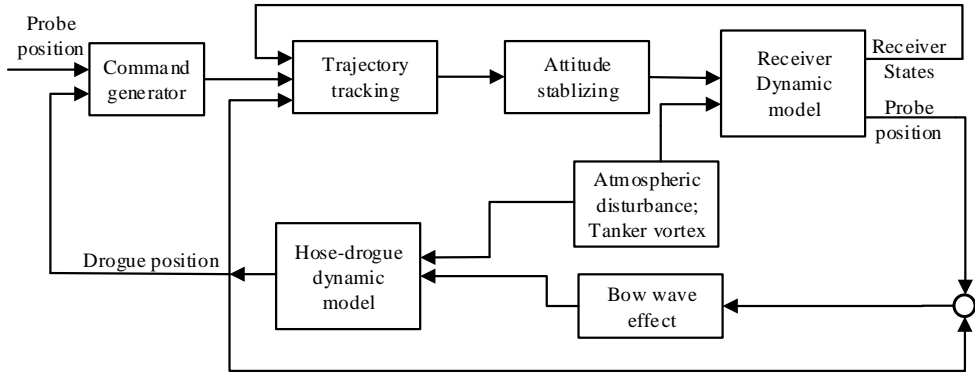


Figure 1.10: Overall structure of the AAR system

motion of the drogue, the control issue in the flying-boom aerial refueling can be basically viewed as a special case of the PDR control issue.

1.4.1 Command generator

For the receiver to successfully complete the formation and refueling tasks in a secure manner, the command generator primarily plans a smooth and practical flight trajectory. There are two reasons for this.

(i) Avoid overshooting. Fixed-wing aircraft often possess nonminimum phase characteristics. In the time domain, nonminimum phase characteristics may cause overshooting, and the amplitude of overshooting is related to the amplitude of the input signal. Therefore, if a far-reaching docking target is directly fed, then a large resulting signal change will cause a large overshooting. Smooth trajectories can weaken the effect of overshooting. In this way, the collision between the receiver and the drogue is avoided while docking in the air. Furthermore, the collision between the receiver and the tanker caused by overshooting can be avoided.

(ii) Avoid induced oscillation. If a large relative position error is directly feedback into the position tracking controller, the controller may produce a large amount of control command, resulting in actuator saturation (the control input value exceeds the actuating capacity or limit of the actuator), which may induce oscillation. Even without induced oscillation, the trajectories may be too aggressive. Docking control in aerial refueling is a high-precision task, but many control methods depend on linear models near the equilibrium point. Large control signals may cause the system to move away from the equilibrium point into nonlinear regions, resulting in that the control accuracy reduces significantly. Therefore, reasonable trajectories must be generated to ensure that the controller command is within acceptable limits.

In this manner, aerial docking is possible without the receiver and drogue/tanker colliding. Various strategies are used to accomplish these objectives, and they can be categorized into five groups.

Method 1: Low pass filter method. A simple method is to make difference between the reference trajectory (the command signal generated by the desired position) and the measured

receiver position, and then feed the error signal into a low-pass filter (LPF) [60] [61], [62], [63], [64], [65]. For example, the low-pass filter used in references [60] and [62] consists of a Proportional-Integral (PI) term and is incorporated directly into the design of the tracking controller. On this basis, in order to track the moving drogue, the reference trajectory becomes a time-varying signal. In this case, the tracking error needs to be smoothed through a low pass filter.

Method 2: Smooth polynomial method. The reference trajectories are generated by simple and smooth polynomial functions to meet the requirement. Reference [66] used three-order polynomials to generate trajectories, while [67], [68] used five-order polynomials. Higher-order polynomials can produce more complex trajectories, but an appropriate order is enough to meet the flight requirements. Reference [69] used two-phase polynomial functions to allow the receiver to catch up with the drogue more quickly in the vertical plane.

Method 3: Terminal guidance method. The idea of this kind of method stems from the terminal guidance of missiles. The exact docking of the receiver and the drogue is similar to a missile hitting a moving target. Reference [70] used Proportional Navigation Guidance (PNG) and Line-of-Sight (LOS) guidance methods, which are derived from missile terminal guidance and autonomous landing of aircraft respectively (It should be noted that reference [70] mainly explained how to guide the tanker to the designated position in the tanker coordinate system. Although it was not docking, the guidance method could be applied to docking). This method calculated in real time how to adjust the attitude or position of the receiver in order to approach the desired position optimally. Reference [63] used the method of differential games, where the reachable region of the receiver and the target region determined by the motion of the drogue are first calculated. Then, the next step is given by calculating the distance between the two regions. Because the way of giving a command is similar to terminal guidance, it is also included in Method 3. Additionally, rendezvous guidance laws for tankers and receivers can also potentially be used for docking [71, 72]. This technique determined in real time how to modify the receiver's attitude or position in order to get closer to the intended position.

Method 4: Intelligent optimization method. An optimum trajectory can be provided by intelligent trajectory optimization. In Ref.[73], the gradient of the docking success rate anticipated by a deep neural network was used to optimize the probe trajectory. Ref.[45] suggested an online trajectory optimization technique to solve the issue that the bow wave is frequently overlooked in the trajectory generator. The optimizer created an ideal docking trajectory by using the bow wave model and the drogue location at the next moment.

Method 5: Preview method. The preview technique [74, 75] is used to address the issue of a slower receiver tracking a faster drogue which can predict the drogue location to compensate for the tracking latency. The reference trajectory takes the predicted drogue motion into account. The preview time is a crucial parameter in deciding the duration of drogue motion prediction. A fuzzy logic controller was used in Ref.[74] to choose the preview time. The controller, however,



primarily depends on human intuition, which might not be optimal. Ref.[75] suggested a learning method that combines deep learning and reinforcement learning to choose the optimal preview time.

1.4.2 Tracking control

The main purpose of tracking control is to transform a tracking control problem into a stabilizing control problem so as to solve the instability of internal dynamics caused by non-minimum phase property.

First, the reference state and the reference input are extracted from the reference trajectory. In the process of converting a tracking problem into a stabilizing control problem, it is necessary to establish an state error dynamics first, which can be obtained by subtracting the reference dynamics from the original dynamics. However, it is not enough to use only the reference output. Thus, the reference state and the reference input have to be obtained first. The non-zero setpoint (NZSP) method proposed in references [60] and [62] was to derive the reference state and the reference input based on the reference output and the receiver model. The NZSP method limits the reference state and the reference input to be constant, that is, the drogue is stationary relative to the tanker. In order to overcome this disadvantage, [61] improved the NZSP method, and further proposed command generator tracker (CGT), which could continuously obtain the reference state and input of the next sampling time with the movement of the drogue. In [67] and [69], Extended State Observers (ESOs) were used to observe the reference state. Reference [76] elaborated on this method in more detail and completeness. The reference trajectory used in reference [66] was a third-order polynomial of time, and the reference acceleration can be obtained by twice differential. In the linearized model based on small-angle approximation, the longitude and lateral acceleration are linearly related to the angle of attack and sideslip angle. Therefore, the reference angles of attack and sideslip angles can be obtained directly by taking the derivative of the trajectory. Then, the ideal system is established. Based on it, the original system can be converted into error dynamics by subtracting it. Then, the tracking goal can be accomplished by stabilizing control for the error dynamics.

Some disturbance rejection terms are also included in tracking control. The integrator is frequently used to address the problem of tracking static error caused by atmospheric turbulence, measurement error, and other random disturbances to a certain extent [60][61][66][77][64]. Furthermore, robust control in Refs. [78],[65] can render the output insensitive to specific noises, primarily atmospheric turbulence, wind gusts, and sensor-induced noise. Another common method is to lump all the unknown disturbances, uncertainties, and some higher-order nonlinearity terms into one disturbance term. Then the lumped disturbance can be estimated and compensated by a disturbance observer[24]. In Ref.[79] a gain-adaptive equivalent sliding mode control scheme based on the ESO was suggested to attenuate the impact of wind disturbances and model uncertainties. In Ref.[80], the disturbance observer approach was used to estimate

the lumped uncertainty containing the tanker wake vortex term, and the dynamic surface control method was chosen to build a position-tracking controller.

AAR is safety-critical, so many scholars are starting to take the fault-tolerant control issue into account[68, 81, 82]. Ref.[68] took control-effector failures into account, and a Structured Adaptive Model Inversion (SAMI) controller was created, which didn't rely on fault-detection data. In Ref.[81], actuator faults and wake vortices were taken into account as a lumped uncertainty and estimated by a disturbance observer in order to accomplish a secure formation flight. Backstepping control was used to accomplish fault-tolerant control based on the estimated uncertainty. Due to the near proximity of the tanker and receiver, the collision avoidance issue was also taken into account in Ref.[83], which transformed it into a state-dependent output-constrained control problem. Then, the backstepping technique and Barrier Lyapunov Function (BLF) were used to create a controller.

It is noteworthy that many studies explicitly design tracking controllers instead of converting the tracking control problem into a stabilizing control problem. This is because the non-minimum phase feature of the receiver is not considered or addressed by other methods. In Refs.[24, 84], the six DOF nonlinear receiver model was considered, and backstepping-based flight controllers were proposed to accomplish high-precision docking control for AAR in the presence of multiple flow disturbances and uncertainties.

The above docking control scheme follows the idea of real-time feedback: trajectory generating tracking control stabilizing control. Reference trajectory design and tracking controller design often rely on accurate models. However, actual models have many uncertainties, such as input delay and parameter uncertainty. In order to deal with uncertainties, the feedback control method with an integrator is often adopted. This method can compensate for uncertain parameters. However, the measurement delay, the input delay, and the phase lag caused by the integrator will affect the dynamic performance, control precision, and even stability. Furthermore, feedback control techniques could cause the receiver to chase the drogue. The drogue moves quickly in the docking process due to its light weight. The chasing action may lead to a significant overshoot and overcontrol for the receiver and may cause impact and damage to the refueling equipment[11]. When the effect does not significantly increase drogue displacement, a rapid approach technique can be used for docking, but this can easily result in HWP. According to NATO aerial refueling standards⁶⁸, this approach strategy is risky and incorrect. On the other hand, if a sluggish approach strategy is used, the receiver's bow wave will significantly shift the drogue.

Inspired by the pilot training process for manned aircraft refueling, the docking control can be formulated as a terminal Iterative Learning Control (ILC) problem or a point-to-point ILC problem[85] [86]. The ILC approach is a model-free control technique that makes use of the repeatability of the considered system to enhance the system's control performance. If a PDR system's docking attempt is unsuccessful, the receiver will withdraw to the standby position in

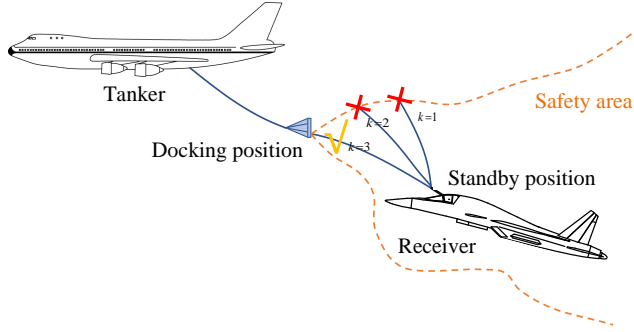


Figure 1.11: ILC-based docking operation in AAR.[88]

preparation for the next docking attempt, as shown in Figure 1.11. That implies that the docking procedure is repetitive. ILC is a viable option to address the docking control problem. The basic idea is to use the data from the most recent unsuccessful docking attempts to change the feedforward input of the docking control. By doing this, it is possible to compensate for the offset and reject the repetitive uncertainties. The problem of the slower dynamic receiver tracking the quicker dynamic drogue may be resolved by ILC. Another advantage of ILC is that it allows identification performed after one docking trial. Compared with real-time identification at each sensor sampling period, the identification here can use more sampling data and has sufficient calculation time. This can reduce the requirement of visual sensor and improve its feasibility. The ILC methods suitable for the probe-and-drogue AAR is different from the traditional ILC in that it cannot guarantee the actual initial position of the receiver is the same as the expected initial value. What is more, the task needs to make full use of model information to reduce the iterative number. The aerial refueling docking controllers in Refs.[41, 87, 88] were designed using iterative learning, which successfully averted the drawbacks of slower dynamics tracking faster dynamics and overcontrol in feedback control. These ILC techniques used an adjoint operator to solve the non-minimum phase problem. Iterative learning control can effectively handle repetitive disturbances but cannot suppress non-repetitive disturbances. The ability to suppress sudden gusts or random turbulences is poor during aerial refueling docking.

1.4.3 Stabilizing Control

To suppress uncertainties and disturbances and enable the error dynamics state to converge to zero, stabilizing control is used. According to the design methods of the traditional flight control system, classical state feedback and Proportional-Integral-Derivative (PID) method can be used to control the system. Reference [70] applied state feedback to stabilize the system. Reference [89] used PID method to design for each single-input-single-output channel for the inner and outer loops. Its outer loop PID coefficients are adjusted adaptively by particle swarm optimization. The modified PID method can restrain the vortex disturbance caused by the tanker wingtip. In contrast, most methods prefer the Linear Quadratic Regulation (LQR) method [60] [61] [67] [66] [90] [91]. Linear quadratic optimization is a convex optimization with a unique

extremum, so this method is often used to design the optimal feedback gain matrix. Some other methods to suppress perturbation and nonlinearity also use quadratic optimization, such as the adaptive dynamic inverse method in [92] and the L1 adaptive method in [63], [64]. Reference [93] used the adaptive control to stabilize the controller and track an adaptive signal. In reference [62], Linear Quadratic Gaussian (LQG) regulator was used to reduce the effect of Gaussian white noise caused by measuring sensors in the system so as to improve the stabilization effect. Although the actual aircraft model is nonlinear, the stabilizing controller design is generally built on linear models. Consequently, when the disturbance is significant, the control performance may suffer. Reference [94] proposed feedback linearization to solve this problem. Few papers are based on the six degrees of freedom (DOF) nonlinear receiver model. For such a purpose, backstepping based flight controller was proposed to solve the AAR docking control problem with high precision in the presence of multiple flow disturbances and uncertainties [24][84].

1.4.4 Station-keeping control

After a successful capture, the receiver and tanker must maintain relatively stationary during the refueling phase to transmit the fuel. In other words, the receiver must hold a specific location under the coordinate frame of the tanker without significantly deviating from it. For two main reasons, station-keeping control for AAR is a challenging task. The first reason is that the receiver is disturbed by atmospheric disturbances and the tanker's wake vortex. The second reason is that the receiver's mass, inertia, and center of mass will alter due to the fuel transfer during the refueling phase.

In order to maintain the location, station-keeping control must first establish the reference state, which transforms the issue into a stabilizing control problem. Generally speaking, by fixing the reference frame on the tanker, reference state can be regarded as a constant value. The station-keeping control method is basically consistent with the stabilizing control mentioned above. For example, the LQR method was adopted in references [77], [95] and [96], the L1 adaptive method was adopted in reference [63], and the PID method was adopted in [97]. In view of the receiver mass change in the process of fuel transferring, the control method of adaptive gain (gain scheduling) was adopted in references [63], [77]. These are based on rigorous and accurate modeling, such as the result in [77], which is based on the variable mass modeling of the receiver under wake vortex disturbance in [98]. Reference [99] proposed that the controlled plant should be the position of the probe rather than the position of the center of gravity of the receiver. Therefore, the relative position of the center of gravity of the receiver and its probe was used to modify the original model, and the controller was then designed. In [22], double power reaching law based sliding mode controller was designed to control the receiver translational motion relative to the tanker aircraft in the outer loop while Active Disturbance Rejection Control (ADRC) technique was applied to the inner loop to stabilize the receiver.

Prior information about the refueling system or disturbances can also be used to solve some

problems encountered in station keeping. Reference [95] dealt with the problem of how to control a receiver when the flight condition of the tanker changes. This paper considered that the position and attitude information of the tanker could be obtained by communication as the feedforward, which was then incorporated into the LQR. The robust design method was consistent with the stabilizing control problem in solving this problem, i.e., to minimize the gain of the disturbance or disturbance on the output as much as possible [90]. Reference [100] adopted the ADRC design method to design the station-keeping controller. In [101], Quantitative Feedback Theory (QFT) was used to design controllers to guide the receiver and tanker formation. This control method was also applied to station keeping [102].

In the past ten years, station-keeping control has drawn some interest. Ref.[22] examined the effects of fuel injection in terms of the receiver's mass change and center-of-gravity change. An inner and outer loop controller structure was considered. The sliding mode controller was developed in the outer loop to regulate the relative motion between the receiver and the tanker, and the ADRC method was used in the inner loop to stabilize the receiver. A station-keeping control based on additive-state-decomposition was suggested in Ref.[103] to take the receiver's nonlinearity into account. With the aid of the additive state decomposition, the effects of nonlinearity and uncertainties were decomposed, making the remaining control design simpler. The predefined-time, finite-time, and fixed-time attitude stabilization controls for receiver aircraft were investigated in Refs.[23, 104, 105] in order to maintain the intended attitude of the receiver for a long period of time to receive fuel while achieving a quicker convergence rate. In Ref.[104], a sliding manifold was created to enable the sliding mode phase achieved within the predetermined time, and after that, a robust stabilization controller was used to accomplish the predefined-time attitude stabilization. The benefit of the method is that the system settling time can be selected arbitrarily and independent of system states. A nonsingular sliding mode based adaptive controller was created in Ref.[23] to accomplish the faster finite-time stability of the closed-loop system while considering the receiver model's uncertain and time-varying inertia, wind disturbances, and change in center of mass. However, the receiver models used in Refs.[23, 104, 105] are merely six-degree-of-freedom models with the force and torque inputs, and the aerodynamic models of force and torque are not considered. Additionally, the chattering of the sliding mode control is still a problem.

1.4.5 Anti-HWP control

The refueling pod is frequently outfitted with a reel system, specifically an HDU[33], in order to maintain the hose tension steady and prevent the hose whipping phenomenon[11]. The hose whipping phenomenon brought on by the receiver's extreme closing speed needs to be repressed, so the HDU control by reeling in/out the hose is required for safety reasons. By adjusting the hose length, HDU can prevent the development of extra slack in the hose and maintain the internal hose tension. The conventional way to rewind the hose is to outfit the refueling pod with a tensator,

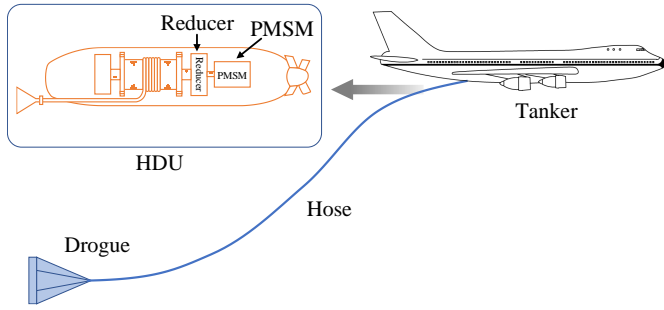


Figure 1.12: Schematic of Hose-Drum Unit[34]

a spring-loaded take-up mechanism. However, the approach is a passive method in nature, and it is challenging to reconstruct the tensator's mechanism. Additionally, because the reel take-up speed is slower than the closing speed, the hose whipping phenomenon is adversely affected. As a result, as seen in Figure 1.12, many scholars have begun to investigate using a Permanent Magnet Synchronous Motor (PMSM) to drive the HDU. Through a reducer, the PMSM directs the HDU to release and retrieve the hose. Ref.[34] converted the hose length control to the angular control of the PMSM, and then suggested an active control strategy based on an integral sliding mode backstepping controller design to prevent the hose whipping phenomenon. However, the suggested backstepping control's computation of higher-order command derivatives will result in a problem with an exponential explosion. A command-filtered backstepping sliding mode controller was suggested in Ref.[106] as a remedy for this problem. It was suggested in Ref.[35] to use two different kinds of HDU controllers to regulate the hose length to stabilize the drogue movement and prevent the hose whipping phenomenon.

1.4.6 Drogue stabilization and control

Some studies concentrated on boosting the damping of drogue motion to slow down the drogue dynamics in order to address the issue of a slower dynamic receiver tracking a fast-moving drogue. These studies included the addition of an active stability control device. The drogue motion can be indirectly controlled by the HDU, which is frequently regarded as a passive control technique. The main topic of this part is the active control using the drogue's built-in control surfaces. Ref.[28] tended to create a drogue with an active controller and self-stabilization. The design aimed to increase the stability of the drogue and make it difficult to be disturbed[28] [107]. The fundamental design of the autonomous drogue is the installation of four control surfaces at the point where the drogue connects to the hose so that the drogue can adjust its location. A self-stabilized drogue's design arrangement, as shown in Figure 1.13, was provided in Ref.[107], and its performance was assessed in a wind tunnel. Ref.[108] also took into account a similar self-stabilized drogue arrangement. Ref.[2] lists some additional self-stabilized drogue designs. The dynamic response of the integrated system, which consists of the hose, the drogue, and the control surfaces, was examined in Ref.[109] by considering the control surfaces placed in the drogue. A fractional-order controller was developed in Ref.[110] to actively regulate the drogue

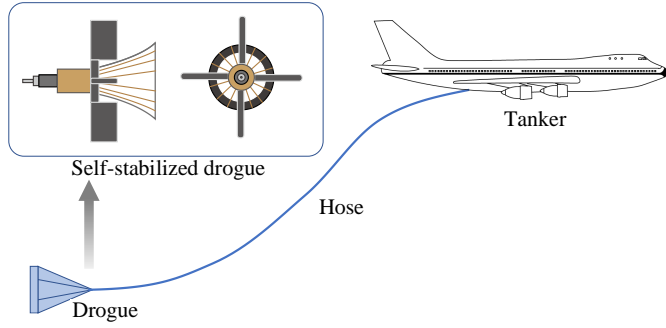


Figure 1.13: Schematic of Hose-Drum Unit[114]

in order to maintain its location within a range. An improved pigeon-inspired optimization technique was suggested in response to the challenge of selecting the controller parameter of the fractional-order controller. Ref.[111] developed active disturbance rejection controllers to improve the drogue's anti-disturbance capabilities.

To increase the control precision during aerial refueling docking, many researchers have studied the vibration control of the hose and drogue assembly using the control surfaces installed on the drogue. By using the backstepping technique to reduce the elastic vibration of the flexible hose, Ref.[39] developed boundary control. Ref.[112] developed a multi-objective adaptive controller to simultaneously address the input nonlinearities of dead-zone, input constraints, and partial state constraints. Additionally, the fault-tolerant control for the refueling hose and drogue assembly with regard to actuator failure was also researched[113, 114], similar to the fault-tolerant control for the receiver. For a refueling hose with variable length and constrained output, Ref.[113] evaluated the partial effectiveness loss of the actuator and suggested an adaptive barrier-based fault-tolerant control. A control strategy that combines adaptive methods and redundancy actuators was used in Ref.[114] to address the possibility of a partial or even complete loss of the actuator's effectiveness.

The active drogue control may offer a fresh approach to the docking control issue. In this situation, a novel control strategy that controls the drogue to connect with the probe could be suggested in place of controlling the probe to dock with the drogue. This method can solve the issue of a fast-moving drogue being tracked by a sluggish dynamic receiver. It is possible to reduce overcontrol and prevent chasing actions while increasing docking safety. There are still some issues, though: If the control surfaces are too big, the interference that they experience may result in significant drogue drift; if the control surfaces are too tiny, they lack sufficient controllability. Furthermore, a power supply for the self-stabilizing drogue is required because it is far from the tanker. Electricity leakage and fire safety must be considered if electronic control is used.

The control for PDR has been examined up to this point, and Table 1.4.6 displays the methods taken and the problems addressed in some research and scholarly papers. It is noteworthy that designs for both flying-boom aerial refueling and probe-and-drogue aerial refueling are included,

with the former's introduction meant to provide some related techniques. Section 1.2 provides a description of the docking characteristics and requirements in the table. Table 1.4.6's symbol “✓” denotes that the method took into account the corresponding requirements and characteristics, while the vacant space denotes the other way around. In Table 1.4.6, U1, U2, U3,U4 mean atmospheric disturbance, bow wave, time-varying mass and inertia, and tanker wake vortex, respectively; R1, R2, R3 denote high precision, high safety, and high efficiency, respectively.



Table 1.3: Summary of control problems and methods during autonomous aerial docking

Reference	Characteristic				Requirement			Controller					Drogue stabilization and control		
	Uncertainty				Slow dyn.	NMP	R1	R2	R3	Docking controller			Station-keeping controller	Anti-HWP control	
	U1	U2	U3	U4						Command generator	Tracking controller	Sta. controller			
[10]	✓	✓	✓		✓	✓	✓	✓							
[60]	✓					✓	✓		✓	Step Signal + PI	NZSP	LQR			
[61]	✓					✓	✓		✓	Time-varying signal + PI	CGT	LQR			
[62]	✓					✓	✓		✓	Step signal + PI	NZSP	LQG			
[67]	✓					✓	✓		✓	5th-order polynomial	Extended state observer	LQR			
[66]	✓					✓	✓		✓	3th-order polynomial	LQR + integrator	LQR			
[93]	✓	✓				✓	✓			Nonlinear reference model	Differential games	Adaptive control			

[63]	✓				✓	✓		✓	Time-varying signal + LPF	LQR + Integrator	L1 Adaptive			
[115]	✓		✓		✓	✓		✓				Gain scheduling + L1 adaptive		
[97]					✓							Gain scheduling + PID		
[70]					✓	✓			PNG + LOS	Integrator + State feedback	State feedback			
[77]	✓		✓		✓	✓		✓				Gain scheduling + LQR		
[101]	✓				✓	✓						QFT		

[78]	✓					✓	✓	✓	1. Robust servomechanism design 2. Model following design 3. H_∞	1. LQR 2. LQR 3. H_∞			
[65]		✓				✓	✓		Tracking error + PI	H_∞	H_∞		
[95]						✓	✓	✓				Feedforward + LQR	
[90]	✓		✓			✓	✓					PID + H_∞	
[96]	✓					✓	✓	✓				LQR + Integrator	
[100]	✓		✓			✓	✓					ADRC	
[69]	✓	✓				✓	✓	✓	Two-phase polynomials	Extended state observer	LQR		
[89]	✓					✓	✓			PID	PID		
[22]	✓		✓	✓								SMC+ ADRC	

[23]	✓		✓	✓						Sliding mode-based adaptive control		
[24]	✓				✓	✓			Backstepping higher order SMC			
[39]							✓					Backstepping control
[45]	✓	✓		✓				Deep learning + Reference observer				
[68]							✓	Fifth-order polynomial	Fault-tolerant SAMI control			
[75]	✓			✓	✓	✓		Learning-based preview method	LQR+HOSM controller			
[87]	✓	✓		✓	✓	✓	✓	TILC				

[106]	✓				✓			✓					Command filtered backstepping SMC	
[111]	✓	✓		✓	✓		✓	✓	✓				ADRC	

1.5 Progress in Safety of PDR

Docking safety is a crucial problem in the refueling phase of PDR. With the gradual maturity of the modeling and control technology of PDR, many researchers started to focus on the safety problem.

1.5.1 Safety Analysis

In practice, the docking safety analysis has important guiding significance for the docking maneuver decision of AAR.

1.5.1.1 Docking success rate evaluation

Currently, most control techniques described in academic and research papers demonstrate accurate docking ability under specific circumstances. However, in the real world, it is extremely challenging to accomplish exact docking every time. In NASA's trial report [10], only three of the six docking flight attempts were successful due to various disturbances. According to Ref.[116], the success rate for docking during manned aerial refueling is approximately 35%, while the success rate for docking during NASA's UAV aerial refueling is approximately 60%. This suggests that the docking success rate will be reduced under challenging circumstances. The docking success rate under disturbances must therefore be taken into account. There is, however, little study on quantitative modeling and examination of the AAR docking success rate. Online and offline evaluations of the docking success rate are available. How to acquire a docking envelope is the subject of the offline assessment. The docking success probability can be predicted using the envelope obtained offline and the receiver's present location and velocity. The Monte Carlo method, a safety evaluation technique for uncertain systems, is a straightforward approach. However, performing numerous Monte Carlo simulations, which takes time, is necessary for a decent assessment outcome. A technique using the likelihood of the drogue center situated in the capture area was suggested to determine the online docking success probability by considering the drogue motions under atmospheric disturbances[116]. The reachability analysis technique, used by Ref.[117], is another theory approach. In Ref.[117], the probability of the receiver joining the target set within a specified time period was calculated using the Markov chain stochastic approximation method, which required much less simulation time than the Monte Carlo method. However, the reachability analysis method's memory and computation needs increase rapidly with dimension. Online computation will be difficult if many parameters are considered or the relative motion model has a large dimension. Additionally, Ref.[73] suggested a real-time safety evaluation network, a neural network based on deep learning, to predict the docking success rate based on the current docking state, preventing the difficult reachability analysis. There was also established a safety margin between the probe and the drogue. But getting lots of training data is a challenge.

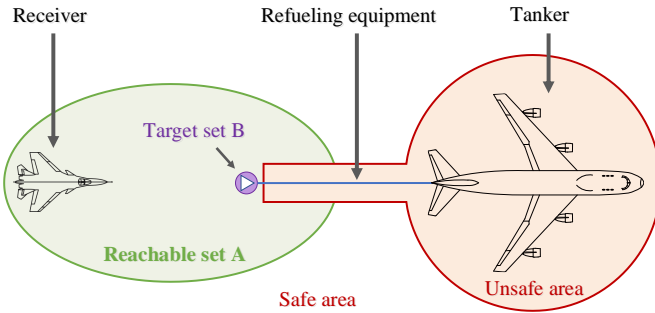


Figure 1.14: Airspace division for aerial refueling

1.5.1.2 Docking reachability calculation

The problem "Is there a controller that satisfies the docking criteria given the uncertainty model and the constraint on the docking success rate?" is the goal of this part. This problem pertains to the calculation of the docking reachable set A that correlates to the docking target set B, as shown in Figure 1.14, and can be seen as an inverse problem of the assessment of the docking success rate. The conventional controllability problem and this one are related. However, it does not examine whether the receiver state can be controlled to the origin, as is the case with conventional controllability, but rather whether the drogue can be caught to a set with the proper relative docking velocities, etc. Another distinction is that docking reachability is a form of probabilistic reachability due to random perturbations and uncertainties. Additionally, certain essential safety requirements will also limit the docking capability. Ref.[118] developed a docking reachability calculation algorithm based on the Hamilton-Jacobi equation and an algorithm for real-time docking success probability estimation regarding the relative distance between the drogue and the probe. However, the drogue position was only possible for a two-dimensional normal distribution in the study. On this basis, we should further define the degree of reachability, as shown in Figure 1.15. If there is no reachability, then we need to abandon the docking. What is more, the degree of reachability can, in turn, propose a demand for the atmospheric environment and the receiver. Aerial refueling docking may not be carried out under any receiver and any docking environment. Many factors may result in that no controller meets the docking requirements, such as the tanker size, atmospheric environment, algorithm processing time and effect, sensor dynamic response and accuracy, control surface dynamic response and accuracy.

On the other hand, most research and academic publications consider the problem of aerial docking as an accurate tracking problem and rarely consider the damage of the drogue and the potential danger in the flight. In Figure 1.16, for example, when the probe passes through the drogue, the docking will be continued by following the idea of tracking control. However, to continue the mandatory docking at this point, a larger pitch command is required, which is prone to a heavy collision between the probe and the drogue. Even without collision, large commands can cause large overshooting and make the drogue damaged, as shown in the video [119]. In

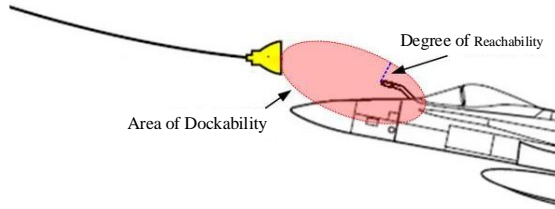


Figure 1.15: Degree of reachability

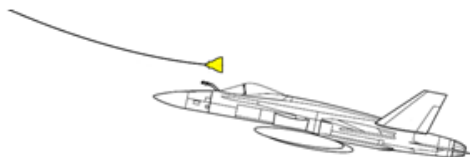


Figure 1.16: A kind of unsafe relative position

order to ensure docking safety, it is necessary to set impassable or unsafe areas (as shown in Figure 13) and allow the receiver to abandon the docking attempt once entering these areas. As shown in Figure 1.17, Ref. [10] designated the "capture" area and the "miss" area (the docking task declared to failed when entering this area) by segmenting the area around the drogue into different areas. When the probe enters the "miss" area, the docking attempt will be immediately aborted. However, this study did not offer a theory or method for the area partition. In Ref.[120], the authors divided the flight safety region for aerial refueling using the controllable region to constrain the flight trajectory. Reference [12] referred to the need for an appropriate capture speed to open the fuel valve without causing hose whip. According to some studies, the controller's command should fall within a reasonable range. The aerial refueling accident shown in the video [121] is caused by unreasonable overshooting. However, the majority of these academic and research publications only provide ad-hoc guidelines based on experience, which calls for additional research.

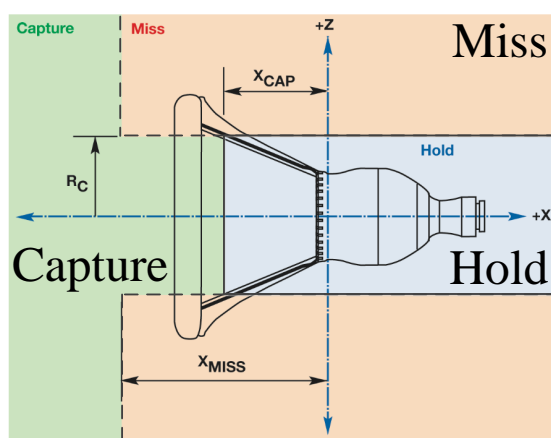


Figure 1.17: Docking area division [10]

1.5.1.3 Optimal flight condition determination

This part pays attention to "At what flight condition (altitude and cruise speed) the docking control has the highest success rate?". Here, the term "optimal flight condition" refers to the altitude and cruise speed that will result in the greatest likelihood of docking success. Different docking altitudes and speeds will produce various receiver models at the equilibrium point, which will then result in various reachability probabilities. Therefore, better docking altitude and speed for the same controller can increase the docking success rate. The solution to the problem is of significance for aerial refueling docking. Ref.[122] used the reachability analysis to create an optimization problem whose solution is the optimal trim state. The altitude and speed that correspond to the largest volume of the reachable set are the optimal trim state.

1.5.2 Safety-oriented decision

In terms of "How to design a safe flight decision for functional failures or mission failures?", only limited studies can be found, or just very simple results are given on the safety-oriented decision-making. In reality, various external factors, such as excessive turbulence that lasts too long to stabilize the aircraft in a particular position or a malfunctioning receiver's navigation system that prevents the drogue from being positioned, can cause the AAR mission to fail. Making safe and trustworthy decision under these unusual circumstances is necessary to guarantee a safe flight. It is necessary to think about how to combine the requirements into a final reliable flight decision-making scheme in addition to the proposed safety requirements. A straightforward safety-oriented docking strategy with six docking modes was proposed in [73] as a solution to this issue. It was based on the safety margin determined using the relative distance between the probe and the drogue and the docking success rate. In order to make decisions for AAR, Ref.[123] proposed a failsafe mechanism based on supervisory control of state tree structures. According to exterior directives and aircraft flight states, the complete failsafe system can direct the receiver's following actions.

1.6 Chapter Summary and possible future work

1.6.1 Chapter Summary

Since the middle of the 20th century, scholars have been interested in PDR because of its huge military and civilian importance. The refueling phase is of particular concern. There are a lot of uncertainties during the PDR's refueling phase, which affect the receiver's motion, the drogue's movement, the receiver model, and the docking's initial state. The receiver also exhibits slower dynamic and non-minimum phase characteristics. High efficiency, high safety, and high precision technical requirements must be met during the refueling phase.

In the refueling phase of probe-and-drogue autonomous aerial refueling, the most recent

advancements and fresh research findings in modeling, control, and safety are compiled in this chapter. The study on modeling, which includes modeling of aircraft, refueling equipment, and wind disturbances, is first given. Due to the hose's flexibility, it should be noted that modeling the refueling equipment is fairly difficult. Then, the control study is divided into six sections: command generator, tracking control, stabilizing control, station-keeping control, anti-HWP control, and drogue stabilization and control. Finally, safety-related technologies are presented, such as safety analysis and safety-focused decision-making, which merit further investigation.

1.6.2 Possible Future Work

Despite all the advancements previously mentioned, numerous issues still need to be researched, and numerous technologies still have room for improvement. Future advancements and research generally tend to make refueling docking safer, more accurate, and more efficient in accordance with the requirements in the refueling phase listed in the Introduction.

1.6.2.1 Possible Future Work for high-safety requirement

For the high-safety requirement, further research could be done in the areas of intelligent autonomous mechanical design, safety assessment, modular controller design, dependable decision-making, and adaptive vision navigation.

(1) Intelligent autonomous mechanical design

The fact that the hose is flexible and the motion of the drogue is rapid and passive is the main cause of PDR's difficulty in docking. Thus, a better docking mechanism could be explored. Currently, drogues with automated control surfaces installed are under consideration. The drogue's movement can be stabilized and controlled by the control surfaces. In this situation, a new control scheme can be suggested where the drogue is controlled to link up with the probe instead of controlling the probe to dock with the drogue. With this plan, the issue of a fast-moving drogue being tracked by a slower dynamic receiver can be solved. It is possible to avoid chasing action and overcontrol, and docking safety can be increased.

(2) Safety assessment

Safety assessment is a further topic that needs to be researched because high safety is the most important requirement for AAR. The safety analysis of PDR has been the subject of some studies thus far, but more consideration and work are still required. The docking success rate assessment, docking reachability calculation, division of safe and unsafe areas, determination of the optimal flight condition, robust margin analysis, etc., are all included in the safety assessment. Deep learning-based methods are a viable option for fitting complex unknown relationships and can be used in safety assessment. However, the mathematical basis for safety analysis must be uncovered because deep learning is somewhat unexplainable. The reachability analysis method is a preferred theoretical approach, in which probabilistic reachability aids in carrying out the safety analysis under stochastic disturbances.

(3) Modular controller design

The modular controller architecture is advantageous for future controller updates and alterations. The control components are linked hierarchically and appropriately to form the overall controller. If the modular controller architecture is used, it will be possible to modify the guidance module while maintaining the low-level control module's original configuration for various tasks. This makes the transition to a new controller simpler. Reusability is essential for safety-critical applications like PDR because many actual flight tests have demonstrated the low-level control module's dependability. Additionally, it is not suggested to access the throttle, elevator, aileron, and rudder directly for safety reasons. It is also time and money efficient for control components to be reused in various applications. Additionally, more investigation into a low-level controller that uses velocity as the input merits attention. The receiver's position control is frequently the target of the velocity controller. But the velocity controller designed here is required to aim at the position control of the probe tip in relation to the receiver's attitude for docking. This presents many difficulties.

(4) Dependable decision-making

In order to control and manage aerial refueling, a reliable decision-making scheme must be developed. On the safety-oriented decision-marking, however, there are few studies available or the findings are very straightforward. The refueling operation can be affected by a variety of factors, such as when the turbulence is too intense for an extended period of time to stabilize the aircraft in a specific position, when the actuator malfunctions for unknown reasons and makes it difficult to control the attitude and position, when an enemy finds the aircraft while it is being refueled, and when the receiver's navigation system is malfunctioning and prevents the drogue from being positioned. Due to these various factors, the aircraft should be able to operate in numerous modes, and multi-mode decision-making is important for regulating the aircraft to ensure safety. One option is to use the Finite State Machine (FSM) technique, which calls for thorough requirements analysis, mode specification, and event definition.

(5) Adaptive vision navigation

During the rendezvous and joining phases of AAR, global positioning and wireless communication technologies frequently provide relative position information. They might, however, be disturbed. In contrast, vision-based navigation devices offer the relative distance and speed between the probe and the drogue during the refueling phase. The system can work fully autonomously, but the observation distance and the field of vision are somewhat at odds with one another, which is a crucial restriction for the system. On the other hand, short focal lenses have a broad field of vision but a close observation distance. On the other hand, telephoto lenses have a narrow field of vision but a long observation distance. As a result, adaptive vision navigation technology is anticipated to achieve both a broad field of view and a long observation distance. The rendezvous, joining, and refueling phases can all use the adaptive vision navigation system. Installing a zoom lens or numerous lenses with various focal lengths as compound eyes is one

option. The related algorithms with these new lenses are rife with difficulty to obtain accurate and robust relative poses in all-weather flight.

1.6.2.2 Possible Future Work for high-precision requirement

For the high-precision requirement, online learning of complex disturbances and image-based visual servo control need more attention.

(1) Online learning of complex disturbances

The refueling phase is characterized by complicated disturbances. The full consideration of disturbances is important for high-precision control. To deal with disturbances, PDR primarily uses two types of control designs. The first is to model disturbances, followed by adding the disturbance model to the aircraft model. The ultimate control-oriented model is then created using the combined model. The second method involves combining all disturbances and unmodeled dynamics into a single disturbance that is estimated by a disturbance observer. Next, the estimated disturbance is compensated for in the control design. The former approach frequently uses offline modeling based on historical data, and the established model may not match the actual system. The online estimation technique, however, can capture actual disturbances. But a lot of factors can have an impact on the estimation inaccuracy. As machine learning technology advances, online learning of complicated disturbances offers a way to handle the disturbance problem. A significant advancement in flight control has been achieved by the control based on disturbance learning[124]. Better anti-disturbance performance can be anticipated if machine learning based online learning of complicated disturbances could be implemented in the PDR.

(2) Image-based visual servo control

Because of their high precision in close vicinity, machine vision technologies are frequently used in the navigation system during the refueling phase to determine the relative distance between the probe and the drogue. If a vision-based navigation system is used, image-based visual servo control is favored. Position-Based Visual Servo (PBVS) and Image-Based Visual Servo (IBVS) are two categories for the current visual servo control methods. The features in PBVS are a collection of 3D parameters that must be estimated from image data. Once the pose estimation is complete, the servo control can be executed. A collection of 2D features that are instantly accessible in the image data makes up the features in IBVS. AAR and robotic systems have benefited from the widespread use of the visual servo control technique in recent years. These works primarily pay attention to PBVS. Due to issues with camera calibration, installation, and 3D object modeling errors, a precise 2D picture observation does not necessarily indicate a precise 3D pose estimation. In order to obtain more accurate docking control, it is therefore preferable to learn IBVS. Ref.99 examined the IBVS control design for PDR. The use of an inner and outer loop controller structure was made to achieve zero image error with the outer loop visual servo controller and intended camera motion with the inner loop stabilization controller.

1.6.2.3 Possible Future Work for high-efficiency requirement

Compound control, simultaneous refueling of multiple UAVs, and global refueling scheduling may be feasible future work for the high-efficiency requirement.

(1) Compound control

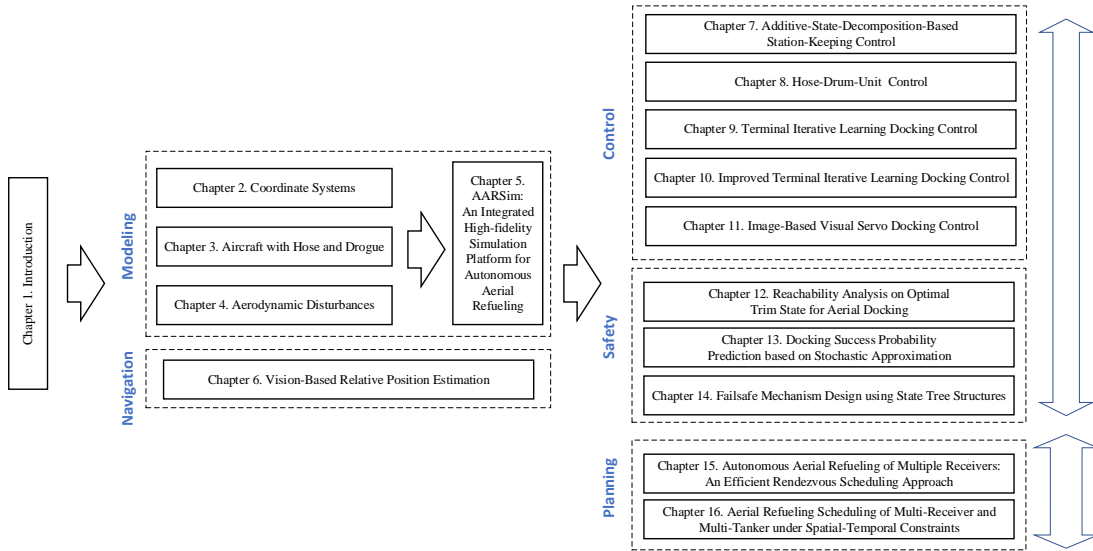
High efficiency and precision are crucial for AAR. In general, feedforward control can accomplish high efficiency, while feedback control can ensure high precision. In order to achieve high precision while maintaining excellent efficiency, compound control (feedforward control + feedback control) is advised. "ILC (learning feedforward) + feedback control" is one potential method. ILC is first designed to mitigate the effects of repetitive uncertainties during the refueling phase, and then feedback control can be further developed to mitigate the effects of nonrepetitive uncertainties. For the "ILC (learning feedforward) + feedback control" system, it is necessary to study their respective control authorities. Furthermore, the final contact velocity is crucial for AAR, but most study has focused primarily on tracking trajectory rather than controlling velocity. If both velocity control and trajectory control are taken into account, the control issue will become an underactuated control problem, necessitating the use of some unique control methods.

(2) Multi-UAVs simultaneous refueling

The demand for multiple aircraft refueling is quickly expanding due to the development of swarm UAV systems. There are two possibilities for refueling multiple aircraft. The first situation involves concurrently refueling multiple receivers, while the second involves sequentially refueling multiple receivers. With multiple refueling pods mounted on a single tanker, PDR has the benefit of allowing up to three receivers to be refueled concurrently. The majority of prior studies, however, only considered one receiver instance and gave little thought to multiple aircraft refueling. Multiple aircraft refueling requires fewer tankers than the AAR of a single receiver. However, as a tanker and several receivers are coupled aerodynamically, the technology involved becomes much more complex. Future research should focus on the AAR for multi-UAVs simultaneous refueling, which also involves cooperative control and decision-making, management of flight paths, modeling for aerodynamic impact from other receivers, and formation mechanism.

(3) Global refueling scheduling

When refueling multiple receivers sequentially, global scheduling is essential. AAR is required when several fighters work together to complete a task over an extended period of time. Additional classifications include "multiple receivers and a single tanker" and "multiple receivers and multiple tankers". The problem of global scheduling gets more challenging when there are more aircraft. The refueling sequence and path should be decided to increase refueling efficiency under the precondition of assuring mission requirements, which can be formulated as an optimization problem, such as the least fuel consumption problem or shortest refueling time problem. The best optimization techniques are then chosen to provide a solution for the constrained optimization problem. Ref.[125] looked at rendezvous scheduling for multiple

**Figure 1.18:** Structure of this book

aircraft' aerial refueling technology. An integer linear programming method was developed to accomplish the fastest refueling.

1.7 The Objective and Structure of the Book

The book aims at solving modeling, control and decision-making problems in the probe-and-drogue AAR. Chapter 1 introduces the significance of AAR through discussing the following questions: why the probe-and-drogue AAR is very important, what are the typical characteristics of such a problem, what is the state-of-the-art technology, and what are the difficulties faced. The remainder of this book has five parts, sixteen chapters, as shown in Figure.1.18.

(i) Part I. Modeling Part

Through this part, readers can have a deeper understanding of the dynamic model of the probe-and-drogue AAR, which will be further used for control in the following. This part contains four chapters, including notation and systems of axes, airflow models, dynamics models of aircraft and drogue and a simulation platform for probe-and-drogue AAR which has connected all the models together for the following control and decision-making design. These correspond to Chaps. 2–5, respectively.

- Chapter 2. Coordinate Systems
- Chapter 3 Aerodynamic Disturbances
- Chapter 4 Aircraft with Hose and Drogue
- Chapter 5 AARSim: An Integrated High-fidelity Simulation Platform for Autonomous Aerial Refueling

This part is mainly based on our work [40],[44],[35]. The paper [40] proposed a lower-order dynamic model to describe drogue dynamics under the bow wave effect. The model consists of two components: one is a second-order transfer function matrix to describe the drogue dynamics,

and the other is a nonlinear function vector to describe the bow wave effect model. To make the modeling easier, the paper [44] analyzed the bow wave effect and presented a simpler stream function based method to model it. With the obtained aerodynamic coefficients, the induced aerodynamic force on the drogue was calculated. We found that the drogue dynamics model with the bow wave was not accurate enough, especially on the vertical position. This is because the HDU is not involved. Since the docking process is an accurate task, and a sub-meter level error may result in a failed docking, in [35], an improved integrated model is proposed by considering the effect of HDU.

(ii) Part II. Navigation Part

Through this part, readers can have a deeper understanding of the relative position estimation in probe-and-drogue AAR by using vision technology. This corresponds to Chap. 6.

- Chapter 6. Vision-Based Relative Position Estimation

This part is mainly based on our work [126].

Introduction to the paper above

(iii) Part III. Control Part

Through this part, readers can have a deeper understanding of the low-level control of the probe-and-drogue AAR, where the station-keeping control and the docking control are proposed. Moreover, relative visual navigation between the receiver and the drogue is proposed especially for docking as it requires higher accuracy than the normal flight. With them in hand, probe-and-drogue AAR can be guided by the decision-making module which will be introduced in Part IV. These correspond to Chaps. 7–11 in the following.

- Chapter 7 Additive-State-Decomposition-Based Station-Keeping Control
- Chapter 8 Hose-Drum-Unit Control
- Chapter 9 Terminal Iterative Learning Docking Control
- Chapter 10 Improved Terminal Iterative Learning Docking Control
- Chapter 11 Image-Based Visual Servo Docking Control

This part is mainly based on our work [41],[29],[87].

Introduction to the papers above

(iv) Part IV. Safety Part

Through this part, readers can have a deeper understanding about the high-level decision-making of probe-and-drogue AAR, where a method to determine the optimal trim state for aerial docking, a docking success rate prediction method and a failsafe mechanism design based on supervisory control theory are proposed. These correspond to Chaps. 12–14, respectively.

- Chapter 12 Reachability Analysis on Optimal Trim State for Aerial Docking
- Chapter 13 Docking Success Probability Prediction based on Stochastic Approximation
- Chapter 14 Failsafe Mechanism Design using State Tree Structures

This part is mainly based on our work [122],[127],[123]. Aerial Refueling is an important method to increase the endurance and flight range of aircraft, but it often suffers from a low success rate.



The altitude and speed of the tanker aircraft in the docking phase have a great influence on the docking success rate. According to this, the optimal trim state, namely the optimal speed and altitude of the tanker aircraft, is investigated through the reachability analysis method in [122]. At the docking phase, the docking risk is high as the receiver aircraft is approaching the tanker aircraft. In order to guarantee the safety of the AAR process, it is important to predict the docking success rate. Motivated by this, a stochastic approximation method is adopted to evaluate the docking success rate of the receiver aircraft by taking random disturbances into account [127]. Dangerous flight maneuvers may be executed when unexpected failures or command conflicts happen. In order to solve this problem, a decision-making logic with the failsafe mechanism based on State Tree Structure (STS) is proposed to make the whole flight safer in [123].

(v) Part V. Planning Part

Through this part, readers can have a deeper understanding of the scheduling and path planning of probe-and-drogue AAR. This corresponds to Chaps. 15-16.

- Chapter 15 Autonomous Aerial Refueling of Multiple receivers: An Efficient Rendezvous Scheduling Approach
- Chapter 16 Aerial refueling scheduling of multi-receiver and multi-tanker under spatial-temporal constraints

This part is mainly based on our work [125],[128].



Chapter 2 Coordinate Systems

In order to describe the attitude and position of aircraft and refueling equipment in aerial refueling systems, it is necessary to establish appropriate coordinate frames. Especially in the modeling process, several frames need to be introduced to describe the relative and absolute states of objects in the system, such as the absolute position and attitude of aircraft, the relative motion among aircraft and refueling equipment, and the forces and moments acting on the aircraft. These frames will also be beneficial to the simplification of analysis and controller design for aerial refueling systems. Besides, choosing an appropriate coordinate system can effectively simplify the establishment and solution of the dynamics and kinematics equations of the aircraft, as well as conveniently describe the relative motion between the probe and the drogue during the aerial refueling process, especially in the docking phase. This chapter mainly introduces several frames commonly used in aerial refueling, along with the mutual conversion relationship among them.

2.1 Definitions and Notation

2.1.1 Right-Hand Rule

In the beginning, the **right-hand rule** needs to be introduced for the definitions of different coordinate frames. A typical coordinate definition in line with the right-hand rule is presented in Fig. 2.1(a), where the right thumb points to the positive direction of the ox axis, the first finger points to the positive direction of the oy axis, and the middle finger points to the positive direction of the oz axis. Furthermore, the right-hand rule is also widely used in determining the positive direction of a rotation transformation as shown in Fig. 2.1(b), where the thumb of the right-hand points the positive direction of the rotation axis and the direction of the bent fingers is the positive direction of the rotation. All the frames and rotation transformations used in this book are defined by the right-hand rule.

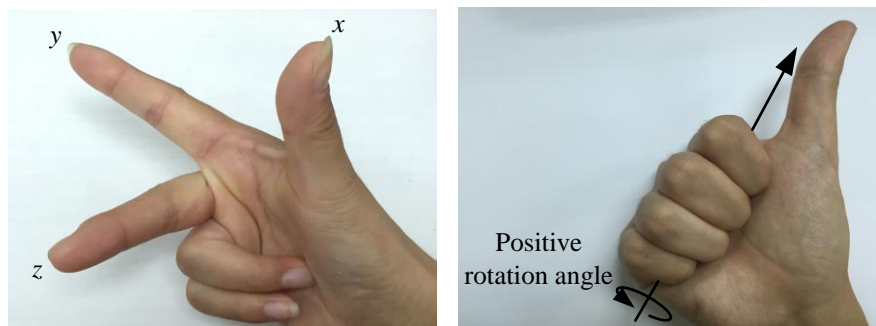


Figure 3.1: Definitions of coordinate axes and positive rotation transformation with the right-hand rule.

Table 2.1: Implication of abbreviation symbols of superscripts and subscripts

Abbreviation symbols	Implication
d	drogue
e	equilibrium position of drogue
f	origin of CFD frame
g	ground
h	hose
n	nose of aircraft head
p	probe
r	receiver
t	tanker
w	wind

2.1.2 Variable Notation

In this paper, scalar variables are represented by normal italic letters, such as the air density $\rho \in \mathbb{R}$; vector variables are represented by bold lowercase letters, such as the velocity vector $\mathbf{v} \in \mathbb{R}^3$; matrix variables are represented by bold capital letters, such as the rotation matrix $\mathbf{R} \in \mathbb{R}^{3 \times 3}$. The superscript or subscript of a variable indicates the concrete meaning of the variable. For example, \mathbf{p}_d denotes the position vector of the drogue, where “d” is the abbreviation of the word “drogue”. The abbreviation symbols commonly-used in this book are shown in Table 2.1.

Based on the literature [129], the following notation is used to describe the motion of objects in aerial refueling systems:

(1) A right superscript on a vector specifies a frame. It denotes a vector and its components are defined in the specified frame. For example, $\mathbf{p}^g = [x^g \ y^g \ z^g]^T$ denotes the position vector in the ground frame (abbreviated as “g”).

(2) Right subscripts are used to designate the meaning of a variable. For example, \mathbf{p}_t denotes the position vector (expressed by bold lowercase letter “p”) of the tanker aircraft (abbreviated as “t”). Besides, a “/” in a subscript means “with respect to”, which represents the relative relationship between two objects. For example, $\mathbf{p}_{p/r}$ denotes the position vector of the probe position (abbreviated as “p”) with respect to the mass center point of the receiver aircraft (abbreviated as “r”).

(3) When a variable is an angle (or rotation matrix), the right subscript “A/B” indicates the angular relationship of the frame A relative to frame B. For example, $\mathbf{R}_{r/t}$ denotes the rotation matrix to describe the angular relationship of the receiver frame “r” relative to the tanker frame “t”, which is also used to describe the transformation of a vector from the tanker frame “t” to the receiver frame “r”.

(4) The components of a vector on the three axes are expressed by a 3×1 array with the subscript inherited from that vector. For example, $\mathbf{v}_t = [v_{t,x} \ v_{t,y} \ v_{t,z}]^T$ represents the three components of the tanker velocity. In order to simplify the derivation process, an exception is

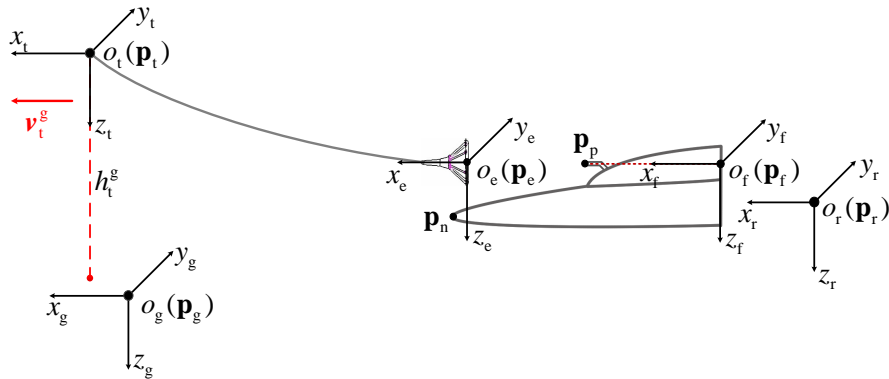


Figure 2.2: Coordinate frames used in the docking process

made for the most frequently-used variables – the position vectors, whose components are simply expressed as $\mathbf{p}_t = [\begin{array}{ccc} x_t & y_t & z_t \end{array}]^T$.

(5) When the reference frame is the tanker frame (see the detailed definition in the next section), the superscript “t” and subscript “/t” of a variable can be omitted for simplicity. This is because, during the docking modeling process, the reference frame for most variables is the tanker frame. For example, $\mathbf{p}_{d/r}^t = [\begin{array}{ccc} x_{d/r}^t & y_{d/r}^t & z_{d/r}^t \end{array}]^T$ represents the relative position between the drogue (“d”) and the receiver aircraft “r”, and the relative position vector is projected in the tanker frame (“t”), then it can be abbreviated as $\mathbf{p}_{d/r} = [\begin{array}{ccc} x_{d/r} & y_{d/r} & z_{d/r} \end{array}]^T$ for simplicity. In addition, $\Theta_{r/t}$ represents the angular relationship between the receiver frame “r” and the tanker frame “t”, then it can be abbreviated as Θ_r .

2.2 Coordinate Frames

There are five coordinate frames commonly used in kinematics and dynamics modeling of aircraft: the ground frame, the body frame, the wind frame and the stability frame. Meanwhile, the CFD frame and the drogue equilibrium position frame (referred to as the drogue frame) will also be introduced for presenting the relative relationship among the drogue, the probe and the receiver aircraft. The frames used in the docking process are shown in Fig. 2.2. These frames are detailed below and the function of each coordinate system and the relationship among them are explained.

2.2.1 The Ground Frame

The ground frame $o_g - x_g y_g z_g$ (also called the flat-earth frame) is defined by ignoring the earth’s curvature on the ground (the earth’s surface is assumed to be flat in a small region), so the ground frame can be treated as an inertial system. The above assumption is also referred to as the flat earth assumption in many references. This assumption is reasonable for this book because the aerial refueling process is operated in a limited region. As shown in Fig. 2.3, the coordinate origin o_g of the ground frame is one fixed point on the ground which is usually selected as the

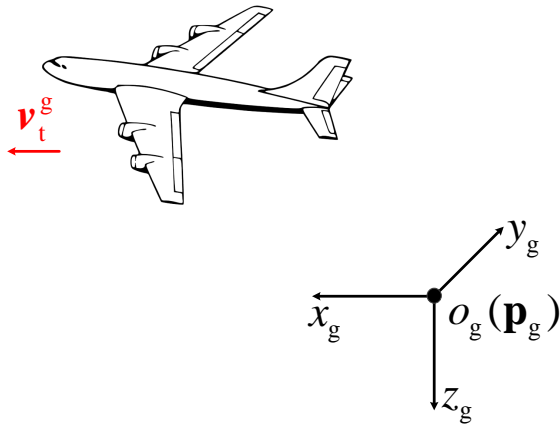


Figure 2.3: Definition of the ground frame

take-off position of an aircraft; the axis o_gx_g usually points to the north or points to the horizontal direction of the aircraft motion for convenience; the axis o_gz_g points vertically downwards to the ground; the axis o_gy_g is determined according to the right-hand rule.

2.2.2 The Body Frames

A coordinate frame fixed to the aircraft body can be called the body frame. The traditional body frame $o_b - x_b y_b z_b$ usually selects the mass center of an aircraft as the origin o_b , and its axis directions are defined as: the axis $o_b x_b$ points to the nose direction in the symmetric plane of the aircraft; the axis $o_b y_b$ is perpendicular to the symmetric plane and points to the right side; the axis $o_b z_b$ is vertical to the axis $o_b x_b$ in the symmetric plane and points to below, which satisfies the right-hand rule. The moment of inertia of an aircraft is usually defined in the above body frame to describe its rotational motion produced by the forces and moments (also described in the body frame) acting on the aircraft. Since there are a tanker aircraft and several receiver aircraft in an aerial refueling system, their body frames are distinguished by the tanker body frame and the receiver body frame, respectively.

2.2.2.1 The Tanker Body Frame

The tanker body frame $o_t - x_t y_t z_t$ is also simplified as the taker frame for short. During the aerial refueling process, the tanker aircraft is commanded to fly straight and level with a constant speed in most situations, so the tanker frame can be assumed to be a moving inertial coordinate frame. For the convenience of describing the movement of the hose, the drogue, and the receivers at the same time, the origin of the tanker body frame is selected as the connection point between the hose and the tanker fuselage as shown in Fig. 2.4, which is different from the definition of traditional body frame whose origin is on the mass center. Then, the axis directions of the tanker frame are defined as follows: the axis $o_t x_t$ points to the horizontal direction of the tanker ground velocity v_t^g ; the axis $o_t z_t$ points vertically downwards to the ground; the $o_t y_t$ axis is determined according to the right-hand rule.

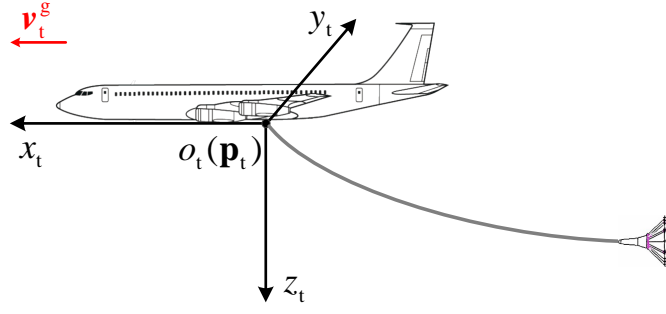


Figure 2.4: The tanker body frame

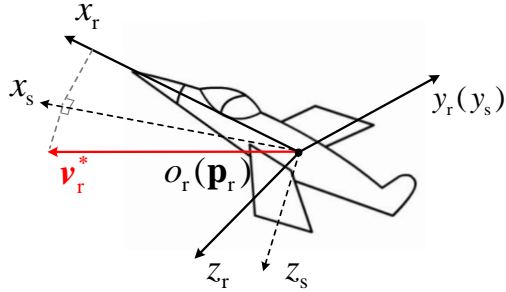


Figure 2.5: The relationship between the receiver body frame and the stability frame

The relative position and attitude between the drogue and the receiver are mainly concerned in the docking phase, where the tanker frame (moving inertial frame) is more convenient for modeling and analysis than the ground frame (fixed inertial frame). In order to further simplify the coordinate transformation among different frames, the direction of the axis o_gx_g of the ground frame is also selected the same as the horizontal moving direction of the tanker, so the tanker frame and the ground frame have the same direction definitions and the rotation transformation between them can be avoided.

Since both the ground frame and the tanker frame are inertial frames, we can use the tanker frame to describe all the relative motion among objects in the aerial refueling system, and use the ground frame to describe their absolute motion relative to the ground.

2.2.2.2 The Receiver Body Frame

The receiver body frame $o_r - x_r y_r z_r$ (or simply “the receiver frame”) is used to describe the physical quantities associated with the attitude angle of the receiver. As shown in Fig. 2.5, the origin o_r of the receiver frame is fixed to the mass center of the receiver p_r , and the direction of the coordinate axis is consistent with the traditional body frame, where the $o_r x_r$ axis points to the nose direction in the symmetric plane of the aircraft; the $o_r y_r$ axis is perpendicular to the symmetric plane and points to the right side; the $o_r z_r$ axis is vertical to the $o_r x_r$ axis in the symmetric plane and points to below, which satisfies the right-hand rule.

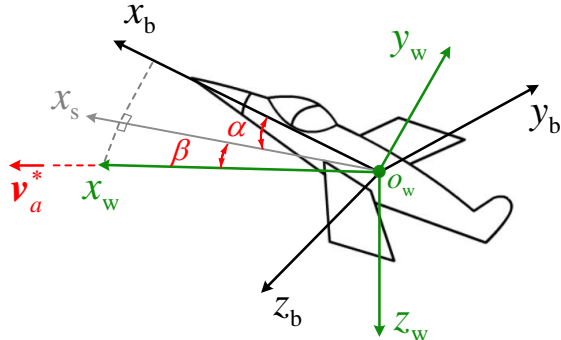


Figure 2.6: The aerodynamic angles

2.2.3 The Stability Frame

The stability frame $o_s - x_s y_s z_s$ is also widely used in the study of the motion characteristics of the aircraft after a small disturbance during steady flight. The stability frame is defined according to the airspeed vector of an aircraft which is defined as the relative velocity of the aircraft to the surrounding air. The tanker's airspeed vector is represented by \mathbf{v}_t , and the receiver's airspeed vector is expressed as \mathbf{v}_r .

As shown in Fig. 2.5, taking the receiver as an example, the origin o_s of the receiver stability frame is fixed to the mass center of the receiver; the axis $o_s x_s$ coincides with the projection within the symmetric plane of the trimmed airspeed vector \mathbf{v}_r^* (the trim methods will be introduced in Chapter 4) based on \mathbf{v}_r ; the axis $o_s z_s$ is perpendicular to the axis $o_s x_s$ in the symmetric plane of the aircraft and points vertically downwards to the ground; $o_s y_s$ points to the right and satisfies the right-hand rule.

2.2.4 The Wind Frame

The wind frame $o_w - x_w y_w z_w$ is very important in aerodynamic modeling of aircraft. The origin o_w of the wind frame is fixed to the mass center of the aircraft; the axis $o_w x_w$ coincides with the trimmed airspeed vector \mathbf{v}_a^* ; the axis $o_w z_w$ is perpendicular to the axis $o_w x_w$ in the symmetric plane of the aircraft and points vertically downwards to the ground; the axis $o_w y_w$ points to the right side and satisfies the right-hand rule.

The aerodynamic angle is determined by the relationship between the wind frame and the body frame. As shown in Fig. 2.6, the aerodynamic angles are defined as follows.

(1) **Angle of attack α :** the angle between the projection of the axis $o_w x_w$ of the wind frame and the axis $o_b x_b$ of the body frame on the symmetric plane of the aircraft, which is equal to the angle between $o_b x_b$ and $o_s x_s$. Note that the angle is positive when the projection of $o_w x_w$ is below $o_b x_b$.

(2) **Sideslip Angle β :** the angle between the $o_w x_w$ axis of the wind frame and the symmetric plane of the aircraft, which is equal to the angle between $o_w x_w$ and $o_s x_s$. Note that the angle is positive when the projection of $o_w x_w$ is on the right of the symmetric plane of the aircraft.

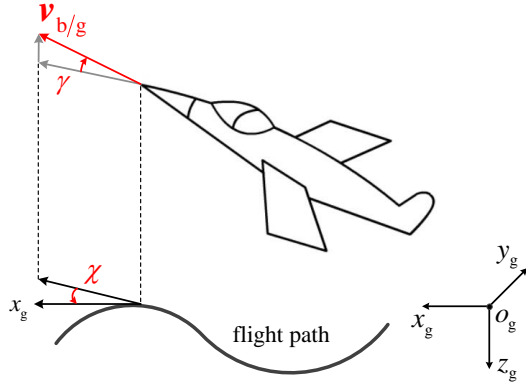


Figure 2.7: The flight path angle and the course angle

The flight path angle and the course angle are determined by the relationship between the wind frame and the ground frame. As shown in Fig. 2.7, taking the receiver as an example, the flight path angle and the course angle are defined as follows.

(1) **Flight Path Angle γ :** The angle between the flight ground velocity $v_{b/g}$ (the velocity of the aircraft relative to the ground) and the horizontal plane, which is positive when the aircraft is flying upwards.

(2) **Course Angle χ :** The angle between the projection of the flight velocity vector $v_{b/g}$ on the horizontal plane and the axis o_gx_g of the ground frame, which is positive when the projection is on the right side of o_gx_g .

2.2.5 The CFD Frame

The CFD frame $o_f - x_f y_f z_f$ is defined for the convenience of studying the aerodynamic interference (also called the bow wave effect) between the receiver forebody and the drogue. As shown in Fig. 2.8, the direction of the CFD frame is the same as the receiver frame while the origin is different. The origin of the CFD frame is a point p_f in the plane $x_r o_r z_r$, and its height is the same as the mounting position of the probe. The reasons for taking p_f as the coordinate origin are as follows.

(1) The height of the axis $o_f z_f$ is consistent with the height of the drogue, because the probe is aligned with the drogue during the docking process, that is, the docking process is completed near this height.

(2) The coordinate origin is selected at the rear of the probe because the pilot's view is roughly at this position, and this position is also convenient for CFD computation.

2.2.6 The Drogue Equilibrium Position Frame

The drogue equilibrium position frame $o_e - x_e y_e z_e$ (or simply “the drogue frame”) is defined for better evaluating the disturbed motion and docking error of the probe and the drogue during the docking phase. Since the tanker is assumed to fly at a uniform speed in a straight line, the

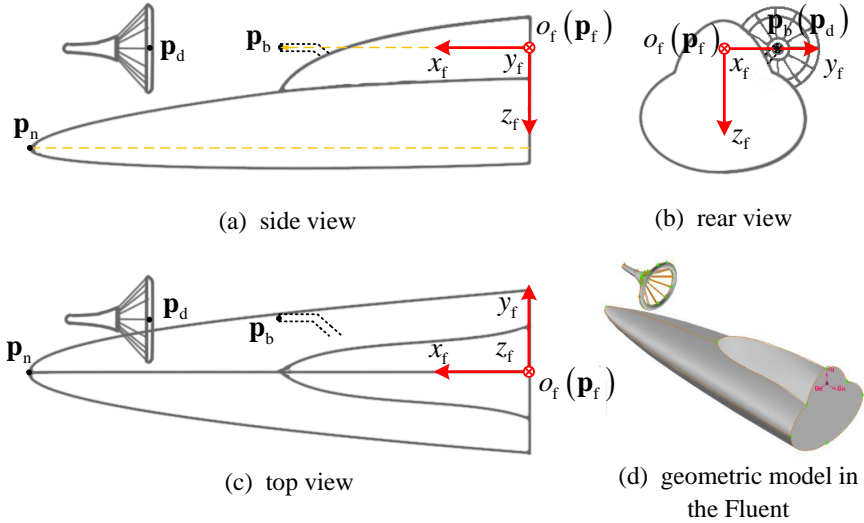


Figure 2.8: Three views of the CFD frame

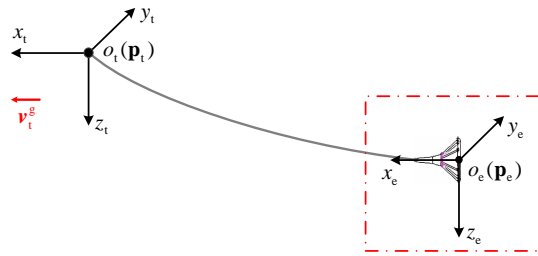


Figure 2.9: The drogue equilibrium position frame

hose-drogue system will finally reach an equilibrium state relative to the tanker body. Then, the drogue position (the center of the drogue canopy) will also reach an equilibrium position or slightly fluctuate around an equilibrium position under disturbances. This equilibrium position (marked with \mathbf{p}_e) is selected as the origin of the drogue frame, which is fixed to the tanker frame and will not move as the drogue moves. As shown in Fig. 2.9, the axis directions of the drogue frame are consistent with the tanker frame. Noteworthy, under different flight altitudes and speeds, the drogue equilibrium position \mathbf{p}_e may be different, but it can be estimated before the docking phase starts.

2.3 Frame Transformation

There are several ways to realize the frame transformation, or to project a vector from one frame to another. Common methods used in aerial refueling systems are: Euler angle method and Direction Cosine Matrix (DCM) method. The two methods will be described separately below.

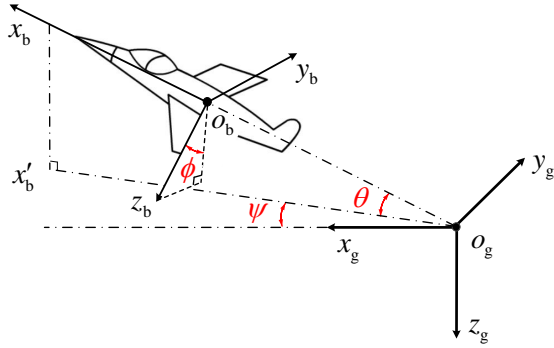


Figure 2.10: The relationship between the body frame and the ground frame

2.3.1 Euler Angle Method

2.3.1.1 Euler Angle Definitions

Based on Euler's theorem, the rotation of a rigid body around one fixed point can be regarded as the composition of several finite rotations around that fixed point. The orientation of a body frame can be achieved by three elemental rotations from the ground frame around one fixed point (usually the mass center). During these elemental rotations, each rotation axis is one of the coordinate axes of the rotated frame, and each rotation angle is defined by one Euler angle. It should be noted that the order of rotation is important, and different rotation orders will result in different frames. For an aircraft, the sequence of rotation axes $z-y-x$ is often used to define its Euler angles.

The attitude of an aircraft, which is often described by the Euler angles, is determined by the relationship between the body frame and the ground frame. As shown in Fig. 2.10, $o_g - x_g y_g z_g$ represents the ground frame and $o_b - x_b y_b z_b$ represents the body frame. Euler angles are defined as follows.

(1) **Yaw angle ψ** : it is the angle between the axis $o_g x_g$ and the projection line from the axis $o_b x_b$ to the plane $o_g x_g y_g$. The yaw angle is positive when the aircraft turns to the right, and its value range is $[-\pi, \pi]$.

(2) **Pitch angle θ** : it is the angle between the axis $o_b x_b$ and the plane $o_g x_g y_g$. The pitch angle is positive when the aircraft nose pitches up, and its value range is $[-\pi/2, \pi/2]$.

(3) **Roll angle ϕ** : it is the angle between the axis $o_b z_b$ and the plane $o_b x_b x'_b$. The roll angle is positive when the aircraft rolls to the right, and its value range is $[-\pi/2, \pi/2]$.

2.3.1.2 Vector Conversion

This section introduces the conversion relationship of vectors among different frames. First of all, vector conversions from the ground frame to the body frame will be presented. As shown in Fig. 2.11, the rotation is composed of three elemental rotations around axes $o z_g$, $o k_2$, and $o n_1$ by angles ψ, θ, ϕ , respectively. More specifically, we first move the origin o_b of the body frame and the origin o_g of the ground frame to the same point o , so the body frame and ground

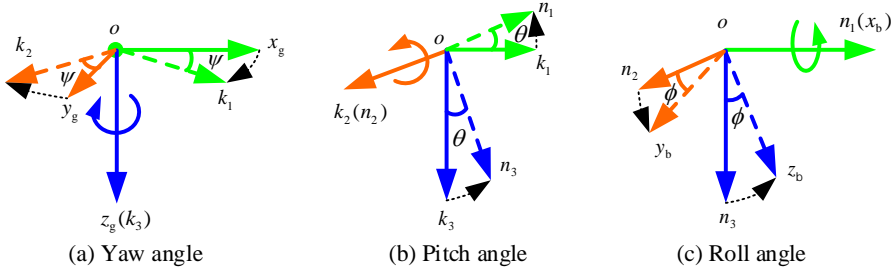


Figure 2.11: Euler angles and frame transformation

frame are presented by $o - x_b y_b z_b$ and $o - x_g y_g z_g$ respectively, and then perform the following operations.

(1) As shown in Fig. 2.11(a), rotate the ground frame $o - x_g y_g z_g$ around the axis oz_g by the yaw angle ψ to obtain a new coordinate frame $o - k_1 k_2 k_3$, so that ox_g turns to ok_1 and oy_g turns to ok_2 . Thus, the axis ok_1 is located in the plane $ox_b z_b$ of the body frame, ok_2 is located in the plane $oy_b z_b$.

(2) As shown in Fig. 2.11(b), rotate the frame $o - k_1 k_2 k_3$ around the axis ok_2 by the pitch angle θ to obtain a new coordinate frame $o - n_1 n_2 n_3$. Thus, on_1 corresponds to the axis ox_b of the body frame, on_3 is located in the plane $oy_b z_b$.

(3) As shown in Fig. 2.11(c), rotate the frame $o - n_1 n_2 n_3$ around the axis on_1 by the roll angle ϕ to obtain body frame $o - x_b y_b z_b$, so that on_2 turns to the axis oy_b of the body frame, on_3 turns to oz_b of the body frame.

The detailed mathematical derivations of the above procedures are presented as follows.

(1) After rotating the yaw angle ψ around oz_g as shown in Fig. 2.11(a), the following equations can be obtained

$$\begin{cases} \mathbf{k}_1 = \mathbf{i}^g \cos \psi + \mathbf{j}^g \sin \psi \\ \mathbf{k}_2 = -\mathbf{i}^g \sin \psi + \mathbf{j}^g \cos \psi \\ \mathbf{k}_3 = \mathbf{k}^g \end{cases} \quad (2.1)$$

where \mathbf{i}^g is the unit vector along ox_g , \mathbf{j}^g is the unit vector along oy_g , and \mathbf{k}^g is the unit vector along oz_g . Note that, the bold symbols $\mathbf{k}_1, \mathbf{k}_2, \mathbf{k}_3$ represent the axial unit vectors of the new frame $o - k_1 k_2 k_3$. Thus, the transformation relationship between $o - k_1 k_2 k_3$ and $o - x_g y_g z_g$ is

$$\begin{bmatrix} k_1 \\ k_2 \\ k_3 \end{bmatrix} = \begin{bmatrix} \cos \psi & \sin \psi & 0 \\ -\sin \psi & \cos \psi & 0 \\ 0 & 0 & 1 \end{bmatrix} \begin{bmatrix} x_g \\ y_g \\ z_g \end{bmatrix}. \quad (2.2)$$

where $[x_g \ y_g \ z_g]^T$ denotes the coordinate values of a vector projected (presented, described or observed) in the frame $o - x_g y_g z_g$, and $[k_1 \ k_2 \ k_3]^T$ denotes the new coordinate values of that vector projected in the frame $o - k_1 k_2 k_3$.

By letting

$$\mathbf{R}_z(\psi) \triangleq \begin{bmatrix} \cos \psi & \sin \psi & 0 \\ -\sin \psi & \cos \psi & 0 \\ 0 & 0 & 1 \end{bmatrix} \quad (2.3)$$

then Eq. (2.2) is rewritten as

$$\begin{bmatrix} k_1 \\ k_2 \\ k_3 \end{bmatrix} = \mathbf{R}_z(\psi) \begin{bmatrix} x_g \\ y_g \\ z_g \end{bmatrix}. \quad (2.4)$$

(2) After rotating the pitch angle θ around ok_2 as shown in Fig. 2.11(b), the following equations can be obtained

$$\begin{cases} \mathbf{n}_1 = \mathbf{k}_1 \cos \theta - \mathbf{k}_3 \sin \theta \\ \mathbf{n}_2 = \mathbf{k}_2 \\ \mathbf{n}_3 = \mathbf{k}_1 \sin \theta + \mathbf{k}_3 \cos \theta \end{cases} \quad (2.5)$$

where the bold symbols $\mathbf{n}_1, \mathbf{n}_2, \mathbf{n}_3$ represent the axial unit vectors of the new frame $o - n_1 n_2 n_3$.

Thus, the transformation relationship between $o - n_1 n_2 n_3$ and $o - k_1 k_2 k_3$ is given by

$$\begin{bmatrix} n_1 \\ n_2 \\ n_3 \end{bmatrix} = \begin{bmatrix} \cos \theta & 0 & -\sin \theta \\ 0 & 1 & 0 \\ \sin \theta & 0 & \cos \theta \end{bmatrix} \begin{bmatrix} k_1 \\ k_2 \\ k_3 \end{bmatrix}. \quad (2.6)$$

By letting

$$\mathbf{R}_y(\theta) \triangleq \begin{bmatrix} \cos \theta & 0 & -\sin \theta \\ 0 & 1 & 0 \\ \sin \theta & 0 & \cos \theta \end{bmatrix} \quad (2.7)$$

one has

$$\begin{bmatrix} n_1 \\ n_2 \\ n_3 \end{bmatrix} = \mathbf{R}_y(\theta) \begin{bmatrix} k_1 \\ k_2 \\ k_3 \end{bmatrix} = \mathbf{R}_y(\theta) \mathbf{R}_z(\psi) \begin{bmatrix} x_g \\ y_g \\ z_g \end{bmatrix} \quad (2.8)$$

(3) After rotating the roll angle ϕ around on_1 as shown in Fig. 2.11(c), the following equation can be obtained

$$\begin{cases} \mathbf{x}_b = \mathbf{n}_1 \\ \mathbf{y}_b = \mathbf{n}_2 \cos \phi + \mathbf{n}_3 \sin \phi \\ \mathbf{z}_b = -\mathbf{n}_2 \sin \phi + \mathbf{n}_3 \cos \phi \end{cases} \quad (2.9)$$

where $\mathbf{x}_b, \mathbf{y}_b, \mathbf{z}_b$ represent the axial unit vectors of the finally obtained aircraft body frame $o - x_b y_b z_b$. Thus, the transformation relationship between $o - x_b y_b z_b$ and $o - n_1 n_2 n_3$ is

$$\begin{bmatrix} x_b \\ y_b \\ z_b \end{bmatrix} = \begin{bmatrix} 1 & 0 & 0 \\ 0 & \cos \phi & \sin \phi \\ 0 & -\sin \phi & \cos \phi \end{bmatrix} \begin{bmatrix} n_1 \\ n_2 \\ n_3 \end{bmatrix} \quad (2.10)$$

By letting

$$\mathbf{R}_x(\phi) \triangleq \begin{bmatrix} 1 & 0 & 0 \\ 0 & \cos \phi & \sin \phi \\ 0 & -\sin \phi & \cos \phi \end{bmatrix} \quad (2.11)$$

one has

$$\begin{bmatrix} x_b \\ y_b \\ z_b \end{bmatrix} = \mathbf{R}_x(\phi) \begin{bmatrix} n_1 \\ n_2 \\ n_3 \end{bmatrix} = \mathbf{R}_x(\phi) \mathbf{R}_y(\theta) \begin{bmatrix} k_1 \\ k_2 \\ k_3 \end{bmatrix} = \mathbf{R}_x(\phi) \mathbf{R}_y(\theta) \mathbf{R}_z(\psi) \begin{bmatrix} x_g \\ y_g \\ z_g \end{bmatrix}. \quad (2.12)$$

Therefore, the rotation matrix $\mathbf{R}_{b/g}$, which represents the rotation from the ground frame to the body frame, can be expressed as

$$\begin{aligned} \mathbf{R}_{b/g} &= \mathbf{R}_x(\phi) \mathbf{R}_y(\theta) \mathbf{R}_z(\psi) \\ &= \begin{bmatrix} 1 & 0 & 0 \\ 0 & \cos \phi & \sin \phi \\ 0 & -\sin \phi & \cos \phi \end{bmatrix} \begin{bmatrix} \cos \theta & 0 & -\sin \theta \\ 0 & 1 & 0 \\ \sin \theta & 0 & \cos \theta \end{bmatrix} \begin{bmatrix} \cos \psi & \sin \psi & 0 \\ -\sin \psi & \cos \psi & 0 \\ 0 & 0 & 1 \end{bmatrix} \\ &= \begin{bmatrix} \cos \theta \cos \psi & \cos \theta \sin \psi & -\sin \theta \\ \sin \theta \sin \phi \cos \psi - \sin \psi \cos \phi & \sin \psi \sin \theta \sin \phi + \cos \psi \cos \phi & \sin \phi \cos \theta \\ \sin \theta \cos \phi \cos \psi + \sin \psi \sin \phi & \sin \psi \sin \theta \cos \phi - \cos \psi \sin \phi & \cos \phi \cos \theta \end{bmatrix} \end{aligned} \quad (2.13)$$

The rotation from the ground frame to the body frame is composed of three elemental steps, which can be represented as

$$\begin{bmatrix} x_g \\ y_g \\ z_g \end{bmatrix} \xrightarrow{\mathbf{R}_z(\psi)} \begin{bmatrix} k_1 \\ k_2 \\ k_3 = z_g \end{bmatrix} \xrightarrow{\mathbf{R}_y(\theta)} \begin{bmatrix} n_1 \\ n_2 = k_2 \\ n_3 \end{bmatrix} \xrightarrow{\mathbf{R}_x(\phi)} \begin{bmatrix} x_b = n_1 \\ y_b \\ z_b \end{bmatrix}. \quad (2.14)$$

In the docking process, the movement of the receiver needs to be converted to the tanker frame for calculating, so it is necessary to know the conversion relationship between the tanker frame and the receiver frame. Since we have previously stated that the tanker frame is equivalent to an inertial system whose direction is consistent with the ground frame, we can directly describe the relationship between the two frames by the attitude angle of the receiver. Here, the attitude of the receiver is defined as $\Theta_r = \Theta_{r/g} = \Theta_{r/t} = [\theta_r \ \phi_r \ \psi_r]^T$, where θ_r, ϕ_r, ψ_r represent the pitch angle, the roll angle and the yaw angle, respectively. Then the rotation matrix can be expressed as

$$\mathbf{R}_{r/t}(\Theta_r) = \begin{bmatrix} \cos \theta_r \cos \psi_r & \cos \theta_r \sin \psi_r & -\sin \theta_r \\ \sin \theta_r \cos \psi_r \sin \phi_r - \sin \psi_r \cos \phi_r & \sin \theta_r \sin \psi_r \sin \phi_r + \cos \psi_r \cos \phi_r & \cos \theta_r \sin \phi_r \\ \sin \theta_r \cos \psi_r \cos \phi_r + \sin \psi_r \sin \phi_r & \sin \theta_r \cos \psi_r \cos \phi_r - \cos \psi_r \sin \phi_r & \cos \theta_r \cos \phi_r \end{bmatrix}. \quad (2.15)$$

The corresponding coordinates satisfy the following conversion relationship

$$\mathbf{p}^r = \mathbf{R}_{r/t}(\Theta_r) \mathbf{p}^t + \mathbf{p}_{t/r}^r \quad (2.16)$$

or

$$\mathbf{p}^t = \mathbf{R}_{r/t}^T(\Theta_r) \mathbf{p}^r + \mathbf{p}_{r/t}^t \quad (2.17)$$

where $\mathbf{p}_{r/t}^t$ and $\mathbf{p}_{r/t}^t$ represent the relative position vector of the tanker and the receiver, respectively.

The rotation from the wind frame to the body frame of an aircraft is presented as follows. It takes two steps to transform vectors from the wind frame $o_w - x_w y_w z_w$ to the body frame $o_b - x_b y_b z_b$.

In the first step, we rotate the wind frame $o_w - x_w y_w z_w$ around the axis $o_w z_w$ by the side slip angle β , which yields the stability frame $o_s - x_s y_s z_s$ as

$$\begin{bmatrix} x_s \\ y_s \\ z_s \end{bmatrix} = \begin{bmatrix} \cos \beta & -\sin \beta & 0 \\ \sin \beta & \cos \beta & 0 \\ 0 & 0 & 1 \end{bmatrix} \begin{bmatrix} x_w \\ y_w \\ z_w \end{bmatrix}. \quad (2.18)$$

The rotation matrix from the wind frame to the stability frame is expressed as

$$\mathbf{R}_{s/w}(\beta) = \begin{bmatrix} \cos \beta & -\sin \beta & 0 \\ \sin \beta & \cos \beta & 0 \\ 0 & 0 & 1 \end{bmatrix}. \quad (2.19)$$

The corresponding coordinates satisfy the following conversion relationship

$$\mathbf{p}^s = \mathbf{R}_{s/w}(\beta) \mathbf{p}^w \quad (2.20)$$

or

$$\mathbf{p}^w = \mathbf{R}_{s/w}^T(\beta) \mathbf{p}^s. \quad (2.21)$$

In the second step, we rotate the obtained stability frame $o_s - x_s y_s z_s$ around the axis $o_s y_s$ by the angle of attack α , which yields the body frame $o_b - x_b y_b z_b$, namely

$$\begin{bmatrix} x_b \\ y_b \\ z_b \end{bmatrix} = \begin{bmatrix} \cos \alpha & 0 & -\sin \alpha \\ 0 & 1 & 0 \\ \sin \alpha & 0 & \cos \alpha \end{bmatrix} \begin{bmatrix} x_s \\ y_s \\ z_s \end{bmatrix}. \quad (2.22)$$

The rotation matrix is expressed as

$$\mathbf{R}_{b/s}(\alpha) = \begin{bmatrix} \cos \alpha & 0 & -\sin \alpha \\ 0 & 1 & 0 \\ \sin \alpha & 0 & \cos \alpha \end{bmatrix}. \quad (2.23)$$

The corresponding coordinates satisfy the following conversion relationship

$$\mathbf{p}^b = \mathbf{R}_{b/s}(\alpha) \mathbf{p}^s \quad (2.24)$$

or

$$\mathbf{p}^s = \mathbf{R}_{b/s}^T(\alpha) \mathbf{p}^b. \quad (2.25)$$

According to Eq. (2.18) and Eq. (2.22), the following equation can be obtained

$$\begin{bmatrix} x_b \\ y_b \\ z_b \end{bmatrix} = \mathbf{R}_{b/s}(\alpha) \begin{bmatrix} x_s \\ y_s \\ z_s \end{bmatrix} = \mathbf{R}_{b/s}(\alpha) \mathbf{R}_{s/w}(\beta) \begin{bmatrix} x_w \\ y_w \\ z_w \end{bmatrix}. \quad (2.26)$$

In summary, the rotation matrix which represents the rotation from the wind frame to the body frame, is expressed as

$$\begin{aligned} \mathbf{R}_{b/w}(\alpha, \beta) &= \mathbf{R}_{b/s}(\alpha) \mathbf{R}_{s/w}(\beta) \\ &= \begin{bmatrix} \cos \alpha & 0 & -\sin \alpha \\ 0 & 1 & 0 \\ \sin \alpha & 0 & \cos \alpha \end{bmatrix} \begin{bmatrix} \cos \beta & -\sin \beta & 0 \\ \sin \beta & \cos \beta & 0 \\ 0 & 0 & 1 \end{bmatrix} \\ &= \begin{bmatrix} \cos \alpha \cos \beta & -\cos \alpha \sin \beta & -\sin \alpha \\ \sin \beta & \cos \beta & 0 \\ \sin \alpha \cos \beta & -\sin \alpha \sin \beta & \cos \alpha \end{bmatrix}. \end{aligned} \quad (2.27)$$

The corresponding coordinates satisfy the following conversion relationship

$$\mathbf{p}^b = \mathbf{R}_{b/w}(\alpha, \beta) \mathbf{p}^w \quad (2.28)$$

or

$$\mathbf{p}^w = \mathbf{R}_{b/w}^T(\alpha, \beta) \mathbf{p}^b. \quad (2.29)$$

2.3.1.3 Air Velocity, Wind Velocity and Ground Velocity

The aerodynamic forces and moments acting on an aircraft depend on the airflow velocity (or simply “air velocity”) of the fuselage relative to the surrounding air (the wind velocity should be considered) instead of the ground velocity. The ground velocity and the air velocity are the same when there is no wind. However, there are always many wind disturbances in the flight environment, and we must carefully distinguish between air velocity $\mathbf{v}_{b/w}^g$ (the relative velocity with respect to the surrounding air) and the ground velocity $\mathbf{v}_{b/g}^g$ (the relative velocity with respect to the ground frame). Their relationship is described as

$$\mathbf{v}_{b/w}^g = \mathbf{v}_{b/g}^g - \mathbf{v}_{w/g}^g \quad (2.30)$$

where $\mathbf{v}_{w/g}^g$ represents the velocity of the wind relative to the ground frame, namely the wind velocity. Eq. (2.30) is described in the ground frame, which should be converted into the body frame for convenience. First, by projecting the ground velocity vector $\mathbf{v}_{b/g}^g$ into the body frame, we obtain vector $\mathbf{v}_{b/g}^b$ whose component form is expressed as

$$\mathbf{v}_{b/g}^b = \begin{bmatrix} u \\ v \\ w \end{bmatrix}. \quad (2.31)$$

Secondly, by projecting the wind velocity vector $\mathbf{v}_{w/g}^g$ in Eq. (2.30) into the body frame, we obtain vector $\mathbf{v}_{w/g}^b$ whose component form is expressed as

$$\mathbf{v}_{w/g}^b = \begin{bmatrix} u_w \\ v_w \\ w_w \end{bmatrix}. \quad (2.32)$$

Finally, projecting the air velocity vector $\mathbf{v}_{b/w}^g$ into the body frame yields $\mathbf{v}_{b/w}^b = [u_a \ v_a \ w_a]^T$, whose relationship with $\mathbf{v}_{b/w}^b$ and $\mathbf{v}_{w/g}^b$ can be derived from Eq. (2.30) as

$$\mathbf{v}_{b/w}^b = \mathbf{v}_{b/w}^b - \mathbf{v}_{w/g}^b \quad (2.33)$$

or written with the component form

$$\begin{bmatrix} u_a \\ v_a \\ w_a \end{bmatrix} = \begin{bmatrix} u \\ v \\ w \end{bmatrix} - \begin{bmatrix} u_w \\ v_w \\ w_w \end{bmatrix} = \begin{bmatrix} u - u_w \\ v - v_w \\ w - w_w \end{bmatrix}. \quad (2.34)$$

Note that, the components u_a , v_a and w_a of $\mathbf{v}_{b/w}^b$ are often used to calculate the aerodynamic forces and moments when building an aircraft dynamics model; The components u , v and w of $\mathbf{v}_{b/w}^b$ are state variables in the aircraft dynamics equations; the components u_w , v_w and w_w of $\mathbf{v}_{w/g}^b$ can be estimated from the flight data, which are usually generated from the wind model in simulations. According to the conversion relationship between the wind frame and the body frame in Eq. (2.28), the following equation can be obtained

$$\mathbf{v}_{b/w}^b = \mathbf{R}_{b/w}(\alpha, \beta) \mathbf{v}_{b/w}^w \quad (2.35)$$

where

$$\begin{aligned} \mathbf{v}_{b/w}^w &= [V_a \ 0 \ 0]^T \\ V_a &= \|\mathbf{v}_{b/w}^b\| \end{aligned}$$

in which V_a is usually called the airspeed and can be measured with an airspeed tube. Then Eq. (2.35) can be written as

$$\begin{bmatrix} u_a \\ v_a \\ w_a \end{bmatrix} = \begin{bmatrix} \cos \alpha \cos \beta & -\cos \alpha \sin \beta & -\sin \alpha \\ \sin \beta & \cos \beta & 0 \\ \sin \alpha \cos \beta & -\sin \alpha \sin \beta & \cos \alpha \end{bmatrix} \begin{bmatrix} V_a \\ 0 \\ 0 \end{bmatrix} \quad (2.36)$$

or

$$\begin{bmatrix} u_a \\ v_a \\ w_a \end{bmatrix} = V_a \begin{bmatrix} \cos \alpha \cos \beta \\ \sin \beta \\ \sin \alpha \cos \beta \end{bmatrix}. \quad (2.37)$$

Thus

$$V_a = \|\mathbf{v}_{b/w}^b\| = \sqrt{u_a^2 + v_a^2 + w_a^2} \quad (2.38)$$

$$\alpha = \tan^{-1} \left(\frac{w_a}{u_a} \right) \quad (2.39)$$

$$\beta = \sin^{-1} \left(\frac{v_a}{V_a} \right). \quad (2.40)$$

Since the aerodynamic forces and moments of the aircraft are usually determined by V_a , α and β , the above expressions are essential for deriving the equations of motion of the aircraft.

2.3.1.4 Angular Velocity

The rates of the change of roll, pitch and yaw angles with time are represented by $\dot{\phi}$, $\dot{\theta}$ and $\dot{\psi}$ respectively, which are critical for computing the Euler angles ϕ , θ , ψ in the flight dynamics simulations, but they are difficult to measure directly in practice. The angle changing rate is usually different from the angular velocity of an aircraft relative to the ground frame, which can be measured by a rate gyro.

As shown in Fig. 2.10, assuming that the angular velocity of the aircraft is $\omega^b = [p \ q \ r]^T$, then the relationship between angular velocity ω^b and the changing rates $\dot{\phi}$, $\dot{\theta}$, $\dot{\psi}$ of Euler angles can be expressed as [130]

$$\omega^b = \dot{\psi} \cdot \mathbf{k}_3^b + \dot{\theta} \cdot \mathbf{n}_2^b + \dot{\phi} \cdot \mathbf{x}_b^b. \quad (2.41)$$

Since

$$\mathbf{n}_2^b = \mathbf{R}_{b/n} \cdot \mathbf{n}_2^g = \mathbf{R}_{b/n} \cdot \mathbf{y}_g \quad (2.42)$$

$$\mathbf{k}_3^b = \mathbf{R}_{b/k} \cdot \mathbf{k}_3^g = \mathbf{R}_{b/k} \cdot \mathbf{z}_g \quad (2.43)$$

$$\mathbf{x}_b^b = \begin{bmatrix} 1 & 0 & 0 \end{bmatrix}^T \quad (2.44)$$

one has

$$\mathbf{n}_2^b = \mathbf{R}_{b/n} \cdot \mathbf{y}_g = \begin{bmatrix} 0 & \cos \phi & -\sin \phi \end{bmatrix}^T \quad (2.45)$$

$$\mathbf{k}_3^b = \mathbf{R}_{b/k} \cdot \mathbf{z}_g = \begin{bmatrix} -\sin \theta & \cos \theta \sin \phi & \cos \theta \cos \phi \end{bmatrix}^T \quad (2.46)$$

where $\mathbf{R}_{b/n} = \mathbf{R}_x(\phi)$, $\mathbf{R}_{b/k} = \mathbf{R}_x(\phi) \mathbf{R}_y(\theta)$. The specific forms of $\mathbf{R}_y(\theta)$ and $\mathbf{R}_x(\phi)$ are given by (2.7) and (2.11). Combining (2.41)-(2.46) yields

$$\begin{bmatrix} p \\ q \\ r \end{bmatrix} = \begin{bmatrix} 1 & 0 & -\sin \theta \\ 0 & \cos \phi & \cos \theta \sin \phi \\ 0 & -\sin \phi & \cos \theta \cos \phi \end{bmatrix} \begin{bmatrix} \dot{\phi} \\ \dot{\theta} \\ \dot{\psi} \end{bmatrix} \quad (2.47)$$

and then

$$\begin{bmatrix} \dot{\phi} \\ \dot{\theta} \\ \dot{\psi} \end{bmatrix} = \begin{bmatrix} 1 & \tan \theta \sin \phi & \tan \theta \cos \phi \\ 0 & \cos \phi & -\sin \phi \\ 0 & \sin \phi / \cos \theta & \cos \phi / \cos \theta \end{bmatrix} \begin{bmatrix} p \\ q \\ r \end{bmatrix}. \quad (2.48)$$

It can be observed from Eq. (2.48) that $\cos \theta$ appears in the denominator, so the value of the

fraction no longer has meaning when $\cos \theta = 0$ or $\theta = \pm \frac{\pi}{2}$, which is called the singularity problem. Therefore, Eq. (2.48) can only be used for aircraft modeling and control when the pitch angle θ is small.

2.3.2 Direction Cosine Matrix method

2.3.2.1 Direction Cosine Matrix

Direction cosine matrix, namely rotation matrix, is widely used in frame transformation. According to the three-step rotation process from the ground frame to the body frame presented in Eq. (2.14), the rotation matrix $\mathbf{R}_{g/b}$ can be described by Euler angles ϕ, θ, ψ as

$$\begin{aligned} \mathbf{R}_{g/b} &= \mathbf{R}_{g/b}^{-1} \\ &= \mathbf{R}_z^{-1}(\psi) \mathbf{R}_y^{-1}(\theta) \mathbf{R}_x^{-1}(\phi) \\ &= \mathbf{R}_z^T(\psi) \mathbf{R}_y^T(\theta) \mathbf{R}_x^T(\phi) \\ &= \begin{bmatrix} \cos \theta \cos \psi & \sin \theta \sin \phi \cos \psi - \sin \psi \cos \phi & \sin \theta \cos \phi \cos \psi + \sin \psi \sin \phi \\ \cos \theta \sin \psi & \sin \psi \sin \theta \sin \phi + \cos \psi \cos \phi & \sin \psi \sin \theta \cos \phi - \cos \psi \sin \phi \\ -\sin \theta & \sin \phi \cos \theta & \cos \phi \cos \theta \end{bmatrix}. \end{aligned} \quad (2.49)$$

Conversely, Euler angles ϕ, θ, ψ can be solved with knowing the rotation matrix $\mathbf{R}_{g/b}$. By letting the rotation matrix be

$$\mathbf{R}_{g/b} \triangleq \begin{bmatrix} r_{11} & r_{12} & r_{13} \\ r_{21} & r_{22} & r_{23} \\ r_{31} & r_{32} & r_{33} \end{bmatrix} \quad (2.50)$$

according to Eq.(2.49), one has

$$\begin{cases} \tan \psi = \frac{r_{21}}{r_{11}} \\ \sin \theta = -r_{31} \\ \tan \phi = \frac{r_{32}}{r_{33}} \end{cases} . \quad (2.51)$$

Since the ranges of Euler angles are $\psi \in [-\pi, \pi]$, $\theta \in [-\pi/2, \pi/2]$, $\phi \in [-\pi/2, \pi/2]$, the solutions to Eq.(2.51) are

$$\begin{cases} \psi = \arctan \frac{r_{21}}{r_{11}} \\ \theta = \arcsin(-r_{31}) \\ \phi = \arctan \frac{r_{32}}{r_{33}} \end{cases} \quad (2.52)$$

where the value ranges of $\arctan(\cdot)$ and $\arcsin(\cdot)$ are $[-\pi/2, \pi/2]$.

2.3.2.2 Relationship Between the Derivative of the Rotation Matrix and the Angular Velocity

If only the rigid body's rotation (without translation) is considered, then the derivative of a vector $\mathbf{r}^g \in \mathbb{R}^3$ with time satisfies

$$\frac{d\mathbf{r}^g}{dt} = \boldsymbol{\omega}^g \times \mathbf{r}^g \quad (2.53)$$

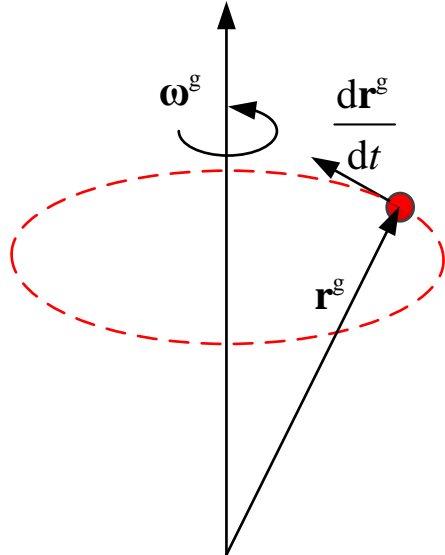


Figure 2.12: The derivative of a vector presented by a circular motion

where the symbol \times represents the cross product of two vectors. The physical significance of Eq. (2.53) can be vividly illustrated by the circular motion in Fig. 2.12.

The cross product of two vectors $\mathbf{a} \triangleq [a_x \ a_y \ a_z]^T$ and $\mathbf{b} \triangleq [b_x \ b_y \ b_z]^T$ is defined as [131]

$$\mathbf{a} \times \mathbf{b} = [\mathbf{a}]_{\times} \mathbf{b} \quad (2.54)$$

where

$$[\mathbf{a}]_{\times} = \begin{bmatrix} 0 & -a_z & a_y \\ a_z & 0 & -a_x \\ -a_y & a_x & 0 \end{bmatrix} \quad (2.55)$$

is a skew-symmetric matrix.

Let $\mathbf{x}_b^b, \mathbf{y}_b^b, \mathbf{z}_b^b$ present the axial unit vectors of the body frame as

$$\begin{aligned} \mathbf{x}_b^b &\triangleq \begin{bmatrix} 1 & 0 & 0 \end{bmatrix}^T \\ \mathbf{y}_b^b &\triangleq \begin{bmatrix} 0 & 1 & 0 \end{bmatrix}^T \\ \mathbf{z}_b^b &\triangleq \begin{bmatrix} 0 & 0 & 1 \end{bmatrix}^T \end{aligned} \quad (2.56)$$

then

$$\begin{bmatrix} \mathbf{x}_b^b & \mathbf{y}_b^b & \mathbf{z}_b^b \end{bmatrix} = \begin{bmatrix} 1 & 0 & 0 \\ 0 & 1 & 0 \\ 0 & 0 & 1 \end{bmatrix} = \mathbf{I}_{3 \times 3}$$

composes an identity matrix. Projecting vectors $\mathbf{x}_b^b, \mathbf{y}_b^b, \mathbf{z}_b^b$ from the body frame to the ground frame, one has

$$\begin{aligned} \mathbf{x}_b^g &= \mathbf{R}_{g/b} \cdot \mathbf{x}_b^b \\ \mathbf{y}_b^g &= \mathbf{R}_{g/b} \cdot \mathbf{y}_b^b \\ \mathbf{z}_b^g &= \mathbf{R}_{g/b} \cdot \mathbf{z}_b^b \end{aligned} \quad (2.57)$$

which yields

$$\begin{aligned} \begin{bmatrix} \mathbf{x}_b^g & \mathbf{y}_b^g & \mathbf{z}_b^g \end{bmatrix} &= \mathbf{R}_{g/b} \cdot \begin{bmatrix} \mathbf{x}_b^b & \mathbf{y}_b^b & \mathbf{z}_b^b \end{bmatrix} \\ &= \mathbf{R}_{g/b} \cdot \mathbf{I}_{3 \times 3} \\ &= \mathbf{R}_{g/b} \end{aligned} \quad (2.58)$$

According to Eq. (2.53), one has

$$\begin{aligned} \frac{d\mathbf{R}_{g/b}}{dt} &= \frac{d}{dt} \begin{bmatrix} \mathbf{x}_b^g & \mathbf{y}_b^g & \mathbf{z}_b^g \end{bmatrix} = \begin{bmatrix} \frac{d\mathbf{x}_b^g}{dt} & \frac{d\mathbf{y}_b^g}{dt} & \frac{d\mathbf{z}_b^g}{dt} \end{bmatrix} \\ &= \begin{bmatrix} \boldsymbol{\omega}^g \times \mathbf{x}_b^g & \boldsymbol{\omega}^g \times \mathbf{y}_b^g & \boldsymbol{\omega}^g \times \mathbf{z}_b^g \end{bmatrix} \end{aligned} \quad (2.59)$$

Since $\boldsymbol{\omega}^g = \mathbf{R}_{g/b} \cdot \boldsymbol{\omega}^b$, by using the properties of the cross product, one has

$$\begin{aligned} \boldsymbol{\omega}^g \times \mathbf{x}_b^g &= (\mathbf{R}_{g/b} \cdot \boldsymbol{\omega}^b) \times (\mathbf{R}_{g/b} \cdot \mathbf{x}_b^b) \\ &= \mathbf{R}_{g/b} \cdot (\boldsymbol{\omega}^b \times \mathbf{x}_b^b) \\ &= \mathbf{R}_{g/b} \cdot [\boldsymbol{\omega}^b]_x \cdot \mathbf{x}_b^b \end{aligned} \quad (2.60)$$

where $[\boldsymbol{\omega}^b]_x$ is the skew-symmetric form of $\boldsymbol{\omega}^b$. Finally, by applying Eq. (2.60) for $\boldsymbol{\omega}^g \times \mathbf{y}_b^g$ and $\boldsymbol{\omega}^g \times \mathbf{z}_b^g$, Eq. (2.59) is rewritten as

$$\begin{aligned} \frac{d\mathbf{R}_{g/b}}{dt} &= \begin{bmatrix} \boldsymbol{\omega}^g \times \mathbf{x}_b^g & \boldsymbol{\omega}^g \times \mathbf{y}_b^g & \boldsymbol{\omega}^g \times \mathbf{z}_b^g \end{bmatrix} \\ &= \mathbf{R}_{g/b} \cdot [\boldsymbol{\omega}^b]_x \cdot \begin{bmatrix} \mathbf{x}_b^b & \mathbf{y}_b^b & \mathbf{z}_b^b \end{bmatrix} \\ &= \mathbf{R}_{g/b} \cdot [\boldsymbol{\omega}^b]_x \end{aligned} \quad (2.61)$$

The use of the rotation matrix can avoid the singularity problem. However, since $\mathbf{R}_{g/b}$ has nine unknown variables, the calculating quantity of solving Eq. (2.61) is large.

2.4 Chapter Summary

This chapter mainly introduces several common frames in the aerial refueling process, including the ground frame, the body frame, the wind frame, the stability frame, the CFD system and the drogue equilibrium position frame. Moreover, two methods for frame conversion are introduced, that is, the Euler angle method and the direction cosine matrix method. This chapter provides all the necessary knowledge for subsequent aerial fueling modeling.

Chapter 3 Aircraft with Hose and Drogue

The successful implementation of aerial refueling is based on the establishment of accurate docking models, including Aerodynamic Disturbance Models, aircraft model and hose-and-drogue model. Among them, Aerodynamic Disturbance Models have been discussed in detail in the previous chapter, and this chapter will mainly introduce the aircraft model and the hose-and-drogue model during the refueling process. Taking F-16 fighter as an example, its kinematics and dynamics models are analyzed, and the models are decoupled and linearized longitudinally and laterally, which provides convenience for controller design. Secondly, the hose-and-drogue model is established to show the dynamic characteristics of the hose-and-drogue system. Finally, a bow wave effect analysis method based on the hose-and-drogue model is introduced.

3.1 Aircraft Model

In the process of refueling in the air, the tanker keeps a constant speed and a level flight with fixed height. Because the duration of each docking operation is short, the tanker frame can be regarded as an inertial frame during this period of time, and does not have other dynamic characteristics. In the process of refueling in the air, the receiver must complete various maneuvers to successfully complete the refueling task. Therefore, the receiver model is an important part of the whole air refueling model. This section mainly discusses the building process of the receiver model in detail. First, the nonlinear model of the receiver is established. Then, the nonlinear model is simplified to the horizontal and longitudinal linear model. Finally, the wind field disturbance is added to the model.

3.1.1 Nonlinear Mass-varying Model of Receiver Aircraft

The actual receiver is a complex dynamic system, its mass is time-varying during flight, and its structure also has the characteristics of elastic deformation. In addition, the rotation of the Earth causes the vehicle to be subject to centrifugal and Gothic acceleration, while the gravitational acceleration also varies with altitude. Therefore, it is not realistic to establish a completely accurate aircraft model, and it is of practical significance to simplify the aircraft model and flight environment appropriately. Before establishing the motion equation of the receiver, the following assumptions are proposed:

1. Ignoring the curvature of the earth, the "flat earth hypothesis" is adopted, and the ground coordinate system is assumed to be an inertial coordinate system. In this case, the tanker maintains uniform speed and flies in a straight line, so the tanker coordinate system is also an inertial coordinate system.

2. The receiver system includes the aircraft mechanical body part and the fuel tank part. The body part of the receiver is a rigid body with constant mass, regardless of the elastic deformation of the fuselage and wing during flight, and the origin of the body coordinate system is located at the mass center of the body part of the receiver. The change of the fuel part of the fuel tank causes the change of the total mass and moment of inertia of the receiver.
3. The mechanical body of the receiver system is assumed to be rigid and symmetric about the $o_r x_r z_r$ plane of the body coordinate system, with both external shape and internal mass symmetry. This assumption is applicable to most aircraft. The advantage of this assumption is that the modeling of the mechanical body of the aerial refueling system can directly use traditional constant mass aircraft modeling methods, and the existing aerodynamic parameters can be directly applied to the modeling process of mass-varying aircraft.
4. Ignoring the fuel mass in the fuel transfer pipe and fuel consumption during normal flight. In other words, the receiver system only experiences a mass change during the refueling phase, while in other phases it is considered as a rigid body with constant mass. The mass-varying model is used only during the refueling phase, while in other phases, the receiver system model remains the same as that of a traditional constant mass aircraft.
5. The receiver system has k fuel tanks, and the positions of the fuel tanks and the distribution of fuel mass are symmetric. Each fuel tank is considered as a variable mass block, where the mass of fuel in the j th fuel tank is $m_j, j \in \{1, 2, \dots, k\}$, and the position vector \mathbf{r}_j from the center of mass o_j to the origin o_r of the aerial refueling system's body coordinate system is constant.

Based on the above assumptions, the six-degrees-of-freedom motion equations of the variable mass receiver system can be established. Fig. 3.1 shows a diagram of an F-16 receiver. The dynamics of the receiver can be described by the variations of position, velocity, attitude angles, and angular velocity with respect to time. In the process of establishing the nonlinear model for the variable mass receiver system, for simplicity, the following notations for the variables are used: $\mathbf{p}_r^e \triangleq \begin{bmatrix} x_r & y_r & h_r \end{bmatrix}^T$ represents the position of the receiver system in the Earth coordinate system; $\mathbf{v}_r^b \triangleq \begin{bmatrix} u_r & v_r & w_r \end{bmatrix}^T$ represents the velocity vector of the receiver system in the body coordinate system, where u is the longitudinal velocity magnitude, v is the lateral velocity magnitude, and w is the normal velocity magnitude; $\Theta_r \triangleq \begin{bmatrix} \phi & \theta & \psi \end{bmatrix}^T$ represents the attitude angles of the receiver system; $\omega_r^b \triangleq \begin{bmatrix} p & q & r \end{bmatrix}^T$ represents the body angular velocity of receiver system; $\mathbf{u}_r \triangleq \begin{bmatrix} \delta_t & \delta_e & \delta_a & \delta_r \end{bmatrix}^T$ represents the control inputs of the receiver system, including the engine input, elevator deflection angle, aileron deflection angle, and rudder deflection angle. It is also defined that a downward deflection of the elevator angle δ_e is considered positive, a leftward deflection of the rudder angle δ_r is considered positive, and an upward deflection of the

left aileron and a downward deflection of the right aileron are considered positive.

According to Newton's second law, the linear equations of motion for the receiver under external forces in an inertial reference frame are as follows

$$\mathbf{F} = \frac{d}{dt} (m\mathbf{v}_r^g) \quad (3.1)$$

where \mathbf{F} represents the total external force acting on the receiver, including aerodynamic forces, engine thrust, and gravity; \mathbf{v}_r^g represents the velocity vector of the center of mass of the receiver system in the Earth coordinate system; m represents the total mass of the receiver system, satisfying the following equation

$$m = m_0 + m_f. \quad (3.2)$$

Here, m_0 is a constant representing the mass of the mechanical body of the aircraft; m_f is a variable representing the mass of the fuel in the fuel tank, satisfying the following equation

$$m_f = \sum_{j=1}^k m_j. \quad (3.3)$$

It can be deduced from Eq. (3.2) and Eq. (3.3) that

$$\dot{m} = \dot{m}_0 + \dot{m}_f = \dot{m}_f = \sum_{j=1}^k \dot{m}_j. \quad (3.4)$$

Therefore, the mass change of the receiver is entirely determined by the fuel mass change in the fuel tank of the receiver.

The equation of angular motion for the receiver under the influence of external torque is as follows

$$\mathbf{M} = \frac{d\mathbf{L}_r^g}{dt} \quad (3.5)$$

where \mathbf{L}_r^g is the angular momentum, \mathbf{M} is the total external torque acting on the receiver, including aerodynamic torque and the torque generated by the gravitational force of the fuel on the aircraft's mechanical center of gravity, as the center of gravity of the fuel in each fuel tank does not coincide with the aircraft's mechanical center of gravity.

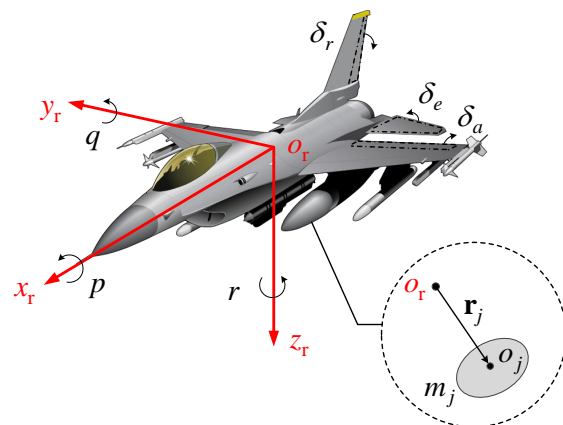


Figure 3.1: Schematic diagram of the F-16 refueling receiver

- Force Equations:

First, consider Eq. (3.1). In order to establish the motion relationship of the receiver relative to the ground coordinate system, the velocity \mathbf{v}_r of the receiver is decomposed in the body coordinate system. In the body coordinate system, Eq. (3.1) can be expressed as

$$\mathbf{F}^b = \frac{d}{dt} (m\mathbf{v}_r^b) + \boldsymbol{\omega}_r^b \times m\mathbf{v}_r^b \quad (3.6)$$

where \mathbf{v}_r^b is the velocity vector of the receiver's center of gravity in the body coordinate system, and $\boldsymbol{\omega}_r^b$ is the total angular velocity vector of the receiver relative to the ground coordinate system.

In the receiver body coordinate system, \mathbf{v}_r^b and $\boldsymbol{\omega}_r^b$ can be decomposed into

$$\mathbf{v}_r^b = \mathbf{i}^b u_r + \mathbf{j}^b v_r + \mathbf{k}^b w_r \quad (3.7)$$

$$\boldsymbol{\omega}_r^b = \mathbf{i}^b p + \mathbf{j}^b q + \mathbf{k}^b r \quad (3.8)$$

where $\mathbf{i}^b, \mathbf{j}^b$ and \mathbf{k}^b are the unit vectors of the $o_r x_r$ -axis, $o_r y_r$ -axis, and $o_r z_r$ -axis of the receiver body coordinate system.

Therefore, the first term of Eq. (3.6) can be expressed as

$$\frac{d}{dt} (m\mathbf{v}_r^b) = \dot{m}\mathbf{v}_r^b + m\dot{\mathbf{v}}_r^b = \mathbf{i}^b (\dot{m}u_r + \dot{m}u_r) + \mathbf{j}^b (\dot{m}v_r + \dot{m}z_r) + \mathbf{k}^b (\dot{m}w_r + \dot{m}w_r) \quad (3.9)$$

where \dot{m} is given by Eq. (3.4). The second term of Eq. (3.6) can be expressed as

$$\boldsymbol{\omega}_r^b \times m\mathbf{v}_r^b = m \begin{vmatrix} \mathbf{i}^b & \mathbf{j}^b & \mathbf{k}^b \\ p & q & r \\ u_r & v_r & w_r \end{vmatrix} = \mathbf{i}^b m (w_r q - v_r r) + \mathbf{j}^b m (u_r r - w_r p) + \mathbf{k}^b m (v_r p - u_r q). \quad (3.10)$$

Represent \mathbf{F} in the form of components in the body coordinate system as

$$\mathbf{F}^b = \mathbf{i}^b F_x^b + \mathbf{j}^b F_y^b + \mathbf{k}^b F_z^b. \quad (3.11)$$

Therefore, substituting Eqs. (3.9), (3.10), and (3.11) into Eq. (3.6), one can obtain

$$\begin{aligned} F_x^b &= m(\dot{u}_r + w_r q - v_r r) + \dot{m}u_r \\ F_y^b &= m(\dot{v}_r + u_r r - w_r p) + \dot{m}v_r \\ F_z^b &= m(\dot{w}_r + v_r p - u_r q) + \dot{m}w_r. \end{aligned} \quad (3.12)$$

The total external force \mathbf{F} includes gravity, aerodynamic force, and engine thrust. Assuming the engine thrust is F_T and its direction is along the $o_r x_r$ -axis of the body coordinate system. In the body coordinate system, the component of gravity is represented as follows

$$\begin{bmatrix} G_x^b \\ G_y^b \\ G_z^b \end{bmatrix} = \begin{bmatrix} -mg \sin \theta \\ mg \cos \theta \sin \phi \\ mg \cos \theta \cos \phi \end{bmatrix} \quad (3.13)$$

where g is the gravitational acceleration. The aerodynamic force components along the three axes of the body coordinate system are denoted as \bar{X}, \bar{Y} and \bar{Z} , and their magnitudes are related to the receiver's airspeed V_r , air density ρ , wing area S , wingspan b , angle of attack α , sideslip angle β , and control surface deflection angle $\delta = [\delta_a, \delta_r, \delta_e, \delta_t]$, etc. The aerodynamic force

components can be represented as follows

$$\begin{aligned}\bar{X} &= \bar{q}SC_{X_T}(\alpha, \beta, p, q, r, \delta, \dots) \\ \bar{Y} &= \bar{q}SC_{Y_T}(\alpha, \beta, p, q, r, \delta, \dots) \\ \bar{Z} &= \bar{q}SC_{Z_T}(\alpha, \beta, p, q, r, \delta, \dots)\end{aligned}\quad (3.14)$$

where $\bar{q} = 0.5\rho V_r^2$ represents dynamic pressure, S is the wing area, and the aerodynamic coefficients C_{X_T} , C_{Y_T} and C_{Z_T} can be obtained from wind tunnel data or flight data. Interested readers can refer to reference [132] for the specific forms of the aerodynamic coefficients.

Thus, the force equations for the receiver in the body coordinate system can be represented as follows

$$\begin{aligned}\dot{u}_r &= rv_r - qw_r - g \sin \theta + \frac{1}{m}(\bar{X} + F_T) - \frac{\dot{m}u_r}{m} \\ \dot{v}_r &= pw_r - ru_r + g \sin \phi \cos \theta + \frac{1}{m}\bar{Y} - \frac{\dot{m}v_r}{m} \\ \dot{w}_r &= qu_r - pv_r + g \cos \phi \cos \theta + \frac{1}{m}\bar{Z} - \frac{\dot{m}w_r}{m}\end{aligned}\quad (3.15)$$

- Moment Equations:

Considering Eq. (3.5), let us decompose the angular momentum \mathbf{L}_r^g in the body coordinate system. In the body coordinate system, Eq. (3.5) can be represented as follows

$$\mathbf{M}^b = \frac{d\mathbf{L}_r^b}{dt} + \omega_r^b \times \mathbf{L}_r^b. \quad (3.16)$$

Assuming that the angular momentum \mathbf{h}_E generated by the engine thrust is in the direction of the positive $o_r x_r$ -axis of the aircraft body, it can be represented in the body coordinate system as follows[133]

$$\mathbf{h}_E^b = \begin{bmatrix} h_E & 0 & 0 \end{bmatrix}^T \quad (3.17)$$

where h_E is the magnitude of the angular momentum generated by the engine thrust. Therefore, the angular momentum can be represented in the body coordinate system as follows

$$\mathbf{L}_r^b = \mathbf{J}\omega_r^b + \mathbf{h}_E^b \quad (3.18)$$

where \mathbf{J} is the inertia matrix of the receiver. Therefore, Eq. (3.16) is represented as follows

$$\begin{aligned}\mathbf{M}^b &= \frac{d}{dt}(\mathbf{J}\omega_r^b + \mathbf{h}_E^b) + \omega_r^b \times (\mathbf{J}\omega_r^b + \mathbf{h}_E^b) \\ &= \mathbf{J}\omega_r^b + \mathbf{J}\dot{\omega}_r^b + \omega_r^b \times (\mathbf{J}\omega_r^b + \mathbf{h}_E^b).\end{aligned}\quad (3.19)$$

Based on Assumptions 2) and 4), it can be concluded that the rotational inertia \mathbf{J} of the receiver consists of two parts: the rotational inertia \mathbf{J}_0 of the mechanical body and the rotational inertia \mathbf{J}_f of the fuel in the tank. According to Ref. [134], the rotational inertia \mathbf{J}_f of the fuel in the tank is represented as follows

$$\mathbf{J}_f = \sum_{j=1}^k m_j (\mathbf{r}_j^T \mathbf{r}_j \mathbf{I}_3 - \mathbf{r}_j \mathbf{r}_j^T) \quad (3.20)$$

where $\mathbf{r}_j \in \mathbb{R}^3$ represents the vector from the center of mass o_j of the fuel in the j th tank to the origin o_r of the receiver's body coordinate system, and \mathbf{I}_3 represents the three-dimensional unit

matrix. According to Assumption 5), \mathbf{r}_j is constant; hence, we have

$$\dot{\mathbf{J}}_f = \sum_{j=1}^k \dot{m}_j \left(\mathbf{r}_j^T \mathbf{r}_j \mathbf{I}_3 - \mathbf{r}_j \mathbf{r}_j^T \right). \quad (3.21)$$

At a specific moment, the total rotational inertia of the receiver is given by

$$\mathbf{J} = \mathbf{J}_0 + \mathbf{J}_f = \begin{bmatrix} J_x & 0 & -J_{xz} \\ 0 & J_y & 0 \\ -J_{xz} & 0 & J_z \end{bmatrix}. \quad (3.22)$$

Specifically, the rotational inertia of the mechanical body part of the receiver \mathbf{J}_0 is represented as follows

$$\mathbf{J}_0 = \begin{bmatrix} J_{x0} & 0 & -J_{xz0} \\ 0 & J_{y0} & 0 \\ -J_{xz0} & 0 & J_{z0} \end{bmatrix}. \quad (3.23)$$

Furthermore, according to Assumption 5), the positions of the fuel tanks and the distribution of fuel mass are symmetric. The rotational inertia \mathbf{J}_f is represented as follows

$$\mathbf{J}_f = \begin{bmatrix} J_{x1} & 0 & -J_{xz1} \\ 0 & J_{y1} & 0 \\ -J_{xz1} & 0 & J_{z1} \end{bmatrix} \quad (3.24)$$

where J_{x0} and J_{x1} represent the rotational inertia of the aircraft body and the fuel in the tanks around the $o_r x_r$ -axis of the body, J_{y0} and J_{y1} represent the rotational inertia around the $o_r y_r$ -axis, J_{z0} and J_{z1} represent the rotational inertia around the $o_r z_r$ -axis, and J_{xz0} and J_{xz1} represent the products of inertia. According to the symmetry assumption, the receiver is symmetric about the $o_r x_r z_r$ plane of the body coordinate system, hence $J_{xy} \equiv J_{yx} \equiv J_{yz} \equiv J_{zy} = 0$. It is worth noting that \mathbf{J}_f is time-varying, by taking the derivative of Eq. (3.24), it can be obtained

$$\dot{\mathbf{J}}_f = \begin{bmatrix} \dot{J}_{x1} & 0 & -\dot{J}_{xz1} \\ 0 & \dot{J}_{y1} & 0 \\ -\dot{J}_{xz1} & 0 & \dot{J}_{z1} \end{bmatrix} \quad (3.25)$$

where the values of each element are dependent on the changes of the receiver's fuel tank mass. Since the rotational inertia \mathbf{J}_0 of the receiver's mechanical body part is constant,

$$\dot{\mathbf{J}} = \dot{\mathbf{J}}_0 + \dot{\mathbf{J}}_f = \dot{\mathbf{J}}_f. \quad (3.26)$$

The total external moment \mathbf{M}^b includes the aerodynamic moment \mathbf{M}_a^b and the moment \mathbf{M}_f^b generated by the gravity of the fuel in the tanks, satisfying the following equation

$$\mathbf{M}^b = \mathbf{M}_a^b + \mathbf{M}_f^b \quad (3.27)$$

where the moment \mathbf{M}_f^b generated by the gravity of the fuel in the tanks can be represented as follows

$$\mathbf{M}_f^b = \sum_{j=1}^k \mathbf{r}_j \times \mathbf{R}_{b/g} \mathbf{G}_j = \mathbf{i}^b \bar{L}_f + \mathbf{j}^b \bar{M}_f + \mathbf{k}^b \bar{N}_f \quad (3.28)$$

where $\mathbf{G}_j = \begin{bmatrix} 0 & 0 & m_j g \end{bmatrix}^T$ represents the gravitational vector of the fuel in the j th tank, and \bar{L}_f , \bar{M}_f , and \bar{N}_f respectively represent the magnitudes of the components of the moment generated by the gravity of the fuel in the tanks along the three axes of the receiver's body coordinate system. The aerodynamic moment \mathbf{M}_a^b can be decomposed into the body coordinate axes as follows

$$\mathbf{M}_a^b = \mathbf{i}^b \bar{L}_a + \mathbf{j}^b \bar{M}_a + \mathbf{k}^b \bar{N}_a \quad (3.29)$$

where \bar{L}_a , \bar{M}_a , and \bar{N}_a represent the magnitudes of the components of the aerodynamic moment of the receiver along the three axes of its body coordinate system. Similar to the aerodynamic force, their magnitudes are related to the receiver's airspeed V_a , air density ρ , wing area S , wingspan b , angle of attack α , sideslip angle β , and control surface deflection angle δ , etc. The specific forms can be represented as follows

$$\begin{aligned} \bar{L}_a &= \bar{q} S b C_{l_T} (\alpha, \beta, p, q, r, \delta, \dots) \\ \bar{M}_a &= \bar{q} S c C_{m_T} (\alpha, \beta, p, q, r, \delta, \dots) \\ \bar{N}_a &= \bar{q} S b C_{n_T} (\alpha, \beta, p, q, r, \delta, \dots) \end{aligned} \quad (3.30)$$

where $\bar{q} = 0.5 \rho V_r^2$ represents dynamic pressure, b is the wingspan, and S is the wing area. The aerodynamic coefficients C_{l_T} , C_{m_T} and C_{n_T} can be obtained from wind tunnel data or flight data. Interested readers can refer to Ref. [132] to understand the specific forms of the aerodynamic coefficients.

According to Eqs. (3.28) and (3.29), Eq. (3.27) can be redefined as follows

$$\mathbf{M}^b = \mathbf{i}^b \bar{L} + \mathbf{j}^b \bar{M} + \mathbf{k}^b \bar{N} = \mathbf{i}^b (\bar{L}_f + \bar{L}_a) + \mathbf{j}^b (\bar{M}_f + \bar{M}_a) + \mathbf{k}^b (\bar{N}_f + \bar{N}_a) \quad (3.31)$$

Furthermore, Eq. (3.19) is expressed as follows

$$\begin{aligned} \mathbf{M}^b &= \frac{d}{dt} \left(\mathbf{J} \boldsymbol{\omega}_r^b + \mathbf{h}_E^b \right) + \boldsymbol{\omega}_r^b \times \left(\mathbf{J} \boldsymbol{\omega}_r^b + \mathbf{h}_E^b \right) \\ &= \underbrace{\mathbf{J} \boldsymbol{\omega}_r^b}_{\text{Constantmasssection}} + \underbrace{\mathbf{J} \boldsymbol{\omega}_r^b + \boldsymbol{\omega}_r^b \times \left(\mathbf{J} \boldsymbol{\omega}_r^b + \mathbf{h}_E^b \right)}_{\text{Variablemasssection}} \\ &= \underbrace{\mathbf{J}_0 \boldsymbol{\omega}_r^b}_{\text{(mechanicalbodysection)}} + \underbrace{\boldsymbol{\omega}_r^b \times \left(\mathbf{J}_0 \boldsymbol{\omega}_r^b + \mathbf{h}_E^b \right) + \mathbf{J}_f \dot{\boldsymbol{\omega}}_r^b + \mathbf{J}_f \boldsymbol{\omega}_r^b + \boldsymbol{\omega}_r^b \times \left(\mathbf{J}_f \boldsymbol{\omega}_r^b \right)}_{\text{(fueltanksection)}}. \end{aligned} \quad (3.32)$$

So far, we have decomposed the moment equation of the variable-mass aircraft model into two parts: the first part represents the constant-mass portion of the aircraft's mechanical body, and the second part represents the variable-mass portion due to the fuel in the tanks. The advantage of this approach is that it facilitates the analysis of the impact of fuel mass changes on the receiver's system.

Next, the moment equation represented by Eq. (3.32) will be expanded into scalar form. From Eq. (3.18), we have

$$\mathbf{L}_r^b = \begin{bmatrix} L_x \\ L_y \\ L_z \end{bmatrix} = \begin{bmatrix} p J_x - r J_{xz} + h_E \\ q J_y \\ r J_z - p J_{xz} \end{bmatrix} \quad (3.33)$$

so

$$\boldsymbol{\omega}_r^b \times \mathbf{L}_r^b = \begin{vmatrix} \mathbf{i}^b & \mathbf{j}^b & \mathbf{k}^b \\ p & q & r \\ L_x & L_y & L_z \end{vmatrix} = \mathbf{i}^b (qL_z - rL_y) + \mathbf{j}^b (rL_x - pL_z) + \mathbf{k}^b (pL_y - qL_x). \quad (3.34)$$

As a result, it can be obtained

$$\mathbf{J}\dot{\boldsymbol{\omega}}_r^b + \boldsymbol{\omega}_r^b \times (\mathbf{J}\boldsymbol{\omega}_r^b + \mathbf{h}_E^b) = \begin{bmatrix} \dot{p}J_x - \dot{r}J_{xz} + q(rJ_z - pJ_{xz}) - qrJ_y \\ \dot{q}J_y + r(pJ_x - rJ_{xz} + h_E) - p(rJ_z - pJ_{xz}) \\ -\dot{p}J_{xz} + \dot{r}J_z + pqJ_y - q(pJ_x - rJ_{xz} + h_E) \end{bmatrix}. \quad (3.35)$$

According to Eq. (3.25), one can obtain

$$\mathbf{J}_f \boldsymbol{\omega}_r = \begin{bmatrix} p\dot{J}_{x1} - r\dot{J}_{xz1} \\ q\dot{J}_{y1} \\ r\dot{J}_{z1} - p\dot{J}_{xz1} \end{bmatrix}. \quad (3.36)$$

Therefore, based on Eqs. (3.31), (3.32), (3.35), and (3.36), one can obtain

$$\begin{cases} \bar{L} = \dot{p}J_x - \dot{r}J_{xz} + qr(J_z - J_y) - pqJ_{xz} + p\dot{J}_{x1} - r\dot{J}_{xz1} \\ \bar{M} = \dot{q}J_y + pr(J_x - J_z) + (p^2 - r^2)J_{xz} + rh_E + q\dot{J}_{y1} \\ \bar{N} = \dot{r}J_z - \dot{p}J_{xz} + pq(J_y - J_x) + qrJ_{xz} - qh_E + r\dot{J}_{z1} - p\dot{J}_{xz1}. \end{cases} \quad (3.37)$$

By rearranging Eq. (3.37), the moment equations of the receiver in the body coordinate system can be obtained

$$\begin{aligned} \dot{p} &= (c_1r + c_2p)q + c_3\bar{L} + c_4(\bar{N} + h_Eq) + \kappa_1p + \kappa_2r \\ \dot{q} &= c_5pr - c_6(p^2 - r^2) + c_7(\bar{M} - h_Er) + \kappa_3q \\ \dot{r} &= (c_8p - c_2r)q + c_4\bar{L} + c_9(\bar{N} + h_Eq) + \kappa_4p - \kappa_5r. \end{aligned} \quad (3.38)$$

where the specific expressions of each coefficient are as follows

$$\begin{aligned} c_1 &= \frac{(J_y - J_z)J_z - J_{xz}^2}{\Sigma}, c_2 = \frac{(J_x - J_y + J_z)J_{xz}}{\Sigma}, c_3 = \frac{J_z}{\Sigma}, c_4 = \frac{J_{xz}}{\Sigma}, c_5 = \frac{J_z - J_x}{J_y}, c_6 = \frac{J_{xz}}{J_y}, \\ c_7 &= \frac{1}{J_y}, c_8 = \frac{J_x(J_x - J_y) + J_{xz}^2}{\Sigma}, c_9 = \frac{J_x}{\Sigma}, \kappa_1 = \frac{J_{xz1}J_{xz} - J_{x1}J_z}{\Sigma}, \kappa_2 = \frac{J_{xz1}J_z - J_{z1}J_{xz}}{\Sigma}, \kappa_3 = \frac{J_{y1}}{J_y}, \\ \kappa_4 &= \frac{J_{x1}J_{xz} - J_xJ_{xz1}}{\Sigma}, \kappa_5 = \frac{J_{x1}J_z - J_{xz1}J_{xz}}{\Sigma}. \Sigma = J_xJ_z - J_{xz}^2. \end{aligned}$$

• Motion Equations:

According to Section 2.3.1.4, there exists the following relationship between the attitude angles and the body angular velocities

$$\begin{bmatrix} \dot{\phi} \\ \dot{\theta} \\ \dot{\psi} \end{bmatrix} = \begin{bmatrix} 1 & \tan \theta \sin \phi & \tan \theta \cos \phi \\ 0 & \cos \phi & -\sin \phi \\ 0 & \sin \phi / \cos \theta & \cos \phi / \cos \theta \end{bmatrix} \begin{bmatrix} p \\ q \\ r \end{bmatrix} \quad (3.39)$$

Therefore, the equations of motion for the receiver can be obtained as follows

$$\begin{aligned} \dot{\phi} &= p + \tan \theta(q \sin \phi + r \cos \phi) \\ \dot{\theta} &= q \cos \phi - r \sin \phi \\ \dot{\psi} &= \frac{q \sin \phi + r \cos \phi}{\cos \theta} \end{aligned} \quad (3.40)$$

The equation above can also be derived from the relationship between the derivative of the direction cosine matrix and the body angular velocity, which is $\dot{\mathbf{R}}_{g/b} = \mathbf{R}_{g/b} [\boldsymbol{\omega}^b]_\times$.

• Navigation Equations:



The position of the receiver in the ground coordinate system is represented as $\mathbf{p}_r^g \triangleq \begin{bmatrix} x_r & y_r & h_r \end{bmatrix}^T$. Based on the relationship between position and velocity, one can obtain the velocity vector in the ground coordinate system as $\mathbf{v}_r^g = \dot{\mathbf{p}}_r^g = \begin{bmatrix} \dot{x}_r & \dot{y}_r & \dot{h}_r \end{bmatrix}^T$. In the body coordinate system, the velocity vector of the receiver is represented as $\mathbf{v}_r^b \triangleq \begin{bmatrix} u_r & v_r & w_r \end{bmatrix}^T$. By using the transformation relationship between the ground coordinate system and the body coordinate system, which is $\mathbf{v}_r^g = \mathbf{R}_{g/b}(\theta, \psi, \phi) \mathbf{v}_r^b$, one can derive the navigation equations for the receiver as follows

$$\begin{aligned}\dot{x}_r &= u_r \cos \psi \cos \theta + v_r (\cos \psi \sin \theta \sin \phi - \sin \psi \cos \phi) + w_r (\cos \psi \sin \theta \cos \phi + \sin \psi \sin \phi) \\ \dot{y}_r &= u_r \sin \psi \cos \theta + v_r (\sin \psi \sin \theta \sin \phi + \cos \psi \cos \phi) + w_r (\sin \psi \sin \theta \cos \phi - \cos \psi \sin \theta) \\ \dot{h}_r &= u_r \sin \theta - v_r \cos \theta \sin \phi - w_r \cos \theta \cos \phi.\end{aligned}\tag{3.41}$$

Until now, the kinematic and dynamic equations of the receiver are established. The nonlinear model of the receiver consists of a total of twelve differential equations, including force equations, moment equations, motion equations, and navigation equations, given by Eqs. (3.15), (3.38), (3.40), and (3.41). Based on these equations, receiver 6-DOF motion equations are presented as follows:

Force equations

$$\begin{aligned}\dot{u}_r &= rv_r - qw_r - g \sin \theta + \frac{1}{m} (\bar{X} + F_T) - \frac{\dot{m}u_r}{m} \\ \dot{v}_r &= pw_r - ru_r + g \sin \phi \cos \theta + \frac{1}{m} \bar{Y} - \frac{\dot{m}v_r}{m} \\ \dot{w}_r &= qu_r - pv_r + g \cos \phi \cos \theta + \frac{1}{m} \bar{Z} - \frac{\dot{m}w_r}{m}\end{aligned}\tag{3.42}$$

Moment equations

$$\begin{aligned}\dot{p} &= (c_1 r + c_2 p) q + c_3 \bar{L} + c_4 (\bar{N} + h_E q) + \kappa_1 p + \kappa_2 r \\ \dot{q} &= c_5 pr - c_6 (p^2 - r^2) + c_7 (\bar{M} - h_E r) + \kappa_3 q \\ \dot{r} &= (c_8 p - c_2 r) q + c_4 \bar{L} + c_9 (\bar{N} + h_E q) + \kappa_4 p - \kappa_5 r\end{aligned}\tag{3.43}$$

Motion equations

$$\begin{aligned}\dot{\phi} &= p + \tan \theta (q \sin \phi + r \cos \phi) \\ \dot{\theta} &= q \cos \phi - r \sin \phi \\ \dot{\psi} &= \frac{q \sin \phi + r \cos \phi}{\cos \theta}\end{aligned}\tag{3.44}$$

Navigation equations

$$\begin{aligned}\dot{x}_r &= u_r \cos \psi \cos \theta + v_r (\cos \psi \sin \theta \sin \phi - \sin \psi \cos \phi) + w_r (\cos \psi \sin \theta \cos \phi + \sin \psi \sin \phi) \\ \dot{y}_r &= u_r \sin \psi \cos \theta + v_r (\sin \psi \sin \theta \sin \phi + \cos \psi \cos \phi) + w_r (\sin \psi \sin \theta \cos \phi - \cos \psi \sin \theta) \\ \dot{h}_r &= u_r \sin \theta - v_r \cos \theta \sin \phi - w_r \cos \theta \cos \phi.\end{aligned}\tag{3.45}$$

Instead of $u_r, v_r, w_r, V_r, \alpha, \beta$ are also usually used to represent the force equations, where V_r is the airspeed magnitude of the receiver, and α and β represent the angle of attack and sideslip



angle, respectively. This is because in practical aircraft, V_r , α and β can be directly measured, and they have a more direct relationship with aerodynamics, moments, and navigation. Ignoring wind disturbances, from Section 1.3.1.2, we know that there exists the following relationship among the velocity vector $\mathbf{v}_r^b \triangleq \begin{bmatrix} u_r & v_r & w_r \end{bmatrix}^T$, airspeed V_r , angle of attack α , and sideslip angle β

$$\begin{aligned} u_r &= V_r \cos \alpha \cos \beta \\ v_r &= V_r \sin \beta \\ w_r &= V_r \sin \alpha \cos \beta \end{aligned} \quad (3.46)$$

Taking its derivative, one can obtain

$$\begin{aligned} \dot{u}_r &= \dot{V}_r \cos \alpha \cos \beta - \dot{\alpha} \cdot V_r \sin \alpha \cos \beta - \dot{\beta} \cdot V_r \cos \alpha \sin \beta \\ \dot{v}_r &= \dot{V}_r \sin \beta + \dot{\beta} \cdot V_r \cos \beta \\ \dot{w}_r &= \dot{V}_r \sin \alpha \cos \beta + \dot{\alpha} \cdot V_r \cos \alpha \cos \beta - \dot{\beta} \cdot V_r \sin \alpha \sin \beta. \end{aligned} \quad (3.47)$$

Simultaneously, the following relationships exist

$$\begin{aligned} V_r &= \|\mathbf{v}_r\| = \sqrt{u_r^2 + v_r^2 + w_r^2} \\ \alpha &= \tan^{-1} \left(\frac{w_r}{u_r} \right) \\ \beta &= \sin^{-1} \left(\frac{v_r}{V_r} \right) \end{aligned} \quad (3.48)$$

Taking its derivative, one can obtain

$$\begin{aligned} \dot{V}_r &= \frac{u_r \dot{u}_r + v_r \dot{v}_r + w_r \dot{w}_r}{V_r} \\ \dot{\alpha} &= \frac{u_r \dot{w}_r - w_r \dot{u}_r}{u_r^2 + w_r^2} \\ \dot{\beta} &= \frac{V_r \dot{v}_r - v_r \dot{V}_r}{V_r^2 \sqrt{1 - \left(\frac{v_r}{V_r} \right)^2}} \end{aligned} \quad (3.49)$$

The process of calculating \dot{V}_r , $\dot{\alpha}$, and $\dot{\beta}$ is as follows: First, use Eq. (3.42) to calculate \dot{u}_r , \dot{v}_r , and \dot{w}_r . Then, use the current values of V_r , α , and β (obtained from instruments) to calculate u_r , v_r , and w_r using Eq. (3.46). Finally, substitute the obtained u_r , v_r , and w_r along with the current flight speed V_r into Eq. (3.49) to get \dot{V}_r , $\dot{\alpha}$, and $\dot{\beta}$. This method avoids the lengthy nonlinear calculation process when directly computing \dot{V}_r , $\dot{\alpha}$, and $\dot{\beta}$ in the airflow coordinate system. It also allows the aircraft's dimensionless aerodynamic coefficients to be used directly in the body coordinate system without the need to convert the coefficients to the airflow coordinate system. In general, the nonlinear model of the receiver consists of Eqs. (3.42), (3.43), (3.44), and (3.45).

In practical applications, Eq. (3.49) is commonly used instead of Eq. (3.42). The new nonlinear model of the receiver consists of Eqs. (3.43), (3.44), (3.45), and (3.49), represented as a nonlinear state equation

$$\dot{\mathbf{x}}_r = \mathbf{f}(\mathbf{x}_r, \mathbf{u}_r) \quad (3.50)$$

where the state variables are represented by $\mathbf{x}_r \triangleq \begin{bmatrix} x_r & y_r & h_r & \phi & \theta & \psi & V_r & \alpha & \beta & p & q & r \end{bmatrix}^T$,

which includes position, attitude angles, aerodynamic angles, and angular velocities. The control inputs are represented by $\mathbf{u}_r \triangleq \begin{bmatrix} \delta_t & \delta_e & \delta_a & \delta_r \end{bmatrix}^T$, which includes throttle, elevator, aileron, and rudder operations.

3.1.2 Nonlinear Model Decoupling and Linearization

3.1.2.1 Decoupling

For the receiver, during the refueling process, it maintains a slightly pitched-up level flight attitude. This state satisfies horizontal no sideslip flight condition, which means that the roll angle and sideslip angle satisfy $\phi = \beta \equiv 0$, and the angle of attack α , yaw angle γ , and pitch angle θ satisfy $\theta = \gamma + \alpha$, while $\dot{\theta} = q$ simultaneously.

In the body coordinate system, gravity is given by Eq. (3.13). When transformed into the airflow coordinate system, it can be obtained

$$\begin{bmatrix} G_x^w \\ G_y^w \\ G_z^w \end{bmatrix} = \begin{bmatrix} mg(-\cos \alpha \cos \beta \sin \theta + \sin \beta \sin \phi \cos \theta + \sin \alpha \cos \beta \cos \phi \cos \theta) \\ mg(\cos \alpha \sin \beta \sin \theta + \cos \beta \sin \phi \cos \theta - \sin \alpha \sin \beta \cos \phi \cos \theta) \\ mg(\sin \alpha \sin \theta + \cos \alpha \cos \phi \cos \theta) \end{bmatrix} \quad (3.51)$$

Considering in the airflow coordinate system, the aerodynamic lift of the receiver is denoted as L , the aerodynamic drag as D , and the side force as Y . According to the transformation relationship between the body coordinate system and the airflow coordinate system, one have

$$\begin{bmatrix} \bar{X} \\ \bar{Y} \\ \bar{Z} \end{bmatrix}_{\text{body}} = \begin{bmatrix} F_T \\ 0 \\ 0 \end{bmatrix}_{\text{body}} + \mathbf{R}_{b/w}(\alpha, \beta) \begin{bmatrix} -D \\ Y \\ -L \end{bmatrix}_{\text{wind}} \quad (3.52)$$

which can be expanded as

$$\begin{aligned} \bar{X} &= F_T + L \sin \alpha - Y \cos \alpha \sin \beta - D \cos \alpha \cos \beta \\ \bar{Y} &= Y \cos \beta - D \sin \beta \\ \bar{Z} &= -L \cos \alpha - Y \sin \alpha \sin \beta - D \sin \alpha \cos \beta \end{aligned} \quad (3.53)$$

Therefore, based on Eqs. (3.47), (3.51), and (3.53), Eq. (3.42) can be transformed into

$$\begin{aligned} m\dot{V}_r &= F_T \cos \alpha \cos \beta - D + G_x^w - \dot{m}V_r \\ mV_r \dot{\beta} &= -F_T \cos \alpha \sin \beta + Y - mV_r (-p \sin \alpha + r \cos \alpha) + G_y^w \\ mV_r \cos \beta \dot{\alpha} &= -F_T \sin \alpha - L + mV_r (-p \cos \alpha \sin \beta + q \cos \beta - r \sin \alpha \sin \beta) + G_z^w \end{aligned} \quad (3.54)$$

By using the condition $p = r \equiv 0$, the second equation in the moment equation group (3.43) can be simplified to

$$\dot{q} = c_7 \bar{M} - \kappa_3 q. \quad (3.55)$$

Combining with Eq. (3.54) and utilizing the horizontal no sideslip flight condition $\phi = \beta \equiv 0$ and $p = r \equiv 0$, the motion equations of the receiver can be decoupled into longitudinal motion that does not depend on lateral-directional states.

(1) The longitudinal motion equations are as follows

$$\begin{cases} m\dot{V}_r = F_T \cos \alpha - D - mg (\cos \alpha \sin \theta - \sin \alpha \cos \theta) - \dot{m}V_r \\ mV_r \dot{\alpha} = -F_T \sin \alpha - L + mV_r q + mg (\sin \alpha \sin \theta + \cos \alpha \cos \theta) \\ \dot{\theta} = q \\ \dot{q} = c_7 \bar{M} - \kappa_3 q \end{cases} \quad (3.56)$$

where the state variable for longitudinal motion is represented by $\mathbf{x}_{\text{long}} \triangleq \begin{bmatrix} V_r & \alpha & \theta & q \end{bmatrix}^T$.

(2) The lateral-directional equations are as follows

$$\begin{cases} mV_r \dot{\beta} = \bar{Y} - mV_r (-p \sin \alpha + r \cos \alpha) \\ \dot{\phi} = p + \tan \theta (q \sin \phi + r \cos \phi) \\ \dot{\psi} = \frac{q \sin \phi + r \cos \phi}{\cos \theta} \\ \dot{p} = (c_1 r + c_2 p) q + c_3 \bar{L} + c_4 (\bar{N} + h_E q) + \kappa_1 p + \kappa_2 r \\ \dot{r} = (c_8 p - c_2 r) q + c_4 \bar{L} + c_9 (\bar{N} + h_E q) + \kappa_4 p - \kappa_5 r \end{cases} \quad (3.57)$$

where the state variable for lateral motion is represented by $\mathbf{x}_{\text{lat}} \triangleq \begin{bmatrix} \beta & \phi & \psi & p & r \end{bmatrix}^T$.

Since the longitudinal motion equation group does not depend on the lateral-directional states, the longitudinal motion state $\begin{bmatrix} V_r & \alpha & \theta & q \end{bmatrix}^T$ can be directly calculated using Eq. (3.56). Then, combining with Eq. (3.57), the lateral motion state $\begin{bmatrix} \beta & \phi & \psi & p & r \end{bmatrix}^T$ can be calculated. By using the navigation equation group (3.45), all the state variables of the receiver's motion $\mathbf{x}_r \triangleq \begin{bmatrix} x & y & h & \phi & \theta & \psi & V_r & \alpha & \beta & p & q & r \end{bmatrix}^T$ can be solved.

3.1.2.2 Trimming

Before linearizing the nonlinear model of the receiver, trim analysis should be considered. The purpose of trim analysis is to balance the longitudinal moment and throttle thrust of the receiver in a certain flight state, obtaining the equilibrium point of the nonlinear model as a reference for linearization. Trim analysis serves as the foundation for linearization. Variations in flight speed, changes in the receiver's center of gravity, modifications in aerodynamic shape, and other factors can cause imbalances in the receiver's moments, affecting normal flight. By performing trim analysis, one can determine the necessary control surface deflections and thrust values to balance the moments and throttle thrust at the equilibrium point for a specific flight state. These values can then be used as input compensation in the controller, effectively eliminating imbalances in forces and moments.

Trim analysis can be divided into different categories based on the flight state, such as straight and level flight trim, hovering trim, etc. The trim analysis for different categories are basically the same. The general approach for trim analysis involves establishing a group of equations based on balances of force and moment and solving for the required control surface deflections and throttle settings. During trim, the linear acceleration and angular acceleration of

the receiver are both zero, meaning they satisfy the following conditions

$$\dot{p} = \dot{q} = \dot{r} = \dot{u} = \dot{v} = \dot{w} = 0 \quad (3.58)$$

or

$$\dot{p} = \dot{q} = \dot{r} = \dot{V}_r = \dot{\alpha} = \dot{\beta} = 0. \quad (3.59)$$

Trim analysis refers to the process of solving the six-degree-of-freedom motion equations of the receiver under specific conditions to determine the input and control variables. Typically, trim conditions may involve non-constant system states, such as during a wing-level steady climbing flight where the change rate of flight altitude \dot{h} is constant, and the flight altitude h increases linearly. Therefore, in general, trim conditions can be represented as follows

$$\dot{\mathbf{x}}_r^* = \mathbf{f}(\mathbf{x}_r^*, \mathbf{u}_r^*) \quad (3.60)$$

where \mathbf{x}_r^* represents the trim state, and \mathbf{u}_r^* represents the trim input.

The trim state and trim input of the receiver can be calculated when the receiver simultaneously satisfies the following conditions:

- (1) Maintaining a constant flight speed V_r^* .
- (2) Maintaining a constant flight path angle γ^* during climbing.
- (3) Maintaining a constant turning radius R^* during turns. The parameters V_r^* , γ^* , and R^* are the input variables used in calculating the trim conditions. It is assumed that $R^* \geq R_{\min}$, where R_{\min} is the minimum turning radius of the receiver. The most common cases for trim calculation are as follows:

1. Trim conditions for level flight at constant altitude, where $\gamma^* = 0$ and $R^* = \infty$.
2. Trim conditions for flight at constant altitude and turning with a radius R^* , where $\gamma^* = 0$.

The calculation of the trim state \mathbf{x}_r^* and trim input \mathbf{u}_r^* is typically done by using numerical methods. A trim algorithm is provided in Ref. [135] for readers to refer to.

3.1.2.3 Linearization

For the nonlinear model of the receiver $\dot{\mathbf{x}}_r = \mathbf{f}(\mathbf{x}_r, \mathbf{u}_r)$, at the trim point $(\mathbf{x}_r^*, \mathbf{u}_r^*)$, it satisfies

$$\dot{\mathbf{x}}_r^* = \mathbf{f}(\mathbf{x}_r^*, \mathbf{u}_r^*) = 0 \quad (3.61)$$

Setting $\tilde{\mathbf{x}}_r \triangleq \mathbf{x}_r - \mathbf{x}_r^*$ and $\tilde{\mathbf{u}}_r = \mathbf{u}_r - \mathbf{u}_r^*$, one have

$$\begin{aligned} \dot{\tilde{\mathbf{x}}}_r &\triangleq \dot{\mathbf{x}}_r - \dot{\mathbf{x}}_r^* \\ &= \mathbf{f}(\mathbf{x}_r, \mathbf{u}_r) - \mathbf{f}(\mathbf{x}_r^*, \mathbf{u}_r^*) \\ &= \mathbf{f}(\mathbf{x}_r + \mathbf{x}_r^* - \mathbf{x}_r^*, \mathbf{u}_r + \mathbf{u}_r^* - \mathbf{u}_r^*) - \mathbf{f}(\mathbf{x}_r^*, \mathbf{u}_r^*) \\ &= \mathbf{f}(\mathbf{x}_r^* + \tilde{\mathbf{x}}_r, \mathbf{u}_r^* + \tilde{\mathbf{u}}_r) - \mathbf{f}(\mathbf{x}_r^*, \mathbf{u}_r^*) \end{aligned}$$

At the trim point, using the Taylor series expansion and retaining only the first-order terms, one have

$$\begin{aligned}\dot{\tilde{\mathbf{x}}}_r &= \mathbf{f}(\mathbf{x}_r^*, \mathbf{u}_r^*) + \frac{\partial \mathbf{f}(\mathbf{x}_r^*, \mathbf{u}_r^*)}{\partial \mathbf{x}_r} \tilde{\mathbf{x}}_r + \frac{\partial \mathbf{f}(\mathbf{x}_r^*, \mathbf{u}_r^*)}{\partial \mathbf{u}_r} \tilde{\mathbf{u}}_r + H.O.T - \mathbf{f}(\mathbf{x}_r^*, \mathbf{u}_r^*) \\ &\approx \frac{\partial \mathbf{f}(\mathbf{x}_r^*, \mathbf{u}_r^*)}{\partial \mathbf{x}} \tilde{\mathbf{x}}_r + \frac{\partial \mathbf{f}(\mathbf{x}_r^*, \mathbf{u}_r^*)}{\partial \mathbf{u}} \tilde{\mathbf{u}}_r\end{aligned}\quad (3.62)$$

Therefore, by calculating $\partial \mathbf{f} / \partial \mathbf{x}_r$ and $\partial \mathbf{f} / \partial \mathbf{u}_r$, the linearized longitudinal and lateral-directional motion equations can be obtained.

(1) Linearization of longitudinal motion equations

Based on the previous content, the state variables for longitudinal motion are represented as $\mathbf{x}_{rlong} \triangleq \begin{bmatrix} V_r & \alpha & \theta & q \end{bmatrix}^T$, and the control inputs are represented as $\mathbf{u}_{rlong} \triangleq \begin{bmatrix} \delta_e & \delta_t \end{bmatrix}^T$. The trim point for longitudinal state can be denoted as $\mathbf{x}_{rlong}^* \triangleq \begin{bmatrix} V_r^* & \alpha^* & \theta^* & q^* \end{bmatrix}^T$, and the corresponding trim input is $\mathbf{u}_{rlong}^* \triangleq \begin{bmatrix} \delta_e^* & \delta_t^* \end{bmatrix}^T$. According to Eq. (3.62), the longitudinal motion can be linearized as follows

$$\dot{\tilde{\mathbf{x}}}_{rlong} = \mathbf{A}_{rlong} \tilde{\mathbf{x}}_{rlong} + \mathbf{B}_{rlong} \tilde{\mathbf{u}}_{rlong} \quad (3.63)$$

where $\mathbf{A}_{rlong} \in \mathbb{R}^{4 \times 4}$, $\mathbf{B}_{rlong} \in \mathbb{R}^{4 \times 2}$.

The Jacobian matrix for the longitudinal motion equations (3.56) is as follows

$$\frac{\partial \mathbf{f}_{rlong}}{\partial \mathbf{x}_{rlong}} = \begin{bmatrix} \frac{\partial \dot{V}_r}{\partial V_r} & \frac{\partial \dot{V}_r}{\partial \alpha} & \frac{\partial \dot{V}_r}{\partial \theta} & \frac{\partial \dot{V}_r}{\partial q} \\ \frac{\partial \dot{\alpha}}{\partial V_r} & \frac{\partial \dot{\alpha}}{\partial \alpha} & \frac{\partial \dot{\alpha}}{\partial \theta} & \frac{\partial \dot{\alpha}}{\partial q} \\ \frac{\partial \dot{\theta}}{\partial V_r} & \frac{\partial \dot{\theta}}{\partial \alpha} & \frac{\partial \dot{\theta}}{\partial \theta} & \frac{\partial \dot{\theta}}{\partial q} \\ \frac{\partial \dot{q}}{\partial V_r} & \frac{\partial \dot{q}}{\partial \alpha} & \frac{\partial \dot{q}}{\partial \theta} & \frac{\partial \dot{q}}{\partial q} \end{bmatrix}, \quad \frac{\partial \mathbf{f}_{rlong}}{\partial \mathbf{u}_{rlong}} = \begin{bmatrix} \frac{\partial \dot{V}_r}{\partial \delta_e} & \frac{\partial \dot{V}_r}{\partial \delta_t} \\ \frac{\partial \dot{\alpha}}{\partial \delta_e} & \frac{\partial \dot{\alpha}}{\partial \delta_t} \\ \frac{\partial \dot{\theta}}{\partial \delta_e} & \frac{\partial \dot{\theta}}{\partial \delta_t} \\ \frac{\partial \dot{q}}{\partial \delta_e} & \frac{\partial \dot{q}}{\partial \delta_t} \end{bmatrix}$$

Calculate derivatives to obtain the linearized lateral-directional state-space equations

$$\begin{bmatrix} \dot{\tilde{V}}_r \\ \dot{\tilde{\alpha}} \\ \dot{\tilde{\theta}} \\ \dot{\tilde{q}} \end{bmatrix} = \begin{bmatrix} a_1 & a_2 & -g \cos(\theta^* - \alpha^*) & -\frac{1}{m} D_q \\ a_3 & a_4 & -\frac{1}{V_r^*} g \sin(\theta^* - \alpha^*) & 1 - \frac{1}{m V_r^*} L_q \\ 0 & 0 & 0 & 1 \\ M_V & M_\alpha & 0 & M_q - \kappa_3 \end{bmatrix} \begin{bmatrix} \tilde{V}_r \\ \tilde{\alpha} \\ \tilde{\theta} \\ \tilde{q} \end{bmatrix} + \begin{bmatrix} -\frac{1}{m} D_{\delta_e} & \frac{1}{m} T_{\delta_t} \cos \alpha^* \\ -\frac{1}{m V_r^*} L_{\delta_e} & -\frac{1}{m V_r^*} T_{\delta_t} \sin \alpha^* \\ 0 & 0 \\ M_{\delta_e} & M_{\delta_t} \end{bmatrix} \begin{bmatrix} \tilde{\delta}_e \\ \tilde{\delta}_t \end{bmatrix} \quad (3.64)$$

where $T_V = \frac{\partial F_T}{\partial V_r}$, $T_{\delta_t} = \frac{\partial T}{\partial \delta_t}$, $D_V = \frac{\partial D}{\partial V_r}$, $D_\alpha = \frac{\partial D}{\partial \alpha}$, $D_q = \frac{\partial D}{\partial q}$, $D_{\delta_e} = \frac{\partial D}{\partial \delta_e}$, $L_V = \frac{\partial L}{\partial V_r}$, $L_\alpha = \frac{\partial L}{\partial \alpha}$, $L_q = \frac{\partial L}{\partial q}$, $L_{\delta_e} = \frac{\partial L}{\partial \delta_e}$, $M_V = \frac{1}{J_{y0}} \frac{\partial M}{\partial V_r}$, $M_\alpha = \frac{1}{J_{y0}} \frac{\partial M}{\partial \alpha}$, $M_q = \frac{1}{J_{y0}} \frac{\partial M}{\partial q}$, $M_{\delta_e} = \frac{1}{J_{y0}} \frac{\partial M}{\partial \delta_e}$, $M_{\delta_t} = \frac{1}{J_{y0}} \frac{\partial M}{\partial \delta_t}$.

(2) Linearization of lateral-directional motion equations

Based on the previous content, the state variables for lateral-directional motion are represented as $\mathbf{x}_{rlat} \triangleq \begin{bmatrix} \beta & \phi & \psi & p & r \end{bmatrix}^T$, and the control inputs are represented as $\mathbf{u}_{rlat} \triangleq \begin{bmatrix} \delta_a & \delta_r \end{bmatrix}^T$. The trim point for lateral-directional state can be denoted as $\mathbf{x}_{rlat}^* \triangleq \begin{bmatrix} \beta^* & \phi^* & \psi^* & p^* & r^* \end{bmatrix}^T$,

and the corresponding trim input is $\mathbf{u}_{\text{rlat}}^* \triangleq \begin{bmatrix} \delta_a^* & \delta_r^* \end{bmatrix}^\top$. According to Eq. (3.62), the lateral-directional motion can be linearized as follows

$$\dot{\tilde{\mathbf{x}}}_{\text{rlat}} = \mathbf{A}_{\text{rlat}} \tilde{\mathbf{x}}_{\text{rlat}} + \mathbf{B}_{\text{rlat}} \tilde{\mathbf{u}}_{\text{rlat}} \quad (3.65)$$

where $\mathbf{A}_{\text{rlat}} \in \mathbb{R}^{5 \times 5}$, $\mathbf{B}_{\text{rlat}} \in \mathbb{R}^{5 \times 2}$.

The Jacobian matrix for the lateral-directional motion equations (3.57) is as follows

$$\frac{\partial \mathbf{f}_{\text{rlat}}}{\partial \mathbf{x}_{\text{rlat}}} = \begin{bmatrix} \frac{\partial \dot{\beta}}{\partial \beta} & \frac{\partial \dot{\beta}}{\partial \phi} & \frac{\partial \dot{\beta}}{\partial \psi} & \frac{\partial \dot{\beta}}{\partial p} & \frac{\partial \dot{\beta}}{\partial r} \\ \frac{\partial \dot{\phi}}{\partial \beta} & \frac{\partial \dot{\phi}}{\partial \phi} & \frac{\partial \dot{\phi}}{\partial \psi} & \frac{\partial \dot{\phi}}{\partial p} & \frac{\partial \dot{\phi}}{\partial r} \\ \frac{\partial \dot{\psi}}{\partial \beta} & \frac{\partial \dot{\psi}}{\partial \phi} & \frac{\partial \dot{\psi}}{\partial \psi} & \frac{\partial \dot{\psi}}{\partial p} & \frac{\partial \dot{\psi}}{\partial r} \\ \frac{\partial \dot{p}}{\partial \beta} & \frac{\partial \dot{p}}{\partial \phi} & \frac{\partial \dot{p}}{\partial \psi} & \frac{\partial \dot{p}}{\partial p} & \frac{\partial \dot{p}}{\partial r} \\ \frac{\partial \dot{r}}{\partial \beta} & \frac{\partial \dot{r}}{\partial \phi} & \frac{\partial \dot{r}}{\partial \psi} & \frac{\partial \dot{r}}{\partial p} & \frac{\partial \dot{r}}{\partial r} \end{bmatrix}, \frac{\partial \mathbf{f}_{\text{rlat}}}{\partial \mathbf{u}_{\text{rlat}}} = \begin{bmatrix} \frac{\partial \dot{\beta}}{\partial \delta_a} & \frac{\partial \dot{\beta}}{\partial \delta_r} \\ \frac{\partial \dot{\phi}}{\partial \delta_a} & \frac{\partial \dot{\phi}}{\partial \delta_r} \\ \frac{\partial \dot{\psi}}{\partial \delta_a} & \frac{\partial \dot{\psi}}{\partial \delta_r} \\ \frac{\partial \dot{p}}{\partial \delta_a} & \frac{\partial \dot{p}}{\partial \delta_r} \\ \frac{\partial \dot{r}}{\partial \delta_a} & \frac{\partial \dot{r}}{\partial \delta_r} \end{bmatrix}$$

Calculate derivatives to obtain the linearized lateral-directional state-space equations

$$\begin{bmatrix} \dot{\tilde{\beta}} \\ \dot{\tilde{\phi}} \\ \dot{\tilde{\psi}} \\ \dot{\tilde{p}} \\ \dot{\tilde{r}} \end{bmatrix} = \begin{bmatrix} Y_\beta & g \cos \theta^* / V_r & 0 & Y_p + \sin \alpha^* & Y_r - \cos \alpha^* \\ 0 & q^* \cos \phi^* \tan \theta^* - r^* \sin \phi^* \tan \theta^* & 0 & 1 & \cos \phi^* \tan \theta^* \\ 0 & q^* \cos \phi^* \sec \theta^* + r^* \sin \phi^* \sec \theta^* & 0 & 0 & \cos \phi^* \sec \theta^* \\ c_3 \bar{L}_\beta + c_4 \bar{N}_\beta & 0 & 0 & b_1 & b_2 \\ c_4 \bar{L}_\beta + c_9 \bar{N}_\beta & 0 & 0 & b_3 & b_4 \end{bmatrix} \begin{bmatrix} \tilde{\beta} \\ \tilde{\phi} \\ \tilde{\psi} \\ \tilde{p} \\ \tilde{r} \end{bmatrix} + \begin{bmatrix} Y_{\delta_a} & Y_{\delta_r} \\ 0 & 0 \\ 0 & 0 \\ c_3 \bar{L}_{\delta_a} + c_4 \bar{N}_{\delta_a} & c_3 \bar{L}_{\delta_r} + c_4 \bar{N}_{\delta_r} \\ c_4 \bar{L}_{\delta_a} + c_9 \bar{N}_{\delta_a} & c_4 \bar{L}_{\delta_r} + c_9 \bar{N}_{\delta_r} \end{bmatrix} \begin{bmatrix} \tilde{\delta}_a \\ \tilde{\delta}_r \end{bmatrix} \quad (3.66)$$

where $Y_\beta = \frac{1}{mV_r} \frac{\partial \bar{Y}}{\partial \beta}$, $Y_p = \frac{1}{mV_r} \frac{\partial \bar{Y}}{\partial p}$, $Y_r = \frac{1}{mV_r} \frac{\partial \bar{Y}}{\partial r}$, $Y_{\delta_a} = \frac{1}{mV_r} \frac{\partial \bar{Y}}{\partial \delta_a}$, $Y_{\delta_r} = \frac{1}{mV_r} \frac{\partial \bar{Y}}{\partial \delta_r}$, $\bar{L}_\beta = \frac{\partial \bar{L}}{\partial \beta}$, $\bar{L}_p = \frac{\partial \bar{L}}{\partial p}$, $\bar{L}_r = \frac{\partial \bar{L}}{\partial r}$, $\bar{L}_{\delta_a} = \frac{\partial \bar{L}}{\partial \delta_a}$, $\bar{L}_{\delta_r} = \frac{\partial \bar{L}}{\partial \delta_r}$, $\bar{N}_\beta = \frac{\partial \bar{N}}{\partial \beta}$, $\bar{N}_p = \frac{\partial \bar{N}}{\partial p}$, $\bar{N}_r = \frac{\partial \bar{N}}{\partial r}$, $\bar{N}_{\delta_a} = \frac{\partial \bar{N}}{\partial \delta_a}$, $\bar{N}_{\delta_r} = \frac{\partial \bar{N}}{\partial \delta_r}$.

3.1.3 Involvement of wind disturbances

The impact of wind field disturbances will be analyzed in the following. Wind field disturbances essentially cause additional perturbations to the state variables. Moreover, wind field disturbances come from various sources, such as atmospheric turbulence, the downwash of the tanker, wind gust, wind shear, etc. In order to facilitate the superposition of these wind fields, they need to be unified in a single coordinate system. According to the description in Chapter 3 about wind disturbances, the total wind field includes three linear velocity components and three angular velocity components. In the ground coordinate system, it can be represented as $\mathbf{w}^g = [u_w^g \ v_w^g \ w_w^g \ p_w^g \ q_w^g \ r_w^g]^\top$. The first three components represent the equivalent velocity of the wind field, and the last three components represent the equivalent rotational angular velocity.

First, let us consider the coordinate transformation. Airspeed refers to the relative airflow velocity around the aircraft with respect to the body coordinate system. Therefore, the ground-based disturbed wind field can be projected onto the body coordinate system of the tanker after coordinate transformation, denoted as $\mathbf{w}^b = \begin{bmatrix} u_w^b & v_w^b & w_w^b & p_w^b & q_w^b & r_w^b \end{bmatrix}^T = \mathbf{C}_{b/g} \mathbf{w}^g$. Specifically, $\mathbf{C}_{b/g}$ is the rotation matrix. Since \mathbf{w}^g is a six-dimensional vector, its projection transformation matrix is given by

$$\mathbf{C}_{b/g} = \begin{bmatrix} \mathbf{R}_{b/g} & \mathbf{0} \\ \mathbf{0} & \mathbf{R}_{b/g} \end{bmatrix} \quad (3.67)$$

where $\mathbf{R}_{b/g}$ is the transformation matrix from the ground coordinate system to the body coordinate system, and its specific form is given by Eq. (2.19). Secondly, in order to incorporate the total disturbed wind field \mathbf{w}^b into the state equation, it is necessary to transform the components of velocity from $\begin{bmatrix} u_w^b & v_w^b & w_w^b \end{bmatrix}^T \rightarrow \begin{bmatrix} V_w & \alpha_w & \beta_w \end{bmatrix}^T$ (airspeed, angle of attack, and sideslip angle) according to Eq. (3.48).

In the equilibrium flight state of level and constant-speed flight, assuming that the aircraft moves along the ground axis $o_g x_g$, the flight state satisfies the following relationships: $\theta \approx \alpha^*, \psi = 0, \phi = 0, \beta = 0$, where α^* represents the angle of attack in the equilibrium state. In this case, the transformation matrix from the ground coordinate system to the body coordinate system is simplified as follows

$$\mathbf{R}_{b/g} \approx \mathbf{R}_{b/g}^* = \begin{bmatrix} \cos \alpha^* & 0 & \sin \alpha^* \\ 0 & 1 & 0 \\ \sin \alpha^* & 0 & \cos \alpha^* \end{bmatrix}. \quad (3.68)$$

If the aerial refueling in a horizontal steady flight with very small angle of attack is considered, the model can be simplified by taking $\mathbf{R}_{b/g} \approx \mathbf{I}_3$, where \mathbf{I}_3 is the three-dimensional identity matrix. This is equivalent to applying the wind field perturbations directly in the body coordinate system.

When the receiver is not subjected to wind field perturbations, the velocity vector in the body coordinate system is represented as $\mathbf{v}_r \triangleq \begin{bmatrix} u_r & v_r & w_r \end{bmatrix}^T$. For simplicity, the wind disturbance in the body coordinate system is expressed as $\mathbf{w}^b = \begin{bmatrix} u_w & v_w & w_w & p_w & q_w & r_w \end{bmatrix}^T$. Considering the addition of wind field perturbations, $\begin{bmatrix} u_r & v_r & w_r \end{bmatrix}^T \rightarrow \begin{bmatrix} u_r + u_w & v_r + v_w & w_r + w_w \end{bmatrix}^T$, and the state variables change to $\begin{bmatrix} V_r + V_w & \alpha + \alpha_w & \beta + \beta_w \end{bmatrix}^T$. Generally, we have $V_r \approx u_r$, $u_r \gg v_r$, and $u_r \gg w_r$. Therefore

$$\begin{aligned} V_r + V_w &= \sqrt{(u_r + u_w)^2 + (v_r + v_w)^2 + (w_r + w_w)^2} \\ &\approx \sqrt{u_r^2 + v_r^2 + w_r^2 + 2u_r u_w} \\ &\approx V_r \sqrt{1 + 2 \frac{u_w}{V_r}} \approx V_r \left(1 + \frac{1}{2} \cdot 2 \frac{u_w}{V_r}\right) \\ &= V_r + u_w. \end{aligned} \quad (3.69)$$

Therefore, $V_w \approx u_w$ can be obtained. Similarly, one have $\alpha_w \approx w_w/V_r$, $\beta_w \approx v_w/V_r$. Thus

$$\begin{bmatrix} V_w \\ \alpha_w \\ \beta_w \end{bmatrix} \approx \begin{bmatrix} 1 & 0 & 0 \\ 0 & 0 & 1/V_r \\ 0 & 1/V_r & 0 \end{bmatrix} \begin{bmatrix} u_w \\ v_w \\ w_w \end{bmatrix}. \quad (3.70)$$

Therefore, the state increments caused by wind disturbance

$$\Delta \mathbf{x}_r \triangleq \begin{bmatrix} 0 & 0 & 0 & 0 & 0 & 0 & V_w & \alpha_w & \beta_w & p_w & q_w & r_w \end{bmatrix}^T \quad (3.71)$$

can be obtained. By substituting it into the system's state equations, it can be obtained

$$\dot{\mathbf{x}}_r = \mathbf{A}(\mathbf{x}_r + \Delta \mathbf{x}_r) + \mathbf{B}\mathbf{u}_r = \mathbf{A}\mathbf{x}_r + \mathbf{B}\mathbf{u}_r + \mathbf{A}\Delta \mathbf{x}_r \quad (3.72)$$

where $\mathbf{A} \in \mathbb{R}^{12 \times 12}$ is the state gain matrix of the receiver, related to the longitudinal state gain matrix \mathbf{A}_{rlong} and lateral-directional state gain matrix \mathbf{A}_{rlat} ; $\mathbf{B} \in \mathbb{R}^{12 \times 4}$ is the input gain matrix of the receiver, related to the longitudinal input gain matrix \mathbf{B}_{rlong} and lateral-directional input gain matrix \mathbf{B}_{rlat} .

3.2 Link-connected hose-dogue Model

3.2.1 Outline

The refueling hose is a flexible body, and it is challenging to express its dynamics accurately. In this section, a link-connected model will be used to describe the dynamic characteristics of the hose. The link-connected model consists of a series of finite cylindrical rigid links connected by frictionless ball joints, as shown in Fig. 3.2. The links themselves have no mass; instead, the mass is equivalent to the ball joint, assuming that half of the mass of the j th link ($j = 1, 2, \dots, N$, where N is the number of links used for modeling, and a larger N provides a closer approximation to the flexible hose) and half of the mass of the $j + 1$ th link are concentrated at the ball joint of the j th link's end. This ball joint is referred to as the j th mass point and is denoted as m_j (note that if the length of the link changes, its mass will also change). The mass of m_N is the sum of half of the mass of the N th link and the mass of the drogue. Additionally, l_j represents the length of the j th link, and its end position is denoted as $\mathbf{p}_j = [x_j \ y_j \ z_j]^T$, while r_j is the radius of the link. For convenience, the origin o_t of the tanker is defined as \mathbf{p}_0 , meaning they represent the same point. $\mathbf{p}_d = [x_d \ y_d \ z_d]^T$ represents the position of the drogue. Therefore

$$\mathbf{p}_d = \mathbf{p}_N - [l_d \ 0 \ 0]^T \quad (3.73)$$

where l_d is the height of the drogue, i.e., the distance from the connection point of the drogue with the hose to the center of the drogue.

3.2.2 Kinematic Equations

The link-connected model is established in the tanker coordinate system. Since the rotation of the link around itself is not considered, the direction of each link can be described using two



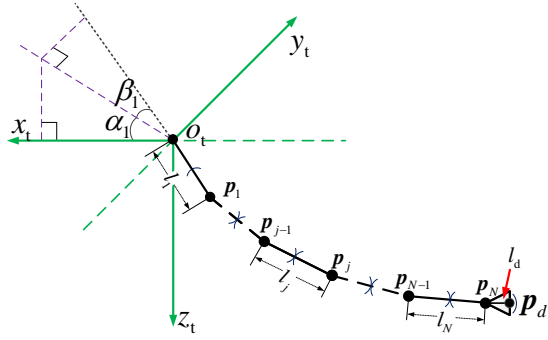


Figure 3.2: Link-connected hose-dogue model

angles, α_j, β_j , as shown in Fig. 3.2. For example, α_1, β_1 represent the direction angles of the first link. Then, the relationship between the two spherical joints can be expressed using these direction angles

$$\mathbf{p}_{j/(j-1)} = -l_j \mathbf{n}_j, j = 1, 2, \dots, N \quad (3.74)$$

where $\mathbf{n}_j \in \mathbb{R}^3$ represents the direction of the j th link and can be obtained from the following equations

$$\mathbf{n}_j = \begin{bmatrix} \cos \alpha_j \cos \beta_j \\ \sin \beta_j \\ -\sin \alpha_j \cos \beta_j \end{bmatrix}. \quad (3.75)$$

According to Eq. (3.74), the position relationship between each mass point can be obtained as follows

$$\mathbf{p}_j = \mathbf{p}_{j-1} + \mathbf{p}_{j/(j-1)}, j = 1, 2, \dots, N \quad (3.76)$$

Taking the derivative of it, the kinematic relationships between each mass point can be obtained as follows

$$\mathbf{v}_j = \mathbf{v}_{j-1} + \dot{\mathbf{p}}_{j/(j-1)}, \mathbf{a}_j = \mathbf{a}_{j-1} + \ddot{\mathbf{p}}_{j/(j-1)}, j = 1, 2, \dots, N \quad (3.77)$$

where \mathbf{v}_j and \mathbf{a}_j represent the velocity and acceleration of the j th mass point, respectively. Note that since this model is established in the tanker coordinate system, and during the docking process, the tanker coordinate system is equivalent to an inertial frame, the effects of the tanker's motion on the model is not considered in this section. If readers need to consider the influence of the tanker's motion on this model, they can refer to Ref. [136].

As described above, the fundamental variables to represent the link-connected model are the attitude angles of each link. Therefore, the kinematic model should ultimately be expressed in terms of these attitude angles. Thus, expanding Eq. (3.77), one can obtain

$$\dot{\mathbf{p}}_{j/(j-1)} = -l_j \mathbf{n}_j - l_j \dot{\mathbf{n}}_j = -l_j \mathbf{n}_j - l_j \left(\frac{\partial \mathbf{n}_j}{\partial \alpha_j} \dot{\alpha}_j + \frac{\partial \mathbf{n}_j}{\partial \beta_j} \dot{\beta}_j \right) \quad (3.78)$$

$$\ddot{\mathbf{p}}_{j/(j-1)} = -l_j \mathbf{n}_j - 2l_j \dot{\mathbf{n}}_j - l_j \left(\frac{\partial \dot{\mathbf{n}}_j}{\partial \alpha_j} \dot{\alpha}_j + \frac{\partial \dot{\mathbf{n}}_j}{\partial \beta_j} \dot{\beta}_j + \frac{\partial \mathbf{n}_j}{\partial \alpha_j} \ddot{\alpha}_j + \frac{\partial \mathbf{n}_j}{\partial \beta_j} \ddot{\beta}_j \right) \quad (3.79)$$

Since \mathbf{n}_j represents a direction vector, then

$$\frac{\partial \mathbf{n}_j^T}{\partial \alpha_j} \cdot \frac{\partial \mathbf{n}_j}{\partial \beta_j} = \frac{\partial \mathbf{n}_j^T}{\partial \alpha_j} \cdot \mathbf{n}_j = \frac{\partial \mathbf{n}_j^T}{\partial \beta_j} \cdot \mathbf{n}_j = \dot{\mathbf{n}}_j^T \cdot \mathbf{n}_j = 0, \|\mathbf{n}_j\| = \|\dot{\mathbf{n}}_j\| = 1 \quad (3.80)$$

From Eqs. (3.75), (3.78), (3.79), and (3.80), one can obtain

$$\begin{cases} \ddot{\alpha}_j = \frac{1}{l_j} \frac{\partial \mathbf{n}_j}{\partial \alpha_j} \left(-(\mathbf{a}_j - \mathbf{a}_{j-1}) - 2l_j \dot{\mathbf{n}}_j - l_j \left(\frac{\partial \dot{\mathbf{n}}_j}{\partial \alpha_j} \dot{\alpha}_j + \frac{\partial \dot{\mathbf{n}}_j}{\partial \beta_j} \dot{\beta}_j \right) \right) \\ \ddot{\beta}_j = \frac{1}{l_j} \frac{\partial \mathbf{n}_j}{\partial \beta_j} \left(-(\mathbf{a}_j - \mathbf{a}_{j-1}) - 2l_j \dot{\mathbf{n}}_j - l_j \left(\frac{\partial \dot{\mathbf{n}}_j}{\partial \alpha_j} \dot{\alpha}_j + \frac{\partial \dot{\mathbf{n}}_j}{\partial \beta_j} \dot{\beta}_j \right) \right) \end{cases} \quad (3.81)$$

which represents the kinematic equations of the link-connected model.

3.2.3 Dynamic Equations

Air flows over the j th link creates frictional drag $\mathbf{D}_{F,j} \in \mathbb{R}^3$ along the link direction and pressure difference drag $\mathbf{D}_{D,j} \in \mathbb{R}^3$ perpendicular to the cylinder's direction. The combination of these forces gives the aerodynamic force $\mathbf{D}_j \in \mathbb{R}^3$ acting on the cylinder. For the link-connected model, the dynamic force acting on each link needs to be distributed equally to its two end mass points, so each mass point is subjected to five forces. Define the airspeed of the tanker and each link as follows

$$\mathbf{v}_{t/w}^g = \mathbf{v}_t^g - \mathbf{v}_w^g, \mathbf{v}_{j/w}^g = \mathbf{v}_j^g - \mathbf{v}_w^g \quad (3.82)$$

Among them, \mathbf{v}_w^g is the local wind speed. As shown in Fig. 3.3, these five forces are the gravity $\mathbf{G}_j \in \mathbb{R}^3$ acting on the mass point, the tension forces $\mathbf{t}_j \in \mathbb{R}^3, \mathbf{t}_{j+1} \in \mathbb{R}^3$ in the two link connectors, and the equivalent forces $\mathbf{D}_j/2, \mathbf{D}_{j+1}/2$ due to the aerodynamic forces acting on the two links at that point. For the last mass point m_N , since the next link is replaced by a drogue, its force situation is different, as shown in Fig. 3.4. The five forces acting on m_N are the tension force t_N in the N th link and its equivalent aerodynamic force $\mathbf{D}_N/2$, the gravity of the mass point and the drogue $\mathbf{G}_N \in \mathbb{R}^3, \mathbf{G}_d \in \mathbb{R}^3$, and the aerodynamic force $\mathbf{G}_d \in \mathbb{R}^3$ acting on the drogue.

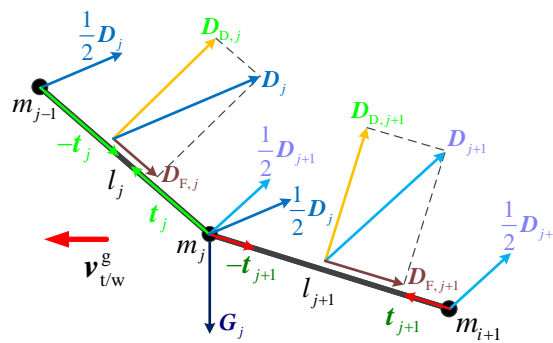
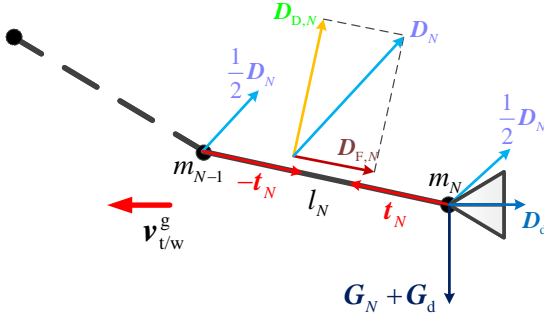


Figure 3.3: Analysis of forces on the first $N - 1$ links

According to aerodynamics principles, the calculation of friction drag and pressure drag is as follows

$$\mathbf{D}_{F,j} = - \left[C_{F,j} \rho_\infty (\mathbf{v}_{j/w}^g \cdot \mathbf{n}_{F,j})^2 (\pi r_j l_j) \right] \mathbf{n}_{F,j} \quad (3.83)$$

$$\mathbf{D}_{D,j} = - \left[C_{D,j} \rho_\infty (\mathbf{n}_{D,j} \cdot \mathbf{n}_{D,j})^2 (\pi r_j l_j) \right] \mathbf{n}_{D,j} \quad (3.84)$$

Figure 3.4: Analysis of forces on the N th link

where ρ_∞ represents the density of the stationary air at that altitude, and $\mathbf{n}_{F,j}, \mathbf{n}_{D,j}$ are the directions of the two forces, which can be expressed as

$$\mathbf{n}_{F,j} = \mathbf{n}_j, \mathbf{n}_{D,j} = \mathbf{v}_{j/w}^g - (\mathbf{v}_{j/w}^g \cdot \mathbf{n}_j) \mathbf{n}_j \quad (3.85)$$

The parameters $C_{F,j}$ and $C_{D,j}$ represent aerodynamic coefficients. According to Ref. [137], before calculating $C_{F,j}$ and $C_{D,j}$, it is necessary to compute the Reynolds number of the fluid at each link's location.

$$Re_j = \frac{\rho_j \|\mathbf{v}_{j/w}^g\| l_{ch,j}}{\nu} \approx \frac{\rho_\infty \|\mathbf{v}_{j/w}^g\| l_{ch,j}}{\nu} \quad (3.86)$$

where ρ_∞ is the local fluid density, and since the airflow compression during the docking process can be neglected, it is approximately equivalent to the density of static atmosphere at that altitude. ν is the dynamic viscosity coefficient of the local atmosphere, and $l_{ch,j}$ is the characteristic length of the j th link, represented as

$$l_{ch,j} = \frac{\pi r_h}{\sin \vartheta_j} \quad (3.87)$$

where ϑ_j is the angle between the link and the airspeed $\mathbf{v}_{j/w}^g$, and r_h is the outer radius of the hose, i.e.

$$\vartheta_j = \arccos \frac{\mathbf{n}_j^T \mathbf{v}_{j/w}^g}{\|\mathbf{n}_j\| \|\mathbf{v}_{j/w}^g\|}. \quad (3.88)$$

After obtaining the Reynolds number, $C_{F,j}$ and $C_{D,j}$ can be determined based on the Reynolds number, as shown in Table 3.1. Additionally, the drogue also experiences aerodynamic forces.

Table 3.1: The relations among $C_{F,j}, C_{D,j}$ and Re_j

Re_j	$C_{F,j}$	Re_j	$C_{D,j}$
$(10^{-2}, 10^4]$	$4.6409 Re^{-0.6667}$	$(10^{-2}, 1]$	$10 Re^{-0.81}$
$(10^4, 10^{10}]$	$0.0464 Re^{-0.1667}$	$(1, 180]$	$10 Re^{-0.4083}$
$(10^{10}, +\infty]$	0.001	$(180, 4 \times 10^5]$	1.2
		$(4 \times 10^5, 4 \times 10^6]$	$0.002128 Re^{-0.3522}$
		$(4 \times 10^6, +\infty]$	0.45

Ref. [138] analyzed the aerodynamic forces acting on the drogue and provided the equation for

the aerodynamic force on the drogue as follows

$$\mathbf{D}_d = \frac{1}{2} C_d \rho_\infty \left((\mathbf{v}_{N/w}^g)^T \mathbf{v}_{N/w}^g \right) (\pi r_d) \left(\frac{\mathbf{v}_{N/w}^g}{\|\mathbf{v}_{N/w}^g\|} \right) \quad (3.89)$$

where r_d is the radius of the drogue canopy, and C_d is a coefficient determined by the drogue strut angle as shown in Fig. 3.5 and the canopy area, and so on. Typically, this coefficient is taken as 0.8 [138]. At this point, all forces except for the tension are known. The following section provides the method for calculating the tension.

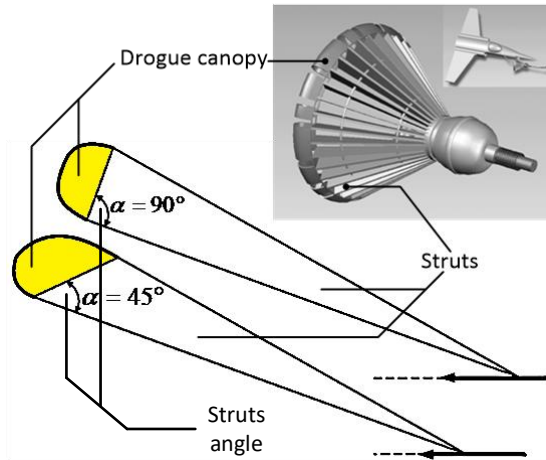


Figure 3.5: Drogue canopy's angle of struts

3.2.4 Calculation of Tension

In the link-connected model, since the tension force is generated internally within the system, it is considered an internal force, while the other forces are external forces. For ease of calculation, the external forces composed of aerodynamic forces and gravity are denoted as $\mathbf{Q}_j \in \mathbb{R}^3$, i.e,

$$\begin{cases} \mathbf{Q}_j = m_j \mathbf{g} + \frac{1}{2} (\mathbf{D}_j + \mathbf{D}_{j+1}), j = 1, 2, \dots, N-1 \\ \mathbf{Q}_N = (m_N + m_d) \mathbf{g} + \frac{1}{2} \mathbf{D}_N + \mathbf{D}_d + \mathbf{F}_b. \end{cases} \quad (3.90)$$

Assume the tension at the two ends of the same link is $t_j \mathbf{n}_j$ and $-t_j \mathbf{n}_j$, where t_j is a constant, which satisfies the property that the tension at both ends of the link has the same magnitude, opposite direction, and along the link. Here, \mathbf{F}_b represents other external disturbances acting on the drogue, and it actually includes the bow wave, which is included in the external forces acting on the last mass point. Therefore, according to Newton's second law, one has

$$\begin{cases} \mathbf{a}_j = \frac{t_j \mathbf{n}_j - t_{j+1} \mathbf{n}_{j+1} + \mathbf{Q}_j}{m_j}, j = 1, 2, \dots, N-1 \\ \mathbf{a}_N = \frac{t_N \mathbf{n}_N + \mathbf{Q}_N}{m_N} \end{cases} \quad (3.91)$$

where \mathbf{a}_j represents the acceleration of the j th link, and \mathbf{a}_N represents the acceleration of the drogue.

On the other hand, since

$$\mathbf{p}_{j/(j-1)}^T \cdot \mathbf{p}_{j/(j-1)} = l_j^2 \quad (3.92)$$

Taking the second derivative of both sides of this equation, it can be obtained

$$\mathbf{n}_j^T \cdot (\mathbf{a}_j - \mathbf{a}_{j-1}) = l_j \dot{\mathbf{n}}_j^T \dot{\mathbf{n}}_j - \ddot{l}_j \quad (3.93)$$

Therefore, by combining Eq. (3.91) and Eq. (3.93) and rearranging them

$$\mathbf{T}^T \mathbf{t} = \mathbf{q} \quad (3.94)$$

where $\mathbf{t} = [t_1 \ t_2 \ \dots \ t_N]^T$, and the coefficient matrix \mathbf{T} is known in terms of \mathbf{q} (its specific form will be described in the next section). With this, the relationship between internal force and external force can be established. By solving Eq. (3.91), we can obtain \mathbf{a}_j and then update it in Eq. (3.81). This completes the entire link-connected model.

The block diagram of the link-connected hose-droge model can be obtained based on the above steps, as shown in the Fig. 3.6.

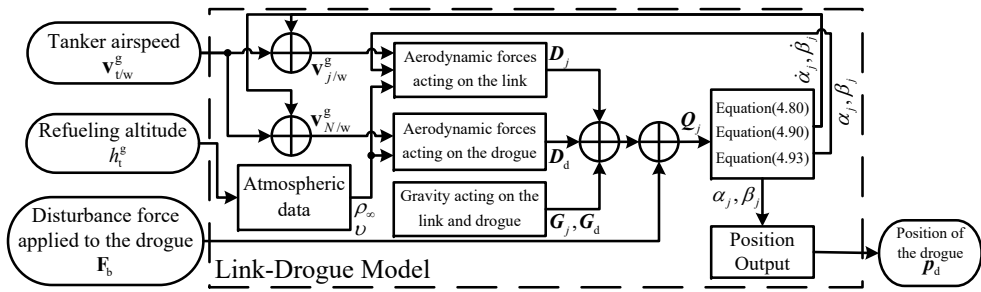


Figure 3.6: Flowchart of the link-connected hose-droge model calculation

3.2.5 Link-connected Model during Hose Contraction

It should be noted that due to the presence of the Hose Drum Unit (HDU) in the system, the hose-droge may retract a certain distance into the refueling pod when subjected to strong disturbances. For the subsequent modeling needs, it is necessary to consider the retraction of the link. If the retraction distance of the link is less than the length of the first link, we will consider the equation for the tension of N links. However, if the disturbances are significant and the retraction length exceeds the length of the first link, the order of the equation will change. Assume that the link visible outside the HDU is the original i th link, then Eq. (3.94) satisfies the following form

$$\begin{bmatrix} \mathbf{0}_{(i-1) \times (i-1)} & \mathbf{0} \\ \mathbf{0} & \bar{\mathbf{T}}_{(N-i+1) \times (N-i+1)} \end{bmatrix} \mathbf{t} = \begin{bmatrix} \mathbf{0}_{(i-1) \times 1} \\ \bar{\mathbf{q}}_{(N-i+1) \times 1} \end{bmatrix} \quad (3.95)$$

where $\bar{\mathbf{T}}$ and $\bar{\mathbf{q}}$ are as follows

$$\bar{\mathbf{T}} = \begin{bmatrix} 1 & -\mathbf{n}_i^T \mathbf{n}_{i+1} & 0 & \cdots & \cdots \\ -\mu_i \mathbf{n}_i^T \mathbf{n}_{i+1} & \mu_i + \mu_{i+1} & -\mu_{i+1} \mathbf{n}_{i+1}^T \mathbf{n}_{i+2} & 0 & \cdots \\ 0 & \ddots & 0 & \cdots & \cdots \\ 0 & -\mu_{j-1} \mathbf{n}_{j-1}^T \mathbf{n}_j & \mu_{j-1} + \mu_j & \mu_j \mathbf{n}_j^T \mathbf{n}_{j+1} & 0 \\ 0 & \cdots & \ddots & 0 & \cdots \\ 0 & 0 & -\mu_{N-2} \mathbf{n}_{N-2}^T \mathbf{n}_{N-1} & \mu_{N-2} + \mu_{N-1} & \mu_{N-1} \mathbf{n}_{N-1}^T \mathbf{n}_N \\ 0 & \cdots & \cdots & -\mu_{N-1} \mathbf{n}_{N-1}^T \mathbf{n}_N & \mu_{N-1} + \mu_N \end{bmatrix} \quad (3.96)$$

$$\bar{\mathbf{q}} = \begin{bmatrix} m_i l_i \dot{\mathbf{n}}_i^2 - \mathbf{Q}_i^T \mathbf{n}_i - m_i \ddot{l}_i \\ l_{i+1} \dot{\mathbf{n}}_{i+1}^2 + (\mu_i \mathbf{Q}_i^T - \mu_{i+1} \mathbf{Q}_{i+1}^T) \mathbf{n}_{i+1} \\ \vdots \\ l_j \dot{\mathbf{n}}_j^2 + (\mu_{j-1} \mathbf{Q}_{j-1}^T - \mu_j \mathbf{Q}_j^T) \mathbf{n}_j \\ \vdots \\ l_{N-1} \dot{\mathbf{n}}_{N-1}^2 + (\mu_{N-2} \mathbf{Q}_{N-2}^T - \mu_{N-1} \mathbf{Q}_{N-1}^T) \mathbf{n}_{N-1} \\ l_N \dot{\mathbf{n}}_N^2 + (\mu_{N-1} \mathbf{Q}_{N-1}^T - \mu_N \mathbf{Q}_N^T) \mathbf{n}_N \end{bmatrix} \quad (3.97)$$

where $\mu_j = 1/m_j$, and when $i = 1$, $\bar{\mathbf{T}} = \mathbf{T}$ and $\bar{\mathbf{q}} = \mathbf{q}$, and in this case only the first link changes. The equation for the i th link being retracted exactly is

$$t_i - \mathbf{n}_i^T \mathbf{n}_{i+1} t_{i+1} = 0 \Rightarrow t_i = \mathbf{n}_i^T \mathbf{n}_{i+1} t_{i+1} \quad (3.98)$$

This means that at this moment, the length of the link is exactly zero, the mass of the link is zero, and the aerodynamic force acting on it is also zero. On the other hand, due to the continuity of the hose, it can be assumed that its direction is aligned with the next link, and the magnitude of the tension is the same. It is seen that Eq. (3.98) corresponds well to this physical process. During numerical simulations, the updating process of the calculation for the first link is illustrated by Fig. 3.7.

In the figure, l_0 represents the length of each link when it is fully extended, j is the counter, and jl_0 represents the total length of j links of the hose that are either retracted or extended. This process takes into account situations where the first link cannot be extended any further after being fully extended, and the last link cannot be retracted any further after being fully retracted. It also considers the possibility of encountering numerical calculation scenarios where multiple links of the hose are retracted or extended in a single step.

3.2.6 Simulation Example of the link-connected hose-drogue model

To validate the effectiveness of the link-connected model, simulations are conducted using the parameters listed in Table 3.2. In the table, the variable ρ_h represents the linear density of the hose, and the aerodynamic parameter C_d for the drogue is typically set to 0.8. It is important to note that in this simulation, the elongation of the hose due to the Hose Drum Unit (HDU) model

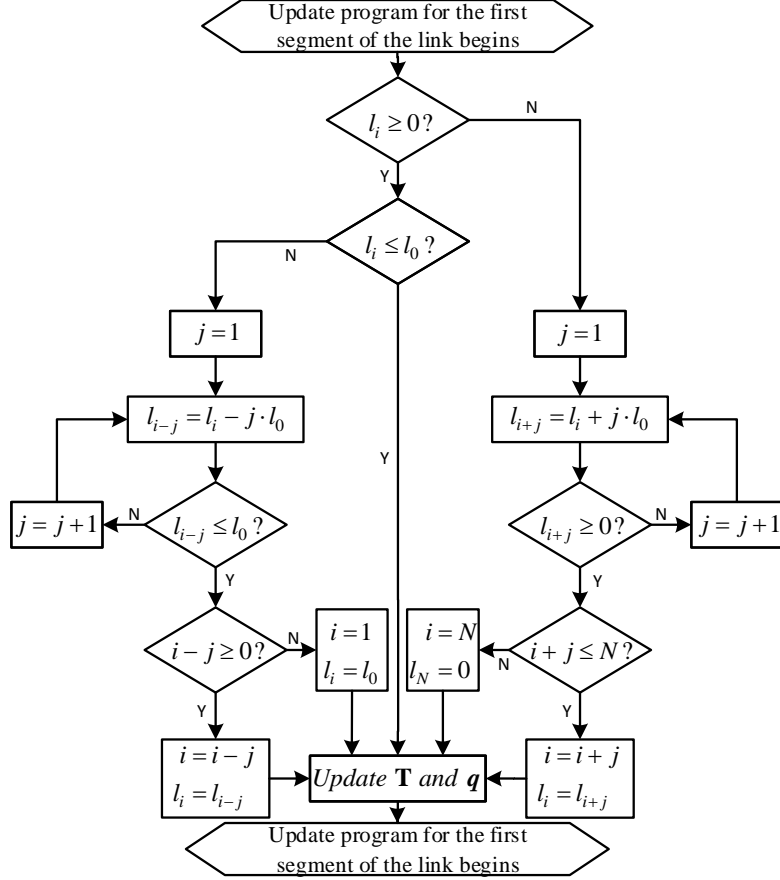


Figure 3.7: Updating Process of the First Link

has not been taken into account.

Table 3.2: Simulation Parameters of the link-connected hose-drogue model

Parameters	Values	Units	Parameters	Values	Units
v_t^g	$\begin{bmatrix} 120 & 0 & 0 \end{bmatrix}^T$	m/s	l_d	0.422	m
h_t^g	3000	m	l_h	15	m
ρ_∞	0.8443	kg/m^3	r_h	0.034	m
ν	1.7894×10^{-5}	m^2/s	ρ_h	4.1	kg/m
r_d	0.305	m	N	20	-
m_d	29.5	kg	w_t^g	$\begin{bmatrix} 0 & 0 & 0 \end{bmatrix}^T$	m/s

(1) Simulation 1: Windless Scenario

In this simulation, the hose is allowed to fall freely from a horizontal position under no wind conditions. Specifically, when the wind velocity $w_t^g = \begin{bmatrix} 0 & 0 & 0 \end{bmatrix}^T$, the hose is fully extended, and the initial conditions for each link are set to $\alpha_j(0) = \beta_j(0) = 0^\circ, j = 1, 2, \dots, N$. The model is then allowed to move freely, and the trajectories of the links and the drogue are observed. The simulation results are depicted in Fig. 3.8. Since there is no crosswind in this simulation, the position in the y_t -direction remains unchanged. Observing the dynamic process, the model reaches a steady state around 20 seconds. Therefore, a moment beyond 20 seconds can be chosen

as the equilibrium point of the model under the environmental conditions specified in Table 3.2.

(2) Simulation 2: Drogue Located at Equilibrium Position

In this simulation, the hose is initially at its equilibrium position, and a lateral perturbation is applied to the drogue at 10 seconds. Specifically, the stable state obtained from Simulation 1 is used as the initial condition for Simulation 2. At 10 seconds, a step disturbance is introduced to the system by setting the force \mathbf{F}_b to increase from $\begin{bmatrix} 0 & 0 & 0 \end{bmatrix}^T$ to $\begin{bmatrix} 0 & 50 & 0 \end{bmatrix}^T$ (Unit is N). The trajectories of the links and the drogue under this scenario are observed. Fig. 3.9 illustrates the trajectory of the drogue in this scenario.

From Fig. 3.9 (d), it can be observed that under the crosswind perturbation, the drogue first swings in the direction of the wind and upwards. Subsequently, it oscillates back, forming a spiral motion, and finally stabilizes at a new equilibrium position. Moreover, Figs. 3.9 (a)-(c) show that the dynamics of the drogue in various directions resemble those of a second-order or even higher-order linear system. This observation serves as the foundation for simplifying the model in subsequent chapters.

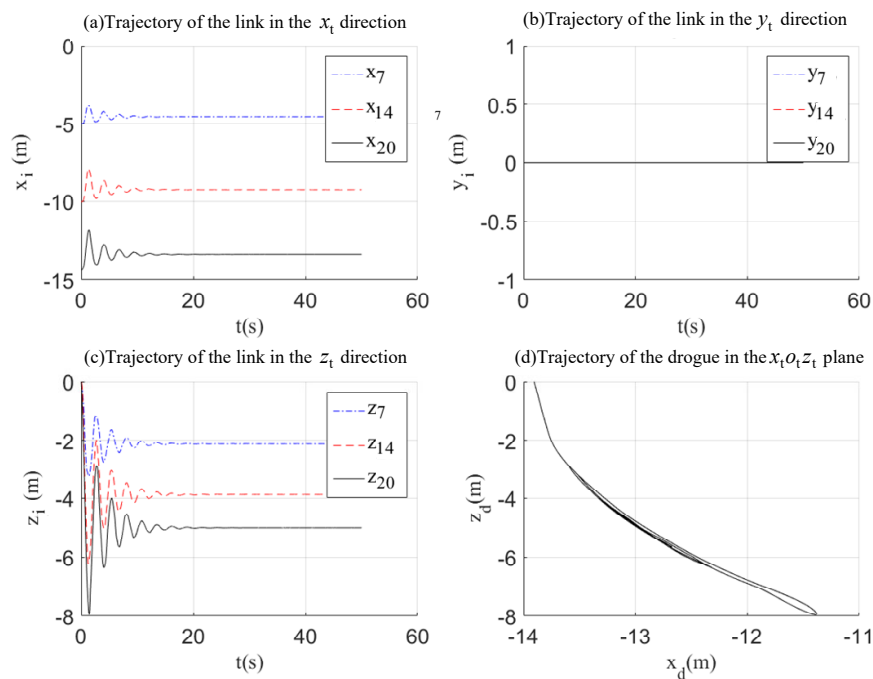


Figure 3.8: Simulation 1: Trajectory of the Hose in Free Fall without Wind

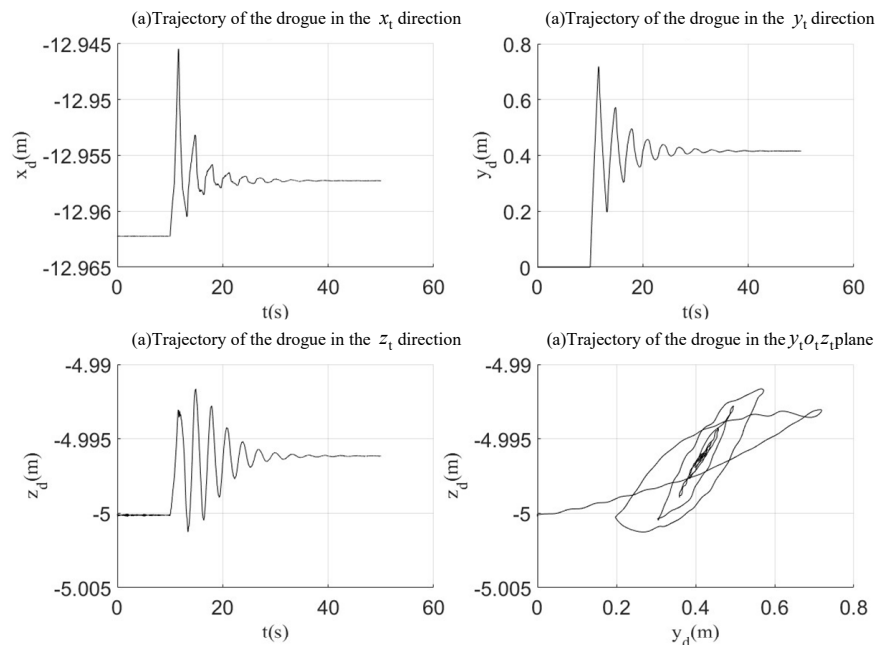


Figure 3.9: Simulation 2: Trajectory of the Drogue Under Crosswind Conditions

Chapter 4 Aerodynamic Disturbances

The aerodynamic disturbances is one of the reasons why the aerial refueling mission is very difficult. The disturbances will act on the tanker and receiver aircraft to cause the aircraft away from the desired flight, and will also act on the hose and the drogue to cause the drogue to swing irregularly. In order to accurately simulate the environment of aerial refueling, the modeling of airflow disturbances is essential. Aerodynamic disturbances are multifaceted, including atmospheric turbulence, wake vortex of the tanker aircraft, wind gust and wind shear, ect. In general, non-uniform wind disturbances can be approximated by decomposing them into a uniform wind disturbance component and a uniform wind gradient component, namely, translational and rotational wind speeds. By decomposing the various wind disturbances into translational and rotational wind speeds and then superimposing them in each direction, the total wind disturbance is obtained. In this chapter, the various wind disturbances encountered during aerial refueling are analyzed in detail.

4.1 Atmospheric Turbulence

Atmospheric turbulence, also known as turbulence, is irregular, three-dimensional small-scale motion in the atmosphere with randomness. Atmospheric turbulence is a particularly common class of atmospheric motion. In general, the atmospheric winds in nature, especially in the aircraft operating environment, are variable and basically have no specific pattern. Through a long period of observation and measurement of the wind field, meteorologists found that in a certain region and a certain period of time, the size of the wind speed always changes near a basic value. The basic value is defined as the average wind, and the fluctuations from the value is called turbulence. Atmospheric turbulence is generally considered to be a bounded random perturbation and is independent of the state of the tanker and the receiver aircraft. This disturbance occurs in all phases of aerial refueling.

The atmospheric turbulence model commonly used in aerospace is the Dryden model[139], which uses a white noise signal of finite bandwidth and unit variance to generate the desired turbulence model output by passing it through a forming filter. The turbulence signal consists of three velocity components u_D^b , v_D^b , w_D^b and three angular velocity components p_D^b , q_D^b , r_D^b , all of which are defined in the body coordinate system. For simplicity, the right superscript will be ignored in the following discussion, namely, the velocity component and the angular velocity component are expressed as u_D , v_D , w_D and p_D , q_D , r_D . According to the U.S. Army military specification MILF_8785C[139][140], the velocity and angular velocity spectral functions of the forming filter in the Dryden model are defined as follows

$$\begin{aligned}
\Phi_{uD}(\omega) &= \frac{2\sigma_u^2 L_u}{\pi V_a} \cdot \frac{1}{1 + \left(L_u \frac{\omega}{V_a}\right)^2} & \Phi_{pD}(\omega) &= \frac{\sigma_w^2}{V_a L_w} \cdot \frac{0.8 \left(\frac{\pi L_w}{4b}\right)^{1/3}}{1 + \left(\frac{4b\omega}{\pi V_a}\right)^2} \\
\Phi_{vD}(\omega) &= \frac{\sigma_v^2 L_v}{\pi V_a} \cdot \frac{1 + 3 \left(L_v \frac{\omega}{V_a}\right)^2}{\left[1 + \left(L_v \frac{\omega}{V_a}\right)^2\right]^2} & \Phi_{rD}(\omega) &= \frac{\left(\frac{\omega}{V_a}\right)^2}{1 + \left(\frac{3b\omega}{\pi V_a}\right)^2} \cdot \Phi_{vD}(\omega) \\
\Phi_{wD}(\omega) &= \frac{\sigma_w^2 L_w}{\pi V_a} \cdot \frac{1 + 3 \left(L_w \frac{\omega}{V_a}\right)^2}{\left[1 + \left(L_w \frac{\omega}{V_a}\right)^2\right]^2} & \Phi_{qD}(\omega) &= \frac{\left(\frac{\omega}{V_a}\right)^2}{1 + \left(\frac{4b\omega}{\pi V_a}\right)^2} \cdot \Phi_{wD}(\omega)
\end{aligned} \tag{4.1}$$

where b denotes aircraft wingspan, V_a denotes the airspeed, L_u , L_v , L_w denote the turbulence scale, and σ_u , σ_v , σ_w denote the turbulence intensity, which have different values at different altitudes. Specifically, when the altitude is less than 1000 ft. the model is called the low altitude model and the values of the parameters are

$$L_w = h, \quad L_u = L_v = \frac{h}{(0.177 + 0.000823h)^{1.2}} \tag{4.2}$$

where h is in feet. In particular, when the altitude is 20 feet (about 6 metres), a wind speed of 15 knots (about 7.7 m/s) is a mild turbulence, a wind speed of 30 knots is a moderate turbulence, and a wind speed of 45 knots is a severe turbulence. Using W_{20} to represent the wind speed at 20 feet above sea level, the turbulence intensity satisfies the

$$\sigma_w = 0.1 W_{20}, \quad \frac{\sigma_u}{\sigma_w} = \frac{\sigma_v}{\sigma_w} = \frac{1}{(0.177 + 0.000823h)^{0.4}} \tag{4.3}$$

When the altitude is greater than 2,000 ft, it is called a medium to high altitude model, and under the assumption of isotropy, there are

$$L_u = L_v = L_w, \quad \sigma_u = \sigma_v = \sigma_w \tag{4.4}$$

Specific values can refer to literature[139]. Besides, one can directly use the corresponding modules in Simulink's Aerospace toolbox. When the altitude is between 1000 and 2000 ft, the turbulent velocity and the turbulent angular velocity can be obtained from by linear interpolation of the values taken at 1000 ft for the low altitude model and 2000 ft for the medium and high altitude model. It should be noted that in the low altitude model, the direction of the turbulent velocity is slightly different from the direction of the ground coordinate system. Specifically, the turbulent velocity component is oriented in the horizontal plane and in the same direction as the mean wind vector.

Based on the spectral square root of the spectral function, the transfer function of the forming filter can be obtained as follows



$$\begin{aligned}
 H_{u_D}(s) &= \sigma_u \sqrt{\frac{2L_{ul}}{\pi V_a}} \cdot \frac{1}{1 + \frac{L_{ul}}{V_a} s} & H_{p_D}(s) &= \sigma_w \sqrt{\frac{0.8}{V_a}} \cdot \frac{\left(\frac{\pi}{4b}\right)^{1/6}}{L_w^{1/3} \left(1 + \left(\frac{4b}{\pi V_a}\right) s\right)} \\
 H_{v_D}(s) &= \sigma_v \sqrt{\frac{L_v}{\pi V_a}} \cdot \frac{1 + \frac{\sqrt{3}L_v}{V_a} s}{\left(1 + \frac{L_v}{V_a} s\right)^2} & H_{r_D}(s) &= \frac{\frac{s}{V_a}}{1 + \left(\frac{3b}{\pi V_a}\right) s} \cdot H_{v_D}(s) \\
 H_{w_D}(s) &= \sigma_w \sqrt{\frac{L_w}{\pi V_a}} \cdot \frac{1 + \frac{\sqrt{3}L_w}{V_a} s}{\left(1 + \frac{L_w}{V_a} s\right)^2} & H_{q_D}(s) &= \frac{\frac{s}{V_a}}{1 + \left(\frac{4b}{\pi V_a}\right) s} \cdot H_{w_D}(s)
 \end{aligned} \tag{4.5}$$

Therefore, by passing the white noise signal with unit variance through this forming filter, the turbulence signal containing three velocity components and three angular velocity components can be obtained.

4.2 Wind Gust Model

A gust, also known as a sudden gust, is a sudden change in wind speed that occurs over a short period of time. The uncertainty of atmospheric motion causes the speed and direction of gusts to change rapidly all the time. It is generally accepted that gusts, like atmospheric turbulence, are bounded random disturbances and are independent of the state of the tanker and the receiver aircraft. This disturbance occurs in all phases of aerial refueling.

A widely used model is the 1-cosine discrete gust model, the shape of which is shown in Fig. 11.1. In this model,

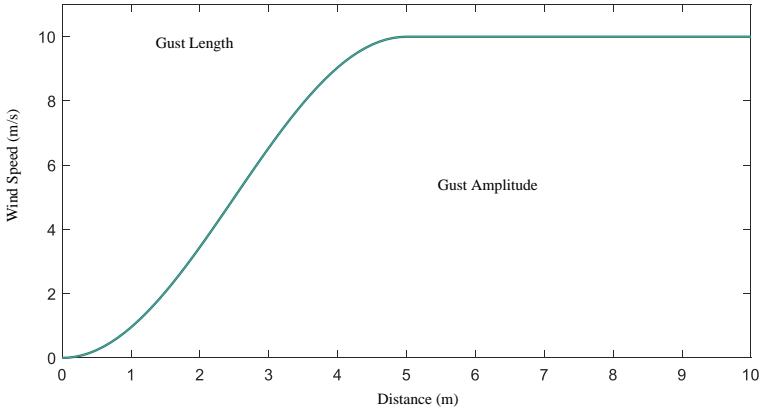


Figure 4.1: Half-wavelength atmospheric disturbance gust modelling[141]

the gust contains three velocity components u_G^b , v_G^b and w_G^b in the body coordinate system and the three velocities are uncorrelated and have the same mathematical model. The 1-cosine discrete gust model is available in both full-wavelength and half-wavelength model. Taking the velocity u_G^b in the direction of the body axis $o_b x_b$ as an example, the full-wavelength 1-cosine discrete gust model is



$$u_G^b(x) = \begin{cases} 0 & x < 0 \\ \frac{V_m}{2} \left(1 - \cos\left(\frac{\pi x}{d_m}\right)\right) & 0 < x < 2d_m \\ 0 & x > 2d_m \end{cases} \quad (4.6)$$

and the half-wavelength 1-cosine discrete gust model is

$$u_G^b(x) = \begin{cases} 0 & x < 0 \\ \frac{V_m}{2} \left(1 - \cos\left(\frac{\pi x}{d_m}\right)\right) & 0 < x < d_m \\ V_m & x > d_m \end{cases} \quad (4.7)$$

where V_m denotes the gust intensity, namely, the maximum value of gust wind speed; d_m denotes the gust scale, namely, the transition distance of gust establishment; x denotes the distance into the gust. By applying the gust model to the three body axes of the aircraft, $u_G^b(x)$, $v_G^b(x)$ and $w_G^b(x)$ can be obtained.

Before the 1980s, the full-wavelength 1-cosine discrete gust model was more often used. With the continuous improvement of numerical simulation technology, the traditional full-wavelength model can no longer satisfy the needs of the study. After the 1980s, the half-wavelength 1-cosine discrete gust model is more often used. Compared with the full-wavelength 1-cosine discrete gust model, the half-wavelength 1-cosine discrete gust model is more convenient and flexible. The half-wavelength 1-cosine discrete gust model is used in the U.S. military specification MIL-F-8785C[139] and has been modularised in Simulink's Aerospace toolbox.

4.3 Wind Shear

Wind shear refers to the sudden change of wind direction or wind speed between any two points in space within a certain period of time, including the sudden vertical shear of horizontal winds, the horizontal shear of horizontal winds and the shear of vertical winds. Research results show that wind shear often occurs in the low and medium-altitude areas where aircraft take off and land, posing a great danger and threat to the safe operation of aircraft.

At present, there are three main ways of modeling wind shear. The first way is to store the Doppler radar measurement data in the form of a grid in the computer, and it is also possible to establish a wind shear incident database. The data is real and the amount of data storage depends on the division of the grid size, and the interpolation method can be adopted to take the values in use. However, the cost required by this method is very high; the second way is to establish and numerically solve the atmospheric dynamics equations in accordance with the laws of hydrodynamics and thermodynamics. The equations of atmospheric dynamics are nonlinearly differential and it generally takes up a lot of memory and machine time to solve to equations numerically. The real-time performance of this method is generally difficult to meet, and it is not suitable for engineering simulation; the third way is to establish an engineering simulation

model, that is, to establish a relatively simplified mathematical model that describes the nature of the wind shear phenomenon, the mechanism and the movement process. This engineering wind shear model is simple and flexible, easy to use, and has better realism, so it is more suitable for atmospheric wind field simulation applications[142].

The most widely used models for wind shear in the ground boundary layer are the logarithmic and exponential models. The Prandtl logarithmic model is expressed as

$$u_S(h) = \frac{u_{S0}}{k} \ln \frac{h}{h_0} \quad (4.8)$$

where h is the altitude; u_{S0} is the friction velocity, which depends on the shear stress on the ground τ_0 and the air density ρ_0 , denoted as $u_{S0} = \sqrt{\tau_0/\rho_0}$; h_0 characterises the effect of the roughness of the ground; and $k = 0.4$ is known as Karman's constant.

The exponential model for wind shear in the ground boundary layer takes the form

$$u_S(h) = u_{SR} \left(\frac{h}{h_R} \right)^m \quad (4.9)$$

where h is the altitude; u_{SR} is the mean wind speed at the reference altitude h_R ; and m is the wind shear index, which is affected by factors such as ground roughness h_0 and temperature gradient dT/dh [143].

In the U.S. Army military specification MIL-F-8785C[139], the logarithmic model used for horizontal wind variation with height is

$$u_S(h) = W_{20} \frac{\ln \left(\frac{h}{z_0} \right)}{\ln \left(\frac{20}{z_0} \right)}, \quad 3ft < h < 1000ft \quad (4.10)$$

where h is the altitude; W_{20} denotes the wind speed at 20 ft above sea level; and z_0 takes the value of 0.15 ft for the Class C phase of flight (specifically defined in the literature [139], which generally refers to the take-off and landing phases), and z_0 takes the value of 2.0 ft for the other phases.

It is worth noting that the wind shear velocity derived from the above model is the horizontal mean wind velocity, which can be projected in the ground coordinate system if the angle between the wind direction and the earth's axis is known. In particular, assuming that the angle between the direction of the wind and the earth's axis o_gx_g is θ_S , the velocity component of the wind shear in the ground coordinate system is expressed as follows

$$\mathbf{v}_S^g(h) = \begin{bmatrix} u_S^g(h) \\ v_S^g(h) \\ w_S^g(h) \end{bmatrix} = \begin{bmatrix} u_S(h) \cos \theta_S \\ u_S(h) \sin \theta_S \\ 0 \end{bmatrix} \quad (4.11)$$

It should be noted that h is the altitude, which is satisfied by $z_g = -h$ in the ground coordinate system. This can then be transformed to the aircraft body coordinate system by means of the

coordinate system transformation method

$$\mathbf{v}_S^b(h) = \begin{bmatrix} u_S^b(h) \\ v_S^b(h) \\ w_S^b(h) \end{bmatrix} = \mathbf{R}_{b/g}(\theta, \psi, \phi) \mathbf{v}_S^g(h) \quad (4.12)$$

where $u_S^b(h)$, $v_S^b(h)$ and $w_S^b(h)$ are the three components of the induced velocity from wind shear on the aircraft body axis.

4.4 Tanker Wake

Tanker wake vortex is a kind of perturbation due to the presence of pressure differences between the upper and lower surfaces of the tanker wing, the airflow on the lower wing surface is reversed upwards around the wing tip under the effect of pressure difference to form a vortex spreading backward, thus affecting the receiver aircraft. It belongs to non-random perturbations, related to the state of the tanker but not related to the state of the receiver. The perturbation occurs in the last four phases when the tanker and receiver aircraft are close to each other, and it can be equated to a constant angle of attack perturbation due to the small change in the relative positions of the tanker and the receiver aircraft in the docking phase.

According to the lift line theory[144]. Vortices from the wing and horizontal tail of a tanker can be modeled as horseshoe Vortices as shown in Fig. 11.2. Four vortex lines along the axis of the airflow coordinate system $o_w x_w$ are trailed by the wing tip and tail tip, which correspond to vortex line ①②③④ in Fig. 11.2; and two vortex lines exist in the direction of the wingspan and the tail, which correspond to vortex line ⑤ and ⑥ in Fig. 11.2, respectively. When the wing generates positive lift, the wing tip vortex rotates inward; when the horizontal tail generates negative lift, the tail tip vortex rotates outward. Thus, the vortices on the wing and tail are in opposite directions. Since the lift generated by the wing is much greater than that generated by the tail, the wing vortices are much stronger than the tail vortices.

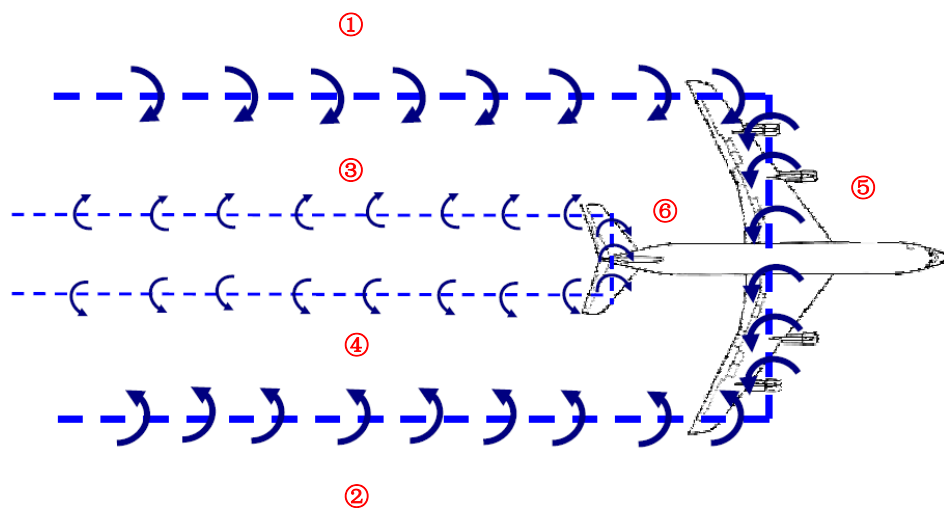


Figure 4.2: Schematic of the wing and horizontal tail saddle vortex[144]

For simplicity of analysis, wingtip vortices are generally considered to be a series of circular swirling motions with the center of the circle located on the vortex line, producing induced velocities tangent to the circle. For any position in the near airspace of the tanker, it is simultaneously affected by the six vortices in Fig. 11.2. By analyzing the effect of each vortex separately and then superimposing them the total effect of the tanker wake on any position in the space can be obtained. As shown in Fig. 11.3, assuming that in the airflow coordinate system, the relative position coordinate of any point \mathbf{p} in space relative to the center of the wingtip vortex \mathbf{o} is $\mathbf{p}_{p/o}^w = [x_{p/o}^w \ y_{p/o}^w \ z_{p/o}^w]^T$; $r_R = \|\mathbf{p}_{p/o}^w\|$ is the radial distance from the position \mathbf{p} to the vortex line; the induced velocity of the left wingtip vortex at the point \mathbf{p} is \mathbf{v}_{LWV}^w , and the direction is tangent to the circular vortex; and the angle of induced velocity θ_{LWV}^w and the axis of $o_w y_w$ in the airflow coordinate system is θ_{LWI} .

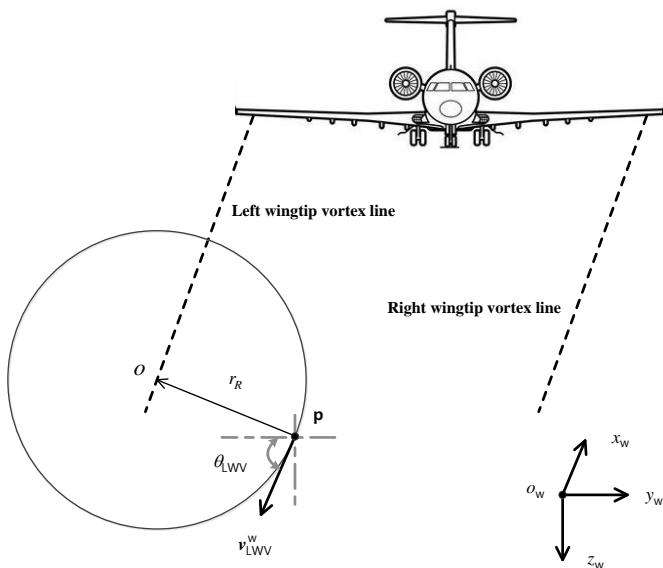


Figure 4.3: Schematic diagram of a tanker wake

According to literature[145], the size of the induced velocity produced by each vortex line at the point \mathbf{p} is

$$V = \frac{\Gamma r_R}{2\pi (r_R^2 + r_c^2)} \left(1 - \exp \left(-\frac{r_R^2}{4\nu\tau} \right) \right) \quad (4.13)$$

where Γ is the vortex strength, r_c is the radius of the vortex core which can be taken as $r_c = 2.24\sqrt{\nu\tau}$, ν is the viscosity coefficient which can be taken as $\nu = 0.06 \times \Gamma$, τ is the vortex time coefficient related to the airspeed of the tanker, $r_R = \|\mathbf{p}_{p/o}^w\|$ is the radial distance from the position \mathbf{p} to the vortex line.

The vortex strength can be calculated by the following equation as follows

$$\Gamma = \frac{L}{\rho V_t (\pi/4)b} \frac{\cos \gamma_1 + \cos \gamma_2}{2} \quad (4.14)$$

where b is the wingspan of the tanker, ρ is the air density, V_t is the airspeed of the tanker, and L is the lift generated by the wings or tail of the tanker; γ_1 and γ_2 is the angle from the end point of the vortex line to the current point. For bound vortices, namely, vortex lines ⑤⑥ in Fig. 11.2,

both γ_1 and γ_2 are non-zero; for tip vortices, namely, vortex lines ①②③④ in Fig. 11.2, γ_1 and γ_2 are equal to zero.

According to Eqs. (13.13) and (13.14), the induced velocities of the six vortices generated at any point \mathbf{p} in the space can be calculated, including left wingtip vortex $\mathbf{v}_{\text{LWV}}^w$, right wingtip vortex $\mathbf{v}_{\text{RWV}}^w$, left tailtip vortex $\mathbf{v}_{\text{LTV}}^w$, right tailtip vortex $\mathbf{v}_{\text{RTV}}^w$, wing spreading vortex \mathbf{v}_{WV}^w and horizontal tail spreading vortex \mathbf{v}_{TV}^w , respectively. The components of $\mathbf{v}_{\text{LWV}}^w$, $\mathbf{v}_{\text{RWV}}^w$, $\mathbf{v}_{\text{LTV}}^w$ and $\mathbf{v}_{\text{RTV}}^w$ lie in the plane of the airflow coordinate system $o_w y_w z_w$ and therefore have a component of 0 along the $o_w x_w$ axis, while \mathbf{v}_{WV}^w and \mathbf{v}_{TV}^w lie in the plane of the airflow coordinate system $o_w x_w z_w$ and therefore have a component of 0 along the $o_w y_w$ axis. Taking the induced velocity $\mathbf{v}_{\text{LWV}}^w$ generated by the left wingtip vortex in Fig. 11.3 as an example, its component in the airflow coordinate system can be expressed as

$$\mathbf{v}_{\text{LWV}}^w = \begin{bmatrix} 0 \\ -V_{\text{LWV}} \cos \theta_{\text{LWV}} \\ V_{\text{LWV}} \sin \theta_{\text{LWV}} \end{bmatrix} \quad (4.15)$$

where V_{LWV} is the magnitude of the induced velocity generated by the left wingtip vortex, which can be calculated according to Eq. (13.13). All other induced velocities can be decomposed into the airflow coordinate system. Specifically, in the aerial refueling process, the point \mathbf{p} is the position of the receiver aircraft, and the direction of induced speed can be determined according to the relative position relationship between the receiver and the tanker.

The total induced velocity \mathbf{v}_V^w generated by the tanker wake at any point in space can be obtained by summing the induced velocity generated by the six eddies at that point, which is expressed as follows

$$\mathbf{v}_V^w(x, y, z) = \mathbf{v}_{\text{LWV}}^w + \mathbf{v}_{\text{RWV}}^w + \mathbf{v}_{\text{LTV}}^w + \mathbf{v}_{\text{RTV}}^w + \mathbf{v}_{\text{WV}}^w + \mathbf{v}_{\text{TV}}^w \quad (4.16)$$

from the analysis, it can be seen that the induced speed generated by the tanker wake is a function of position. The total induced velocity \mathbf{v}_V^w is decomposed into three components along the axial direction in the airflow coordinate system

$$\mathbf{v}_V^w(x, y, z) = \begin{bmatrix} u_V^w & v_V^w & w_V^w \end{bmatrix}^T \quad (4.17)$$

According to the coordinate system conversion method introduced in chapter 2, the total induced velocity \mathbf{v}_V^w in the airflow coordinate system can be transformed into the receiver aircraft body coordinate system. In the receiver aircraft body coordinate system, Eq. (13.16) can be rewritten as

$$\mathbf{v}_V^r(x, y, z) = \mathbf{R}_{r/w}(\alpha, \beta) \mathbf{v}_V^w(x, y, z) = \begin{bmatrix} u_V^r & v_V^r & w_V^r \end{bmatrix}^T \quad (4.18)$$

where $\mathbf{R}_{r/w}(\alpha, \beta) = \mathbf{R}_{b/w}(\alpha, \beta)$, α and β are the angle of attack and side slip angle of the receiver, respectively, and the velocity components u_V^r , v_V^r and w_V^r are all functions of position.

Based on the literature[144], the non-uniform wind field can be approximately decomposed into a uniform wind disturbance component and a uniform wind gradient component, namely, translational wind speed and rotating wind speed. Therefore, the induced angular velocity

$\omega_V^r(x, y, z) = \begin{bmatrix} p_V^r & q_V^r & r_V^r \end{bmatrix}^T$ generated by the tanker wake can be obtained as

$$\begin{aligned} p_V^r &= \frac{\partial w_V^r}{\partial y} - \frac{\partial v_V^r}{\partial z} \\ q_V^r &= \frac{\partial u_V^r}{\partial z} - \frac{\partial w_V^r}{\partial x} \\ r_V^r &= \frac{\partial v_V^r}{\partial x} - \frac{\partial u_V^r}{\partial y} \end{aligned} \quad (4.19)$$

where p_V^r , q_V^r and r_V^r are the components of the induced angular velocity generated by the tanker wake stream on the receiver aircraft body axis, respectively.

4.5 Bow Wave Effect

In the probe-and-drogue aerial refueling docking process, when the drogue and the receiver aircraft are very close to each other, the airflow near the nose of the receiver aircraft produces a strong aerodynamic disturbance to the drogue, pushing the drogue away from the probe. This phenomenon is called as the bow wave effect. It should be noted that the modeling of the bow wave is different from the modeling of the bow wave effect. The bow wave effect is essentially due to that the airflow changes after passing over the nose of the aircraft. The drogue swings in the changed flow field, and experiences a force similar to the repulsive force generated by the aircraft's nose. The term "bow wave" refers to the airflow that has passed over the aircraft's nose. Modeling the bow wave involves modeling the flow field of this airflow, which is unrelated to the drogue. On the other hand, the term "bow wave effect" pertains to the changes experienced by the drogue due to the bow wave. Essentially, modeling the bow wave effect involves capturing the disturbances affecting the drogue, such as modeling the forces acting on the drogue in the presence of the bow wave.

From the perspective of flow field theory, this section will first model the bow wave, namely, the flow field near the nose, and then analyze the force of the drogue in the flow field. According to the classical fluid dynamics theory, the flow of uniform velocity air over some simple objects, such as cylinders and symmetric wings, can be modeled by the method of stream function. However, the stream function approach is only applicable to non-viscous fluids. If the viscosity of air want to be considered, additional calibration functions need to be incorporated. To reduce the model complexity, this section first introduces the modeling method of the two-dimensional flow field of the nose profile, which is then mapped to the three-dimensional spatial flow field distribution. After obtaining the flow field distribution, a similar method of aircraft wind disturbance modeling can be used to obtain the magnitude and direction of the force subjected to the drogue, which can then be substituted into the dynamic equation of the hose-drogue system to better simulate the dynamic motion of the drogue under the receiver aircraft bow wave disturbance.



4.5.1 Stream functions

By varying the distribution and intensity of the basic flow field unit (source, sink, doublet), some complex flow fields bypassing something can be described, for example, the induced flow field when the airflow flows through the aircraft nose. Line doublet are well suited for modeling the three-dimensional flow field around the nose and fuselage, but they are not effective for modeling the flow field of a pressurized body (e.g. a wing). As shown in Fig. 11.4, considering the longitudinal section of the nose, a two-dimensional stream function coordinate system oxy is established by taking the apex of the nose as the origin. Considering that the bow wave effect only arises when the distance between the receiver and the drogue is very close, and the bow wave effect decreases sharply with the increase of the distance between the receiver and the drogue. Meanwhile, the drogue only moves in a limited area during the docking stage. Therefore, the modeling region is set as the dashed box region in Fig. 11.4. According to the literature [146], assuming that the linear doublet intensity distribution function distributed on the $[x_a, x_b]$ interval of the x -axis satisfies $f_m(x)$, the stream function $\psi(x, y)$ corresponding to this pair of doublet can be expressed as

$$\psi(x, y) = V_\infty y - V_\infty y \int_{x_a}^{x_b} \frac{f_m(s)}{(x - s)^2 + y^2} ds \quad (4.20)$$

where V_∞ is the free stream velocity, which is equal in magnitude and opposite in direction to the receiver airspeed, and $f_m(s)$ depends only on the shape of the nose. In practice, x_a and x_b should be selected first, and then $f_m(s)$ should be obtained by solving the boundary conditions. In general, $x_a \geq 0$ and $x_b \geq 1.5l$, where l is the length of the nose in the modeled region.

The conditions that need to be satisfied for the doublet-constructed stream function to coincide with the actual nose flow field are called boundary conditions. A boundary condition is a constraint on a streamline that defines a boundary that no streamline can cross. By solving $\psi(x, y) = 0$, a closed curve in the plane can be obtained, which corresponds to the innermost streamline in Fig. 11.4 and is called “0 streamline”. When the 0-flowline, $\psi(x, y) = 0$, coincides with the nose contour line, OA , all the outer flowlines, $\psi > 0$, flow along the 0-flowline layer but not through it. Therefore, this stream function can be used for an equivalent flow around the curve $\psi(x, y) = 0$ (nose contour) when the boundary conditions are met.

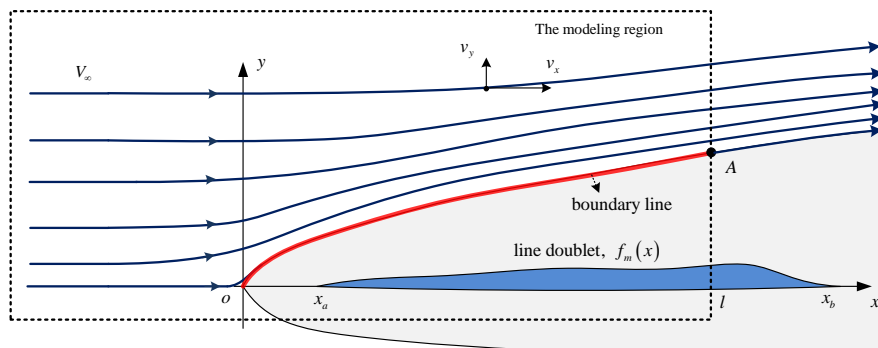


Figure 4.4: Airflow in the nose described by doublet stream function

In Fig. 11.4, the contour line OA on the upper side of the nose is selected as the boundary line, then the boundary condition can be expressed as

$$\forall (x_{ci}, y_{ci}) \in OA \Rightarrow \psi(x_{ci}, y_{ci}) = 0 \quad (4.21)$$

Eq. (11.24) shows that $\psi(x, y) = 0$ is satisfied at any point on the boundary line OA . Combining Eq. (13.20) with the assumption of $y_{ci} \neq 0$, the boundary condition reduces to

$$\forall (x_{ci}, y_{ci}) \in OA \Rightarrow \int_{x_a}^{x_b} \frac{f_m(s)}{(x_{ci} - s)^2 + y_{ci}^2} ds = 1 \quad (4.22)$$

$f_m(s)$ can be obtained by solving Eq. (11.25), and then the stream function $\psi(x, y)$ can be determined from Eq. (13.20).

A numerical calculation method to calculate the linear doublet intensity distribution function $f_m(x)$ is introduced below. As shown in Fig. 11.5, the n points $\mathbf{p}_i (i = 1, 2, \dots, n)$ are selected on the upper side contour line OA of the nose, and the corresponding coordinates are $(x_{ci}, y_{ci}) (i = 1, 2, \dots, n)$, respectively, while the linear doublet is divided into equal-length $m (m < n)$ segments on the interval $[x_a, x_b]$. Thus, the numerical form of Eq. (11.25) can be expressed numerically as

$$\sum_{j=1}^m \frac{f_m(s_j) \Delta s}{(x_{ci} - s_j)^2 + y_{ci}^2} = 1, i = 1, \dots, n \quad (4.23)$$

where

$$\Delta s = \frac{x_b - x_a}{m}, s_j = x_a + \frac{j}{2} \Delta s. \quad (4.24)$$

let

$$a_{ij} = \frac{\Delta s}{(x_{ci} - s_j)^2 + y_{ci}^2} \quad (4.25)$$

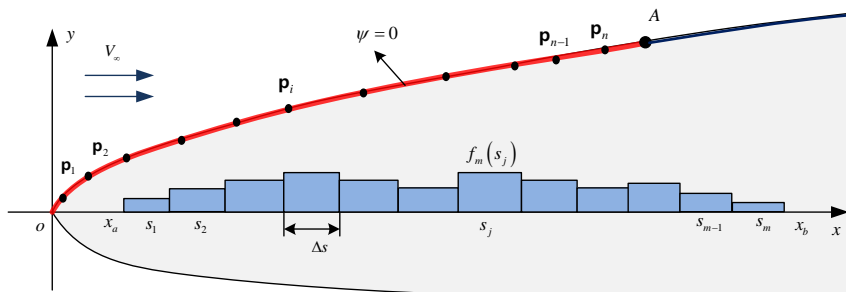


Figure 4.5: Numerical approach to solving boundary conditions

Eq. (11.26) can be expressed as

$$\sum_{j=1}^m a_{ij} f_m(s_j) = 1, i = 1, \dots, n \quad (4.26)$$

or expressed as a matrix

$$\mathbf{A} \begin{bmatrix} f_m(s_1) \\ f_m(s_2) \\ \vdots \\ f_m(s_m) \end{bmatrix} = \mathbf{I}_{n \times 1} \quad (4.27)$$

where $\mathbf{A} = (a_{ij})_{n \times m}$. Therefore, the least squares method can be used to solve Eq. (11.30) in $f_m(s_1), f_m(s_1), \dots, f_m(s_m)$. Thus, the numerical stream function applicable to the modeling of the flow field can be obtained

$$\psi(x, y) = V_\infty y - V_\infty y \sum_{j=1}^m \frac{f_m(s_j) \Delta s}{(x - s_j)^2 + y^2} \quad (4.28)$$

when m is large enough, the stream function obtained by the above equation has a high accuracy, but it will produce a large amount of computation, and at the same time, this method is not conducive to theoretical analysis. Thus, another analytical method for solving the stream function is introduced below.

After $f_m(s_1), f_m(s_1), \dots, f_m(s_m)$ are obtained from Eq. (11.30), the analytical solution of $f_m(s)$ can be obtained by polynomial fitting method. For example, when the accuracy requirement is not high, a first order polynomial can be used for fitting

$$f_m(s) = m_0 + m_1 s \quad (4.29)$$

where m_0 and m_1 are polynomial coefficients that can be obtained by fitting. Then the Eqs. (11.33) is substituted into (13.20), to get the analytical form of the stream function

$$\begin{aligned} \psi(x, y) &= V_\infty y - V_\infty \cdot \int_{x_a}^{x_b} \frac{(m_0 + m_1 x) y}{(x - s)^2 + y^2} ds \\ &= V_\infty y - V_\infty (m_0 + m_1 x) \left(\tan^{-1} \left(\frac{x_b - x}{y} \right) - \tan^{-1} \left(\frac{x_a - x}{y} \right) \right) \\ &\quad - 0.5 m_1 V_\infty y \left(\ln \left(\left(\frac{x_b - x}{y} \right)^2 + 1 \right) - \ln \left(\left(\frac{x_a - x}{y} \right)^2 + 1 \right) \right). \end{aligned} \quad (4.30)$$

The resulting analytical solution of the stream function is more suitable for theoretical analysis and nonlinear controller design. However, when the shape of the nose of the receiver is relatively complex, the first-order polynomial in Eq. (11.33) is challenging to achieve the accuracy requirements, so the higher-order polynomial functions are required. As the order of the polynomial increases, the Eq. (11.34) becomes very complex. Therefore, there is a trade-off between accuracy and complexity in practical applications.

To verify the validity of the stream function method introduced above, parameters $x_a = 0.1$ and $x_b = 2.5$ of the linear doublet distribution interval were taken, and $n = 30$ sampling points were taken on the boundary line for simulation experiments. The experimental results are shown in Fig. 11.6. The streamlines of Fig. 11.6 (a), (b) are obtained from the numerical stream function Eq. (11.31), where the parameter values are $m = 9$ and $m = 20$, respectively. The streamlines in Fig. 11.6 (c) is obtained from the analytic stream function Eq. (11.34), where the parameters are $m_0 = 0.03$ and $m_1 = 0.09$.

From Fig. 11.6, it can be observed that the horizontal streamlines flow along the boundary line in the presence of a linear doublet, which is in line with the desired result. Comparing Fig. 11.6 (a) and Fig. 11.6 (b), it can be observed that when m is large enough, the numerical stream function Eq. (11.31) produces smooth enough streamlines. At the same time, the simplified

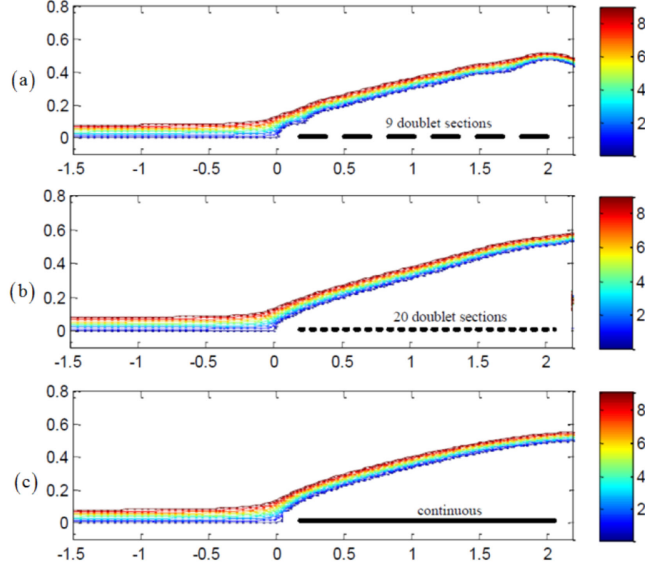


Figure 4.6: Streamlines generated by linear doublet with different distributions

analytical stream function Eq. (11.34) can produce streamlines that are close to those of the numerical method, but the computational effort is much smaller than that of the numerical method.

4.5.2 Two-dimensional flow field and correction of the aircraft nose

After obtaining the stream function $\psi(x, y)$, the distribution of the flow velocity around the aircraft nose can be obtained by the following partial differential equation[146]

$$v_x(x, y) = \frac{\partial \psi(x, y)}{\partial y}, v_y(x, y) = -\frac{\partial \psi(x, y)}{\partial x}. \quad (4.31)$$

In the two-dimensional stream function coordinate system shown in Fig. 11.4, since the original velocity is $v_x = V_\infty$, $v_y = 0$, the induced velocity components u_p and u_n due to the bow wave effect can be expressed as

$$u_p = v_x - V_\infty, u_n = v_y. \quad (4.32)$$

where u_p is along the ox axis and u_n is along the oy axis. Substituting the expression of $\psi(x, y)$, leads to

$$\begin{cases} u_p(x, y) = -V_\infty \int_{x_a}^{x_b} \frac{f_m(s)((x-s)^2-y^2)}{((x-s)^2+y^2)^2} ds \\ u_n(x, y) = -V_\infty \int_{x_a}^{x_b} \frac{2f_m(s)(x-s)y}{((x-s)^2+y^2)^2} ds \end{cases} \quad (4.33)$$

It should be noted that the classical stream function method is proposed under the assumption that the air is an ideal steady flow with no viscosity, but in fact, the viscosity of the air and the friction of the nose surface will accelerate the attenuation of the flow field. After many CFD simulations and verifications, a correction function is introduced to compensate for air viscosity,

friction, turbulence and other factors, and its expression can be expressed as

$$\begin{bmatrix} \bar{u}_p(x, y) \\ \bar{u}_n(x, y) \end{bmatrix} = \begin{bmatrix} u_p(x, y)e^{-k_{up}r_u(x, y)} \\ u_n(x, y)e^{-k_{un}r_u(x, y)} \end{bmatrix} \quad (4.34)$$

where $k_u \approx 1$ is the attenuation coefficient and $r_u(x, y)$ is a distance function that describes the distance from the point (x, y) to the surface of the nose, which can be approximated by the stream function $\psi(x, y)$

$$r_u(x, y) = \begin{cases} \frac{|\psi(x, y)|}{V_\infty} & , x \geq 0 \quad m \\ \frac{\sqrt{\psi(x, y)^2 + (V_\infty y)^2}}{V_\infty} & , x < 0 \quad m \end{cases} \quad (4.35)$$

Fig. 11.7 depicts the isogram of $r_u(x, y)$ in the above equation. The result shows that Eq. (11.38) can measure the distance from any point to the boundary line very well. More importantly, the distance function can make full use of the calculated result $\psi(x, y)$ of Eq. (13.20), which makes the calculation easier.



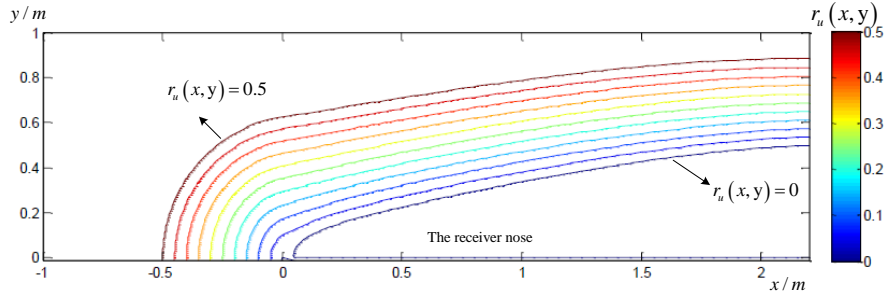


Figure 4.7: Isogram of the distance function $r_u(x, y)$ in the range $0 < r_u < 0.5m$

The comparison between the final obtained velocity field distribution in the nose and the CFD experimental results is shown in Fig. 11.8, where the left figures show the results of the CFD test, and the top figure and bottom figure correspond to the velocity distributions in the directions of the x and y axes, respectively, and the right figures are the results obtained by the proposed method in the paper. The comparison results verify that the proposed scheme can simulate the nose-induced flow field better.

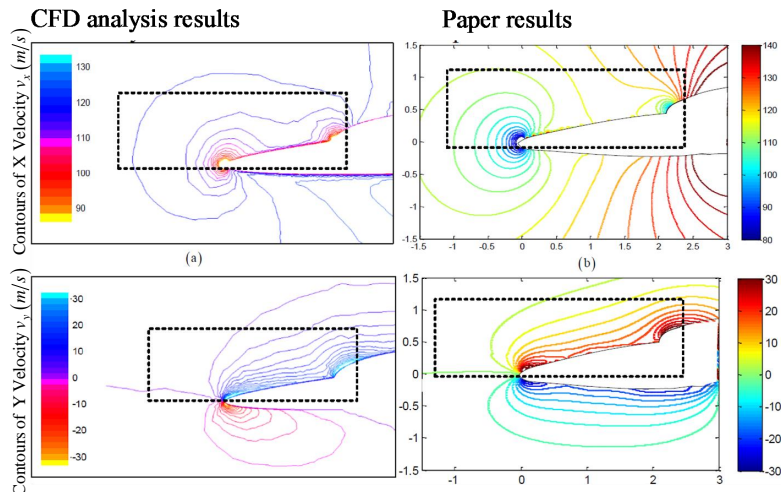


Figure 4.8: Validation of the stream function approach to model the bow wave flow field

4.5.3 Establishment of three-dimensional flow field of the aircraft nose

Since the nose is usually a conical or ellipsoidal shape, rotationally symmetric about the center axis. Therefore, when the flow field of the nose profile is acquired, the profile two-dimensional flow field can be mapped to three-dimensional according to the method of rotational mapping as shown in Fig. 4.9. Specifically, the nose vertex is taken as the origin to establish the three-dimensional stream function coordinate system $o - xyz$, whose direction is the same as the direction of the receiver aircraft body coordinate system. For the \mathbf{p} with coordinates (x, y, z) in the stream function coordinate system, the coordinates of its projection in the radial plane oo_1o_2 are (x_p, y_p) . The radial plane oo_1o_2 defined here corresponds to the two-dimensional stream function coordinate system defined in Fig. 11.4, and the mapping relationship between

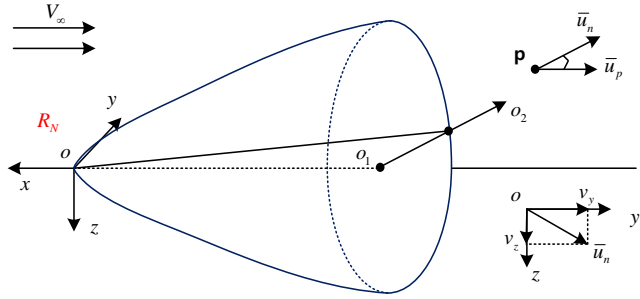


Figure 4.9: Schematic figure of the mapping of the two-dimensional flow field of the profile to three-dimensional flow field

the two-dimensional coordinates and three-dimensional coordinates is as follows

$$\begin{cases} x_p = -x \\ y_p = \sqrt{y^2 + z^2} \end{cases} . \quad (4.36)$$

According to Eq. (11.36) and Eq. (11.37), the two-dimensional modified velocity vector $[\bar{u}_p \quad \bar{u}_n]^T$ at the point (x_p, y_p) can be obtained, and then by decomposing \bar{u}_p and \bar{u}_n in the three directional axes of the three-dimensional stream function coordinate system $o-xyz$, the three-dimensional velocity vector $\mathbf{v}_B = [u_B \quad v_B \quad w_B]^T$ can be obtained, which is denoted by

$$\begin{cases} u_B = -\bar{u}_p(x_p, y_p) \\ v_B = \frac{y}{\sqrt{y^2 + z^2}}\bar{u}_n(x_p, y_p) \\ w_B = \frac{z}{\sqrt{y^2 + z^2}}\bar{u}_n(x_p, y_p) \end{cases} \quad (4.37)$$

The above coordinate mapping method applies to the case where the cross-section of the nose of the receiver aircraft is circular, but for most of the receiver aircraft, such as the F-16, the cross-section of the nose is approximated to be elliptical. Therefore, a scale change is first needed to transform the ellipse into a circle. As shown in Fig. 4.10, an ellipse in the xyz plane with a long axis radius of b and a short axis radius of a is mapped to a circle with a radius of a in the $oy'z'$ plane. The scale transformation relationship between the two coordinate systems can be expressed as

$$x' = x, y' = \frac{a}{b}y, z' = z \quad (4.38)$$

By substituting the converted coordinates (x', y', z') into Eqs. (11.39) and (11.40), the three-dimensional velocity vector $\mathbf{v}'_B = [u'_B \quad v'_B \quad w'_B]^T$ can be obtained, and then the coordinate inverse transformation is performed to obtain the velocity component under the original coordinate system

$$v_x = v'_x, v_y = \frac{b}{a}v'_y, v_z = v'_z \quad (4.39)$$

Thus, the three-dimensional velocity vector with elliptical cross-section $\mathbf{v}_B = [u_B \quad v_B \quad w_B]^T$ can be obtained. It is worth noting that, since the three-dimensional stream function coordinate system $o-xyz$ is in the same direction as the receiver aircraft body coordinate system, it satisfies $\mathbf{v}_B^b = \mathbf{v}_B$, namely, the three-dimensional velocity vector obtained by this method is the induced

velocity generated by the bow wave effect in the receiver body coordinate system.

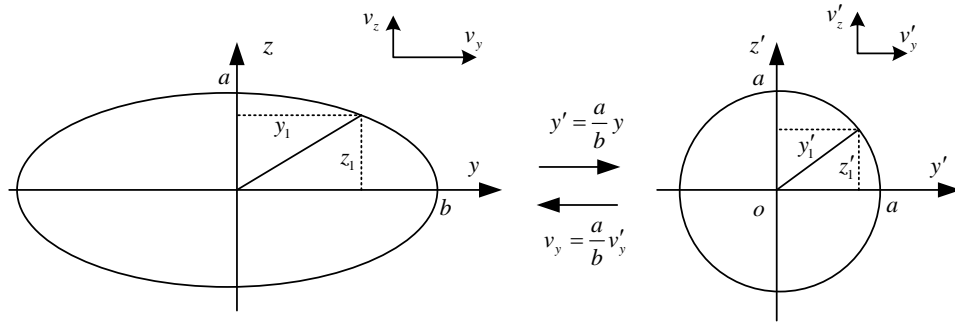


Figure 4.10: Scale transformation from ellipse to circle

When the drogue enters the flow field range of the bow wave, it can be seen from the simulation results of CFD in Fig. 11.8 that the flow field around the nose is drastically changing, which means that the flow velocity corresponding to different positions of the drogue is different. To solve this problem, an averaging method as shown in Fig. 4.11 is used[145].

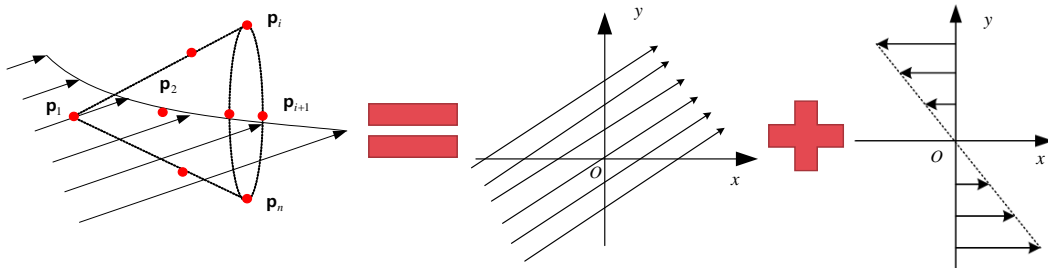


Figure 4.11: The flow field of the drogue is averaged into a uniform wind field with uniform rotation

Sample the wind field at n key points on the drogue \mathbf{v}_B (\mathbf{p}_i), and then by using the averaging method, the non-uniform wind field in which the drogue is located can be transformed to a constant (constant size and direction) wind field, and a rotating wind field. Due to the small size of the drogue, the induced moments generated by the rotating wind field are negligible. Therefore, the averaging algorithm can be expressed as

$$\bar{\mathbf{v}}_B^b = \frac{1}{n} \sum_{i=1}^n \mathbf{v}_B(\mathbf{p}_i) \quad (4.40)$$

Assuming that the effects of atmospheric turbulence, wind gust, wind shear and the effect on the drogue of the perturbation velocity generated by the tanker wake are not taken into account in the body coordinate system, the velocity of the drogue with respect to the surrounding air $\mathbf{v}_{d/w}^b$ can be expressed as

$$\mathbf{v}_{d/w}^b = \mathbf{v}_\infty + \bar{\mathbf{v}}_B^b \quad (4.41)$$

where $\mathbf{v}_\infty = [-V_\infty \ 0 \ 0]^T$ represents the free stream velocity vector, which meets the relation $\mathbf{v}_\infty = -\mathbf{v}_r$ with the receiver airspeed vector \mathbf{v}_r , and the negative sign indicates the opposite direction. If $\mathbf{v}_{d/w}^b = [u_d \ v_d \ w_d]^T$ is used, then the airspeed of the drogue V_d , the attack angle

α_d and the side slip angle β_d can be expressed as follows

$$\begin{cases} V_d = \sqrt{u_d^2 + v_d^2 + w_d^2} \\ \alpha_d = \tan^{-1} \left(\frac{v_d}{u_d} \right) \\ \beta_d = \sin^{-1} \left(\frac{v_d}{V_d} \right) \end{cases} \quad (4.42)$$

After obtaining the velocity of the drogue relative to the surrounding air, the aerodynamic force on the drogue can be solved by using the same methods as that of the aerodynamic modeling of aircraft. The aerodynamic force on the drogue can be equivalent to an equation related to the dynamic pressure (the flow velocity is related to the air density), the windward area, and the aerodynamic coefficient, either by wind tunnel testing or computational fluid dynamics. In this case, the aerodynamic coefficient of the drogue can be expressed as follows, based on the symmetrical characteristics of the drogue

$$\begin{cases} C_{dX}(\alpha_d, \beta_d) = C_{dX_0} + C_{dX_\alpha} \alpha_d^2 + C_{dX_\beta} \beta_d^2 \\ C_{dY}(\beta_d) = C_{dY_\beta} \beta_d \\ C_{dZ}(\alpha_d) = C_{dZ_\alpha} \alpha_d \end{cases} \quad (4.43)$$

where C_{dX} , C_{dY} , C_{dZ} denote the aerodynamic coefficients of the drogue defined along the body, and C_{dX_0} , C_{dX_α} , C_{dX_β} , C_{dY_β} and C_{dZ_α} are the drogue coefficients, respectively, which need to be obtained by CFD simulation or wind tunnel testing.

4.5.4 Derivation and validation of the force model for the drogue

Using the method of aerodynamic coefficients commonly used in aircraft modeling, the final force on the drogue can be expressed as follows when only the bow wave effect is taken into account (if other perturbations are considered, a modification of Eq. (4.41) is sufficient), the final force on the drogue can be expressed as

$$\mathbf{F}_d = f_d(\rho, \mathbf{v}_{d/w}^b) = \frac{1}{2} \rho V_d^2 S_d \mathbf{C}_d \quad (4.44)$$

where V_d is the magnitude of the airspeed of the drogue, S_d is the reference area of the drogue, ρ is the air density, and $\mathbf{C}_d = [C_{dX}(\alpha_d, \beta_d) \ C_{dY}(\beta_d) \ C_{dZ}(\alpha_d)]^T$ is the matrix of aerodynamic parameters of the drogue, which is defined with reference to the aerodynamic parameters of the aircraft, and the measurements can be obtained using wind tunnel or CFD simulation.

Let $\mathbf{v}_{d/w}^b = \mathbf{v}_\infty^b = [-V_\infty \ 0 \ 0]^T$, namely, without considering the bow wave effect, the force on the drogue can be expressed as

$$\mathbf{F}_{d0} = f_d(\rho, \mathbf{v}_\infty) = \frac{1}{2} \rho V_\infty^2 S_d \mathbf{C}_{d0} \quad (4.45)$$

where $\mathbf{C}_{d0} = [C_{dX_0} \ 0 \ 0]^T$. Thus, the induced force on the drogue due to the bow wave effect alone can be obtained as

$$\Delta \mathbf{F}_d = \begin{bmatrix} \Delta F_{dX} \\ \Delta F_{dY} \\ \Delta F_{dZ} \end{bmatrix} = \mathbf{F}_d - \mathbf{F}_{d0} = \frac{1}{2} \rho V_d^2 S_d \begin{bmatrix} C_{dX}(\alpha_d, \beta_d) \\ C_{dY}(\beta_d) \\ C_{dZ}(\alpha_d) \end{bmatrix} - \frac{1}{2} \rho V_\infty^2 S_d \begin{bmatrix} C_{dX_0} \\ 0 \\ 0 \end{bmatrix} \quad (4.46)$$

After simulation verification. Through comparing the induced force generated by the bow wave effect on the drogue (Fig. 4.24 right) with the CFD simulation results (Fig. 4.24 left), it can be concluded that the modeling of the bow wave effect using this method has a high accuracy.

4.6 Bow Wave Effect Model Based on link-connected model

In Section 3.4, an analysis of "bow wave" has been done from the perspective of flow field theory. The bow wave model was first established, which refers to the flow field near the nose of the aircraft. Subsequently, the forces acting on the drogue in this flow field was analyzed. It is important to note that modeling the bow wave and modeling the bow wave effect are different concepts. The bow wave effect is essentially due to that the airflow changes after passing over the nose of the aircraft. The drogue swings in the changed flow field, and experiences a force similar to the repulsive force generated by the aircraft's nose. The term "bow wave" refers to the airflow that has passed over the aircraft's nose. Modeling the bow wave involves modeling the flow field of this airflow, which is unrelated to the drogue. On the other hand, the term "bow wave effect" pertains to the changes experienced by the drogue due to the bow wave. Essentially, modeling the bow wave effect involves capturing the disturbances affecting the drogue, such as modeling the forces acting on the drogue in the presence of the bow wave.

In this section, the bow wave effect will be analysed from a different perspective?directly modeling the bow wave effect without analyzing the flow field near the aircraft's nose. We begin by describing the bow wave effect and outlining the modeling steps. Subsequently, we divide the modeling process into two main parts: collecting Computational Fluid Dynamics (CFD) data and conducting multidimensional nonlinear fitting. Finally, we integrate the link-connected hose-drogue model to conduct simulations, analyze the bow wave effect, and further validate the model. Throughout this section, if no special instructions, lengths are in meters, and forces are in Newtons.

4.6.1 Problem Description and Modeling Approach of the Bow Wave Effect Model

First, the following assumptions are made.

Assumption 1: During the docking process, $\Theta_r \approx \mathbf{0}$.

Assumption 2: During the docking process, $\mathbf{v}_{r/w}^g \approx \mathbf{v}_{t/w}^g$.

For Assumption 1, since the tanker undergoes fine adjustments in attitude angles throughout the entire docking process to achieve position changes, the attitude angles of the tanker remain relatively small during the docking process. Therefore, it can be assumed that $\Theta_r \approx \mathbf{0}$ in this process, where $\Theta_r = \begin{bmatrix} \theta_r & \psi_r & \phi_r \end{bmatrix}^T$. Therefore, Assumption 1 holds.

Regarding Assumption 2, its significance lies in considering that the receiver's airspeed is equal to the tanker's airspeed during the docking process, and remains unchanged. This is

because the relative velocity between the receiver and the tanker is significantly lower compared to the velocity of the tanker. Therefore, Assumption 2 holds.

4.6.1.1 Problem Description of the Bow Wave Effect Model

The influence of the bow wave effect extends approximately from a short distance in front of the aircraft's nose. In other words, the range of the bow wave effect is relatively short. Therefore, it can be considered that it only affects the drogue and doesn't exert any aerodynamic influence on the hose. Based on the modeling of the refueling equipment described in Section 4.2, we can use the following equation to describe the bow wave effect

$$\begin{cases} \dot{\mathbf{x}}_h = f_{h0}(\mathbf{x}_h, \mathbf{x}_d, \mathbf{v}_{t/w}^g, h_t^g) \\ \dot{\mathbf{x}}_d = f_{d0}(\mathbf{x}_h, \mathbf{x}_d, \mathbf{v}_{t/w}^g, h_t^g, \mathbf{F}_b) \\ \mathbf{p}_d = f_y(\mathbf{x}_h, \mathbf{x}_d) \end{cases} \quad (4.47)$$

Here, the functions f_{h0} , f_{d0} and f_y are formed by the link-connected hose-drogue model. The variables \mathbf{x}_h and \mathbf{x}_d represent the state variables composed of the directional angles and angular velocities of each link. The output is the position \mathbf{p}_d of the drogue in the tanker's coordinate system. The input to this system is the force $\mathbf{F}_b \in \mathbb{R}^3$ exerted on the drogue due to the bow wave effect.

Based on experience, \mathbf{F}_b is expected to be a force generated by the relative states between the tanker and the drogue. The bow wave effect aims to discuss the relationship between \mathbf{F}_b , the tanker, and the drogue, as well as the dynamic behavior of the drogue under the influence of \mathbf{F}_b .

Firstly, it can be inferred that \mathbf{F}_b is mainly related to the position of the drogue \mathbf{p}_d^r in the coordinate frame of the receiver and the receiver's airspeed $\mathbf{v}_{r/w}^g$. It can be expressed as

$$\mathbf{F}_b = \mathbf{R}_{r/t}^T(\theta_r) \mathbf{F}_b^r = \mathbf{R}_{r/t}^T(\theta_r) f_{b1}(\mathbf{p}_d^r, \mathbf{v}_{r/w}^g) \quad (4.48)$$

The above equation represents the model for the bow wave effect. According to Assumption 2, one have

$$\mathbf{F}_b = f_{b2}(\mathbf{p}_d^r) \quad (4.49)$$

where $f_{b2}(\mathbf{p}_d^r) \triangleq f_{b1}(\mathbf{p}_d^r, \mathbf{v}_{r/w}^g)$. The utilization of Assumption 2 in this context is consistent with the actual situation:

(1) The reason for the correlation between the function relationship f_{b1} and $\mathbf{v}_{r/w}^g$ is that the aerodynamic force generated by the bow wave is related to the airspeed of the receiver. However, the airspeed of the receiver can be expressed as

$$\mathbf{v}_{r/w}^g = \mathbf{v}_{r/t}^g + \mathbf{v}_{t/w}^g \quad (4.50)$$

During the docking process, $\mathbf{v}_{r/t}^g \ll \mathbf{v}_{t/w}^g$, so it can be neglected, which means that $\mathbf{v}_{r/w}^g \approx \mathbf{v}_{t/w}^g$.

(2) According to the NATO AAR Manual [137], pilots have two approaches during the refueling process: the first one is a rapid approach, characterized by a larger $\mathbf{v}_{r/t}$, allowing for quick docking before the drogue deviates significantly from its equilibrium position due to

the bow wave; the second approach involves estimating the drogue's deviation beforehand and executing a slow approach with a smaller $v_{r/t}$. Although the first method enables docking before substantial drogue drift occurs, controlling the relative velocity for engaging the refueling valve can be challenging, potentially leading to refueling accidents. On the other hand, the second method may result in drogue drift but is considered safer. Due to the high-risk nature of aerial refueling, the manual deems the second approach more reasonable. This further explains the reasonableness of neglecting the effect of $v_{r/t}$ in practical operations.

On the other hand, in the process of modeling the bow wave effect, it is necessary to use CFD software to generate training data. In this process, the CFD coordinate system is made use of, which was briefly introduced in *Chapter 2*. Therefore, \mathbf{p}_d^r is transformed into this coordinate system

$$\mathbf{p}_d^r = \mathbf{p}_{d/r}^r = \mathbf{p}_{d/f}^r + \mathbf{p}_{f/r}^r = \mathbf{p}_d^f + \mathbf{p}_f^r \quad (4.51)$$

According to Assumption 1, it can be deduced that \mathbf{p}_d^f can also be expressed as

$$\mathbf{p}_d^f = \mathbf{p}_d - \mathbf{p}_f \quad (4.52)$$

Therefore, the bow wave effect model can be further rewritten as

$$\mathbf{F}_b = f_b(\mathbf{p}_d^f) \quad (4.53)$$

where $f_b(\mathbf{p}_d^f) \triangleq f_{b1}(\mathbf{p}_d^f + \mathbf{p}_f^r)$.

Thus, based on Eq. (4.47) and Eq. (4.53), we can derive the relationship between the bow wave effect generated by the relative position of the tanker and drogue and the link-connected hose-drogue model, as shown in Fig. 4.12. Here, $\mathbf{p}_r(0)$ represents the initial position of the receiver in the tanker's coordinate system, and $\Delta\mathbf{p}_r$ indicates the docking trajectory of the receiver relative to the initial position.

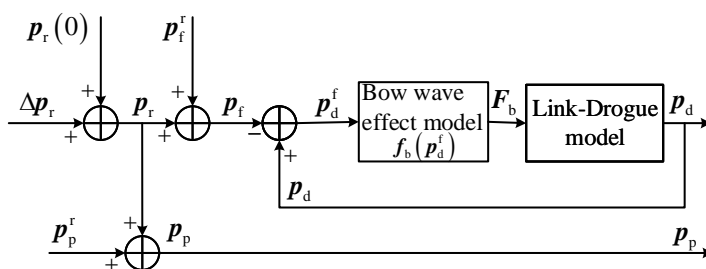


Figure 4.12: Relationship between Bow Wave Effect Model and link-connected hose-drogue model

4.6.1.2 Modeling Approach for the Bow Wave Effect Model

There are mainly two methods for modeling the bow wave effect. One method is the approach introduced in Section 3.4, where the theoretical derivation is used to gradually approximate the distribution of the flow field using multiple dipoles. Although this method can provide a good approximation of the model, as the model's precision improves, the number of dipoles significantly increases, leading to a high number of model parameters and overall complexity. In

this section, the modeling approach presented in Ref. [147] is adopted. This approach involves the following five steps:

- (1) Establish the CFD simulation environment and define its position in the receiver's coordinate system.
- (2) Select spatial points within the primary operational region of the bow wave effect $f_b(p_d^f)$ and generate a large set of training data.
- (3) Infer the functional form of the bow wave effect model with parameter estimations based on the profiles of the training data.
- (4) Employ nonlinear regression to calculate the specific parameters in $f_b(p_d^f)$, resulting in a concrete bow wave effect model.
- (5) Perform initial validation to assess the effectiveness of the parameters.

The first two steps belong to the CFD data acquisition phase, which will be elaborated in Section 4.3.2. The subsequent three steps are related to the bow wave effect model and parameter estimation, which will be discussed in Section 4.3.3. In Section 4.3.4, the obtained bow wave effect will be integrated with the link-connected hode-drogue model for the analysis of the bow wave effect. A comparison will also be made against a set of publicly available simulation and experimental data from the United States, providing further validation of the model's effectiveness.

Analyzing the bow wave effect using a mechanistic model involves two main steps. First, modeling the flow field generated by the bow wave formation, and then analyzing the aerodynamic coefficients of the drogue in this flow field to determine the resulting forces on the drogue. Due to the inherent complexity of the bow wave model itself and the irregular shape of the drogue with hollow features, it becomes challenging to establish a bow wave effect model directly from mechanistic principles. This approach, based on data and fitting methods, provides a way to bypass the complexity of this analysis and directly obtain a model for the bow wave effect.

The bow wave effect model established through this process exhibits a certain universality for aircraft with nose shapes resembling ellipsoids (such as F-16, J-8, etc.). However, the parameters within the model are influenced by factors like the shape parameters of the aircraft's nose, the aerodynamic parameters of the drogue, and the airspeed. This method requires a substantial amount of Computational Fluid Dynamics (CFD) data to derive a generalized functional form with a limited number of parameters. Consequently, when modeling for different scenarios, this model can be applied with relatively fewer data points. To achieve a more accurate model, wind tunnel testing can also be employed in the data collection phase. The limited parameter amount significantly reduces the workload required for simulation or experimentation.

4.6.2 Collection of CFD Data for Bow Wave Effect

4.6.2.1 Establishment of CFD Simulation Environment

(1) Creating a 3D Model

Fluent is utilized as the simulation software for Computational Fluid Dynamics (CFD). Initially, the object for analyzing the bow wave effect was established. Fig. 4.13 (d) presents the 3D model constructed using Gambit, while Figs. 4.13 (a)-(c) show its corresponding three views. The aircraft nose model was set with parameters resembling those of the F-16 nose. Fig. 4.14 provides a detailed exhibit of the 3D model.

It is important to note that during the process of collecting CFD data, a substantial amount of data is required for subsequent extrapolation of the functional form and parameter calculation. Hence, it is essential to minimize computation while maintaining a certain level of accuracy. Therefore, in the 3D modeling, certain aspects that have minimal impact were deliberately omitted. Specifically, these include:

- 1) The rear part of the fuselage behind the nose was neglected. Since the bow wave effect is primarily a result of the airflow passing over the nose and affecting the drogue, the region generating the bow wave is mainly the nose. Additionally, the impact on the drogue is limited by the docking distance, and the rear part of the aircraft will not significantly affect the drogue. Hence, the portion behind the nose was omitted, significantly reducing the total grid count.

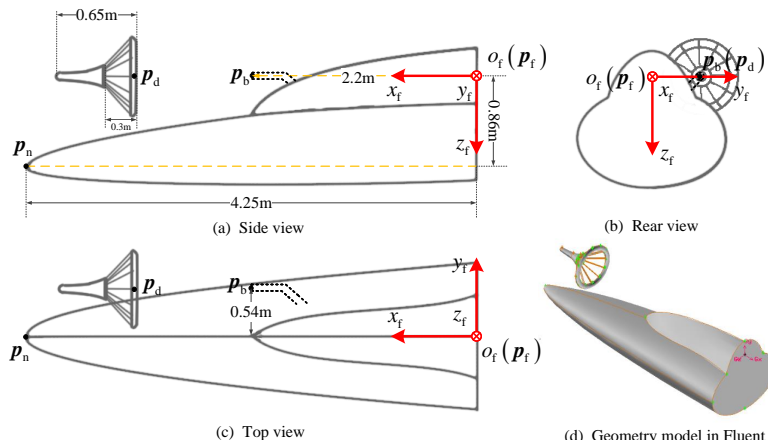


Figure 4.13: Three-dimensional Model in Fluent and its Three Views

- 2) The probe was neglected. From Fig. 4.14, it can be observed that the probe was actually excluded in the CFD simulation. Similar to the previous point, the bow wave caused by the probe (every object generates a bow wave) has a very limited impact distance. By the time the drogue enters the region affected by the probe's bow wave, the docking process is almost completed. Furthermore, the magnitude of the bow wave is influenced by the size of the object. Due to the small volume of the probe, the alteration in the bow wave it induces is minimal. Therefore, the probe's effect on the drogue is short in time and small in magnitude, allowing it to be disregarded.

- 3) The drogue's crown section was replaced with a rigid body. The crown of the drogue is

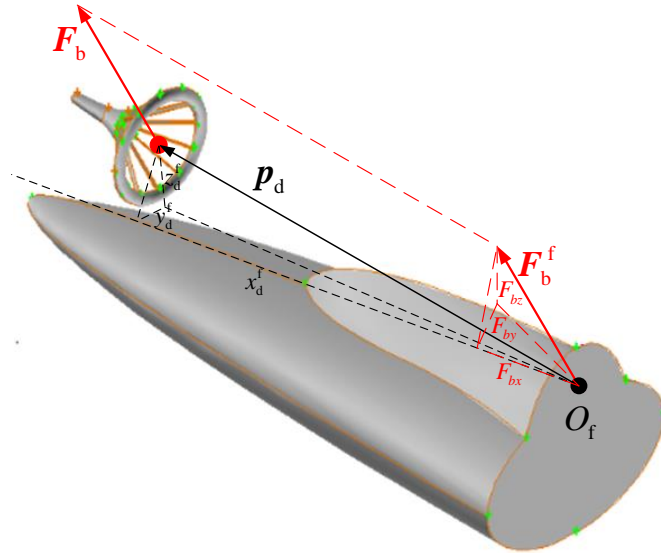


Figure 4.14: Details of the Three-dimensional Model

actually a flexible structure with an opening. However, in flight, due to high-speed airflow, this part extends and behaves more like a rigid body. Using a rigid body to represent this flexible section simplifies the modeling process and reduces computational complexity. For readers seeking a more precise drogue modeling, Ref. [138] can be consulted.

4) The hose is disregarded. As explained in Section 4.3.1.1, this is due to the short range of the bow wave's influence. The impact on the hose can be ignored.

(2) Establishing a Coordinate System for CFD Simulation

Use the CFD coordinate system established in Section 2.2.5.

(3) Generation and Solving of Fluent Mesh

Create a cubic grid with dimensions of $10\text{m} \times 6\text{m} \times 6\text{m}$ around the aircraft and drogue, as illustrated in Fig. 4.15. This grid comprises approximately 2.6×10^6 cells and is a hybrid mesh type. To achieve an appropriate grid density for obtaining higher accuracy data, the grid spacing on the surfaces of the drogue and aircraft is set to approximately 0.005m. The length of these grid cells is around 1/20 of the length of the edge grid cells. The k-epsilon turbulence model is employed for solving.

4.6.2.2 Collection of CFD Data

(1) Training Data

In the CFD simulation environment described in Section 4.3.2.1, change the relative positions of the drogue and aircraft to collect data. Each relative position corresponds to a position $\mathbf{p}_{d,i}^f = \begin{bmatrix} x_{d,i}^f & y_{d,i}^f & z_{d,i}^f \end{bmatrix}^T$ of the drogue in the CFD coordinate system. A simulation is performed using Fluent to calculate the corresponding force data $\mathbf{F}_{b,i} = \begin{bmatrix} F_{bx,i} & F_{by,i} & F_{bz,i} \end{bmatrix}^T$ acting on the drogue. According to Assumption 2 and the definition of the CFD coordinate system, it is known that $\mathbf{F}_{b,i} = \mathbf{F}_{b,i}^f$. Hence, the force data $\mathbf{F}_{b,i}$ is directly recorded in the

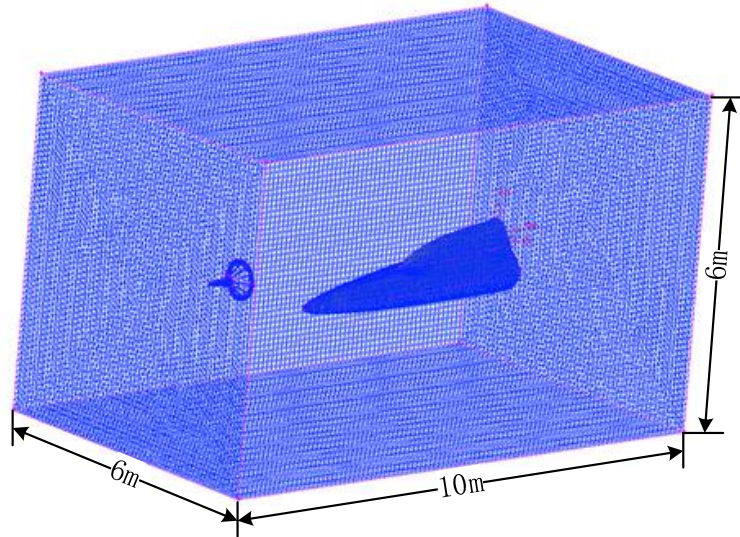


Figure 4.15: Mesh Generated in Fluent

tanker coordinate system. In this manner, for each relative position, the collected training data is represented as the i -th set $\left[\begin{array}{cc} \mathbf{p}_{d,i}^f & \mathbf{F}_{b,i} \end{array} \right]$.

Taking the simulation at $\mathbf{p}_{d,i}^f = \begin{bmatrix} 3.5 & 0 & 0 \end{bmatrix}^T$ as an example, after performing the simulation using Fluent, analysis results such as the contour plot of fluid velocity magnitude, as shown in Fig. 4.16, can be obtained. Simultaneously, the force data acting on the drogue's mass center can be read as $\mathbf{F}_{b,i} = \begin{bmatrix} 82.5566 & 0.2014 & 41.0140 \end{bmatrix}^T$.

(2) Collection of Training Data

Over 200 training data points are collected from the region $\mathbf{p}_{d,i}^f \in [2, 6] \times [-2, 2] \times [-0.5, 0.1]$. The reason for choosing this region is that, during the docking process, the drogue primarily operates within the region affected by the bow wave. All the training data has been provided in the Appendix of Section 4.3.5 of this chapter. It should be noted that the data directly collected

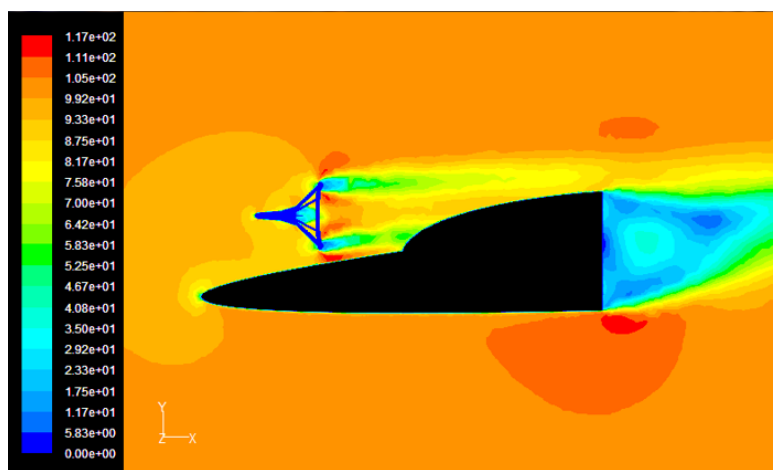


Figure 4.16: Contour Plot of Fluid Velocity Magnitude when $\mathbf{p}_{d,i}^f = [3.5, 0, 0]^T$

from CFD needs to undergo certain processing before it can be used as training data:

- 1) The software's coordinate axis direction definition is different from ours, so the collected

F_{bx} values need to be taken with the opposite sign to match the definition in the CFD coordinate system (indicated in the table header).

2) In the absence of bow wave disturbance, the drogue will also experience a force $F_{bx\infty}$ in the $o_f x_f$ direction. The bow wave reduces this force, and Fluent provides the reduced force directly. Therefore, the actual training data should be obtained from $F_{bx} = F_{bx\infty} - F_{bx0}$, where F_{bx0} is the force without bow wave disturbance. We take $F_{bx0} = F_{bx\infty}$ at $\mathbf{p}_d^f = [5.75 \ 0 \ 0]^T$, i.e., $F_{bx\infty} = 1978.988$, because at this point, the drogue is far enough from the aircraft nose, and it can be considered as the force under no bow wave disturbance.

3) Due to the aircraft nose's symmetry about the $x_f o_f z_f$ plane, we can appropriately increase some training data using symmetry to facilitate inferring the functional form of $f_b(\mathbf{p}_d^f)$.

For instance, using the first row of data in the table $\begin{bmatrix} 2 & 0.4 & 0 & 1935.152 & 49.97507 & 67.78349 \end{bmatrix}$, we can obtain the transformed data $\begin{bmatrix} 2 & -0.4 & 0 & 1935.152 & -49.97507 & 67.78349 \end{bmatrix}$.

Following the above steps, the collection of all training data can be completed. Fig. 4.17 provides training data for several important planes. The next section will analyze and derive the bow wave effect model based on these data.

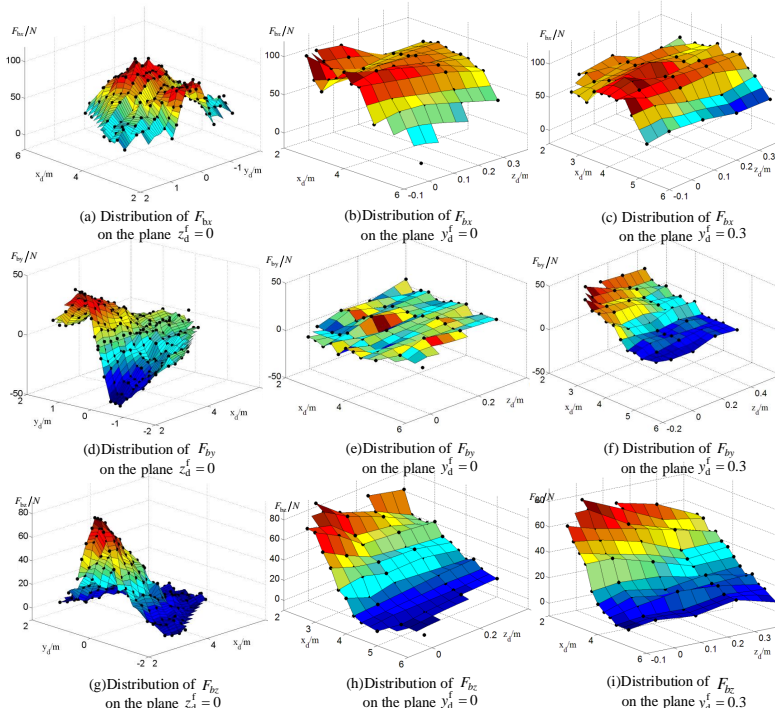


Figure 4.17: Distribution of Training Data on Three Main Planes

4.6.3 Bow Wave Effect Model and Parameter Estimation

In this section, the form of the function $\mathbf{F}_b(\mathbf{p}_d^f)$ will be first speculated, then the parameters in the model will be estimated using the training data, and finally the model will be validated using all the training data. If the validation is successful, it confirms the correctness of the speculated function form.

4.6.3.1 Speculating the Functional Form of the Bow Wave Effect Model

(1) Functional Form

First, the speculated form of the function is provided

$$\mathbf{f}_b(\mathbf{p}_d^f) = \begin{bmatrix} f_{bx}(\mathbf{p}_d^f) \\ f_{by}(\mathbf{p}_d^f) \\ f_{bz}(\mathbf{p}_d^f) \end{bmatrix} = \begin{bmatrix} F_{bx} \\ F_{by} \\ F_{bz} \end{bmatrix} = \begin{bmatrix} F_{bx_nose} + F_{bx_cockpit} \\ F_{by} \\ F_{bz} \end{bmatrix} \quad (4.54)$$

where

$$\begin{cases} F_{bx_nose} = C_{x1} \left[1 - C_{x2} (x_d^f - C_{x3})^2 \right] e^{-\frac{(y_d^f)^2}{C_{x4}}} e^{\frac{z_d^f}{C_{x5}}} s \left(\frac{1}{\sqrt{C_{x2}}} + C_{x3} - x_d^f \right) \\ F_{bx_cockpit} = C_{x6} \left(1 - C_{x7} x_d^f \right) e^{-\frac{(y_d^f)^2}{C_{x8}}} e^{\frac{z_d^f}{C_{x9}}} s \left(\frac{1}{C_{x7}} - x_d^f \right) \\ F_{by} = C_{y1} \left(1 - C_{x2} x_d^f \right) y_d^f e^{-\frac{(y_d^f)^2}{C_{y3}}} e^{\frac{z_d^f}{C_{y4}}} s \left(\frac{1}{C_{y2}} - x_d^f \right) \\ F_{bz} = -C_{z1} \left(1 - C_{z2} x_d^f \right) e^{-\frac{(y_d^f)^2}{C_{z3}}} e^{\frac{z_d^f}{C_{z4}}} s \left(\frac{1}{C_{z2}} - x_d^f \right) \end{cases} \quad (4.55)$$

Here, $C_{(\cdot)} \in \mathbb{R}_+$ represents the parameters to be identified in the model, and the function $s(\sigma)$ is a step function defined as

$$s(\sigma) = \begin{cases} 1, & \sigma \geq 0 \\ 0, & \sigma < 0 \end{cases} \quad (4.56)$$

This function also represents the effective range of the bow wave in the $o_f x_f$ direction. When the position of the drogue is farther from χ , the bow wave has no effect, that is, $\mathbf{F}_b = \mathbf{0}$. The bow wave only comes into play within the range of χ . It should be noted that F_{bx} is decomposed into two parts: one part is caused by the aircraft nose, denoted as F_{bx_nose} , and the other part is caused by the receiver aircraft fuselage, denoted as $F_{bx_cockpit}$. We will explain why this is done in the subsequent sections.

(2) Process of Speculating Functional Form

Taking $f_{bz}(\mathbf{p}_d^f)$ as an example, let's explain the process of inferring the functional form. The process of inferring other functions is similar. Fig. 4.18 illustrates the three profiles of F_{bz} , which are derived from Fig. 4.17 (g) and (h). (Note that the training data in Fig. 4.18 has been processed, so the direction is opposite to that in Fig. 4.17.)

Step one: Estimate the three functional relationships $h_{z-x}(x_d)$, $h_{z-y}(y_d)$ and $h_{z-z}(z_d)$ based on these three profile plots. (Note that the issue of sign will be considered in the second step.)

1) The curve in Fig. 4.18 (a) is nearly linear in the first half, and due to the fact that the bow wave cannot affect the drogue when it is far from the aircraft nose, the second half of the curve must be zero. Therefore, this curve can be expressed by the following equation.

$$h_{z-x}(x_d^f) = \left(1 - C_{z2} x_d^f \right) \cdot s \left(\frac{1}{C_{z2}} - x_d^f \right) \quad (4.57)$$

2) The curve in Fig. 4.18 (b) approximates a normal distribution curve, thus it can be expressed

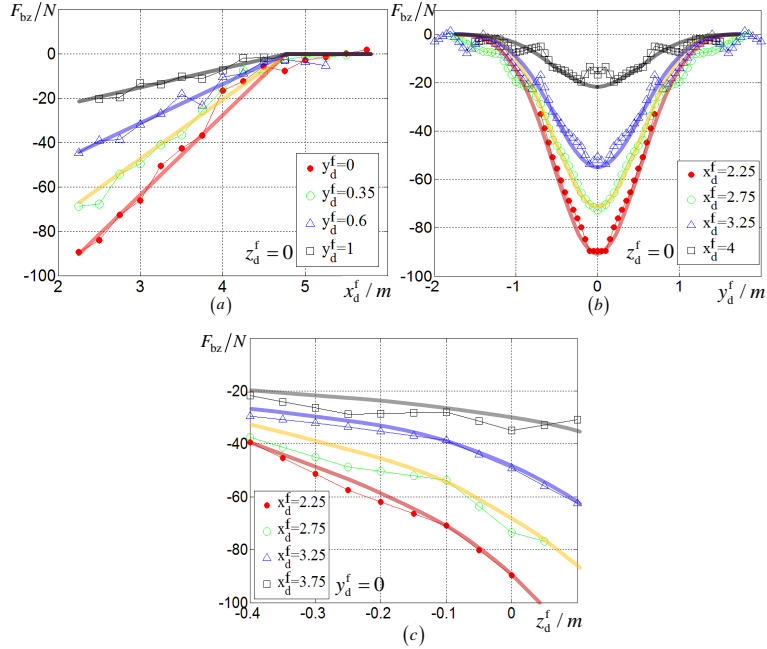


Figure 4.18: Distribution of Training Data on Three Main Planes

using the following equation

$$h_{z-y}(y_d^f) = e^{-\frac{(y_d^f)^2}{C_{z3}}} \quad (4.58)$$

3) The curve in Fig. 4.18 (c) increases in velocity as it progresses, hence it can be expressed using an exponential function.

$$h_{z-z}(z_d^f) = e^{\frac{z_d^f}{C_{z4}}} \quad (4.59)$$

Step two: Assuming the coupling relationships between different directions are

$$f_{bz}(\mathbf{p}_d^f) = -C_{z1} h_{z-x}(x_d^f) h_{z-y}(y_d^f) h_{z-z}(z_d^f) \quad (4.60)$$

where C_{z1} represents the gain in the function, and due to the fact that f_{bz} is always positive when in the docking region, there is a negative sign.

The estimation method for $f_{bx}(\mathbf{p}_d^f)$ and $f_{by}(\mathbf{p}_d^f)$ is similar to that for $f_{bz}(\mathbf{p}_d^f)$, but $f_{bx}(\mathbf{p}_d^f)$ is more specific. The following provides the special treatment for it.

(3) Special Treatment of $f_{bx}(\mathbf{p}_d^f)$

Fig. 4.19 shows the cross-sectional profile of F_{bx} within the $z_d^f = 0$ plane. During the subsequent parameter fitting process, it is found that using a single function to express $h_{x-x}(x_d^f)$ alone cannot pass the goodness-of-fit test based on the determination coefficient (see Section 4.3.3.3). Therefore, according to Fig. 4.19, separating the two components that influence f_{bx} and fitting them separately yields a well-fitted result. These two components are a parabola and a straight line, and further analysis reveals that they correspond to two distinct parts of the bow wave: the bow wave from the aircraft nose and the bow wave from the cockpit.

4.6.3.2 Parameter Estimation of the Model

Estimating the parameters in Eq. (4.55) using the training data is the next step. Similarly, take $f_{bx}(\mathbf{p}_d^f)$ as an example. Since it involves parameters, it can be rewritten as $f_{bx}(\mathbf{p}_d^f, \mathbf{C}_z)$, where $\mathbf{C}_z = [C_{z1} \ C_{z2} \ C_{z3} \ C_{z4}]^T \in \mathbb{R}_+^4$ represents the unknown parameters. Accordingly, the corresponding optimization problem can be expressed as

$$\mathbf{C}_z^* = \arg \min_{\mathbf{C}_z \in \mathbb{R}_+^4} \sum_{i=1}^{N_f} [F_{bx,i} - f_{bx}(\mathbf{p}_{d,i}^f, \mathbf{C}_z)]^2 \quad (4.61)$$

where N_f represents the number of training data points used for parameter estimation. For the initial value selection of this optimization, one can perform a single function fitting on the curves within the profiles and use the obtained parameters as initial values. For example, when estimating $f_{bx}(\mathbf{p}_d^f, \mathbf{C}_z)$, one can choose the initial value as $\mathbf{C}_{z0} = [170 \ 0.2 \ 0.5 \ 0.6]^T$. After setting the initial values, one can use the nonlinear fitting function `nlinfit` provided by

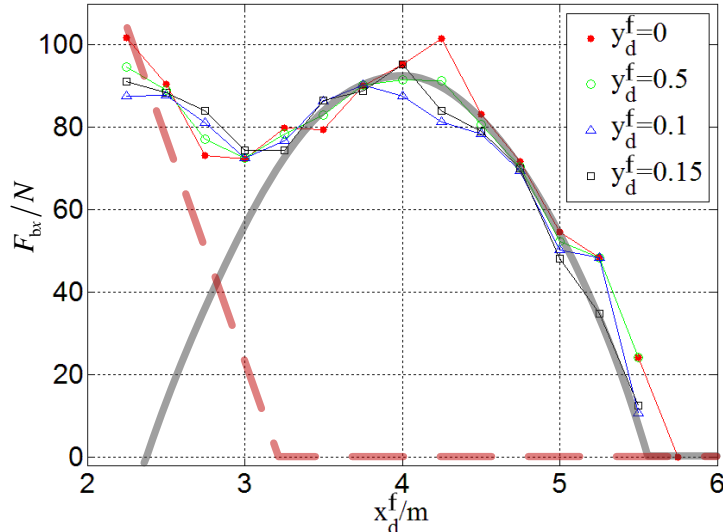


Figure 4.19: Two Components Constituting F_{bx}

MATLAB® to obtain \mathbf{C}_z^* . The estimation method for \mathbf{C}_y^* in $f_{by}(\mathbf{p}_d^f, \mathbf{C}_y)$ is the same as for \mathbf{C}_z^* . As for $f_{bx}(\mathbf{p}_d^f, \mathbf{C}_x)$, the contribution from the nose section can be first estimated. Then, subtract the estimated nose contribution from the training data to obtain new training data, and estimate the cockpit contribution from this data. By substituting the estimated values of \mathbf{C}_x^* , \mathbf{C}_y^* and \mathbf{C}_z^* into Eq. (4.55), the bow wave effect model can be obtained under these conditions as follows

$$\begin{cases} F_{bx_nose} = 91.6170 \left[1 - 0.3220(x_d^f - 3.8870)^2 \right] e^{-\frac{(y_d^f)^2}{2.7395}} e^{\frac{z_d^f}{2.4838}} s(5.6493 - x_d^f) \\ F_{bx_cockpit} = 309.7709 \left(1 - 0.3237x_d^f \right) e^{-\frac{(y_d^f)^2}{0.3851}} e^{\frac{z_d^f}{1.1471}} s(3.0893 - x_d^f) \\ F_{by} = 223.3210 \left(1 - 0.2082x_d^f \right) y_d^f e^{-\frac{(y_d^f)^2}{0.8102}} e^{\frac{z_d^f}{0.6555}} s(4.8031 - x_d^f) \\ F_{bz} = -173.2021 \left(1 - 0.2141x_d^f \right) e^{-\frac{(y_d^f)^2}{0.5697}} e^{\frac{z_d^f}{0.7038}} s(4.6707 - x_d^f) \end{cases} \quad (4.62)$$



4.6.3.3 Validating the Effectiveness of the Parameters

To validate the effectiveness of the parameters, the coefficient of determination [148] is chosen as the criterion for evaluating the fitting performance, denoted as R^2 . Taking $f_{bz}(\mathbf{p}_d^f, \mathbf{C}_z)$ as an example, its corresponding coefficient of determination is defined as

$$R_z^2 = 1 - \frac{\text{SSE}_z}{\text{SST}_z} \quad (4.63)$$

where

$$\begin{cases} \text{SSE}_z = \sum_{i=1}^{N_v} \left[f_{bz,i} - F_{bz}(\mathbf{p}_{d,i}^f, \mathbf{C}_z^*) \right]^2 \\ \text{SST}_z = \sum_{i=1}^{N_v} \left[f_{bz,i} - \frac{1}{N_f} \sum_{i=1}^{N_v} f_{bz,i} \right]^2 \end{cases} \quad (4.64)$$

where N_v is the number of training points used for validation. According to this definition, it can be derived

$$R_x^2 = 0.8866, R_y^2 = 0.9536, R_z^2 = 0.9671 \quad (4.65)$$

Generally speaking, when $R^2 > 0.7$, the fitting results are considered good. Therefore, based on Eq. (4.65), it can be concluded that the speculated model and the estimated parameters are consistent with the bow wave effect.

Fig. 4.20 presents the comparison between the surface formed by $f_{bz}(\mathbf{p}_d^f, \mathbf{C}_z^*)$ on the plane $z_d^f = 0$ and the training data of F_{bx} (represented by the black dots in the figure), corresponding to Fig. 4.17(a). The function f_{bz} is one of the more complex functions in the bow wave effect model, and Fig. 4.20 intuitively demonstrates how well $f_{bz}(\mathbf{p}_d^f, \mathbf{C}_z^*)$ captures the trend of F_{bx} changing with the relative position of the drogue and the receiver aircraft.

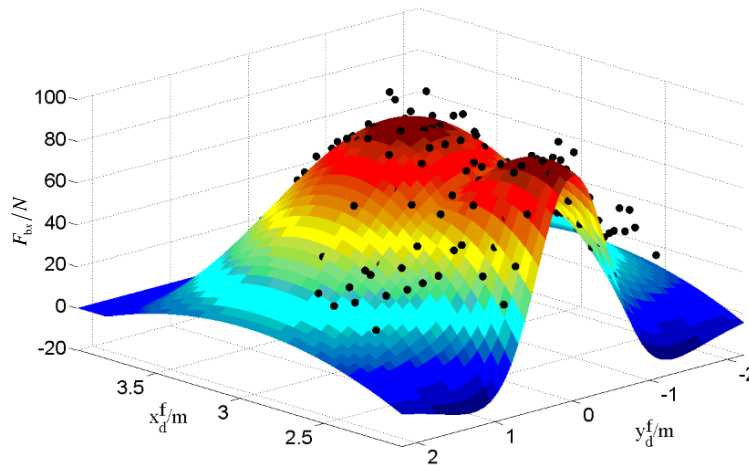


Figure 4.20: Fitting Effect of F_{bx}

4.6.3.4 Matters Needing Attention for Applying the Bow Wave Effect Model

The modeling method for the bow wave effect described in this chapter, while providing an example model for a specific environment (as shown in Table 3.2) and a specific aircraft type, can be extended to model bow wave effects for different aircraft types in various environments. However, when applying this method or model, it's important to consider its application conditions and scope.

(1) Application Conditions: The model (4.55) is developed based on aircraft with an ellipsoidal cone nose, making this function form suitable for such aircraft types as F-16, F-18, J-8, and similar ones. For aircraft with non-ellipsoidal cone nose, the modeling process remains applicable, but the function form would need to be adjusted compared with Eq. (4.54). For instance, aircraft like the X-47B, which has already undergone autonomous docking experiments and features a flying-wing design, can be considered to have a two-dimensional nose rather than a three-dimensional one, leading to a relatively simpler model. Another scenario involves aircraft with canard wings, like the J-10; if the canards are mounted toward the front, they would also need to be included in the modeling process.

(2) Application Scope: The data used to establish this model is obtained from the $\mathbf{p}_{d,i}^f \in [2,6] \times [-2,2] \times [-0.5,0.1]$ region. As a result, the model is more accurate within this specific area. Nevertheless, the model remains applicable in the surrounding areas of this region. Furthermore, considering that $\mathbf{F}_b = \mathbf{0}$ when $x_d^f > 6$ due to the bow wave not affecting the drogue, it is evident that model (4.54) fulfills this condition. Consequently, the model (4.54) is equally applicable within the region where $x_d^f > 6$.

Additionally, there are two points that require clarification:

(1) When modeling the force F_{bx} , the force was divided into two components: the forces from the nose and the cockpit. However, when modeling F_{by} and F_{bz} , the cockpit was not taken into consideration. The reason for this lies in Eq. (4.61), which indicates that the range of force in the F_{bx} direction is relatively extensive. Referring to the parameters in Figure 4.11, it can be observed that F_{bx_nose} becomes effective at approximately 1.2 meters in front of the nose, whereas the effective range of F_{by} and F_{bz} is only about 0.5 meters in front of the nose. This situation implies that, before the probe docks with the drogue, the force component $F_{bx_cockpit}$ from the cockpit has an effect, while the cockpit hasn't yet influenced the other two directions. Therefore, it was not included in the modeling. However, if the position of the probe continues to shift backward, this component will also need to be included in the modeling. This is also why aircraft with canard wings need to be accounted for in the model.

(2) The use of a linear expression for the portion related to x_d^f in the model is due to the relatively good linearity of this part within the docking region. However, in reality, if viewed over a larger range, this part is not necessarily linear. For example, the effect of F_{bx_nose} caused by the nose section with respect to x_d^f follows a quadratic curve. Therefore, the choice of function form is closely related to the range considered.

4.6.4 Simulation Analysis and Model Validation of the Bow Wave Effect

By incorporating the bow wave effect model into the link-connected hose-drogue model, the motion trajectory of the drogue under the influence of the bow wave effect can be derived. By comparing this with the publicly available experimental data from NASA [149], we can further validate the effectiveness of the model. Additionally, this allows to analyze the motion of the drogue during the docking process.

4.6.4.1 Setting of Simulation Environment and Simulation Results

The bow wave effect model and the link-connected hose-drogue model (without HDU and with fixed-length hose) are integrated into the same simulation, as depicted in Fig. 4.21. In order to closely replicate experimental conditions, white noise and a low-pass filter are introduced to simulate the impact of atmospheric turbulence on the drogue. A total of six sets of experimental data are provided in Ref. [149]. Among them, the sixth set of experiments had relatively stable airflow, making it suitable for observing the bow wave effect. Hence, this set of experiments is selected as the control group. Since the experiments in the reference used the drogue equilibrium point coordinate system, we also transformed all the data into the drogue equilibrium point coordinate system.

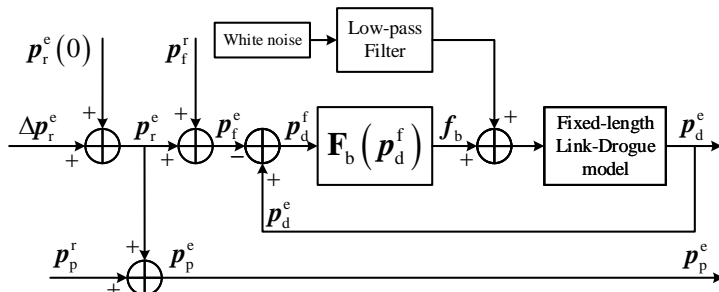


Figure 4.21: Schematic Diagram of Drogue Dynamics Simulation under Bow Wave Effect

Ref. [149] does not provide the docking environment parameters or specific docking controller details. Therefore, we still assume the environment to be the same as in Table 3.2. The specific parameters of the receiver aircraft are as shown in Fig. 4.13. In the absence of a docking controller, we assume the receiver aircraft flies at a constant speed. Although this approach may introduce some deviations, it is sufficient for qualitative analysis of the drogue's dynamics. To ensure that the receiver aircraft's trajectory is closer to the trajectory of Experiment 6 in Ref. [149], we set its initial position as $\mathbf{p}_r^e(0) = [-12 \ -0.54 \ 0.86]^T$ and its trajectory as $\Delta\mathbf{p}_r^e = [\Delta x_r^e \ 0 \ 0]^T$, where Δx_r^e satisfies the following equation

$$[\Delta x_r^e(t)]''' = \begin{cases} 0, & t = 0 \cup t \in (16, +\infty) \\ 0.047, & t \in (0, 4] \cup t \in (12, 16] , \Delta x_r^e(0) = 0 \\ -0.047, & t \in (4, 12] \end{cases} \quad (4.66)$$

Under the influence of $\Delta\mathbf{p}_r^e$, the motion trajectory of the drogue and the probe can be seen in Fig.

4.22. In this figure, figures (a), (c), and (e) show the original data from Experiment 6 in Ref. [149], while figures. (b), (d), and (f) display the simulation results. "Longitudinal" corresponds to the $o_e x_e$ direction, "Lateral" to the $o_e y_e$ direction, and "Vertical" to the $-o_e z_e$ direction (in the experiment, upward is positive, so it is opposite to the $o_e z_e$ direction).

The symbol X_{MISS} represents the position where the probe contacts the plane of the drogue's parachute in the $o_e x_e$ direction, and X_{CAP} is the position where the probe and the drogue are connected to complete the docking. It's worth noting that due to the use of the imperial system in the experiment, the length units in this figure have all been converted to feet. To provide a more intuitive view of this process, we utilized the Virtual Reality toolbox provided by MATLAB® to record a video of this process (as shown in Fig. 4.23). This video can be viewed in Ref. [150]. In the video, Viewpoint 1 represents the pilot's perspective, Viewpoint 2 provides a side view, Viewpoint 3 offers the tanker's perspective, and Viewpoint 4 demonstrates the relationship between the drogue and the probe in the vertical plane.

4.6.4.2 Simulation Analysis and Model Validation

(1) Dynamic Analysis of Drogue under Bow Wave Effect

From the simulation results, the dynamic behavior of the drogue under the influence of the bow wave during the docking process can be summarized as follows:

- 1) As shown in Fig. 4.22, during the time interval from 0s to 8s, the aircraft's nose is far from the drogue, so the drogue is not affected by the bow wave effect.
- 2) As depicted in Figs. 4.22 (e) and (f), from 8s to 10s, the aircraft's nose begins to approach the drogue, and due to the influence of f_{bx_nose} , the drogue starts to descend.
- 3) As shown in Figs. 4.22 (c), (d), (e), and (f), from 10s to $t_{X_{MISS}}$, the aircraft's nose surpasses the drogue, causing the drogue to swing upwards and to the right. Here, $t_{X_{MISS}}$ represents the moment when the aircraft's nose reaches X_{MISS} .
- 4) Based on the simulation results, the motion of the drogue appears to exhibit characteristics similar to those of a second-order dynamic system. Thus, it can be observed from the simulation that if the drogue were to move freely, its trajectory in the final stage would resemble a three-dimensional spiral. In other words, if the docking is not successful, the drogue would swing back. During this time, if the receiver does not retract promptly, the drogue is likely to collide with the probe.

Please note that these descriptions are based on the simulation results and provide insights into the potential behavior of the drogue under the influence of the bow wave effect during the docking process.

(2) Comparison Analysis between Simulation and Experiment

From the dashed ellipses in Fig. 4.22, it can be observed that despite the differences in conditions between simulation and experiment, the overall trend of the drogue's dynamics in the simulation closely matches the experimental data. This further validates the effectiveness of the

bow wave effect model. However, there are still some differences between the simulation and experimental trajectories, which can be analyzed based on the discrepancies between the two.

1) In the experiment, the encounter between the drogue and the probe has already occurred at $t_{X_{MISS}}$, and the drogue's subsequent data lacks meaning.

2) Due to the absence of docking controllers in the provided literature [12], the simulation does not include such a controller. Consequently, the simulated probe does not actively approach the drogue.

3) There is a time drift between the simulation and experiment. This is because in the experiment, the probe approaches the drogue earlier at $t_{X_{MISS}}$, as shown in Figs. 4.22 (a) and (b), which causes a drift in Figs. 4.22 (c), (d), (e), and (f).

4) As indicated by the boxed lines in Figs. 4.22 (c) and (d), the simulated drogue rises and then falls in the $o_e y_e$ direction, whereas this descent phenomenon does not occur in the experiment. This is due to the presence of docking controllers in the experiment, which causes the receiver to approach the drogue and increase F_{by} , preventing the drogue from descending. Since the simulation lacks docking controllers, this phenomenon is absent.

5) As shown within the circles in Figs. 4.22 (e) and (f), the simulated drogue's descent is significantly greater than that observed in the experiment. This phenomenon occurs around 8s to 10s, when only F_{bx_nose} is active. This discrepancy suggests that the drogue experienced an $o_e z_e$ displacement when subjected to the $o_e x_e$ direction force in the simulation, possibly due to inadequate consideration of drogue dynamics.

In summary, the first four differences are primarily due to variations in the simulation environment and the presence of docking controllers, unrelated to the model established. However, the last point results from insufficient consideration of the drogue's dynamics. This is mainly because the link-connected hose-drogue model employed here does not consider the dynamic effects of the Hose Drum Unit (HDU). Thus, in the next section, we will discuss the impact of the HDU on the drogue's dynamics during the docking process and simplify the complex link-connected hose-drogue model.

4.6.5 Appendix: Training Data for CFD Simulation

Table 4.1: Training Data for CFD Simulation

x_d^f	y_d^f	z_d^f	f_{bxo}	f_{by}	$-f_{bz}$
2	0.4	0	1935.152	49.97507	67.78349
2	0.55	0	1962.551	49.90587	56.38194
2	0.7	0	1965.541	53.56217	42.26877
2.25	0	0	1877.09	-1.38444	89.50524
2.25	0.1	0	1891.363	8.478858	89.55186

Continued on next page

Table 4.1 – continued from previous page

x_d^f	y_d^f	z_d^f	f_{bx0}	f_{by}	$-f_{bz}$
2.25	0.2	0	1884.143	23.14848	79.688
2.25	0.4	0	1907.8	42.64901	65.19876
2.25	0.55	0	1931.28	43.14221	50.70876
2.25	0.7	0	1948.082	44.39585	32.93854
2.5	0	0	1888.471	-3.3283	84.03368
2.5	0.1	0	1891.097	12.75222	78.3916
2.5	0.2	0	1889.646	17.89514	77.71612
2.5	0.3	0	1891.902	29.18447	70.80311
2.5	0.4	0	1912.455	38.22988	64.80012
2.5	0.55	0	1925.106	37.56345	41.95024
2.5	0.7	0	1937.53	40.44554	33.88661
2.75	0	0	1905.588	-1.54709	72.78587
2.75	0.1	0	1897.696	10.06669	70.35958
2.75	0.2	0	1891.794	14.38844	65.44239
2.75	0.4	0	1916.689	29.95287	50.69795
2.75	0.55	0	1908.102	29.90309	43.66149
2.75	0.7	0	1925.605	34.67043	28.83245
2.75	0.8	0	1927.103	30.74913	22.5957
2.75	1	0	1937.375	31.89542	19.73628
2.75	1.2	0	1938.813	24.55119	8.037597
2.75	1.4	0	1939.96	17.54958	7.166264
2.75	1.8	0	1955.324	7.74839	0.674521
3	0	0	1906.439	-1.93069	66.10936
3	0.1	0	1906.326	8.260492	59.66183
3	0.2	0	1902.461	7.931259	54.39062
3	0.4	0	1912.583	27.5208	48.09717
3	0.55	0	1906.338	29.47111	37.75587
3	0.7	0	1913.876	30.55886	20.71366
3	0.8	0	1928.057	27.42648	25.23526
3	1	0	1926.199	23.35419	13.32988
3	1.2	0	1934.61	19.23117	4.650642
3	1.4	0	1945.862	12.55815	4.357155
3	1.6	0	1933.849	2.665652	6.048263
3	1.8	0	1945.159	7.973973	-0.90967
3.25	0	0	1899.066	2.701695	50.60028

Continued on next page



Table 4.1 – continued from previous page

x_d^f	y_d^f	z_d^f	f_{bx0}	f_{by}	$-f_{bz}$
3.25	0.1	0	1902.078	11.80255	53.75233
3.25	0.2	0	1906.683	8.608786	46.28071
3.25	0.4	0	1915.213	20.88915	39.34686
3.25	0.55	0	1913.535	21.34352	32.07226
3.25	0.7	0	1923.002	29.24078	16.97864
3.25	0.8	0	1911.378	22.94512	22.62798
3.25	1	0	1928.837	22.81941	13.89667
3.25	1.2	0	1936.018	13.35212	5.372196
3.25	1.4	0	1936.732	8.931533	0.147386
3.25	1.6	0	1942.781	2.066532	7.839279
3.25	1.8	0	1949.75	4.850519	-1.29908
3.25	2	0	1941.735	-1.58934	3.100472
3.5	0	0	1899.424	-2.44892	42.78738
3.5	0.1	0	1892.472	6.468319	45.3292
3.5	0.3	0	1892.072	13.19065	41.90424
3.5	0.4	0	1898.64	16.06715	31.44417
3.5	0.55	0	1906.189	18.75113	18.16805
3.5	0.7	0	1908.816	24.11334	18.15747
3.5	0.8	0	1926.448	16.00554	17.08064
3.5	1.2	0	1937.009	12.01171	3.48231
3.5	1.4	0	1940.195	6.617393	7.853269
3.5	1.6	0	1949.275	1.33581	3.097204
3.75	0	0	1888.775	-0.351	36.97307
3.75	0.1	0	1888.495	-1.31786	36.81176
3.75	0.2	0	1891.718	8.350181	23.12941
3.75	0.4	0	1885.92	19.98882	26.67769
3.75	0.55	0	1895.868	17.93918	27.03524
3.75	0.7	0	1907.38	21.44813	16.06237
3.75	1	0	1915.853	15.08807	11.17834
3.75	1.4	0	1936.246	8.582346	2.163225
4	0	0	1883.635	-1.66483	16.67866
4	0.1	0	1891.216	0.260463	13.353
4	0.2	0	1876.017	5.131186	19.66199
4	0.4	0	1895.766	7.498112	15.06
4	0.55	0	1891.179	15.68732	13.53941

Continued on next page



Table 4.1 – continued from previous page

x_d^f	y_d^f	z_d^f	f_{bx0}	f_{by}	$-f_{bz}$
4	0.7	0	1912.026	12.41592	4.921065
4	1	0	1919.772	14.14816	7.568582
4.25	0	0	1877.409	-4.07732	12.53402
4.25	0.1	0	1897.548	1.496633	15.18791
4.25	0.2	0	1892.1	-0.32216	10.86199
4.25	0.4	0	1896.437	5.904054	6.594666
4.25	0.55	0	1894.221	8.80662	13.47059
4.25	0.7	0	1915.939	9.192991	-0.07344
4.5	0	0	1895.776	0.884979	5.717911
4.5	0.1	0	1900.439	-4.3517	4.330609
4.5	0.2	0	1899.418	3.932347	4.831711
4.5	0.4	0	1900.141	6.1575	9.969199
4.5	0.7	0	1923.698	2.226699	0.41099
4.75	0	0	1907.242	3.912367	7.87268
4.75	0.1	0	1909.358	-2.89677	-0.17089
4.75	0.2	0	1908.356	-0.61287	3.951506
4.75	0.4	0	1910.193	6.424881	2.374755
4.75	0.55	0	1916.29	2.779272	4.436689
4.75	0.7	0	1934.05	2.925473	-0.80836
5	0	0	1924.306	-1.45821	2.837799
5.25	0.1	0	1930.548	-4.36341	1.57146
5.25	0.2	0	1957.479	0.402683	-3.21645
5.25	0.4	0	1950.309	6.477548	3.397986
5.25	0.55	0	1945.299	3.043292	6.797494
5.25	0.7	0	1956.483	2.057735	3.033184
5.75	0	0	1978.988	-4.12688	-1.64644
2	0	0.25	1931.061	-2.39221	70.12786
2	0	0.4	1927.641	6.536772	61.68861
2.25	0	0	1877.538	-2.363	89.7203
2.25	0	0.1	1881.266	5.154949	70.77319
2.25	0	0.25	1910.434	2.421267	57.38434
2.25	0	0.4	1913.352	-4.77149	39.3706
2.5	0	0	1888.471	-3.3283	84.03368
2.5	0	0.1	1893.673	7.470213	69.98457
2.5	0	0.25	1906.001	-2.35917	55.1411

Continued on next page



Table 4.1 – continued from previous page

x_d^f	y_d^f	z_d^f	f_{bx0}	f_{by}	$-f_{bz}$
2.5	0	0.4	1903.965	0.503217	37.26331
2.75	0	-0.1	1867.638	2.020421	79.98985
2.75	0	0	1894.259	-2.66836	73.55091
2.75	0	0.1	1907.699	0.300437	53.76503
2.75	0	0.25	1900.796	1.030111	48.61658
2.75	0	0.4	1902.461	1.787676	37.46697
3	0	-0.1	1896.243	1.749572	79.04185
3	0	0	1906.25	-1.97176	66.0885
3	0	0.1	1901.812	6.220172	48.13084
3	0	0.25	1898.426	2.548486	45.2492
3	0	0.4	1898.788	-3.49069	41.38231
3.25	0	-0.1	1908.33	-1.91339	62.55213
3.25	0	0	1897.847	2.588771	49.27016
3.25	0	0.1	1897.717	10.70473	38.66476
3.25	0	0.25	1897.128	1.039912	33.55502
3.25	0	0.4	1901.85	-3.02839	29.51895
3.5	0	-0.1	1889.657	4.732341	49.68154
3.5	0	0	1896.321	0.201368	41.01397
3.5	0	0.1	1891.197	-3.74036	36.1753
3.5	0	0.25	1893.489	-0.44333	34.37979
3.5	0	0.4	1905.265	0.667469	26.54286
3.75	0	-0.1	1884.474	-4.37587	30.88381
3.75	0	0	1887.277	2.651545	34.84399
3.75	0	0.1	1899.717	2.033757	28.03109
3.75	0	0.25	1901.549	2.809562	28.74055
3.75	0	0.4	1903.798	1.676934	21.73364
4	0	-0.1	1872.461	4.864983	25.39089
4	0	0	1883.635	-1.66483	16.67866
4	0	0.1	1885.352	0.922932	21.73873
4	0	0.4	1906.227	3.922466	15.4815
4.25	0	-0.1	1884.459	4.201428	11.05799
4.25	0	0	1877.409	-4.07732	12.53402
4.25	0	0.25	1895.835	6.581223	17.15091
4.25	0	0.4	1914.089	-6.55676	18.80595
4.5	0	-0.1	1884.904	0.95923	7.187963

Continued on next page



Table 4.1 – continued from previous page

x_d^f	y_d^f	z_d^f	f_{bx0}	f_{by}	$-f_{bz}$
4.5	0	0.25	1901.812	3.516881	12.20134
4.5	0	0.4	1915.519	-0.7898	11.78431
4.75	0	0	1907.242	3.912367	7.87268
4.75	0	0.25	1921.814	0.565272	8.179273
5	0	-0.1	1927.734	4.233589	4.53449
5	0	0	1921.123	0.154792	1.352383
5	0	0.1	1922.571	8.74117	4.09685
5	0	0.25	1934.563	2.122329	6.912462
5	0	0.4	1947.859	-0.2652	8.198037
5.75	0	0	1978.878	-3.87453	-0.23906
2	0.3	0.15	1939.605	31.1767	68.08053
2	0.3	0.3	1948.11	28.52947	60.72145
2	0.3	0.45	1945.238	26.07339	46.26502
2.25	0.3	0	1905.073	39.33223	78.97865
2.25	0.3	0.15	1899.559	27.29833	65.06013
2.25	0.3	0.3	1924.632	17.94953	50.38094
2.25	0.3	0.45	1916.371	16.09782	45.0788
2.5	0.3	0	1899.669	31.27909	73.05958
2.5	0.3	0.15	1908.215	28.14702	55.2124
2.5	0.3	0.3	1915.878	19.77477	45.73813
2.5	0.3	0.45	1925.867	12.91631	36.37103
2.75	0.3	-0.1	1908.274	38.04318	66.04627
2.75	0.3	0	1907.453	25.69103	59.8806
2.75	0.3	0.15	1900.271	22.8196	53.3856
2.75	0.3	0.3	1901.308	13.45491	46.14612
2.75	0.3	0.45	1916.663	16.6892	38.44371
3	0.3	-0.1	1908.868	28.98864	55.74809
3	0.3	0	1901.447	27.26497	52.83898
3	0.3	0.15	1900.88	23.85431	44.99321
3	0.3	0.3	1908.674	13.00684	32.09362
3	0.3	0.45	1916	8.28878	32.6655
3.25	0.3	-0.1	1914.709	28.87577	48.37326
3.25	0.3	0	1897.285	24.02913	43.44238
3.25	0.3	0.15	1895.12	22.67347	36.8537
3.25	0.3	0.3	1906.299	12.15394	26.77808

Continued on next page

Table 4.1 – continued from previous page

x_d^f	y_d^f	z_d^f	f_{bxo}	f_{by}	$-f_{bz}$
3.25	0.3	0.45	1912.954	11.94831	29.95766
3.5	0.3	-0.1	1894.835	23.45421	41.70473
3.5	0.3	0	1892.072	13.19065	41.90424
3.5	0.3	0.15	1887.557	14.94957	32.81424
3.5	0.3	0.3	1908.499	8.885591	23.14094
3.5	0.3	0.45	1904.284	6.429515	24.04007
3.75	0.3	-0.1	1892.979	22.87695	22.15732
3.75	0.3	0	1883.841	12.55068	24.79043
3.75	0.3	0.15	1909.842	8.420726	23.07135
3.75	0.3	0.3	1909.629	15.34369	16.50582
3.75	0.3	0.45	1918.944	12.5867	18.59137
4	0.3	-0.1	1892.007	10.01279	13.69089
4	0.3	0	1885.085	7.68627	20.52778
4	0.3	0.15	1900.667	3.350723	15.17055
4	0.3	0.3	1898.646	5.950576	19.67752
4	0.3	0.45	1908.654	1.735995	13.48066
4.25	0.3	-0.1	1894.251	0.82695	9.271547
4.25	0.3	0	1894.003	6.529135	16.85438
4.25	0.3	0.15	1896.117	2.782244	12.11096
4.25	0.3	0.3	1902.856	7.714981	14.86567
4.25	0.3	0.45	1907.181	1.118459	16.04109
4.5	0.3	-0.1	1886.941	1.930626	7.097323
4.5	0.3	0	1901.498	5.961144	11.53257
4.5	0.3	0.15	1908.773	4.297838	16.774
4.5	0.3	0.3	1908.571	2.657928	14.90869
4.5	0.3	0.45	1924.211	1.63737	9.567619
4.75	0.3	-0.1	1908.523	-1.65388	3.04914
4.75	0.3	0	1908.724	-0.61661	5.661158
4.75	0.3	0.15	1925.177	2.912454	4.77448
4.75	0.3	0.3	1936.655	4.833992	9.875234
4.75	0.3	0.45	1931.258	2.087447	7.782806
5.25	0.3	-0.1	1943.176	1.556812	2.777204
5.25	0.3	0	1938.94	-2.25769	6.091156
5.25	0.3	0.15	1944.1	-3.02404	3.298745
5.25	0.3	0.3	1956.328	4.404246	9.308514

Continued on next page



Table 4.1 – continued from previous page

x_d^f	y_d^f	z_d^f	f_{bx0}	f_{by}	$-f_{bz}$
5.25	0.3	0.45	1957.553	1.449844	0.974527
3.25	0.1	-0.1	1895.803	8.854423	67.84669
3.25	0.1	0.1	1895.3	4.972096	37.03752
3.25	0.1	0.25	1894.38	-2.45197	34.62555
3.25	0.1	0.4	1907.695	1.958618	26.62141
3.25	0.2	-0.1	1903.085	14.18456	56.57365
3.25	0.2	0.1	1893.247	16.68875	41.00027
3.25	0.2	0.25	1912.751	4.595699	30.76815
3.25	0.2	0.4	1912.762	7.867481	31.73922
3.25	0.4	0.1	1899.886	21.54362	35.46951
3.25	0.4	0.25	1898.468	16.23446	28.86395
3.25	0.4	0.4	1905.133	9.082244	34.99778
3.25	0.6	0.6	1907.977	14.59208	26.47914
3.25	0.6	0.8	1920.977	1.388453	12.05727
3.25	0.6	0.8	1911.67	2.043233	18.45201
3.25	0.6	1.2	1916.547	-3.44422	22.94979
3.25	0.8	1.2	1907.557	4.363414	23.55074
3.25	0.9	0.6	1925.953	10.2258	18.85932
3.25	0.9	1	1941.524	0.007668	13.3116
3.25	0.9	1.2	1926.785	3.835454	13.94848
3.25	1	1.2	1917.73	-1.89124	21.21302
3.25	1.2	0.6	1931.372	12.84287	19.83434
3.25	1.2	1.2	1907.535	9.779163	16.48193

4.7 Chapter Summary

This chapter introduces various wind disturbance models during aerial refueling, including the atmospheric turbulence model, wind gust model, wind shear model, tanker wake model and bow wave effect model. Here, the atmospheric turbulence model adopts the Dryden model commonly used in the aerospace field, which is based on the principle of using a white noise signal with limited bandwidth and unit variance to generate the desired turbulence model output through a forming filter; the wind gust model adopts the 1-cosine discrete gust model, which can generate three velocity components varying with the distance; and the commonly used logarithmic and exponential models are introduced for the wind shear model. The tanker wake is modeled using the lift line theory, which can obtain the induced velocity and angular velocity. Finally, the effect of the bow wave generated by the receiver aircraft during the docking phase of

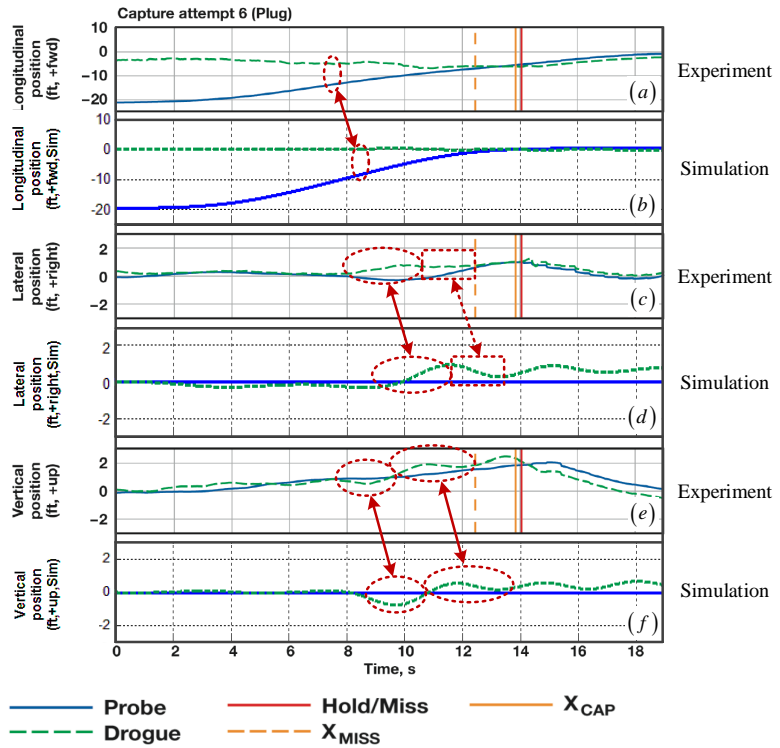


Figure 4.22: Comparison of Simulation Data with Experiments in Ref. [149]

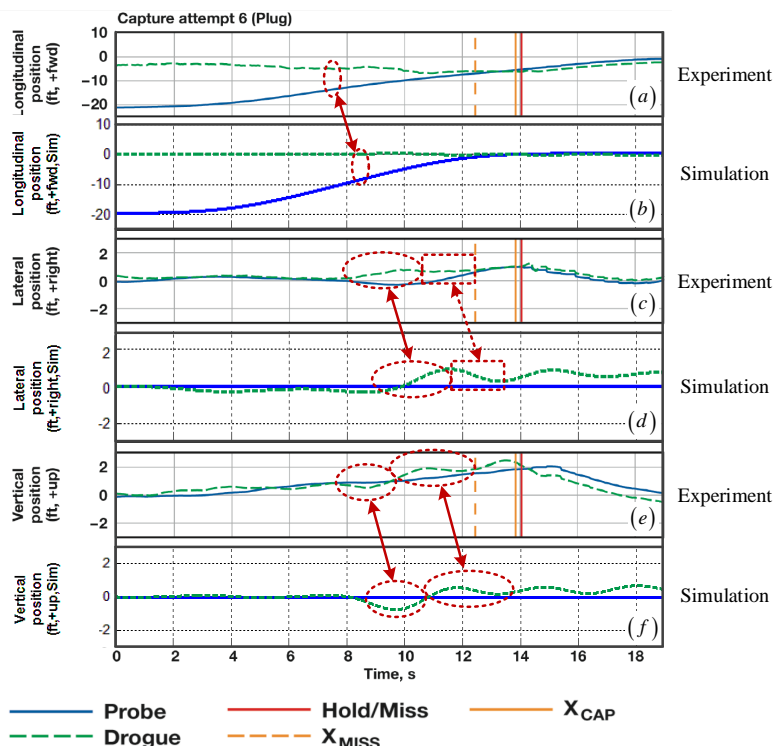


Figure 4.23: Screenshots from Simulation Videos

aerial refueling on the drogue is analyzed.

In addition, the Aerospace toolbox of MATLAB/Simulink software has modularized the atmospheric turbulence model, wind gust model and wind shear model according to the model introduced in the US military specification MIL-F-8785C, and users can directly set relevant parameters for easy use.



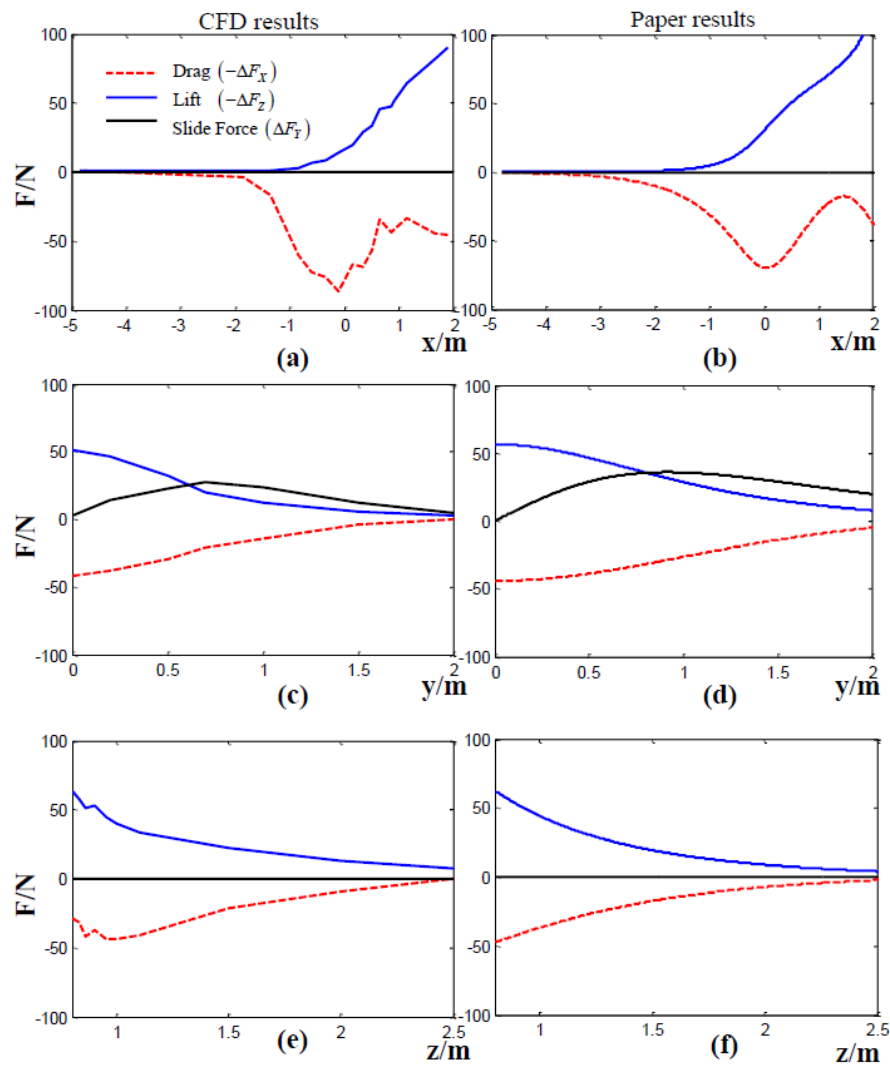


Figure 4.24: Validation of bow wave effect force model of the drogue against CFD results

Chapter 5 AARSim: An Integrated High-fidelity Simulation Platform for Autonomous Aerial Refueling

Aerial refueling has been extensively researched over the last decade and received conspicuous achievements because of its advantages of increasing the endurance and range of aircraft. A complete aerial refueling process includes a variety of interdisciplinary platform modeling (aircraft aerodynamic modeling, flexible hose modeling, complex wind interference, airflow interference between aircraft, etc.) and various complex perception and control tasks (robust visual recognition and tracking, reliable flight control, formation, and coordination control, high-precision air docking control). Existing platforms focus on some aspects of aerial refueling due to the lack of a complete set of high-fidelity simulation, test, and development platforms suitable for the entire process of aerial refueling. Therefore, this paper proposes an integrated high-fidelity simulation platform for autonomous aerial refueling. The platform includes high-precision motion models (including receiver model, tanker model, and hose-drogue model), a high-fidelity 3D simulation that supports visual sensors' output, multi-functional control interface (unmanned autonomous controller, manual joystick control), multiple complex disturbance models and injection interfaces such as wind disturbance and the mass change of receiver. Hence the platform can simulate the dynamics and kinematics of motion models, support selection, setting, and output of different sensors, and demonstrate the entire aerial refueling process in a high-fidelity 3D simulation. Furthermore, algorithms test and development can also be implemented in this platform. In the verification part, two demos implemented in the platform show that the proposed platform can accomplish the entire aerial refueling mission by designing the guidance, navigation, and control algorithms with autonomous and manual methods. The source code of this platform is released, making it easier to study the related work of aerial refueling.

5.1 Introduction

Autonomous aerial refueling (AAR) has become increasingly popular because of the rapid development and use of unmanned aerial vehicles (UAV)[3, 151, 152] which attract the attention of many scholars in colleges and institutions. Significant progress has been made over the last decade. Autonomous refueling programs were drawn up by the US at the beginning of this century and were mainly implemented by three agencies, NASA, USAF, and US Navy. NASA's Autonomous Airborne Refueling Demonstration (AARD) project has been declared successful with the X-47B completing its first mid-air refueling in April 2015. US Navy completed the

mid-air refueling test[153] with F/A-18F in the summer of 2021. In March 2023, Airbus Defense and Space announced that it had conducted an autonomous aerial refueling test with a multi-role tanker transport (MRTT) that can control the UAV without human intervention[154].

However, it is almost impossible for researchers in colleges or other institutions to conduct aerial refueling flight tests, which puts forward requirements to build integrated high-fidelity simulation platforms. This motivates some institutes to build aerial refueling simulation platforms. Aerospace Vehicles Technology Assessment and Simulation(AVTAS) laboratory established a human-in-the-loop refueling scenario using simulation consoles for a boom operator, tanker pilot, and UAV operator, which is built on the commercially available simulation platform D-Six and can run one tanker and four UAV aerodynamics models[46]. This AAR real-time simulation platform with a high-fidelity boom operator station is comparatively complicated and only supports flying boom refueling. In Ref[155], a virtual platform for UAVs' aerial refueling using the probe-and-drogue method is established based on MATLABTM/Simulink and commercial software DynaWORLDS. However, the platform is mainly used to test vision-based algorithms. German Aerospace Center gave a general overview of the performed modeling work, some specifics in selected parts of the model, and the developed simulation infrastructure for the aerial refueling scenario. However, the proposed AVES full-flight research simulator is challenging to build for other researchers[156].

To facilitate the comprehensive modeling, simulation, test, and development of AAR, this paper establishes a high-fidelity simulation platform for aerial refueling based on MATLABTM/Simulink, named AARSim. As shown in Figure 5.1, current aerial refueling systems can be divided into three types: flying-boom type, probe-and-drogue type, and boom-drogue-adapter type. AARSim adopts the probe-and-drogue type because the modeling, disturbances, and control of this type are more complicated. What's more, this type can be applied in multi-aircraft refueling, which is helpful for swarm combat. Users can re-develop other types of platforms based on AARSim.



Figure 5.1: Three types of aerial refueling systems.

The modeling of AARSim is as follows. In a typical AAR process, a tanker enters a racetrack orbit to wait for rendezvousing with receivers, which requires that the tanker not perform a high maneuver. As a result, it is generally assumed that the tanker maintains steady-state flight. A hose with a drogue at its end is attached to a hose-drum-unit (HDU) in the tanker, which is modeled by the finite element method[40]. The HDU is a reel take-up system abling to effectively suppress the hose whip (HWP)[11, 34, 35, 157]. The tanker can generate wake turbulence

trailing from its lifting surfaces. The modeling includes the vortex lattice model, the roll-up vortex model, and so on. Besides wake turbulence, the Dryden[158] model usually represents atmospheric turbulence and the “1-cosin” Gust model for wind gusts. The bow wave effect is modeled with explicit equations to simulate the real flight conditions[40, 44]. The aircraft models (including tanker and receiver) usually take the form of 6-DoF rigid body dynamics. Refueling can change the receiver’s state more than that of the tanker because tankers are often bigger. As a result, a mass-varying receiver model is adopted[159]. Particularly, the 3D visualization model supports the real-time dynamic status display of the aircraft and the hose-drogue model, perception of visual[160] information obtained by sensors[161]. The control in AAR mainly refers to the receiver. For the receiver, there are three distinct control tasks through the refueling process: (1) trajectory generation for rendezvousing, (2) station keeping with the tanker, and (3) docking the drogue. Various control methods can be employed, such as the feedback method, the linear quadratic regulator(LQR), terminal iterative learning controller[29, 41], additive-state-decomposition-based method[88], and novel docking controller[162]. In addition, AARSim supports co-simulation between Simulink and Python through User Datagram Protocol (UDP); hence a variety of interfaces of RflySim[163] can be employed in AARSim.

With this platform, users can study (1) comprehensive interfaces provided from settings like initial environment state settings, aircraft conditions, sensor selection and location, and wind disturbance effect; (2) algorithm design such as perception, guidance, navigation, and control; (3) analysis including hose tension, hose whip effect, and control performance. A provided demo has shown a whole process of a receiver accomplishing autonomous aerial refueling.

The outline of this paper is as follows. Section 5.2 presents the framework containing the architecture and realization of the simulation platform. Section 5.3 introduces the coordinate system and models of the AAR system in detail. The functions and usage of each subsystem in the platform built in MATLABTM/Simulink are demonstrated in Section 5.4. In Section 5.5, two demos in a video are presented on the platform. Finally, concluding remarks are stated in Section 5.6.

5.2 AARSim framework

5.2.1 Architecture

A typical AAR system includes a natural wind model, hose-drogue model, receiver model, tanker model, and flight control system. As shown in Figure 5.2, AARSim established in this paper contains all necessary subsystems.

① Environment model

The block incorporates natural wind and wake turbulence caused by tankers, resulting in a vortex-induced wind field acting on the receiver aircraft.

② Tanker model



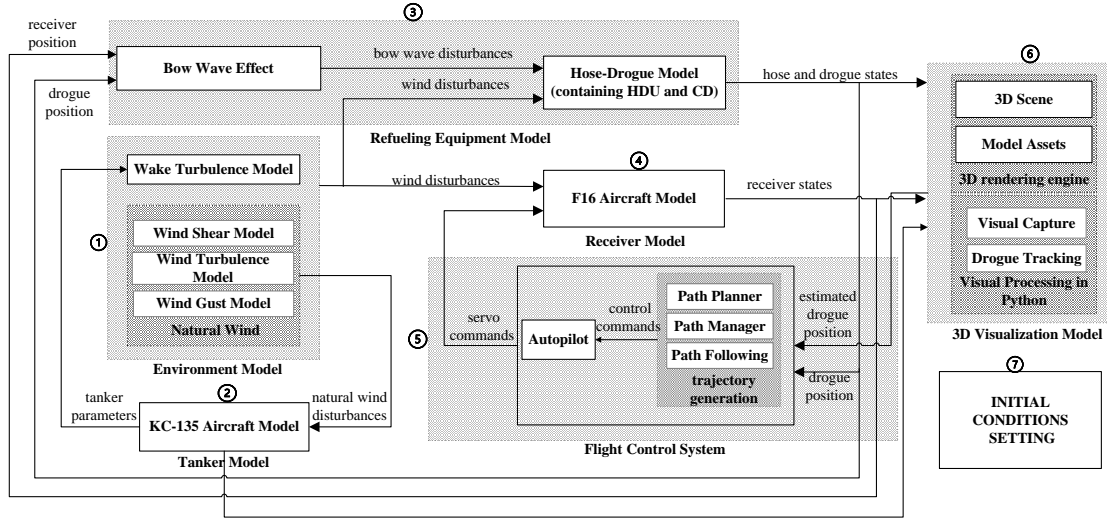


Figure 5.2: The architecture of AARSim.

The tanker is supposed to be in steady flight mode. Hence the disturbances come from natural wind. Meanwhile, the tanker's states lead to wake turbulence.

③ Refueling equipment model

The block contains a “Bow wave effect” block, “Collision Detection” (CD) block, and “DR-dynamics” block. The hose-drogue model is represented by a link-connected system. Precisely, a series of rigid links are adopted according to the finite element method to express the motion of the hose and drogue in the “DRdynamics” block. By iteratively calculating each link’s states (rotation and translation), the position and attitude can be determined at any moment. To avoid excessive contact with drogue and HWP mentioned above, an HDU model is adopted. Besides, the CD block can simulate the collision between the probe and the drogue. Furthermore, with the addition of the “Bow wave effect” determined by the relative position of the receiver and drogue, an additional wind field would superpose the dynamics of the “DRdynamics” block.

④ Receiver model

The receiver is modeled as a 6-DoF rigid body, and the states are determined by translational and rotational kinematics and dynamics.

⑤ Flight control system

Receiver states are determined by the commands of its “Flight control system” and the wind turbulence. The “Flight control system” utilizes the estimated drogue position obtained by perception algorithms from the “3D visualization model” to generate a trajectory for accomplishing autonomous rendezvous and docking. The true drogue position from the “Refueling equipment model” can be used to assess the estimation accuracy and the controller performance.

⑥ 3D visualization model

The block provides typical scenarios associated with the refueling maneuvers and supports visual algorithms development for visual processing, including vision capture and drogue tracking.

∅ Initial condition setting

Many parameters need to be initialized before starting the AAR simulation process. The parameters can be divided into flight conditions, receiver and tanker status, hose-drogue status, and so on, which will be listed explicitly in Table 5.2.

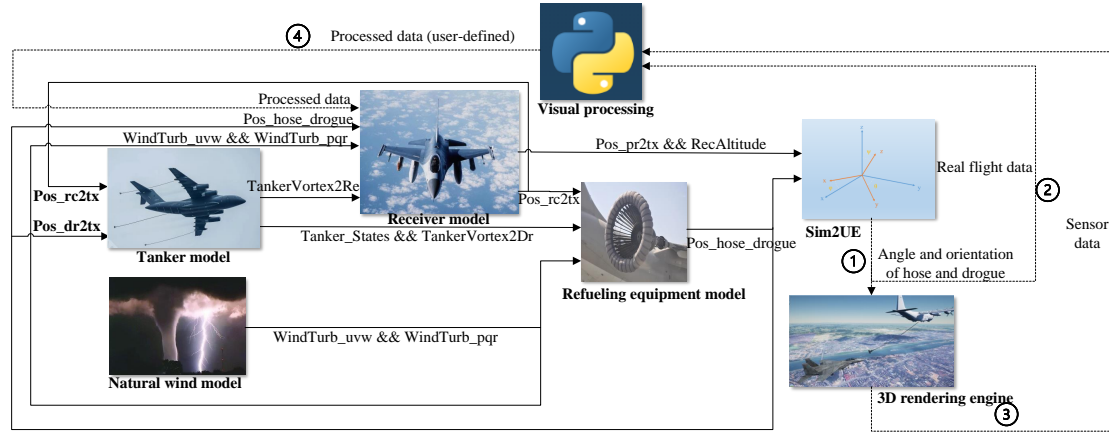


Figure 5.3: The realization of AARSim.

5.2.2 Realization

A comprehensive toolbox is released to improve the efficiency of studies concerning AAR and to make re-searchers study further. As shown in Figure 5.3, the relationships among the receiver system, turbulence, and refueling equipment model are described clearly, which corresponds to Figure 5.2.

The complete toolbox's MATLABTM/Simulink source code and experimental videos can be obtained in the following part of the paper.

The dataflows of AARSim are displayed by solid lines and dashed lines which represent different natures in Figure 5.3. The solid lines are the interior communication in Simulink, while the dashed are the external communication among Simulink®, the 3D rendering engine, and Python.

(1) Solid line signals

The meanings of the signals are consistent with the dataflows among different blocks in Figure 5.2.

(2) Dashed line signals

The dataflows are separated into three parts.

∅ Simulink → 3D rendering engine

The information containing angles and orientations of models is sent to the “3D rendering engine” to display.

∅ Simulink → Visual processing

The real flight data is transmitted to the “Visual processing” block to verify the information obtained by sensors. There are a total of 20 float types of data available. By setting the port

address, users can send the real position and attitude of the tanker to Python.

③ 3D rendering engine → Visual processing

The sensors installed on the receiver can grasp information from the “3D rendering engine” to process for further control. The information, such as images and depth, can be processed by some third-party vision libraries’ functions when performing vision-in-the-loop for AAR simulation.

④ Visual processing → Simulink

The processed data are sent back to Simulink for navigation. Specifically, the length of the processed data is set to 136 bits, the outputs are the ID of aircraft and the concrete data whose types are integers. In the vision-in-the-loop experiment, the output data are the estimated position of the drogue’s central point calculated by user-defined vision algorithms, the distance of the depth camera mounted in the receiver, and the drogue’s central point. The left 13 bits of data are reserved.

5.2.3 Interface usage

The usage of interfaces and the specific implementation of each model mentioned above are introduced in detail. Corresponding to Figure 5.3, they are introduced in order: natural wind model, tanker model, receiver model, refueling equipment model, and sim2UE & 3D rendering engine & visual processing.

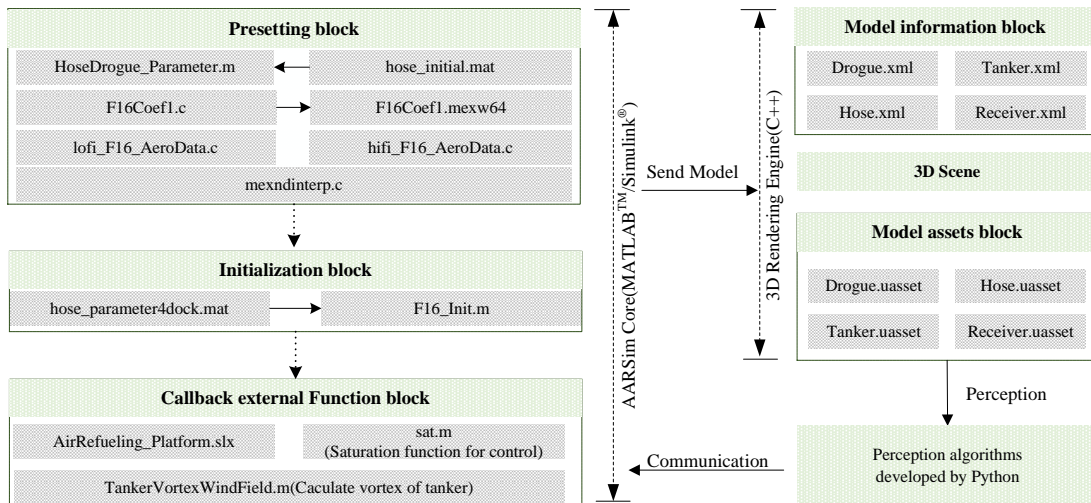


Figure 5.4: Source code structure of AARSim.

(1) Natural wind model

The simulation incorporates both the Dryden model, which accounts for the effects of flight altitude and air-speed, and a discrete gust wind model that includes specific parameters such as time, amplitude, and length. The parameters in the natural wind model can be set to accommodate the AAR conditions.

(2) Tanker model

The calculation method of wake turbulence block generated by the tanker's vortex that influences the receiver and drogue's position is in the script file named "TankerVortexWindField.m".

(3) Receiver model

Wake turbulence, tanker vortex, and control instructions constitute the receiver's input. The "Guidance" block and "Controller" block are responsible for guiding and controlling the receiver to the demand position. The "Controller" block contains two control schemes that support automatic controls via the LQR controller and manual control by handling a joystick connected to the simulation computer.

(4) Refueling equipment model

The bow wave effect, which is determined by the relative distance between the drogue and the receiver, and the parameters of the receiver nose, can be obtained by the method of system identification[40]. The "HDU" block in "DRdynamics" adopts the control method proposed in the previous work[35]. The "Collision Detection" block takes the relative speed and position of the drogue and probe into consideration to generate force feedback which adopts a proportional controller to simulate the collision of the real docking process.

(5) Sim2UE & 3D rendering engine & Visual Processing

Considering the initial parameters of the hose and drogue, the influence of wake turbulence, and the bow wave effect, "Sim2UE" will calculate and send the position and attitude of each link of the hose and drogue to the "3D rendering engine". The "Visual Processing" block is used to develop perception algorithms, which consists of "detect-realtime.py" for recognition and tracking, and "Config.json" for settings.

To introduce more explicitly, the source code structure and interaction of each part are shown in Figure 5.4. The programming environment is separated into three parts: "AARSim Core (MATLABTM/Simulink)", "3D Rendering Engine (C++) ",c and "Perception algorithms developed by Python".

In AARSim Core, the "Presettings block" has the parameters of the hose and aircraft model generated by the function previously. "HoseDrogue_Parameter.m" loads and processes the data of the hose from "hose_initial.mat" and then saves the data in "hose_parameter4dock.mat". The "hose_parameter4dock.mat" stores the parameters of hose, drogue, and HDU shown in Table 5.2. The file ended with ".c" and ".mexw64" are the settings of the receiver.

Then, by running the initialization function "F16_Init.m" and "AirRefuelingPlatform.slx" in order. The functions named "TankerVortexWindField.m" and "sat.m" is used during the simulation. The former is used to calculate the vortex of the tanker; the latter is utilized to generate control commands that incorporate saturation limits.

In "3D Rendering Engine", the model assets and 3D scenes are pre-defined in the UE4 engine directory. The perception algorithms can be developed stand-alone to optimize the recognition results. The AARSim Core sends the model's position and orientation to the 3D Rendering Engine as well as perception algorithms. The 3D Render-ing Engine constructs a high-fidelity

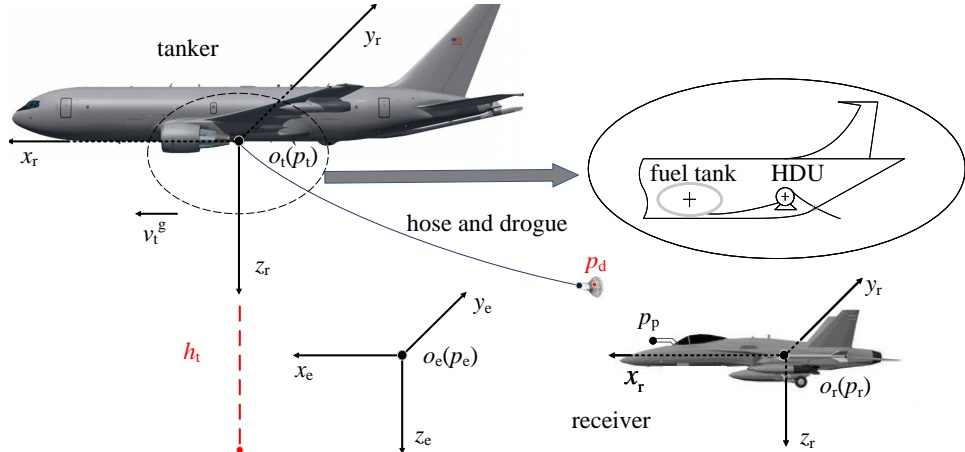


Figure 5.5: Coordinate frames used in this paper and HDU unit.

environment based on the information from MATLABTM/Simulink and the model's properties, which can also be preceived by Python algorithms.

5.3 AAR System Modeling

As mentioned before, a typical AAR system should include the wind model, hose-drogue model, aircraft model, and flight control system, among which the receiver aircraft plays an essential role in probe-drogue refueling on account of performing a maneuver to accomplish rendezvous, formation with tanker aircraft as well as docking with the drogue. In this section, the design model of the AAR system is introduced in detail. For the convenience of building a mathematical model of every sub-system of the AAR system, the coordinate systems used in this paper are shown as follows (refer to Figure 5.5).

(1) Earth-Fixed Coordinate Frame ($o_e - x_e y_e z_e$): This frame is used to study the states of tanker and receiver aircraft relative to the surface of the earth, which is assumed to be flat. The $o_e x_e$ axis is aligned with the projection of the velocity of the tanker v_t^g on the ground for convenience, and the $o_e z_e$ axis points perpendicularly to the ground, and the $o_e y_e$ axis is determined according to the right-hand rule.

(2) Tanker Coordinate Frame ($o_t - x_t y_t z_t$): This frame is used to study the states of receiver aircraft and hose-drogue relative to the tanker aircraft. The origin of this frame p_t is fixed to the conjunctive point between the tanker and the hose. The $o_t x_t$ axis is identical to the velocity of the tanker v_t^g , and the $o_t z_t$ axis points belly down, and the $o_t y_t$ axis is determined according to the right-hand rule.

(3) Receiver Coordinate Frame ($o_r - x_r y_r z_r$): This frame is used to study the states of receiver aircraft. The origin of this frame is fixed to the mass center of the receiver aircraft, namely p_r . The $o_r x_r$ axis points to the nose direction in the symmetric plane of the receiver aircraft, and the axis is in the symmetric plane of the receiver aircraft, pointing downward, which is perpendicular to the $o_r x_r$ axis, and the $o_r y_r$ axis is determined according to the right-hand rule.

5.3.1 Aircraft model

5.3.1.1 Tanker aircraft model

In an actual aerial refueling process, the tanker aircraft usually enters a racetrack orbit pattern to wait for rendezvousing with the receiver aircraft[164]. Hence, it is felicitously assumed that the tanker aircraft maintains steady-state flight in a straight line with constant airspeed and altitude to simplify the problem without loss of generality. A KC-130 mass-point tanker aircraft model is used in our AAR platform with the flight condition of $h_t = 3000$ m and $v_t = 120$ m/s .

5.3.1.2 Receiver aircraft model

The receiver aircraft used in the AAR platform is an F-16. The University of Minnesota puts forward a nonlinear F-16 aircraft model package, which is built on MATLABTM/Simulink software including a low-fidelity model and a high-fidelity model with a more extensive aerodynamic data range, and leading-edge flap[165]. The high-fidelity model has an additional control surface, namely the leading-edge flap, which is governed by the angle of attack, and the aircraft's static and dynamic pressures. It allows the aircraft to fly at higher angles of attack. Thus, the nonlinear F-16 aircraft model in the package is used as a receiver aircraft model in the AAR platform. The control input units and ranges of the F-16 aircraft model are shown in Table 5.1.

Table 5.1: Control input units and ranges of the F-16.

Control Input	Units	Min Value	Max Value	Rate Limit
Thrust	lbs.	1000	19000	10000 lbs/s
Elevator	deg.	-25	25	60 deg/s
Aileron	deg.	-21.5	21.5	80 deg/s
Rudder	deg.	-30	30	30120 deg/s

In AAR operation, the receiver aircraft with respect to the tanker's position and orientation rather than with respect to the earth-fixed frame is emphatically concerned, which indicates that it is necessary to model the receiver aircraft in the tanker frame. It will be convenient to model the receiver aircraft in the receiver frame with a well-developed method and then transform it into a tanker frame.

The platform provides a mass-varying receiver model which is close to the actual AAR process. The mass of the receiver will increase with the amount of fuel added during the refueling process. The total weight and moment of inertia of the receiver will be influenced by the fuel tanker's change. The mass-varying receiver model ignores the refueling weight in the hose and the consumption, and it is only needed in the refueling phase which means the invariant mass receiver model can be utilized in the left phase of the AAR process. The force equations, moment equations, kinematic equations, and navigation equations of the invariant

mass receiver model, and the detailed formulas derivation of the varying mass receiver model refers to Ref[159].

5.3.2 Refueling equipment model

In the probe-and-drogue system, there are usually two types to mount the central part of the refueling system on the tanker, including under the centerline, or using a pod under the wing. The centerline hose and drogue refueling is considered in AARSim, the wing-pod refueling can also be adopted. To suppress the hose whip behavior, the HDU utilizes a reel take-up system which is located in the front end of the flexible hose[33] as shown in Figure 5.5. When fully deployed, the hose has a trailing length of 15 m , while a diameter of 0.068 m and a specific linear density of 4.1 kg/m is assumed. Besides, the high-speed drogue is modeled with a diameter of 0.70 m and a weight of 29.5 kg .

A physically deduced multi-body model, namely the link-connected model, is used to describe the flexible hose-drogue dynamic model according to the finite element method, where the hose-drogue is regarded as ten rigid links. As shown in Figure 5.6, the orientation angles of each link with length $l_j \in \mathbb{R}$ are described by $\alpha_j \in \mathbb{R}$ and $\beta_j \in \mathbb{R}$, where $j = 1, 2, \dots, N$ and $N \in \mathbb{Z}^+$ is the number of rigid links ($N = 10$ in AARSim). It is assumed that the masses and loads associated with each link are concentrated at the joints whose positions $P_j \in \mathbb{R}^3$ And the drogue's position is expressed by P_d . The effects of HDU and wind turbulence are also displayed in Figure 5.6. The resultant external force, including both gravitational and aerodynamic forces, acts on each lumped mass, whereas aerodynamic forces are due to the wake of the tanker, steady wind, and atmospheric turbulence. The drogue is modeled as a rigid body with a conical geometry and fine aerodynamics creating longitudinal and lateral forces, which is significant to respond realistically to the bow wave.

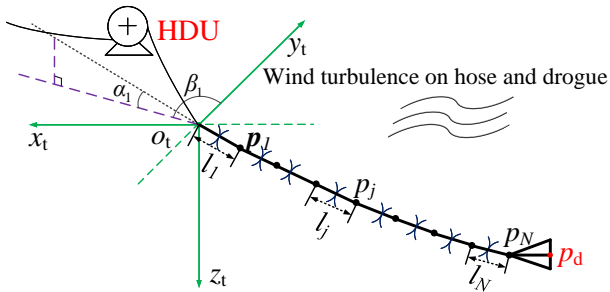


Figure 5.6: The link-connected model of hose and drogue.

The reel take-up system is used to retract the hose when hose tension drops below the static catenary value during drogue and probe coupling. To describe this scene, the link length is considered variable, which allows for studying the dynamic effects of the hose-drogue model, like hose whip behavior. However, for a reel take-up modeling purpose, only the first hose segment is modeled as having variable length. A modified HDU controller proposed in Ref.[35] based on Ref.[33, 166] has a good transient response.

5.3.3 Natural wind model

The air disturbance includes natural wind, wake turbulence of tanker, and bow wave, while bow wave only influences the hose-drogue model. What follows in this subsection will establish the natural wind model in detail.

5.3.3.1 Natural wind

Wind turbulence and wind gusts are known as a part of perturbation that affects aircraft and refueling equipment seriously. Turbulence is a stochastic process defined by velocity spectra. According to the American Military Specification MIL-F-8785C[167], the Dryden wind turbulence model uses the Dryden spectral representation to add turbulence to the aerospace model by passing band-limited white noise through appropriate forming filters.

The turbulence intensities are determined from a lookup table that provides the turbulence intensity as a function of altitude and the probability of the turbulence intensity being exceeded. At altitudes between 1000 feet and 2000 feet, the turbulence velocities, and turbulence angular rates are determined by linearly interpolating between the value of low and high.

5.3.3.2 Wake turbulence

The vortices that trail from the tanker's lifting surfaces generate considerable turbulence for the receiver as well as probe-drogue, to which the Helmholtz horseshoe-vortex model is applicable[151, 168]. The part of the vortex sheet along the span of the wing or horizontal tail is the bound vortex, whereas the parts that continue in the downstream direction are the tip vortices. Moreover, wing vortices rotate inward, and tail vortices rotate outward[145] as shown in Figure 5.7. There is a total of six vortex filaments, including two bound vortices and four tip vortices. The velocity of the wind induced by the wake of the tanker at a given point is the vector sum from all six filaments.

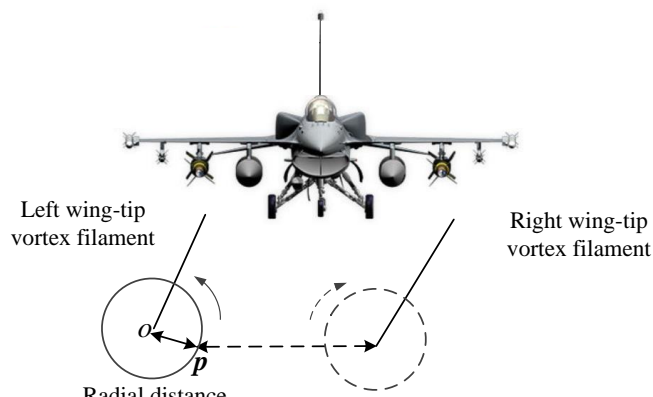


Figure 5.7: Wing tip vortices induced by tanker aircraft.

For a given point in wind axes, the velocity of the wind induced by the left-wing tip vortex can be computed by the vortex effect modeling technique[145].

5.3.4 Bow wave effect

In a probe and drogue aerial refueling system, the bow wave of the receiver aircraft will produce a robust aerodynamic effect on the drogue at the docking phase. The bow wave effect occurs when the receiver aircraft approaches the drogue into the area of influence (AOI) of the bow wave effect, which is a significant difficulty of docking control in probe and drogue aerial refueling[9, 169].

Two approaches are used to model the bow wave effect. The first approach represented in Ref[44] can obtain an analytical form model which adopts stream function defined by the superposition of fundamental stream singularities to model the inviscid flow field around the forebody of the receiver. Then the aerodynamic coefficients are used to calculate the induced aerodynamic force on the drogue.

The other approach is represented in Ref[40], where the bow wave effect model is figured out in the form of a nonlinear function vector with undetermined parameters based on profiles of training data within AOI which are obtained by Computational Fluid Dynamics (CFD) software, the undetermined parameters can be determined by nonlinear regression based on these training data. To work with the hose-drogue dynamic model, this bow wave effect model is suitable to simulate the behavior of the drogue with receiver aircraft approaching. Besides, this model applies to dock controller design to overcome the bow wave effect actively.

5.3.5 Successful docking criterion

During the refueling process, it is not easy for the receiver aircraft to contact the drogue. In addition, more serious is that the drogue occasionally causes damage to the receiver, such as cracked or broken canopies and damage to the probe. Therefore, the NASA AARD project[170] represents a two-dimensional cross-section of the capture and miss criteria. A similar capture criterion of successful or failed docking attempts is defined in this platform. As shown in Figure 5.8, the capture radius R_c is defined as 0.1m inside the outer ring of the drogue, which would reach a 90% success rate with minimal vertical and lateral velocity, according to the recommendation of pilots. The success rate can also be predicted by the method proposed in Ref[73].

A relative closing speed is required to capture successfully during the refueling scenario[40]. Therefore, a successful docking attempt should satisfy

$$\sqrt{\Delta y^2 + \Delta z^2} < R_c \quad (5.1)$$

$$v_{\min} < v_{r,x} - v_{d,x} < v_{\max} \quad s.t. \Delta x = 0$$

where Δx , Δy and Δz represent the longitudinal, lateral, and vertical distance between probe and drogue; $v_{r,x}$, $v_{d,x}$ are the longitudinal speed of the receiver and the drogue; and v_{\min} , v_{\max} are the minimum and maximum relative closing speed thresholds. The criterion[29] implies that the radial error reaches within the capture radius, and the relative closing speed is within a range, indicating a successful docking attempt.

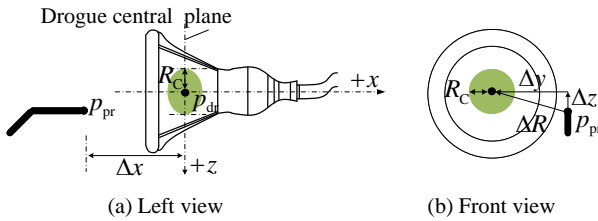


Figure 5.8: Criteria of successful or failed docking attempt.

When the docking phase starts, the simulation data will be recorded to calculate the docking errors while the demonstration running in the 3D rendering engine. Once the criterion set up for docking has been satisfied, the probe and the drogue will be connected to fly with relative static mode. The simulation can be paused and terminated manually or ends when the set time is up.

5.3.6 3D visualization model

The simulation outputs are linked to a 3D rendering engine constructed by Unreal Engine 4 to provide typical scenarios associated with the refueling maneuvers. Such a 3D rendering engine can display real-time information of receiver, tanker, and hose-drogue within the simulation, which contains position, orientation, and attitude on the foundation of taking account of wind turbulence and bow wave effect. It also allows users to explicitly observe the relative relationships (position, etc.) among objects in the simulation and the whole dynamic docking process. Users can switch viewpoints at any time conveniently and observe the process of docking at any viewpoint to get the desired view of the scenarios. Figure 5.9 shows three different views: side view, front view, and back view from Figure 5.9(a)-(c). Thus, the intuitive movement of the aircraft as well as the hose-drogue model is provided by the 3D rendering engine. Meanwhile, since the variety of the external environment is essential to the perception and control of aircraft, users can switch the scenarios in the 3D rendering engine to meet the actual needs of AAR.

The information is sent to the corresponding processing software through the transmission interface of the 3D rendering engine. The processing results can be transferred back to MATLABTM/Simulink for control. A complete control closed loop is built, and users can develop and verify the aerial docking algorithms on this basis. Using the 3D rendering engine of the simulation platform can provide a high-fidelity display for the development and verification of the algorithm for aerial refueling. More importantly, the algorithm can be quickly iterated on the platform, which can significantly improve the development efficiency of the algorithm.

5.4 Platform's function

After modeling the AAR system, this paper will introduce the entire aerial refueling process, the initial settings, algorithms design, and model analysis in the platform.

5.4.1 AAR process

As shown in Figure 5.10, a typical AAR probe-drogue refueling procedure incorporates joining from the rendezvous position to the observation area where receivers enter an echeloned queue, and then the receivers maneuver to the astern of the tanker aircraft, namely the trail position in the designated refueling line which may be either the centerline or from a wing-mounted pod. Afterward, the receivers approach the drogue stably. Once refueled, the receiver disengages, falls back, and maneuvers starboard to the reform area. In general, there are five phases during the aerial refueling process: rendezvousing, formation-flying, docking, refueling, and reforming.

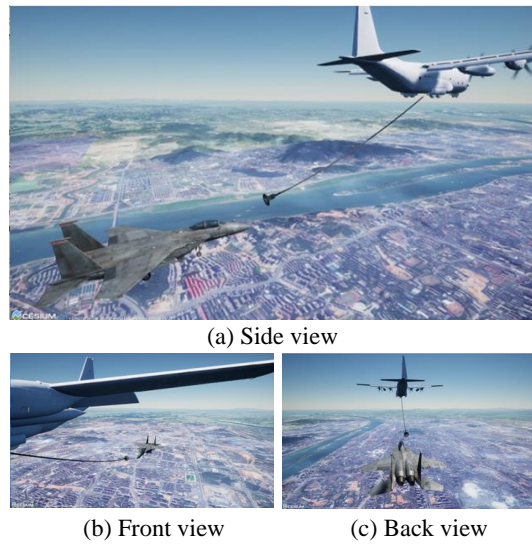


Figure 5.9: Different viewpoints of the modeled virtual world.

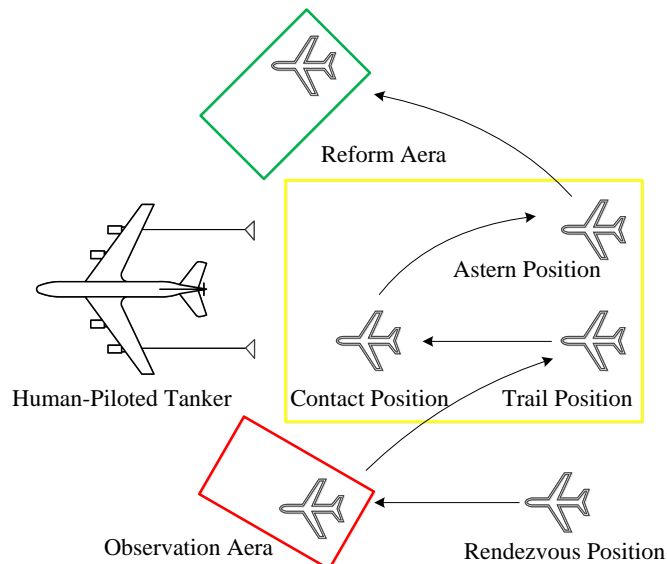


Figure 5.10: Typical AAR refueling procedure.

The built AAR platform can simulate these scenarios to provide a convenient way to study AAR. As previously mentioned, a complete aerial refueling process includes five phases. More

precisely, several modes can be divided during the aerial refueling process, such as rendezvous mode, station-keeping mode, join mode, refueling mode, reforming mode, and so forth.

5.4.2 Initial condition setting

5.4.2.1 Flight status

Some parameters should be initialized before starting the simulation. To be more specific, as shown in Table 5.2, many parameters can be defined by users to initialize the simulation environment which corresponds to the script file named “F16_Init.m”. Take the linearized aircraft models as examples, the nominal conditions, including altitude and airspeed, are specific flight conditions of a tanker, around which the receiver aircraft is also linearized. Due to the nominal altitude of the tanker being 3000 m, the initial position of the tanker in the earth-fixed frame can be defined as $p_{t0}^e = \begin{bmatrix} 0 & 0 & -3000 \end{bmatrix}^T$, while the receiver's initial position is defined as $p_{r0}^e = \begin{bmatrix} -30 & 1 & -2992 \end{bmatrix}^T$. Considering the relationship between the earth-fixed frame and the tanker frame, the receiver's initial position in the tanker frame represents the trail position at the docking phase.

Parameters listed in Table 5.2 are dependent on the model's materials such as the drag coefficient of the drogue, linear density, and radius of the hose; or specifications like the receiver's probe position, the tanker's wingspan and weight. Drogue's parameters left are predefined by the models themselves.

The number of links can be adjusted by modifying the block in the simulation. If users want to adjust the length and the first link's length, change them in an initialization file. The parameters in HDU can be adjusted without constraints as long as it works better. The constrained parameters are nominal altitude, nominal airspeed, and trim-states of the receiver. The nominal altitude and airspeed are supposed to match the aircraft's performance, and the trim state can be set for specific conditions according to users' demands.

5.4.2.2 Sensors

Multiple types and numbers of sensors are supplied for the perception of AAR in the platform. As shown in Figure 5.3, the installation of sensors can be initialized in the perception algorithm when constructing the communication with Simulink. To recognize and locate the drogue, the receiver needs to mount various sensors to get relevant information such as an RGB camera for color images and a depth camera for distance. At the same time, the types of sensors mounted on the receiver vary according to different conditions. For example, the infrared camera is applied in a situation that lacks visible light. If a more accurate perception is needed, point cloud data obtained by Light Detection and Ranging (LiDAR) is also available. The sensors' effects of depth image and RGB image are shown in Figure 5.11. Particularly, the darker the black, the closer the distance is in Figure 5.11(a).



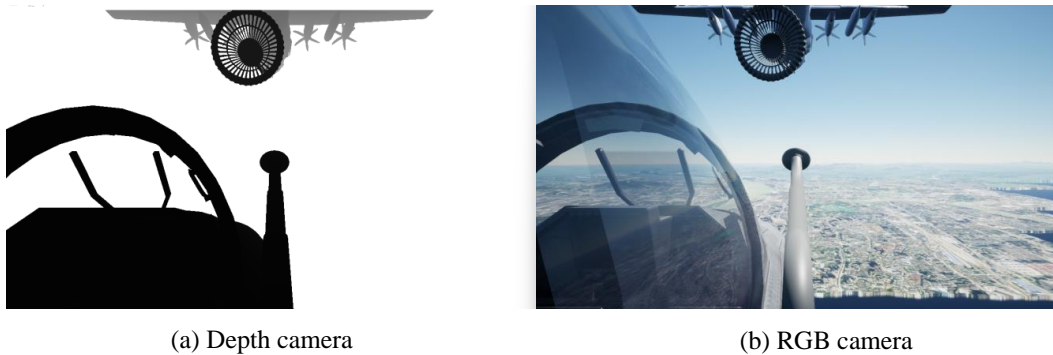
Table 5.2: Initialized parameters with default values.

Parameters		Symbol in "F16_Init.m"	Default Value	Unit
Flight Conditions	nominal altitude	<i>altitude</i>	9843	
	Nominal airspeed	Airspeed	393.72	
Receiver	initial position	<i>p0_rc</i>	$[-30 \ 1 \ 8]^T$	
	attitude angle	<i>Euler_0</i>	[0 trimAlpha 0]	rad
	angular velocity	<i>pqr_0</i>	$[0 \ 0 \ 0]^T$	rad/s
	probe position	<i>d_pr_rc</i>	$[7.6 \ 0.5 \ -2.44]^T$	
	weight	<i>mass</i>	639.64	s
Tanker	initial position	<i>xyz_0</i>	$[0 \ 0 \ -3000]^T$	
	wingspan	<i>wingspan</i>	40	
	weight	<i>tankerWeight</i>	8000	
Parameters		Symbols in "hose_parameter4dock.mat"	Default Value	Unit
Drogue	drag coefficient	<i>Cdr_</i>	0.8	
	weight	<i>Mdr</i>	29.5	
	radius	<i>Rdr</i>	0.305	
Hose	number of links	<i>N</i>	10	
	length	<i>length</i>	15	
	linear density	<i>I_density</i>	4.1	kg/m
	linear radius (external)	<i>RI</i>	0.0336	
	radius (internal)	-	0.0254	
	length of first link	<i>I1</i>	2	
HDU	coefficient	<i>k_reel</i>	0.5	
	coefficient	<i>kd</i>	500	
	Static tension force	<i>T_reel_initial</i>	1610	
Criteria	capture radius	-	0.15	

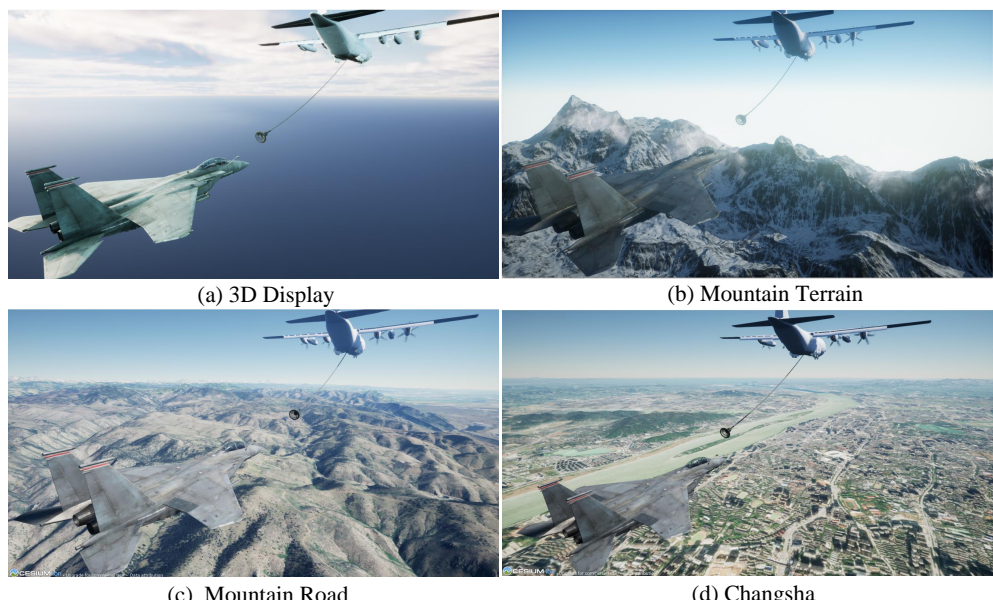
5.4.2.3 3D Scenarios and model assets

As shown in Figure 5.12, external environment conditions are essential to the perception and control of aircraft during the AAR process. The scenarios cover wide areas to satisfy long-distance experiments. Users can switch different AAR scenarios and develop user-defined scenarios in the 3D rendering engine. In addition, real satellite imagery scenes can be introduced if needed.

Model assets can also be replaced so users can select proper models of aircraft or place markers on drogue and flexible hose models for recognition in the UE4 engine which corresponds to the Model assets part in Figure 5.4. AARism provides maps such as “3D Display”, “Mountain Terrain”, “Mountain Road” and “Changsha” which correspond to Figure 5.12(a)-(d) respectively. Users can switch different maps when entering the 3D visualization model by inputting the key

**Figure 5.11:** Images obtained by sensors.

“M”.

**Figure 5.12:** Scenarios of AAR.

5.4.3 Algorithm design

5.4.3.1 Navigation algorithm

The drogue’s position needs to be recognized precisely for docking during the process. Therefore, the navigation algorithm designs are fundamental and significant tasks that rely on the data obtained by sensors. The platform supports the perception algorithms’ development and deployment in the “3D visualization model”. As mentioned above, communication has been established between Simulink and Python which can be used to transmit information generated by the user-designed vision algorithms. Due to the diversity of sensors’ data, users can determine certain or multisensory fusion perception algorithms.

5.4.3.2 Guidance algorithm

The development of a guidance algorithm has a close relationship with the navigation algorithm. The interface of visual capture and drogue tracking is provided to design the navigation algorithms that control and navigate the aircraft's flight. The Python block in Figure 5.3 obtains the information collected by sensors in the 3D rendering engine, and then the drogue's position is calculated by the vision algorithms and sent back to Simulink for guidance and control. In the vision-in-the-loop experiment, the processed data from Python can be added to the navigator block to improve the performance of the AAR, which fully demonstrates the practicability and extensivity of the platform.

5.4.3.3 Control algorithm

Different controllers must be designed to meet various task requirements, or the controller parameters must be changed to accommodate various conditions. A position-tracking controller can guide the receiver to the target location by following the generated reference trajectory when the receiver plans to maneuver from the rendezvous position to the observation area or from the observation area to the trail position. In contrast, it probably does not apply to docking control because of the severe air disturbance, especially the bow wave effect acting on the drogue at the docking phase. Therefore, an interface is provided for designing the controller to achieve a different task in the AAR simulation platform.

5.4.4 Model analysis

According to the initial settings and algorithm designs, the analysis concerned system stability and periodicity, station-keeping controller, wind disturbance, HDU controller, and docking accuracy can be implemented. Table 5.3 shows the crucial parameters to analyze in “F16_Init.m”. Users can exert a pulse signal to the system to observe the outputs of the system to analyze the system stability and motion mode as well as the station-keeping controller's performance. The analysis of wind turbulence and HDU controller is recommended to record the data while running.

Table 5.3: Analysis parameters.

Analysis item	Parameter1	Parameter2	Parameter3
Stability motion mode	A_lon	B_lon	$C_lon_xd_h$
station-keeping controller	k_lon	k_la	-
wind turbulence	<i>The parameters are in “Total Turbulence” block</i>		
HDU controller	T_hose	dl_1	-



The parameters of the receiver's state space equation are listed in "F16_Init.m". Take the longitude equation as an example to analyze the stability and motion mode, the parameters are "A_lon", "B_lon" and "C_lon_xd_h". The station-keeping controller is designed as an LQR controller, the parameters are "k_lon" and "k_b_la" which represent the feedback of longitude and lateral direction respectively. Attention must be paid to the "Total Turbulence" in block "Refueling equipment model" to analyze the wind turbulence. For the HDU controller, "Tu_hose" and "dl_1"m are the tension and the slack rate of the hose after running the simulation.

5.5 Demos

5.5.1 Demo objectives

Objective 1: The first demo will demonstrate the complete process of using the platform to simulate AAR. A vision navigation method is adopted to recognize the drogue and perform docking tasks considering the error of satellite navigation signals and the dynamic characteristics of the drogue in close range. The initial settings, algorithm design, results, and analysis will be introduced in detail. As shown in Figure.??, the entire AAR task is performed in this section.

Objective 2: To enhance the effectiveness of pilot training on the ground, AARSim provides support for both automatic and manual control using a joystick connected to the simulation computer. Objective 2 is similar to Objective 1, but it replaces the LQR controller of the "Controller" block with a physical joystick in the receiver model as shown in Figure 5.3. This feature can provide a more realistic flight simulation environment, which can aid pilots in becoming more familiar with the aircraft's operation and help them develop their emergency response skills. The joystick control interface is open, allowing users to design the transfer function of the joystick's input.

5.5.2 Initial settings

The setting of flight status is consistent with the default values in Table 5.2, as shown in Figure 5.13(a). In Figure 5.13 (b), an RGB camera and a depth camera are selected to mount on the receiver to capture images and depth information during AAR. The sensors' parameters such as type, location, and angle of installation are set in advance in "Config.json" which will be utilized to initialize sensors when the navigation algorithm starts. The model assets and scenarios are kept as default.

5.5.3 Implement of two objectives

The built platform can realize typical aerial refueling tasks, such as station keeping, docking control, and joining from the rendezvous position to the observation area, with a nonlinear aircraft model.

F16_Init.m	Config.json
<pre> 1 %% — Parameters of Hose and Drogue Model 2 load hose_parameter4dock.mat 3 %% — Receiver Parameters (F-16) 4 % aircraft model parameters 5 fi_flag = 1; % '1' for the high fidelity model; '0' for the low fidelity model 6 mass = 636.94; % aircraft mass (slugs),namely $kg/(lbf \cdot m/ft/N)$ 7 Inertia = [9496.0, -982.0, 0.55814.0; -982.0, 0.63100.0]; % inertia matrix 8 S_ref = 300.0; % Reference area (m) 9 b_ref = 30.0; % Reference span (m) 10 d_ref = 11.32; % Reference length or mean chord length (m) 11 % flight condition 12 altitude = 9843; % altitude (ft) 13 airSpeed = 393.72; % airSpeed (ft/s) ... 61 %% — Tanker Parameters (KC-135) 62 wingSpan = 40; % wingSpan (m) 63 tankerWeight = 8000; % generally set as the half of the max-load capacity (146000kg) </pre>	<pre> 1 { 2 "VisionSensors": [3 { 4 "SeqID": 0, % index of the current sensor 5 "TypeID": 1, % RGB camera 6 "TargetCopter": 1, % The ID of the copter on which the sensor is mounted 7 "TargetMountType": 0, % relative coordinate of copter 8 "DataWidth": 1280, % The width of captured picture 9 "DataHeight": 720, % The height of captured picture 10 "DataCheckFreq": 30, % The update frequency of checking data 11 "SendProtocol": [0,127,0.0,1999.0,0], % Transmission mode,IP address,port number 12 "CameraFOV": 90, % Field of view 13 "SensorPosXYZ": [4.7, 0.54, -1.45], % location of the sensor 14 "SensorAngEular": [0, 0, 0], % angles of the sensor 15 "otherParams": [0,0,0,0,0,0] % reserved 16 }, 17 { 18 ... 19 } 20] 21 } 22 } 23 } 24 } 25 } 26 } 27 } 28 } 29 } 30 } 31 } 32 } 33 } </pre>

(a) F-16's parameters

(b) Sensor's configuration

Figure 5.13: Initialization files.

Researchers who pay attention to the design of linear models can also deploy concerned algorithms in the platform. A linearized model is introduced in this part for controller design. After trimming the nonlinear equation, linearizing the nonlinear model at a steady level flight condition ($\mathbf{X}_r^*, \mathbf{U}_r^*$), and letting $\tilde{\mathbf{X}}_r \stackrel{\Delta}{=} \mathbf{X}_r - \mathbf{X}_r^*$ with the perturbations, then the linearized equation of the receiver in state-space form can be obtained as

$$\dot{\tilde{\mathbf{X}}}_r = \mathbf{A}\tilde{\mathbf{X}}_r + \mathbf{B}\tilde{\mathbf{U}}_r \quad (5.2)$$

where $\mathbf{A} = \partial f_r / \partial x_r \in \mathbb{R}^{12 \times 12}$ and $\mathbf{B} = \partial f_r / \partial u_r \in \mathbb{R}^{12 \times 4}$ are Jacobian matrix, known as state matrix and input matrix respectively, and there are a lot of numerical algorithms to calculate \mathbf{A} and \mathbf{B} [171–173], making it easier to linearize nonlinear aircraft model. Although here a simplified linear model is applied, the simulation platform can support nonlinear models for more complex and comprehensive analysis.

5.5.4 Implement of Objective 1

In navigation algorithms, a robust and fast deep learning algorithm named you only look once version 5 (YOLOv5) is applied for visual recognition and tracking [174, 175]. After running the “AirRefueling_Platform.slx” file, the AAR scenarios are displayed in the 3D rendering engine. Then start the perception algorithm “detect-realtime.py” and the information transmission is established. The information obtained from sensors can be transmitted to a Python file to process and the processed data consists of the drogue’s center point coordinate and the distance between the probe and the drogue’s center point can be sent back to Simulink for further control.

For control algorithms, LQR controllers are used for position control, and HDU is used to control the tension of the hose to avoid HWP. For guidance algorithms, since recognition and control are separated, which is different from the visual scheme [79, 176, 177], the terminal iterative learning controller will take the processed data as input to dock because the controller can learn the process to minimize the docking error.

Overall, the perception algorithm processes the raw image and depth data and estimates the relative position between the drogue and the probe. Then the estimated data are sent to the port named “EstimatePos” for generating navigation commands which is the demand position for the

receiver to fly. Finally, the LQR controller utilizes the demand position to control the receiver. The data relationship among perception data, navigation controller, and LQR controller in the “Receiver model” block is shown in Figure 5.14.

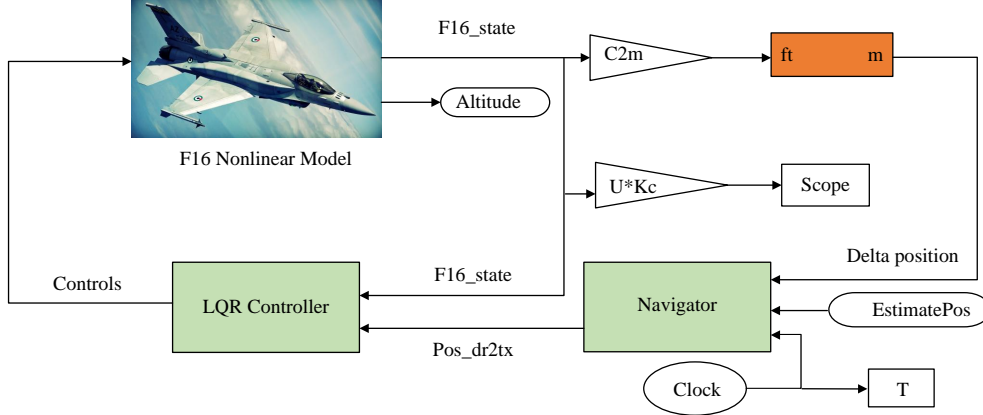


Figure 5.14: The dataflow of Objective 1.

5.5.5 Implement of Objective 2

Compared to Objective 1, the LQR controller is replaced with manual control via a joystick to complete the docking process. The pilot uses information of the receiver’s states and relative position from the tanker to control the joystick for docking in Figure 5.15.

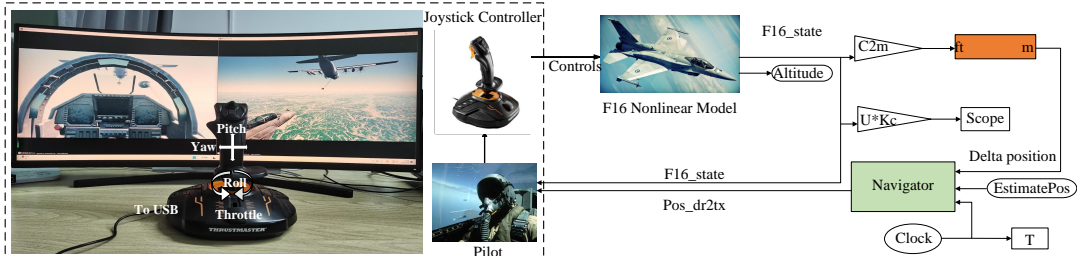


Figure 5.15: The dataflow of Objective 2.

To be specific, the joystick is connected to the simulation computer via USB to establish a connection with the simulation platform. As shown in Figure 5.15, the forward and backward movement of the joystick corresponds to the pitch of the receiver, while the left and right movement corresponds to the yaw. Clockwise and counterclockwise rotation corresponds to the roll, and the bottom slider corresponds to the throttle.

5.5.6 Results and analysis

Objective 2 is the same as Objective 1, hence the results and analysis of Objective 1 are presented in this part. Based on the settings and designs before, several successful docking attempts are accomplished. Figure 5.16 shows the moment of both failed and successful docking. And the whole process of the AAR in the simulation of different phases is shown in Figure 5.17

that corresponds to Figure 5.12. The analysis will be illustrated from stability and motion mode, wind turbulence, hose tension monitoring, and docking accuracy respectively.



Figure 5.16: The docking moment.

5.5.7 Stability and motion mode

The linearized system can be divided into lateral and longitudinal systems to design controllers which should take the stability and the flight mode of the receiver into consideration. To avoid repeating the analysis of the system, the section takes the longitudinal system as an example. When giving the receiver a pulse of the elevator deflection, the responses of each state variable of the longitudinal motion are shown in Figure 5.18. The variation of airspeed and attack angle are selected to illustrate the different modes of the receiver. The variation of the speed corresponds to the phugoid mode which is determined by a pair of small conjugate complex roots. It has the characteristics of a long oscillation period and slow decay. The variation of the attack angle corresponds to the short period mode which is determined by a pair of roots with larger values. The oscillation period is shorter, decay is faster.

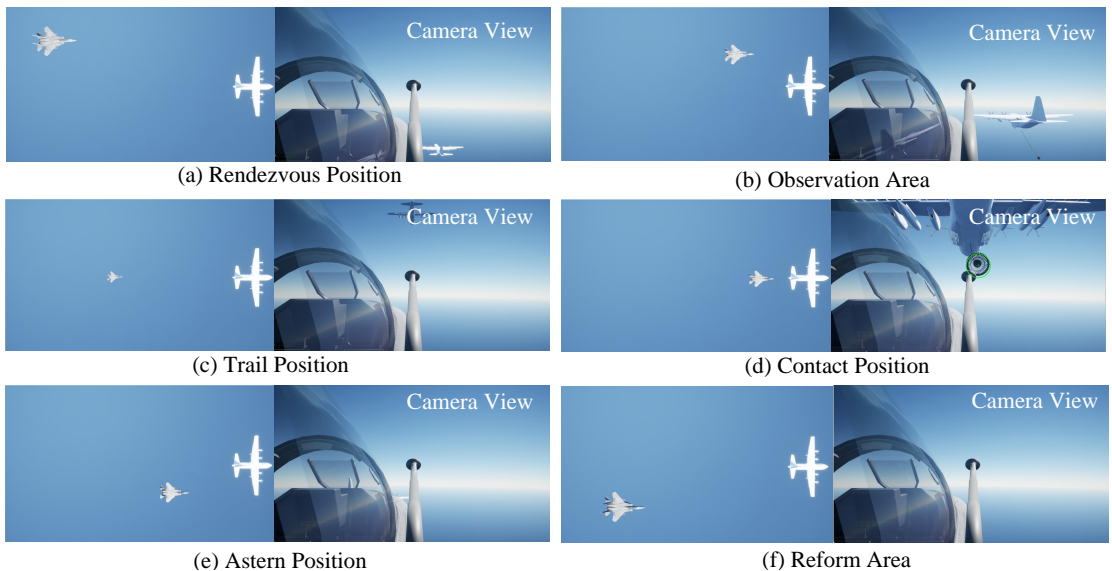


Figure 5.17: God view(left) and onboard camera view(right).

Figure 5.18 shows the system cannot keep stable when input has changed, hence the LQR controller is introduced to improve the system's performance. The results with and without the

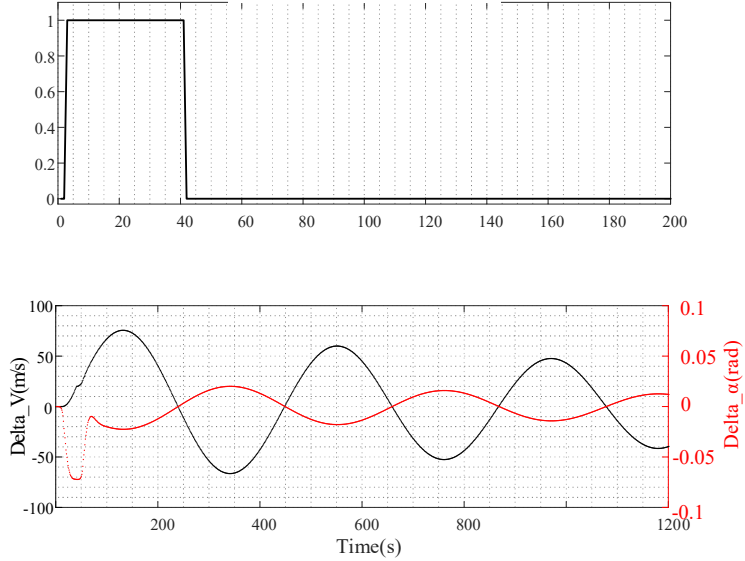


Figure 5.18: Response of elevator pulse.

LQR controller are compared in Figure 5.19. On the condition of adopting the LQR controller, the aircraft climbed to a certain position swiftly and become stabilized, which demonstrates great maneuverability and stability.

5.5.8 Wind turbulence and hose tension monitoring

Then, the model is applied to the platform to simulate a docking process. During the process, the turbulence and the hose tension can be obtained for analysis. As mentioned above, the wind turbulences will disturb the drogue's movement and the HDU can suppress HWP. The turbulences containing bow wave effect, wake turbulence and natural wind, and hose tension are shown in Figure 5.20(a)-(c), which show the variety of the force caused by total turbulence in 7 successful docking processes. The curve shows the significant influence of the bow wave effect since they share a similar trend which just differs in offsets. When the probe approaches the drogue, the force in total turbulence increases tremendously. In addition, the HDU model has been applied to control the hose-drogue model which prevents excessive contact and the HWP effect. The real-time monitoring data of the hose tension is shown in Figure 5.20 (d). The original tension of the hose is set to 1610 N and every trough represents the successful docking during the simulation.

The HDU controller exerts an influence on the adjustment of the hose tension to prevent excessive contact in a complete docking process. In Figure 5.21(a), the receiver starts to approach the tanker from 30s to t_1 and the probe gets in contact with the drogue at t_1 . The hose remains the same length during this period. Then the probe drives the drogue to fly forward between t_1 and t_2 . The slack degree of the hose varies for the contact, which will lead to a change of the tension. At the same time, the HDU controller keeps the slack degree of the hose at a minimal value to accommodate this period. The probe and the drogue fly forward with a relatively static

mode from t_2 to t_3 . The hose slack rate degree returns to 0 quickly and almost no changes after 38s. The probe breaks away from the drogue at t_3 which means a successful docking has been finished. The delta offset in the y axis and z axis are kept in a small region to ensure the accuracy and stationarity of the docking. In Figure 5.21(b), the distributions of the three parameters are all very close to zero, and their fluctuations are very small. Some of the outliers correspond to the peaks and valleys in Figure 5.21 (a). The reason for these outliers is that the position of the drogue is deviated due to the wind disturbance during the flight process. Hence the HDU controller can effectively avoid HWP and guarantee the stationarity and safety of the refueling system.

5.5.9 Docking accuracy

A successful docking has been shown in Figure 5.22. The refueling phase matches the time from the 40th second to the 50th second. The error is $e_{dr}^{pr} = [0.023 - 0.050.069]^T$ which satisfies the requirement $\Delta R = 0.0884 < R_C$. After performing the refueling task, the receiver maneuvers back to the initial position which means the accomplishment of the third and the fourth phase.

5.5.10 Source code and video

The MATLABTM/Simulink source code of AARSim is published on GitHub:

<https://github.com/kelearnliu/AARSim>

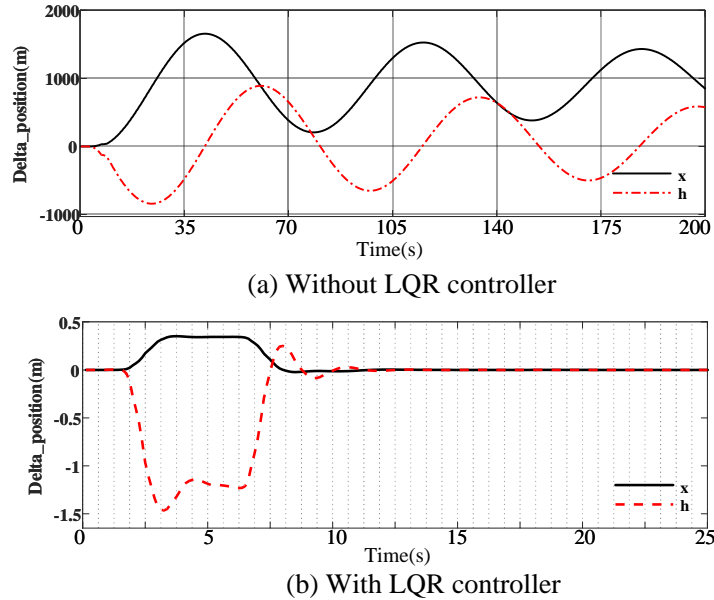
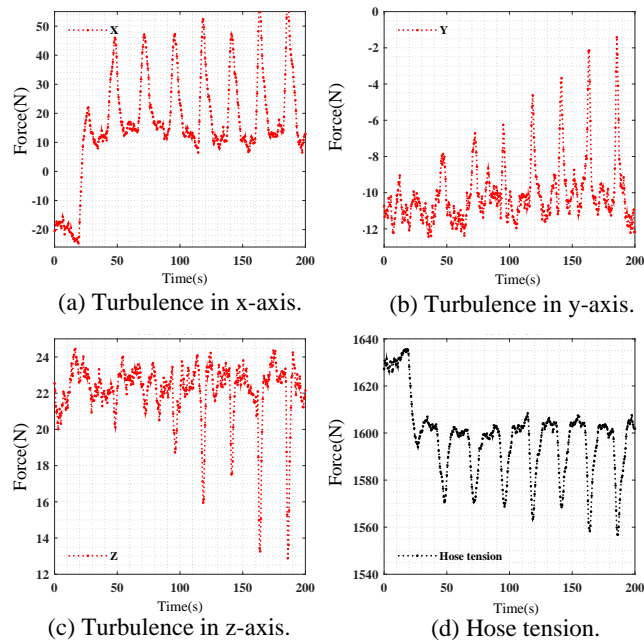
A video has been published to demonstrate AARSim, which includes an introduction to the platform, simulation procedures, and two demos as illustrated in Section 5.5.1:

https://v.youku.com/v_show/id_XNTk2NTAzMTMzMg==.html

5.6 Chapter Summary

This paper proposes a simulation platform for AAR that is of great help to scientific research and education. AARSim is developed based on MATLABTM/Simulink which contains aircraft models, refueling equipment model (with HDU model), and air disturbance models (incorporated with wind turbulence, wind gust, and wake turbulence of tanker) and bow wave effect. More importantly, a 3D rendering engine is used to create high-fidelity scenarios and visualize the entire phases based on comprehensively modeling the process of AAR. The information relationship among various models and the interfaces provided in each subsystem which can be modified according to the actual situation is illustrated in detail. The platform not only supports the more deep-going and more refined modeling of every model in the AAR process in modular form but improves the development efficiency of concerned algorithms tremendously with low cost. Meanwhile, the co-simulation of Python and MATLABTM/Simulink extends the availability, which can utilize abundant methods in perception and control.



**Figure 5.19:** The effect of the LQR controller.**Figure 5.20:** Hose tension and total turbulence.

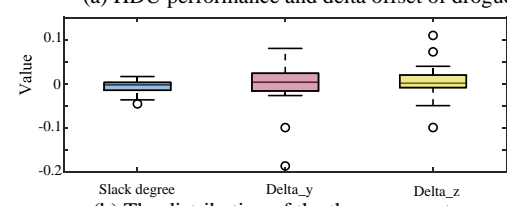
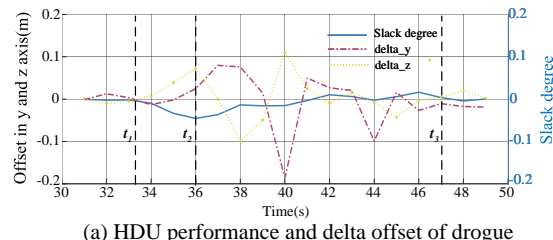


Figure 5.21: HDU controller performance.

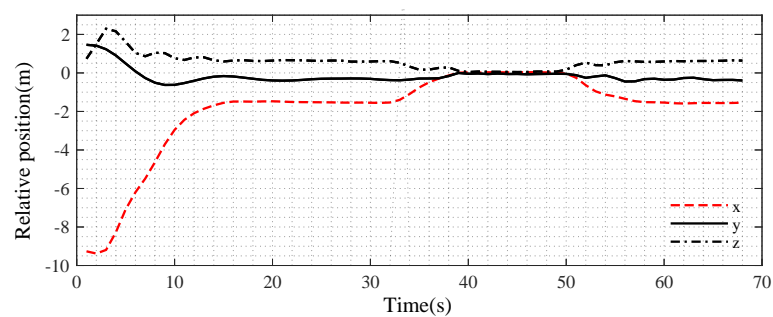


Figure 5.22: Successful docking process.

Chapter 6 Vision-Based Relative Position Estimation

Probe-and-drogue refueling is widely used owing to its simple requirement for refueling equipment and flexibility. For autonomous aerial refueling, determining the distance between an unmanned receiver aircraft and a tanker aircraft is of great importance. In this chapter, a vision-based method is proposed to estimate the position of the drogue by using a camera. This method is a two-step process. The first step is to detect the markers fixed on the drogue and match them as a circle. The second step is to improve the image robustness. In addition, the proposed method is verified in the simulation with a virtual reality toolbox. Simulation results indicate that the proposed method can track the circle steadily and estimate its position in real time..

6.1 Introduction

Along with the development of the UAV technology, Autonomous Aerial Refueling (AAR) systems are urgently needed. However, the probe-and-drogue system has an apparent drawback, which is susceptible to disturbances, making docking very difficult [178]. Thus, the autonomous aerial refueling requires precise relative position between the receiver aircraft and the drogue of the refueling system [179].

During the past decades, researchers have been making significant efforts to design position estimation methods, including Inertial Measurement Unit (IMU), Global Positioning System (GPS) [180], and vision-based position estimation method [181]. One aspect to note is that, due to the restriction of the safety, it is not permitted to attach electronic devices onto the drogue. Relative position information can be obtained from IMU measurements, but zero drift and accumulative error result in its accuracy not meeting the requirements. The GPS method has been made in 5cm to 10cm accuracy for formation flying, but problems emerge with accuracy decreasing because of signal blocked or other interference factors. In addition, it is hard to attach the GPS equipment to the drogue. Thus, as a newly-developed contactless method, the vision-based position sensor like a camera is a preferable solution to get the relative position [182].

The research on vision-based position estimation has been developing in the world, and many meaningful achievements have been made [183–185]. The existing schemes of vision-based refueling systems can be classified into two groups: image-based algorithm and feature tracking algorithm. The image-based algorithm regards the visual sensor as a two-dimensional sensor, whose characteristics such as image Jacobian matrix and gray value can be integrated into the control law. A typical example of this kind of method is the algorithm using the predictive

image for vision aids [184]. The feature tracking algorithm is to obtain the relative position by means of acquiring and tracking specific features (points, lines, etc.) from a visual sensor. Typical examples of this kind of method include visual positioning systems based on infrared vision sensors [186] and VisNAV active vision navigation systems [187, 188].

In this chapter, the main algorithm is a kind of feature tracking algorithm. For example, in the VisNAV system, the position and attitude information is obtained by LHM [189] algorithm which is based on a monocular camera and some infrared Light Emitting Diode (LED) marking points. Nevertheless, the LHM algorithm is an iterative algorithm, which is somewhat time-consuming. In face of such a situation, in this chapter, a simpler feature point detecting and matching method with relatively high efficiency and reliability is proposed. In addition, some extra measures are also taken to improve the robustness of the system.

The main features of this chapter are as follows.

- 1) A feature point algorithm of detecting and matching the markers as a circle is proposed.
- 2) In order to improve the robustness of the system, a Kalman filter (KF) based method to reduce observation errors is proposed. In addition, several general correspondence methods are proposed to reduce the influence of noise, redundant and losing points.
- 3) Simulations are carried out to validate the effectiveness of the proposed methods.

This chapter is organized as follows. Some preliminaries and problem formulation are introduced in Section II. In Section III, the main algorithms used in this chapter are presented. Then, in Section IV, the details and results of the simulations are expressed. Finally, in Section V, the conclusions are presented.

6.2 Preliminaries and Problem Formulation

6.2.1 The Layout of Markers

In order to determine the distance among the receiver aircraft, the tanker aircraft and the drogue of the refueling system, it is necessary to place some markers on the surface of the latter two. Moreover, in order to represent the geometric characteristics of the drogue, the markers (see Fig. 11.2) can be distributed on the circle of the drogue canopy with different intervals between them. Combined with physical and algorithmic filtering methods, markers can be easily extracted from the image.

6.2.2 Coordinate System Transformation

In this chapter, the coordinate systems are defined as follows (see Fig. 11.3). The camera coordinate system $o_c - x_c y_c z_c$ is attached to the camera. Its origin is the optical center of the camera, with x_c axis pointing forward, y_c axis pointing right, z_c axis pointing downward. The other coordinate system is the drogue coordinate system $o_d - x_d y_d z_d$, whose origin is the center of the drogue. Moreover, its orientation is the same as the camera coordinate system.



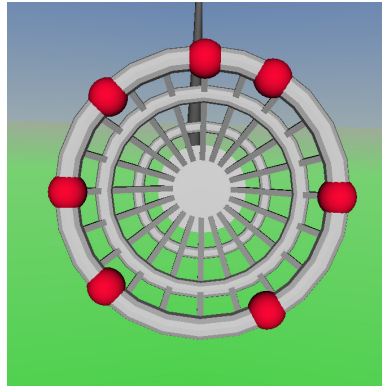


Figure 6.1: Markers located at the drogue

Assume that vectors $\mathbf{p}_c \triangleq [x_c \ y_c \ z_c]^T$ and $\mathbf{p}_d \triangleq [x_d \ y_d \ z_d]^T$ are in two coordinate systems above, which satisfy [190]:

$$\mathbf{p}_c = \mathbf{R}_d^c \mathbf{p}_d + \mathbf{t}_d^c \quad (6.1)$$

where $\mathbf{R}_d^c \in \mathbb{R}^{3 \times 3}$ is the rotation matrix, and $\mathbf{t}_d^c \in \mathbb{R}^3$ is the translation vector. The rotation matrix \mathbf{R}_d^c from the drogue coordinate system to the camera coordinate system can be shown as

$$\mathbf{R}_d^c = \mathbf{R}_z^T(\psi) \mathbf{R}_y^T(\theta) \mathbf{R}_x^T(\phi). \quad (6.2)$$

In the equation above, with three principal axes, a rotation of angle ϕ about the x-axis is defined as

$$\mathbf{R}_x(\phi) \triangleq \begin{bmatrix} 1 & 0 & 0 \\ 0 & \cos \phi & \sin \phi \\ 0 & -\sin \phi & \cos \phi \end{bmatrix}. \quad (6.3)$$

Similarly, a rotation of angle θ about the y-axis is defined as

$$\mathbf{R}_y(\theta) \triangleq \begin{bmatrix} \cos \theta & 0 & -\sin \theta \\ 0 & 1 & 0 \\ \sin \theta & 0 & \cos \theta \end{bmatrix}. \quad (6.4)$$

Besides, a rotation of angle ψ about the z-axis is defined as

$$\mathbf{R}_z(\psi) \triangleq \begin{bmatrix} \cos \psi & \sin \psi & 0 \\ -\sin \psi & \cos \psi & 0 \\ 0 & 0 & 1 \end{bmatrix} \quad (6.5)$$

where ψ , θ and ϕ are the Euler angles.

In the process of aerial refueling, the rotation between the receiver aircraft and the drogue is limited in a small range to ensure the safety, which can be ignored. Thus, assume that there is only translation which can be expressed as

$$\mathbf{p}_c = \mathbf{p}_d + \mathbf{t}_d^c. \quad (6.6)$$

Using (11.39), equations of position parameters can be established and solved.

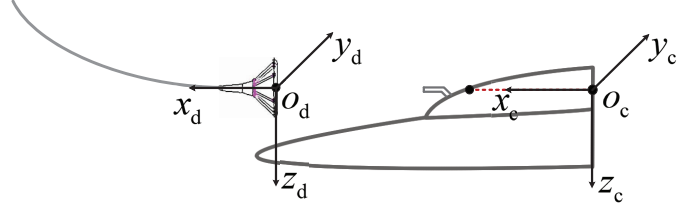


Figure 6.2: The coordinate systems of the refueling system [191]

6.2.3 Camera Pinhole Model

Assume that a vector $\mathbf{p}_i \triangleq [u \ v]^T$ is in the image coordinate system $o_i - x_i y_i$. The camera pinhole model (see Fig. 11.1) is used to transform \mathbf{p}_c and \mathbf{p}_d to \mathbf{p}_i as follows

$$l \begin{bmatrix} u \\ v \\ 1 \end{bmatrix} = \begin{bmatrix} \alpha_x & 0 & u_0 & 0 \\ 0 & \alpha_y & v_0 & 0 \\ 0 & 0 & 1 & 0 \end{bmatrix} \begin{bmatrix} x_c \\ y_c \\ z_c \\ 1 \end{bmatrix} = \mathbf{M} \begin{bmatrix} \mathbf{R}_d^c & \mathbf{t}_d^c \\ 0 & 1 \end{bmatrix} \begin{bmatrix} x_d \\ y_d \\ z_d \\ 1 \end{bmatrix}, \quad (6.7)$$

and

$$\mathbf{M} = \begin{bmatrix} \alpha_x & 0 & u_0 \\ 0 & \alpha_y & v_0 \\ 0 & 0 & 1 \end{bmatrix}, \quad (6.8)$$

where l in (13.12) is the scaling factor; \mathbf{M} is the camera intrinsic matrix, in which α_x , α_y , u_0 and v_0 are determined by camera calibration [191].

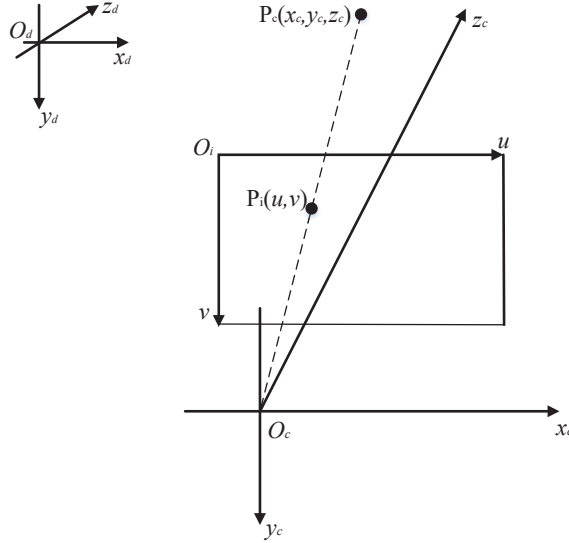


Figure 6.3: Camera pinhole model [192]

6.2.4 Problem Formulation

According to the descriptions above, it is obtained that some markers are placed on the drogue. Let the number of the markers be N . As all markers are placed in the same plane, their

depth information is identical, which can be expressed as s . Thus the markers in the image can be described as (u_i, v_i, s) , $i = 1, 2, \dots, N$. Since the markers compose a circle, it is necessary to obtain the center coordinate and radius of the circle, which can be expressed as (a, b, r) with (a, b) denoting the center coordinate of the circle, r the radius of the circle. With these parameters, the relative distance between the drogue and the receiver aircraft is obtained. However, since the external environment is complicated and full of interferences, some essential measures should be taken, which can ensure the accuracy of the parameters and improve the robustness of the whole system.

There are two major tasks in this chapter: drogue recognition and enhancing detection robustness. Enhancing detection robustness is based on the prediction of the markers' coordinates, and it can be divided into three parts corresponding to different situations. Therefore, for simplicity, they are formulated into the following four steps.

- 1) Step 1: Assume that there is no disturbance and the whole refueling system works well. According to the known parameters (u_i, v_i, s) , $i = 1, 2, \dots, N$, get the the center and radius of the circle (a, b, r) .
- 2) Step 2: According to the relative distance between the drogue and the receiver aircraft got in Step 1, estimate the coordinates of the markers at the next moment and revise the current data.
- 3) Step 3: Assume that there are some noise and redundant points in the image. According to the known parameters (u_i, v_i, s) , $i = 1, 2, \dots, N$ and the equation of the circle, eliminate the influence of interferences.
- 4) Step 4: Assume that there are some markers undetectable. According to the current and predictive coordinates of the markers, bring forward corresponding measures.

Next, the main algorithm will be introduced in Section III in detail.

6.3 Main Algorithm for Position Estimation

6.3.1 Markers Detecting and Matching

As shown above, markers placed on the drogue are arranged as a circle. In the process of aerial refueling, the receiver aircraft should track the tanker aircraft with high accuracy. Thus, the angle of attack of the receiver aircraft is very small, according to which the drogue can be approximated as a circle. Its projection on the image can be expressed in the function form as

$$(x - a)^2 + (y - b)^2 = r^2 \quad (6.9)$$

Let N be the number of all detected markers. The detected markers can be expressed as $\mathbf{p}_i \triangleq [x_i \ y_i]^T$, $i = 1, 2, \dots, N$. In order to describe the difference between the observed value and the estimated value, the residuals ε_i is used, which can be shown as

$$\varepsilon_i = (x_i - a)^2 + (y_i - b)^2 - r^2. \quad (6.10)$$



The cost function can be the sum of the residuals' square, that is

$$J = \sum_{i=1}^N \varepsilon_i^2 = \sum_{i=1}^N [(x_i - a)^2 + (y_i - b)^2 - r^2]^2. \quad (6.11)$$

According to the principle of the least square, when the partial derivative of the cost function equals zero, the optimal fitting result is achieved, which can be written in the numerical form as

$$\begin{cases} \frac{\partial J}{\partial a} = -4(x_i - a) \sum_{i=1}^N [(x_i - a)^2 + (y_i - b)^2 - r^2] = 0 \\ \frac{\partial J}{\partial b} = -4(y_i - b) \sum_{i=1}^N [(x_i - a)^2 + (y_i - b)^2 - r^2] = 0 \\ \frac{\partial J}{\partial r} = -4r \sum_{i=1}^N [(x_i - a)^2 + (y_i - b)^2 - r^2] = 0. \end{cases} \quad (6.12)$$

With these functions, the parameters of the circle are obtained as

$$\begin{cases} a = \frac{(\bar{x}^2 \cdot \bar{x} + \bar{x} \cdot \bar{y}^2 - \bar{x}^3 - \bar{x}\bar{y}^2)(\bar{y}^2 - \bar{y}^2)}{2(\bar{x}^2 - \bar{x}^2)(\bar{y}^2 - \bar{y}^2) - 2(\bar{x} \cdot \bar{y} - \bar{x}\bar{y})^2} - \\ \frac{(\bar{x}^2 \cdot \bar{y} + \bar{y} \cdot \bar{y}^2 - \bar{x}^2\bar{y} - \bar{y}^3)(\bar{x} \cdot \bar{y} - \bar{x}\bar{y})}{2(\bar{x}^2 - \bar{x}^2)(\bar{y}^2 - \bar{y}^2) - 2(\bar{x} \cdot \bar{y} - \bar{x}\bar{y})^2} \\ b = \frac{(\bar{x}^2 \cdot \bar{y} + \bar{y} \cdot \bar{y}^2 - \bar{x}^2\bar{y} - \bar{y}^3)(\bar{x}^2 - \bar{x}^2)}{2(\bar{x}^2 - \bar{x}^2)(\bar{y}^2 - \bar{y}^2) - 2(\bar{x} \cdot \bar{y} - \bar{x}\bar{y})^2} - \\ \frac{(\bar{x}^2 \cdot \bar{x} + \bar{x} \cdot \bar{y}^2 - \bar{x}^3 - \bar{x}\bar{y}^2)(\bar{x} \cdot \bar{y} - \bar{x}\bar{y})}{2(\bar{x}^2 - \bar{x}^2)(\bar{y}^2 - \bar{y}^2) - 2(\bar{x} \cdot \bar{y} - \bar{x}\bar{y})^2} \\ r = \sqrt{a^2 - 2\bar{x}a + b^2 - 2\bar{y}b + \bar{x}^2 + \bar{y}^2} \end{cases} \quad (6.13)$$

where \bar{x} and \bar{y} denote the average values of x and y , and $\bar{x}^m\bar{y}^n = \frac{\sum_{i=1}^N x_i^m y_i^n}{N}$, $m, n \in [0, 3]$.

On the basis of camera pinhole model, the depth s of the plane at which the markers are located can be obtained by the radius of the circle. The function is as follows

$$\frac{R_{dr}}{s + f} = \frac{r}{f} \quad (6.14)$$

where R_{dr} is the actual radius, f is the focal length of the camera. Let the coordinate of the probe in the image be $\mathbf{p}_i \triangleq [u \ v]^T$, and the distance between the probe and the camera in z-axis be d . The relative distance between the drogue and the probe can be expressed as

$$\begin{cases} \Delta x = |a - u| \cdot \frac{R_{dr}}{r} \\ \Delta y = |b - v| \cdot \frac{R_{dr}}{r} \\ \Delta z = \left| \frac{f R_{dr}}{r} - f - d \right|. \end{cases} \quad (6.15)$$

Although the form of this algorithm is complex, its time complexity is just $O(n)$, which is

suitable for computer implementation.

6.3.2 KF and Robust Image Tracking Algorithm

In this subsection, KF is applied to estimate the position of markers, which can reduce the influence of error points and improve the matching accuracy. The equations of state and measurement are given as follows

$$\mathbf{x}(k+1) = \Phi(k+1, k)\mathbf{x}(k) + \Gamma(k+1, k)\mathbf{W}(k) \quad (6.16)$$

$$\mathbf{z}(k) = \mathbf{H}(k)\mathbf{x}(k) + \mathbf{V}(k). \quad (6.17)$$

In above functions, $\mathbf{x}(k) \in \mathbb{R}^6$ is the state vector of the system state, which is written as

$$\mathbf{x} = \begin{bmatrix} \Delta x & \Delta y & \Delta z & \Delta v_x & \Delta v_y & \Delta v_z \end{bmatrix}^T \quad (6.18)$$

where $\Delta x, \Delta y, \Delta z$ are the relative distances between the receiver aircraft and the drogue along three axes, respectively. And $\Delta v_x, \Delta v_y, \Delta v_z$ are velocity differences; $\mathbf{z}(k) \in \mathbb{R}^3$ is the observation vector, which is expressed as

$$\mathbf{z} = \begin{bmatrix} u & v & s \end{bmatrix}^T. \quad (6.19)$$

and $\mathbf{H}(k)$ can be obtained from the correspondence of the image and the real world. Besides, other parameters can be expressed as

$$\Phi(k+1, k) = \begin{bmatrix} \mathbf{0}_3 & \mathbf{I}_3 \\ \mathbf{0}_3 & \mathbf{0}_3 \end{bmatrix} \quad (6.20)$$

$$\Gamma(k+1, k) = \begin{bmatrix} \mathbf{0}_3 \\ \mathbf{I}_3 \end{bmatrix}. \quad (6.21)$$

Given the initial value, the well-known KF consisting of prediction and estimation parts can start to iterate. The estimation of the states can be sent to the autopilot for the docking control. KF can also improve the system robustness performance enormously which will ensure the normal operation of the whole refueling system.

6.3.3 The Dispose of Noise and Redundant Points

As the environment around the refueling equipment is complex, it is a common phenomenon that some noise and redundant points appear in the image, which may affect the matching of the drogue. These redundant points may emerge for the following reasons: direct sunlight, light reflecting on the surface of the tanker aircraft, the noise points generated by the camera. The corresponding measures are given as follows.

For the drogue of the refueling system, let the center coordinate of estimation in world space be $\mathbf{z} = [\Delta x \ \Delta y \ \Delta z]^T$. According to the projection relation, the next center and radius of the circle in the image can be forecasted as (a, b) and r , and the estimation errors are $\Delta a, \Delta b, \Delta r$, respectively. For the image point (u, v) at the next moment, the judgment rules can be expressed



as follows

$$\sqrt{(u_i - a)^2 + (v_i - b)^2} > \sqrt{\Delta a^2 + \Delta b^2} + r + \Delta r \quad (6.22)$$

or

$$\sqrt{(u_i - a)^2 + (v_i - b)^2} < r - \Delta r. \quad (6.23)$$

The two formulas have a similar effect, which can distinguish the unwanted points with high efficiency. If the point satisfies the condition (11.36) or (11.37), it will be removed.

In addition, as the markers located at the drogue are placed as a circle, let the current circle in the image be (a, b, r) . If the fitting error is greater than the threshold value ε set earlier, this point should be removed. The function can be expressed as

$$\frac{(u_i - a)^2 + (v_i - b)^2 - r^2}{r} > \varepsilon. \quad (6.24)$$

In actual operation, the value of ε can be got from real experiments.

The first algorithm shown above removes the unsuitable points in the aspect of the markers' movement tendency, while the other does the same in the aspect of markers' geometry distribution property. Together with other necessary logical judgments, most errors can be discovered and got rid of, which can ensure the accuracy of position estimation.

6.3.4 The Algorithm of Losing Points

When the probe-and-drogue refueling system is operating, there is a common phenomenon that some of the markers may be out of the camera's view or obscured by the probe or other obstacles. Due to the determination of parameters of the circle (a, b, r) , three detectable markers should be obtained at least. By estimating the coordinates of the markers in the image, whether or not there are markers out of sight can be determined in advance. Different states and necessary countermeasures are listed as follows.

State 1: If some of the markers are out of sight, and other visible markers are near the probe, this situation means that the invisible markers are obscured by the probe. If they are just out of sight for a short time, which is less than the threshold value t_i , the estimation results of KF can fill the missing data directly, which can maintain system normal operation. However, at the same time, an alarm is provided until all return to normal.

State 2: If some markers are blocked by the probe for such a long time that exceeds the threshold value t_i , it is necessary to check the number of markers available. If the number is less than three, it is illustrated that the position estimation system is in bad condition, which may lead to huge safety risks. Thus, the receiver aircraft should stop refueling process immediately. Until the receiver aircraft returns to a safe place, a next refueling attempt is allowed to begin.

State 3: If some markers are out of sight, and the existing markers are near the four boundaries of the camera's view, it means that the invisible markers are beyond the camera's view. If this situation occurs, it implies that there is something wrong with the relative position

between the receiver aircraft and the tanker aircraft. If all the missing markers return to view after a short period, which is less than the threshold value t_p , the refueling process can be permitted to carry on. If not, the refueling process must be stopped at once. An alarm is also required in this situation.

The threshold values t_i and t_p can be got from real experiments. However, according to the intensity of the events, t_p is much smaller than t_i . With these countermeasures, the robustness of the whole refueling system can be highly improved.

6.4 Deep Learning-Based Drogue Detection

The target-based detection algorithms are susceptible to light interference and sensitive to weather conditions. Object detection algorithms based on deep learning, on the other hand, can directly learn the features of objects from images, eliminating the need for target installation on drogue and providing strong robustness. Early object detection algorithms consisted of two steps, namely candidate box generation and candidate box classification and localization, referred to as two-stage algorithms, such as R-CNN[193], Faster-RCNN[194], and FPN[195]. In contrast to two-stage algorithms, one-stage algorithms merge the two steps into one, significantly improving detection speed. Examples of one-stage algorithms include YOLO[196], SSD[197], and RetinaNet[198], with the YOLO series being the most widely used at present. In this chapter, the YOLOv5 algorithm is employed for drogue detection.

6.4.1 Network Architecture

The network architecture of YOLOv5 is illustrated in Fig. 6.4 and can be divided into four components: Input, Backbone, Neck, and Output. A key feature of YOLOv5 is its ability to detect objects on three different scales of feature maps, obtained through downsampling, corresponding to 1/32, 1/16, and 1/8 of the input image dimensions. The largest feature map is responsible for detecting small objects. For each point on the feature map, predictions are made using three anchor boxes as priors.

6.4.1.1 Input

(i) **Mosaic data augmentation.** The Mosaic data augmentation method was introduced in YOLOv4[199]. Its main idea is to concatenate four images together by randomly scaling, cropping, and arranging them. This concatenated image is then used as training data. The advantage of this approach is that it enhances the background diversity of the images and effectively increases the training batch size by combining four images into one.

(ii) **Adaptive anchor box computation.** In the algorithm, initial anchor boxes with pre-defined aspect ratios are set for different datasets. During the training process, the network computes predicted boxes based on these initial anchor boxes, compares them with the ground



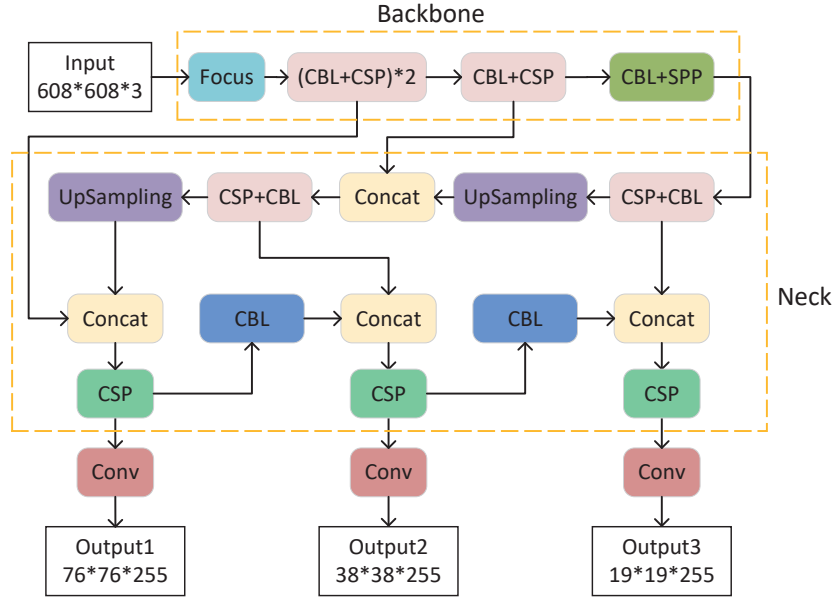


Figure 4.4: The network architecture of YOLOv5

truth boxes, measures the differences between the two, and then updates the network parameters in a backward manner. YOLOv5 incorporates the functionality of adaptive computation of initial anchor boxes into the code, automatically calculating the optimal anchor box values for different training sets during each training iteration.

(iii) **Adaptive image scaling.** In the process of collecting datasets, it is common for images to have varying dimensions. A commonly used approach is to uniformly scale the images during data preprocessing to obtain a standardized size before inputting them into the network. Popular sizes used in the YOLO algorithm include 416×416 and 608×608 . To achieve the standardized size, padding is applied to the edges of the images that fall short after scaling. In the prediction stage, YOLOv5 optimizes the padding algorithm, minimizing the extent of padding required and thereby improving the speed of object detection.

6.4.1.2 Backbone

(i) **Focus structure.** The most critical aspect of the Focus structure is the slicing operation. In YOLOv5, a $608 \times 608 \times 3$ image enters the Focus structure, undergoes the slicing operation, resulting in a $304 \times 304 \times 12$ feature map. Subsequently, a convolution operation with a kernel size of 32 is performed, transforming it into a $304 \times 304 \times 32$ feature map.

(ii) **CSP structure.** The CSP structure, inspired by CSPNet[200], addresses the issue of excessive computational complexity in inference from the perspective of network architecture design. YOLOv5 incorporates two types of CSP structures, with the CSP1_X structure applied to the Backbone and the CSP2_X structure utilized in the Neck.

6.4.1.3 Neck

The Neck network employs the FPN+PAN structure, drawing inspiration from PANet[201]. FPN is a top-down structure that utilizes upsampling to propagate and fuse high-level feature information, generating feature maps for prediction. YOLOv5 introduces a bottom-up feature pyramid after the FPN layer, which includes two RAN structures. By combining these two components, the FPN structure can transmit strong semantic features from top to bottom, while the feature pyramid is responsible for propagating strong localization features from bottom to top. The combination of these two components performs parameter aggregation operations on different detection layers from different backbone layers.

6.4.1.4 Output

(i) **Loss function.** The loss function for object detection tasks typically consists of two components: classification loss and bounding box regression loss. YOLOv5 adopts the CIoU Loss[202] as its loss function, which is derived from the DIoU Loss[203]. The CIoU Loss combines the considerations of overlapping area, center point distance, and aspect ratio of bounding boxes. It can be represented as

$$L_{\text{CIoU}} = 1 - \text{CIoU} = 1 - (\text{IoU} - \frac{\text{Distance_2}^2}{\text{Distance_C}^2} - \frac{v^2}{(1 - \text{IoU}) + v}) \quad (6.25)$$

where v is defined as a measure of aspect ratio consistency, plays a role in assessing the consistency of object's width and height ratios. It is defined as

$$v = \frac{4}{\pi^2} (\arctan \frac{w^{gt}}{h^{gt}} - \arctan \frac{w^p}{h^p}). \quad (6.26)$$

(ii) **Non-Maximum suppression.** During the post-processing stage of object detection, multiple bounding boxes may be predicted for a single object, leading to overlapping detections. Non-Maximum Suppression (NMS) is commonly employed to identify the most relevant bounding box among them. Since CIoU incorporates the factor v , and there is no ground truth information available during prediction, DIoU is used instead. Firstly, the boxes for a specific class are sorted in descending order based on their confidence scores. Next, DIoU is computed, and boxes with DIoU values below a threshold are retained. Finally, the resulting output consists of the object's center position (u, v) , width w , height h , confidence score p , and class probability $c_0, c_1, c_2, \dots, c_{nc-1}$, as depicted in Fig. 6.5.

Among them, nc represents the number of categories, and the class probabilities are represented as a vector of length nc . The index corresponding to the maximum value in the vector indicates the predicted class. Since only the detection of a single object, namely "drogue" is performed, nc is set to 1.

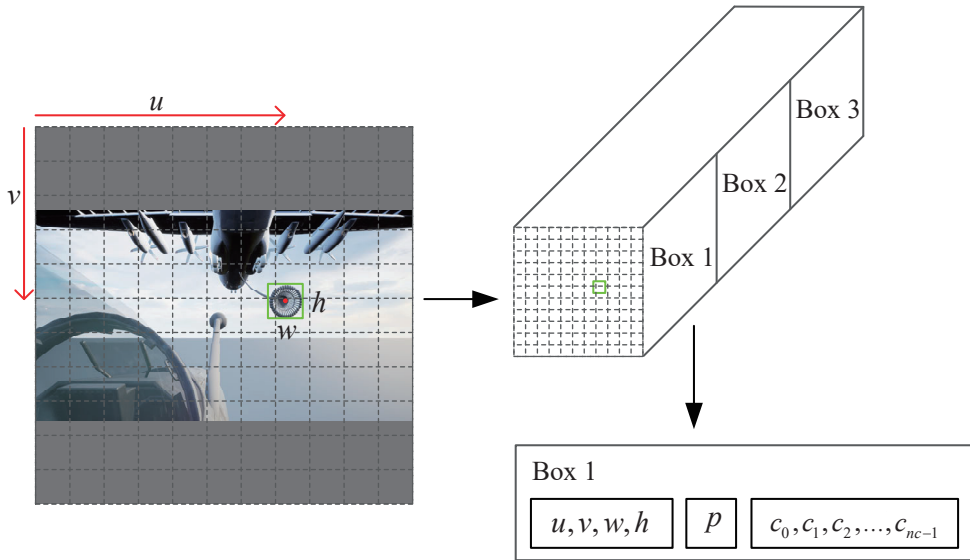


Figure 6.5: The network architecture of YOLOv5

Table 6.1: The training parameter settings for the experiment

Parameters	Value
Model	YOLOv5s
Epochs	300
Image size	640×640
Batch size	16
Learning rate	0.01
Optimizer	SGD

6.4.2 Position esitimation

From the depth image, the depth value s of the drogue's center point coordinates (u, v) can be obtained. Using (13.12), the cone cover's coordinates p_c in the camera coordinate system can be derived, which subsequently leads to the calculation of p_d .

6.4.3 Dataset

In AARSim, the data collection process for the dataset is highly convenient. By adjusting the position of the tanker, images can be obtained at arbitrary distances and angles. Additionally, the camera resolution can be adjusted, with a resolution of 1280×720 set for this experiment.

6.4.4 Training approach

The experiment was conducted using an Intel(R) Core(TM) i7-10700F CPU, 32GB of RAM, and an NVIDIA RTX 2060 SUPER 8G GPU, on the Windows 11 operating system. PyCharm was utilized for development, and training, validation, and testing were performed with the same parameters. The training parameter settings for the experiment are presented in Table 6.1.

6.5 Simulation and Results

6.5.1 Simulation Environment

In order to observe the simulation results intuitively, a three-dimensional (3D) simulation model is created by the virtual reality toolbox of Matlab, which emulates the process of aerial refueling precisely. The interface of this model is shown as follows (see Fig. 11.4).

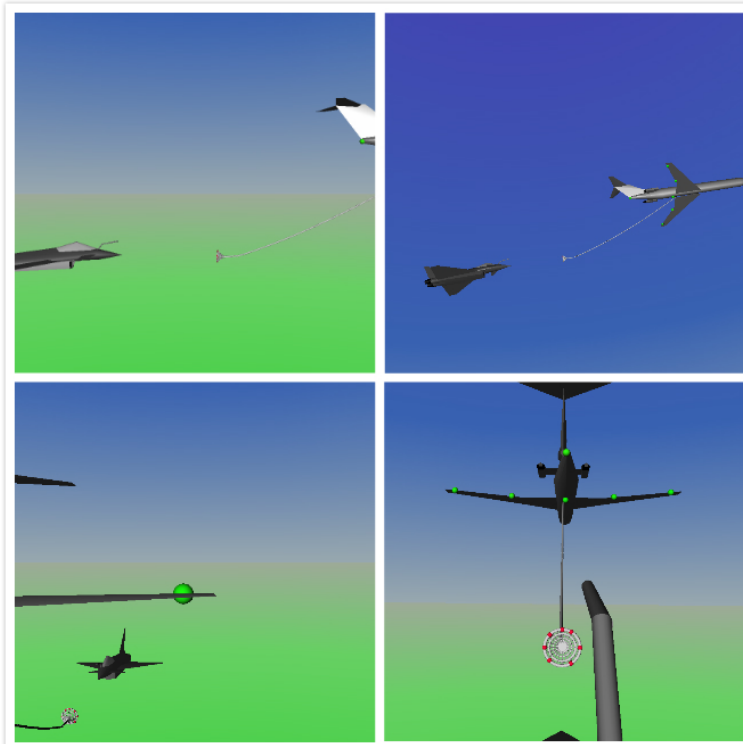


Figure 6.6: Aerial refueling of VR simulation.

The coordinate system of the virtual camera in this simulation model is different from the one in Section 2. Its origin is the current location set by the user, with x_c axis pointing forward, y_c pointing upward, z_c pointing right. In addition, the pixel resolution of the virtual camera is 860 pixels \times 480 pixels. Moreover, its maximum frame rate is 50 frames per second. What is more, its angle of view is 90 degrees.

In order to test the effectiveness and practicability of the vision-based algorithm proposed in Section III, let the drogue stay still in a series of simulations, and at the same time, the receiver aircraft moves along the trajectory set in advance, for example, sinusoidal movement in three axes. According to the image acquired by the virtual camera on the receiver aircraft, the relative distance between the receiver aircraft and the drogue can be calculated.

6.5.2 Marker Identification

For the convenience of establishing the model, some colored spheres substitute for the passive reflectors are attached to the drogue and the tanker aircraft. The color of the spheres

on the drogue is set to be red, while green on the tanker aircraft. The two kinds of spheres are distinguished by color, and then treated differently.

In the image obtained by the virtual camera, the markers appear to be bright. Thus, image gray processing (11.40) and thresholding function (11.41) are sufficient to detect markers. Then erode the bright pixel blob to eliminate noise according to the threshold value w . Finally, the center coordinates of the pixel blob can be obtained, namely, pixel coordinates of the markers.

$$\text{Gray}(u, v) = 2\mathbf{R}(u, v) - \mathbf{G}(u, v) - \mathbf{B}(u, v) \quad (6.27)$$

$$\text{Gray}(u, v) = \begin{cases} 255, & \text{if } \text{Gray}(u, v) \geq w \\ 0, & \text{otherwise} \end{cases}. \quad (6.28)$$

6.5.3 Simulation Results

The whole simulation lasts for 200 seconds, while real-time pictures are displayed in two windows. The images of different situations are listed as follows (see Figs. 11.5 and 11.6)

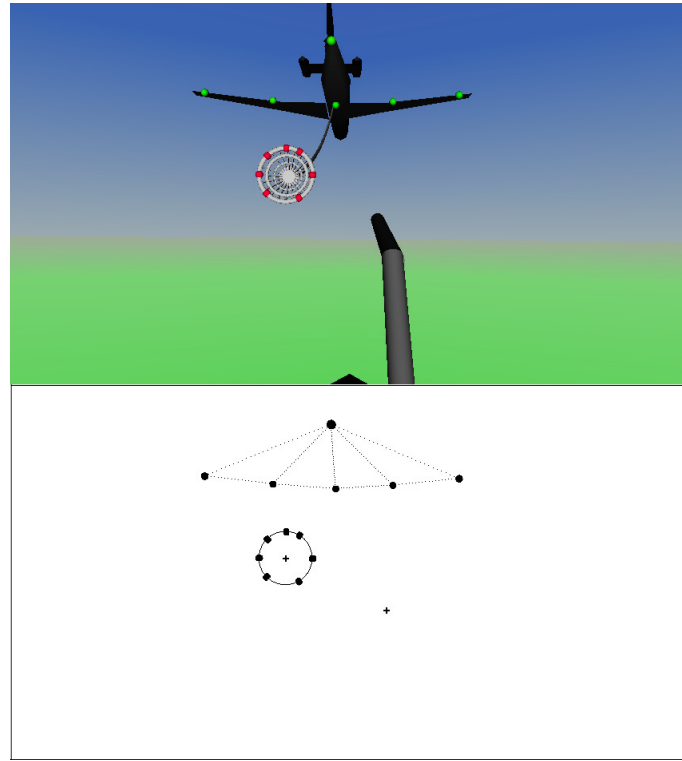


Figure 6.7: All markers are identified properly

From these figures, it is obtained that the circle matching algorithm can work well even if some markers are blocked or beyond the boundary. Besides, even though the external environment is complex, the system can ensure a high-precision position estimation. These results show the high robustness of this position estimation system. The positioning data and actual data are compared as follows (see Fig. 11.8)

In Fig. 11.8, the dotted line represents the relative distance solved by vision-based position estimation algorithm, while the solid line represents the real distance. It can be obtained that the

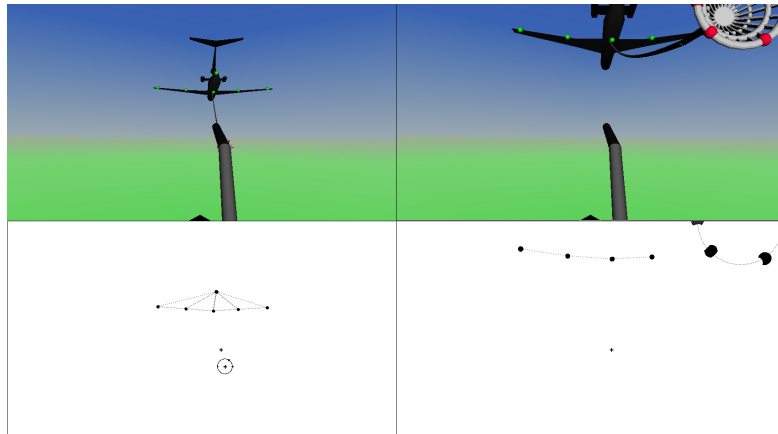


Figure 6.8: 85% and 50% of the drogue is blocked.

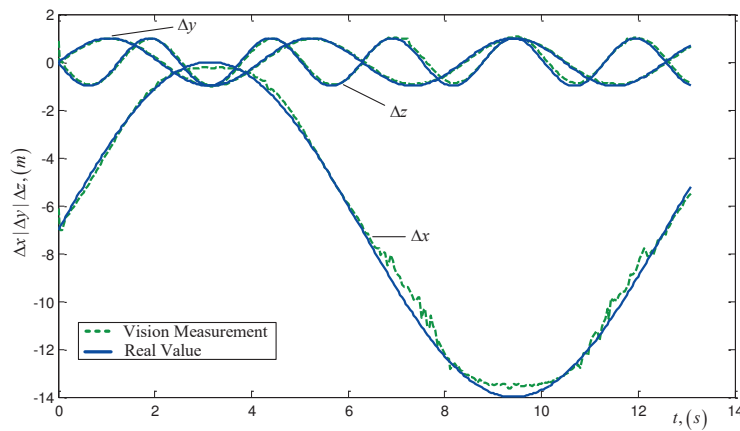


Figure 6.9: The effect of visual location and tracking.

system can obtain fairly good localization information of the drogue.

6.6 Chapter Summary

In this research, a vision-based position estimation method for probe-and-drogue refueling systems is presented. These real-time detecting and matching algorithms are of strong robustness. Through the simulation, the effectiveness and accuracy of the proposed method have been demonstrated. Therefore, the proposed vision-based position estimation method is promising to acquire the relative distance information between the drogue and the receiver aircraft, which can be later applied to the autonomous aerial refueling system.

In future research, the proposed method could be tested with a real camera, such as in a hardware-in-the-loop simulation. Besides, some other extreme circumstances which may happen in real flight should be considered.

Chapter 7 Additive-State-Decomposition-Based Station-Keeping Control

Station-keeping control is the basis of autonomous aerial refueling. However, there exist strong external disturbances including the atmospheric turbulence and the wake vortex of the tanker, and the system change caused by the fuel transfer. These present challenges in station-keeping control design. This chapter proposes an additive-state-decomposition-based station-keeping control method for autonomous aerial refueling. This method ‘additively’ decomposes the original tracking problem into two more tractable problems, namely a tracking problem for a linear time-invariant primary system and a stabilization problem for a deterministic nonlinear secondary system. Based on the decomposition, a proportional-integral controller is designed for the primary system to track the reference trajectory, and a feedback linearization controller is adopted to solve the stabilization problem for the secondary system. Finally, the two designed controllers are combined to achieve the original control objective. By using additive state decomposition, the proposed control method with two degrees of freedom can satisfy the control requirements of station keeping with constant mass and varying mass. Simulation results demonstrate the effectiveness and robustness of the proposed station-keeping controller.

7.1 Introduction

Aerial refueling consists of four phases: rendezvous phase, joining phase, refueling phase and reform phase. The studied station-keeping control focuses on the phases except the docking subphase. Thus, station-keeping control is the basis of autonomous aerial refueling (AAR). To perform aerial refueling, the controller must have the capability of maintaining and moving among the standby point, observation area, pre-contact point during a flight. The existing aerial refueling systems mainly include the flying-boom type and the probe-and-drogue type. The control problem in the flying-boom aerial refueling can actually be considered as a special case of the control problem in the probe-and-drogue aerial refueling without the motion of the drogue considered. In the station-keeping flight, the tanker aircraft and the receiver aircraft rather than the drogue and the probe are the focuses. Thus, station-keeping control for these two main aerial refueling methods is basically the same. The station-keeping control for AAR is a difficult task for two main reasons. First, the receiver is disturbed by the atmospheric turbulence and the wake vortex of the tanker. Secondly, due to the fuel injection in the refueling process, the mass and the center of mass of the receiver will change. Therefore, the station-keeping controller design for AAR is important and challenging.

Station-keeping control can be considered as a special case of tracking control between the

tanker aircraft and the receiver aircraft. If the receiver aircraft is focused, station-keeping control first needs to determine the reference state or reference trajectory so that the receiver can be maintained in the reference state or track the reference trajectory. Many research efforts have focused on developing station-keeping control methods for AAR. The linear quadratic regulator (LQR) method was adopted in references [77], [95] and [96]; the L1 adaptive control method was utilized in reference [63]; and the proportional-integral-derivative (PID) control method was adopted in [97]. In view of the receiver mass change in the process of fuel transferring, the control method with adaptive gain (or gain scheduling) was used in references [77], [63]. These control methods are based on rigorous and accurate modeling, such as the result in [77], which is based on the variable mass modeling of the receiver under the wake vortex disturbance in [98]. Reference [99] proposed that the controlled plant should be the position of the probe rather than the position of the center of gravity of the receiver. Therefore, the relative position of the center of gravity of the receiver and its probe was used to modify the original model, and the controller was then designed. In [22], a double power reaching law based sliding mode controller was designed to control the receiver translational motion relative to the tanker aircraft in the outer loop while active disturbance rejection control (ADRC) technique [204] was applied to the inner loop to stabilize the receiver.

Prior information about the refueling system or disturbances can also be used to solve some problems encountered in station keeping. Reference [95] dealt with the problem of how to control a receiver when the flight condition of the tanker changes. This chapter considered that the position and attitude information of the tanker could be obtained by communication as the feedforward, which was then incorporated into the LQR. Robust control methods aim to minimize the gain of the disturbance on the output as much as possible [90]. Reference [100] adopted the ADRC method to design the station-keeping controller. In [101], quantitative feedback theory (QFT) was used to design controllers to guide the formation of the tanker and the receiver. This control method was also applied to station keeping [102]. Among these existing methods, most station-keeping controllers are designed by using some control methods for linear systems after linearizing the nonlinear receiver system directly. However, abandoning the nonlinear term directly may limit the control effect and make the final closed-loop system fragile to system perturbation and external disturbances. If the nonlinearity information of the nonlinear receiver system can be considered properly, better control effect would be expected.

In this chapter, an additive-state-decomposition-based (ASD) [205] station-keeping control method is proposed for the probe-and-drogue AAR, a typical representative of AAR. The basic idea of the control design is to additively decompose the original tracking problem into two more tractable problems, namely a tracking problem for a linear time-invariant (LTI) primary system and a stabilization problem for a deterministic nonlinear secondary system. After the additive state decomposition (ASD), a conventional proportional-integral (PI) controller is designed for the tracking problem, and a feedback linearization controller is adopted to solve the stabilization

problem. The advantage of the ASD-based control method lies in the decomposition of the original problem into two well-solved control problems. As long as the two control problems are well-solved, the original control problem is solved.

The main contributions of this chapter are twofold.

(i) An ASD-based control method is proposed to solve the station keeping problem for AAR. The trajectory tracking and position holding in the presence of unknown disturbances and varying mass can be achieved.

(ii) The proposed control method is a type of two-degree-of-freedom control method, which separates the nonlinear stabilization task from a tracking task. Introducing ASD simplifies the design and also increases the flexibility of controller design.

7.2 Model Description and Problem Statement

The studied AAR is the probe-and-drogue refueling (PDR), a typical benchmark. Aerial refueling consists of four phases: rendezvous phase, joining phase, refueling phase, and reform phase. The studied station-keeping control focuses on the phases except the docking subphase. In the docking subphase, docking control [206], [87] is adopted; in other phases, station-keeping control is adopted instead.

7.2.1 AAR system model

An AAR system model includes a tanker model, a receiver model, refueling equipment model (hose-drogue dynamic model and hose-drum unit model), and aerodynamic disturbance model. When establishing the AAR system model, three commonly used coordinate frames are the ground frame (o_g - $x_g y_g z_g$), the tanker frame (o_t - $x_t y_t z_t$), and the drogue equilibrium-point frame (o_d - $x_d y_d z_d$), which are shown in Fig. 7.1. The definition of these coordinate frames can be found in reference [40]. Because of fuel transfer in refueling, the receiver aircraft is a system of varying mass and moments of inertia. For station-keeping control, taking the variable mass receiver model into account is a big difference from other conventional control. Thus, only variable mass receiver model is described in this section. Readers can refer to [95] for the tanker model, [207] for the refueling equipment model and [54] for the aerodynamic disturbance model.

7.2.1.1 Variable mass receiver model

The complexity of the receiver system would make the system modelling difficult. To facilitate the derivation of the dynamics equations including the effect of fuel transfer, the following assumptions are introduced.

Assumption 1. A receiver system comprises two parts: a solid main part and fuel tanks. The solid part is considered to be rigid, and the total change of mass and inertial moment of the

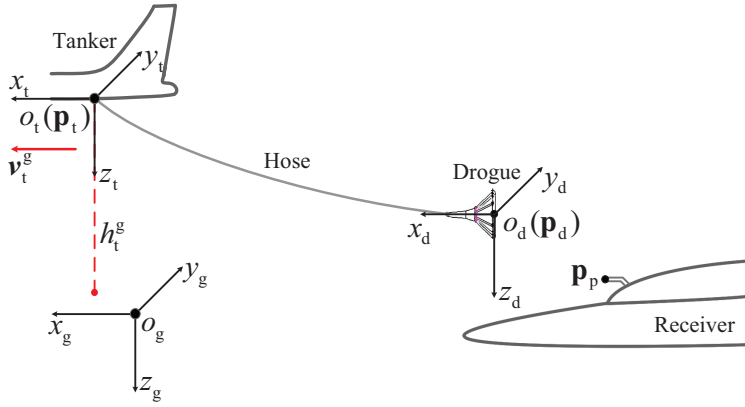


Figure 7.1: Coordinate frames for the PDR system.

receiver is caused by that of fuel tanks.

Assumption 2. The solid part is symmetric about the plane $o_r x_r z_r$. Not only the geometric shape but also the mass distribution are symmetric.

Assumption 3. The mass only changes during the fuel transfer.

Assumption 4. The receiver has k fuel tanks. The tank position and fuel mass distribution are symmetric about the plane $o_r x_r z_r$. The mass of fuel in the j th tank is $m_j, j = 1, 2, \dots, k$, and the distance vector \mathbf{r}_j from its mass center o_j to the mass center of the receiver body o_r is constant.

Based on these assumptions, the six-degree-of-freedom variable mass receiver model (F-16 aircraft is considered) [208] including dynamic equations and kinematic equations is given as below. First, some variable definitions are given. $\mathbf{p}_r = [x_r \ y_r \ h_r]^T$ denotes the receiver position in the tanker frame with x_r for the x -axis position value, y_r for the y -axis position value, and h_r for the z -axis height value. $\mathbf{v}_r = [u_r \ v_r \ w_r]^T$ denotes the receiver velocity in the tanker frame with u_r for the x -axis velocity value, v_r for the y -axis velocity value, and w_r for the z -axis velocity value. $\Theta_r = [\phi \ \theta \ \psi]^T$ denotes the receiver attitude angle with ϕ for the roll angle, θ for the pitch angle, and ψ for the yaw angle. $\omega_r = [p \ q \ r]^T$ denotes the receiver body angular velocity with p for the roll rate, q for the pitch rate, and r for the yaw rate. The control input for the receiver is $\mathbf{u}_r = [\delta_t \ \delta_e \ \delta_a \ \delta_r]^T$ with $\delta_t, \delta_e, \delta_a$ and δ_r denoting the thrust input and three control surface deflections of the elevator, the aileron, and the rudder, respectively.

Translational dynamic equations:

$$\begin{aligned}\dot{u}_r &= rv_r - qw_r - g \sin \theta + \frac{1}{m} (\bar{X} + F_T) - \frac{\dot{m}u_r}{m} \\ \dot{v}_r &= pw_r - ru_r + g \sin \phi \cos \theta + \frac{1}{m} \bar{Y} - \frac{\dot{m}v_r}{m} \\ \dot{w}_r &= qu_r - pv_r - g \cos \phi \cos \theta + \frac{1}{m} \bar{Z} - \frac{\dot{m}w_r}{m}.\end{aligned}\tag{7.1}$$

Rotational dynamic equations:

$$\begin{aligned}\dot{p} &= (c_1 r + c_2 p) q + c_3 \bar{L} + c_4 (\bar{N} + h_E q) + \kappa_1 p + \kappa_2 r \\ \dot{q} &= c_5 p r - c_6 (p^2 - r^2) + c_7 (\bar{M} - h_E r) + \kappa_3 q \\ \dot{r} &= (c_8 p - c_2 r) q + c_4 \bar{L} + c_9 (\bar{N} + h_E q) + \kappa_4 p + \kappa_5 r.\end{aligned}\quad (7.2)$$

Rotational kinematical equations:

$$\begin{aligned}\dot{\phi} &= p + \tan \theta (q \sin \phi + r \cos \phi) \\ \dot{\theta} &= q \cos \phi - r \sin \phi \\ \dot{\psi} &= \frac{q \sin \phi + r \cos \phi}{\cos \theta}.\end{aligned}\quad (7.3)$$

Translational kinematical equations:

$$\begin{aligned}\dot{x}_r &= u_r \cos \psi \cos \theta + v_r (\cos \psi \sin \theta \sin \phi - \sin \psi \cos \phi) \\ &\quad + w_r (\cos \psi \sin \theta \cos \phi + \sin \psi \sin \phi) \\ \dot{y}_r &= u_r \sin \psi \cos \theta + v_r (\sin \psi \sin \theta \sin \phi - \cos \psi \cos \phi) \\ &\quad + w_r (\sin \psi \sin \theta \cos \phi + \cos \psi \sin \theta) \\ \dot{h}_r &= u_r \sin \theta - v_r \cos \theta \sin \phi - w_r \cos \theta \cos \phi.\end{aligned}\quad (7.4)$$

Please refer to [98] for the detailed derivation process. The definition and expression of other parameters in the above equations are given in *Appendix A*. The translational dynamic equations (7.1) and the rotational dynamic equations (7.2) are different from their constant mass counterparts, while the rotational kinematical equations (7.3) and the translational kinematical equations (7.4) are the same as their constant mass counterparts. Concretely, the change of mass has an effect on the translational dynamic equations (7.1), and the change of the inertia moment has an effect on the rotational dynamic equations (7.2).

In the tanker frame, the variable mass receiver model consisting of (7.1), (7.2), (7.3), (7.4) can be represented by a compact form

$$\mathbf{x}_r = \mathbf{f}(\mathbf{x}_r, \mathbf{u}_r, \mathbf{d}) \quad (7.5)$$

where the state vector $\mathbf{x}_r = \begin{bmatrix} x_r & y_r & h_r & \phi & \theta & \psi & u_r & v_r & w_r & p & q & r \end{bmatrix}^T$, the input vector $\mathbf{u}_r = \begin{bmatrix} \delta_t & \delta_e & \delta_a & \delta_r \end{bmatrix}^T$, \mathbf{d} denotes various aerodynamic disturbances including the atmospheric turbulence and the tanker vortex.

7.2.2 Problem statement

Suppose that, in the level and forward flight, $u_r = v_r = w_r = p = q = r = 0$. Under this trim condition, the trimmed state and trimmed input are \mathbf{x}_r^* and \mathbf{u}_r^* , which satisfy

$$\mathbf{x}_r^* = \mathbf{f}(\mathbf{x}_r^*, \mathbf{u}_r^*). \quad (7.6)$$

By defining the disturbed state and disturbed input as $\tilde{\mathbf{x}}_r = \mathbf{x}_r - \mathbf{x}_r^*$, $\tilde{\mathbf{u}}_r = \mathbf{u}_r - \mathbf{u}_r^*$, the disturbed system can be written as

$$\begin{aligned}\tilde{\mathbf{x}}_r &= \mathbf{A}\tilde{\mathbf{x}}_r + \mathbf{B}\tilde{\mathbf{u}}_r + \mathbf{g}(\tilde{\mathbf{x}}_r) + \mathbf{d}(\tilde{\mathbf{x}}_r, \tilde{\mathbf{u}}_r) \\ \tilde{\mathbf{y}}_r &= \mathbf{C}\tilde{\mathbf{x}}_r, \tilde{\mathbf{x}}_r(0) = \tilde{\mathbf{x}}_{r0}\end{aligned}\quad (7.7)$$

where $\mathbf{A} \triangleq \frac{\partial \mathbf{f}(\mathbf{x}_r, \mathbf{u}_r)}{\partial \mathbf{x}_r} \Big|_{\mathbf{x}_r=\mathbf{x}_r^*, \mathbf{u}_r=\mathbf{u}_r^*}$, $\mathbf{B} \triangleq \frac{\partial \mathbf{f}(\mathbf{x}_r, \mathbf{u}_r)}{\partial \mathbf{u}_r} \Big|_{\mathbf{x}_r=\mathbf{x}_r^*, \mathbf{u}_r=\mathbf{u}_r^*}$, $\mathbf{g}(\tilde{\mathbf{x}}_r)$ denotes nonlinear terms, and $\mathbf{d}(\tilde{\mathbf{x}}_r, \tilde{\mathbf{u}}_r)$ includes unmodelled dynamics and disturbances. The output matrix $\mathbf{C} \in \mathbb{R}^{3 \times 12}$, and $\tilde{\mathbf{y}}_r = \mathbf{p}_r - \mathbf{p}_r^*$ with \mathbf{p}_r^* for the trimmed position. $\tilde{\mathbf{x}}_{r0} \in \mathbb{R}^{12}$ is the initial state value.

Control objective: Design a station keeping controller \mathbf{u}_r for the receiver system (7.5) such that $\mathbf{p}_r(t) - \mathbf{p}_r^d(t) \rightarrow \mathbf{0}$ or $\mathbf{p}_r(t) - \mathbf{p}_r^d(t) \rightarrow \mathcal{B}(\mathbf{0}_{3 \times 1}, \delta)$ ¹ as $t \rightarrow \infty$, $\delta \in \mathbb{R}_+ \cup \{0\}$. Equivalently, design a tracking controller \mathbf{u}_r for the system (7.7) such that $\tilde{\mathbf{y}}_r(t) - \tilde{\mathbf{y}}_r^d(t) \rightarrow \mathbf{0}$ or $\tilde{\mathbf{y}}_r(t) - \tilde{\mathbf{y}}_r^d(t) \rightarrow \mathcal{B}(\mathbf{0}_{3 \times 1}, \delta)$ as $t \rightarrow \infty$ when there exist disturbances, where \mathbf{p}_r^d is the reference trajectory, $\tilde{\mathbf{y}}_r^d = \mathbf{p}_r^d - \mathbf{p}_r^*$ is the disturbed reference trajectory.

The system (7.7) is a multi-input multi-output (MIMO) nonlinear system with nonminimum-phase, multi-disturbance, and variable-mass features. Thus, the latter control design needs to deal with nonlinearity, uncertainty, and disturbances simultaneously. ASD-based control can provide an effective solution to this problem.

7.3 ASD-based Station-keeping Controller Design

This section presents the station-keeping controller design. First, based on additive state decomposition, the considered system (7.7) is decomposed into two subsystems: an LTI primary system (7.11) including all disturbances and a deterministic nonlinear secondary system (7.12). Correspondingly, the original tracking task for system (7.7) is decomposed into two subtasks: a tracking subtask for (7.11) and a stabilization subtask for (7.12).

7.3.1 Basic control idea

Conventionally, most station-keeping controllers are designed by using control methods for linear systems after linearizing the nonlinear receiver system directly, as shown in Fig. 7.2(a). However, abandoning the nonlinear term directly may limit the control effect and make the final closed-loop system fragile to system perturbation and external disturbances. If the nonlinearity information of the nonlinear receiver system can be considered properly, better control effect would be expected. Thus, in this chapter, a new control idea displayed in Fig. 7.2(b) is proposed. Based on ASD, we aim to consider the nonlinear part of the receiver system in the secondary system. Then, the primary system from the input \mathbf{u}_p to the state \mathbf{x}_p is an LTI system, which can still adopt the conventional station-keeping controller. The closed-loop system of the secondary

¹ $\mathcal{B}(\mathbf{0}, \delta) \triangleq \{\xi \in \mathbb{R}^3 \mid \|\xi - \mathbf{0}\| \leq \delta\}$, and the notation $\mathbf{x}(t) \rightarrow \mathcal{B}(\mathbf{0}, \delta)$ means $\min_{\mathbf{y} \in \mathcal{B}(\mathbf{0}, \delta)} \|\mathbf{x}(t) - \mathbf{y}\| \rightarrow 0$.

system can be realized by a computer, and the primary system ($B - C$) can be obtained by subtracting the complementary secondary system (C) from the original system (A).

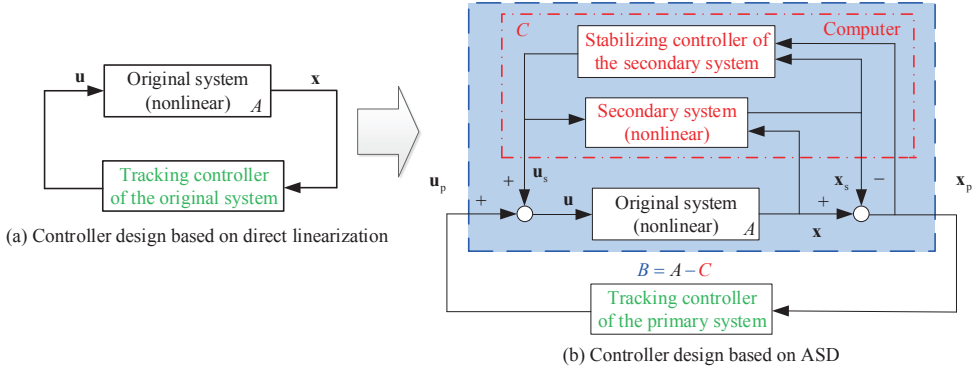


Figure 7.2: Two control ideas.

7.3.2 Additive state decomposition

Additive state decomposition (ASD) [205] is a decomposition method for nonlinear systems just like superposition principle for linear systems. In the following, ASD is introduced to decompose the aforementioned receiver model into two subsystems to make the following controller design more flexible and easier.

Consider system (7.7) as the original system. By applying ASD, the primary system is chosen as

$$\begin{aligned}\tilde{\mathbf{x}}_{r,p} &= \mathbf{A}\tilde{\mathbf{x}}_{r,p} + \mathbf{B}\tilde{\mathbf{u}}_{r,p} + \mathbf{d}(\tilde{\mathbf{x}}_r, \tilde{\mathbf{u}}_r) \\ \tilde{\mathbf{y}}_{r,p} &= \mathbf{C}\tilde{\mathbf{x}}_{r,p}, \tilde{\mathbf{x}}_{r,p}(0) = \tilde{\mathbf{x}}_{r0}.\end{aligned}\quad (7.8)$$

Then, subtracting the primary system (7.8) from the original system (7.7) gives

$$\begin{aligned}\tilde{\mathbf{x}}_r - \tilde{\mathbf{x}}_{r,p} &= \mathbf{A}(\tilde{\mathbf{x}}_r - \tilde{\mathbf{x}}_{r,p}) + \mathbf{B}(\tilde{\mathbf{u}}_r - \tilde{\mathbf{u}}_{r,p}) + \mathbf{g}(\tilde{\mathbf{x}}_r) \\ \tilde{\mathbf{y}}_r - \tilde{\mathbf{y}}_{r,p} &= \mathbf{C}(\tilde{\mathbf{x}}_r - \tilde{\mathbf{x}}_{r,p}), \tilde{\mathbf{x}}_r(0) - \tilde{\mathbf{x}}_{r,p}(0) = \mathbf{0}.\end{aligned}\quad (7.9)$$

Next, by defining

$$\tilde{\mathbf{x}}_{r,s} = \tilde{\mathbf{x}}_r - \tilde{\mathbf{x}}_{r,p}, \tilde{\mathbf{y}}_{r,s} = \tilde{\mathbf{y}}_r - \tilde{\mathbf{y}}_{r,p}, \tilde{\mathbf{u}}_{r,s} = \tilde{\mathbf{u}}_r - \tilde{\mathbf{u}}_{r,p} \quad (7.10)$$

system (7.8) and system (7.9) become

$$\text{Primary system: } \begin{cases} \tilde{\mathbf{x}}_{r,p} = \mathbf{A}\tilde{\mathbf{x}}_{r,p} + \mathbf{B}\tilde{\mathbf{u}}_{r,p} + \mathbf{d}(\tilde{\mathbf{x}}_{r,s} + \tilde{\mathbf{x}}_{r,p}, \tilde{\mathbf{u}}_{r,p} + \tilde{\mathbf{u}}_{r,s}) \\ \tilde{\mathbf{y}}_{r,p} = \mathbf{C}\tilde{\mathbf{x}}_{r,p}, \tilde{\mathbf{x}}_{r,p}(0) = \tilde{\mathbf{x}}_{r0} \end{cases} \quad (7.11)$$

$$\text{Secondary system: } \begin{cases} \tilde{\mathbf{x}}_{r,s} = \mathbf{A}\tilde{\mathbf{x}}_{r,s} + \mathbf{B}\tilde{\mathbf{u}}_{r,s} + \mathbf{g}(\tilde{\mathbf{x}}_{r,s} + \tilde{\mathbf{x}}_{r,p}) \\ \tilde{\mathbf{y}}_{r,s} = \mathbf{C}\tilde{\mathbf{x}}_{r,s}, \tilde{\mathbf{x}}_{r,s}(0) = \mathbf{0}. \end{cases} \quad (7.12)$$

The two decomposed systems have the same dimensions with the original system (7.7). Conversely, the original system (7.7) can be replaced by putting the primary system (7.11) and the secondary system (7.12) together, which means the state and the output satisfy

$$\tilde{\mathbf{x}}_r = \tilde{\mathbf{x}}_{r,s} + \tilde{\mathbf{x}}_{r,p}, \tilde{\mathbf{y}}_r = \tilde{\mathbf{y}}_{r,s} + \tilde{\mathbf{y}}_{r,p}, \tilde{\mathbf{u}}_r = \tilde{\mathbf{u}}_{r,s} + \tilde{\mathbf{u}}_{r,p}. \quad (7.13)$$

It is clear from equations (7.11)-(7.13) that if the controller $\tilde{\mathbf{u}}_{r,p}$ drives $\tilde{\mathbf{y}}_{r,p}(t) - \tilde{\mathbf{y}}_r^d(t) \rightarrow \mathbf{0}$ or $\tilde{\mathbf{y}}_{r,p}(t) - \tilde{\mathbf{y}}_r^d(t) \rightarrow \mathcal{B}(\mathbf{0}_{3 \times 1}, \delta)$ as $t \rightarrow \infty$ and the controller $\tilde{\mathbf{u}}_{r,s}$ drives $\tilde{\mathbf{x}}_{r,s}(t) \rightarrow \mathbf{0}$ as $t \rightarrow \infty$, then $\tilde{\mathbf{y}}_r(t) - \tilde{\mathbf{y}}_r^d(t) \rightarrow \mathbf{0}$ or $\tilde{\mathbf{y}}_r(t) - \tilde{\mathbf{y}}_r^d(t) \rightarrow \mathcal{B}(\mathbf{0}_{3 \times 1}, \delta)$ as $t \rightarrow \infty$. The strategy here is to assign the tracking subtask to the primary system (7.11) and the stabilization subtask to the secondary system (7.12), which is shown in Fig. 7.3. Since system (7.11) is an LTI system including all disturbances, standard design methods in either frequency domain or time domain, such as the PI control method, can be used to handle the tracking problem. On the other hand, system (7.12) is a deterministic nonlinear system, many nonlinear stabilizing control methods can be applied to solve the stabilization problem. It should be noticed that the ASD offers a two-degree-of-freedom way to tackle a tracking task under disturbances and a nonlinear stabilization task respectively, which reduces the difficulty of the original problem. The primary controller designed for the tracking task and the secondary controller designed for the nonlinear stabilization task can be viewed as two one-degree-of-freedom controllers. The final two-degree-of-freedom controller can be obtained by combining the primary controller and the secondary controller.

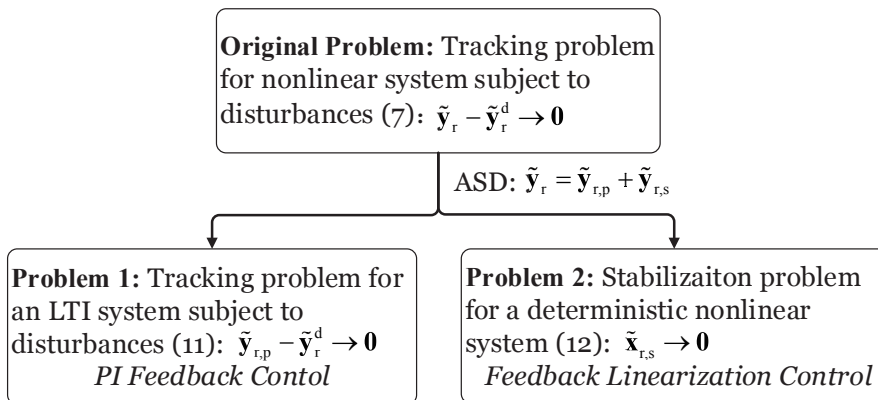


Figure 7.3: Additive state decomposition of system (7.7).

7.3.3 Controller design for the primary and secondary systems

So far, the considered system has been decomposed into two subsystems in charge of corresponding subtasks. In this section, the controller design is investigated in the form of two problems with respect to two subtasks, respectively. Because the system dimension of the receiver is high, controllers are often designed for the decoupled longitudinal channel and lateral channel respectively. In the following, the controller design for the longitudinal channel is taken into consideration for an illustration (a subscript ‘lon’ is added to every variable in the following, while ‘lat’ stands for the lateral channel). The control idea and design process of the lateral channel is similar, and thus omitted here. The longitudinal channel has the state $\mathbf{x}_{rlon} = [x_r \ h_r \ \theta \ V_r \ \alpha \ q]^T$ and the input $\mathbf{u}_{rlon} = [\delta_t \ \delta_e]^T$, while the lateral channel has the state $\mathbf{x}_{rlat} = [y_r \ \psi \ \phi \ \beta \ p \ r]^T$ and the input $\mathbf{u}_{rlat} = [\delta_a \ \delta_r]^T$.

7.3.3.1 Problem 1. Tracking problem

For (7.11), design a PI tracking controller

$$\tilde{\mathbf{u}}_{rlon,p} = \tilde{\mathbf{u}}_{rlon,p} \left(\tilde{\mathbf{x}}_{rlon,p}, \int_0^t (\tilde{\mathbf{y}}_{rlon,p}(s) - \tilde{\mathbf{y}}_{rlon}^d(s)) ds \right) \quad (7.14)$$

such that $\mathbf{e}_{rlon,p} = \tilde{\mathbf{y}}_{rlon,p}(t) - \tilde{\mathbf{y}}_{rlon}^d(t) \rightarrow \mathbf{0}$ as $t \rightarrow \infty$, meanwhile keeping $\tilde{\mathbf{x}}_{rlon,p}$ bounded.

Intuitively, to remove the tracking error, an integral action must be employed in the controller

$$\mathbf{q}_{rlon,p} = \int_0^t \mathbf{e}_{rlon,p}(s) ds = \int_0^t (\tilde{\mathbf{y}}_{rlon,p}(s) - \tilde{\mathbf{y}}_{rlon}^d(s)) ds. \quad (7.15)$$

By combining (7.11) with (7.15), the manipulated augmented system of (7.11) is

$$\begin{bmatrix} \tilde{\mathbf{x}}_{rlon,p} \\ \mathbf{q}_{rlon,p} \end{bmatrix} = \begin{bmatrix} \mathbf{A}_{lon} & \mathbf{0} \\ \mathbf{C}_{lon} & \mathbf{0} \end{bmatrix} \begin{bmatrix} \tilde{\mathbf{x}}_{rlon,p} \\ \mathbf{q}_{rlon,p} \end{bmatrix} + \begin{bmatrix} \mathbf{B}_{lon} \\ \mathbf{0} \end{bmatrix} \tilde{\mathbf{u}}_{rlon,p} - \begin{bmatrix} \mathbf{0} \\ \mathbf{I} \end{bmatrix} \tilde{\mathbf{y}}_{rlon}^d + \begin{bmatrix} \mathbf{I} \\ \mathbf{0} \end{bmatrix} \mathbf{d}(\tilde{\mathbf{x}}_{rlon}, \tilde{\mathbf{u}}_{rlon}).$$

According to [209], a state feedback controller can be designed as

$$\tilde{\mathbf{u}}_{rlon,p} = -\mathbf{K}_{xlon} \tilde{\mathbf{x}}_{rlon,p} - \mathbf{K}_{elon} \mathbf{q}_{rlon,p} \quad (7.16)$$

where $\mathbf{K}_{xlon} \in \mathbb{R}^{2 \times 6}$, $\mathbf{K}_{elon} \in \mathbb{R}^{2 \times 2}$. The LQR method is utilized to determine the feedback matrices \mathbf{K}_{xlon} , \mathbf{K}_{elon} , and the cost function is

$$J(\tilde{\mathbf{u}}_{rlon,p}) = \arg \min_{\mathbf{K}_{xlon}, \mathbf{K}_{elon}} \int_0^\infty \left\{ \left[\begin{array}{cc} \tilde{\mathbf{x}}_{rlon,p}^T & \mathbf{q}_{rlon,p}^T \end{array} \right] \mathbf{Q}_{rlon} \begin{bmatrix} \tilde{\mathbf{x}}_{rlon,p} \\ \mathbf{q}_{rlon,p} \end{bmatrix} + \tilde{\mathbf{u}}_{rlon,p}^T \mathbf{R}_{rlon} \tilde{\mathbf{u}}_{rlon,p} \right\} dt.$$

The feedback matrices \mathbf{K}_{xlon} , \mathbf{K}_{elon} can be determined by choosing proper \mathbf{Q}_{rlon} and \mathbf{R}_{rlon} . The structure of the closed-loop primary system is displayed in Fig. 7.4.

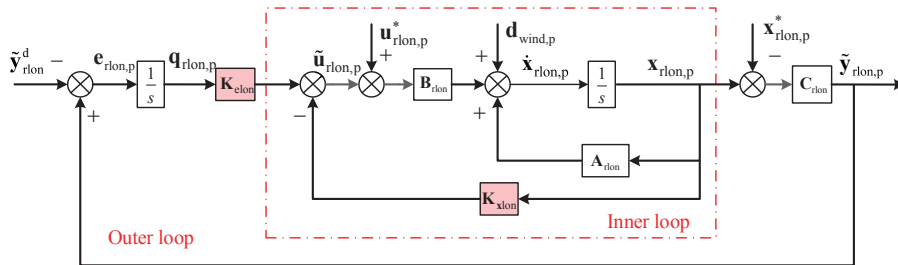


Figure 7.4: Closed-loop primary system.

Theorem 1. For system (7.11), if the controller is designed as

$$\tilde{\mathbf{u}}_{rlon,p} = -\mathbf{K}_{xlon} \tilde{\mathbf{x}}_{rlon,p} - \mathbf{K}_{elon} \mathbf{q}_{rlon,p} \quad (7.17)$$

then $\tilde{\mathbf{y}}_{rlon,p}(t) - \tilde{\mathbf{y}}_{rlon}^d(t) \rightarrow \mathbf{0}$ as $t \rightarrow \infty$, and $\tilde{\mathbf{x}}_{rlon,p}$ is bounded.

Proof. See [209]. \square

7.3.3.2 Problem 2. Stabilization problem

For (7.12), design a stabilizing controller

$$\tilde{\mathbf{u}}_{rlon,s} = \tilde{\mathbf{u}}_{rlon,s}(\tilde{\mathbf{x}}_{rlon,s}, \tilde{\mathbf{x}}_{rlon,p}) \quad (7.18)$$

such that $\tilde{\mathbf{x}}_{rlon,s}(t) \rightarrow \mathbf{0}$ as $t \rightarrow \infty$.

In the following, a feedback linearization controller will be designed. In order to make the controller design easier, a virtual output variable is defined as

$$\bar{y}_{rlon,s} = \mathbf{C}_{slon}\tilde{x}_{rlon,s} \quad (7.19)$$

where $\mathbf{C}_{slon} \in \mathbb{R}^{2 \times 6}$. If the new output matrix \mathbf{C}_{slon} makes the system from $\tilde{u}_{rlon,s}$ to $\bar{y}_{rlon,s}$ be a minimum-phase system, then $\bar{y}_{rlon,s} \rightarrow \mathbf{0}$ implies $\tilde{x}_{rlon,s} \rightarrow \mathbf{0}$. A method for determining the output matrix \mathbf{C}_{slon} is given in [210]. After obtaining feedback matrix \mathbf{K}_{xlon} , $\mathbf{A}_{lon} + \mathbf{B}_{lon}\mathbf{K}_{xlon}$ is stable. Thus, according to Lyapunov function, there exist \mathbf{P} and \mathbf{M} such that

$$\mathbf{P}(\mathbf{A}_{lon} + \mathbf{B}_{lon}\mathbf{K}_{xlon}) + (\mathbf{A}_{lon} + \mathbf{B}_{lon}\mathbf{K}_{xlon})^T\mathbf{P} = -\mathbf{M}.$$

Then, the output matrix \mathbf{C}_{slon} can be determined as

$$\mathbf{C}_{slon} = \mathbf{P}\mathbf{B}_{lon}.$$

Differentiating Eq. (7.19), one has

$$\bar{y}_{rlon,s} = \mathbf{C}_{slon}\mathbf{A}_{lon}\tilde{x}_{rlon,s} + \mathbf{C}_{slon}\mathbf{B}_{lon}\tilde{u}_{rlon,s} + \mathbf{C}_{slon}\mathbf{g}(\tilde{x}_{rlon,s} + \tilde{x}_{rlon,p}). \quad (7.20)$$

A control input can be designed as

$$\tilde{u}_{rlon,s} = (\mathbf{C}_{slon}\mathbf{B}_{lon})^{-1}(\mathbf{v}_{rlon,s} - \mathbf{C}_{slon}\mathbf{A}_{lon}\tilde{x}_{rlon,s} - \mathbf{C}_{slon}\mathbf{g}(\tilde{x}_{rlon,s} + \tilde{x}_{rlon,p})) \quad (7.21)$$

where $\mathbf{v}_{rlon,s}$ is a virtual input. The choice of \mathbf{C}_{slon} needs to make $\mathbf{C}_{slon}\mathbf{B}_{lon}$ invertible. Then, it can be obtained

$$\bar{y}_{rlon,s} = \mathbf{v}_{rlon,s}.$$

Design

$$\mathbf{v}_{rlon,s} = -\mathbf{K}_{rlon}\bar{y}_{rlon,s}$$

where $\mathbf{K}_{rlon} \in \mathbb{R}^{2 \times 2}$ is the controller parameter. Then, one has

$$\bar{y}_{rlon,s} = -\mathbf{K}_{rlon}\bar{y}_{rlon,s}$$

which can guarantee that $\bar{y}_{rlon,s} \rightarrow \mathbf{0}$ exponentially, and further can guarantee that $\tilde{x}_{rlon,s} \rightarrow \mathbf{0}$ exponentially.

Theorem 2. For system (7.12), if there exists a control input

$$\tilde{u}_{rlon,s} = (\mathbf{C}_{slon}\mathbf{B}_{lon})^{-1}(-\mathbf{K}_{rlon}\bar{y}_{rlon,s} - \mathbf{C}_{slon}\mathbf{A}_{lon}\tilde{x}_{rlon,s} - \mathbf{C}_{slon}\mathbf{g}(\tilde{x}_{rlon,s} + \tilde{x}_{rlon,p})) \quad (7.22)$$

where $\mathbf{K}_{rlon} \in \mathbb{R}^{2 \times 2}$ and $\mathbf{C}_{slon} = \mathbf{P}\mathbf{B}_{lon}$, such that

$$\bar{y}_{rlon,s} = -\mathbf{K}_{rlon}\bar{y}_{rlon,s} \quad (7.23)$$

is stable, then $\tilde{x}_{rlon,s}(t) \rightarrow \mathbf{0}$ as $t \rightarrow \infty$.

Proof. See [210]. \square

Controller design for the decomposed systems (7.11) and (7.12) requires their states and outputs as feedback variables. However, they are virtual and unknown. For such a purpose, an observer is designed in *Theorem 3* to estimate $\tilde{x}_{rlon,p}$, $\tilde{x}_{rlon,s}$ and $\tilde{y}_{rlon,p}$.

Theorem 3. Suppose that an observer is designed to estimate $\tilde{x}_{rlon,p}$, $\tilde{x}_{rlon,s}$ and $\tilde{y}_{rlon,p}$ in

(7.11) and (7.12) as

$$\begin{aligned}\hat{\tilde{x}}_{rlon,s} &= \mathbf{A}_{lon}\hat{\tilde{x}}_{rlon,s} + \mathbf{B}_{lon}\tilde{u}_{rlon,s} + \mathbf{g}(\tilde{x}_{rlon}), \hat{\tilde{x}}_{rlon,s} = \mathbf{0}, \\ \hat{\tilde{x}}_{rlon,p} &= \tilde{x}_{rlon} - \hat{\tilde{x}}_{rlon,s} \\ \hat{\tilde{y}}_{rlon,p} &= \mathbf{C}_{lon}\hat{\tilde{x}}_{rlon,p}.\end{aligned}\quad (7.24)$$

Then $\hat{\tilde{x}}_{rlon,p} \equiv \tilde{x}_{rlon,p}$, $\hat{\tilde{x}}_{rlon,s} \equiv \tilde{x}_{rlon,s}$ and $\hat{\tilde{y}}_{rlon,p} \equiv \tilde{y}_{rlon,p}$.

Proof. [205]. \square

7.3.4 Controller integration

With the solutions to the two problems in hand, one is ready to claim *Theorem 4*.

Theorem 4. Under Assumptions 1-4, suppose (i) Problems 1 and 2 are solved; (ii) the controller for system (7.7) is designed as

Longitudinal-channel Observer:

$$\begin{aligned}\hat{\tilde{x}}_{rlon,s} &= \mathbf{A}_{lon}\hat{\tilde{x}}_{rlon,s} + \mathbf{B}_{lon}\tilde{u}_{rlon,s} + \mathbf{g}(\tilde{x}_{rlon}), \hat{\tilde{x}}_{rlon,s} = \mathbf{0}, \\ \hat{\tilde{x}}_{rlon,p} &= \tilde{x}_{rlon} - \hat{\tilde{x}}_{rlon,s} \\ \hat{\tilde{y}}_{rlon,p} &= \mathbf{C}_{lon}\hat{\tilde{x}}_{rlon,p}.\end{aligned}\quad (7.25)$$

Longitudinal-channel Controller:

$$\tilde{u}_{rlon} = \tilde{u}_{rlon,p} \left(\hat{\tilde{x}}_{rlon,p}, \int_0^t (\hat{\tilde{y}}_{rlon,p}(s) - \tilde{y}_{rlon}^d(s)) ds \right) + \tilde{u}_{rlon,s} \left(\hat{\tilde{x}}_{rlon,s}, \hat{\tilde{x}}_{rlon,p} \right). \quad (7.26)$$

Lateral-channel Observer:

$$\begin{aligned}\hat{\tilde{x}}_{rlat,s} &= \mathbf{A}_{lat}\hat{\tilde{x}}_{rlat,s} + \mathbf{B}_{lat}\tilde{u}_{rlat,s} + \mathbf{g}(\tilde{x}_{rlat}), \hat{\tilde{x}}_{rlat,s} = \mathbf{0}, \\ \hat{\tilde{x}}_{rlat,p} &= \tilde{x}_{rlat} - \hat{\tilde{x}}_{rlat,s} \\ \hat{\tilde{y}}_{rlat,p} &= \mathbf{C}_{lat}\hat{\tilde{x}}_{rlat,p}.\end{aligned}\quad (7.27)$$

Lateral-channel Controller:

$$\tilde{u}_{rlat} = \tilde{u}_{rlat,p} \left(\hat{\tilde{x}}_{rlat,p}, \int_0^t (\hat{\tilde{y}}_{rlat,p}(s) - \tilde{y}_{rlat}^d(s)) ds \right) + \tilde{u}_{rlat,s} \left(\hat{\tilde{x}}_{rlat,s}, \hat{\tilde{x}}_{rlat,p} \right). \quad (7.28)$$

Integrated Controller:

$$\tilde{u}_r = \begin{bmatrix} \tilde{u}_{rlon} \\ \tilde{u}_{rlat} \end{bmatrix} = \begin{bmatrix} \tilde{u}_{rlon,p} + \tilde{u}_{rlon,s} \\ \tilde{u}_{rlat,p} + \tilde{u}_{rlat,s} \end{bmatrix} \quad (7.29)$$

$$= \tilde{u}_{r,p} + \tilde{u}_{r,s} = \begin{bmatrix} \tilde{u}_{rlon,p} \\ \tilde{u}_{rlat,p} \end{bmatrix} + \begin{bmatrix} \tilde{u}_{rlon,s} \\ \tilde{u}_{rlat,s} \end{bmatrix}. \quad (7.30)$$

Then, the output of system (7.7) satisfies $\tilde{y}_r(t) - \tilde{y}_r^d(t) \rightarrow \mathbf{0}$ as $t \rightarrow \infty$.

Proof. For the longitudinal channel, according to *Theorem 3*, observer (7.25) will make $\hat{\tilde{x}}_{rlon,p} \equiv \tilde{x}_{rlon,p}$, $\hat{\tilde{x}}_{rlon,s} \equiv \tilde{x}_{rlon,s}$ and $\hat{\tilde{y}}_{rlon,p} \equiv \tilde{y}_{rlon,p}$. Under condition (i), the controller $\tilde{u}_{rlon,p}$ drives $\tilde{y}_{rlon,p}(t) - \tilde{y}_{rlon}^d(t) \rightarrow \mathbf{0}$ as $t \rightarrow \infty$ for system (7.11) (*Theorem 1*), and the controller $\tilde{u}_{rlon,s}$ drives $\tilde{x}_{rlon,s}(t) \rightarrow \mathbf{0}$ as $t \rightarrow \infty$ for system (7.12) (*Theorem 2*). Then the controller $\tilde{u}_{rlon} = \tilde{u}_{rlon,p} + \tilde{u}_{rlon,s}$ guarantees $\tilde{y}_{rlon}(t) - \tilde{y}_{rlon}^d(t) \rightarrow \mathbf{0}$ as $t \rightarrow \infty$. For the lateral channel, it can be concluded that the

controller $\tilde{\mathbf{u}}_{rlat} = \tilde{\mathbf{u}}_{rlat,p} + \tilde{\mathbf{u}}_{rlat,s}$ guarantees $\tilde{\mathbf{y}}_{rlat}(t) - \tilde{\mathbf{y}}_{rlat}^d(t) \rightarrow \mathbf{0}$ as $t \rightarrow \infty$ in a similar way. Then the controller $\tilde{\mathbf{u}}_r = \tilde{\mathbf{u}}_{r,p} + \tilde{\mathbf{u}}_{r,s}$ guarantees $\tilde{\mathbf{y}}_r(t) - \tilde{\mathbf{y}}_r^d(t) \rightarrow \mathbf{0}$ as $t \rightarrow \infty$ for system (7.7). \square

The structure of the overall closed-loop system is depicted in Fig. 7.5.

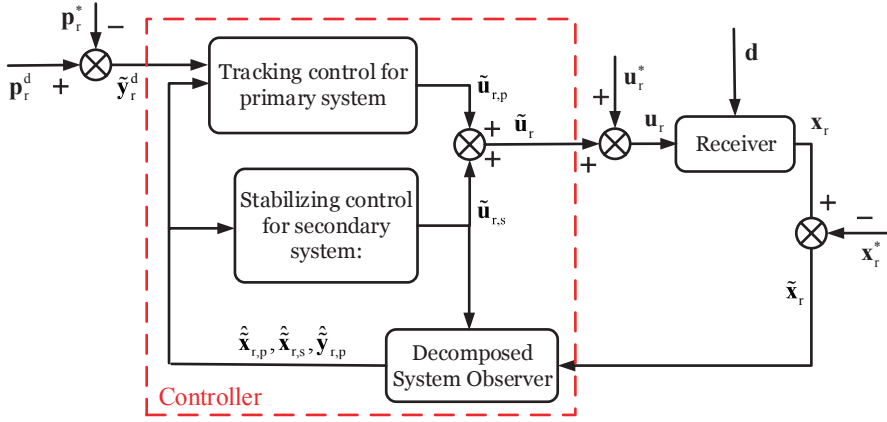


Figure 7.5: Structure of the closed-loop system with ASD-based control.

7.4 Simulation Studies

In this section, the feasibility and the performance of the proposed ASD-based station-keeping controller are investigated through the simulation.

7.4.1 Simulation configuration

A MATLAB/SIMULINK-based simulation environment with a three-dimensional virtual-reality display has been developed by the authors' research laboratory to simulate the PDR. The detailed information about the modeling procedure, model parameters, and simulation environment can refer to previous works [87], [40].

In the simulation, the trim condition is the level and forward flight with the height $h_t^g = 3000\text{m}$ (9843ft) and the velocity $v_t^g = 120\text{m/s}$ (393.72ft/s), as shown in Fig. 7.1. Controller parameters are set as follows.

Longitudinal-channel primary controller parameters:

$$\mathbf{Q}_{rlon} = \text{diag}(4, 10, 10, 1, 10, 10, 1, 3), \mathbf{R}_{rlon} = \text{diag}(50, 50)$$

$$\mathbf{K}_{xlon} = \begin{bmatrix} 0.6690 & 0.1816 & 72.926 & 1.3386 & -75.589 & 1.0669 \\ 0.0974 & -0.7903 & -354.56 & 0.0628 & 246.25 & -50.082 \end{bmatrix}, \mathbf{K}_{elon} = \begin{bmatrix} 0.1392 & 0.0433 \\ 0.0250 & -0.2411 \end{bmatrix}$$

Longitudinal-channel secondary controller parameters:

$$\mathbf{C}_{s1on} = \begin{bmatrix} -14.068 & 196.526 & 143428.581 & 2406.307 & -147654.857 & 2428.098 \\ 194.075 & 76.508 & 44066.609 & 904.369 & -48027.709 & -41.490 \end{bmatrix}, \mathbf{K}_{rlon} = \begin{bmatrix} 1 & 0 \\ 0 & 1 \end{bmatrix}$$

Lateral-channel primary controller parameters:

$$\mathbf{Q}_{\text{rlat}} = \text{diag}(10, 2, 4, 4, 2, 2, 4), \mathbf{R}_{\text{rlat}} = \text{diag}(50, 50)$$

$$\mathbf{K}_{\text{xlat}} = \begin{bmatrix} -0.3833 & 9.6773 & -287.58 & -250.74 & -5.7648 & -34.536 \end{bmatrix}, \mathbf{K}_{\text{elat}} = \begin{bmatrix} -0.0876 \\ -0.0180 \end{bmatrix}$$

Lateral-channel secondary controller parameters:

$$\mathbf{C}_{\text{slat}} = \begin{bmatrix} -1.272 & 55.046 & -880.467 & -775.037 & -7.652 & -52.170 \\ -0.143 & 9.216 & -173.189 & -149.751 & -1.826 & -13.936 \end{bmatrix}, \mathbf{K}_{\text{rlat}} = \begin{bmatrix} 1 & 0 \\ 0 & 1 \end{bmatrix}$$

7.4.2 Simulation results

7.4.2.1 Station-keeping with constant mass

In the first group of simulations, the joining phase from the standby point A to the observation position B and the pre-refueling phase from B to the pre-contact point C are studied. During these phases, the receiver mass remains unchanged. The position A is set as $\mathbf{p}_{r0}^t = \begin{bmatrix} -60 & -50 & 5 \end{bmatrix}^T$, the position B is set as $\mathbf{p}_{r1}^t = \begin{bmatrix} -10 & -50 & 5 \end{bmatrix}^T$, and the position C is set as $\mathbf{p}_{r2}^t = \begin{bmatrix} -25 & 0 & 5 \end{bmatrix}^T$ in the tanker frame. The total simulation time is $T = 200$ s. The first phase from A to B begins when $t = 10$ s, and the second phase from B to C begins when $t = 90$ s. First, when the tanker vortex is considered, the tracking response is presented in Fig. 7.6. During the beginning 10s, the receiver stays relatively still to the tanker. Then, the receiver moves forward slowly, and reaches the observation position B at about 75s. After staying still for 15s, the receiver begins to move backward and to the right to approach C , and gets there at about 160s. It can also be seen that, during the whole flight, the receiver tracks the reference trajectory well. The actual flight trajectory is smooth, and the steady-state error is zero. The corresponding control inputs including the thrust and the actuator deflection are displayed in Fig. 7.7. Other nine states are displayed in Fig. 7.8. They all meet the control requirements. Then, taking the atmospheric turbulence into consideration, the tracking response is presented in Fig. 7.9. The maximum velocity of the induced wind field by the atmospheric turbulence can reach 1m/s. Under this circumstance, the receiver tracks the reference trajectory under slight fluctuation. The whole tracking effect is satisfactory. Thus, the designed controller can achieve good control effect in the presence of the wind disturbances.

7.4.2.2 Station-keeping with varying mass

In the second group of simulations, the fuel transferring phase, namely the receiver and the tanker keep relatively stationary to transfer the fuel, is considered. During this phase, the receiver mass increases gradually as the fuel transfers. The receiver mass before fuel transfer is $m_0 = 9295$ kg, and the receiver mass after fuel transfer is $m_1 = 11295$ kg. Total 2000kg fuel is transferred. If the fuel transferring speed is $v_{ft} = \dot{m} = 20$ kg/s, then the fuelling time is $T_{ft} = 100$ s.

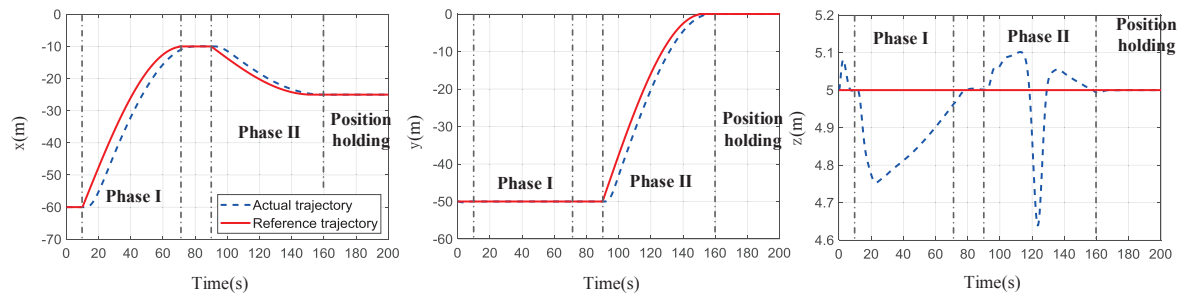


Figure 7.6: Trajectory tracking response under the tanker vortex.

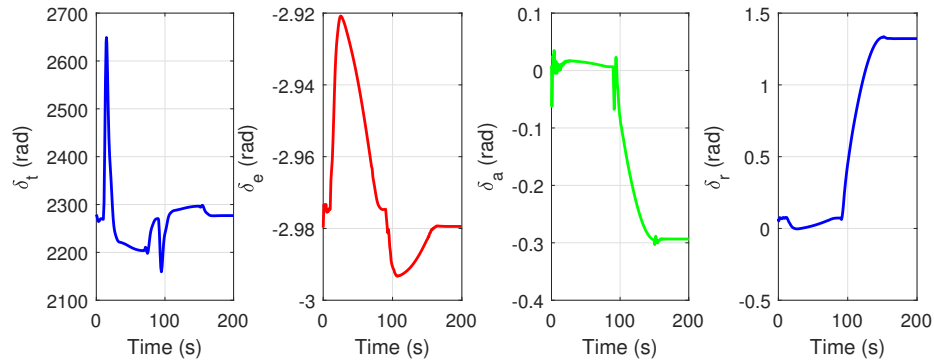


Figure 7.7: Control inputs.

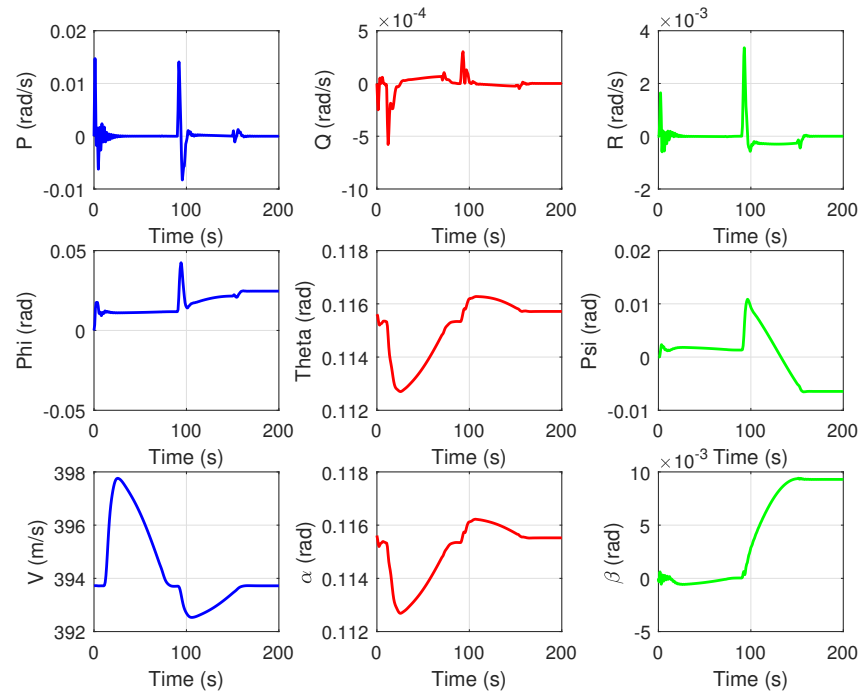


Figure 7.8: State response.

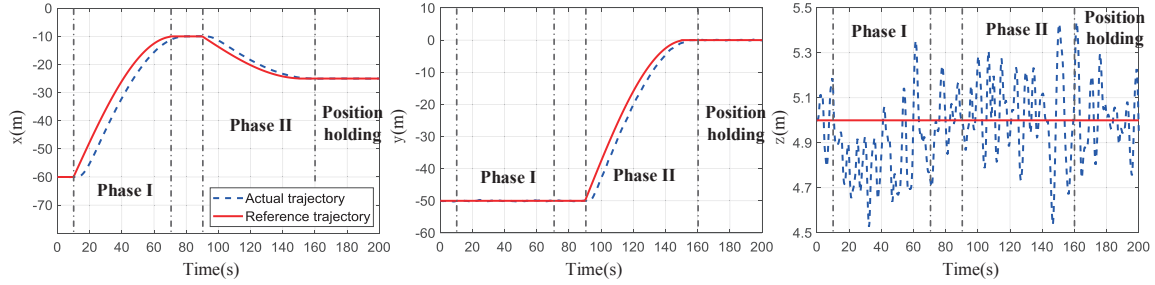


Figure 7.9: Trajectory tracking response under the atmospheric turbulence.

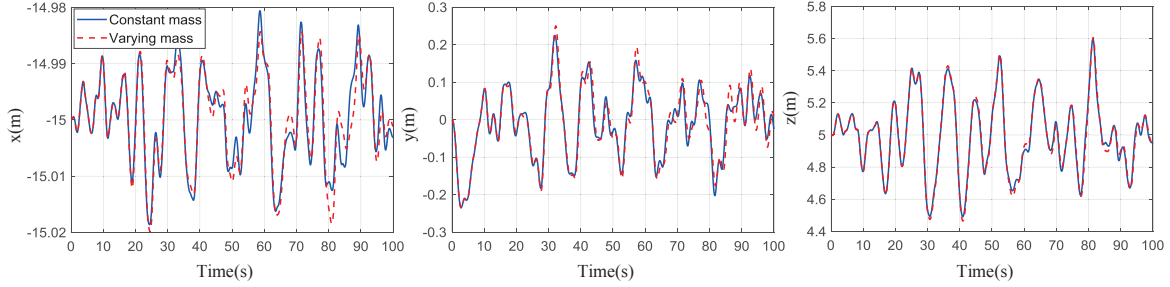


Figure 7.10: Position holding effect of the varying mass receiver.

Suppose that, in the tanker frame, the reference position of the receiver is $\mathbf{p}_d^t = \begin{bmatrix} -15 & 0 & 5 \end{bmatrix}^T$. The position holding response is displayed in Fig. 7.10. It can be seen that the mass-varying receiver holds in the refueling position well and the response under varying mass is just slightly different from the response under the constant mass. This means the proposed controller has robustness against the receiver mass change.

7.5 Chapter Summary

In this study, the station keeping problem for AAR has been addressed by an ASD-based control method. In order to demonstrate its effectiveness, the control method is applied to the PDR. Based on ASD, the original receiver system is decomposed into a primary system and a secondary system. Through designing a PI controller and a feedback linearization controller for these two decomposed systems respectively, the final control input can be obtained by combining these two controllers. Simulation results show that the designed ASD-based station-keeping controller can satisfy the control requirements of the trajectory tracking and position holding in the presence of unknown disturbances and varying mass. While PI control and feedback linearization control are not new, the salient feature of the proposed control method lies in the fusion of them by using ASD to solve a challenging nonlinear tracking problem. In future research, stability margin could be introduced into the linear primary system to study the stability and robustness of the full system in a more accurate and quantitative way. Furthermore, frequency-domain compensation methods could be introduced into the primary system to study the robustness performance improvement of the full system.

Chapter 8 Hose-Drum-Unit Control

Aerial refueling (AR) is an effective method of increasing the endurance and range of aircraft by refueling them in flight [2], [211]. Among the aerial refueling methods in operation today, the probe-drogue refueling (PDR) [9] is the most widely adopted one owing to its flexibility and simple requirement for equipment. In this chapter, the low-level flight control for PDR is focused, where the station-keeping control and the docking control are included. First, the station-keeping control is the basis of autonomous aerial refueling. However, there exist strong external disturbances including the atmospheric turbulence and the wake vortex of the tanker, and the system perturbation caused by the fuel transfer. These pose challenges to station-keeping control design. This chapter proposes an additive-state-decomposition-based (or state-compensation-linearization-based) station-keeping control method for autonomous aerial refueling. Moreover, designing a controller for the docking maneuver in PDR is the most important but challenging task, due to the complex system model and the high precision requirement. In order to overcome the disadvantage of only feedback control, a additive-state-decomposition-based feedforward control scheme known as iterative learning control (ILC) proposed in *Chapter 6* is adopted here.

8.1 Introduction

Autonomous Aerial Refueling (AAR) is an effective method of increasing the endurance and range of Unmanned Aerial Vehicles (UAVs) [212–214] by refueling them in flight [215]. The Probe-and-Drogue Refueling (PDR) is widely adopted in AAR owing to its simple requirement of equipment and flexibility. In a PDR system, there is a hose payout and reel-in device which is called Hose-Drum Unit (HDU) [216] (also known as the reel take-up system [217, 218]). It consists of a hose-drum motor and a motor control unit, and determines the motion of the upper end of the hose [216]. It is an important device to suppress the hose whipping phenomenon (HWP), which can result in severe damage to the probe or the drogue [219].

The HWP is caused by the excessive contact between the probe and the drogue. The existing literature focused on how to design an HDU controller to maintain the tension of the hose and suppress HWP, such as [217, 219]. In practice, the drogue will remain relatively static if the hose-drogue system is not affected by wind disturbances. In this situation, the “excessive contact” is hard to happen because tracking a static target is a relatively easy and simple task. However, when affected by wind disturbances, the drogue is always moving, so the receiver has to speed up to chase the drogue which may result in excessive contact and HWP. In addition to suppressing the HWP after the contact, this chapter tries to reveal that the HDU can also be applied as a feedback damper to reduce the frequency and amplitude of the drogue position fluctuation under wind

disturbances, which has not attracted enough attention in the previous research. Fortunately, the basic models were established by the existing literature, which can be employed to analyze the dynamics of the drogue with HDU controller. The hose-drogue dynamic model is established and the behavior of the drogue in the docking stage is analyzed by references [216–218, 220?].

In the whole refueling process, the motion of the drogue is influenced by many types of wind disturbances, such as the aerodynamic influence of the tanker [221], atmospheric turbulence [222], the bow wave effect [223], and so on. According to the NASA flight test results [223] as shown in Fig. 8.1(a), the drogue fluctuates with the amplitude about 0.1~0.2m (mainly caused by atmospheric turbulence, and the amplitude depends on the weather condition) in a low frequency when the receiver is far away. When the receiver comes close to the drogue, the drogue is quickly pushed away by the bow wave flow field with offset about 0.4m (dotted ellipse region in Fig. 8.1(a)), and this docking attempt is failed because the probe is too slow to chase the drogue. As a result, in the docking stage, the bow wave of the receiver is the most substantial one. Thus, the hose-drogue model under the bow wave is simplified by reference [224, 225], which is called the drogue dynamic model. Moreover, the motion of the drogue under the bow wave and its control methods are studied in [29, 41?]. However, there were some differences (the dotted ellipse regions in Fig. 8.1) between the simulation results generated by the drogue dynamic model (see Fig. 8.1(b)) and the flight test experiment (see Fig. 8.1(a)) [223], where the simulation results are about 40% larger than the experimental results, especially for the vertical position. One of the main reasons is that the effects of HDU were not considered by the drogue dynamic model. Thus, the results of reference [224] are improved in this chapter by considering the effects of HDU. Meanwhile, the traditional HDU control methods mainly feedback the hose tension to reduce the drogue fluctuation and suppress HWP to some extent, but it cannot avoid HWP essentially because it cannot detect whether the HWP is happening and its degree. Since the HWP is essentially caused by the over-slack of the hose due to excessive contact on the drogue, this chapter proposed an anti-HWP control method to monitor the state of the hose and control the hose length to stabilize the drogue movement.

In summary, the main contributions of this chapter are: (i) a more precise modeling method for hose-and-drogue system is proposed based on the previous study; (ii) by considering the effects of HDU controller, an improved integrated model is proposed to describe more accurately the behavior of the drogue under wind disturbances, and a simplified drogue dynamic model is obtained through system identification for the convenience of docking controller design of the receiver aircraft; (iii) improvements are proposed for the traditional HDU controllers to realize a better performance to stabilize the drogue position under disturbances before the contact happens; (iv) for the excessive contact situations, an anti-HWP control method is proposed to significantly reduce the effect of hose whipping phenomenon and improve the safety of aerial refueling systems.

This chapter is organized as follows. Section II describes the drogue dynamic model with

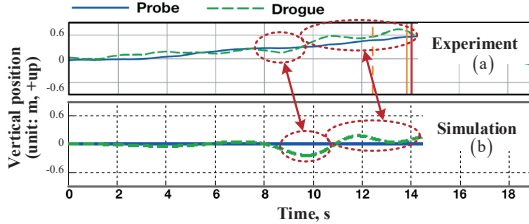


Figure 8.1: The vertical motion of the drogue in reference [224]

HDU and demonstrates the procedure of researching the effects of HDU. Section III compares two types of controllers for HDU, and the corresponding drogue dynamic models with HDU controllers are obtained by following the procedure of the simulation as mentioned in Section II. Their performances are also compared in this section. The anti-HWP control method is proposed and verified in Section IV. Finally, the conclusions are given in Section V.

8.2 Drogue Dynamic Model with HDU

The HDU is situated within the refueling pod, as shown in Fig. 8.2. It primarily consists of a drum (reel) that winds the hose, a motor responsible for controlling the rotation of the drum, and a controller for the motor. The rotation of the motor is primarily controlled based on the status of the upper end of the hose connected to the refueling pod. This device regulates the hose tension by adjusting the length of the hose exposed outside when the hose tension is insufficient. It effectively mitigates the phenomenon of hose whipping by reducing the risk of sudden tension changes, thereby minimizing potential refueling accidents caused by such effects. Currently,

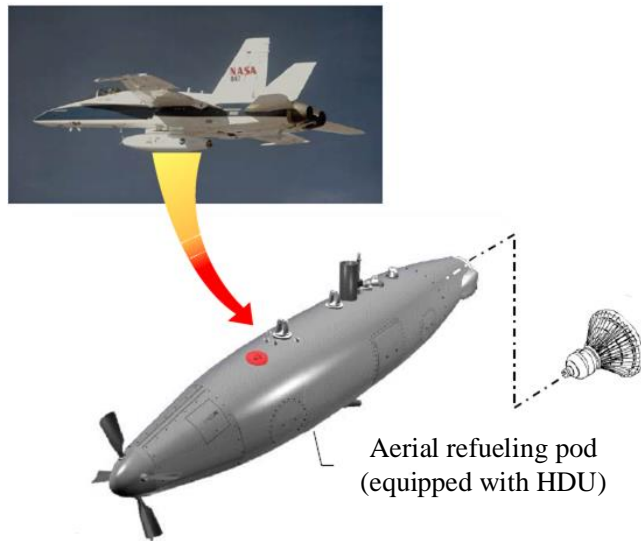


Figure 8.2: Refueling Pod and HDU Schematic

research on the HDU primarily focuses on designing controllers to regulate the hose tension and suppress hose whipping phenomenon. Hose whipping usually occurs after the docking of the drogue and probe, but the HDU's role in suppressing hose whipping also affects the dynamics of the hose-drogue assembly during the docking process. However, this aspect has

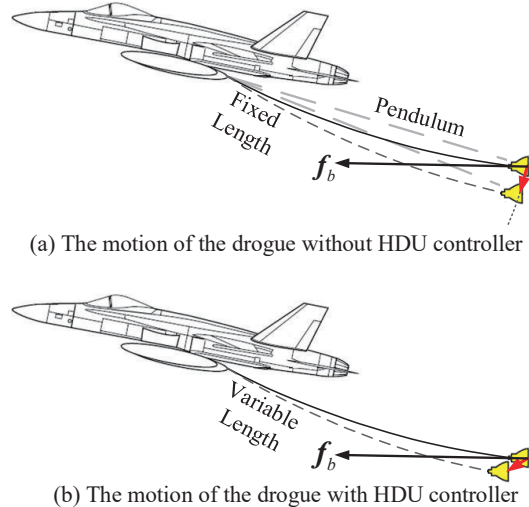


Figure 8.3: The motion of the drogue with and without HDU controller

received relatively little attention in current research. Therefore, this section will provide an initial analysis of this impact.

8.2.1 Analysis of Fixed-Length link-connected model Deficiencies

Based on the analysis in Section 4.3.4, the significant downward movement of the drogue in the $o_t z_t$ direction compared to the experiment can be observed. From this phenomenon and the corresponding time of occurrence, it can be inferred that this dynamic motion of the drogue in the $o_t z_t$ direction is caused by the component of the bow wave in the $o_t x_t$ direction, meaning that the force in the $o_t x_t$ direction induces a substantial displacement of the drogue in the $o_t z_t$ direction. The reason behind this phenomenon is that the hose-drogue system is under tension when in a steady state, making the hose behave more rigidly. The hose-drogue system is approximately similar to a simple pendulum near its equilibrium position [226], as depicted in Fig. 8.3.

In the absence of the HDU, the pendulum length remains unchanged, as shown in Fig. 8.3(a). Within the equilibrium range, applying a force to the endpoint of the pendulum, apart from the force direction normal to the equilibrium position, will result in a tangential motion of the pendulum due to forces acting in other directions. In a steady state, the hose tends to be in a more horizontal position, causing both F_{bx} and F_{bz} to primarily induce displacement of the drogue along the $o_t z_t$ direction. This also indicates a significant coupling of the drogue's dynamics in the absence of the HDU. When the HDU is considered, it adjusts the length of the exposed hose outside the aircraft in response to changes in hose tension, as depicted in Fig. 8.3(b). When the drogue experiences a longitudinal force F_{bx} from the bow wave, the HDU reduces the length of the exposed hose, thereby changing the primary direction of movement of the drogue from downward to forward. It is evident that the HDU modifies the dynamics of the drogue during the docking process.

8.2.2 Model of the HDU

The model of the HDU typically employs a reel model[227], and its dynamics can be expressed as follows

$$(T_{\text{reel}} - T_{\text{hose}}) r_{\text{reel}} = I_{\text{reel}} \alpha_{\text{reel}} \quad (8.1)$$

where T_{reel} and T_{hose} represent the tension in the reel and the tension at the upper end of the hose, respectively. Since the direction of force is not analyzed here, scalar magnitudes of tension are used. The symbols r_{reel} , I_{reel} and α_{reel} represent the radius of the reel, moment of inertia, and angular acceleration around its central axis. Furthermore, if the reel is considered as a cylindrical object, one have

$$I_{\text{reel}} = m_{\text{reel}} r_{\text{reel}}^2. \quad (8.2)$$

On the other hand, expressing α_{reel} in terms of linear acceleration

$$\alpha_{\text{reel}} = \frac{\ddot{l}_1}{r_{\text{reel}}}. \quad (8.3)$$

It should be noted that the change in the length of the hose is replaced by the change in the length of the first link. Although from Section 4.2 it can be understood that the one exposed is the i th link, due to the relatively small retraction of the hose during the docking process, extending the original length of the first link appropriately ensures that the first link is always exposed. Of course, the model of variable first link in Section 4.2.5 can also be used, but it involves more complex calculations. Substituting Eqs. (8.2) and (8.3) into Eq. (8.1), the kinematic model of HDU can be obtained as

$$\ddot{l}_1 = \frac{T_{\text{reel}} - T_{\text{hose}}}{m_{\text{reel}}}. \quad (8.4)$$

The relation of the bow wave model, the variable length hose-drogue model and the HDU model is shown in Fig. 8.4(b), while the relation of the models used in reference [228] is shown in Fig. 8.4(a).

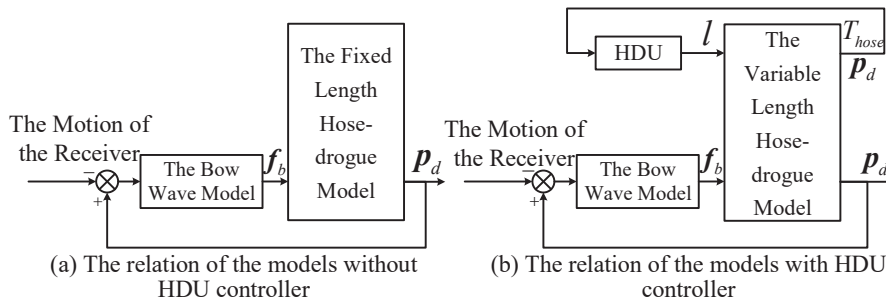


Figure 8.4: The relation between the models with and without HDU controller

The dynamic model of the HDU is determined by its controller, which will be elaborated on in the next section.

8.2.3 HDU Controller and Qualitative Analysis of its Control Effect

The controller of the HDU adjusts T_{reel} by using the state variables of the hose (such as T_{hose} , l_1 and \dot{l}_1) to indirectly control the length of the exposed hose, thereby regulating the hose tension and achieving equilibrium without causing hose whipping phenomenon. Fig. 8.5 illustrates the structural diagram of the link-connected hose-drogue model with the inclusion of the HDU.

(1) Two Types of Controllers for HDU

The first type of controller is the one proposed in Refs. [136, 227].

$$T_{\text{reel}}(t) = T_{\text{reel}}(0) \left[\frac{l_1(t)}{l_1(0)} \right]^k, 0 < l_1(t) \leq l_1(0) \quad (8.5)$$

That is, at $t = 0$, when the hose is just fully extended, $T_{\text{reel}}(0)$ represents the tension at that moment, $l_1(0)$ is the length of the first link at that moment, and $k \in \mathbb{R}_+$ is the parameter of the controller. It can be observed from Eqs. (8.4) and (8.5) that when the hose is completely extended (which corresponds to the state at $t = 0$), the controller achieves equilibrium, and there is no change in the hose length. While the first type of controller does regulate the hose tension,

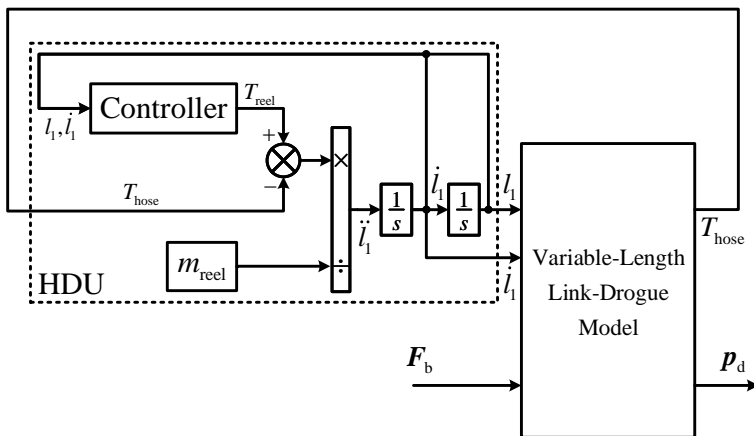


Figure 8.5: Schematic of link-connected hose-drogue model with HDU

its transient behavior is suboptimal. Therefore, based on the first type of controller, the second type of controller is proposed

$$T_{\text{reel}}(t) = T_{\text{reel}}(0) \left[\frac{l_1(t)}{l_1(0)} \right]^k + k_d \dot{l}_1(t), 0 < l_1(t) \leq l_1(0) \quad (8.6)$$

where $k_d \in \mathbb{R}_+$. The second type of controller introduces a damping term $k_d \dot{l}_1(t)$, which can effectively improve the transient performance. Furthermore, since we can directly measure the linear velocity of the hose length change, or indirectly obtain the hose length change through the rotation speed of the drum, this controller is easy to implement.

Next, the HDU and the variable-length link-connected hose-drogue model will be used to simulate the control effects of the two types of controllers and analyze the effects of different k values on each type of controller.

(2) Simulation and Qualitative Analysis of Two Types of Controllers

Firstly, establish the simulation model as shown in Fig. 8.5. The basic settings of the simulation environment are outlined in Table II in Section 4.2. For the sake of convenience in simulation, some of the parameters listed in Table II in Section 4.2 have been modified in this chapter's simulations. Additionally, new simulation parameters related to the HDU have been added, as depicted in Table III in Section 4.3.

Let the force f_b experience a step change from $\begin{bmatrix} 0 & 0 & 0 \end{bmatrix}^T$ to $\begin{bmatrix} 75 & 0 & 0 \end{bmatrix}^T$ at 100 seconds. This is done to mimic the force difference in the $o_t x_t$ direction that contributed to the disparities between simulations and experiments in Section 4.3.4. For both the first type of controller and the second type of controller, select the controller parameters as $k = \{0.3, 0.5, 1, 3\}$, with $k_d = 500$ for the second type of controller.

The simulation results are presented in Fig. 8.6. Subfigures (a1)-(a4) depict the control effects of the first type of controller, while subfigures (b1)-(b4) illustrate the control effects of the second type of controller. Through comparison, the following conclusions can be qualitatively drawn:

- 1) Comparing subfigures (a1)-(a4) and (b1)-(b4) in Fig. 8.6, it can be observed that the first type of controller leads to pronounced oscillations with a longer settling time. In contrast, the second type of controller exhibits significant improvements in both tension adjustment and drogue position control, showing smoother transition dynamics than the first type of controller.
- 2) Comparing Fig. 8.6 (a1) with Fig. 8.6 (b1), it can be deduced that the parameter k does not influence the steady-state value of the final hose tension.
- 3) Comparing Fig. 8.6 (a1) with Fig. 8.6 (b1), it can be observed that the parameter k significantly affects the retraction length of the hose. When k is smaller, the HDU needs to retract a longer length of the hose to achieve the same steady-state tension value. Conversely, if a minimal change in hose length is desired, a larger k value can be chosen.
- 4) A larger value of k brings about a noticeable negative effect, which makes the HDU-hose-drogue system unstable. This can be observed from Figs. 8.6 (a1)-(a4), where the adjustment time of various quantities significantly increases with the increase in k . In fact, for the first type of controller with $k = 4$, the outputs of various quantities have already diverged. In contrast, comparing Figs. 8.6 (b1)-(b4) reveals that the second type of controller shows significant improvement in addressing this phenomenon.
- 5) From Figs. 8.6 (a3) and (a4) and Figs 8.6 (b3) and (b4), it can be observed that the parameter k indirectly influences the dynamics of the drogue in various directions by affecting the length of the hose. This characteristic will be further discussed in the subsequent sections of this chapter.

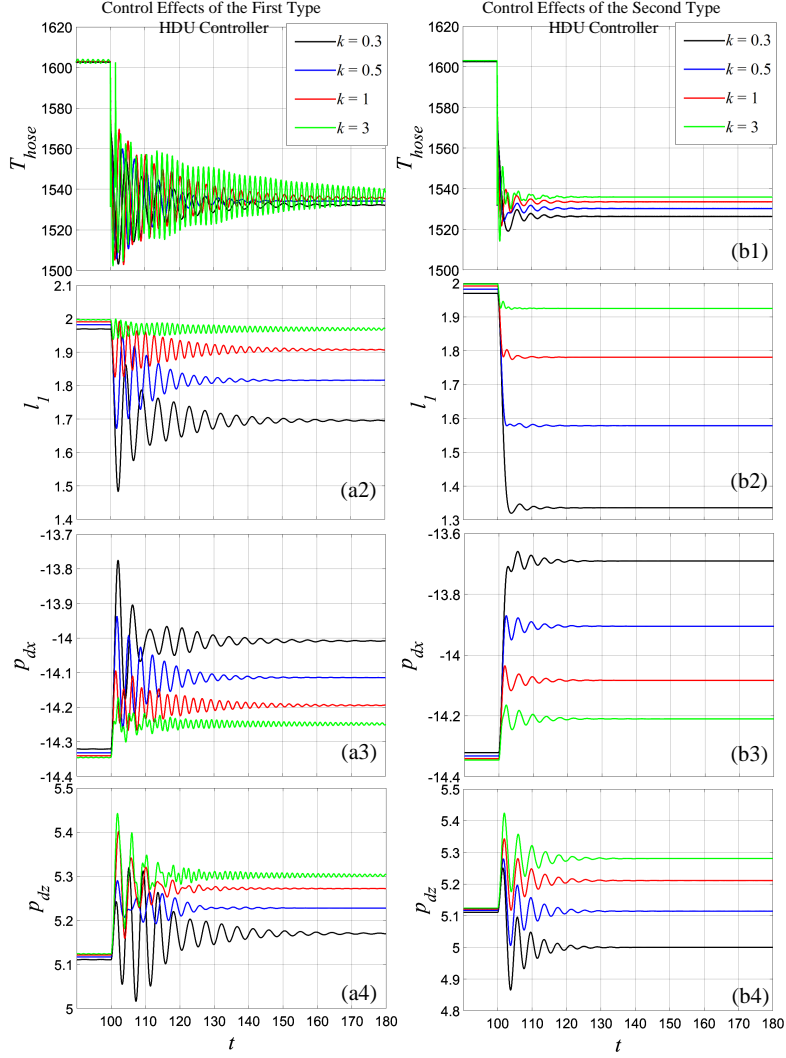


Figure 8.6: Control Effects of Two Types of HDU Controllers

8.3 Simplified Drogue Dynamic Model

Regardless of whether the link-connected hose-drogue model includes the HDU, the model is too complex. As described in Section 4.2, to better simulate the dynamics of the hose, a significant number of links are required, with each link having multiple state variables such as $\alpha_j, \beta_j, \dot{\alpha}_j, \dot{\beta}_j, l_j, \dot{l}_j$, etc. This complexity results in a high-order link-connected hose-drogue model. Additionally, the presence of nonlinear operations in model calculations further increases its complexity. However, when designing a docking controller, only the dynamics of the drogue are concerned with, and the dynamics of other links become redundant. Therefore, this section aims to simplify the link-connected hose-drogue model in order to obtain a model that solely expresses the dynamics of the drogue. This simplified model is referred to as the drogue dynamics model. It has a lower order and is suitable for controller design in subsequent chapters. Furthermore, it allows for quantitative analysis of the drogue's dynamics under different HDU models.

8.3.1 Problem Description and Modeling Approach for Drogue Dynamic Model

(1) Problem Description for Drogue Dynamic Model

In Section 4.3.1, the link-plexity results in a high-order connected hose-drogue model was represented using Eq. (98). If taking the HDU model into account, with the drogue's forces as inputs and the drogue's position as output, the system can be expressed as follows

$$\begin{cases} \dot{\mathbf{x}}_{\text{reel}} = \mathbf{f}_{\text{reel}}(\mathbf{x}_{\text{reel}}, \mathbf{x}_h) \\ \dot{\mathbf{x}}_h = \mathbf{f}_{h0}(\mathbf{x}_h, \mathbf{x}_d, v_{t/w}^g, h_t^g) \\ \dot{\mathbf{x}}_d = \mathbf{f}_{d0}(\mathbf{x}_h, \mathbf{x}_d, v_{t/w}^g, h_t^g, \mathbf{F}_b) \\ \mathbf{p}_d = \mathbf{f}_y(\mathbf{x}_h, \mathbf{x}_d) \end{cases} \quad (8.7)$$

where \mathbf{x}_{reel} represents the state variables of the HDU, and \mathbf{f}_{reel} represents the function related to the dynamics of the HDU as described in Section 8.4. Under a constant tanker altitude h_0 and airspeed v_0 , the model is simplified to

$$\begin{cases} \dot{\mathbf{x}}_{\text{reel}} = \mathbf{f}_{\text{reel}}(\mathbf{x}_{\text{reel}}, \mathbf{x}_h) \\ \dot{\mathbf{x}}_h = \mathbf{f}_h(\mathbf{x}_{\text{reel}}, \mathbf{x}_h, \mathbf{x}_d) \\ \dot{\mathbf{x}}_d = \mathbf{f}_d(\mathbf{x}_h, \mathbf{x}_d, \mathbf{F}_b) \\ \mathbf{p}_d = \mathbf{f}_y(\mathbf{x}_h, \mathbf{x}_d) \end{cases} \quad (8.8)$$

where $\mathbf{f}_h(\mathbf{x}_h, \mathbf{x}_d) \triangleq \mathbf{f}_{h0}(\mathbf{x}_h, \mathbf{x}_d, v_0, h_0)$, $\mathbf{f}_d(\mathbf{x}_h, \mathbf{x}_d, \mathbf{F}_b) \triangleq \mathbf{f}_{d0}(\mathbf{x}_h, \mathbf{x}_d, v_0, h_0, \mathbf{F}_b)$. Then, for each set of (v_0, h_0) , and when the system (8.8) is subjected to zero input (i.e., $\mathbf{F}_b = \mathbf{0}$), the system will reach a steady-state position. Denote the state of the system at this time as the equilibrium state

$$\mathbf{x}_{\text{reel}} = \mathbf{x}_{\text{reel}}^*, \mathbf{x}_h = \mathbf{x}_h^*, \mathbf{x}_d = \mathbf{x}_d^* \quad (8.9)$$

At this moment, the system satisfies the equation

$$\begin{cases} \dot{\mathbf{x}}_{\text{reel}}^* = \mathbf{f}_{\text{reel}}(\mathbf{x}_{\text{reel}}^*, \mathbf{x}_h^*) \\ \dot{\mathbf{x}}_h^* = \mathbf{f}_h(\mathbf{x}_{\text{reel}}^*, \mathbf{x}_h^*, \mathbf{x}_d^*) \\ \dot{\mathbf{x}}_d^* = \mathbf{f}_d(\mathbf{x}_h^*, \mathbf{x}_d^*, \mathbf{0}) \\ \mathbf{p}_d^* = \mathbf{f}_y(\mathbf{x}_h^*, \mathbf{x}_d^*) \end{cases} \quad (8.10)$$

Linearizing the system (8.8) at the equilibrium point (8.10), we can obtain

$$\begin{cases} \begin{bmatrix} \Delta \dot{\mathbf{x}}_{\text{reel}} \\ \Delta \dot{\mathbf{x}}_h \\ \Delta \dot{\mathbf{x}}_d \end{bmatrix} = \underbrace{\begin{bmatrix} \mathbf{A}_{11} & \mathbf{A}_{12} & \mathbf{0} \\ \mathbf{A}_{21} & \mathbf{A}_{22} & \mathbf{A}_{23} \\ \mathbf{0} & \mathbf{A}_{32} & \mathbf{A}_{33} \end{bmatrix}}_{\mathbf{A}} \begin{bmatrix} \Delta \mathbf{x}_{\text{reel}} \\ \Delta \mathbf{x}_h \\ \Delta \mathbf{x}_d \end{bmatrix} + \underbrace{\begin{bmatrix} \mathbf{0} \\ \mathbf{0} \\ \mathbf{B}_3 \end{bmatrix}}_{\mathbf{B}} \mathbf{F}_b + \begin{bmatrix} o(\Delta \mathbf{x}_{\text{reel}}, \Delta \mathbf{x}_h) \\ o(\Delta \mathbf{x}_{\text{reel}}, \Delta \mathbf{x}_h, \Delta \mathbf{x}_d) \\ o(\Delta \mathbf{x}_h, \Delta \mathbf{x}_d, F_b) \end{bmatrix} \\ \Delta \mathbf{p}_d = \underbrace{\begin{bmatrix} \mathbf{0} & \mathbf{C}_2 & \mathbf{C}_3 \end{bmatrix}}_{\mathbf{C}} \begin{bmatrix} \Delta \mathbf{x}_{\text{reel}} \\ \Delta \mathbf{x}_h \\ \Delta \mathbf{x}_d \end{bmatrix} + o(\Delta \mathbf{x}_h, \Delta \mathbf{x}_d) \end{cases} \quad (8.11)$$

where

$$\begin{aligned}
 \mathbf{A}_{11} &= \frac{\partial f_{\text{reel}}}{\partial \mathbf{x}_{\text{reel}}} \Big|_{\substack{\mathbf{x}_{\text{reel}}=\mathbf{x}_{\text{reel}}^* \\ \mathbf{x}_h=\mathbf{x}_h^*}}, \quad \mathbf{A}_{12} = \frac{\partial f_{\text{reel}}}{\partial \mathbf{x}_h} \Big|_{\substack{\mathbf{x}_{\text{reel}}=\mathbf{x}_{\text{reel}}^* \\ \mathbf{x}_h=\mathbf{x}_h^*}}, \quad \mathbf{A}_{21} = \frac{\partial f_h}{\partial \mathbf{x}_{\text{reel}}} \Big|_{\substack{\mathbf{x}_{\text{reel}}=\mathbf{x}_{\text{reel}}^* \\ \mathbf{x}_h=\mathbf{x}_h^* \\ \mathbf{x}_d=\mathbf{x}_d^*}}, \quad \mathbf{A}_{22} = \frac{\partial f_h}{\partial \mathbf{x}_h} \Big|_{\substack{\mathbf{x}_{\text{reel}}=\mathbf{x}_{\text{reel}}^* \\ \mathbf{x}_h=\mathbf{x}_h^* \\ \mathbf{x}_d=\mathbf{x}_d^*}}, \\
 \mathbf{A}_{23} &= \frac{\partial f_h}{\partial \mathbf{x}_d} \Big|_{\substack{\mathbf{x}_{\text{reel}}=\mathbf{x}_{\text{reel}}^* \\ \mathbf{x}_h=\mathbf{x}_h^* \\ \mathbf{x}_d=\mathbf{x}_d^*}}, \quad \mathbf{A}_{32} = \frac{\partial f_d}{\partial \mathbf{x}_h} \Big|_{\substack{\mathbf{x}_h=\mathbf{x}_h^* \\ \mathbf{x}_d=\mathbf{x}_d^* \\ F_b=0}}, \quad \mathbf{A}_{33} = \frac{\partial f_d}{\partial \mathbf{x}_d} \Big|_{\substack{\mathbf{x}_h=\mathbf{x}_h^* \\ \mathbf{x}_d=\mathbf{x}_d^* \\ F_b=0}}, \quad \mathbf{B}_3 = \frac{\partial f_d}{\partial F_b} \Big|_{\substack{\mathbf{x}_h=\mathbf{x}_h^* \\ \mathbf{x}_d=\mathbf{x}_d^* \\ F_b=0}}, \\
 \mathbf{C}_2 &= \frac{\partial f_y}{\partial \mathbf{x}_h} \Big|_{\substack{\mathbf{x}_h=\mathbf{x}_h^* \\ \mathbf{x}_d=\mathbf{x}_d^*}}, \quad \mathbf{C}_3 = \frac{\partial f_y}{\partial \mathbf{x}_d} \Big|_{\substack{\mathbf{x}_h=\mathbf{x}_h^* \\ \mathbf{x}_d=\mathbf{x}_d^*}}
 \end{aligned} \tag{8.12}$$

and $\Delta \mathbf{x}_{\text{reel}} = \mathbf{x}_{\text{reel}} - \mathbf{x}_{\text{reel}}^*$, $\Delta \mathbf{x}_h = \mathbf{x}_h - \mathbf{x}_h^*$, $\Delta \mathbf{x}_d = \mathbf{x}_d - \mathbf{x}_d^*$, $\Delta \mathbf{p}_d = \mathbf{p}_d - \mathbf{p}_d^*$, according to the drogue equilibrium coordinate system, it can be observed that $\Delta \mathbf{p}_d = \mathbf{p}_d^e$, and $o(\cdot)$ represents higher-order infinitesimal terms in the linearization. Since the changes in the state of the hose and the drogue are relatively small during the docking process, i.e., $\Delta \mathbf{x}_{\text{reel}}$, $\Delta \mathbf{x}_h$ and $\Delta \mathbf{x}_d$ are infinitesimal terms that can be neglected. Additionally, if the subsequent model simplification can be validated through the process described in section 8.3.4, it would also indicate the reasonableness of omitting infinitesimal terms here. After neglecting infinitesimal terms, the system (8.11) becomes a linear system. Subsequently, through Laplace transformation, the transfer function of this linear system can be expressed as

$$\mathbf{p}_d^e(s) = \underbrace{\mathbf{C}(s\mathbf{I} - \mathbf{A})^{-1}\mathbf{B}F_b(s)}_{\mathbf{G}_d(s)} \tag{8.13}$$

This equation is commonly referred to as the drogue dynamic model.

(2) Modeling Approach for Drogue Dynamic Model

The model (8.13) includes $\mathbf{G}_d(s)$, which represents the drogue's dynamics. Next, system identification methods will be used to obtain $\mathbf{G}_d(s)$, and the following steps outline this process:

- 1) Utilize axial force to infer the coupling relationships among different channels, and then obtain the basic form of $\mathbf{G}_d(s)$.
- 2) Employ Generalized Binary Noise (GBN) as an input to excite the system and identify system parameters.
- 3) Validate the identified results using a Chirp Signal.

In Sections 8.3.2-8.3.4, we will combine an example of a fixed-length link-connected model to explain the above process. The object to be identified in this example is the same as the one in Section 4.2.5. The obtained drogue dynamic model can be analyzed and compared with the later derived link-connected hose-drogue model with HDU.

8.3.2 Speculation on the Form of $\mathbf{G}_d(s)$

Five simulations are conducted, each applying an axial force in a different direction to \mathbf{F}_b . The forces were as follows $\mathbf{F}_{bx+} = [50 \ 0 \ 0]^T$, $\mathbf{F}_{by+} = [0 \ 50 \ 0]^T$, $\mathbf{F}_{by-} = [0 \ -50 \ 0]^T$, $\mathbf{F}_{bz+} = [0 \ 0 \ 50]^T$, $\mathbf{F}_{bz-} = [0 \ 0 \ -50]^T$. The reason for not using forces in the \mathbf{F}_{bx-} direction for simulation is that, under normal circumstances, the receiver does



not generate disturbances in the negative direction against the drogue. The choice of an amplitude of $50N$ is because the maximum bow wave effect during the docking process is around $100N$, and $50N$ serves as a representative intermediate value for the bow wave effect. The results of these five simulations are presented in Table 8.1. In the table, $(\cdot)_{\max}$ represents the maximum drift position of the drogue in the current simulation, while $(\cdot)_{\text{final}}$ represents the final drift position of the drogue in the current simulation.

Table 8.1: Parameters Used in HDU Simulation

Parameters	Values	Units
Number of Link Segments N	10	-
Full length of the hose, L_h	15	m
Initial Length of the First Link $l_1(0)$	2	m
Lengths of the Remaining Links $l_j(0), j = 2, 3, \dots, N$	13/9	m
The Mass of the Reel m_{reel}	68	kg
Initial Tension of the Reel	1610	N

According to Table 8.1, the following conclusions can be drawn: 1) The x and z channels are coupled. 2) It can be assumed that the y channel is decoupled from x and z channels, as the effects of $\mathbf{F}_{\text{by}+}$ and $\mathbf{F}_{\text{by}-}$ on $x_{d/t}$ and $z_{d/t}$ are much smaller than the forces in other directions. Therefore, the basic form of $\mathbf{G}_d(s)$ can be obtained as follows

$$\mathbf{G}_d(s) = \begin{bmatrix} G_{xx}(s) & 0 & G_{xz}(s) \\ 0 & G_{yy}(s) & 0 \\ G_{zx}(s) & 0 & G_{zz}(s) \end{bmatrix} \quad (8.14)$$

Additionally, in Section 4.2.5, it has been mentioned that the inherent dynamics of the drogue are of second order. Therefore, it can be inferred that the elements within $\mathbf{G}_d(s)$ are also of second order.

8.3.3 System identification of the link-connected hose-drogue model

Using a GBN (Generalized Binary Noise) signal with an amplitude of $50N$ to excite the system, as shown in Fig. 8.7, the parameters within $\mathbf{G}_d(s)$ are identified using the Output-Error (OE) model [229]. The results can be obtained as follows

$$\left\{ \begin{array}{l} G_{xx}(s) = \frac{0.002185}{s^2 + 0.3071s + 2.682} \\ G_{xz}(s) = \frac{0.006169}{s^2 + 0.3013s + 2.689} \\ G_{yy}(s) = \frac{0.01712}{s^2 + 0.2422s + 2.081} \\ G_{zx}(s) = \frac{0.005824}{s^2 + 0.3223s + 2.687} \\ G_{zz}(s) = \frac{0.01782}{s^2 + 0.3391s + 2.687} \end{array} \right. . \quad (8.15)$$

8.3.4 Frequency sweep verification

A frequency sweep signal is simultaneously applied to both the link-connected hose-drogue model (Equation 8.8) and the drogue dynamics model (Equation 8.13), as shown in Fig. 8.8.

By comparing the output results of the two systems, the simulation results are presented in Fig. 8.9. The curves in Fig. 8.9(b) are obtained by subtracting the two dashed lines from Fig. 8.9(a). The frequency sweep signal is a signal with a fixed amplitude and a frequency that uniformly increases from ζ_0 to ζ_T over the interval $[0, T]$, and its mathematical expression is

$$c(t) = K_c \sin \left[2\pi \left(\zeta_0 + \frac{\zeta_T - \zeta_0}{T} t \right) t \right] \quad (8.16)$$

where $K_c = 50$, $\zeta_0 = 0.05\text{Hz}$, $\zeta_T = 0.5\text{Hz}$ and $T = 200\text{s}$. From Fig. 8.9 (b), it can be observed

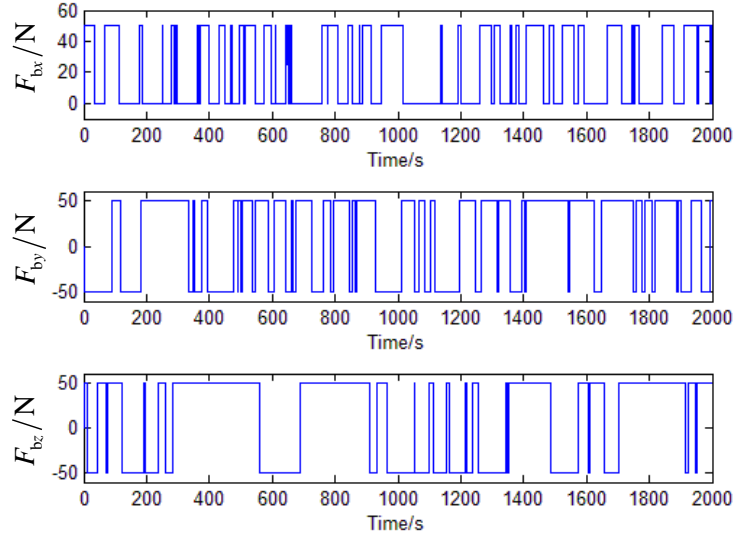


Figure 8.7: GBN Signal Used to Excite the System

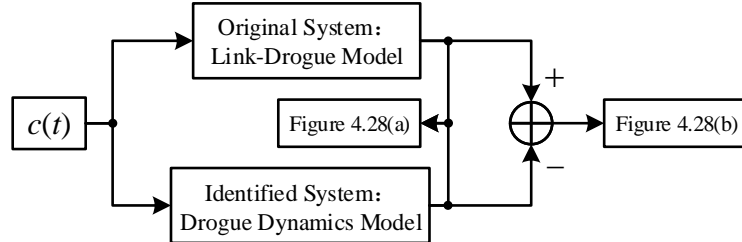


Figure 8.8: Verification Simulation Framework for Identification Results

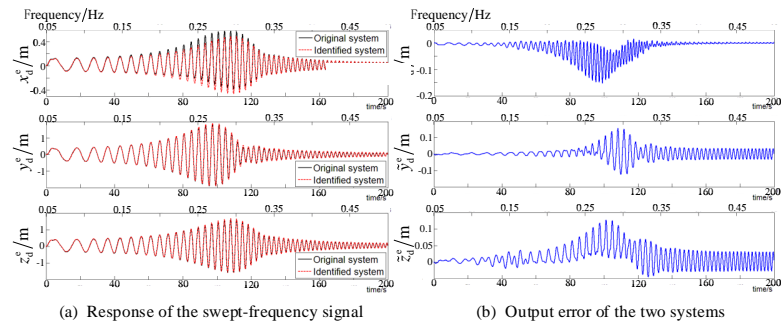


Figure 8.9: Effectiveness of System Identification

that the system's tracking error is minimal in the low-frequency range below 0.2 Hz, increases

in the mid-frequency range between 0.2 Hz and 0.35 Hz, and remains relatively small in the high-frequency range above 0.35 Hz. The outputs y_d^e and z_d^e from both models are very close to each other, while the performance of x_d^e is relatively poorer. This is mainly due to the higher nonlinearity exhibited by the link-connected hose-drogue model when subjected to \mathbf{F}_{bx-} , which occurs rarely in actual docking scenarios. Therefore, the identified drogue dynamics model effectively captures the drogue dynamics of the link-connected hose-drogue model.

It should be noted that the above model was derived under the assumption of no crosswind or minimal crosswind. In the presence of a crosswind, the y -axis becomes coupled with the other axes, meaning that all elements within Eq. (8.14) would be non-zero. However, the drogue dynamics model can still be obtained using the identification method described above. Since the refueling process allows for adjustments in the direction of the aircraft's velocity to minimize the impact of crosswind disturbances, this chapter primarily focuses on the model under the assumption of no crosswind.

8.3.5 Dynamic Model of Drogue with HDU and Quantitative Analysis

Using the system identification steps described in Sections 8.3.2-8.3.4, the simplified drogue dynamics model for the link-connected hose-drogue system with HDU was obtained. The identification results are presented in Table 8.2. The controller choices are as shown in Section 4.3.3: for the first type of HDU controller (8.5), the parameter is set as $k = 0.5$, and for the second type of HDU controller (8.6), the parameters are chosen as $k = 0.5$ and $k_d = 500$. In the table, the fitness metric is used to represent the identification performance, defined as $1 - \|\mathbf{y} - \hat{\mathbf{y}}\|/\|\mathbf{y} - \bar{\mathbf{y}}\|$, where \mathbf{y} , $\hat{\mathbf{y}}$ and $\bar{\mathbf{y}}$ represent the output of the original model, the the output of the identification model, and the mean of the output of the original model, respectively.

Table 8.2: Drift positions of the drogue under the influence of \mathbf{F}_b in different directions

\mathbf{F}_b	\mathbf{F}_{bx+}	\mathbf{F}_{by+}	\mathbf{F}_{by-}	\mathbf{F}_{bz+}	\mathbf{F}_{bz-}
$(x_{d/t})_{\max}$	0.07	0.015	0.015	0.204	0.177
$(x_{d/t})_{\text{final}}$	0.04	0.005	0.005	0.109	0.105
$(y_{d/t})_{\max}$	0	0.724	-0.724	0	0
$(y_{d/t})_{\text{final}}$	0	0.41	-0.41	0	0
$(z_{d/t})_{\max}$	0.199	-0.012	-0.012	0.56	-0.588
$(z_{d/t})_{\text{final}}$	0.115	-0.004	-0.004	0.324	-0.447

Unlike the drogue dynamics without considering HDU (Eq. (8.13)), the identification in Table 8.2 utilizes a fourth-order model. The reason behind this choice is that the drogue dynamics without HDU are second-order, while the HDU itself introduces an additional second-order dynamics. Hence, a fourth-order model is employed to identify the link-connected hose-drogue system with HDU. Moreover, judging from the fitness values in the identification results, the fourth-order model also performs better than the second-order model. From Table 8.2, the following conclusions regarding the drogue dynamics can be drawn:



1) The transition process under the control of the second-class controller exhibits significantly better performance compared with the first-class controller. This is due to the fact that, in comparison to the first-class controller, the poles of the drogue dynamic model under the second-class controller are far from the imaginary axis.

2) From the fitness values in Table 8.2, it is evident that the identification results of the drogue dynamics under the control of the first-class controller are inferior to those under the second-class controller. This is due to the higher level of nonlinearity exhibited by the drogue dynamics under the first-class controller, which is also evident from Figs. 8.6 (a3) and (a4). Therefore, if a more accurate drogue dynamic model is desired, employing the second-class controller for HDU control is more appropriate.

Table 8.3: Drogue Dynamic Model Considering HDU (Controller Parameter $k = 0.5$)

Controller \ Results	Transfer function	Fitness
First-Class HDU Controller	$G_{xx}(s) = \frac{0.012s^2+0.012s+0.052}{s^4+2.15s^3+9.17s^2+7.54s+18.21}$	89.4%
	$G_{xz}(s) = \frac{0.0010s^2+0.0057s+0.046}{s^4+13.49s^3+19.29s^2+35.69s+29.50}$	70.9%
	$G_{yy}(s) = \frac{0.026s^2+0.0034s+0.42}{s^4+0.39s^3+24.02s^2+5.76s+49.66}$	99.5%
	$G_{zx}(s) = \frac{0.0026s^2+0.010s+0.032}{s^4+1.76s^3+11.03s^2+7.04s+20.01}$	85.1%
	$G_{zz}(s) = \frac{0.027s^2+0.0011s+0.38}{s^4+0.56s^3+24.22s^2+7.06s+53.95}$	94.5%
	$G_{xx}(s) = \frac{0.0090s^2+0.011s+0.021}{s^4+4.01s^3+6.61s^2+10.48s+7.38}$	98.3%
Second-Class HDU Controller	$G_{xz}(s) = \frac{0.0048s^2+0.019s+0.0085}{s^4+3.29s^3+5.77s^2+8.44s+5.80}$	98.5%
	$G_{yy}(s) = \frac{0.026s^2+0.0033s+0.42}{s^4+0.40s^3+24.01s^2+5.75s+49.62}$	99.6%
	$G_{zx}(s) = \frac{0.0051s^2+0.0091s+0.0051}{s^4+1.96s^3+4.32s^2+4.71s+3.14}$	93.2%
	$G_{zz}(s) = \frac{0.027s^2+0.0046s+0.39}{s^4+0.61s^3+24.05s^2+7.71s+55.76}$	89.4%

3) By comparing Table 8.2 with the transfer function in Eq. (8.13), it can be observed that the presence or absence of HDU significantly affects the drogue dynamics. Next, the impact of HDU on the drogue dynamics will be further analyzed by comparing their Direct Current Gain (DC Gain) of the transfer functions [230]. Taking the coefficients of the two classes of controllers as $k = \{0.3, 0.5, 1, 3\}$, the results are shown in Table 8.3.

Based on Table 8.3, the following conclusions can be drawn regarding the drogue dynamics.

1) The gains of the drogue dynamics models under both types of controllers are similar. In other words, the second type of controller only affects the transient behavior, while the steady-state values of both types are the same.

2) The primary factor influencing the DC gain is the controller coefficient k . The smaller the value of k , the more pronounced the impact, especially on $G_{xx}(s)$ and $G_{zx}(s)$. In this case, the decoupling between the x -channel and z -channel is better, indicated by the fact that the gains of $G_{zx}(s)$ and $G_{xz}(s)$ are much smaller than those of $G_{xx}(s)$ and $G_{zz}(s)$. Conversely, as k increases, coupling becomes more pronounced. For instance, when $k = 3$, the DC gain of the drogue dynamics model with HDU is already approaching that of the model without HDU.

3) The impact of HDU on the DC gain of the y -axis is not significant.

In summary, when designing HDU controllers with the aim of mitigating the hose whipping phenomenon, a larger value of k should be selected. This choice would require fewer adjustments to achieve regulation and speed up the adjustment process. On the other hand, if the intention is to decouple the dynamics of the drogue, facilitating controller design, a smaller value of k should be chosen. Therefore, the selection of k should balance between these two aspects.

Table 8.4: DC gain of drogue dynamic model model with or without HDU (order of magnitude is 10^{-4})

Transfer function \ Drogue model type	Considering HDU					Without cons
	HDU Controller	$k = 0.3$	$k = 0.5$	$k = 1$	$k = 3$	
$G_{xx}(s)$	First-Class	41.6	28.69	18.96	12.59	8.1
	Second-Class	42.04	28.98	19.15	12.64	
$G_{xz}(s)$	First-Class	8.08	14.48	20.07	23.56	22.1
	Second-Class	7.42	14.56	19.93	23.52	
$G_{yy}(s)$	First-Class	84.65	84.58	84.72	84.75	82.1
	Second-Class	84.65	84.68	84.73	84.75	
$G_{zx}(s)$	First-Class	11.81	15.98	19.78	21.77	8.1
	Second-Class	11.48	16.31	19.54	21.78	
$G_{zz}(s)$	First-Class	72.42	69.99	68.22	67.13	66.1
	Second-Class	72.02	69.76	68.2	67.08	

If establishing a simulation environment similar to the one in Section 4.3.4 and replacing the link-connected hose-drogue model with the drogue dynamic model with HDU (as shown in Table 8.2), simulation results as depicted in Fig. 8.10 can be obtained. To visually display the differences in drogue dynamics with and without HDU during the docking process, as well as the differences in drogue dynamics under different controllers, a video have also been recorded. Readers can refer to Ref. [231] for the video, and a screenshot from the video is shown in Fig. 8.11. In the screenshot, View 1 represents the pilot's perspective, and View 2 provides a lateral view. The HDU used in the screenshot employs the first type of controller, which is common in current HDU designs. This choice accurately reflects the flight conditions in the experiment. To compare with the results from Ref. [149], the units for position are given in feet. Based on Fig. 8.10, the HDU has a slight influence on the drogue dynamics. However, during the docking process, even a small error of a few centimeters can lead to docking failure. Therefore, this influence remains significant. The two subplots Fig. 8.10 (e) and (f) illustrate the differences in drogue dynamics in the vertical direction during docking, which is in accordance with the issue highlighted in the conclusions of Section 4.3. Additionally, from Fig. 8.11, it's even more evident that compared with the scenario without HDU, the vertical descent of the drogue with HDU is significantly reduced. In other words, the drogue dynamics considering the HDU model closely resemble the drogue dynamics observed in experiments.

On the other hand, from Fig. 8.10, it is evident that the drogue dynamics under the control of the second type of controller differ from those without HDU and those under the control of the first type of controller. Although the swing amplitude of the drogue increases under the second type of controller, its adjustment speed is faster, which is more conducive to suppressing the hose

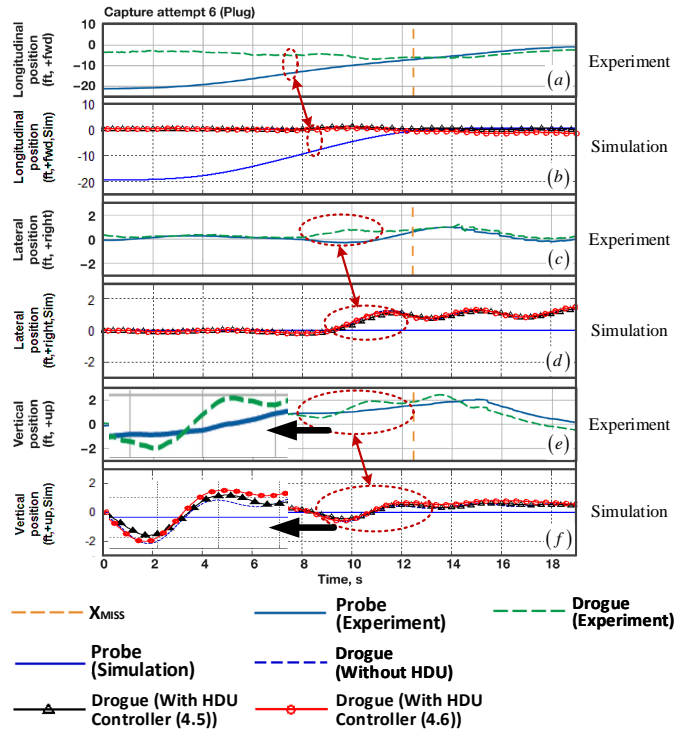


Figure 8.10: Comparison of Drogue Dynamics during the Docking Process

whipping phenomenon. Furthermore, it can lead to a more accurate linearization of the model for the link-connected hose-drogue system with HDU. Therefore, it is still recommended to use the second type of controller for future HDU controller design.

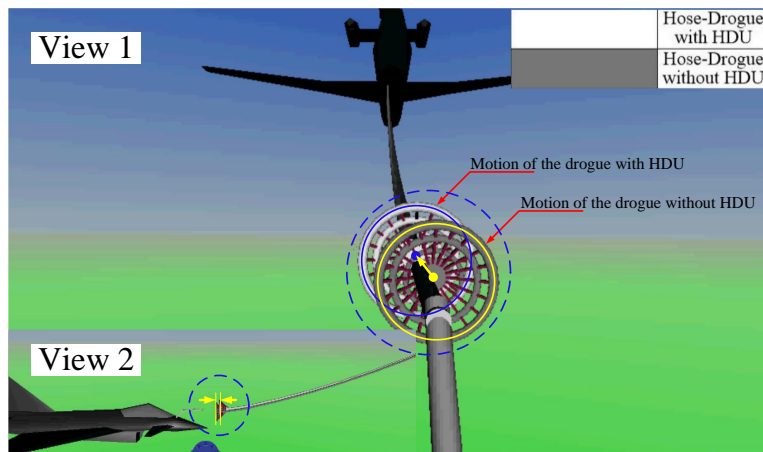


Figure 8.11: Screenshot of the Simulation Video at Maximum Drogue Subsidence

8.3.6 The Effect of HWP Suppression of Traditional HDU control methods

In order to estimate the effect that the traditional HDU control methods suppress the HWP after the excessive contact between the probe and the drogue, comparison simulations are performed and the results are shown in Fig. 8.12, where an impulse disturbance ($500\text{N}\cdot\text{s}$) is injected into the hose-drogue system at 5s to simulate the excessive contact on the drogue. It can be observed from Fig. 8.12 that the hose-drogue system with HDU controller has a larger

longitudinal offset and a smaller vertical offset than those of the hose-drogue system without HDU controller, where the larger longitudinal offset is caused by the hose being reeled up by the HDU controller to avoid vertical offset. The vertical offset indicates that the current HDU control methods can suppress the HWP to some extent, but the effect is very limit and it cannot avoid the HWP essentially. In the next section, a new HDU controller is proposed to avoid the HWP and improve the safety of probe-and-drogue systems.

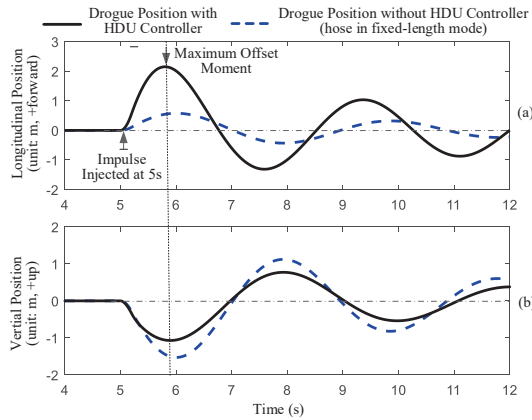


Figure 8.12: Comparison of motions of the drogue after excessive contact.

8.4 Anti-HWP Control Method for HDU

The traditional HDU control methods mainly feedback the hose tension to reduce the drogue fluctuation and suppress HWP to some extent, but it cannot avoid HWP essentially because it cannot detect whether the HWP happens. For example, when the probe is docked into the drogue, it may drive the drogue to continue to move forward a distance, which may cause the hose slack and reach to a new equilibrium state as shown in Fig. 8.13(b). In this situation, the hose tension remains unchanged so the traditional HDU control methods cannot work correctly, but HWP will happen if the probe accidentally breaks away from the drogue. Therefore, the HWP is essentially caused by the over-slack of the hose due to excessive contact on the drogue. In order to avoid HWP, the HDU controller must be able to observe the hose slack degree and roll up the hose with an appropriate control method. This section will present an anti-HWP control method from three aspects: HWP observation, control method, and simulation verification.

8.4.1 HWP observation

8.4.1.1 Drogue Position Estimation

The most direct way to detect HWP is to observe the shape of the hose through computer vision methods, but it is impractical and unreliable for real aerial refueling systems. Observing the position of the drogue \mathbf{p}_d to estimate the hose slack degree indirectly for HWP is a more feasible way, which is adopted in this chapter. The drogue position \mathbf{p}_d is essential for the docking



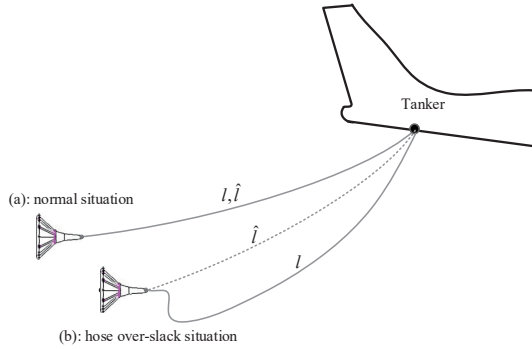


Figure 8.13: Schematic diagram for HWP. The symbol l is the hose length and \hat{l} is the desired hose length.

control of autonomous aerial refueling system to estimate the relative position between the probe and the drogue. There are many mature methods to estimate the drogue position, among which the vision-based methods [223, 232] are the most convenient and widely used one. These methods can be applied to estimate the drogue position for the following HDU control method.

8.4.1.2 Hose Slack Degree

With the drogue position \mathbf{p}_d and the total hose length l , how to define the hose slack degree and how to estimate it are presented in this subsection. First of all, the normal situation with no hose slack is presented as shown in Fig. 8.13(a), which is the equilibrium state of the hose when the desired hose length \hat{l} is defined to equal to the hose length l , i.e., $l = \hat{l}$. Second, when the hose is over-slack as presented in Fig. 8.13(b), the hose length should be larger than its desired value, i.e., $l > \hat{l}$. Consequently, the hose slack degree μ_{slack} can be defined as

$$\mu_{\text{slack}} \triangleq \left| \frac{l - \hat{l}}{\hat{l}} \right| \quad (8.17)$$

which can be used to describe the hose state and predict the degree of HWP. The slack degree $\mu_{\text{slack}} = 0$ indicates that the hose is in the desired state with no over-slack. The more the slack degree μ_{slack} increases, the more the hose is bent which indicates a more serious HWP is ready to happen.

In order to obtain μ_{slack} , the method to obtain the desired hose length \hat{l} should be given first. As shown in Fig. 8.13(a), the desired hose shape is a smooth curve, whose length \hat{l} can be written as a function that depends on the drogue position \mathbf{p}_d as

$$\hat{l} = f_{\hat{l}}(\mathbf{p}_d) \quad (8.18)$$

where $f_{\hat{l}}(\cdot)$ can be obtained by hose modeling methods [216, 219] or look-up table methods. However, in practice, the precise expressions of \hat{l} for different flight conditions (altitude and speed) are very complicated and unobtainable. Alternatively, an approximate estimation method for \hat{l} is developed in this chapter. Based on the simulation results with the hose model [216, 219], the estimation expression for the desired length \hat{l} is approximate to a function of the straight-line

distance of the drogue $\|\mathbf{p}_d\|$ as

$$\hat{l} \approx f_{\hat{l}}'(\|\mathbf{p}_d\|) \approx \frac{\|\mathbf{p}_d\|}{\|\mathbf{p}_{d0}\|} \cdot l_0 \quad (8.19)$$

where \mathbf{p}_{d0} and l_0 are the initial equilibrium drogue position and hose length. The maximum estimated error $\varepsilon_{\hat{l}}$ for (8.19) is given by

$$\varepsilon_{\hat{l}} = \max_{\mathbf{p}_d \in \Omega} \frac{\left| \hat{l} - \frac{\|\mathbf{p}_d\|}{\|\mathbf{p}_{d0}\|} \cdot l_0 \right|}{\hat{l}} \quad (8.20)$$

where Ω denotes a safe region for the normal drogue movement. According to the simulation results, $\varepsilon_{\hat{l}}$ is very small but still the following anti-HWP control method will well consider this error and hand it for robustness requirements.

8.4.1.3 HWP Detection

Safety is always the most fundamental requirement for any aerial refueling system. To avoid the damage of HWP after excessive or abnormal impact on the drogue, this subsection presents a method to detect the hose state and classify it into three situations based on its hazardous degree.

(i) **Normal Situation.** Ideally, the normal situation should be $\mu_{\text{slack}} = 0$; namely, the hose coincides exactly with the desired hose curve as shown in Fig. 8.13(A). However, it is unreachable in practice due to the estimated error of (8.19) and other uncertain errors, such as the small fluctuation of the hose under atmospheric turbulence. Therefore, a minimum slack threshold ε_{\min} is defined as shown in Fig. 8.14. The normal situation of the hose is defined by the criterion

$$\mu_{\text{slack}} \leq \varepsilon_{\min} \text{ and } \mathbf{p}_d \in \Omega \quad (8.21)$$

where the threshold ε_{\min} should cover the estimation error ($\varepsilon_{\min} > \varepsilon_{\hat{l}}$) and other uncertain errors for robustness requirements. For simplicity, it can be select as $\varepsilon_{\min} = 2\varepsilon_{\hat{l}}$ for a 100% safe margin. In (8.21), the safe region $\mathbf{p}_d \in \Omega$ is presented as the meshed region in 8.14. If the drogue is out of this region ($\mathbf{p}_d \notin \Omega$), it indicates that an abnormal big swing is already appearing and emergency measures should be taken immediately.

(ii) **Over-slack Situation.** The over-slack situation is defined as that the hose slack degree μ_{slack} is out of “normal range” in (8.21) and it is within the controllable region for the HDU controller to safely reduce the slack degree μ_{slack} to the normal situation. Similar to (8.21), the over-slack situation can be defined by the following criterion

$$\varepsilon_{\min} < \mu_{\text{slack}} \leq \varepsilon_{\max} \text{ and } \mathbf{p}_d \in \Omega \quad (8.22)$$

where ε_{\max} is the maximum slack threshold as shown in Fig. 8.14, which is selected based on the safety requirement and controller performance.

(iii) **Unsafe Situation.** The unsafe situation is defined as the complementary set of (8.21)(8.22)

$$\mu_{\text{slack}} > \varepsilon_{\max} \text{ or } \mathbf{p}_d \notin \Omega. \quad (8.23)$$

When the drogue-drogue system reaches this situation, it means that a serious HWP is happening or ready to happen. To ensure the safety of the hose-and-droge system, emergency measures should be applied immediately. For example, rolling up the hose with maximum speed to avoid a collision on the receiver aircraft.

For the above three situations, different control strategies will be adopted to avoid the HWP and ensure the safety of the drogue-hose system. When the hose is in the normal situation, it indicates that no impact or abnormal oscillation is happening on the drogue, so the traditional HDU control methods as presented in Section 8.2 can be applied to reduce the drogue position fluctuation for improving the docking success rate. When the hose is in the unsafe situation, emergency control measures should be carried out to avoid further damage on the receiver aircraft or equipment. For example, HDU controller rolls up the hose with the maximum speed to leave a safe distance between the hose and the receiver aircraft. Since the over-slack situation is the most important stage to handle impact on the drogue and avoid HWP, the next subsection will focus on the anti-HWP controller design in this situation.

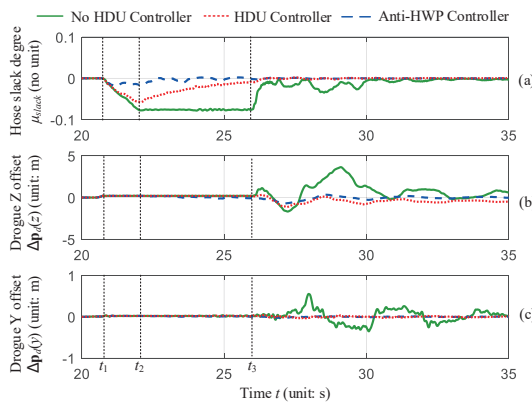


Figure 8.14: Safety criteria for the hose-droge system.

8.4.2 Anti-HWP Control

The objective of the anti-HWP controller for HDU is to smoothly control the hose length to change the hose state from the over-slack situation ($\varepsilon_{\min} < \mu_{\text{slack}} \leq \varepsilon_{\max}$) to the normal situation ($\mu_{\text{slack}} \leq \varepsilon_{\min}$). Then, the traditional HDU controller is capable of stabilizing the hose-and-droge system to an equilibrium state in the normal situation.

First of all, a speed feedback control is given by

$$T_{\text{reel}} = T_{\text{hose}} - m_{\text{reel}} \cdot k_d \cdot (i - \hat{i}) \quad (8.24)$$

where \hat{i} is an indirect control input signal that indicates the desired increasing speed of the hose length, and $k_d > 0$ is a controller parameter. Substituting (8.24) into the HDU model (8.4) gives

$$\ddot{i} = \frac{T_{\text{reel}} - T_{\text{hose}}}{m_{\text{reel}}} = -k_d \cdot (i - \hat{i}). \quad (8.25)$$

which is an exponentially convergent system that ensures the HDU track the given speed as $i \rightarrow \hat{i}$.

Second, the desired speed input \hat{l} is further given by

$$\hat{l} = -k_p \cdot (l - \hat{l}) \quad (8.26)$$

where $k_p > 0$ is a controller parameter. Note that, in practice, a saturation function can be added to (8.26) to prevent the drogue from pulling out the probe if the hose rolls up too fast. Finally, by combining (8.19)(8.24)(8.26), the anti-HWP controller can be written as

$$\begin{aligned} T_{\text{reel}} = & T_{\text{hose}} + m_{\text{reel}} k_d \frac{\|\mathbf{p}_d\|}{\|\mathbf{p}_{d0}\|} l_0 \\ & - m_{\text{reel}} k_d \cdot \dot{l} - m_{\text{reel}} k_d k_p \cdot l \end{aligned} \quad (8.27)$$

The following theorem provides the convergence condition under which one can conclude the convergence property of the designed TILC controller in (8.27).

Theorem 1. Consider a hose-and-drogue system with the HDU structure described by (8.1)(8.4). Suppose (i) the hose state is in over-slack situation (8.22); (ii) the anti-HWP controller is designed as (8.27) with its parameters satisfy

$$k_p > 0, k_d > 0 \quad (8.28)$$

Then, the hose slack degree μ_{slack} can converge to zero, i.e., $\mu_{\text{slack}}(t) \rightarrow 0$.

Proof. Combining (8.25)(8.26) gives

$$\ddot{l} + k_d \dot{l} + k_d k_p (\dot{l} - \hat{l}) = 0. \quad (8.29)$$

By letting $\Delta l \triangleq l - \hat{l}$, for constant value \hat{l} , (8.29) can be rewritten as

$$\ddot{\Delta l} + k_d \Delta \dot{l} + k_d k_p \Delta l = 0. \quad (8.30)$$

It can be observed from (8.30) that controller (8.27) is essentially a PD (Proportion Differentiation) controller with proportion coefficient k_p and differentiation coefficient k_d . Therefore, (8.30) is a stable second-order linear system when $k_d > 0$ and $k_d > 0$, which will converge exponentially to zero

$$\lim_{t \rightarrow \infty} |l(t) - \hat{l}| = \lim_{t \rightarrow \infty} |\Delta l(t)| = 0. \quad (8.31)$$

Then, according to the definition of μ_{slack} in (8.17), it can be derived from (8.31) that

$$\mu_{\text{slack}}(t) \triangleq \left| \frac{l(t) - \hat{l}}{\hat{l}} \right| = \frac{|\Delta l(t)|}{\hat{l}} \rightarrow 0 \quad (8.32)$$

which indicates that the hose slack degree μ_{slack} can converge to zero under controller (8.27). *f*

According to *Theorem 1*, when the hose slack degree is in the range $\varepsilon_{\min} < \mu_{\text{slack}} \leq \varepsilon_{\max}$, it will always converge to zero, which means the slack degree can eventually be reduced into region $\mu_{\text{slack}} \leq \varepsilon_{\min}$. Then, the traditional HDU controller will take over the control privilege. According to research in [41], the hose-and-drogue system is a self-stabilizing system, and it will be stabilized to an equilibrium state under the effect of gravity, air drag and air viscous.

8.4.3 Simulation Verification

A series of simulations are performed to verify the effect of the proposed anti-HWP controller. The basic parameters are listed in Table 8.1, and additional parameters are given below

$$\varepsilon_{\min} = 0.004, \varepsilon_{\max} = 0.05, k_d = 10, k_p = 3.$$

The variable length hose-drogue model [219] with the link number $N = 20$ is used in these simulations for better simulation accuracy and display effect. A video has also been released to introduce the simulation environment and demonstrate the control effect of the proposed anti-HWP controller method. The URL of the video is <https://youtu.be/s9XgGICqKtA>.

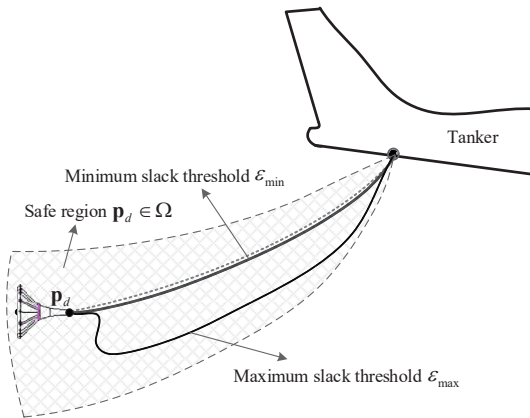


Figure 8.15: Simulations of probe-and-drogue system with and without anti-HWP controller.

Fig. 8.15 presents three typical comparative simulation results: 1) the simulation results (solid green curves in Fig. 8.15) with no HDU controller, where the HDU controller is not enabled, and the hose length remains unchanged during the whole simulation; 2) the simulation results (dotted red curves in Fig. 8.15) with the existing HDU control method, where the HDU controller is enabled to control the hose length to weaken HWP; 3) the simulation results (dash blue curves in Fig. 8.15) with the proposed anti-HWP method, where the anti-HWP controller is enabled to control the hose length to avoid HWP safely. The above three simulations all contain the following stages: (i) the receiver flies close to the drogue from time $0s \sim t_1$; (ii) the contact between the probe and the drogue happens at t_1 ; (iii) the probe drives the drogue fly forward a distance from time $t_1 \sim t_2$; (iv) the probe holds the drogue and remains relatively static from time $t_2 \sim t_3$; (v) the receiver suddenly breaks away from drogue at time t_3 and flies backward from time $t_3 \sim 35s$.

It can be observed from Fig. 8.15(a): 1) the hose slack degree increase to a large for simulation curve with no HDU controller, which indicates a serious HWP is happening; 2) the hose slack degree increase to a medium value for simulation curve with an HDU controller but its slack degree is much smaller than the simulation curve with no HDU controller, which indicates that the existing HDU control methods can suppress HWP but cannot completely avoid it; 3) there is almost no hose slack for simulation curve with anti-HWP controller, which indicates the HWP is successfully avoided. Figs. 8.16(a)(b) show the slack states of the hose with no

HDU controller and with the proposed anti-HWP controller. Due to the over-slack state of the hose, a significant HWP is observed in the simulation without the anti-HWP controller, which is reflected in the drastic position fluctuation along Y and Z directions in Fig. 8.15(b)(c). By contrast, the hose and drogue states are both very steady with the proposed anti-HWP controller, and no HWP happens as expected. The above results indicate that, compared with the existing HDU control methods, the proposed anti-HWP control method can effectively avoid the HWP and ensure the safety of hose-and-drogue systems.

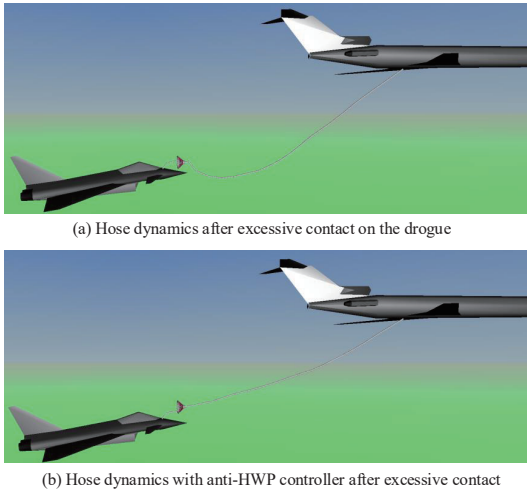


Figure 8.16: Visual display of the hose-and-drogue systems under excessive contact.

8.5 Chapter Summary

It is critical to analyze the dynamics of the drogue under the bow wave, for designing docking controllers and docking simulations. However, this problem is not considered comprehensively in the existing literature. This chapter integrates the HDU model, the bow wave model and the variable length hose-drogue model into an integrated model. Then, two types of controllers are designed for HDU. One type is the commonly used controller used in the real PDR, and the other one is an improved one based on the commonly used controller. Based on the integrated model, the drogue dynamic models under different HDU controllers are obtained through system identification, and the performance of them are analyzed. By considering the effects of HDU, the dynamics of the proposed method is in better agreement with the real experiment than our previous study. Meanwhile, the traditional HDU control methods mainly feedback the hose tension to reduce the drogue fluctuation and suppress HWP to some extent, but it cannot avoid HWP essentially. An anti-HWP control method is proposed to significantly reduce the effect of the hose whipping phenomenon and improve the safety of aerial refueling systems. Finally, the effectiveness of the proposed modeling method and the anti-HWP control method are well verified by simulations and comparisons.

Chapter 9 Terminal Iterative Learning Docking Control

9.1 Introduction

Aerial refueling has demonstrated significant benefits to aviation by extending the range and endurance of aircraft [4]. The development of autonomous aerial refueling (AAR) techniques for unmanned aerial vehicles (UAVs) makes new missions and capabilities possible [10], like the ability for long range or long time flight. As the most widely used aerial refueling method, the probe-drogue refueling (PDR) system is considered to be more flexible and compact than other refueling systems. However, a drawback of PDR is that the drogue is passive and susceptible to aerodynamic disturbances [2]. Therefore, it is difficult to design an AAR system to control the probe on the receiver to capture the moving drogue within centimeter level in the docking stage.

It used to be thought that the aerodynamic disturbances in the aerial refueling mainly include the tanker vortex, wind gust, and atmospheric turbulence. According to NASA Autonomous Aerial Refueling Demonstration (AARD) project [10], the forebody flow field of the receiver may also significantly affect the docking control of AAR, which is called “the bow wave effect” [233]. As a result, the modeling and simulation methods for the bow wave effect were studied in our previous works [40, 44]. Since the obtained mathematical models are somewhat complex and there may be some uncertain factors in practice, this paper aims to use a model-free method to compensate for the docking error caused by aerodynamic disturbances including the bow wave effect.

Most of the existing studies on AAR docking control do not consider the bow wave effect. In [67, 207, 234], the drogue is assumed to be relatively static (or oscillates around the equilibrium) and not affected by the flow field of the receiver forebody. However, in practice, the receiver aircraft is affected by aerodynamic disturbances, and the drogue is affected by both the wind disturbances and the receiver forebody bow wave. As a major difficulty in the control of AAR, the aerodynamic disturbances, especially the bow wave effect, attract increasing attention in these years. In [54, 96], the wind effects from the tanker vortex, the wind gust, and the atmospheric turbulence are analyzed, and in [40, 44, 235], the modeling and simulation methods for the receiver forebody bow wave effect are studied, but no control methods are proposed. In [233], simulations show that the bow wave effect can be compensated by adding an offset value to the reference trajectory, but the method for obtaining the offset value is not given.

Since the accurate mathematical models for the aerodynamic disturbances are usually difficult to obtain [44], iterative learning control (ILC) is a possible choice for the docking control

of AAR. According to [236], the ILC is a model-free control method which can improve the performance of a system by learning from the previous repetitive executions or iterations. ILC methods have been proved to be effective to solve the control problems for complex systems with no need for the exact mathematical model [237]. For an actual AAR system, the relative position between the probe and the drogue is usually measured by vision localization methods [238] whose measurement precision depends on the relative distance (higher precision in a closer distance). Therefore, compared with the trajectory data, the terminal positions of the probe and the drogue are usually easier to measure in practice. As a result, terminal iterative learning control (TILC) methods are suitable for AAR systems because TILC methods need only the terminal states or outputs instead of the whole trajectories [239, 240].

This paper studies the model of the probe-drogue aerial refueling system under aerodynamic disturbances, and proposes a docking control method based on TILC to compensate for the docking errors caused by aerodynamic disturbances. In the ATP-56(B) issued by NATO [241], chasing the drogue directly is identified as a dangerous operation which may cause the overcontrol of the receiver. Therefore, the proposed TILC controller is designed by imitating the docking operations of human pilots to predict the terminal position of the drogue with an offset to compensate for the docking errors caused by aerodynamic disturbances. The designed controller works as an additional unit for the trajectory generation of the original autopilot system. Simulations based on our previously published MATLAB/SIMULINK environment [40, 44] show that the proposed control method has a fast learning speed to achieve a successful docking control under aerodynamic disturbances including the bow wave effect.

9.2 Problem Formulation

9.2.1 Frames and Notations

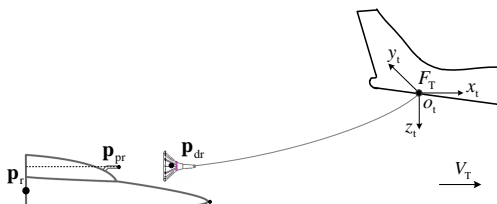


Figure 9.1: Simplified schematic diagram of PDR systems.

Since the tanker moves at a uniform speed in a straight and level line during the docking stage of AAR, a frame fixed to the tanker body can be treated as an inertial reference frame to describe the relative motion between the receiver and the drogue. As shown in Fig. 9.1, a tanker joint frame F_T is defined with the origin O_t fixed to the joint between the tanker body and the hose. F_T is a right-handed coordinate system, whose x_t horizontally points to the flight direction of the tanker, z_t vertically points to the ground, and y_t points to the right. For simplicity, the following rules are defined:

(i) All position or state vectors are defined under the tanker joint frame F_T , unless explicitly stated.

(ii) The drogue position vector is expressed as $\mathbf{p}_{dr} \triangleq [x_{dr} \ y_{dr} \ z_{dr}]^T$, and the probe position vector is $\mathbf{p}_{pr} \triangleq [x_{pr} \ y_{pr} \ z_{pr}]^T$. In a similar way, the position error between the probe and the drogue is expressed as

$$\Delta\mathbf{p}_{dr/pr}(t) \triangleq \mathbf{p}_{dr}(t) - \mathbf{p}_{pr}(t) \quad (9.1)$$

whose decomposition form is represented by $\Delta\mathbf{p}_{dr/pr} \triangleq [\Delta x_{dr/pr} \ \Delta y_{dr/pr} \ \Delta z_{dr/pr}]^T$.

(iii) One docking attempt ends at the terminal time $T \in \mathbb{R}_+$ when the probe contacts with the central plane of the drogue ($\Delta x_{dr/pr} = 0$) for the first time, which is defined as

$$T = \min_t \{\Delta x_{dr/pr}(t) = 0\}. \quad (9.2)$$

The value at time $t = T$ is called the terminal value. For example, $\mathbf{p}_{dr}(T)$ is the terminal position of the drogue and $\Delta\mathbf{p}_{dr/pr}(T)$ is the terminal position error.

(iv) The value in the k^{th} docking attempt is marked by a right superscript. For example, $\mathbf{p}_{dr}^{(k)}$ denotes the drogue position \mathbf{p}_{dr} in the k^{th} docking attempt, $T^{(k)}$ denotes the k^{th} terminal time, and $\mathbf{p}_{dr}^{(k)}(T^{(k)})$ denotes the k^{th} terminal position of the drogue.

9.2.2 System Overview

The overall structure of the AAR system proposed in this paper is shown in Fig. 9.2, where the whole AAR system is divided into two parts: the mathematical model and the control system. The AAR Mathematical model contains three components: the aerodynamic disturbance model, the hose-drogue dynamic model, and the receiver dynamic model; the control system contains two components: the autopilot and the TILC controller. The autopilot focuses on stabilizing the aircraft attitude and tracking the given reference trajectory, and the TILC controller works as a human pilot that learns from historical experience and sends trajectory commands to the autopilot. This paper focuses on the design of the TILC controller.

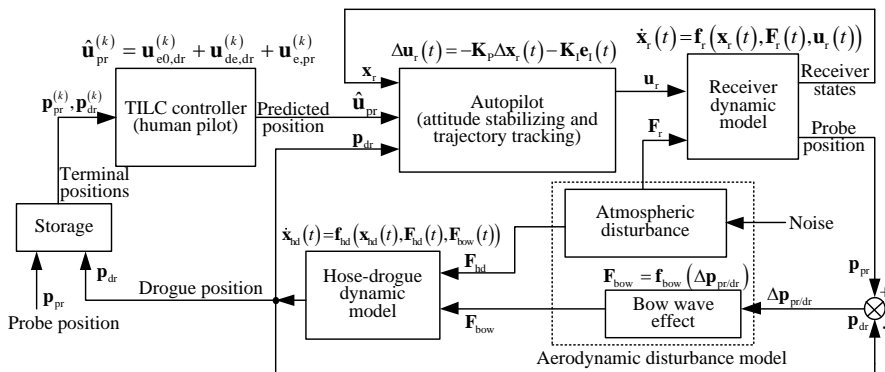


Figure 9.2: Overall structure of the AAR system.

9.2.3 Mathematical Model

9.2.3.1 Aerodynamic Disturbance Model

The aerodynamic disturbances will change the flow field around the receiver and the drogue, then produce disturbance forces on them to affect their relative motions. There are mainly two sources of aerodynamic disturbances: one is from the atmospheric environment such as the tanker vortex, the wind gust and the atmospheric turbulence [54]; the other is from the bow wave flow field of the receiver forebody. In an AAR system, the receiver mainly suffers the atmospheric disturbance force $\mathbf{F}_r \in \mathbb{R}^3$, while the hose-drogue suffers both the atmospheric disturbance force $\mathbf{F}_{hd} \in \mathbb{R}^3$ and the bow wave disturbance force $\mathbf{F}_{bow} \in \mathbb{R}^3$.

The modeling and simulation methods for \mathbf{F}_r and \mathbf{F}_{hd} have been well studied in the existing literature, where the detailed mathematical expression for \mathbf{F}_r can be found in [54], the detailed mathematical expression for \mathbf{F}_{hd} can be found in [44][54]. The bow wave disturbance force \mathbf{F}_{bow} , according to [44], is determined by the position error between the drogue and the probe $\Delta\mathbf{p}_{dr/pr}$, which can be expressed as

$$\mathbf{F}_{bow} = \mathbf{f}_{bow}(\Delta\mathbf{p}_{dr/pr}) \quad (9.3)$$

where $\mathbf{f}_{bow}(\cdot)$ is the bow wave effect function whose expression can be obtained by the method proposed in [44].

Among these disturbances, \mathbf{F}_r and \mathbf{F}_{hd} are independent of the states of the AAR system, and the corresponding control methods are mature; \mathbf{F}_{bow} is strongly coupled with the system output $\Delta\mathbf{p}_{dr/pr}$, the control strategy for which is challenging and still lacking. Therefore, this paper puts more effort on the control of the bow wave effect.

9.2.3.2 Hose-drogue Model

The soft hose can be modeled by a finite number of cylinder-shaped rigid links based on the finite-element theory [27]. Then, the hose-drogue dynamic equation can be written as

$$\begin{cases} \mathbf{x}_{hd}(t) = \mathbf{f}_{hd}(\mathbf{x}_{hd}(t), \mathbf{F}_{hd}(t), \mathbf{F}_{bow}(t)) \\ \mathbf{p}_{dr}(t) = \mathbf{g}_{hd}(\mathbf{x}_{hd}(t)) \end{cases} \quad (9.4)$$

where $\mathbf{f}_{hd}(\cdot)$ is a nonlinear vector function, \mathbf{x}_{hd} is the hose-drogue state vector, and $\mathbf{F}_{hd}(t)$ and $\mathbf{F}_{bow}(t)$ are the disturbance forces acting on the drogue. The dimensions of \mathbf{x}_{hd} and $\mathbf{f}_{hd}(\cdot)$ depend on the number of the links that the hose is divided into.

The most concerned value in the TILC method is the terminal position of the drogue. Therefore, it is necessary to study the terminal state of the hose-drogue system (9.4). According to [40], when there is no random disturbance, the drogue will eventually settle at an equilibrium position marked as \mathbf{p}_{dr}^{e0} . Then, under the bow wave effect, the drogue will be pushed to a new terminal position $\mathbf{p}_{dr}(T)$. The drogue position offset $\Delta\mathbf{p}_{dr}^e \in \mathbb{R}^3$ is defined as

$$\Delta\mathbf{p}_{dr}^e = \mathbf{p}_{dr}(T) - \mathbf{p}_{dr}^{e0} \quad (9.5)$$

where $\Delta\mathbf{p}_{\text{dr}}^e$ is further determined by the strength of terminal bow wave disturbance force $\mathbf{F}_{\text{bow}}(T)$ as

$$\Delta\mathbf{p}_{\text{dr}}^e = \mathbf{f}_{\text{dr}}(\mathbf{F}_{\text{bow}}(T)). \quad (9.6)$$

Then, substituting Eq. (9.3) into Eq. (9.6) yields

$$\Delta\mathbf{p}_{\text{dr}}^e = \mathbf{f}_{\text{dr}}(\mathbf{f}_{\text{bow}}(\Delta\mathbf{p}_{\text{dr/pr}}(T))) \triangleq \bar{\mathbf{f}}_{\text{dr}}(\Delta\mathbf{p}_{\text{dr/pr}}(T)). \quad (9.7)$$

Noticing that $\Delta\mathbf{p}_{\text{dr/pr}}(T) \approx \mathbf{0}$, the Taylor Expansion can be applied to Eq. (9.7), which results in

$$\Delta\mathbf{p}_{\text{dr}}^e \approx \mathbf{m}_0 + \mathbf{M}_1 \cdot \Delta\mathbf{p}_{\text{dr/pr}}(T) \quad (9.8)$$

where

$$\mathbf{m}_0 \triangleq \bar{\mathbf{f}}_{\text{dr}}(\mathbf{0}), \quad \mathbf{M}_1 \triangleq \left. \frac{\partial \bar{\mathbf{f}}_{\text{dr}}(\mathbf{x})}{\partial \mathbf{x}} \right|_{\mathbf{x}=\mathbf{0}}. \quad (9.9)$$

In practice, the drogue is sensitive to the aerodynamic disturbances, and the actual terminal position of the drogue always oscillates around its stable position. Therefore, a bounded disturbance term $\mathbf{v}_{\text{dr}} \in \mathbb{R}^3$ should be added to Eq. (9.7) as

$$\Delta\mathbf{p}_{\text{dr}}^e = \mathbf{m}_0 + \mathbf{M}_1 \cdot \Delta\mathbf{p}_{\text{dr/pr}}(T) + \mathbf{v}_{\text{dr}} \quad (9.10)$$

where $\|\mathbf{v}_{\text{dr}}\| \leq B_{\text{dr}}$ represents the position fluctuation of the drogue due to random disturbances such as atmospheric turbulence. According to Eq. (9.10), there is a functional relationship between the terminal docking error $\Delta\mathbf{p}_{\text{dr/pr}}(T)$ and the drogue bow wave offset $\Delta\mathbf{p}_{\text{dr}}^e$. Therefore, it is possible to use TILC methods to compensate for the bow wave position offset $\Delta\mathbf{p}_{\text{dr}}^e$ with the terminal docking error $\Delta\mathbf{p}_{\text{dr/pr}}(T)$.

The detailed mathematical expression of $\bar{\mathbf{f}}_{\text{dr}}(\cdot)$ can be obtained through methods in [44], then the Jacobian matrix \mathbf{M}_1 can be obtained from Eq. (9.9). Since $\bar{\mathbf{f}}_{\text{dr}}(\cdot)$ is monotonically decreasing along each axial direction, for the receiver aircraft with symmetrical forebody layout, it is easy to verify that \mathbf{M}_1 is a negative definite matrix.

9.2.3.3 Receiver Aircraft Model

As previously mentioned, in the docking stage, the tanker joint frame F_T can be simplified as an inertial frame. Under this situation, the commonly used aircraft modeling methods as presented in [129] can be applied to the receiver aircraft with the following form

$$\begin{cases} \mathbf{x}_r(t) = \mathbf{f}_r(\mathbf{x}_r(t), \mathbf{F}_r(t), \mathbf{u}_r(t)) \\ \mathbf{p}_{\text{pr}}(t) = \mathbf{g}_{\text{pr}}(\mathbf{x}_r(t)) \end{cases} \quad (9.11)$$

where $\mathbf{f}_r(\cdot)$ is a nonlinear function, \mathbf{x}_r is the state of the receiver and \mathbf{u}_r is the control input of the receiver aircraft.

Since the nonlinear model (9.11) is too complex for controller design, a linearization method [129] is applied to Eq. (9.11) to simplify the receiver dynamic model. Assume the receiver equilibrium state is \mathbf{x}_{r0} and the trimming control is \mathbf{u}_{r0} , then the linear model can be

expressed as

$$\begin{cases} \Delta \mathbf{x}_r(t) = \mathbf{A}_r \cdot \Delta \mathbf{x}_r(t) + \mathbf{B}_r \cdot \Delta \mathbf{u}_r(t) + \mathbf{G}_r \cdot \mathbf{F}_r(t) \\ \Delta \mathbf{p}_{pr}(t) = \mathbf{C}_r \cdot \Delta \mathbf{x}_r(t) \end{cases} \quad (9.12)$$

where $\Delta \mathbf{x}_r \triangleq \mathbf{x}_r - \mathbf{x}_{r0}$ is the state vector of the linearized system, $\Delta \mathbf{u}_r \triangleq \mathbf{u}_r - \mathbf{u}_{r0}$ is the linearized control input vector and $\Delta \mathbf{p}_{pr} \triangleq \mathbf{p}_{pr} - \mathbf{p}_{pr0}$ is the probe position offset from the initial probe position \mathbf{p}_{pr0} .

9.2.4 Control System

9.2.4.1 Autopilot

Based on the linear model (9.12), the autopilot can be simplified as a state feedback controller [96] in the form as

$$\Delta \mathbf{u}_r(t) = -\mathbf{K}_P \cdot \Delta \mathbf{x}_r(t) - \mathbf{K}_I \cdot \mathbf{e}_I(t) \quad (9.13)$$

$$\mathbf{e}_I(t) = \mathbf{p}_{pr}(t) - \hat{\mathbf{u}}_{pr}(t) \quad (9.14)$$

where $\hat{\mathbf{u}}_{pr}(t) \in \mathbb{R}^3$ is the reference trajectory vector of the probe, \mathbf{K}_P and \mathbf{K}_I are the gain matrices. Essentially, Eq. (9.13) is a PI controller, where $-\mathbf{K}_P \cdot \Delta \mathbf{x}_r(t)$ is the state feedback control term for stabilizing the aircraft, and $-\mathbf{K}_I \cdot \mathbf{e}_I(t)$ is the integral control term for tracking the given trajectory. Since it is very convenient to obtain \mathbf{K}_P and \mathbf{K}_I through LQR function in MATLAB, the procedures are omitted here. In practice, a saturation function is required for $\mathbf{e}_I(t)$ in Eq. (9.13) to slow down the response speed and resist integral saturation. For instance, the approaching speed should be constrained within a reasonable range, because the probe should have enough closure speed to open the valve on the drogue safely [10].

As analyzed in [96, 129], when the autopilot (9.13) is well designed and the disturbance force $\mathbf{F}_r(t) \equiv \mathbf{0}$, the tracking error can converge to zero

$$\hat{\mathbf{u}}_{pr}(t) - \mathbf{p}_{pr}(t) \rightarrow \mathbf{0}, \text{ as } t \rightarrow \infty. \quad (9.15)$$

However, in practice, the disturbance force $\mathbf{F}_r(t) \neq \mathbf{0}$ and the terminal time $T \ll \infty$, then the tracking error cannot reach zero at terminal time T . Therefore, an error term should be added to Eq. (9.15) at T as

$$\hat{\mathbf{u}}_{pr}(T) - \mathbf{p}_{pr}(T) = \mathbf{v}_{pr} \quad (9.16)$$

where $\mathbf{v}_{pr} \in \mathbb{R}^3$ is a bounded random disturbance term with $\|\mathbf{v}_{pr}\| \leq B_{pr}$. The random disturbance \mathbf{v}_{pr} may come from the unrepeatable disturbances such as atmospheric turbulence.

9.2.4.2 Objective of Docking Control

According to [10], in each docking attempt, the receiver should follow the drogue for seconds until the hose-drogue levels off. Then, the receiver starts to drive the probe to approach the drogue with a slow constant speed, until the probe hits the central plane of the drogue as shown in Fig. 9.3. The basic requirement for the AAR system is that the relative position between

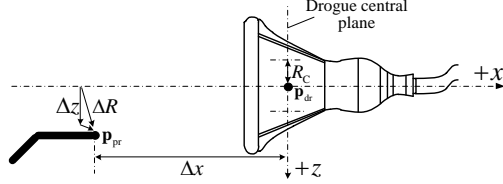


Figure 9.3: Success and failure criteria of a docking attempt [10].

the probe and the drogue (represented by the docking error $\Delta \mathbf{p}_{\text{dr/pr}}$) can reach zero at the terminal time T . In practice, the radial error $\Delta R_{\text{dr/pr}} \in \mathbb{R}_+$ is an important evaluation index for the docking performance which defined in oyz plane as

$$\Delta R_{\text{dr/pr}}(t) \triangleq \sqrt{\Delta y_{\text{dr/pr}}^2(t) + \Delta z_{\text{dr/pr}}^2(t)}. \quad (9.17)$$

Since the docking error is inevitable due to disturbances, a threshold radius (criterion radius) $R_C \in \mathbb{R}_+$ should be defined as

$$\Delta R_{\text{dr/pr}}(T) < R_C. \quad (9.18)$$

If criterion (9.18) is satisfied, a success docking is declared for this docking attempt [10]. Otherwise, a failure or miss is declared. In fact, according to the previous definition, there is $\Delta x_{\text{dr/pr}}(T) \equiv 0$. Therefore, the terminal radial error $\Delta R_{\text{dr/pr}}(T)$ always equals to the terminal docking error $\Delta \mathbf{p}_{\text{dr/pr}}(T)$.

9.3 TILC Design

As shown in Fig. 9.2, the role of the TILC controller in AAR system is the same as the human pilot in manned aerial refueling system. The inputs of the TILC controller are the historical terminal positions of the probe $\mathbf{p}_{\text{pr}}(T)$ and the drogue $\mathbf{p}_{\text{dr}}(T)$, and the output is the reference tracking trajectory $\hat{\mathbf{u}}_{\text{pr}}(t)$ which is further sent to the autopilot.

9.3.1 TILC Controller

The docking errors of the AAR system are mainly caused by two factors: the drogue offset caused by the bow wave effect as described in Eq. (9.5); and the tracking error caused by the response lag of the receiver as described in Eq. (9.16). In order to compensate for these docking errors, a simple and safe control strategy is letting the probe always aims at a predicted fixed position $\hat{\mathbf{u}}_{\text{pr}}^{(k)}(t) \equiv \hat{\mathbf{u}}_{\text{pr}}^{(k)}$ during the docking stage. The predicted position $\hat{\mathbf{u}}_{\text{pr}}^{(k)}$ for the autopilot should have the following form

$$\hat{\mathbf{u}}_{\text{pr}}^{(k)} = \mathbf{p}_{\text{dr}}^{\text{e}0,(k)} + \mathbf{u}_{\text{de,dr}}^{(k)} + \mathbf{u}_{\text{e,pr}}^{(k)} \quad (9.19)$$

where $\mathbf{p}_{\text{dr}}^{\text{e}0,(k)} \in \mathbb{R}^3$ is the original stable position of the drogue, $\mathbf{u}_{\text{de,dr}}^{(k)} \in \mathbb{R}^3$ is an estimation term for the drogue position offset, and $\mathbf{u}_{\text{e,pr}}^{(k)} \in \mathbb{R}^3$ is an ILC term to compensate for the tracking error of the probe. Note that, since $\mathbf{p}_{\text{dr}}^{\text{e}0,(k)}$ can be directly measured during the flight, it is treated as a known parameter here. Then, $\mathbf{u}_{\text{de,dr}}^{(k)}$ and $\mathbf{u}_{\text{e,pr}}^{(k)}$ should be updated in each iteration, and the

updating laws are given below.

(1) the updating law of $\mathbf{u}_{\text{de,dr}}^{(k)}$ is given by

$$\mathbf{u}_{\text{de,dr}}^{(k)} = \mathbf{K}_\alpha \cdot \mathbf{u}_{\text{de,dr}}^{(k-1)} + (\mathbf{I} - \mathbf{K}_\alpha) \cdot \Delta \mathbf{p}_{\text{dr}}^{\text{e},(k-1)} \quad (9.20)$$

where $\mathbf{K}_\alpha = \text{diag}(k_{\alpha_1}, k_{\alpha_2}, k_{\alpha_3})$ with $k_{\alpha_1}, k_{\alpha_2}, k_{\alpha_3} \in (0, 1)$ is a constant diagonal matrix, and $\Delta \mathbf{p}_{\text{dr}}^{\text{e}}$ is the drogue terminal offset position as defined in Eq. (9.5) whose iterative feature can be written as

$$\Delta \mathbf{p}_{\text{dr}}^{\text{e},(k)} \triangleq \mathbf{p}_{\text{dr}}^{(k)}(T^{(k)}) - \mathbf{p}_{\text{dr}}^{\text{e},(k)}. \quad (9.21)$$

(2) the updating law of $\mathbf{u}_{\text{e,pr}}^{(k)}$ is given by

$$\mathbf{u}_{\text{e,pr}}^{(k)} = \mathbf{u}_{\text{e,pr}}^{(k-1)} + \mathbf{K}_p \cdot \mathbf{e}_{\text{pr}}^{(k-1)} \quad (9.22)$$

where $\mathbf{K}_p = \text{diag}(k_{p_1}, k_{p_2}, k_{p_3})$ is a constant diagonal matrices with $k_{p_1}, k_{p_2}, k_{p_3} \in (0, 1)$ and \mathbf{e}_{pr} represents the probe terminal tracking error with the k^{th} iterative feature defined as

$$\mathbf{e}_{\text{pr}}^{(k)} \triangleq \mathbf{p}_{\text{dr}}^{\text{e},(k)} + \mathbf{u}_{\text{de,dr}}^{(k)} - \mathbf{p}_{\text{pr}}^{(k)}(T^{(k)}). \quad (9.23)$$

9.3.2 Convergence Analysis

The following theorem provides the convergence condition under which one can conclude the convergence property of the designed TILC controller in Eq. (9.19).

Theorem 1. Consider the AAR system described by Eqs. (9.4)(9.11)(9.13) with the structure shown in Fig. 9.2. Suppose (i) the autopilot of the receiver aircraft in Eq. (9.13) is well designed, and the probe terminal position satisfies Eq. (9.16); (ii) the TILC controller is designed as Eq. (9.19), and its parameters satisfy

$$0 \leq k_{\alpha_i} < 1, 0 < k_{p_i} \leq 1, i = 1, 2, 3. \quad (9.24)$$

Then, through the repetitive docking attempts, the docking error $\Delta \mathbf{p}_{\text{dr/pr}}^{(k)}(T^{(k)})$ will converge to a bound

$$\lim_{k \rightarrow \infty} \left\| \Delta \mathbf{p}_{\text{dr/pr}}^{(k)}(T^{(k)}) \right\| \leq B_{\text{dr/pr}} \quad (9.25)$$

where

$$B_{\text{dr/pr}} = 2 \sqrt{B_{\text{pr}}^2 + B_{\text{dr}}^2} \quad (9.26)$$

in which B_{dr} is the random disturbance bound of the drogue position fluctuation as defined in Eq. (9.10) and B_{pr} is the random disturbance bound of the probe tracking error as defined Eq. (9.16). In particular, if the random disturbances are negligible, i.e., $B_{\text{dr}} = 0, B_{\text{pr}} = 0$, then the docking error will converge to zero as

$$\left\| \Delta \mathbf{p}_{\text{dr/pr}}^{(k)}(T^{(k)}) \right\| \rightarrow 0, \text{ as } k \rightarrow \infty. \quad (9.27)$$

Proof. See Appendix A. \square

9.3.3 Discussion

Essentially, the term $\mathbf{u}_{de,dr}^{(k)}$ works as a low-pass filter, which is expected to provide a smooth and robust estimation of the drogue offset caused by disturbances. Then, with this term in $\hat{\mathbf{u}}_{pr}^{(k)}$, the drogue offset can be compensated. The low-pass filter is adopted instead of using the drogue offset position directly, which is because the drogue is sensitive to disturbances.

The initial value for the proposed TILC method in Eq. (9.19) should be set to zero ($\mathbf{u}_{de,dr}^{(0)} = \mathbf{0}$, $\mathbf{u}_{e,pr}^{(0)} = \mathbf{0}$) when there is no historical learning data. In practice, $\mathbf{u}_{de,dr}^{(0)}$ has physical significance, namely the drogue position offset caused by the receiver forebody flow field. Therefore, the initial value for $\mathbf{u}_{de,dr}^{(0)}$ can be estimated according to the historical learning data, the experience of human pilots, or the calculation result from the hose-drogue model [27] and the bow wave effect model [44]. With the pre-estimated initial value, the iteration speed of the proposed TILC method can be improved.

Unlike other conventional ILC methods, the proposed TILC method does not require the exact value of the terminal time T and does not require T to be the same between iterations. It only requires the terminal positions of the drogue and the probe, which is practical for an actual AAR system.

9.4 Simulation and Verification

9.4.1 Simulation Configuration

A MATLAB/SIMULINK-based simulation environment has been developed to simulate the docking stage of the AAR. The detailed introduction of the modeling methods and the simulation parameters can be found in the authors' previous work [44]. A video has also been released to introduce the AAR simulation environment and demonstrate the TILC simulation results. The URL of the video is <https://youtu.be/Vop1DA6D5fA>.

9.4.2 TILC Simulation Results

9.4.2.1 Iterative Learning Process

In order to verify the effectiveness of the proposed TILC method, all the initial values in Eq. (9.19) are set zeroes as $\mathbf{u}_{de,dr}^{(0)} = \mathbf{0}$, $\mathbf{u}_{e,pr}^{(0)} = \mathbf{0}$, and the learning procedures are shown in Fig. 9.4.

In Fig. 9.4, there are four docking attempts performed in sequence (the four docking attempts start at time 50s, 100s, 150s and 200s respectively), where the first two docking attempts fail, and the following two attempts both succeed. In each attempt, the probe moves close to until contact with the drogue at $T^{(k)}$ (marked by the vertical dotted lines), then the probe returns to the standby postilion and gets ready for the next docking attempt.

In the first docking attempt as shown in Fig. 9.4, the receiver remains at the standby position (5m behind the drogue, with simulation time from 50s to 60s) to observe the drogue movement



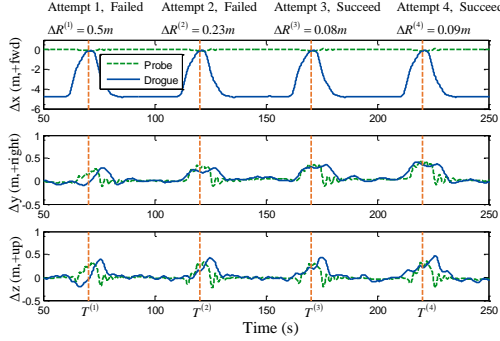


Figure 9.4: Learning process with the proposed TILC method.

and estimate the equilibrium position of the drogue. Then, the receiver approaches the drogue to perform a docking attempt during the simulation time from 60s to 71s in Fig. 9.4. The docking control ends at the terminal time $T^{(1)} = 71\text{s}$, and this docking attempt is declared as a failure because the radial error $\Delta R_{\text{dr/pr}}^{(1)} = 0.5\text{m}$ is larger than the desired radial error threshold $R_C = 0.15\text{m}$.

With more docking attempts (not presented in Fig. 9.4) are simulated, a docking success rate over 90% will be obtained under the given threshold $R_C = 0.15\text{m}$. According to the Monte Carlo simulations, the success rate depends on many factors including the docking error threshold R_C , the strength of the atmospheric turbulence, and other random disturbances. The simulation results are consistent with results in [10][233]. When the aerodynamic disturbances are strong, both the drogue position oscillation and the receiver tracking error will be significant, then the success rate will be low.

9.4.2.2 Aerodynamic Disturbance Simulations

Fig. 9.5 presents the total aerodynamic disturbance force $\mathbf{F}_{\text{total}} = [\Delta F_x, \Delta F_y, \Delta F_z]^T$ applied on the drogue during the first docking attempt (50s~71s) in Fig. 9.4. In this simulation, the tanker vortex disturbance comes from the model presented in [54], the wind gust and the atmospheric turbulence come from the MATLAB/SIMULINK Aerospace Blockset based on the mathematical representations from Military Specification MIL-F-8785C, and the bow wave effect disturbance comes from the authors' previous work [40]. When the receiver remains at the standby position (50s~60s in Fig. 9.5), the drogue is far away from the receiver and the disturbance forces mainly come from the tanker vortex and the atmospheric turbulence as illustrated on the left half of Fig. 9.5. As the receiver moves closer to the drogue, the receiver bow wave starts to cause a large disturbance force on the drogue as illustrated on the right half of Fig. 9.5.

A comprehensive simulation is performed to verify the performance of the proposed TILC method with the initial value from the previous learning results. In addition to the atmospheric turbulence and the bow wave disturbance as shown in Fig. 9.5, a wind gust (5m/s in the lateral direction and vertical direction respectively) is added at 100s to verify the control effect of the proposed method under aerodynamic disturbances. The simulation results are presented in

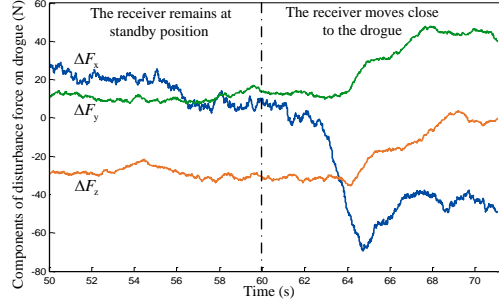


Figure 9.5: Total aerodynamic disturbing force applied on the drogue.

Fig. 9.6.

It can be observed from Fig. 9.6 that, with a good initial value, the docking control succeeds at the first attempt. Then, the second docking attempt (115s in Fig. 9.6) fails due to the addition of a strong wind gust at 100s. In the next two docking attempts (165s and 215s in Fig. 9.6), the controller can rapidly recover and achieve successful docking control without being much affected by the wind gust disturbance. The simulation results demonstrate that the proposed TILC method has a certain ability to resist the aerodynamic disturbances.

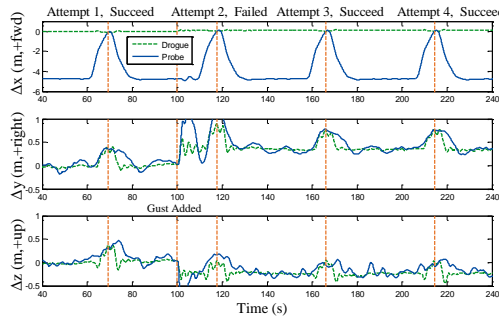


Figure 9.6: Simulation with the initial value and the wind gust disturbance.

9.5 Chapter Summary

This paper studies the model of the probe-drogue aerial refueling system under aerodynamic disturbances, and proposes a docking control method based on terminal iterative learning control to compensate for the docking errors caused by aerodynamic disturbances. The designed controller works as an additional unit for the trajectory generation function of the original autopilot system. Simulations based on our previously published simulation environment show that the proposed control method has a fast learning speed to achieve a successful docking control under aerodynamic disturbances including the bow wave effect.

Chapter 10 Improved Terminal Iterative Learning

Docking Control

10.1 Introduction

Autonomous aerial refueling (AAR) is an important method to increase the voyage and endurance of unmanned aerial vehicles (UAVs) and avoid the conflict between the takeoff weight and the payload weight [151, 152]. Among the aerial refueling methods in operation today, the probe-drogue refueling (PDR) [9] is the most widely adopted one owing to its flexibility and simple requirement for equipment. There are five stages in the process of PDR, docking is the most critical and difficult stage because it is more susceptible to disturbances, which directly affects the success of AAR. The docking control task is to control the probe on the receiver link up with the drogue for fuel transfer. The docking control for PDR is a difficult task for two main reasons. The first reason is that the system model in the docking stage is a multi-input-multi-output (MIMO) higher-order nonlinear system with nonminimum-phase, multi-agent, and multi-disturbance features, which is complex for control design. Moreover, the dynamics of the receiver is slower than that of the drogue, so it is hard for the probe on the receiver to capture the moving drogue. The second reason is that the precision requirement for the PDR docking control is high. The docking error should be controlled within centimeter level, and the relative velocity between the probe and the drogue should be controlled within a small range, such as 1~1.5 m/s [241]. Therefore, the docking controller design for PDR is important and challenging.

Many research efforts have focused on developing docking control methods for PDR. First, the most commonly used method is the linear quadratic regulator (LQR) [66, 67] because it is simple, and the optimal feedback gain matrix can be obtained. It is a linear model based method, and the control quality may deteriorate in the presence of large disturbances. A second method is nonzero setpoint (NZSP) [238], which transforms a tracking problem into a stabilization problem. However, the reference state and reference input are limited to be constant, namely the drogue is relatively static to the tanker. It means that the receiver just needs to perform a set-point tracking task. Some improved work is then carried out to track a moving drogue [61], but the trajectory of the drogue is assumed to be known in advance. Thirdly, to reject complex disturbances and uncertainties during the docking stage, active disturbance rejection control (ADRC) [206] and adaptive-based control [64, 242] have received much attention recently. Generally, when ADRC is applied to the trajectory tracking of aircraft, the flight control system is designed by using scale separation. The considered system is usually divided into several loops, which leads to a complex control configuration. Adaptive-based control is also relatively complex. Moreover,

fault-tolerant control is also studied. A fault-tolerant adaptive model inversion control for vision-based PDR is developed in [68]. Last but not least, backstepping control is adopted in [34], which relies on the modeling precision of the PDR system.

On the whole, there still exist some challenges to designing a docking controller for PDR. First, the PDR system is complicated. Moreover, as one of the main disturbances in the docking stage, the bow wave effect is a repetitive nonlinear disturbance and highly related to the states of the receiver and the drogue, which also makes docking control difficult [40, 44]. Secondly, the problem of the “slow dynamics” to track the “fast dynamics” becomes tougher if the bow wave effect is taken into account. Some feedback control methods may result in a chasing process between the receiver and the drogue, which may cause overcontrol. Besides, the chasing action may lead to impact and damage to the drogue and the probe, which is very dangerous and needs to be avoided according to ATP-56(B) issued by NATO (North Atlantic Treaty Organisation) [241]. Thirdly, there are more than twenty states in the PDR system, so it is quite demanding for sensors to detect so many states accurately. In practice, the global positioning system (GPS) and vision-based navigation systems are common precise positioning methods for PDR [151]. Influenced by the environment, some unexpected sensor delay may happen. Besides, real-time online state feedback is time-consuming. As a consequence, the stability and reliability of the docking operation may deteriorate.

In order to cope with the aforementioned three challenges, a reliable docking control scheme for PDR is proposed in this study. Here, “reliability” means small docking error, certain robustness against disturbances and uncertainties, little dependence on the system model and sensors. The terminal iterative learning control (TILC) method is utilized in the docking control scheme. TILC has captured extensive attention from many fields since it was first presented by [243]. Iterative learning control (ILC) [244] is an effective cycle-to-cycle control approach to achieve entire output trajectory tracking within a given time interval. When only the end-point needs to be tracked, TILC is a good choice. In practice, when a pilot performs a docking operation, he/she adjusts the control input or the initial position of the receiver by learning from historical experience and sending feedforward commands to achieve a successful docking. Similarly, TILC gives feedforward control inputs or initial states based on the terminal output error from the last iteration. Noteworthy, the three challenges mentioned earlier can be solved to some extent by TILC. First, TILC is basically a model-free control method, and little system model knowledge is required. Secondly, the control input of the receiver is a feedforward signal, which is calculated by the iterative learning process, so the docking safety problem caused by some feedback control methods, which are mentioned in the last paragraph, can be avoided. Thirdly, only terminal output information instead of all states is needed for TILC. Besides, TILC takes advantage of the repeatability of the docking stage. Given the advantages TILC has in tackling these challenges, TILC is a preferable way to solve the docking control problem for PDR.

In this paper, a TILC controller is designed for the PDR system (a MIMO higher-order nonlinear system), and convergence analysis is also carried out without linearization. The proposed controller selects the combination of control inputs and initial values as its learning object, which is consistent with the pilots' operation. Besides, the iterative optimization method is adopted to generate a suitable basis function for the proposed TILC controller to achieve fast convergence, and to control the docking process. By combining the generation of basis function and the proposed TILC controller, a reliable docking control scheme for PDR is established.

A previous paper of ours [41] employed terminal iterative learning to forecast the terminal position of the drogue and then generate the tracking trajectory for the original autopilot system. However, it is not a conventional TILC, and the low-level driving signals still come from the original autopilot. There are significant differences between the work presented in this paper and that presented in [41]: i) The TILC controller works as an additional unit for the trajectory generation of the original autopilot system in [41], while the designed TILC controller in this study is a low-level controller without a given trajectory. ii) The proposed TILC controller is a hybrid controller with control input learning and initial position learning, whereas only the docking error learning is utilized in [41]. iii) A basis function is introduced into TILC for faster convergence. iv) The controlling of the x-axis relative velocity is achieved by the trajectory planning of the x-axis relative position rather than a saturation bound.

The main contributions of the study are twofold:

From the practical perspective, the contribution of this study is that: A reliable docking control scheme is proposed based on TILC. With this control scheme, the PDR system can achieve a successful docking quickly, accurately, and safely. TILC is a kind of model-free feedforward learning control, which can avoid the chasing action and reduce sensor burden, and thus possesses some advantages over model-based control and real-time feedback control in terms of the docking control problem.

From the theoretical perspective, the contribution of this study is that: TILC design problem for a class of MIMO higher-order nonlinear system is addressed with two key problems solved. One is that convergence analysis is carried out without linearization; the other is that a suitable basis function is selected by the iterative optimization method. Moreover, the partial state controllability is also considered in the TILC design.

The paper is organized as follows. The model description and problem statement are presented in Section 10.2 to transform the practical docking control problem into a theoretical TILC control problem. Section 10.3 gives a reliable docking control scheme including the generation of the basis function and the TILC controller implementation. In Section 10.4, a suitable basis function is generated for the TILC controller. Section 10.5 is devoted to the details of the TILC controller design with the convergence analysis. Illustrative simulations are provided in Section 10.6 to show the effectiveness of the proposed scheme. Section 10.7 concludes the paper.



10.2 Model Description and Problem Statement

10.2.1 PDR system model in the docking stage

Fig. 7.1 and Fig. 10.1 show the PDR system, which consists of a tanker aircraft with a flexible hose that trails behind and below the tanker, a cone-shaped drogue mounted at the end of the hose, and a receiver aircraft equipped with a rigid probe protruding from its nose. The docking control task is to control the probe link up with the drogue for fuel transfer. When establishing the PDR system model in the docking stage, three commonly used coordinate frames are the ground frame ($o_g-x_gy_gz_g$), the tanker frame ($o_t-x_ty_tz_t$), and the drogue equilibrium-point frame ($o_d-x_dy_dz_d$), which are shown in Fig. 7.1. The definition of these coordinate frames can be found in [40].

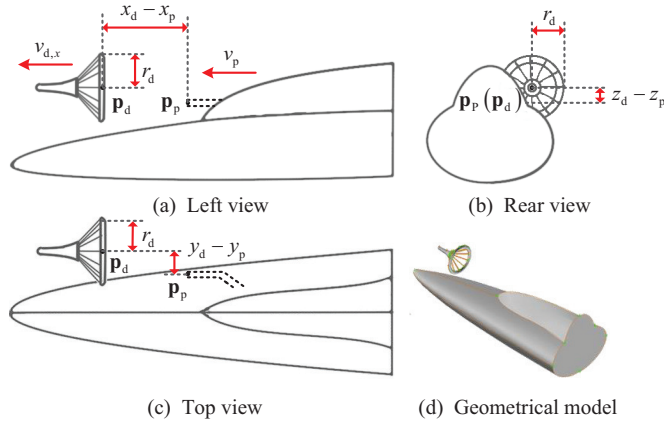


Figure 10.1: Three views and geometrical model of the PDR system.

According to [93, 245], the receiver aircraft (F-16 aircraft is considered) is modeled as

$$\begin{cases} \mathbf{x}_r = \mathbf{A}_r \mathbf{x}_r + \mathbf{B}_r \mathbf{u}_r + \mathbf{G}_r \mathbf{f}_a \\ \begin{bmatrix} \mathbf{p}_r \\ v_r \end{bmatrix} = \mathbf{C}_r \mathbf{x}_r \end{cases}, \quad (10.1)$$

$$\begin{bmatrix} \mathbf{p}_p \\ v_p \end{bmatrix} = \begin{bmatrix} \mathbf{p}_r \\ v_r \end{bmatrix} + \begin{bmatrix} \mathbf{p}_{p/r} \\ 0 \end{bmatrix}, \quad (10.2)$$

where $\mathbf{x}_r \in \mathbb{R}^{12}$ is the state vector of the receiver, $\mathbf{u}_r \in \mathbb{R}^4$ is the control input vector consisting of throttle $\delta_T \in \mathbb{R}$, elevator $\delta_e \in \mathbb{R}$, rudder $\delta_r \in \mathbb{R}$ and aileron $\delta_a \in \mathbb{R}$. The receiver mainly suffers from the atmospheric turbulence force $\mathbf{f}_a \in \mathbb{R}^3$. The modeling and simulation methods for \mathbf{f}_a have been extensively studied in the existing literature [67, 166]. The vector $\mathbf{p}_r = [x_r \ y_r \ z_r]^T \in \mathbb{R}^3$ denotes the position of the receiver's center of mass under the tank frame, which is combined with the velocity of the receiver $v_r \in \mathbb{R}$ to be the system output. The vector $\mathbf{p}_p = [x_p \ y_p \ z_p]^T \in \mathbb{R}^3$ and $v_p \in \mathbb{R}$ are the position and velocity of the front-end of the probe, and $\mathbf{p}_{p/r} \in \mathbb{R}^3$ denotes the relative position from \mathbf{p}_r to \mathbf{p}_p . Note that, all the system matrices $\mathbf{A}_r, \mathbf{B}_r, \mathbf{G}_r, \mathbf{C}_r$ are time-invariant and of appropriate dimensions. Moreover, stability augmentation control is often adopted for the

receiver to place the poles of the receiver system to reasonable positions in the left-half s -plane [245]. To this end, a state feedback matrix $\mathbf{K}_r \in \mathbb{R}^{4 \times 12}$ can be designed, and then the matrix \mathbf{A}_r becomes

$$\bar{\mathbf{A}}_r = \mathbf{A}_r - \mathbf{B}_r \mathbf{K}_r. \quad (10.3)$$

According to [40], the drogue dynamics is expressed by a transfer function, whose corresponding state-space representation is

$$\begin{cases} \mathbf{x}_d = \mathbf{A}_d \mathbf{x}_d + \mathbf{G}_d (\mathbf{f}_b + \mathbf{f}_a) \\ \begin{bmatrix} \mathbf{p}_d \\ v_{d,x} \end{bmatrix} = \mathbf{C}_d \mathbf{x}_d \end{cases}, \quad (10.4)$$

where $\mathbf{x}_d \in \mathbb{R}^{10}$ is the state of the drogue, whose dimension is determined by the order of the fitting model in the identification, the input $\mathbf{f}_b, \mathbf{f}_a \in \mathbb{R}^3$ are the bow wave effect force [169] and the atmospheric turbulence force. The vector $\mathbf{p}_d = [x_d \ y_d \ z_d]^T \in \mathbb{R}^3$ is the position of the drogue under the tank frame, which is combined with the velocity of the drogue in the x -axis direction of the tank frame $v_{d,x} \in \mathbb{R}$ to be the system output. Similar to the receiver model, all the system matrices $\mathbf{A}_d, \mathbf{G}_d, \mathbf{C}_d$ are time-invariant and of appropriate dimensions. Furthermore, the bow wave effect can be represented by a nonlinear function [40]

$$\mathbf{f}_b = \phi_0 (\mathbf{p}_d - \mathbf{p}_p). \quad (10.5)$$

Apart from the disturbance forces \mathbf{f}_b and \mathbf{f}_a , there are no other control inputs in the drogue dynamics (10.4). Therefore, the drogue position is passively affected by the aerodynamic disturbances from the receiver (in a close range) and the atmospheric environment, which is a difficulty for the docking control design.

On the whole, by combining Eqs. (10.1), (10.2), (10.3), (10.4) and (10.5), a comprehensive model for the PDR system is described as

$$\begin{cases} \underbrace{\begin{bmatrix} \mathbf{x}_d \\ \mathbf{x}_r \end{bmatrix}}_{\mathbf{x}} = \underbrace{\begin{bmatrix} \mathbf{A}_d & \mathbf{0} \\ \mathbf{0} & \bar{\mathbf{A}}_r \end{bmatrix}}_{\mathbf{A}} \underbrace{\begin{bmatrix} \mathbf{x}_d \\ \mathbf{x}_r \end{bmatrix}}_{\mathbf{x}} + \underbrace{\begin{bmatrix} \mathbf{0} \\ \mathbf{B}_r \end{bmatrix}}_{\mathbf{u}} \underbrace{\mathbf{u}}_{\mathbf{u}} + \underbrace{\begin{bmatrix} \mathbf{G}_d \phi_0 (\mathbf{p}_d - \mathbf{p}_p) \\ \mathbf{0} \end{bmatrix}}_{\phi(\mathbf{y})} + \underbrace{\begin{bmatrix} \mathbf{G}_d \mathbf{f}_a \\ \mathbf{G}_r \mathbf{f}_a \end{bmatrix}}_{\varphi} \\ \underbrace{\begin{bmatrix} \mathbf{p}_d - \mathbf{p}_p \\ v_{d,x} - v_p \end{bmatrix}}_{\mathbf{y}} = \underbrace{\begin{bmatrix} \mathbf{C}_d & -\mathbf{C}_r \end{bmatrix}}_{\mathbf{C}} \underbrace{\begin{bmatrix} \mathbf{x}_d \\ \mathbf{x}_r \end{bmatrix}}_{\mathbf{x}} + \underbrace{\begin{bmatrix} -\mathbf{p}_{p/r} \\ \mathbf{0} \end{bmatrix}}_{\mathbf{d}} \end{cases}. \quad (10.6)$$

When Eq. (10.6) is established in the drogue equilibrium-point frame, the initial states are

$$\mathbf{x}_d(0) = \mathbf{0}, \mathbf{x}_r(0) = \mathbf{x}_{r0}. \quad (10.7)$$

The physical meaning of Eq. (10.7) is that: when $t = 0$, the drogue is still and steady, and the receiver stays away from the drogue at an initial position \mathbf{x}_{r0} .

In practice, it is expected that the docking process lasts from t_{start} to t_{end} . The docking stage

terminates when

$$t_{\text{dock}} = \arg \min_t |x_d(t) - x_p(t)|, \quad (10.8)$$

which is expected to be equal to t_{end} (desired docking moment). At this moment, if

$$\begin{aligned} e_{\text{dock}} &= \left\| [y_d(t_{\text{dock}}) \ z_d(t_{\text{dock}})]^T - [y_p(t_{\text{dock}}) \ z_p(t_{\text{dock}})]^T \right\| < r_d, \\ -v_{\max} &< v_{d,x}(t_{\text{dock}}) - v_p(t_{\text{dock}}) < -v_{\min}, \end{aligned} \quad (10.9)$$

the docking attempt is regarded as successful [10], where v_{\max}, v_{\min} are the threshold of relative velocity to open the fuel valve at the docking moment, and r_d is the radius of the drogue as shown in Fig. 10.1.

10.2.2 TILC problem statement

Regarding the control design, there are four outputs $x_{d/p}, y_{d/p}, z_{d/p}, v_{dx/p}$ ($\mathbf{p}_d - \mathbf{p}_p \triangleq [x_{d/p} \ y_{d/p} \ z_{d/p}]^T, v_{d,x} - v_p \triangleq v_{dx/p}$) to be controlled. The controlling of $v_{dx/p}$ can be achieved by the trajectory planning of $x_{d/p}$. Thus, the following system from (10.6) is left to be considered

$$\begin{cases} \mathbf{x} = \mathbf{Ax} + \mathbf{Bu} + \boldsymbol{\phi}(\bar{\mathbf{y}}) + \boldsymbol{\varphi} \\ \bar{\mathbf{y}} = \bar{\mathbf{Cx}} + \bar{\mathbf{d}} \end{cases}, \quad (10.10)$$

where $\bar{\mathbf{y}} = [x_{d/p} \ y_{d/p} \ z_{d/p}]^T$, $\mathbf{u} = [\delta_T \ \delta_e \ \delta_a \ \delta_r]^T$, $\bar{\mathbf{C}}$ is generated from \mathbf{C} by removing the last row, $\bar{\mathbf{d}}$ is generated from \mathbf{d} by removing the last row.

According to Section 10.1, TILC is a preferable way to solve the docking control problem. Thus, system (10.10) is rewritten as a model for controller design:

$$\begin{cases} \mathbf{x}_k(t) = \mathbf{Ax}_k(t) + \mathbf{Bu}_k(t) + \boldsymbol{\phi}(\bar{\mathbf{y}}_k(t)) + \boldsymbol{\varphi}_k \\ \bar{\mathbf{y}}_k(t) = \bar{\mathbf{Cx}}_k(t) + \bar{\mathbf{d}}, \mathbf{x}_k(0) = \mathbf{x}_{0,k} \end{cases}, \quad (10.11)$$

where $t \in [0, T]$ is the time with the cycle period $T = t_{\text{end}} - t_{\text{start}}$, the subscript $k \in \mathbb{N}_+$ is the cycle number, $\mathbf{x}_k \in \mathbb{R}^{22}$, $\mathbf{u}_k \in \mathbb{R}^4$, $\bar{\mathbf{y}}_k \in \mathbb{R}^3$. The desired terminal output $\bar{\mathbf{y}}_d(T)$ is known. Henceforth, for convenience, the variables t and k will be omitted except when necessary. The following assumptions are made on system (10.11).

Assumption 1. The initial state $\mathbf{x}_k(0)$ can be reset at every iteration k .

Assumption 2. The atmospheric turbulence force is bounded and $\|\boldsymbol{\varphi}_k - \boldsymbol{\varphi}_{k-1}\| \leq D$.

Assumption 3. The function $\boldsymbol{\phi}(\bar{\mathbf{y}})$ satisfies the local Lipschitz condition on M , namely $\|\boldsymbol{\phi}(\bar{\mathbf{y}}_k) - \boldsymbol{\phi}(\bar{\mathbf{y}}_{k-1})\| \leq l_{\boldsymbol{\phi}} \|\bar{\mathbf{y}}_k - \bar{\mathbf{y}}_{k-1}\|$, where $M = \{\bar{\mathbf{y}} | \bar{\mathbf{y}} - \bar{\mathbf{y}}_d(T) \in \mathcal{B}(\mathbf{0}_{3 \times 1}, \delta)\}$ is an open connected set with $\mathcal{B}(\mathbf{0}_{3 \times 1}, \delta) \triangleq \{\xi \in \mathbb{R}^3 | \|\xi - \mathbf{0}_{3 \times 1}\| \leq \delta, \delta \in \mathbb{R}_+\}$ denoting a neighborhood with the radius δ around the origin $\mathbf{0}_{3 \times 1}$, and $l_{\boldsymbol{\phi}}$ is a positive Lipschitz constant.

In practice, if a docking attempt fails, the receiver will retreat to the standby position for the next attempt [41], which means the initial state $\mathbf{x}_k(0)$ can be reset at every iteration k , namely *Assumption 1*. The initial state $\mathbf{x}_k(0)$ can be measured by various types of sensors, for example vision-based systems [68]. *Assumption 2* is an assumption on the disturbance $\boldsymbol{\varphi}$. It is well known that ILC can remove repetitive disturbances. Thus one only needs to know the variations of disturbances in any two consecutive cycles. *Assumption 2* describes the bounds



of such variations. Because the docking operation is just allowed in calm days, atmospheric turbulence force can be bounded [67, 166]. As for *Assumption 3*, the nonlinear term $\phi(\bar{y})$ comes from the bow wave effect, whose concrete expression satisfies the local Lipschitz condition [40]. Thus, all the three assumptions above are reasonable for the PDR docking control problem.

For an actual PDR system, the drogue position and the relative position between the probe and the drogue are usually measured by vision-based sensors whose measurement precision depends on the relative distance (higher precision in the closer distance). Therefore, compared with the trajectory data, the terminal positions of the probe and the drogue are usually easier to measure in practice. Then, the controller directly uses the terminal docking error (relative position between the drogue and the probe at the docking moment) to give the next control input. Filters can also be used to remove the sensor noise.

Objective. The control objective is to construct a sequence of control $\mathbf{u}_k(t)$, $t \in [0, T]$ for system (10.11) such that

$$\|\bar{\mathbf{y}}_d(T) - \bar{\mathbf{y}}_k(T)\| < r_d \text{ as } k \rightarrow \infty, \quad (10.12)$$

where $\bar{\mathbf{y}}_k(T)$ is the corresponding output at the terminal time T driven by $\mathbf{u}_k(t)$.

10.3 A Reliable Docking Control Scheme

With the control problem (10.12) in hand, a docking control scheme aiming for fast and reliable PDR docking is put forward in this section, which is depicted in Fig. 10.2. The control scheme includes two parts:

- (i) Design a TILC controller to achieve the control objective (10.12).
- (ii) Generate a basis function for the designed TILC controller to obtain fast convergence, and to control the docking process.

The generation of the basis function matrix belongs to the preparation stage of docking control, and the designed TILC controller works in the implementation stage of docking control. In the preparation stage, there is no need to consider the complex PDR model directly. The receiver system with SAC (10.13) is considered to get a suitable basis function for the TILC design based on the actual PDR system in the implementation stage. Through the preparation work, a satisfactory basis function can be attained offline before the docking operation. During the implementation stage, the designed TILC controller works in a repetitive and learning way to achieve a successful docking eventually. Based on the established basis function matrix, the TILC controller is simple and easy to apply. The details of the two parts of the proposed docking control scheme will be described in the subsequent sections.

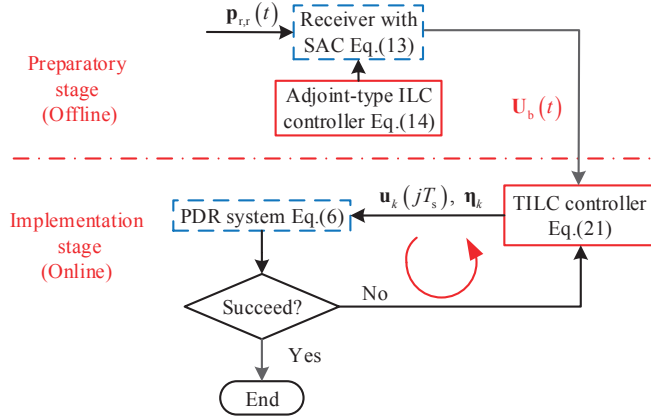


Figure 10.2: A TILC-based reliable docking control scheme.

10.4 Offline Generation of Basis Function

A better basis function leads to a faster convergence for TILC. Since the iterative process of the docking control for PDR is expected to be successfully finished within 2~3 attempts, the basis function $\mathbf{U}_b(t)$ should be carefully selected here. Regarding the selection of the basis function, the common practice is: First, the output profile is parameterized into a polynomial or other functions. Then, the unknown parameters in the proposed function are calculated based on known conditions, which means the output profile is determined. Finally, with the known output profile and a simplified system model, one may obtain the corresponding input which can be used to determine a suitable basis function [243]. In this section, a suitable basis function matrix is chosen by iterative optimization method for better performance. First, a reference docking trajectory $\mathbf{p}_{r,r}(t)$ should be provided. Then, it is aimed to obtain the corresponding reference inputs leading to the given reference docking trajectory $\mathbf{p}_{r,r}(t)$, and the obtained reference inputs make up the desired basis function matrix $\mathbf{U}_b(t)$.

A reference docking trajectory is a reasonable smooth flight trajectory for the receiver to finish the docking task. To this end, the existing work mainly adopts three methods: low-pass filter method [65], polynomial interpolation method [66], terminal guidance method [70]. To establish basis function matrix $\mathbf{U}_b(t)$, a reference output trajectory $\mathbf{p}_{r,r}(t)$ is pre-designed to satisfy the docking requirements of PDR systems and especially to guarantee the terminal docking error. Such a reference output trajectory also needs to give a docking relative velocity of 1~1.5 m/s. The generation of reference docking trajectory is well studied and omitted here.

As mentioned in Section 10.1, ILC is a method to generate inputs that can achieve a perfect tracking of the reference docking trajectory. However, the receiver is nonminimum-phase, so adjoint-type ILC is considered here. For the receiver with SAC

$$\begin{cases} \mathbf{x}_r = \bar{\mathbf{A}}_r \mathbf{x}_r + \mathbf{B}_r \mathbf{u}_r \\ \mathbf{p}_r = \bar{\mathbf{C}}_r \mathbf{x}_r \end{cases}, \quad (10.13)$$

an adjoint-type ILC is designed as

$$\mathbf{u}_{r,k+1} = \mathbf{u}_{r,k} + \alpha_k \mathcal{G}^* (\mathbf{p}_{r,r}(t) - \mathbf{p}_r(t)), \quad (10.14)$$

where $\mathbf{u}_r = [\delta_T \delta_a \delta_e \delta_r]^T$, $\tilde{\mathbf{C}}_r$ is generated from \mathbf{C}_r by removing the last row, \mathcal{G} is the operator of system (10.13), \mathcal{G}^* is the adjoint operator of \mathcal{G} . One can refer to [246] for the selection of α_k and other details. After twenty offline iterations, the actual outputs track the reference docking trajectory completely as shown in Fig. 10.3. The corresponding reference inputs $\delta_{T,r}, \delta_{a,r}, \delta_{e,r}, \delta_{r,r}$ are depicted in Fig. 10.4. Then, the desired basis function matrix is obtained as

$$\mathbf{U}_b(t) = \begin{bmatrix} \delta_{T,r}(t) & 0 & 0 & 0 \\ 0 & \delta_{a,r}(t) & 0 & 0 \\ 0 & 0 & \delta_{e,r}(t) & 0 \\ 0 & 0 & 0 & \delta_{r,r}(t) \end{bmatrix}. \quad (10.15)$$

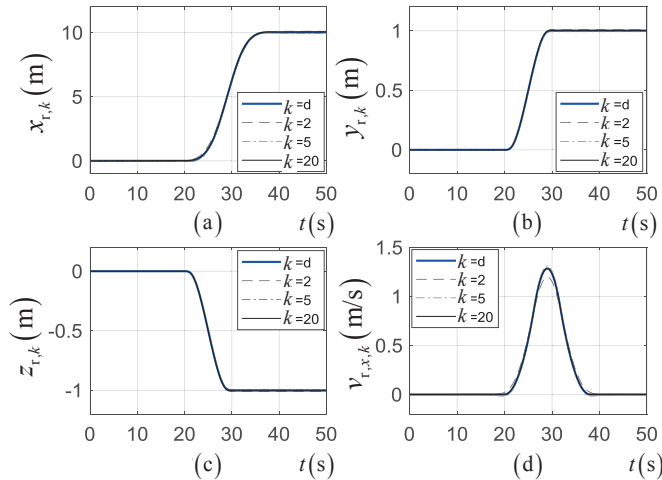


Figure 10.3: Iterative tracking for the given reference docking trajectory $\mathbf{p}_{r,r}(t)$ by the adjoint-type ILC.

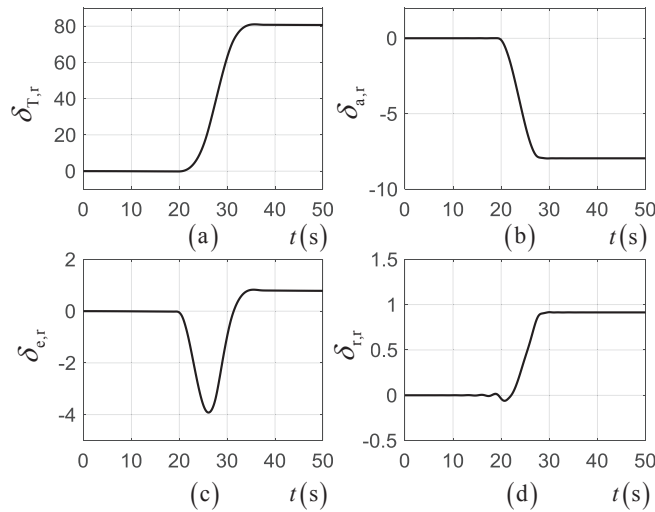


Figure 10.4: Reference inputs leading to the given reference docking trajectory $\mathbf{p}_{r,r}(t)$.

In practice, in the presence of successful docking experiences, one can directly select a prac-

tical docking trajectory as a reference docking trajectory $\mathbf{p}_{r,r}(t)$ and then obtain the corresponding basis function $\mathbf{U}_b(t)$, or select a practical pilots' operation as the basis function $\mathbf{U}_b(t)$.

Until now, the desired basis function matrix $\mathbf{U}_b(t)$ has been generated, namely the preparation work of docking control has been done. Next, a TILC controller based on the generated basis function matrix $\mathbf{U}_b(t)$ is to be designed.

10.5 TILC Controller Design

This section presents the TILC controller design for the MIMO higher-order nonlinear system (10.11) to achieve the control objective (10.12). For most of the time, traditional TILC controllers use the control input or initial state value as their learning object, while a hybrid TILC controller aiming to improve the controller performance by a combined learning object is developed in this paper. Taking the proposed TILC controller into consideration, the overall closed-loop block diagram of a PDR system during the docking process is depicted in Fig. 10.5.

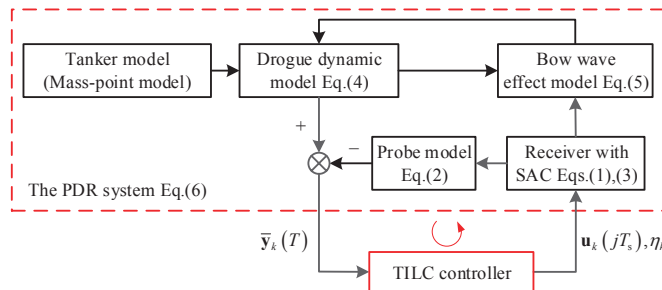


Figure 10.5: Closed-loop system block diagram of a PDR system with the proposed TILC controller.

In general, only partial initial states are controllable, such as, in the docking stage, the initial position of the receiver is controllable. The initial position of the receiver can be changed in every docking attempt to perform a successful docking. According to the state controllability, the initial state can be rewritten as

$$\mathbf{x}_{0,k} = [\boldsymbol{\xi}^T \boldsymbol{\eta}_k^T]^T = \mathbf{M}_1 \boldsymbol{\xi} + \mathbf{M}_2 \boldsymbol{\eta}_k, \quad (10.16)$$

where $\boldsymbol{\xi} \in \mathbb{R}^{19}$ denotes the uncontrollable initial state, and $\boldsymbol{\eta}_k \in \mathbb{R}^3 (\mathbf{p}_r)$ denotes the controllable initial state, which will be utilized in the next iteration; $\mathbf{M}_1 = [\mathbf{I}_{19}^T \mathbf{0}_{3 \times 19}^T]^T$, $\mathbf{M}_2 = [\mathbf{0}_{19 \times 3}^T \mathbf{I}_3^T]^T$. The system whose initial state does not fit the order can be transformed into the form of (10.16) by changing the state order.

The learning control law for system (10.11) is designed as

$$\mathbf{u}_k(t) = \mathbf{U}_b(t) \mathbf{q}_k, \quad (10.17)$$

where $\mathbf{q}_k \in \mathbb{R}^4$ is a constant parameter vector, $\mathbf{U}_b(t) \in \mathbb{R}^{4 \times 4}$ is a diagonal basis function matrix, which has been generated in the last section.

Because the combination of the control input and initial state value is chosen as the learning

object, the learning update law of \mathbf{q}_k and $\boldsymbol{\eta}_k$ is proposed as

$$\begin{bmatrix} \mathbf{q}_k \\ \boldsymbol{\eta}_k \end{bmatrix} = \begin{bmatrix} \mathbf{q}_{k-1} \\ \boldsymbol{\eta}_{k-1} \end{bmatrix} + \begin{bmatrix} \mathbf{L}_1 \\ \mathbf{L}_2 \end{bmatrix} \mathbf{e}_{k-1}(T), \quad (10.18)$$

where $\mathbf{L}_1 \in \mathbb{R}^{4 \times 3}$, $\mathbf{L}_2 \in \mathbb{R}^{3 \times 3}$ are constant parameter matrices, $\mathbf{e}_k(T) \triangleq \bar{\mathbf{y}}_d(T) - \bar{\mathbf{y}}_k(T)$ is the docking error. Then, the following theorem provides the convergence condition of the designed controller including Eqs. (10.17) and (10.18).

Theorem 1. For system (10.11), suppose that i) *Assumptions 1-3* are satisfied; ii) the control law and update law of TILC are designed as Eq. (10.17) and Eq. (10.18), respectively. If the following inequality

$$\alpha + \gamma < 1 \quad (10.19)$$

holds, then the docking error

$$\|\mathbf{e}_k(T)\| \rightarrow \frac{\varepsilon}{1 - \alpha - \gamma} \quad (10.20)$$

as $k \rightarrow \infty$, where

$$\begin{aligned} \alpha &= \left\| \mathbf{I}_3 - \bar{\mathbf{C}} \mathbf{M}_2 \mathbf{L}_2 - \int_0^T \bar{\mathbf{C}} \mathbf{B} \mathbf{U}_b(\tau) \mathbf{L}_1 d\tau \right\|, \\ \gamma &= \int_0^T \left(\|\bar{\mathbf{C}} \mathbf{A}\| + l_{\phi} \|\bar{\mathbf{C}}\|^2 \right) \beta(\tau) d\tau, \\ \beta(t) &= \|\mathbf{M}_2 \mathbf{L}_2\| e^{(\|\mathbf{A}\| + l_{\phi} \|\bar{\mathbf{C}}\|)t} + \int_0^t e^{(\|\mathbf{A}\| + l_{\phi} \|\bar{\mathbf{C}}\|)(t-\tau)} \|\mathbf{B} \mathbf{U}_b(\tau) \mathbf{L}_1\| d\tau, \\ \varepsilon &= DT \|\bar{\mathbf{C}}\| + \int_0^T \left(\|\bar{\mathbf{C}} \mathbf{A}\| + l_{\phi} \|\bar{\mathbf{C}}\|^2 \right) DT e^{(\|\mathbf{A}\| + l_{\phi} \|\bar{\mathbf{C}}\|)\tau} d\tau. \end{aligned}$$

Moreover, if there is no atmospheric turbulence disturbance, namely $D = 0$, $\varepsilon = 0$, then $\|\mathbf{e}_k(T)\| \rightarrow 0$.

Proof. Refer to Appendix A. \square

Because of the introduction of basis function matrix $\mathbf{U}_b(t)$, the iterative learning object is transformed from the control input $\mathbf{u}_k(t)$ to a parameter vector \mathbf{q}_k , which makes the controller implementation simpler. Besides, because the basis function matrix $\mathbf{U}_b(t)$ is generated by using adjoint-type ILC to solve the nonminimum-phase problem in Section 10.4, the designed TILC control law (10.17) can apply to the PDR system with nonminimum-phase feature.

As the real PDR system is computer-controlled, a sampled-data controller is preferred, which can be obtained by discretizing the designed continuous controller. According to the controller emulation design [247], a continuous-time controller is first designed based on the continuous-time plant model (6). Then, the obtained continuous-time controller is discretized according to the sampling period T_s .

For the proposed continuous-time terminal iterative controller (10.17), (10.18), controller discretization is relatively easy. Because \mathbf{q}_k , $\boldsymbol{\eta}_k$, \mathbf{L}_1 , \mathbf{L}_2 , $\mathbf{e}_k(T)$ are all constant matrices or vectors, only the basis function $\mathbf{U}_b(t)$ needs to be discretized to $\mathbf{U}_b(jT_s), j = 0, 1, \dots, N, T = NT_s$. Furthermore, the basis function $\mathbf{U}_b(t)$ is established in the preparatory stage and remains

unchanged in the implementation stage, thus it can be directly discretized by sampling. The final sampled-data controller is the N-sample sequence of the control input as follows

$$\begin{aligned} \mathbf{u}_k(jT_s) &= \mathbf{U}_b(jT_s) \mathbf{q}_k, \\ \begin{bmatrix} \mathbf{q}_k \\ \boldsymbol{\eta}_k \end{bmatrix} &= \begin{bmatrix} \mathbf{q}_{k-1} \\ \boldsymbol{\eta}_{k-1} \end{bmatrix} + \begin{bmatrix} \mathbf{L}_1 \\ \mathbf{L}_2 \end{bmatrix} \mathbf{e}_{k-1}(T), \end{aligned} \quad (10.21)$$

Genetic algorithm (GA) is a little bit similar to TILC, because they both work in an iterative way. However, they have different origins, different definitions, and different applications. GA is a metaheuristic inspired by the process of natural selection that belongs to the larger class of evolutionary algorithms (EA). Genetic algorithms are commonly used to generate high-quality solutions to optimization and search problems by relying on bio-inspired operators such as mutation, crossover, and selection. The iterative convergence speed of TILC is much higher than GA. This makes TILC a better method for PDR because the iterative process of the docking control for PDR is expected to be successfully finished within 2~3 attempts [241]. Moreover, GA is related to probability, but that is not the case for TILC. There is also a connection between them in that GA can be used to determine the optimal TILC controller parameters.

10.6 Simulation

In this section, the feasibility and the performance of the proposed TILC-based control scheme are investigated through the simulation.

10.6.1 Simulation configuration

A MATLAB/SIMULINK based simulation environment with 3D virtual-reality display has been developed by the authors' research lab to simulate the docking stage of PDR. The detailed information about the modeling procedure, model parameters, and simulation environment can refer to our previous works in [40, 44]. Noteworthy, although the drogue dynamics (10.4) is considered in the controller design, the link-connected model of the hose-drogue system is adopted in the simulation environment. A hose-drum unit (HDU) is also included to improve the fitness of the simulation model. Moreover, the actuator dynamics of the aircraft is also considered.

The TILC controller parameters used in this paper are set as

$$\mathbf{q}_1 = \begin{bmatrix} 1 \\ 1 \\ 1 \\ 1 \end{bmatrix}, \mathbf{L}_1 = \begin{bmatrix} 0.1 & 0 & 0 \\ 0 & -0.4 & 0 \\ 0 & 0 & -1 \\ 0 & 14 & 0 \end{bmatrix}, \mathbf{L}_2 = \begin{bmatrix} 0.3 & 0 & 0 \\ 0 & 0.4 & 0 \\ 0 & 0 & 0.4 \end{bmatrix}.$$

The values for $\mathbf{L}_1, \mathbf{L}_2$ used in this paper are selected by manual tuning, in which the physical meaning of position error feedforward can be utilized. Some other optimization methods, for example, genetic algorithm (GA), ant colony algorithm (ACA), and machine learning can be

used to obtain optimal parameters for the proposed controllers. These methods are powerful but time-consuming. Furthermore, the optimal parameter may not be achievable in practice because the full accurate knowledge about the model is not available. The video of the docking control performance by using the proposed control scheme can be viewed online [248].

10.6.2 Basic simulation

First, traditional TILC controllers which use control inputs or initial state values as their learning objects are considered for comparison. By letting $\mathbf{q}_1 = [1 \ 1 \ 1]^T$, $\mathbf{L}_1 = [0.1 \ 0 \ 0; 0 \ -0.4 \ 0; 0 \ 0 \ -1; 0 \ 14 \ 0]$, $\mathbf{L}_2 = \mathbf{0}_{3 \times 3}$, the TILC controller with control input learning (Controller 2) is obtained. By letting $\mathbf{q}_1 = [1 \ 1 \ 1 \ 1]^T$, $\mathbf{L}_1 = \mathbf{0}_{4 \times 3}$, $\mathbf{L}_2 = \text{diag}(0.9, 0.5, 0.5)$, the TILC controller with the initial value learning (Controller 3) is obtained. The convergence of the terminal docking error for the proposed hybrid TILC controller (Controller 1) and the two traditional TILC controllers is compared in Fig. 10.6, from which one can see that the convergence speed of the three controllers can be ordered as: Controller 1 > Controller 2 > Controller 3. It is consistent with the theoretical analysis that the hybrid TILC controller with both control input learning and initial value learning has the best convergence property. As iteration number k increases, the terminal docking errors decrease. A successful docking can be achieved at the second docking attempt, which meets the docking requirements of the PDR system.

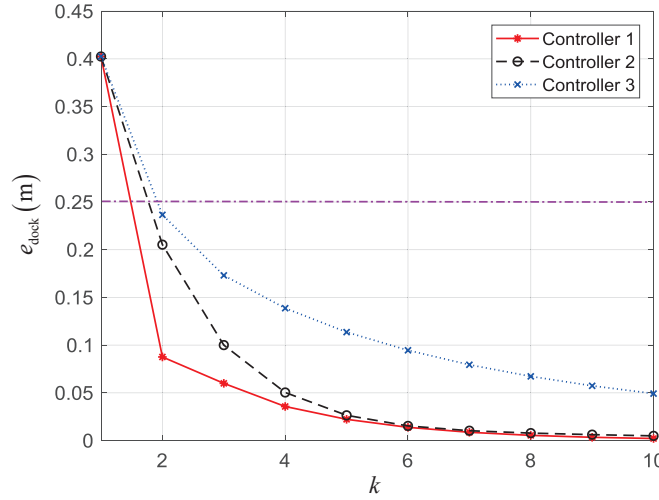


Figure 10.6: Comparison of the convergence of the terminal docking error between the proposed TILC controller (controller 1) and two traditional TILC controllers. (Since $r_d = 0.305\text{m}$ as shown in Fig. 10.1, a docking attempt is regarded as successful if the docking error is less than 0.25m here.)

In the following, the simulation verification for the proposed hybrid TILC controller will be focused on. The iterative process of the system outputs is displayed in Fig. 10.7, which shows that the change of initial position incurs a trajectory translation during the first half (before the 20s). While in the second half, not just a trajectory translation effect is incurred because of the system nonlinearity and the change of control inputs. Actually, the docking terminates at $t_{end} = 30\text{s}$, and it is for a better display to give the later outputs in the 30 ~ 50s. It also can be seen that the drogue

deviates from the equilibrium position under the bow wave effect when the receiver approaches the drogue. It is demonstrated in Fig. 10.7(d) that the docking relative velocity stays around -1.25 m/s at the docking moment. Because a good basis function is selected, the velocity overshoot is small. The final successful three-dimension docking trajectory is illustrated in Fig. 10.8. The probe successfully docks into the drogue in the end, and the solid red line shows the motion of the moving drogue.

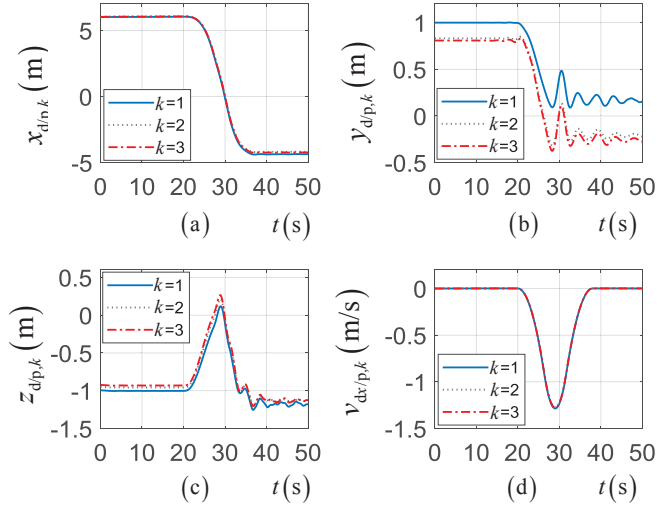


Figure 10.7: The iteration of the relative position and relative velocity between the drogue and the probe during the docking process.

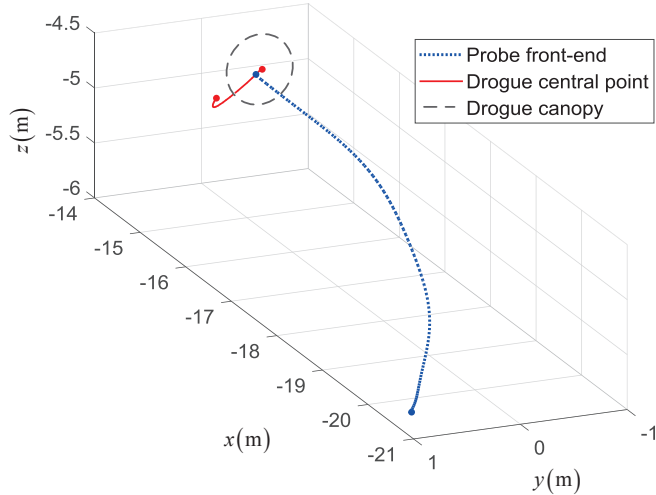


Figure 10.8: A successful three-dimension docking trajectory of the probe and the drogue.

10.6.3 Simulation with uncertainties and disturbances

In this part, in order to evaluate the robustness of the proposed hybrid TILC controller, the following system uncertainties and disturbances are considered:

- (i) Add uncertainties to actuators by multiplying actuator inputs by a factor of 0.6, 0.8, 1.2, 1.4, respectively.

- (ii) Change the actual bow wave effect to 1.2 times of the modeled bow wave effect.
- (iii) Add a side wind disturbance to the atmospheric environment.
- (iv) Add the Dryden wind-turbulence model to the PDR system.

Noteworthy, the uncertainties (i), (ii) and disturbance (iii) are repetitive, while the disturbance (iv) is stochastic and non-repetitive. The aforementioned four changes just apply to the plant, while controller design is still based on the model built previously. Based on the uncertainties and disturbances (i), (ii), (iii) and (iv), three scenarios are considered.

Scenario 1: Only the uncertainty (i) is considered.

Scenario 2: The actuator uncertainty factor is fixed to 0.6, and the uncertainties and disturbances (ii), (iii) are also considered.

Scenario 3: The actuator uncertainty factor is fixed to 0.6, and the uncertainties and disturbances (ii), (iii), (iv) are all considered.

Under these scenarios, the convergence of the terminal docking error of the proposed TILC controller is depicted in Figs. 10.9-10.10. Fig. 10.9 shows that the convergence speed of the proposed TILC controller decreases when there exist actuator uncertainties. The bigger the actuator uncertainty is, the more the convergence speed decreases. Fig. 10.10 shows that the docking error of the proposed TILC controller can still converge to zero when there exist the uncertainties and disturbances (i), (ii), (iii), which are repetitive. When there also exists the stochastic uncertainty (iv), the docking error cannot converge to zero, but it is bounded. The proposed TILC controller can achieve successful docking at the third attempt, which illustrates that the proposed controller can guarantee the docking performance under these uncertainties and disturbances.

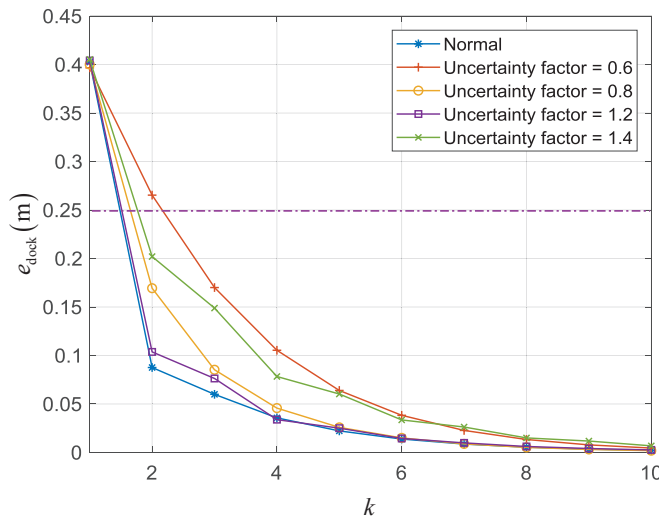


Figure 10.9: Convergence of the terminal docking error when there exist actuator uncertainties (Scenario 1).

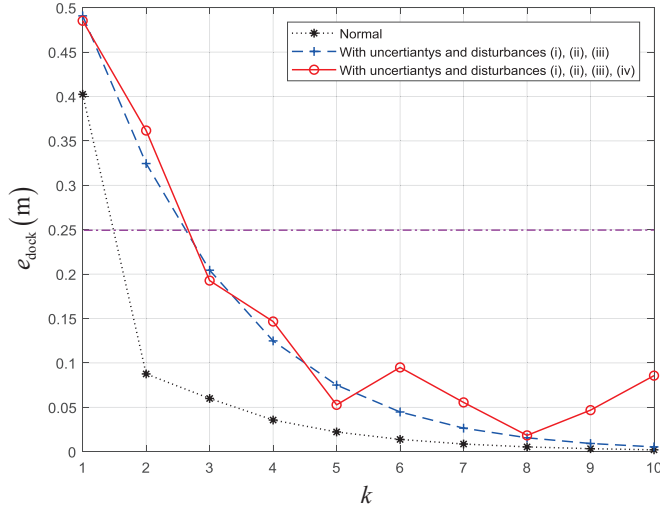


Figure 10.10: Convergence of the terminal docking error when there exist uncertainties and uncertainties (Scenario 2 and Scenario 3).

10.6.4 Discussion

The simulation exhibits favorable results. The proposed TILC controller does not adopt real-time tracking method to track the moving drogue, so the problem of the “slow dynamics” to track the “fast dynamics” is solved. Because a good basis function matrix is constructed in the preparation stage, the overshoot at the docking moment is under control. Additionally, TILC is basically model-free and robust, which can achieve successful docking without knowing the drogue dynamics and the bow wave model. The proposed controller can also provide successful docking in the presence of system uncertainties and disturbances. These make the docking process safer and more reliable.

10.7 Chapter Summary

With the aim of achieving precise docking for the PDR system, a reliable control scheme with a TILC docking control method is proposed to make the receiver contact with the nonstationary drogue. The combination of control inputs and initial state values is chosen as the learning object of TILC, and the convergence condition is derived. The simulation results illustrate that the docking precision is guaranteed after a few iteration cycles. Compared with two traditional TILC controllers, the proposed hybrid TILC controller gives the highest convergence speed.

Chapter 11 Image-Based Visual Servo Docking Control

Autonomous aerial refueling (AAR) can effectively increase the combat range of aircraft, which is crucial to the future development of long-endurance aircraft. However, AAR has a high accident rate, and it has become increasingly urgent to design efficient and safe methods or algorithms for solving AAR problems. The probe-and-drogue refueling (PDR) system is considered simpler, lighter, and more easy-to-install than other aerial refueling systems. However, the docking difficulty of PDR is high. Apart from the various aerodynamic disturbances, another problem is the pose estimation error caused by the camera installation error, calibration error, and/or 3D object modeling error, which may violate the highly accurate docking requirement. This paper aims to implement an image-based visual servo control method for the AAR docking control problem. The corresponding image-based visual servo controller is designed after the establishment of an image-based visual servo model involving the receiver's dynamics. Simulation results indicate that the proposed method can make the system dock successfully under complicated environments and meanwhile improve the robustness against pose estimation error.

11.1 INTRODUCTION

Autonomous aerial refueling (AAR) can effectively increase the combat range of unmanned aerial vehicles (UAVs), which is crucial to the future development of long-endurance aircraft. [152]. The probe-and-drogue refueling (PDR) system is considered simpler, lighter, and more easy-to-install than other aerial refueling systems. However, the control problem of PDR is more complicated than other aerial refueling methods. The drogue is susceptible to aerodynamic disturbances in PDR because of the flexibility of the hose-drogue assembly [249–251]. Moreover, PDR calls for high-precision requirements of the relative ‘tanker-receiver’ or ‘drogue-probe’ position and orientation during the docking stage. Therefore, it is challenging to design a reliable and robust docking controller for the receiver aircraft.

Various sensing technologies have been employed in PDR, including the global positioning system (GPS), inertial navigation systems, electro-optical systems, etc. [249, 252]. Although these sensors can be adopted for autonomous aerial docking, they all have limitations in practice. For instance, the receiver's GPS signals might be unavailable when shadowed or distorted by the tanker. In recent years, machine vision technologies have been proposed to complement these technologies [161]. Some vision-based navigation systems can be found in Refs. [238, 252, 253]. Ref. [254] combined the GPS navigation system with vision systems. Ref. [255] adopted GPS

navigation when the probe is far from the drogue and adopted bionic visual navigation for close-range situations.

With the development of visual navigation systems, visual servo control has become increasingly popular in AAR. The existing visual servo control schemes are classified as position-based visual servos (PBVS) and image-based visual servos (IBVS). The main difference between PBVS and IBVS is how the features are designed. In PBVS, the features are 3D parameters, for example, the pose of the camera relative to some coordinate frames, which must be calculated from image information [256–258]. The most commonly-used method is to deploy marks on the parachute part of a drogue by using infrared light emitting diodes (LEDs) [253], and then use the Gaussian least-square-differential-correction (GLSDC) algorithm [238] or a deep learning method [45, 259] to obtain relative pose. In IBVS, the features consist of 2D features that are immediately available from the image information [256]. The visual servo control method has been applied to AAR systems by many researchers [67, 68, 79, 255]. Ref. [79] designed a docking controller based on sliding mode control and backstepping design after precise pose estimation by visual navigation methods. Moreover, control methods like iterative learning control [41, 87] and fault-tolerant control [68] have also received much attention. These studies mainly focus on pose estimation methods and corresponding controller design to provide the relative ?tanker-receiver? and ?drogue-probe? position and achieve a robust and safe approach and docking.

On the whole, there still exist some challenges in visual servo control for PDR. First, the system model of the PDR docking is complicated. The hose is flexible, and whose motion is easily affected by disturbances. Besides, there are complex disturbances during the docking process. For example, the bow wave disturbance around the receiver nose is state-dependent and nonlinear [250, 251]. Moreover, it should be noted that a high-precision 2D image observation does not imply a high-precision pose estimation due to the camera installation error, calibration error, and/or 3D object modeling error [260]. Existing works [41, 68, 79, 87] are mainly based on PBVS, where a high-precision 3D pose estimation is crucial since it appears that both the pose estimation error and the interaction matrix need to be regulated to zero. Coarse estimation will not only cause perturbations on the trajectory realized but will also affect the accuracy of the pose reached.

A reliable docking control method based on IBVS for PDR is proposed in this paper to cope with the challenges mentioned above. Compared with PBVS, in IBVS, 2D image error is used to control the receiver to reach its desired pose directly and make the probe dock with the drogue indirectly. What is more, the linear quadratic regulator (LQR) method is used here to reject various disturbances and uncertainties, including the bow wave effect. The main contributions of this paper are as follows.

- An IBVS model is established, which describes the relationship between image errors and the camera's linear and angular velocities, and the relationship between the camera's



motion and the receiver's motion.

- An inner-and-outer-loop controller is designed. The outer-loop control makes the 2D image error converge to zero, and the inner-loop control uses the LQR method to get the optimal inputs while rejecting disturbances. The proposed control method is robust against the pose estimation error.
- Simulations are carried out to prove the validity of the proposed IBVS controller subject to aerodynamic disturbances and bow wave disturbances. Besides, a comparison is made between IBVS and PBVS subject to the pose estimation error.

This paper is organized as follows. The system description and problem statement are introduced in Sec. II. In Sec. III, the main algorithm of IBVS docking control is described. Then, simulations are presented in Sec. IV. Finally, Sec. V concludes the paper.

11.2 System Description and Problem Formulation

In order to describe the PDR docking control problem, basic coordinate frames, aircraft models, and the camera pinhole model are first introduced. Then, the visual servo control problem is formulated.

11.2.1 PDR system model at the docking stage

The PDR docking control is to control the receiver aircraft to approach the tanker and then make the probe tip dock with the drogue. There are five commonly-used coordinate frames when establishing the PDR system model at the docking stage, which are the ground coordinate frame ($o_gx_gy_gz_g$), the receiver coordinate frame ($o_rx_ry_rz_r$), the tanker coordinate frame ($o_tx_ty_tz_t$), the camera coordinate frame ($o_cx_cy_cz_c$) and the reference coordinate frame ($o_{re}x_{re}y_{re}z_{re}$), which are shown in Fig. 11.1. Noteworthy, the origin of the reference coordinate frame coincides with that of the tanker coordinate frame, and its coordinate axis direction is consistent with the camera coordinate frame. The relative position and attitude between the drogue and the probe are mainly concerned in the docking phase, where the tanker frame (a moving inertial frame) is more convenient for modeling and analysis than the ground frame (a fixed inertial frame). In order to further simplify the coordinate transformation among different coordinate frames, the direction of the axis o_gx_g of the ground frame is selected the same as the horizontal moving direction of the tanker. Besides, $\mathbf{R}_{r/t}$ denotes the *rotation matrix* to describe the angular relationship of the receiver frame “r” relative to the tanker frame “t”. The symbolic operation rules here are defined as

$$\begin{cases} \mathbf{R}_{i/j}\mathbf{x}_k^j = \mathbf{x}_k^i \\ \mathbf{x}_i^j - \mathbf{x}_k^j = \mathbf{x}_i^k \end{cases}$$

where i, j or k denotes a coordinate system that \mathbf{x} is in when it is superscript or denotes an object that \mathbf{x} belongs to when it is subscript. For instance, V_t^g is the forward flight velocity of the tanker

in the ground frame and \mathbf{p}_c^r is the position vector of the camera in the receiver frame, which are illustrated in Fig. 11.1. Refer to Ref. [251] for more information about these coordinate frames.

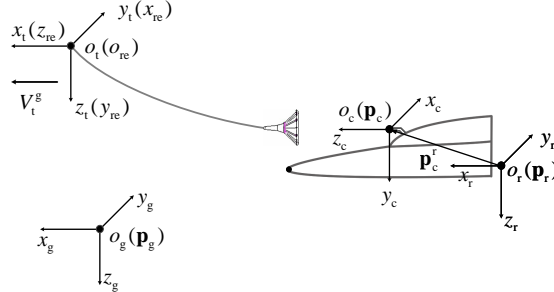


Figure 11.1: Coordinate frames used in the PDR docking process

During the docking stage, the receiver performs a level flight. Motion equations of the receiver [172] under the tanker coordinate frame are decoupled into a longitudinal motion that does not depend on lateral states

$$\left\{ \begin{array}{l} \dot{x}_r = V_r^g \cos(\theta - \alpha) \\ \dot{h}_r = V_r^g \sin(\theta - \alpha) \\ \dot{\theta} = q \\ \dot{V}_r^g = T \cos \alpha / m - D / m - g (\cos \alpha \sin \theta - \sin \alpha \cos \theta) \\ \dot{\alpha} = -T \sin \alpha / m V_r^g - L / m V_r^g + q \\ \quad + g (\sin \alpha \sin \theta + \cos \alpha \cos \theta) / V_r^g \\ \dot{q} = c_7 \bar{M} \end{array} \right. \quad (11.1)$$

and the corresponding lateral motion

$$\left\{ \begin{array}{l} \dot{y}_r = V_r^g \cos(\theta - \alpha) \sin(\psi + \beta) \\ \dot{\psi} = (q \sin \phi + r \cos \phi) / \cos \theta \\ \dot{\phi} = p + \tan \theta (q \sin \phi + r \cos \phi) \\ \dot{\beta} = \bar{Y} / m V_r^g + p \sin \alpha - r \cos \alpha \\ \dot{p} = (c_1 r + c_2 p) q + c_3 \bar{L} + c_4 N \\ \dot{r} = (c_8 p - c_2 r) q + c_4 \bar{L} + c_9 N \end{array} \right. \quad (11.2)$$

where the lift, drag, and thrust forces, the roll, pitch, and yaw moments, and the aerodynamic side force are denoted by L , D , T , \bar{L} , \bar{M} , N , and \bar{Y} , respectively. Besides, c_1 - c_9 denote the inertia moment and inertia product components. Eqs. (13.1) and (13.2) can be simply represented as

$$\dot{\mathbf{x}}_r = \mathbf{f}(\mathbf{x}_r, \mathbf{u}_r) \quad (11.3)$$

where $\mathbf{x}_r = [x_r \ y_r \ h_r \ \phi \ \theta \ \psi \ V_r^g \ \alpha \ \beta \ p \ q \ r]^T$ denotes the receiver's state, which comprises position, Euler angles, speed, aerodynamic angles, and angular rates. The vector $\mathbf{u}_r = [\delta_t \ \delta_e \ \delta_a \ \delta_r]^T$ denotes the control input, which comprises the throttle, elevator, aileron, and rudder inputs.

It is challenging to design a control law directly for the decoupled nonlinear models (13.1)

and (13.2), so it is necessary to linearize and simplify the nonlinear models accordingly. Trimming should be considered before linearizing to obtain the equilibrium point of the nonlinear models by balancing the aerodynamic forces and moments of the receiver in a certain state. The process of trimming is to solve the trim states and inputs of Eq. (13.3). In general, trim conditions can be expressed as

$$\dot{\mathbf{x}}_r^* = \mathbf{f}(\mathbf{x}_r^*, \mathbf{u}_r^*) \quad (11.4)$$

where \mathbf{x}_r^* denotes the trim state and \mathbf{u}_r^* denotes the trim input. Here, the trim conditions are selected with respect to the state of the tanker $\mathbf{v}_t^* = [V_t^g \ 0 \ 0]^T$, and the results can be calculated by the numerical method [261].

As for the nonlinear model $\dot{\mathbf{x}}_r = \mathbf{f}(\mathbf{x}_r, \mathbf{u}_r)$, under the equilibrium point $(\mathbf{x}_r^*, \mathbf{u}_r^*)$, define $\tilde{\mathbf{x}}_r \triangleq \mathbf{x}_r - \mathbf{x}_r^*$ and $\tilde{\mathbf{u}}_r \triangleq \mathbf{u}_r - \mathbf{u}_r^*$. Then, by using Taylor series expansion at the equilibrium point and retaining only the primary term, the linear model of the receiver is obtained as

$$\dot{\tilde{\mathbf{x}}}_r = \mathbf{A}\tilde{\mathbf{x}}_r + \mathbf{B}\tilde{\mathbf{u}}_r \quad (11.5)$$

where $\mathbf{A} = \frac{\partial \mathbf{f}(\mathbf{x}_r, \mathbf{u}_r)}{\partial \mathbf{x}_r} |_{\mathbf{x}_r=\mathbf{x}_r^*, \mathbf{u}_r=\mathbf{u}_r^*}$, $\mathbf{B} = \frac{\partial \mathbf{f}(\mathbf{x}_r, \mathbf{u}_r)}{\partial \mathbf{u}_r} |_{\mathbf{x}_r=\mathbf{x}_r^*, \mathbf{u}_r=\mathbf{u}_r^*}$. Furthermore, according to Eq. (13.5), the decoupled models (13.1) and (13.2) become

$$\begin{cases} \dot{\tilde{\mathbf{x}}}_{rlon} = \mathbf{A}_{rlon}\tilde{\mathbf{x}}_{rlon} + \mathbf{B}_{rlon}\tilde{\mathbf{u}}_{rlon} \\ \dot{\tilde{\mathbf{x}}}_{rlat} = \mathbf{A}_{rlat}\tilde{\mathbf{x}}_{rlat} + \mathbf{B}_{rlat}\tilde{\mathbf{u}}_{rlat} \end{cases} \quad (11.6)$$

where $\tilde{\mathbf{u}}_{rlon} = [\tilde{\delta}_a \ \tilde{\delta}_r]^T$, $\tilde{\mathbf{u}}_{rlat} = [\tilde{\delta}_e \ \tilde{\delta}_t]^T$, $\tilde{\mathbf{x}}_{rlon} = [\tilde{x}_r \ \tilde{h}_r \ \tilde{\theta} \ \tilde{V}_r^g \ \tilde{\alpha} \ \tilde{q}]^T$ and $\tilde{\mathbf{x}}_{rlat} = [\tilde{y}_r \ \tilde{\psi} \ \tilde{\phi} \ \tilde{\beta} \ \tilde{p} \ \tilde{r}]^T$. Here, the subscripts “rlon” and “rlat” refer to the longitudinal and lateral channels of the receiver, respectively. Besides, \mathbf{A}_{rlon} , \mathbf{A}_{rlat} , \mathbf{B}_{rlon} , \mathbf{B}_{rlat} are known time-invariant matrices with appropriate dimensions.

11.2.2 Camera Pinhole Model

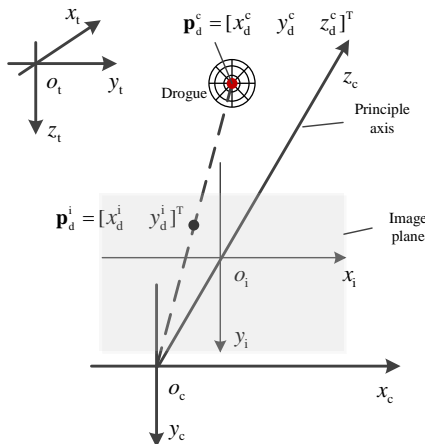


Figure 11.2: Camera pinhole model. $o_t x_t y_t z_t$ is the tanker coordinate frame; $o_c x_c y_c z_c$ is the camera coordinate frame; $o_i x_i y_i$ is the image coordinate frame.

Assume that a vector $\mathbf{p}_d^i = [x_d^i \ y_d^i]^T$ is in the image coordinate system $o_i - x_i y_i$. \mathbf{p}_d^c and \mathbf{p}_d^t

can be transformed to \mathbf{p}_d^i by using the camera pinhole model [255, 262] (see Fig. 11.2) as follows

$$s \begin{bmatrix} x_d^i \\ y_d^i \\ 1 \end{bmatrix} = \begin{bmatrix} \alpha_x & 0 & u_0 & 0 \\ 0 & \alpha_y & v_0 & 0 \\ 0 & 0 & 1 & 0 \end{bmatrix} \begin{bmatrix} x_d^c \\ y_d^c \\ z_d^c \\ 1 \end{bmatrix} = \mathbf{M} \begin{bmatrix} \mathbf{R}_t^c & \mathbf{t}_t^c \\ 0 & 1 \end{bmatrix} \begin{bmatrix} x_d^t \\ y_d^t \\ z_d^t \\ 1 \end{bmatrix} \quad (11.7)$$

and

$$\mathbf{M} = \begin{bmatrix} \alpha_x & 0 & u_0 \\ 0 & \alpha_y & v_0 \\ 0 & 0 & 1 \end{bmatrix} \quad (11.8)$$

where s in (11.7) is the scaling factor. $\mathbf{R}_t^c \in \mathbf{R}^{3 \times 3}$ is the rotation matrix from the tanker frame to the camera frame, and $\mathbf{t}_t^c \in \mathbf{R}^3$ is the translation vector from the tanker frame to the camera frame. \mathbf{M} is the camera intrinsic matrix, and its elements α_x , α_y , u_0 and v_0 are determined by camera calibration [251].

In the PBVS control, the position information of the drogue $\mathbf{p}_d^t = [x_d^t \ y_d^t \ z_d^t]^T$ needs be obtained based on the relationship described in Eq. (11.7), and the detailed calculation procedure can be found in [262]. If there exist pointing errors of the camera, $\mathbf{R}_t^c \in \mathbf{R}^{3 \times 3}$ will be incorrect. If there exist installation position errors of the camera, $\mathbf{t}_t^c \in \mathbf{R}^3$ will be incorrect. As a result, the obtained position information of the drogue will be incorrect, which will affect the control performance of the PBVS control. On the contrary, the IBVS control adopts image information $\mathbf{p}_d^i = [x_d^i \ y_d^i]^T$ rather than position information to design a docking controller, which is more robust against the pose estimation error.

11.2.3 Problem Formulation

In this paper, the situation is considered that a forward-looking monocular camera is mounted on the probe tip of the receiver. The drogue image is the emphasis in the visual servo control for PDR. Define the coordinate of the drogue center in the camera coordinate frame as $\mathbf{p}_d^c = [x_d^c \ y_d^c \ z_d^c]^T$, which is projected in the image as a 2D point with coordinates $\mathbf{p}_d^i = [x_d^i \ y_d^i]^T$ as shown in Fig. 11.2. The image tracking error is defined as

$$\mathbf{e} = \begin{bmatrix} e_x \\ e_y \end{bmatrix} = \begin{bmatrix} x_d^i - x_o^i \\ y_d^i - y_o^i \end{bmatrix} \quad (11.9)$$

where (x_o^i, y_o^i) is the convergence point of the drogue image, which is the origin of the image frame here.

Besides, the docking depth z_d^c , as shown in Fig. 11.3, is the position difference between the camera and the plane of the drogue center (where LEDs are installed) along the z_c axis. After the image tracking error converges to zero, in order to achieve a successful docking, the docking depth z_d^c also needs to be controlled to zero, meanwhile ensuring the docking velocity within the required range 1-1.5m/s [241] at the docking moment.

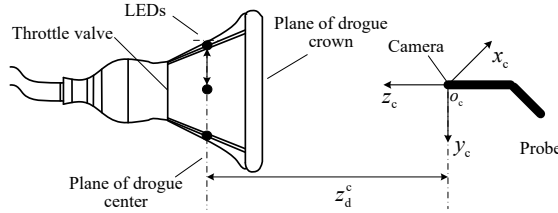


Figure 11.3: Schematic diagram of docking depth.

In image-based visual servo, except for the image tracking error, the docking depth must be obtained. Laser distance measuring technology is commonly adopted [263]. In this study, the docking depth is acquired using the pinhole imaging principle [262]. According to the pinhole imaging principle, one has

$$\frac{R_{\text{dr}}}{z_d^c} = \frac{r}{f} \quad (11.10)$$

where R_{dr} is the actual drogue radius, r is the drogue radius in the image, f is the focal length of the adopted monocular camera. Thus, the docking depth is determined as

$$z_d^c = \frac{R_{\text{dr}} f}{r} \quad (11.11)$$

On the whole, after the camera data processing, one can obtain the spatial errors e_x , e_y and the docking depth z_d^c , which will be used in the feedback controller design later.

Before proceeding further, four assumptions are made in the following.

Assumption 1. The visual tracking module of the receiver can accurately capture the drogue's central coordinate \mathbf{p}_d^i from images in real time.

Assumption 2. The tanker is in a steady flight during the entire docking process, while the receiver keeps a certain distance relative to the tanker with the trim state $\mathbf{v}_r^* = \mathbf{v}_t^*$.

Assumption 3. During the docking process, the pitch, roll, and yaw angles of the receiver are small.

Assumption 4. The camera installation position coincides with the probe tip, as shown in Fig. 11.1. The transformation matrix from the tanker coordinate frame to the camera coordinate frame is

$$\mathbf{R}_{c/t} = \begin{bmatrix} 0 & 1 & 0 \\ 0 & 0 & 1 \\ 1 & 0 & 0 \end{bmatrix}. \quad (11.12)$$

Based on Assumptions 1-4, the *Visual Servo Control Problem* for the PDR docking is to design a proper control input $\tilde{\mathbf{u}}_r = [\tilde{\delta}_a \tilde{\delta}_r \tilde{\delta}_e \tilde{\delta}_t]^T$ for system (13.6) to make the image tracking error converge to zero ($\mathbf{e}(t) \rightarrow 0$) as $t \rightarrow \infty$ and the depth error converge to zero ($z_d^c(t) \rightarrow 0$) slower than ($\mathbf{e}(t) \rightarrow 0$).

11.3 IBVS controller design

In this section, an IBVS model with a forward-looking monocular camera mounted on the receiver is established, which describes the relationship between image errors and the camera's linear and angular velocities, and the relationship between the camera's motion and the receiver's motion. Besides, based on the obtained model, an IBVS controller is designed.

11.3.1 Outer-loop visual servo model based on the Jacobian matrix

By applying the basic equation of IBVS [256] in the PDR system, the relationship between $\dot{\mathbf{e}}$ and \mathbf{v}_d^c , ω_d^c is

$$\dot{\mathbf{e}} = \underbrace{\begin{bmatrix} -\frac{1}{z_d^c} & 0 & \frac{x_d^i}{z_d^c} & x_d^i y_d^i & -(1 + x_d^i)^2 & y_d^i \\ 0 & -\frac{1}{z_d^c} & \frac{y_d^i}{z_d^c} & 1 + y_d^i)^2 & -x_d^i y_d^i & -x_d^i \end{bmatrix}}_{\mathbf{L}} \begin{bmatrix} v_{d,x}^c \\ v_{d,y}^c \\ v_{d,z}^c \\ \omega_{d,x}^c \\ \omega_{d,y}^c \\ \omega_{d,z}^c \end{bmatrix} \quad (11.13)$$

where $\mathbf{L} \in \mathbb{R}^{2 \times 6}$ is the Jacobian matrix, $\mathbf{u}_d^c = [\mathbf{v}_d^c]^T [\omega_d^c]^T]^T$ with $\mathbf{v}_d^c = [v_{d,x}^c \ v_{d,y}^c \ v_{d,z}^c]^T = \mathbf{v}_d^t - \mathbf{v}_c^t = \mathbf{v}_d^{\text{re}} - \mathbf{v}_c^{\text{re}}$ and $\omega_d^c = [\omega_{d,x}^c \ \omega_{d,y}^c \ \omega_{d,z}^c]^T$ are the drogue velocity and angular velocity in the camera coordinate frame. Specially, $\mathbf{v}_c^{\text{re}} = [v_{c,x}^{\text{re}} \ v_{c,y}^{\text{re}} \ v_{c,z}^{\text{re}}]^T$ and \mathbf{v}_d^{re} are the velocity of the camera and the drogue under the reference coordinate frame. In order to simplify the later controller design, Eq. (13.11) is further decomposed into a longitudinal channel and a lateral channel.

- Longitudinal channel: In the $x_c - z_c$ plane, state variables are $v_{d,x}^c, v_{d,z}^c, \omega_{d,y}^c$ with $v_{d,y}^c = 0, \omega_{d,x}^c = 0, \omega_{d,z}^c = 0$. One can obtain

$$\dot{e}_x = -\frac{v_{d,x}^c}{z_d^c} + \frac{e_x v_{d,z}^c}{z_d^c} - (1 + e_x^2) \omega_{d,y}^c. \quad (11.14)$$

- Lateral channel: In the $y_c - z_c$ plane, state variables are $v_{d,y}^c, v_{d,z}^c, \omega_{d,x}^c$ with $v_{d,x}^c = 0, \omega_{d,y}^c = 0, \omega_{d,z}^c = 0$. One can obtain

$$\dot{e}_y = -\frac{v_{d,y}^c}{z_d^c} + \frac{e_y v_{d,z}^c}{z_d^c} - (1 + e_y^2) \omega_{d,x}^c. \quad (11.15)$$

11.3.2 Inner-loop dynamic model

For the Jacobian matrix based visual servo model (13.11), the input variable is $\mathbf{v}_d^c = [v_{d,x}^c \ v_{d,y}^c \ v_{d,z}^c]^T$ based on that the change of $\omega_d^c = [\omega_{d,x}^c \ \omega_{d,y}^c \ \omega_{d,z}^c]^T$ is small in the docking process which can be ignored. In practice, since $\mathbf{v}_d^c = \mathbf{v}_d^{\text{re}} - \mathbf{v}_c^{\text{re}}$, one can only control \mathbf{v}_c^{re} rather than \mathbf{v}_d^{re} ,

because \mathbf{v}_d^{re} is the dynamics of the drogue, which is passive. Thus, the camera motion needs to be controlled, which is indirectly controlled by the receiver. Roughly, $\mathbf{v}_{c,des}^{re} = -\mathbf{v}_{d,des}^c$ will be used by taking \mathbf{v}_d^{re} as a disturbance, which is expressed in a decoupled form as

$$\mathbf{v}_{c,des}^{re} = \begin{bmatrix} \mathbf{v}_{rlon,des}^{re} \\ \mathbf{v}_{rlat,des}^{re} \end{bmatrix} \quad (11.16)$$

where $\mathbf{v}_{rlon,des}^{re} = [v_{d,ydes}^c \ v_{d,zdes}^c]^T$, $v_{rlat,des}^{re} = v_{d,xdes}^c$. The task of the inner-loop controller is to make \mathbf{v}_c^{re} track $\mathbf{v}_{c,des}^{re}$ and reject disturbances. In this part, the inner-loop dynamic model from the receiver inputs $\tilde{\mathbf{u}}_{rlon}$ and $\tilde{\mathbf{u}}_{rlat}$ to \mathbf{v}_{rlon}^{re} and \mathbf{v}_{rlat}^{re} will be derived. Based on the inner-loop dynamic model, the inner-loop visual servo control can then be designed.

The receiver can be taken as a rigid body, and the camera's linear velocity is equal to the vector sum of the velocity of the receiver's center of mass and the velocity of the camera rotating around the receiver's center of mass under the tanker coordinate frame, i.e.,

$$\mathbf{v}_c^t = \omega_r^t \times \mathbf{p}_c^r + \mathbf{v}_r^t \quad (11.17)$$

where $\mathbf{v}_c^t = [v_{c,x}^t \ v_{c,y}^t \ v_{c,z}^t]^T$ and $\mathbf{v}_r^t = [v_{r,x}^t \ v_{r,y}^t \ v_{r,z}^t]^T$ denote the linear velocity of the camera and the receiver, $\omega_r^t = [\omega_{r,x}^t \ \omega_{r,y}^t \ \omega_{r,z}^t]^T$ denotes the angular velocity of the receiver and $\mathbf{p}_c^r = [x_c^r \ y_c^r \ z_c^r]^T$ is the camera's coordinate under the receiver coordinate frame as shown in Fig. 11.1.

In the PDR docking, the rotation between the receiver and the tanker is kept small for safety considerations. Thus, the transformation matrix from the receiver coordinate frame to the tanker coordinate frame is approximated as

$$\mathbf{R}_{t/r} = \mathbf{I}_3. \quad (11.18)$$

With Eq. (13.15), Eq. (13.14) becomes

$$\begin{aligned} \mathbf{v}_c^t &= \omega_r^t \times \mathbf{p}_c^r + \mathbf{v}_r^t \\ &= \mathbf{R}_{t/r} \omega_r^r \times \mathbf{p}_c^r + \mathbf{R}_{t/r} \mathbf{v}_r^r \\ &= \omega_r^r \times \mathbf{p}_c^r + \mathbf{v}_r^r \end{aligned} \quad (11.19)$$

where $\omega_r^r = [\tilde{p} \ \tilde{q} \ \tilde{r}]^T$ and $\mathbf{v}_r^r = [\tilde{u} \ \tilde{v} \ \tilde{w}]^T$. Based on Eq. (13.16), the camera's linear velocity \mathbf{v}_c^{re} can be expressed as

$$\begin{aligned} \mathbf{v}_c^{re} &= \mathbf{R}_{re/t} \mathbf{v}_c^t \\ &= \mathbf{R}_{re/t} (\omega_r^r \times \mathbf{p}_c^r + \mathbf{v}_r^r). \end{aligned} \quad (11.20)$$

According to Ref [172], \mathbf{v}_r^r can be further written as

$$\begin{cases} \tilde{u} = \tilde{V}_r^g \cos \tilde{\alpha} \cos \tilde{\beta} \\ \tilde{v} = \tilde{V}_r^g \sin \tilde{\beta} \\ \tilde{w} = \tilde{V}_r^g \sin \tilde{\alpha} \cos \tilde{\beta} \end{cases} \quad (11.21)$$

Then, Eq. (13.17) becomes

$$\begin{cases} v_{c,x}^{\text{re}} = \tilde{V}_r^g \sin \tilde{\beta} + x_c^r \tilde{r} - z_c^r \tilde{p} \\ v_{c,y}^{\text{re}} = \tilde{V}_r^g \sin \tilde{\alpha} \cos \tilde{\beta} + y_c^r \tilde{p} - x_c^r \tilde{q} \\ v_{c,z}^{\text{re}} = \tilde{V}_r^g \cos \tilde{\alpha} \cos \tilde{\beta} + z_c^r \tilde{q} - y_c^r \tilde{r}. \end{cases} \quad (11.22)$$

Based on the decoupling conditions $\tilde{p} = \tilde{r} = 0$, $\tilde{\beta} = 0$ and omitting the higher-order items, Eq. (13.19) becomes

$$\begin{cases} v_{c,x}^{\text{re}} = x_c^r \tilde{r} - z_c^r \tilde{p} \\ v_{c,y}^{\text{re}} = -x_c^r \tilde{q} \\ v_{c,z}^{\text{re}} = \tilde{V}_r^g + z_c^r \tilde{q}. \end{cases} \quad (11.23)$$

Combining Eq. (13.6) and Eq. (13.20), the longitudinal model is obtained

$$\begin{cases} \dot{\tilde{x}}_{\text{rlon}} = \mathbf{A}_{\text{rlon}} \tilde{x}_{\text{rlon}} + \mathbf{B}_{\text{rlon}} \tilde{u}_{\text{rlon}} \\ \mathbf{v}_{\text{rlon}}^{\text{re}} = \begin{bmatrix} v_{c,y}^{\text{re}} \\ v_{c,z}^{\text{re}} \end{bmatrix} = \underbrace{\begin{bmatrix} 0 & 0 & 0 & 0 & 0 & -x_c^r \\ 0 & 0 & 0 & 1 & 0 & z_c^r \end{bmatrix}}_{\mathbf{C}_{\text{rlon}}} \tilde{x}_{\text{rlon}} \end{cases} \quad (11.24)$$

and the lateral model is denoted by

$$\begin{cases} \dot{\tilde{x}}_{\text{rlat}} = \mathbf{A}_{\text{rlat}} \tilde{x}_{\text{rlat}} + \mathbf{B}_{\text{rlat}} \tilde{u}_{\text{rlat}} \\ v_{\text{rlat}}^{\text{re}} = v_{c,x}^{\text{re}} = \underbrace{\begin{bmatrix} 0 & 0 & 0 & 0 & -z_c^r & x_c^r \end{bmatrix}}_{\mathbf{C}_{\text{rlat}}} \tilde{x}_{\text{rlat}} \end{cases} \quad (11.25)$$

11.3.3 Visual servo controller design

Based on the models (13.12), (13.13), (11.24) and (11.25), the IBVS controller design is divided into a longitudinal channel control problem and a lateral channel control problem.

Problem 1. (Lateral channel control). For systems (13.13) and (11.25), design \tilde{u}_{rlat} , such that the lateral image tracking error converges to zero, i.e., $e_x(t) \rightarrow 0$ as $t \rightarrow \infty$.

Problem 2. (Longitudinal channel control). For systems (13.12) and (11.24), design \tilde{u}_{rlon} , such that the longitudinal image tracking error converges to zero and the probe docks with the drogue, i.e., $e_y(t) \rightarrow 0$ as $t \rightarrow \infty$, $z_d^c(t) \rightarrow 0$ slower than ($\mathbf{e}(t) \rightarrow 0$).

In order to make the controller design simpler, an inner-and-outer-loop control architecture is adopted. The outer controller aims to obtain the desired velocities $v_{d,x\text{des}}^c$, $v_{d,y\text{des}}^c$ and $v_{d,z\text{des}}^c$ which can guarantee $e_x(t) \rightarrow 0$, $e_y(t) \rightarrow 0$, $z_d^c(t) \rightarrow 0$ as $t \rightarrow \infty$ based on the models (13.12) and (13.13), while the inner controller tends to acquire the needed control inputs \tilde{u}_{rlat} and \tilde{u}_{rlon} which can guarantee $\mathbf{v}_d^c \rightarrow \mathbf{v}_{d,\text{des}}^c$ based on the models (11.24) and (11.25).

11.3.3.1 Outer-loop controller design

- Lateral channel controller design



For *Problem 1*, consider that the change of $\omega_{d,y}^c$ is small in the docking process, which can be ignored. Then the desired velocity for $v_{d,x}^c$ is designed as

$$v_{d,xdes}^c = k_1 e_x. \quad (11.26)$$

With it, if $v_{d,x}^c = v_{d,xdes}^c$, then Eq. (13.12) becomes

$$\dot{e}_x = -\lambda_1 e_x \quad (11.27)$$

where $\lambda_1 = \frac{k_1 - v_{d,z}^c}{z_d^c}$ and k_1 is chosen as $k_1 > \max(v_{d,z}^c)$. In this case, we have $\lim_{t \rightarrow \infty} |e_x(t)| = 0$.

- Longitudinal channel controller design

For *Problem 2*, consider that the change of $\omega_{d,x}^c$ is small in the docking process, which can be ignored. Then the desired velocity for $v_{d,y}^c$ is designed as

$$v_{d,ydes}^c = k_2 e_y. \quad (11.28)$$

With it, if $v_{d,y}^c = v_{d,ydes}^c$, Eq. (13.13) becomes

$$\dot{e}_y = -\lambda_2 e_y \quad (11.29)$$

where $\lambda_2 = \frac{k_2 - v_{d,z}^c}{z_d^c}$ and k_2 is chosen as $k_2 > \max(v_{d,z}^c)$. In this case, we have $\lim_{t \rightarrow \infty} |e_y(t)| = 0$. Besides, the desired velocity for $v_{d,z}^c$ is designed as

$$v_{d,zdes}^c = -k_3 z_d^c \quad (11.30)$$

With it, if $v_{d,z}^c = v_{d,zdes}^c$ and $k_3 > 0$, one have $\lim_{t \rightarrow \infty} |z_d^c(t)| = 0$.

Remark 1: The docking control problem has been essentially decoupled to two problems, namely the 2D position error of the drogue in the camera frame going to zero, and the depth error going to zero. However, in order to ensure a successful docking, the controller needs to close the gap to the drogue before closing the lateral distance error. Thus, k_3 should be selected smaller compared with k_1 and k_2 to guarantee $e_y(t) \rightarrow 0$ and $e_x(t) \rightarrow 0$ faster than $z_d^c(t) \rightarrow 0$.

In the following, improvements are made on (11.30). First, in order to prevent the receiver passing the drogue too fast and to guarantee $e_y(t) \rightarrow 0$ and $e_x(t) \rightarrow 0$ faster than $z_d^c(t) \rightarrow 0$, the term “ $-k_4 |e_x| - k_5 |e_y|$ ” is introduced into (11.30) to adjust the speed as follows

$$v_{d,zdes}^c = -k_3 z_d^c - k_4 |e_x| - k_5 |e_y|. \quad (11.31)$$

If $|e_x|, |e_y|$ is large, the term can slow down the approach speed to avoid overshooting. Introducing the term can prevent $v_{d,zdes}^c$ from going to zero in this case that $|e_x|, |e_y|$ is large or even be negative to allow the receiver to retreat and try again.

Besides, the degree to which the forward speed should be changed depends on how far the probe is away from the drogue. For instance, if $e_x = 1\text{m}$ but $z_d^c = 20\text{m}$, perhaps a positive approach speed is still desired. But if $e_x = 1\text{m}$ and $z_d^c = 1\text{m}$, one should probably stop advancing at all. Thus, the change in the approach speed is not just a linear function of e_x and e_y regardless of the value of z_d^c . In reality, it should be normalized by z_d^c . This is equivalent to using angular errors rather than position errors to adjust the approach speed [264]. Thus, the controller (11.31)

should be changed into

$$v_{d,zdes}^c = -k_3 z_d^c - k_4 \frac{|e_x|}{z_d^c} - k_5 \frac{|e_y|}{z_d^c}. \quad (11.32)$$

Secondly, when $|e_x|, |e_y|$ is small, which means the probe is nearly docked with the drogue, saturation limits need to be added for the $v_{d,zdes}^c$ to guarantee the receiver still flies at a certain forward velocity after $z_d^c(t) = 0$, because the receiver should hit to open the throttle valve with a certain relative speed at the docking moment, as shown in Fig. 11.3, but the camera cannot capture the LEDs after $z_d^c(t) = 0$. The final controller is designed as

$$v_{d,zdes}^c = \text{sat}\left(-k_3 z_d^c - k_4 \frac{|e_x|}{z_d^c} - k_5 \frac{|e_y|}{z_d^c}, a\right) \quad (11.33)$$

where $k_3, k_4, k_5 > 0$ and the saturation function is

$$\text{sat}(x(t), a) = \begin{cases} x(t), & |x(t)| \leq a \\ a \cdot \text{sign}(x(t)), & |x(t)| > a \end{cases}$$

where $a > 0$ is a constant. Based on Eq. (11.33), the approach speed can be controlled within a range at the docking moment.

Up to now, the outer-loop controllers for longitudinal and lateral channels have been designed as (11.26), (11.28), and (11.33), and the desired velocity for \mathbf{v}_d^c is obtained, which can be denoted as

$$\mathbf{v}_{d,des}^c = \begin{bmatrix} v_{d,xdes}^c & v_{d,ydes}^c & v_{d,zdes}^c \end{bmatrix}^T. \quad (11.34)$$

11.3.3.2 Inner-loop controller design

- Longitudinal channel controller design

Define the velocity tracking error as $\mathbf{e}_{rlon} = \mathbf{v}_{rlon}^{re} - \mathbf{v}_{rlon,des}^{re}$. In order to reject disturbances, an integral term is used here, which is defined as

$$\mathbf{q}_{rlon} = \int_0^t \mathbf{e}_{rlon}(\tau) d\tau = \int_0^t (\mathbf{v}_{rlon}^{re}(\tau) - \mathbf{v}_{rlon,des}^{re}(\tau)) d\tau. \quad (11.35)$$

Putting Eq. (11.35) to Eq. (11.24) yields

$$\begin{bmatrix} \dot{\tilde{\mathbf{x}}}_{rlon} \\ \dot{\mathbf{q}}_{rlon} \end{bmatrix} = \begin{bmatrix} \mathbf{A}_{rlon} & \mathbf{0}_{6 \times 2} \\ \mathbf{C}_{rlon} & \mathbf{0}_{2 \times 2} \end{bmatrix} \begin{bmatrix} \tilde{\mathbf{x}}_{rlon} \\ \mathbf{q}_{rlon} \end{bmatrix} + \begin{bmatrix} \mathbf{B}_{rlon} \\ \mathbf{0}_{2 \times 2} \end{bmatrix} \tilde{\mathbf{u}}_{rlon} - \begin{bmatrix} \mathbf{0}_{6 \times 2} \\ \mathbf{I}_{2 \times 2} \end{bmatrix} \mathbf{v}_{rlon,des}^{re}. \quad (11.36)$$

The controller is designed as follows

$$\tilde{\mathbf{u}}_{rlon} = -\mathbf{K}_{x1} \tilde{\mathbf{x}}_{rlon} - \mathbf{K}_{e1} \mathbf{q}_{rlon} \quad (11.37)$$

where $\mathbf{K}_{x1} \in \mathbb{R}^{2 \times 6}$, $\mathbf{K}_{e1} \in \mathbb{R}^{2 \times 2}$. \mathbf{K}_{x1} and \mathbf{K}_{e1} are selected to minimize the quadratic cost function as follows

$$J_{rlon} = \int_0^\infty \{ \tilde{\mathbf{x}}_{rlon}^T \mathbf{Q}_{rlon} \tilde{\mathbf{x}}_{rlon} + \tilde{\mathbf{u}}_{rlon}^T \mathbf{R}_{rlon} \tilde{\mathbf{u}}_{rlon} \} dt \quad (11.38)$$

where $\tilde{\mathbf{X}}_{rlon} = \begin{bmatrix} \tilde{\mathbf{x}}_{rlon} & q_{rlon} \end{bmatrix}^T$, $\mathbf{Q}_{rlon} \geq 0$ and $\mathbf{R}_{rlon} > 0$ are weighting matrices.

- Lateral channel controller design

Similarly, define the velocity tracking error as $e_{rlat} = v_{rlat}^{re} - v_{rlat,des}^{re}$ and an integral term is defined as

$$q_{rlat} = \int_0^t e_{rlat}(\tau) d\tau = \int_0^t (v_{rlat}^{re}(\tau) - v_{rlat,des}^{re}(\tau)) d\tau. \quad (11.39)$$

Putting Eq. (11.39) to Eq. (11.25) yields

$$\begin{bmatrix} \dot{\tilde{\mathbf{x}}}_{rlat} \\ \dot{q}_{rlat} \end{bmatrix} = \begin{bmatrix} \mathbf{A}_{rlat} & \mathbf{0}_{6 \times 2} \\ \mathbf{C}_{rlat} & \mathbf{0}_{2 \times 2} \end{bmatrix} \begin{bmatrix} \tilde{\mathbf{x}}_{rlat} \\ q_{rlat} \end{bmatrix} + \begin{bmatrix} \mathbf{B}_{rlat} \\ \mathbf{0}_{2 \times 2} \end{bmatrix} \tilde{\mathbf{u}}_{rlat} - \begin{bmatrix} \mathbf{0}_{6 \times 2} \\ \mathbf{I}_{2 \times 2} \end{bmatrix} v_{rlat,des}^{re}. \quad (11.40)$$

The controller is designed as

$$\tilde{\mathbf{u}}_{rlat} = -\mathbf{K}_{x2}\tilde{\mathbf{x}}_{rlat} - \mathbf{K}_{e2}q_{rlat} \quad (11.41)$$

where $\mathbf{K}_{x2} \in \mathbb{R}^{2 \times 6}$, $\mathbf{K}_{e2} \in \mathbb{R}^2$. \mathbf{K}_{x2} and \mathbf{K}_{e2} are selected to minimize the quadratic cost function as follows

$$J_{rlat} = \int_0^\infty \{ \tilde{\mathbf{X}}_{rlat}^T \mathbf{Q}_{rlat} \tilde{\mathbf{X}}_{rlat} + \tilde{\mathbf{u}}_{rlat}^T \mathbf{R}_{rlat} \tilde{\mathbf{u}}_{rlat} \} dt \quad (11.42)$$

where $\tilde{\mathbf{X}}_{rlat} = \begin{bmatrix} \tilde{\mathbf{x}}_{rlat} & q_{rlat} \end{bmatrix}^T$, $\mathbf{Q}_{rlat} \geq 0$ and $\mathbf{R}_{rlat} > 0$ are weighting matrices.

11.3.3.3 Final IBVS controller

Up to now, based on the models (13.12), (13.13), (11.24) and (11.25), and under the Assumptions 1-4, the final controller is obtained as follows

$$\begin{cases} v_{d,xdes}^c = k_1 e_x \\ v_{d,ydes}^c = k_2 e_y \\ v_{d,zdes}^c = \text{sat} \left(-k_3 z_d^c - k_4 \frac{|e_x|}{z_d^c} - k_5 \frac{|e_y|}{z_d^c}, a \right) \\ \tilde{\mathbf{u}}_{rlon} = -\mathbf{K}_{x1}\tilde{\mathbf{x}}_{rlon} - \mathbf{K}_{e1}\mathbf{q}_{rlon} \\ \tilde{\mathbf{u}}_{rlat} = -\mathbf{K}_{x2}\tilde{\mathbf{x}}_{rlat} - \mathbf{K}_{e2}q_{rlat} \end{cases} \quad (11.43)$$

where $k_i > 0$, $i = 1, 2, \dots, 5$, $\mathbf{K}_{x1}, \mathbf{K}_{e1}, \mathbf{K}_{x2}, \mathbf{K}_{e2}$ are control gains. The closed-loop system composed of the PDR system and the IBVS controller is shown in Fig. 11.4.

11.4 Simulation and Verification

In this section, various disturbances such as aerodynamic disturbance, tanker vortex disturbance, bow wave effect, and pose estimation errors are considered in the simulation to prove the validity of the designed controller.

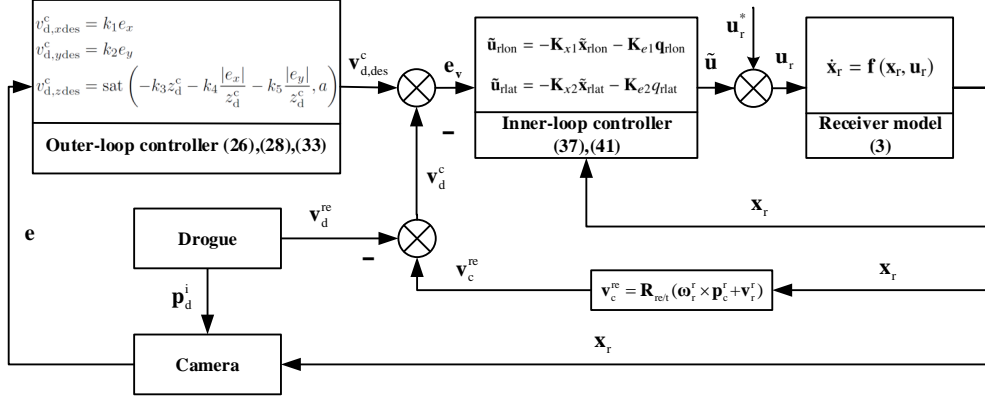


Figure 11.4: The closed-loop structure based on the designed IBVS controller.

11.4.1 Simulation environment

A high-fidelity simulation platform with a 3D virtual-reality visual display is built based on MATLAB/SIMULINK to simulate PDR docking. The basic information about this simulation platform can be referred to Refs. [250, 251]. In this paper, the previous controller used in Refs. [250] is changed to the proposed IBVS controller.

11.4.2 Simulation results

Different disturbances are set in the simulation environment to illustrate the performance of the designed IBVS controller. Besides, pose estimation errors are considered when making a comparison between IBVS and PBVS.

11.4.2.1 Simulations under Aerodynamic Disturbance

The controller parameters of the outer-loop visual servo controller are set to the values in Table 11.1. At first, different intensities of the atmospheric disturbance are added. The intensity of the atmospheric disturbance is negatively correlated with the probability of the turbulence intensity being exceeded. In general, the intensity of the atmospheric disturbance of level I means that the probability of the turbulence intensity being exceeded is 10^{-1} and the maximum velocity of atmospheric disturbance is about 3 feet per second. The level II means that the probability of the turbulence intensity being exceeded is 10^{-2} and the maximum velocity of atmospheric disturbance is about 5 feet per second.

Table 11.1: Parameters of the outer-loop controller

Parameters	k_1	k_2	k_3	k_4	k_5
Values	1	3	0.5	3	1

In Fig. 11.5, the intensity of aerodynamic disturbance is set at level I while the intensity of aerodynamic disturbance is set at level II in Fig. 11.6. It can be found that although the receiver's movement trajectory fluctuates with the increase of the wind disturbance intensity, the success

of docking is ensured meanwhile the trajectory is relatively smooth due to the effect of the PI controller. Then, a bow wave effect is added in Fig. 11.7 in which the controller parameters of the outer-loop visual servo controller are adjusted to the values in Table 11.2. Noteworthy, although the image tracking error fluctuates at the beginning, it can still guarantee the success of docking.

Table 11.2: Parameters of the outer-loop controller under the bow wave effect and Level I aerodynamic disturbances

Parameters	k_1	k_2	k_3	k_4	k_5
Values	1.6	5	0.5	3	1

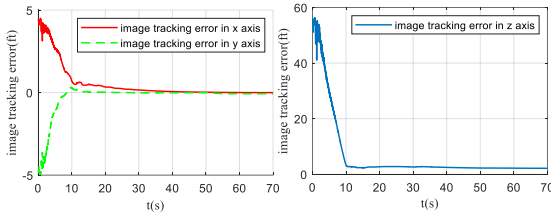


Figure 11.5: Image tracking error under different aerodynamic disturbances (Level I)

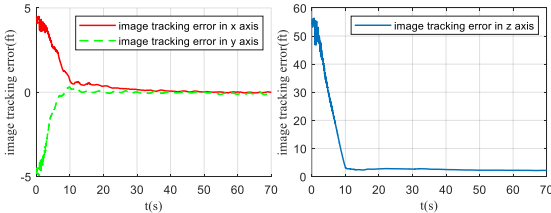


Figure 11.6: Image tracking error under different aerodynamic disturbances (Level II)

11.4.2.2 Simulations under Position Measurement Error

Consider that the pose estimation error affects the docking control in two aspects: the camera installation position does not change, but the distance measurement may be inaccurate, or the distance measurement is precise, but the actual position of the camera deviates from the original installation position. In order to simulate the situation that there are pose estimation errors during the PDR docking, $\Delta \mathbf{p}_c^r = [1 \ 0 \ -0.5]^T$ is added to both IBVS and PBVS controllers, and the corresponding simulation results are shown in Fig. 11.8. It can be observed that the IBVS controller can perform successful docking while the PBVS cannot.

In order to better evaluate the docking performance and reliability of the proposed IBVS controller in the presence of pose estimation errors, a simple Monte Carlo simulation is also carried out. Position errors $\Delta \mathbf{p}_c^r = [\Delta \mathbf{p}_{c,x}^r, \Delta \mathbf{p}_{c,y}^r, \Delta \mathbf{p}_{c,z}^r]^T$ used in the Monte Carlo simulations are listed in Table 11.3.

From the Monte Carlo simulations, the final docking success rate (DSR) can be obtained as shown in Table 11.4. It can be seen that IBVS control can achieve a 100% docking success rate under light atmospheric turbulence, while the PBVS control can achieve a 70% docking success

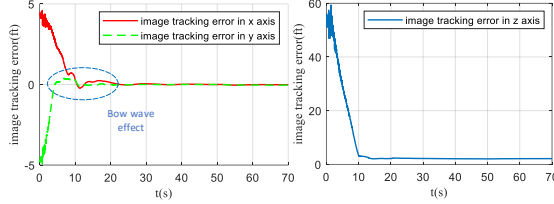


Figure 11.7: Image tracking error under bow wave effect and Level I aerodynamic disturbances

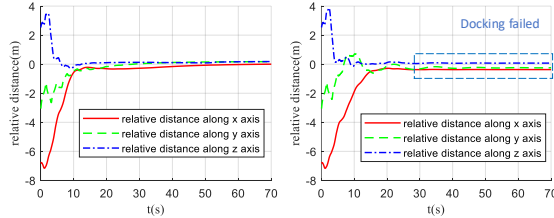


Figure 11.8: Image tracking error under position measurement error

rate under the same situation. When there exists strong atmospheric turbulence, the docking success rate of the IBVS and PBVS control all get worse, but the DSR of the IBVS control is still higher than the DSR of the PBVS control. Thus, it can be concluded that the IBVS control outperforms the PBVS control in the presence of position errors. Besides, it can be seen that the atmospheric turbulence intensity has a significant effect on the docking success.

11.4.2.3 Discussion

For the visual servo control, as long as high-precision image information can be obtained, the calculated 3D relative position may be inaccurate due to the camera installation error, calibration error, and/or 3D object modeling error. In the simulation, the PBVS takes the 3D relative position as the outer-loop feedback. A PI controller can make the feedback error zero. However, there exists a position measurement error, and so the docking finally fails. On the contrary, the proposed IBVS takes the relative 2D image error as the outer-loop feedback. Errors existing in the inner loop are taken as constant disturbances. Besides, the depth error does not determine the docking success that much like the 2D image error. As a result, the IBVS controller is more robust against measurement errors than the PBVS controller.

11.5 Chapter Summary

This paper proposes an IBVS model for the probe-and-drogue refueling and an IBVS docking control method. Concretely, the IBVS control for the outer loop and the LQR control for the inner loop are designed to improve the robustness of the docking control. Simulations show that the proposed IBVS controller has enough robustness, which can achieve a successful docking in the presence of complex disturbances and pose estimation errors. Here, the control surfaces and the throttle are control inputs of the system. However, the low-level controller has always been finished or cannot be changed for safety in practice. Therefore, further research, based

Table 11.3: Position errors used in the Monte Carlo simulations

Pos. error	Nom. value	Max.	Min.	Distribution type
$\Delta p_{c,x}^r$	0	1	-1	Uniform
$\Delta p_{c,y}^r$	0	1	-1	Uniform
$\Delta p_{c,z}^r$	0	1	-1	Uniform

Table 11.4: Docking success rate of IBVS and PBVS control in the presence of position errors and turbulence disturbances

DSR Controller \ Controller	light tur.	strong tur.
IBVS	100%	40%
PBVS	70%	10%

on an existing low-level controller, where the velocity is adopted as the control input is worth studying. Besides, the velocity controller often aims at the receiver's position control. However, the velocity controller for PDR docking needs to control the position of the probe tip, which is related to the receiver's attitude. This is full of challenges.

Chapter 12 Reachability Analysis on Optimal Trim State for Aerial Docking

Aerial refueling is an important capability to increase the endurance and flight range of aircraft, but it often suffers from a low success rate. The altitude and speed of the tanker aircraft in the docking phase play a great role in the docking success rate. According to this, the optimal trim state, namely the optimal speed and altitude of the tanker aircraft, is investigated through the reachability analysis method in this paper. The optimal problem is transformed to find the trim state corresponding to the maximum volume of the reachable set. First, a relative motion model of the receiver aircraft with respect to the drogue is proposed. Then, based on reachability analysis, an optimization problem is formulated and a solution procedure is given in detail. In the simulation, the volumes of reachable sets are plotted with respect to the given discrete speeds and altitudes, based on which the optimal trim state of the docking phase is determined. Finally, the determined optimal trim state is verified by using numerous docking control simulations and the degree of controllability from another aspect. The effectiveness of the proposed method is demonstrated.

12.1 Introduction

Currently, AR processes are realized by experienced pilots of manned aircraft or autopilots of Unmanned Aerial Vehicles (UAVs) which often suffer from low success rates. In fact, inappropriate docking speeds and docking altitudes will affect the docking success rate, but little attention has been paid. The related references about existing chosen docking speeds and docking altitudes are summarized in Table 12.1. In [265], a deep learning based trajectory optimization method was provided to decrease the bow wave effect on the drogue, where the refueling altitude was set to be 7010 m and the speed of tanker aircraft was 200 m/s. In [266], a back-stepping based flight controller for the receiver aircraft was designed, where the speed of tanker aircraft was 200 m/s and the docking altitude was 7010 m. In [267], an adaptive control method was used to reject the trailing vortex, where the altitude was 1524 m and the docking speed was 152 m/s. A command filtered backstepping sliding mode controller for the hose whipping phenomenon in aerial refueling was designed in [268], where the refueling altitude and the speed of the tanker aircraft were set to be 7620 m and 200 m/s respectively. The receiver forebody aerodynamic effect on the drogue transient motion was considered in [269], where the speed of tanker aircraft was 118 m/s and the docking altitude was 2286 m. Furthermore, a lower order dynamic model involving the receiver forebody aerodynamic effect was proposed to describe drogue dynamics in [270], where the docking altitude in this paper was set to be 3000 m and the docking speed

Table 12.1: Summary of the Simulation Experiments and the Actual Flight Test Experiments

Ref.	The Tanker	The Receiver	Altitude	Docking Speed
[265]	NA	NA	7010m	200m/s
[266]	NA	NA	7010m	200m/s
[267]	NA	NA	1524	152m/s
[268]	NA	NA	7620	200m/s
[269]	NA	NA	2286	118m/s
[270]	NA	NA	3000m	120m/s
[271]	Boeing 707	F/A-18B	3000m	120m/s
[272]	NA	NA	7010m	200m/s
[273]	F/A-18	F/A-18	2286, 3200, 7620, 9144m	90 ~ 152m/s
[274]	Boeing 707-300	F/A-18	NA	NA
[275]	VC-10, KC-10	F-16A	1524 ~ 6096m	118 ~ 165m/s

was 120 m/s. In [271], a simple method was used to model the receiver forebody aerodynamic effect, where the altitude of the tanker aircraft was 3000 m and the docking speed was 120 m/s. The type of the tanker aircraft is Boeing 707 and the receiver aircraft is F/A-18B. In [272], the dynamic modeling and simulation application of the receiver aircraft are studied, where the altitude of the tanker aircraft was 7010 m and the docking speed was 200 m/s. In [273], the actual flight test experiment was performed by NASA. The type of the tanker aircraft and the receiver aircraft is F/A-18. The docking altitudes were 2286 m, 3200 m, 7620 m, 9144 m and the range of the docking speed was from 90 m/s to 152 m/s. In [274], another NASA flight test experiment was made to reveal the forebody flow field of the receiver aircraft and two out of six capture attempts were successful. The capture criteria and miss criteria at the docking phase were also provided. The type of the tanker aircraft is Boeing 707-300 and the type of the receiver aircraft is F/A-18. The docking altitude and speed were both set to be constant. The actual flight test experiments were also conducted by North Atlantic Treaty Organization (NATO). In the ATP-56(B) issued by NATO [275], the tanker aircrafts are VC-10 and KC-10, and receiver aircraft is F-16A. The altitude range for refueling was from 1524 m to 6096 m and the speed range was from 118m/s to 165 m/s. By facing different docking speeds and altitudes, a problem arises that what docking speed and altitude can make docking most easily. Motivated by this, this paper aims at studying the optimal speed and altitude based on the reachability analysis method. Concretely, different docking speeds and altitudes will correspond to different volumes of the reachable set at the docking phase, because they will change the relative motion model of the receiver aircraft with respect to the center of the drogue. Therefore, the speed and altitude corresponding to the maximum volume of reachable set are regarded as the optimal trim state.

It is reasonable to use the volume of the reachable set to measure how easy the docking is. The subset of the state space that can reach the target set while remaining in the acceptable range is called the reachable set [276]. With respect to the docking phase, the target set represents the set of successful docking states, and the reachable set is a set of the receiver aircraft states

from which the docking maneuver can be accomplished within a finite time horizon. Thus, the larger the volume of the reachable set is, the higher probability the pilot or the UAV autopilot can drive the receiver aircraft to dock successfully. This further implies that it is more easily to dock. So far, the reachability analysis method has been applied to solve many problems, such as collision avoidance [276], control law design for safe aerobatic maneuvers [277] [278], safety verification of autoland maneuvers [279] and a ground moving target tracking [280]. In [281], the reachability analysis method was first applied to an AR process. The AR process has been divided into several maneuver sequences and the reachability analysis method was used to design a maneuver decision to ensure safe operation of a sequential mode transition. Unlike [281], the aim of this paper is to determine the optimal trim state of the docking phase in terms of reachability.

The reachable set can be calculated by the Level Set Toolbox [282] based on the level set method [283]. Concretely, the computation of the optimal trim state for the considered docking phase of an AR process is divided into four phases. First, the trim state of the tanker aircraft is specified which is used in the relative motion model of the receiver aircraft with respect to the center of the drogue. Secondly, the state space is divided into grid points and the reachable set of the receiver aircraft is computed at each trim state. Thirdly, by comparing the volume of the reachable set at different trim states, the trim state of the tanker aircraft with the largest reachable set volume is regarded as the optimal trim state. Finally, the optimal trim state is verified by the docking control simulations and the degree of controllability from another aspect, showing that the docking success rate is the highest at the optimal altitude and speed. Therefore, the effectiveness of the proposed method is demonstrated. The contribution of this note is the idea and process of determining the optimal trim state for aerial docking *for the first time*.

12.2 Problem Formulation

12.2.1 Relative Motion Model

Fig.12.1 shows the docking phase of an AR process, where the origin of the system is at the center of the drogue of the tanker aircraft. The continuous-time dynamics between the tip of the probe and the center of the drogue in relative coordinates at the docking phase are considered at the docking phase. The state vector $\Delta\mathbf{x} = [\Delta V \Delta\gamma \Delta x \Delta h]^T$, whose elements represent the speed, flight path angle, longitudinal distance and altitude of the tip of the probe with respect to the center of the drogue, respectively. The longitudinal dynamics of the aircraft focused lie on two reasons: 1) it is more important than the lateral dynamics at the docking phase; 2) the objective is to determine the optimal trim state, for which longitudinal dynamics can simplify the problem without loss of generality.

The longitudinal dynamics of the receiver aircraft are modeled by using the reference frame shown in Fig.12.2. The receiver aircraft is subject to the force of thrust T , lift L , drag D and



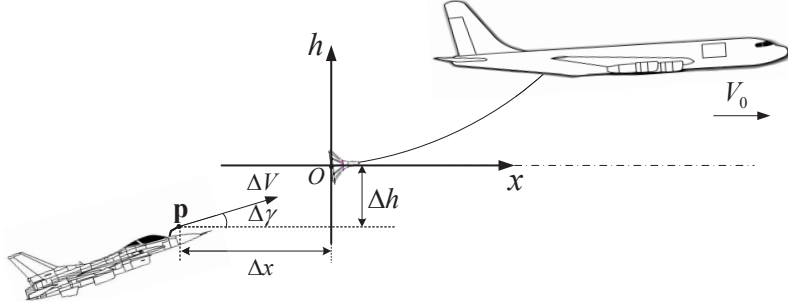


Figure 12.1: Relative coordinate system of the docking phase of an AR process

gravity G . The state vector is $\mathbf{x}_r = [V_r \gamma_r x_r h_r]^T$, whose elements represent the speed, flight path angle, longitudinal distance and altitude of the mass center of the receiver aircraft, respectively. The control input is $\mathbf{u} = [T_r \alpha_r]^T$ whose elements denote the thrust and the angle of attack of the receiver aircraft, respectively. Therefore, the longitudinal dynamics of the mass center of the receiver aircraft are written as follows [279] [284]:

$$\begin{bmatrix} \dot{V}_r \\ \dot{\gamma}_r \\ \dot{x}_r \\ \dot{h}_r \end{bmatrix} = \begin{bmatrix} \frac{1}{m} (T_r \cos \alpha_r - D(\alpha_r, V_r) - mg \sin \gamma_r) \\ \frac{1}{mV_r} (T_r \sin \alpha_r + L(\alpha_r, V_r) - mg \cos \gamma_r) \\ V_r \cos \gamma_r \\ V_r \sin \gamma_r \end{bmatrix}. \quad (12.1)$$

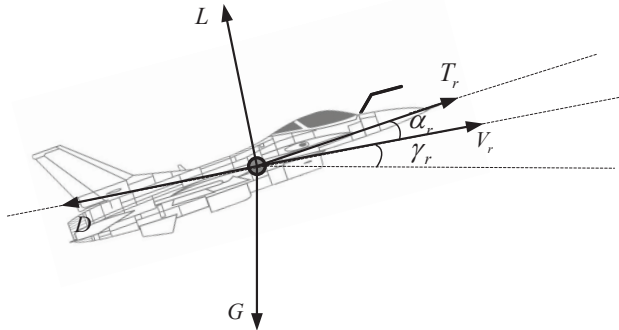


Figure 12.2: Longitudinal dynamics of the receiver aircraft

The state vector of the tanker aircraft is $\mathbf{x}_t = [V_t \gamma_t x_t h_t]^T$, the elements of which represent the speed, the flight path angle, longitudinal distance and the altitude of the tanker aircraft, respectively. The state parameters V_t, h_t are assumed to be constant at the docking phase, namely

$$\dot{V}_t = 0, \dot{x}_t = V_t, \dot{h}_t = 0.$$

This implies $\gamma_t = 0$. To dock successfully, the receiver aircraft's speed should keep the same as the tanker aircraft. As a result, the trim state of the dynamic system Eq.(12.1) is $(V^* \gamma^* T^* \alpha^*)$, where $V^* = V_t, \gamma^* = 0$. Based on the trim state and input, define

$$\Delta V_r = V_r - V^*, \Delta \gamma_r = \gamma_r - \gamma^*,$$

$$\Delta T_r = T_r - T^*, \Delta \alpha_r = \alpha_r - \alpha^*.$$

Then, Eq.(12.1) is rearranged to

$$\underbrace{\begin{bmatrix} \Delta\dot{V}_r \\ \Delta\dot{\gamma}_r \\ \Delta\dot{x}_r \\ \Delta\dot{h}_r \end{bmatrix}}_{\Delta\mathbf{x}_r} = \underbrace{\begin{bmatrix} \frac{1}{m} \begin{pmatrix} (T^* + \Delta T_r) \cos(\alpha^* + \Delta\alpha_r) \\ -D(\alpha^* + \Delta\alpha_r, V^* + \Delta V_r) - mg \sin(\gamma^* + \Delta\gamma_r) \end{pmatrix} \\ \frac{1}{m(V^* + \Delta V_r)} \begin{pmatrix} (T^* + \Delta T_r) \sin(\alpha^* + \Delta\alpha_r) \\ +L(\alpha^* + \Delta\alpha_r, V^* + \Delta V_r) - mg \cos(\gamma^* + \Delta\gamma_r) \end{pmatrix} \\ (V^* + \Delta V_r) \cos(\gamma^* + \Delta\gamma_r) - V^* \\ (V^* + \Delta V_r) \sin(\gamma^* + \Delta\gamma_r) \end{bmatrix}}_{\mathbf{f}_{h^*, V^*}(\Delta\mathbf{x}_r)}, \quad (12.2)$$

where the state vector $\Delta\mathbf{x}_r = [\Delta V_r \Delta\gamma_r \Delta x_r \Delta h_r]^T$ represents the speed, flight path angle, longitudinal distance and altitude of the mass center of the receiver aircraft with respect to the center of the drogue, respectively. Here, the lift and drag are expressed as [285]

$$\begin{aligned} L &= \frac{1}{2}\rho(V^* + \Delta V_r)^2 C_L S \\ D &= \frac{1}{2}\rho(V^* + \Delta V_r)^2 C_D S \end{aligned}, \quad (12.3)$$

where ρ is the air density which is determined by the altitude of the tanker aircraft h_0 at the docking phase and S represents the wing area of the receiver aircraft. The lift coefficient C_L is a linear function of α_r given by

$$C_L = C_{L_0} + C_{L_\alpha}(\alpha^* + \Delta\alpha_r), \quad (12.4)$$

where C_{L_0} is the lift coefficient at zero angle of attack and C_{L_α} is the lift coefficient slope. The drag coefficient C_D is computed by the following equation

$$C_D = C_{D_0} + K C_L^2, \quad (12.5)$$

where C_{D_0} is the zero lift drag coefficient which accounts for the drag of the body, the slats, the flaps and the landing gear. The constant K is the lift-induced drag coefficient. According to Eqs.(12.3)(12.4)(12.5), the lift and drag depend on the parameters V_0 and h_0 . It implies that the speed and altitude of the tanker aircraft affect the lift and drag of the receiver aircraft, and further determine the dynamic model represented by Eq.(12.2).

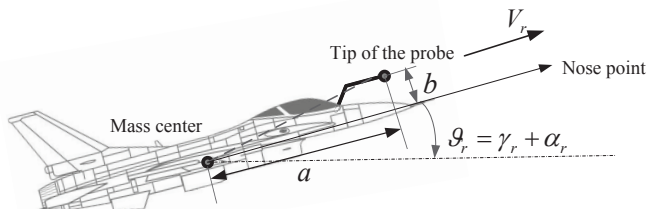


Figure 12.3: Relative position of the tip of the probe with respect to the mass center of the receiver aircraft

12.2.2 Assumptions and Objective

The relative position between the tip of the probe and the mass center of the receiver aircraft is presented in Fig.12.3. As shown, ϑ_r is the angle of pitch, a and b represent the relative longitudinal distance and the relative altitude of the tip of the probe with respect to the mass center of the receiver aircraft. The relative position between the tip of the probe and the center of the drogue is

$$\begin{aligned}\Delta x &= \Delta x_r + (a \cos \vartheta_r - b \sin \vartheta_r) \\ \Delta h &= \Delta h_r + (a \sin \vartheta_r + b \cos \vartheta_r)\end{aligned}. \quad (12.6)$$

The following assumptions are further made.

Assumption 1. At the docking phase, the control inputs of the receiver aircraft are limited by

$$\begin{aligned}\Delta T_{\min} &\leq \Delta T_r \leq \Delta T_{\max} \\ \Delta \alpha_{\min} &\leq \Delta \alpha_r \leq \Delta \alpha_{\max}\end{aligned}. \quad (12.7)$$

Assumption 2. The speed and the flight path angle of the tip of the probe are equal to those of the receiver aircraft, given by

$$\begin{aligned}\Delta V &= \Delta V_r \\ \Delta \gamma &= \Delta \gamma_r\end{aligned}. \quad (12.8)$$

Remark 1. The pilot of the manned aircraft or the UAV autopilot cannot change the control inputs aggressively during the docking phase. Thus, *Assumption 1* is reasonable. At the docking phase, the pitch rate is small. Consequently, its effect on the speed and the flight path angle of the probe is ignored. Thus, *Assumption 2* is also reasonable.

According to Eqs.(12.6)(12.8), the relative motion between the center of the drogue and the tip of the probe is expressed as

$$\Delta \mathbf{x} = \mathbf{g}(\Delta \mathbf{x}_r). \quad (12.9)$$

Based on the *Assumptions 1-2*, the objective of this paper is to study the optimal trim state, including the optimal altitude and speed of the tanker aircraft at the docking phase by using the reachability analysis method. The optimal altitude and speed will be used to determine the trim state of the dynamic model described by Eq.(12.2). The docking speed and altitude of the tanker aircraft corresponding to the maximum volume of the reachable set is regarded as the optimal speed and altitude at the docking phase.

12.3 Computing Procedure of the Optimal Trim State

For the docking phase of the AR process, the target set represents the state set of docking successfully and the reachable set is the state set of the receiver aircraft from which the docking phase can be completed within a finite time horizon $t \in [-\tau, 0]$. The target set \mathcal{D} and the reachable set $pre_\tau(\mathcal{D})$ can be regarded as the zero level set of the cost function $J(\mathbf{x}, t)$ at $t = 0$ and $t = -\tau$,

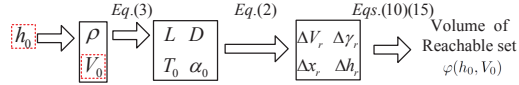


Figure 12.4: Relationship between the docking speed V_0 docking altitude h_0 and the volume of reachable set $\varphi(h_0, V_0)$

respectively. The reachable set $pre_\tau(\mathcal{D})$ is computed by solving the following Hamilton-Jacobi Partial Differential Equation (HJ PDE) [276]

$$\begin{aligned} D_t J(\mathbf{x}, t) &= -H(\mathbf{x}, D_{\mathbf{x}} J(\mathbf{x}, t)) \\ \mathbf{x} \in \mathcal{X}, t < 0 \end{aligned} \quad (12.10)$$

$$J(\mathbf{x}, 0) = J_0(\mathbf{x}), t = 0$$

backward from $t = 0$ until $H(\mathbf{x}, D_{\mathbf{x}} J(\mathbf{x}, t)) \approx 0$ or $t = -\tau$ and $D_t J(\mathbf{x}, t)$ represents the derivative of the cost function $J(\mathbf{x}, t)$. All the states of the target set \mathcal{D} and the reachable set $pre_\tau(\mathcal{D})$ are restricted by the state constraint set \mathcal{X} .

For the problem considered in this paper, the target set with respect to $\Delta \mathbf{x}$ showing in Fig.12.1 can be expressed as

$$\mathcal{D}_{\mathbf{x}} = \{\Delta \mathbf{x} \in \mathbb{R}^4 | J(\Delta \mathbf{x}, 0) \leq 0\}. \quad (12.11)$$

Based on Eq.(12.9), the target set with respect to $\Delta \mathbf{x}_r$ can be written as

$$\mathcal{D}_{\mathbf{x}_r} = \{\Delta \mathbf{x}_r \in \mathbb{R}^4 | J(\mathbf{g}(\Delta \mathbf{x}_r), 0) \leq 0\}. \quad (12.12)$$

Through Eq.(12.12), the target set has been transformed into the range of states $\Delta \mathbf{x}_r$. Thus, the dynamic model $\Delta \mathbf{x}_r = \mathbf{f}_{h_0, V_0}(\Delta \mathbf{x}_r)$ described in Eq.(12.2) is adopted to compute the volume of the reachable set.

Given altitude and speed (h_0, V_0) of the tanker aircraft at the docking phase, the cost function $J(\mathbf{x}, t)$ is rewritten as

$$J(\Delta \mathbf{x}_r, t, h_0, V_0) = J(\Delta \mathbf{x}_r, t)|_{h_0, V_0}. \quad (12.13)$$

The reachable set is denoted as

$$\Phi(h_0, V_0) = \{\Delta \mathbf{x}_r \in \mathcal{X}_r | J(\Delta \mathbf{x}_r, t, h_0, V_0) \leq 0, -\tau \leq t \leq 0\}, \quad (12.14)$$

where \mathcal{X}_r represents the state constraint set of the docking phase.

The volume of the reachable set with respect to (h_0, V_0) is defined by

$$\varphi(h_0, V_0) = |\Phi(h_0, V_0)|, \quad (12.15)$$

where $|\cdot|$ represents the volume of the reachable set. The relationship between the trim state (h_0, V_0) of the tanker aircraft and the volume of the reachable set is shown in Fig.12.4. The docking speed V_0 and altitude h_0 affect the volume of the reachable set through determining the trim state of Eq.(12.2).

The objective of this paper is to obtain the optimal trim state of the tanker aircraft at the docking phase. The optimal problem is transformed to find the optimal altitude and speed of the tanker aircraft to maximize the corresponding volume of the reachable set. The optimization

problem is formulated as

$$\max_{h_0 \in [h_{\min}, h_{\max}], V_0 \in [V_{\min}, V_{\max}]} \varphi(h_0, V_0), \quad (12.16)$$

where $\varphi(h_0, V_0)$ is defined in Eq.(12.15). In the computing procedure, the reachable set is calculated on each grid of the continuous state space \mathcal{X}_r . The value $J(\Delta\mathbf{x}_r, t, h_0, V_0)$ of each grid of the reachable set is negative, thus the volume of the reachable set is measured by the number of negative grids in the state space \mathcal{X}_r . Thus, the optimal target is rewritten as

$$\max_{h_0 \in [h_{\min}, h_{\max}], V_0 \in [V_{\min}, V_{\max}]} \bar{\varphi}(h_0, V_0), \quad (12.17)$$

where $\bar{\varphi}(h_0, V_0)$ is a function representing the number of negative grids. The optimal solution to Eq.(12.17) can be seen as the approximate solution of Eq.(12.16), namely

$$\begin{aligned} (h_{\text{op}}, V_{\text{op}}) &= \arg \max_{h_0 \in [h_{\min}, h_{\max}], V_0 \in [V_{\min}, V_{\max}]} \varphi(h_0, V_0) \\ &\approx \arg \max_{h_0 \in [h_{\min}, h_{\max}], V_0 \in [V_{\min}, V_{\max}]} \bar{\varphi}(h_0, V_0). \end{aligned} \quad (12.18)$$

The simulation time step is set to $\Delta t = 0.1\text{s}$ and the backward computation time is $t = -i \times \Delta t$, $i = 1, 2, \dots, 10$. The computing procedure of the optimal trim state of the tanker aircraft is presented as follows:

Step1. Initialize the state space, target set and the corresponding grid points.

Step2. For the specified docking altitude h_0 and docking speed V_0 , calculate T_0 and α_0 .

Step3. Repeat

Solve the HJ PDE (12.10) at each backward computation time $t = -i \times \Delta t$ to get the reachable set

until $t = -1\text{s}$ or $H(\mathbf{x}, D_{\mathbf{x}}J(\mathbf{x}, t)) \approx 0$.

Step4. Calculate the volume of the reachable set for the selected docking altitude h_0 and docking speed V_0 according to $\bar{\varphi}(h_0, V_0)$.

Step5. Obtain the optimal docking altitude h_{op} and speed V_{op} which correspond to the maximum volume of the reachable set.

12.4 Simulation analysis on the Optimal Docking Altitude and Speed of F-16 aircraft

12.4.1 Simulation Description

A simplified nonlinear F-16 aircraft model is used to compute the optimal trim state based on the computing procedure proposed in Section III. In this section, the system parameters of Eq.(12.2), the control constraint set, the state constraint set, the target set at the docking phase are provided.

(i) System Parameters. The physical parameters of the F-16 aircraft model are shown in Table 12.2. The related parameters used in Eq.(12.2) are given in Table 12.3. The lift coefficient

Table 12.2: Physical parameters of F-16 aircraft model

Parameters	m	g	S
Value	20500 lbs	9.8 m/s^2	300 ft^2

Table 12.3: Related parameters of dynamic model

Parameters	C_{L_0}	C_{L_α}	C_{D_0}	K	a	b
Value	0.1	0.06	-0.021	0.35	3m	0.5m

C_L and drag coefficient C_D are obtained through the linear interpolation in the lift curve and drag curve of the F-16 aircraft [279].

(ii) Control Constraint Set. As presented in Section II, $T_r = T^* + \Delta T_r$ and $\alpha_r = \alpha^* + \Delta \alpha_r$. As shown in Fig.12.4, T_0 and α_0 are determined by the trim state (h_0, V_0) of the tanker aircraft. The limits of the control inputs of the Eq.(12.2) are provided in Table 12.4.

(iii) State Constraint Set. The Cartesian grid is used to approximate the state space X_r . The ranges of the states of the system and the grid division are shown in Table 12.5. If the states are out of the ranges, then the docking is considered to fail.

(iv) Target Set. A neighborhood around the desired final states at the docking phase is chosen as the target set. For the considered system, the target set with respect to Δx is

$$\mathcal{D}_x = \left\{ \Delta x \in \mathbb{R}^4 \mid J(\Delta x, 0) = \max \begin{pmatrix} \max(\Delta \tilde{V} - \Delta V_{\text{up}}, \Delta V_{\text{low}} - \Delta \tilde{V}), \\ \max(\Delta \tilde{\gamma} - \Delta \gamma_{\text{up}}, \Delta \gamma_{\text{low}} - \Delta \tilde{\gamma}), \\ \max(\Delta \tilde{x} - \Delta x_{\text{up}}, \Delta x_{\text{low}} - \Delta \tilde{x}), \\ \max(\Delta \tilde{h} - \Delta h_{\text{up}}, \Delta h_{\text{low}} - \Delta \tilde{h}) \end{pmatrix} \leq 0 \right\}, \quad (12.19)$$

where $\Delta \tilde{x} = [\Delta \tilde{V} \Delta \tilde{\gamma} \Delta \tilde{x} \Delta \tilde{h}]^T$ represents the state vector of each grid point and $\Delta V_{\text{up}} = 2\text{m/s}$, $\Delta V_{\text{low}} = -0.2\text{m/s}$, $\Delta \gamma_{\text{up}} = 0.5^\circ$, $\Delta \gamma_{\text{low}} = -0.5^\circ$, $\Delta x_{\text{up}} = 0\text{m}$, $\Delta x_{\text{low}} = -0.3\text{m}$, $\Delta h_{\text{up}} = 1\text{m}$, $\Delta h_{\text{low}} = -1\text{m}$ which represent the upper and lower boundary of the target set. Based on Eq.(12.19), the target set can be rewritten as

$$\mathcal{D}_x = \left\{ \Delta x \in \mathbb{R}^4 \mid \begin{array}{l} -0.2\text{m/s} \leq \Delta V \leq 2\text{m/s}, -0.5^\circ \leq \Delta \gamma \leq 0.5^\circ, \\ -0.3\text{m} \leq \Delta x \leq 0\text{m}, -1\text{m} \leq \Delta h \leq 1\text{m} \end{array} \right\}. \quad (12.20)$$

At the docking phase γ_t and γ_r approach zero degree, namely $\gamma_t = \gamma_r \approx 0^\circ$. Thus, in Fig.12.3, $\vartheta_r \approx \alpha_r$. The parameter α_r is small at the docking phase leading to $\vartheta_r \approx 0^\circ$. Through the transformation of Eq.(12.12), the target set specified in the relative coordinate system is

Table 12.4: Limits of the variations of the control inputs of the dynamic model

Variations of the control inputs	Min	Max
ΔT_r	-2000N	2000N
$\Delta \alpha_r$	-2°	2°

Table 12.5: Grid division of the state space

Parameters	$\Delta V_r(m/s)$	$\Delta \gamma_r(\text{deg})$	$\Delta x_r(m)$	$\Delta h_r(m)$
Range	[-2,7]	[-10,5]	[-4,0.5]	[-1,1]
Grid numbers	40	30	20	20
Step size	0.23	0.5	0.23	0.1

expressed by

$$\mathcal{D}_{x_r} = \left\{ \Delta \mathbf{x}_r \in \mathbb{R}^4 \mid \begin{array}{l} -0.2m/s \leq \Delta V_r \leq 2m/s, \\ -0.5^\circ \leq \Delta \gamma_r \leq 0.5^\circ, \\ (-0.3 - a)m \leq \Delta x_r \leq (-a)m, \\ (-1 - b)m \leq \Delta h_r \leq (1 - b)m \end{array} \right\}, \quad (12.21)$$

where the target set \mathcal{D}_{x_r} is a small hypercube.

Remark 2. The target set is a four-dimensional (4D) hypercube. So, the function $J(\Delta \mathbf{x}, 0)$ in Eq.(12.19) is not differentiable. However, the HJ PDE can be still solved by a numerical method. According to Eq.(12.19), the distance between each grid point and the boundary of the target set can be obtained by the function "shapeRectangleByCorners" in the ToolboxLS [282]. For the discrete grid points, the derivative of $J(\Delta \mathbf{x}_r, t)|_{h_0, V_0}$ can be computed.

Remark 3. The primary weakness of the reachability analysis method is that memory and computational time requirements rise exponentially with dimension. In practice, systems of dimensions 1~3 can be examined interactively [276]. The dimension of the longitudinal dynamics of the mass center of the receiver aircraft is four. It is slow but feasible on a computer with sufficient memory. Since the exact computation of reachable set is typically done off-line, the over-approximating reachable set can allow for real-time computation [277].

12.4.2 Optimal docking speed and docking altitude

In this section, the volumes of the reachable set at different docking altitudes and speeds are depicted in Fig.12.5. The computation of reachable set is typically done off-line in Matlab, and run on a desktop with 2.4GHz CPU and 2GB RAM. The computation time is 986.878 seconds at each discrete altitude and speed. Furthermore, the computation time of the volumes of the reachable set is 0.000046s. The Matlab source code of the paper is presented in our research group website <http://rfly.buaa.edu.cn/resources/>. The altitude and speed of the F-16 aircraft at the docking phase is confined to 1000m~ 8000m with the interval 1000m and 120m/s~ 180m/s with the interval 10m/s, respectively. The volume of the reachable set at discrete altitude and speed is

$$\begin{aligned} RS_{ij} &= \bar{\varphi}(h(i), V(j)) \\ h(i) &= 1000 + 1000 * i, \quad i = 0, 1, 2, \dots, 7 \\ V(j) &= 120 + 10 * j, \quad j = 0, 1, 2, \dots, 6 \end{aligned} \quad (12.22)$$

From the obtained results in Fig.12.5, three observations can be concluded. (i) As the altitude

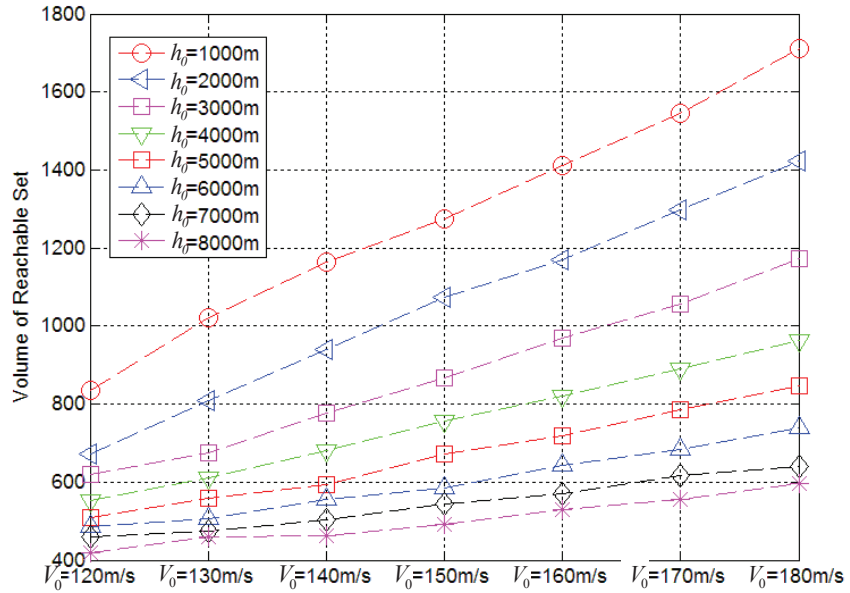


Figure 12.5: Volume of reachable set at different altitudes and different docking speeds

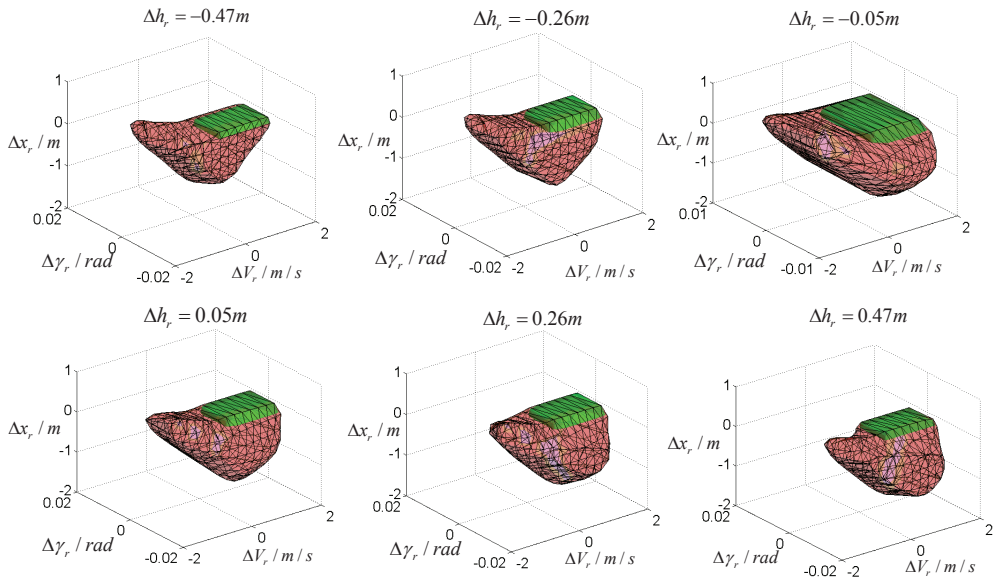


Figure 12.6: Target set (green) and reachable set (red) for three-dimensional (3D) slices of the four-dimensional (4D) reachable set with the optimal altitude $h_{op} = 1000m$ and the optimal docking speed $V_{op} = 180m/s$.

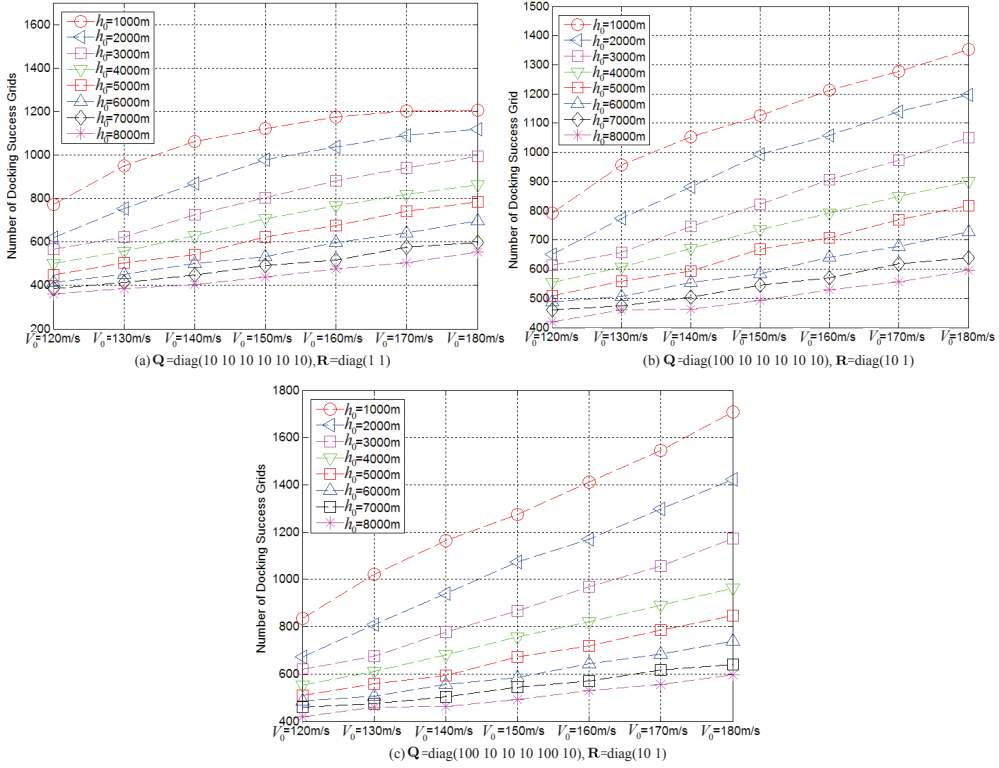


Figure 12.7: For different matrix \mathbf{Q} and \mathbf{R} , the numbers of docking success grid at different altitudes and speeds

changes from 1000m to 8000m, the volume of the reachable set $\bar{\varphi}(h_0, V_0)$ is monotonously decreased. (ii) The volume of the reachable set $\bar{\varphi}(h_0, V_0)$ at a high altitude is always small regardless of the docking speed. (iii) As the speed changes from 120m/s to 180m/s, the volume of the reachable set $\bar{\varphi}(h_0, V_0)$ is monotonously increased. This implies that the faster the tanker aircraft is, the bigger state space the receiver aircraft can be operated in. Then, the optimal docking altitude h_{op} and optimal speed V_{op} are obtained by

$$(h_{\text{op}}, V_{\text{op}}) = \arg \max_{h_0 \in [h_{\min}, h_{\max}] V_0 \in [V_{\min}, V_{\max}]} \bar{\varphi}(h_0, V_0). \quad (12.23)$$

They are $h_{\text{op}} = 1000\text{m}$ and $V_{\text{op}} = 180\text{m/s}$. The corresponding maximum volume of the reachable set is $\bar{\varphi}(h_{\text{op}}, V_{\text{op}}) = 1710$.

The reasons for these observations are summarized as follows. (i) As the altitude is increased, the air density is decreased. Therefore, the receiver aircraft should increase the speed to balance the gravity and the drag force. Meanwhile, the maneuverability of the aircraft becomes worse at a high altitude, resulting in a small volume of the reachable set. (ii) The air density is increased as the altitude is decreased, and the maneuverability of the aircraft becomes better. Thus, the corresponding volume of the reachable set is bigger. This implies that it is suitable for docking at a low altitude. However, by considering the air turbulence and the operational risk of the pilots, it is better to dock at a medium altitude and a medium speed for safety considerations.

The further explanation is provided as follows. The maneuverability is roughly related to the feasible control input of an aircraft. The larger the maneuverability, the more margin the

feasible control can offer, implying a larger reachability roughly [286]. Compared with the maneuverability, the proposed reachability is more exact as it has taken both control input and the system dynamics into consideration. Often, the maneuverability of an aircraft is measured by the normal load factor n_y which can be expressed as $n_y = L/G$. The gravity G is constant. If the lift L is larger, its corresponding normal load n_y is larger, i.e., the maneuverability is better. According to the Fig.12.5, two cases are considered. In the first case, the speed V is set to be constant and the altitude h_1 is set to be higher than the altitude h_2 which are both between 1000m and 8000m. The air densities at the altitudes h_1 and h_2 are supposed to be ρ_1 and ρ_2 , respectively. The formula of the Mach number is $M = V/V_a$, where V_a represents the speed of sound. The Mach number at the altitude h_1 and h_2 are set to be M_1 and M_2 , respectively. According to the formula of the lift L which has been provided in Eq.(12.3), the lift at the altitude h_1 and h_2 can be expressed as $L_1 = \frac{1}{2}\rho_1 V^2 C_{L1} S$ and $L_2 = \frac{1}{2}\rho_2 V^2 C_{L2} S$. As the altitude is increased, the air density ρ is decreased, namely $\rho_1 < \rho_2$. Meanwhile, the speed of sound V_a is also decreased, implying the Mach number $M_1 > M_2$ and the corresponding lift coefficient $C_{L1} < C_{L2}$. Thus, the lift L_2 is larger than the lift L_1 and then the maneuverability at the altitude h_2 is better. This means that if the aircraft speed V is constant, then the volumes of the reachable set at altitude h_2 is larger because the maneuverability at the altitude h_2 is better. In the second case, the altitude h is set to be constant and the speed V_1 is set to be larger than the speed V_2 which are both between 120m/s and 180m/s. According to the definition of the lift L , the lifts at the speed V_1 and the speed V_2 can be expressed as $L_1 = \frac{1}{2}\rho V_1^2 C_L S$ and $L_2 = \frac{1}{2}\rho V_2^2 C_L S$, respectively. It is obvious that the lift L_1 is larger than L_2 . This implies that the maneuverability at the speed V_1 is better than that at the speed V_2 . Therefore, if the aircraft altitude h is set to be constant, then the volume of the reachable set at speed V_1 is larger than that at the speed V_2 .

The Fig.12.6 shows the 3D slices of the 4D maximum reachable set. The 4D maximal reachable set is the largest controllable set from which the receiver aircraft can dock successfully.

12.4.3 Verification

12.4.3.1 Verification by using LQR controllers

In this section, LQR controllers are used to verify the optimal trim state at the docking phase. It is reasonable to adopt LQR controller to verify the simulation results owing the fact that LQR approach is often employed to design the docking control laws for the AR process [265] [287] [288]. The number of docking success grids of the reachable set at different altitudes and speeds within a specified time horizon is used to measure how difficult the docking is. If the number is larger, it means that it is easier to dock with the corresponding controller. The main steps of verification are shown as follows:

Step1. Calculate T_0 and α_0 at the docking altitude h_0 and docking speed V_0 .

Step2. Linearize the dynamic model of the system as in Eq.(12.2) which is written as

$$\Delta \mathbf{x}_r = \mathbf{A}_r \Delta \mathbf{x}_r + \mathbf{B}_r \mathbf{u},$$

where

$$\mathbf{A}_r = \begin{bmatrix} -\frac{\rho V_0 S C_d}{m} & -g \cos \gamma_0 & 0 & 0 \\ \frac{\frac{1}{2} \rho V_0^2 S C_L - T_0 \sin \alpha_0 + mg \cos \gamma_0}{m V_0^2} & \frac{g \sin \gamma_0}{V} & 0 & 0 \\ \cos \gamma_0 & -V_0 \sin \gamma_0 & 0 & 0 \\ \sin \gamma_0 & V_0 \cos \gamma_0 & 0 & 0 \end{bmatrix},$$

$$\mathbf{B}_r = \begin{bmatrix} \frac{-T_0 \sin \alpha_0}{m} & \frac{\cos \alpha_0}{m} \\ \frac{-T_0 \cos \alpha_0}{m V_0} & \frac{\sin \alpha_0}{m V_0} \\ 0 & 0 \\ 0 & 0 \end{bmatrix}.$$

Step3. Each grid point of the reachable set at the selected docking altitude h_0 and docking speed V_0 is taken as the initial state of the LQR controllers (see the *Appendix* for details). The controllers are used to drive the state of the receiver aircraft into the target set \mathcal{D} . The control time is set to be 5s, which is longer than the backward computation time of the reachable set. This is because the LQR controllers need enough time to converge.

Step4. Record the number of docking success grid of the reachable set which can be defined as $\tilde{\varphi}(h_i, V_j)$ at different altitudes and speeds.

The numbers of docking success grid for three LQR controllers are depicted in Fig.12.7. As shown, two observations can be concluded. (i) The $\tilde{\varphi}(h_i, V_j)$ is proportional with $\varphi(h_i, V_j)$. (ii) The maximum number of the docking success grid for different LQR controllers are 1207, 1353 and 1708 with altitude $h_i = 1000\text{m}$ and docking speed $V_j = 180\text{m/s}$ which corresponds with the maximum volume of the reachable set. The verification of the results leads to the following conclusions. (i) The success rate of the LQR controller is proportional with the volume of reachable set. (ii) It is more suitable to design controllers at the optimal trim state at the docking phase.

12.4.3.2 Verification by using degree of controllability

In this section, a degree of controllability (DoC) is adopted to verify the effectiveness of the proposed method from another aspect. The linear dynamical model of the system is $\Delta \mathbf{x}_r = \mathbf{A}_r \Delta \mathbf{x}_r + \mathbf{B}_r \mathbf{u}$, where the control input $\mathbf{u} = [T_r \alpha_r]^T \in \Omega$. The definitions of recovery region and DoC are obtained according to [289].

Definition 1. For the linear dynamical model of the system, the recovery region \mathcal{R} within time t_r is defined as

$$\mathcal{R}(t_r) = \{\Delta \mathbf{x}_r(0) \mid \exists \mathbf{u}(t) \in \Omega, t \in [0, t_r], \text{s.t. } \Delta \mathbf{x}_r(t_r) = \mathbf{0}\} \quad (12.24)$$

Definition 2. For the linear dynamical model of the system, the DoC ρ within time t_r is

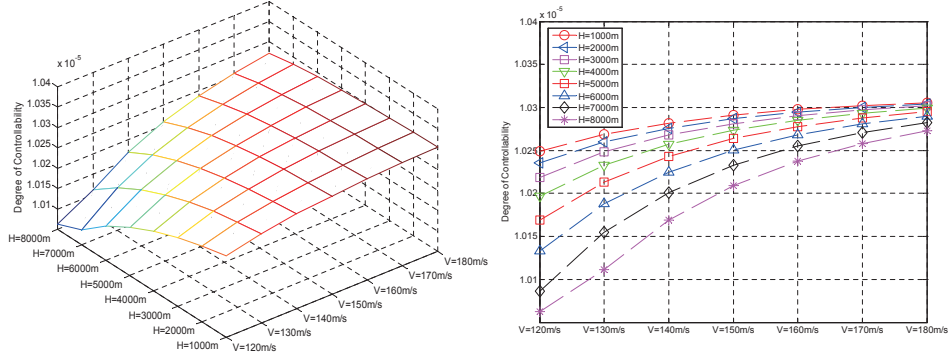


Figure 12.8: (Left) Three-dimensional surface and (right) two-dimensional curve of the value of ρ_{doc} at different altitudes and speeds

defined as

$$\rho_{\text{doc}} = \inf \|\Delta \mathbf{x}_r(0)\| \quad \forall \Delta \mathbf{x}_r(0) \notin \mathcal{R}(t_r) \quad (12.25)$$

where $\|\cdot\|$ represents the Euclidean norm.

From *Definition 2*, it is observed that the minimal distance from the origin to the boundary of the recovery region is considered to be the DoC of the system. The value of ρ_{doc} represents how controllable the system is. The larger the value of ρ_{doc} , the stronger the system control ability is. The values of ρ_{doc} at different altitudes and speeds can be defined as $\rho_{\text{doc}}(h_i, V_j)$ which are shown in Fig.12.8. As shown in Fig.12.8, the $\rho_{\text{doc}}(h_i, V_j)$ is proportional with $\bar{\varphi}(h_i, V_j)$. This shows the feasibility of our simulation results from another aspect. The use of DoC is not used to replace with the reachability analysis but is only taken as a verification for the reachability analysis, because i) the target set is only zero rather than a set as in Eq.(12.12) for reachability analysis here; ii) a linear model is used rather than nonlinear model used for the reachability analysis.

12.5 Chapter Summary

In order to improve the success rate of docking in an AR process, the reachability analysis method is used to obtain the optimal trim state of the tanker aircraft at the docking phase. The optimal trim state is defined as the docking state of the tanker aircraft corresponding to the maximum volume of the reachable set. First, in order to find the optimal trim state of the tanker aircraft at the docking phase, 4D relative motion model between the receiver aircraft and the center of the drogue is proposed. Based on it, a step-by-step computing procedure to obtain the optimal docking speed and altitude is proposed. Then, the simulation on a simplified nonlinear F-16 aircraft model is studied comprehensively. From the simulation, the success rate of the proposed LQR controller is proportional with the volume of the reachable set so that the proposed method to obtain the optimal trim state of the tanker aircraft is reasonable. Furthermore, a DoC method is also used to verify the feasibility of the optimal trim state from another aspect.

For the simulation results, the brute force search method is used to determine the optimal trim state. From the simulation results obtained, the problem seems like convex optimization problem. But it is difficult to verify the convexity of the simulation results, the major reason for which is the function of the volume of the reachable set is not easy to use an analytical function to express. But the convexity of the simulation results is also a problem which is needed to be solved. The verification of its convexity of the optimization problem is regarded as the further study.



Chapter 13 Docking Success Probability Prediction

based on Stochastic Approximation

Aerial Refueling (AR) is an important capability to increase the endurance and flight range of aircraft. But at the docking phase, the docking risk is high as the receiver aircraft is approaching the tanker aircraft. In order to guarantee the safety of the AR process, it is important to predict the probability of docking success. Motivated by this, a stochastic approximation method is adopted to evaluate the docking success probability of the receiver aircraft by taking random disturbance into account. First, a stochastic dynamic model of the probe with respect to the drogue is proposed, and the target set of the docking phase is defined. Then, based on a stochastic approximation method, the backward computing procedure of the docking success probability is given, and the level curves and probability isosurface of the docking phase are plotted. Finally, by comparing the simulation results between the stochastic approximation method and Monte Carlo method, the effectiveness of the proposed method is demonstrated.

13.1 Introduction

Aerial Refueling (AR) is a main method of extending the endurance and range of aircraft in aviation field[3, 152]. During an AR process, the receiver aircraft first breaks away from its formation, and then approaches the rear of the tanker aircraft for docking. Once the receiver aircraft completes refueling, the receiver aircraft disconnects with the tanker aircraft and rejoins the formation again. Therefore, the entire AR process can be decomposed into three phases: the approaching tanker phase, the docking phase, and the rejoin formation phase [151]. This paper will focus on the docking phase which is a very key step of an AR process. Currently, the docking phase of a regular AR process is realized by experienced pilots of the aircraft or the autopilot of the Unmanned Aerial Vehicles (UAVs), which often suffers from high risk due to the close relative distance between the receiver aircraft and the tanker aircraft. Thus, a problem arises that how to evaluate the probability of the docking success at the docking phase. If the probability of the docking success is lower than a specified value when closing to the drogue, the receiver aircraft can decrease the speed and increase the relative distance between the receiver aircraft and the tanker aircraft to reduce the risk.

At present, most of the research on AR mainly focuses on modeling [44, 116, 208] and controlling[40, 290], while there is not much research on evaluating the safety of docking phase. In Ref.[170] provided by NASA, the region around the drogue is separated into two parts, the safe region and the un-docking region. However, the region partition lacks a theoretical support. In Ref.[120], the reachable analysis method has been applied to an AR process to ensure safe

operation of a sequential mode transition. The reachable set is a boundary range. For the state of the reachable set, there exists at least one control input to drive the state into the target set within a finite time horizon. However, the probability of docking success of the state cannot be given. Actually, the docking phase is affected strongly by the wind perturbation. This paper aims to determine the probability of docking success at the docking phase. There are mainly three methods to solve the problem of stochastic disturbances, namely the model abstract method[291–293], the over-approximation method[294–296] and the Monte Carlo simulation method[297, 298]. The stochastic approximation method is a kind of model abstract method and the distinguishing feature of the method is that it approximates the solution of the stochastic differential equations by using Markov chains. So far, stochastic approximation method has been used to solve the problems of aircraft conflict detection[299], safety assessment of autonomous cars[300] and the large geostatistical data analysis[301]. With respect to the docking phase, the target set represents the state set of successful docking states, and the probability of completing the docking maneuver within a finite time horizon is computed by stochastic approximation method[291].

In this paper, the stochastic approximation method is used to obtain the docking success probability of the state of the receiver at the docking phase. With respect to the docking phase, the target set represents the set of successful docking states. The probability of entering the target set is computed by appropriately propagating the transition probabilities of the Markov chain backward starting from the target set during the specified time horizon. With properly chosen transition probabilities, the Markov chain converges weakly to the solution of the stochastic differential equations. Concretely, the computation of the probability of docking success is divided into three phases. First, the relative motion model of the receiver aircraft with respect to the center of the drogue is provided. Secondly, the Markov chain is obtained by gridding the state space of the stochastic dynamic system and defining the transition probabilities of the discrete state set. Thirdly, the probability of entering the target set is computed backward starting from the target set during the specified time horizon. For a specified grid point of the state space, the probability of docking success is computed.

The contributions of this paper are as follows: (i) This paper studies the safety of AR process from the perspective of the docking success probability to provide a support for safety decision-making, which is different from most current studies focusing on accurate control or navigation. (ii) This paper proposes a fast calculation method of backward docking success probability in the AR process, which is more efficient than the regular Monte Carlo method.

13.2 Modeling and Problem Formulation

Fig.13.1 shows the relative position between the receiver and the tanker at the docking phase of the AR process, which contains two types of coordinate systems, namely the earth-fixed



coordinate system $O_gx_gy_gh_g$ and relative coordinate system O_{xyh} . The origin of the relative coordinate system is at the center of the drogue, and the x -axis is aligned with the airspeed vector V_t of the tanker. As shown in Fig.13.1, P represents the tip of the probe, V_t and V_r represent the speed of tanker and receiver respectively, $\Delta\gamma$ and $\Delta\varphi$ represent the relative flight path angle and the relative azimuth angle between receiver and tanker respectively. Assume the flight path angle and the azimuth angle of the tanker are 0° at the docking phase. Then, $\Delta\gamma$ and $\Delta\varphi$ satisfy $\Delta\gamma = \gamma_r$ and $\Delta\varphi = \varphi_r$, where γ_r represents the flight path angle of the receiver and φ_r represents the azimuth angle of the receiver. The region in front of the drogue in Fig.13.1, which is represented by the target set \mathcal{D} [302], is defined as the successful docking region. A successful docking maneuver is made once the probe enters the region.

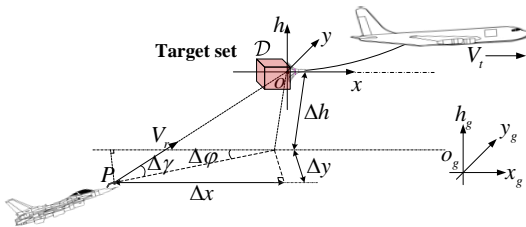


Figure 13.1: The relative position between the receiver and the tanker.

The relative position between the tip of the probe and the center of the drogue in relative coordinates at the docking phase is considered. At the docking phase, the wind is the main source of the uncertainty on the relative position of the tip of the probe and the center of the drogue. The motions of the tip of the receiver probe and the drogue hauled by the tanker is hauling can be described by the following stochastic differential equations[303]

$$d\mathbf{x}_r(t) = \mathbf{a}_1(t) dt + \mathbf{f}(\mathbf{x}_r, t) dt + \Gamma d\mathbf{B}(\mathbf{x}_r, t) \quad (13.1)$$

$$d\mathbf{x}_t(t) = \mathbf{a}_2(t) dt + \mathbf{f}(\mathbf{x}_t, t) dt + \Gamma d\mathbf{B}(\mathbf{x}_t, t) \quad (13.2)$$

where the state vector $\mathbf{x}_r = [x_r \ y_r \ h_r]^T$ represents the longitudinal distance, latitudinal distance and altitude of the tip of the probe in the earth-fixed coordinate system, and $\mathbf{x}_t = [x_t \ y_t \ h_t]^T$ represents the longitudinal distance, latitudinal distance and altitude of the center of the drogue in the earth-fixed coordinate system. Functions $\mathbf{a}_1 : [0, \infty) \rightarrow \mathbb{R}^3$ and $\mathbf{a}_2 : [0, \infty) \rightarrow \mathbb{R}^3$ represent the kinematic states of the tip of the probe and the drogue in the earth-fixed coordinate system. Concretely, $\mathbf{a}_1(t)$ represents the kinematic equation of the probe in the earth-fixed coordinate system, and $\mathbf{a}_2(t)$ represents the kinematic equation of the drogue in the earth-fixed coordinate system. Due to the tanker always in steady flight with a constant speed V_t at the docking phase, $\mathbf{a}_1(t)$ and $\mathbf{a}_2(t)$ satisfy

$$\mathbf{a}_1(t) = \begin{bmatrix} V_r(t) \cos \gamma_r(t) \cos \varphi_r(t) \\ V_r(t) \cos \gamma_r(t) \sin \varphi_r(t) \\ V_r(t) \sin \gamma_r(t) \end{bmatrix}, \quad \mathbf{a}_2(t) \equiv \begin{bmatrix} V_t \\ 0 \\ 0 \end{bmatrix}.$$

The function $\mathbf{f} : \mathbb{R}^3 \times [0, \infty) \rightarrow \mathbb{R}^3$ represents the wind field. The function $\mathbf{f}(\mathbf{x}, t)$ is

affine transformation in \mathbf{x} and can be represented as $\mathbf{f}(\mathbf{x}, t) = \mathbf{r}(t)\mathbf{x} + \mathbf{l}(t)$, where $\mathbf{r} : [0, \infty) \rightarrow \mathbb{R}^{3 \times 3}, \mathbf{l} : [0, \infty) \rightarrow \mathbb{R}^3$. The matrix $\boldsymbol{\Gamma}$ is used to change the variance of the random perturbation. To simplify the problem, $\boldsymbol{\Gamma}$ is assumed to be a constant diagonal matrix given by $\boldsymbol{\Gamma} = \text{diag}(\sigma_1, \sigma_2, \sigma_3), \sigma_1, \sigma_2, \sigma_3 > 0$. The function $\mathbf{B} : \mathbb{R}^3 \times [0, \infty) \rightarrow \mathbb{R}^3$ denotes stochastic perturbation, $\mathbf{B}(\mathbf{x}, t)$ is not a standard Brownian motion but a function related to the current state \mathbf{x} . However, $\mathbf{B}(\mathbf{x}_0, t)$ is a standard Brownian motion for a specific position $\mathbf{x}_0 \in \mathbb{R}^3$. The covariance of $\mathbf{B}(\cdot)$ can be represented as[304]

$$E \left((\mathbf{B}(\mathbf{x}_1, t_2) - \mathbf{B}(\mathbf{x}_1, t_1)) (\mathbf{B}(\mathbf{y}_1, t_2) - \mathbf{B}(\mathbf{y}_1, t_1))^T \right) = \rho(\mathbf{x}_1 - \mathbf{y}_1)(t_2 - t_1) \mathbf{I}_3 \quad \mathbf{x}_1, \mathbf{y}_1 \in \mathbb{R}^3 \quad t_1 < t_2 \quad (13.3)$$

where \mathbf{x}_1 and \mathbf{y}_1 represent the position of the tip of probe and center of the drogue, \mathbf{I}_3 represents the 3-by-3 identity matrix and $\rho : \mathbb{R}^3 \rightarrow \mathbb{R}$ represents the spatial correlation function. Supposing that the drogue is in the same position as the tip of the probe, namely $\mathbf{x}_1 - \mathbf{y}_1 = 0$, then $\rho(\mathbf{x}_1 - \mathbf{y}_1) = 1$; if the distance between probe and drogue is infinite, then $\rho(\mathbf{x}_1 - \mathbf{y}_1) = 0$. It means that the closer the tip of the probe and the center of the drogue are in the space, the more similar the wind speeds at the two positions are. If the tip of the probe and the center of the drogue move farther away from each other, the wind speeds of the two positions become more independent.

Subtracting Eq. (13.2) from Eq. (13.1), the relative position of the tip of the probe and the center of the drogue is written as

$$d\tilde{\mathbf{x}}_{r/t}(t) = \mathbf{u}(t)dt + r(t)\tilde{\mathbf{x}}_{r/t}(t)dt + \boldsymbol{\Gamma}d\mathbf{z}(t) \quad (13.4)$$

where $\tilde{\mathbf{x}}_{r/t} = \mathbf{x}_r - \mathbf{x}_t$ and $\tilde{\mathbf{x}}_{r/t} = [\Delta x \Delta y \Delta h]^T$ represents the longitudinal distance, latitudinal distance and altitude of the tip of the probe with respect to the center of the drogue, respectively; $\mathbf{u}(t) = \mathbf{a}_1(t) - \mathbf{a}_2(t)$ represents the kinematic states of the tip of the probe with respect to the center of the drogue. Based on Eq. (13.3), define $\mathbf{z}(t) = \mathbf{B}(\mathbf{x}_r, t) - \mathbf{B}(\mathbf{x}_t, t)$, where $\mathbf{z}(t)$ is a Gaussian process with the covariance

$$E \left((\mathbf{z}(t_2) - \mathbf{z}(t_1)) (\mathbf{z}(t_2) - \mathbf{z}(t_1))^T \right) = 2(1 - \rho(\tilde{\mathbf{x}}_{r/t})) (t_2 - t_1) \mathbf{I}_3 \quad t_1 < t_2 \quad (13.5)$$

The concrete proof of Eq. (13.5) is presented in Appendix.

According to Eq. (13.5), one can get $z(t) = \sqrt{2(1 - \rho(\tilde{\mathbf{x}}_{r/t}))} \mathbf{W}(t)$. Then, Eq. (13.4) is rewritten as

$$\begin{aligned} d\tilde{\mathbf{x}}_{r/t}(t) &= \mathbf{u}(t)dt + \mathbf{r}(t)\tilde{\mathbf{x}}_{r/t}(t)dt + \sqrt{2(1 - \rho(\tilde{\mathbf{x}}_{r/t}))}\boldsymbol{\Gamma}d\mathbf{W}(t) \\ &= (\mathbf{u}(t) + r(t)\tilde{\mathbf{x}}_{r/t}(t))dt + \sqrt{2(1 - \rho(\tilde{\mathbf{x}}_{r/t}))}\boldsymbol{\Gamma}d\mathbf{W}(t) \\ &= \alpha(\tilde{\mathbf{x}}_{r/t}, t)dt + \beta(\tilde{\mathbf{x}}_{r/t})\boldsymbol{\Gamma}d\mathbf{W}(t) \end{aligned} \quad (13.6)$$

where $\mathbf{W}(t)$ is a standard 3D Brownian motion, $\alpha(\tilde{\mathbf{x}}_{r/t}, t) = \mathbf{u}(t) + r(t)\tilde{\mathbf{x}}_{r/t}$ is the drift term and $\beta(\tilde{\mathbf{x}}_{r/t}) = \sqrt{2(1 - \rho(\tilde{\mathbf{x}}_{r/t}))}$ represents the diffusion term. Eq. (13.6) is a standard stochastic differential equation. According to Eq. (6), the relative motion model between the center of the

drogue and the tip of the probe is expressed as

$$d \begin{bmatrix} \Delta x \\ \Delta y \\ \Delta h \end{bmatrix} = \begin{bmatrix} -V_t + V_r(t) \cos \gamma_r(t) \cos \varphi_r(t) \\ V_r(t) \cos \gamma_r(t) \sin \varphi_r(t) \\ V_r(t) \sin \gamma_r(t) \end{bmatrix} dt + \mathbf{r}(t) \begin{bmatrix} \Delta x \\ \Delta y \\ \Delta h \end{bmatrix} dt + \sqrt{2[1 - \rho(\tilde{\mathbf{x}}_{r/t})]} \begin{bmatrix} \sigma_h & 0 & 0 \\ 0 & \sigma_h & 0 \\ 0 & 0 & \sigma_v \end{bmatrix} d\mathbf{W}(t) \quad (13.7)$$

Here, $\tilde{\mathbf{x}}_{r/t}$ is restricted by state constraint $\chi \subset \mathbb{R}^3$, where χ represents the feasible position of the tip of the probe with respect to the center of the drogue at the docking phase. The speed of the tanker is constant and the control variable is the state parameters of the receiver namely V_r , γ_r and φ_r at the docking phase. The values σ_h and σ_v are adopted to describe the variation of stochastic perturbation. The larger the values are, the larger the variation in perturbation of the corresponding dimension is.

The spatial correlation function $\rho(\tilde{\mathbf{x}}_{r/t})$ can be expressed as [301]

$$\rho(\tilde{\mathbf{x}}_{r/t}) = \exp(-c_h \|\tilde{\mathbf{x}}_{r/t}\|_h - c_v \|\tilde{\mathbf{x}}_{r/t}\|_v) \quad (13.8)$$

where $c_h > 0$ and $c_v > 0$ represent the longitudinal correlation coefficient and latitudinal correlation coefficient. If $c_h > c_v$, then the correlation of the wind perturbations in the vertical direction is greater than that in the horizontal plane. In Eq. (13.7), one has

$$\|\tilde{\mathbf{x}}_{r/t}\|_h = \sqrt{\Delta x^2 + \Delta y^2}, \|\tilde{\mathbf{x}}_{r/t}\|_v = |\Delta h| \quad (13.9)$$

A neighborhood around the desired final states at the docking phase is defined as the target set \mathcal{D} . For the relative motion model Eq. (13.7), the target set \mathcal{D} is a cube.

Definition 1: Given a target set \mathcal{D} , the probability of docking success for the initial state $\tilde{\mathbf{x}}_{r/t}$ at the docking phase over the time horizon $t \in [0, t_f]$ is

$$P \stackrel{\Delta}{=} P\{\tilde{\mathbf{x}}_{r/t}(t_f) \in \mathcal{D} | \tilde{\mathbf{x}}_{r/t}(0) \in \mathcal{X}, t \in [0, t_f]\} \quad (13.10)$$

which satisfies the state constraint Eq. (13.7), where $t_f > 0$ represents the end time of the docking phase.

13.3 Docking Success Probability Evaluation

To make this paper self-contained, some preliminary results on the stochastic approximation method is recalled firstly. Then the computing procedure of the probability of docking success is provided.

13.3.1 General ideas

The objective is to determine the probability of docking success of the states at the docking phase, as shown in Eq. (13.10). The stochastic approximation method is adopted to evaluate the probability of docking success based on the Markov chain approximation scheme, where the Cartesian grid is used to approximate the state space in the Markov chain. It is necessary to consider the uncertainty of state transition due to the stochastic perturbations.

The general ideas of determining the probability of docking success of the states using the stochastic approximation method are described in the following.

- First, determine the state space during the docking phase. The state space set is divided into three sets, which are the target set \mathcal{D} , the state constraint set χ , and the state space which is outside the target set but inside χ can be denoted by $\mathcal{L} = \chi \setminus \mathcal{D}$.

- Second, discretize the state space. Divide the state space \mathcal{L} into grids, with the grid size being $\delta > 0$. The set of grids Q in the state space \mathcal{L} is further divided into boundary grids $\partial Q_{\mathcal{L}} = \partial Q_{\chi} \cup \partial Q_{\mathcal{D}}$ and interior grids $Q_0 = Q \setminus \partial Q_{\mathcal{L}}$. The state space and its partition are shown in Fig. 13.2.

- Third, define the Markov chain Q_k . Based on the discretization of the state space, the probability of the current grid point q transferring to the adjacent grid point set N_q and to the grid point itself is described by using the transition probability of Markov chain. For interior grid points $q \in Q_0$, its adjacent grid point set is N_q . For the three-dimensional state equation shown in equation (13.7), the state transition from the current grid point q to the adjacent grid point set N_q and to the grid point itself can be described by Fig. 13.3. As shown in 13.3, the adjacent grid point set of q includes $q_{1+}, q_{1-}, q_{2+}, q_{2-}, q_{3+}$ and q_{3-} , which are specifically expressed as $q_{i+} = q_i + \eta_i \delta$ and $q_{i-} = q_i - \eta_i \delta$ ($i = 1, 2, 3$). Here, η_i ($i = 1, 2, 3$) are related to the parameters in the constant diagonal matrix Γ and specifically expressed as $\eta_i = \sigma_i / \bar{\sigma}$ ($i = 1, 2, 3$), where $\sigma_1 = \sigma_2 = \sigma_h$, $\sigma_3 = \sigma_v$ and $\bar{\sigma} = \max \sigma_i$.

- Fourth, the probability of docking success of the corresponding grid points in the state space \mathcal{L} are finally obtained by appropriately propagating the transition probabilities of the Markov chain backward starting from the target set.

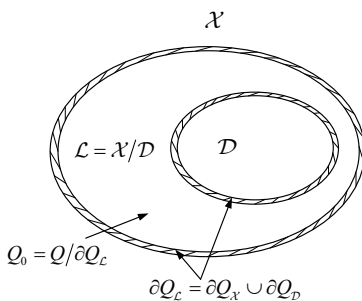


Figure 13.2: State space and its partition.

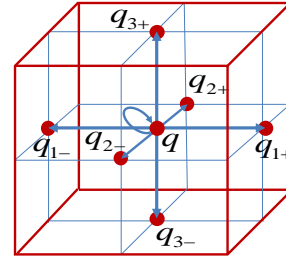


Figure 13.3: Graph description of state transition.

13.3.2 The transition probability of Markov chain

The transition probability of Markov chain is used in stochastic approximation method to describe the change of the states. It is provided as follows[291]:

(1) If $q \in \partial Q_{\mathcal{L}}$, the transition probability is expressed as

$$P \{ Q_{k+1} = q' | Q_k = q \} = \begin{cases} 1 & q' = q \\ 0 & otherwise \end{cases} \quad (13.11)$$

The grid point q will not transfer to another grid point, as the set $\partial Q_{\mathcal{L}}$ is an absorbing region.

(2) If $q \in Q_0$, the transition probability from the grid point q to the adjacent grid $q' \in N_q$ is expressed by

$$P\{Q_{k+1} = q' | Q_k = q\} = \begin{cases} p_{q'}^k(q) & q' \in N_q \cup \{q\} \\ 0 & \text{otherwise} \end{cases} \quad (13.12)$$

where $p_{q'}^k(q)$ represents the probability of transition from the grid point q to the grid point q' in the k -th step. For the discrete state space, the drift term and diffusion term can be denoted by $\alpha(q, k\Delta t)$ and $\beta(q)$ respectively, where Δt represents the time step. Thus, $p_{q'}^k(q)$ can be expressed by

$$p_{q'}^k(q) = \begin{cases} p_q^k(q) = \frac{\xi_0^k(q)}{C_q^k}, & q' = q \\ p_{q_{i+}}^k(q) = \frac{\exp(\delta\xi_i^k(q))}{C_q^k}, & q' = q_{i+}, i = 1, 2, 3 \\ p_{q_{i-}}^k(q) = \frac{\exp(-\delta\xi_i^k(q))}{C_q^k}, & q' = q_{i-}, i = 1, 2, 3 \end{cases} \quad (13.13)$$

where

$$\xi_0^k(q) = \frac{2}{\lambda\bar{\sigma}^2\beta(q)^2} - 2n, \xi_i^k(q) = \frac{(\alpha(q, k\Delta t))_i}{\eta_i\bar{\sigma}^2\beta(q)^2}, C_q^k = \sum_{i=1}^3 \left(\exp(\delta\xi_i^k(q)) + \exp(-\delta\xi_i^k(q)) \right) + \xi_0^k(q)$$

and λ is a positive constant. Here, according to Eq. (13.7), the definitions of $\alpha(q, k\Delta t), \beta(q)$ are

$$\alpha(q, k\Delta t) = \begin{bmatrix} -V_t + V_r(k\Delta t) \cos \gamma_r(k\Delta t) \cos \varphi_r(k\Delta t) \\ V_r(k\Delta t) \cos \gamma_r(k\Delta t) \sin \varphi_r(k\Delta t) \\ V_r(k\Delta t) \sin \gamma_r(k\Delta t) \end{bmatrix} + \mathbf{r}(k\Delta t) \begin{bmatrix} \Delta x(k\Delta t) \\ \Delta y(k\Delta t) \\ \Delta h(k\Delta t) \end{bmatrix}$$

and $\beta(q) = \sqrt{2(1 - \rho(\tilde{x}_{r/t}(k\Delta t)))}$.

To ensure the accuracy of the calculation, the time step Δt is determined by the constant λ and the grid size δ , namely $\Delta t = \lambda\delta^2$. The reference[296] has proved that the Markov chain mentioned converges weakly to the solution of the stochastic differential equation when the grid size $\delta \rightarrow 0$. Therefore, Markov chain can be used to approximate the state equation of the system, and the solution of the stochastic differential equation can be approximated by the probability distribution of the state at a certain moment.

13.3.3 Computing procedure of the probability of docking success

In this section, the computing procedure of the backward probability of docking success is provided. At the docking phase, the target set \mathcal{D} is a cube representing the state set of successful docking. The probability of entering the target set \mathcal{D} for each grid point is computed by appropriately propagating the transition probabilities of the Markov chain backward starting from the target set during the specified time horizon t . The probability of docking success $P^{(k)}(q)$

satisfies the following recursive equation

$$P^{(k)}(q) = \begin{cases} p_q^k(q) P^{(k+1)}(q) + \sum_{q' \in N_q} p_{q'}^k(q) P^{(k+1)}(q'), & q \in Q_0 \\ 1 & q \in \partial Q_D \\ 0 & q \in \partial Q_X \end{cases} \quad (13.14)$$

where recursive step $k \in [0, k_f] \in \mathbb{Z}$, time horizon $t \in [0, t_f]$, thus $k_f = \lfloor t_f / \Delta t \rfloor$; $p_q^k(q)$ and $p_{q'}^k(q)$ represent the transition probability from the grid point q to itself and to the adjacent grid point $q' \in N_q$ in the k -th step, respectively. $P^{(k+1)}(q)$ and $P^{(k+1)}(q')$ represent the probability transited to the grid point q and probability transited to the adjacent grid point $q' \in N_q$ in the $(k+1)$ -th step. As $q \in \partial Q_D$ represents the state has reached the boundary of the target set and ∂Q_D is an absorbing region, the probability of docking success is 1 when $q \in \partial Q_D$. As $q \in \partial Q_X$ represents the state has reached the boundary of the state space X and ∂Q_X also is an absorbing region, the probability of docking success is 0 when $q \in \partial Q_X$.

The initial condition of Eq. (13.14) is

$$P^{(k)}(q) = \begin{cases} 1, & \text{if } q \in \partial Q_D \\ 0, & \text{otherwise} \end{cases} \quad (13.15)$$

According to Eq. (13.14) (13.15), the probability that the state corresponding to any grid points in the state space \mathcal{L} enters the target set \mathcal{D} can be obtained.

Therefore, the computing procedure of the probability of docking success is as follows.

Step 1: Initialize the state space X , the target set \mathcal{D} and the state space $\mathcal{L} = X / \mathcal{D}$, determine the grid size δ and discretize the state space.

Step 2: Define the initial conditions according to Eq. (13.15).

Step 3: Obtain $P^{(k)}(q)$ by backward propagating from initial condition according to Eq. (13.14).

Step 4: Print the probability level curves and the probability isosurface according to $P^{k_f}(q)$.

The flow chart of the computation of the docking success probability based on stochastic approximation method is shown in Fig. 13.4.

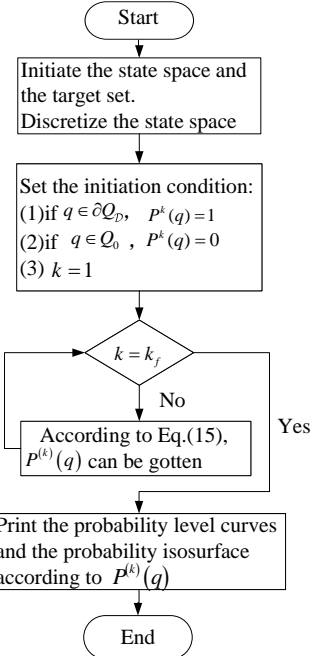
13.4 Simulation analysis on probability of docking success

13.4.1 Description of the simulation parameters

Based on the computing procedure proposed in Section 13.3, the state parameters of Eq. (13.7), the state constraint set and the target set at the docking phase are provided.

(i) State parameters. At the docking phase, the speed of the tanker aircraft is set to be $V_t = 120\text{m/s}$. The related parameters used in Eq. (13.13) is given in Table 13.1. The docking phase is divided into two stages and the time horizon of each stage is 1s. The parameters of each stage are provided in Table 13.2.

(ii) State constraint set. The Cartesian grid is used to approximate the state space X . The

**Figure 13.4:** The flow chart of the computation of the docking success probability.

ranges of the states of the system and the grid division are shown in Table 13.3. If the states are out of the ranges, then the docking is considered to fail. According to the constant λ and the grid size δ , the time step is $\Delta t = \lambda\delta^2 = 0.006s$.

(iii) Target set. A neighborhood around the desired final states at the docking phase is chosen as the target set. For the considered system, the target set with respect to $\tilde{x}_{r/t}$ is

$$\mathcal{D} = \{\tilde{x}_{r/t} \in \mathbb{R}^3 \mid -0.3m \leq \Delta x \leq 0m, -0.5m \leq \Delta y \leq 0.5m, -0.5m \leq \Delta h \leq 0.5m\} \quad (13.16)$$

Table 13.1: Related parameters of the state equations. **Table 13.2:** Parameter values of the two stages.

Paramete	Value
t	2s
λ	0.15
c_v	0.2
c_h	0.05
σ_h	1
σ_v	1

Time interval	Parameter	Value
$t \in [0s, 1s]$	V_r	122m/s
	γ_r	1
	φ_r	1
$t \in [1s, 2s]$	V_r	125m/s
	γ_r	2
	φ_r	2

Table 13.3: Grid division of the state space.

Parameter	Δx (m)	Δy (m)	Δh (m)
Range	[-20, 1]	[-10, 10]	[-10, 10]
Grid numbers	95	100	100
Grid size	0.2	0.2	0.2

13.4.2 The probability of docking success

The simulation results of the probability of docking success are provided in this section. Specifically, two situations are considered, namely considering the lateral deviation and without considering the lateral deviation.

13.4.2.1 Without considering the lateral deviation

Without considering the lateral deviation, the receiver only needs to adjust the longitudinal distance and altitude deviation between the drogue of the tanker and the probe of the receiver to complete the docking during the docking phase. Thus, Eq. (13.9) is rewritten as

$$\|\tilde{\mathbf{x}}_{r/t}\|_h = |\Delta x|, \quad \|\tilde{\mathbf{x}}_{r/t}\|_v = |\Delta h| \quad (13.17)$$

The wind field is set to be

$$\mathbf{r}(k\Delta t)\tilde{\mathbf{x}}_{r/t} = \begin{bmatrix} \frac{1}{5}k\Delta t & 0 \\ 0 & -\frac{1}{5}k\Delta t \end{bmatrix} \begin{bmatrix} \Delta x \\ \Delta h \end{bmatrix} \quad (13.18)$$

The probability of docking success is depicted in Fig. 13.5 when the wind field is not considered, where the numbers on the contour represent the probability of successful docking and the rectangular area with a probability of 1 is the target set. While, the probability of docking success is shown in Fig. 6 when the wind field is considered. Comparing Fig. 13.5 and Fig. 13.6, for a given wind field in Eq. (13.18), the wind field makes the curves of probability be bent counterclockwise.

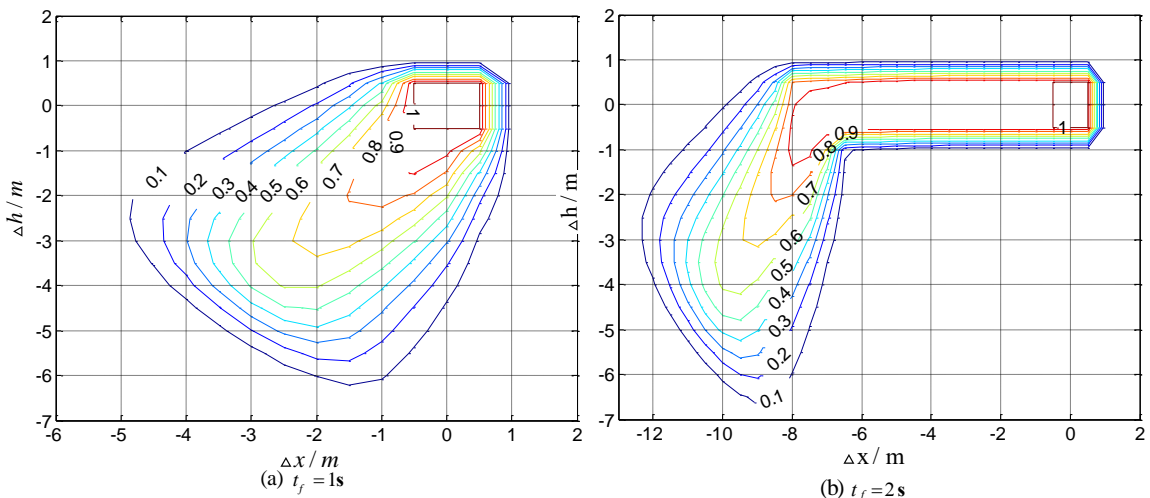


Figure 13.5: Level curves of the probability of docking success without considering wind field.

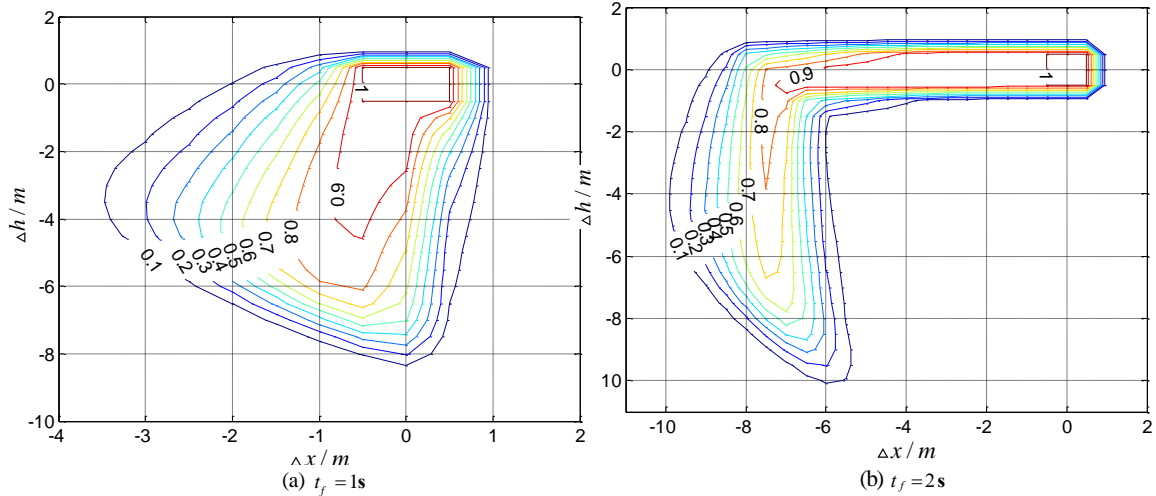


Figure 13.6: Level curves of the probability of docking success without considering wind field.

13.4.2.2 Considering the lateral deviation

Considering the lateral deviation implies the receiver needs to adjust the longitudinal distance, altitude deviation and lateral deviation between the drogue of the tanker and the probe of the receiver to complete the docking during the docking phase. The wind field is set to be

$$\mathbf{r}(k\Delta t)\tilde{\mathbf{x}}_{t/t} = \begin{bmatrix} \frac{1}{5}k\Delta t & 0 & 0 \\ 0 & -\frac{1}{5}k\Delta t & 0 \\ 0 & 0 & \frac{1}{5}k\Delta t \end{bmatrix} \begin{bmatrix} \Delta x \\ \Delta y \\ \Delta h \end{bmatrix} \quad (13.19)$$

The probability of docking success is depicted in Fig. 13.7 when the wind field is not considered, where the green cube is the target set and the values of the isosurfaces of different colors from inside to outside are 0.2, 0.4, 0.6 and 0.8, respectively. The probability of docking success is depicted in Fig. 13.8 when the wind field is considered. Comparing Fig. 13.7 and Fig. 13.8, the 3D wind field has the effect on the isosurface of the probability. The range of the probability of docking success with the isosurface values 0.2, 0.4, 0.6 and 0.8 in Fig. 13.7 is smaller than that in Fig. 13.8. Thus, it is more difficult to dock under the wind perturbation.

Depending on the skill and experience of the pilot, and the performance of the autopilot, the threshold selection varies from each other. Therefore, the partition of state space probabilistic contour and isosurface can provide decision support for successful docking.

13.4.3 Verification of the results

In this section, the Monte Carlo method[305] is used to verify the correctness of the results which are obtained in Sec. 13.4.2. The grid points are randomly selected in the state space \mathcal{L} , where the probability of docking success has been obtained using the stochastic approximation method, and the probabilities of docking success of these grid points are calculated by Monte Carlo method again. Later, the correlation coefficient is adopted to evaluate the relevance of the probabilities of docking success which are obtained by the two methods. The correlation

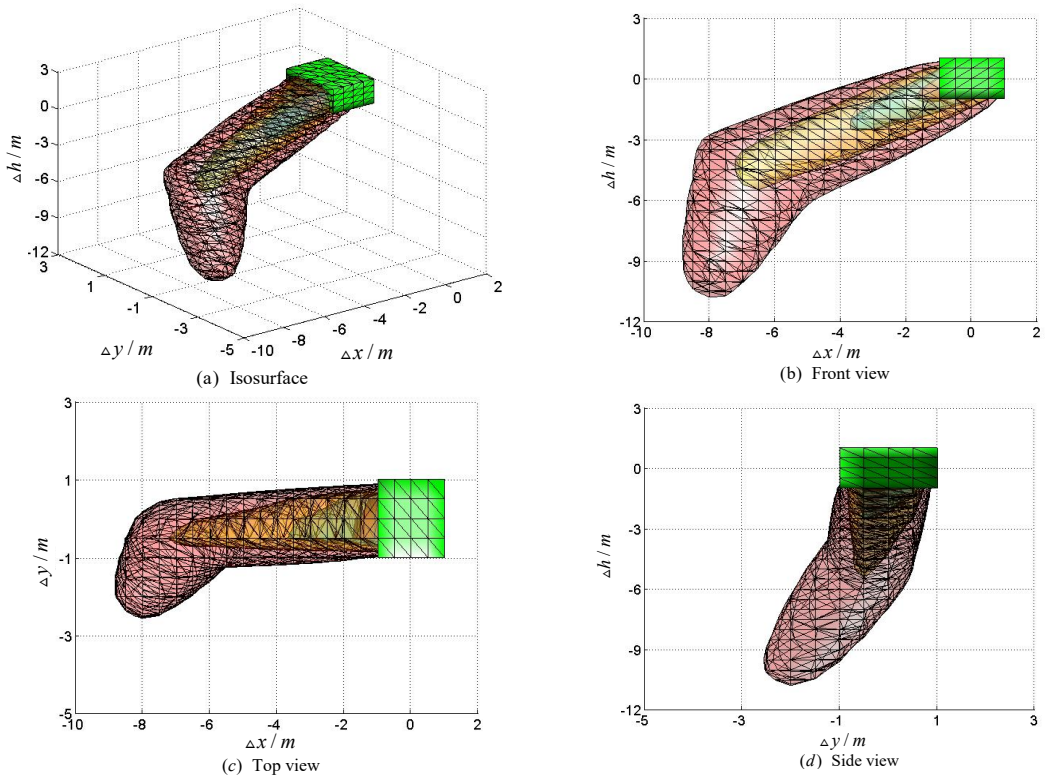


Figure 13.7: Isosurface and the corresponding front view of the probability of docking success without considering the wind field.

coefficient is computed by

$$r = \frac{\sum_{j=1}^N (P_j - \bar{P}) \sum_{j=1}^N (P_{MC,j} - \bar{P}_{MC,j})}{\sqrt{\sum_{j=1}^N (P_j - \bar{P})^2 \sum_{j=1}^N (P_{MC,j} - \bar{P}_{MC,j})^2}} \quad (13.20)$$

where N represents the number of the chosen grid points, P_j and $P_{MC,j}$ represent the probabilities of docking success which are obtained by the stochastic approximation method and Monte Carlo method, respectively. The value $P_{MC,j}$ is expressed as $P_{MC,j} = n_{P_{MC,j}} / m$, where $n_{P_{MC,j}}$ represents the number of the state getting into the target set within the horizon time $t \in [0, t_f]$ and m denotes the testing number for the grid point q_j . The \bar{P} and $\bar{P}_{MC,j}$ represent the average probability and can be denoted by $\bar{P} = \sum_{j=1}^N P_j / N$ and $\bar{P}_{MC,j} = \sum_{j=1}^N P_{MC,j} / N$.

The specific steps of using the Monte Carlo method to get the probabilities of docking success of the grids in state space are as follow:

Step 1: Initialize the state space, target set and the grid points which correspond with that in Sec. 13.4.1.

Step 2: Select $N = 1000$ grid points randomly in the state space, where the probability of docking success has been obtained using the stochastic approximation method. The selected grid points are denoted as $q_j, j = 1, \dots, 1000$. For each grid point, P_j is known and the testing number is set to be $m = 100$.

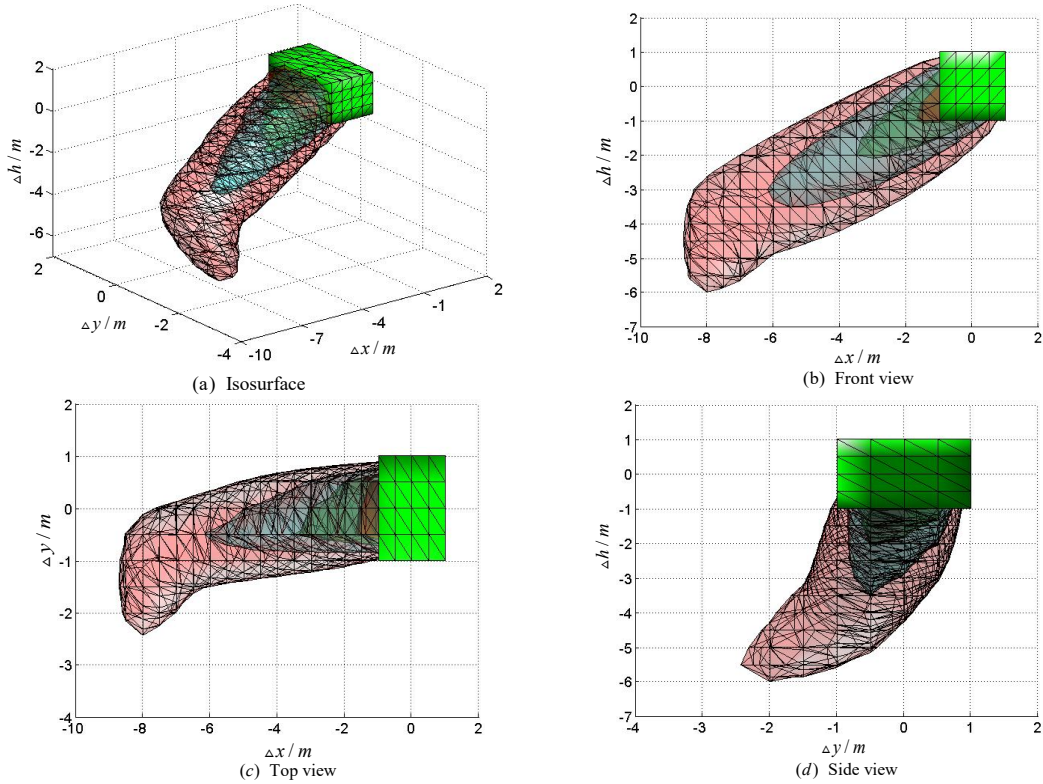


Figure 13.8: Isosurface and the corresponding front view of the probability of docking success considering the wind field.

Step 3: The state corresponding to the grid points q_j is taken as the initial state of Eq. (13.7). The function $\mathbf{W}(t)$ in Eq. (13.7) is a standard 3D Brownian motion, and the mean value and the covariance of $d\mathbf{W}(t)$ are set to be 0 and $\sqrt{\Delta t}$, respectively. By Eq. (13.8), whether the corresponding state of q_j gets into the target set within the time horizon $t \in [0, t_f]$ can be determined. If q_j can get into the target set, then $n_{P_{MC,j}} = n_{P_{MC,j}} + 1$.

Step 4: Substitute the results obtained in the above step into Eq. (13.20) to obtain the correlation coefficient.

The result shows that the correlation coefficient is 0.96 for $t \in [0, 1]$ and 0.91 for $t \in [0, 2]$. Therefore, the correctness of the stochastic approximation method to obtain the probability of docking success is demonstrated. Meanwhile, the comparison between the stochastic approximation method and the Monte Carlo method in obtaining the probability of docking success is listed in Table 13.4. The simulation is performed on Matlab R2010a on an ordinary laptop which has a window 7 operating system with a 2.4 GHz processor and 2 GB of RAM. From Table 13.4, it can be observed that the stochastic approximation method is more efficient in calculating the probability of docking success than the Monte Carlo method. The reason for this is that the probability of docking success of each grid point in the state space is calculated directly by the stochastic approximation method. But each grid point in the state space needs to be tested $m = 100$ to get the probability of docking success using the Monte Carlo method.

Table 13.4: The comparison of the simulation times of the two methods.

t_f	Simulation time of Monte Carlo method	Simulation time of stochastic approximation method
1s	22.70s	0.22s
2s	38.17s	0.32s

13.5 Chapter Summary

In order to ensure the docking safety in an AR process, a stochastic approximation method is used to obtain the probability of docking success at the docking phase, and the partition of state space probabilistic contour and isosurface can provide decision support for a successful docking.

1) The stochastic differential equation is used in this paper to describe the position of the receiver relative to the tanker, and the wind field and stochastic disturbance are considered in the docking phase.

2) The stochastic approximation method is a kind of model abstract method. By properly choosing the transition probabilities, the solutions of stochastic differential equations are approximated by the discrete-time Markov chain.

3) The probability of docking success of grid points in state space is obtained finally by solving the stochastic differential equations by using the stochastic approximation method.

4) The Monte Carlo method is used to verify the effectiveness of the simulation results. In addition, compared with the Monte Carlo method, the stochastic approximation method can greatly reduce the runtime (See Table 13.4) and thus is more efficient.

In this paper, stochastic differential equations are used to describe the docking phase of aerial refueling, by taking into account wind fields and location-dependent random perturbations. However, in the docking process, since the perturbations situation is complicated, it is a future work to seek a balance between the complicated model and the time consuming to satisfy the real-time estimate for docking success rate.



Chapter 14 Failsafe Mechanism Design using State Tree Structures

Autonomous Aerial Refueling (AAR) is vulnerable to various failures and involves cooperation among autonomous receivers, tankers and remote pilots. Dangerous flight maneuvers may be executed when unexpected failures or command conflicts happen. To solve this problem, a failsafe mechanism based on State Tree Structures (STS) is proposed. The failsafe mechanism is a control logic that guides what subsequent actions the autonomous receiver should take, by observing real-time information of internal low-level subsystems such as guidance and drogue&probe and external instructions from tankers and pilots. To generate such a controller using STS, the AAR procedure is decomposed into several modes, and safety issues related with seven low-level subsystems are summarized. Then common functional demands and safety requirements are textually described. On this basis, the AAR plants and specifications are modeled by STS, and a supervisor is synthesized to control the AAR model. To prove its feasibility and correctness, a simulation environment incorporating such a logic supervisor is built and tested. The design procedures presented in this paper can be used in decision-making strategies for similar flight tasks. Supporting materials can be downloaded in [Github¹](#), including related software, input documents and output files.

14.1 Introduction

Autonomous Aerial Refueling (AAR) is an effective approach to increase the range and endurance of Unmanned Aerial Vehicles (UAV) by refueling them in air. Since the first successful AAR concept demonstration by the Boeing company, several ambitious AAR projects have been carried on by the NASA [170], US Air Force and US Navy [249], which demonstrate the feasibility and reliability of AAR. During an AAR operation, as shown in Fig. 14.1, a UAV (or a receiver) detaches from its formation and approaches the rear of a tanker for refueling. Once refueled and cleared, the receiver disengages from the tanker and rejoins the formation. The boom system or drogue&probe system is used for fuel transfer, and this paper focuses on the drogue&probe system, as shown in Fig. 14.2, for the drogue&probe's advantages for autonomous systems. [170, 306]

¹<https://github.com/KevinDong0810/Failsafe-Design-for-AAR-using-STS>

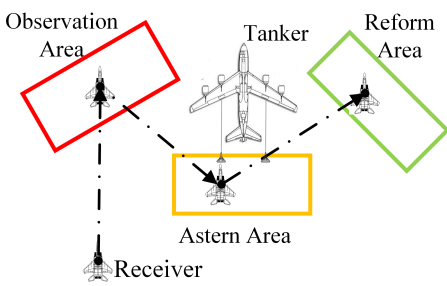


Figure 14.1: JOINING-INIT MODE.



Figure 14.2: JOINING-WAIT MODE.

The AAR is a semi-automated process, where the control of unmanned receivers relies on frequent interactions among the on-board receiver controller, external tanker controller and remote human pilots. Therefore, command conflicts may happen and jeopardize the refueling task. Besides, an AAR process is vulnerable to various system failures like probe damage and unsteady airflow. Therefore, a high-level logic controller that coordinates all these control components and produces the desired safe functionality in the presence of faults and failures is needed, namely a *failsafe mechanism*. A wealth of researches have been done in this domain. Ref [307] formalized the general framework for formal verification of human-automaton interface, where both automaton and human controller share the authority over the system. Refs [302] and [308] investigated the safe path planning in AAR to avoid collision with consideration of receiver-pilot interaction. In the Research Flight Control System developed by [170] in NASA, human-machine interface is put into practice. But none of them has taken system failures into consideration for logic design, under which dangerous maneuvers may happen. In contrast, fault-related literature is mainly focused on low-level controllers, such as fault detection techniques [309] and fault-tolerant control algorithms [310, 311]. As far as the authors know, no high-level logic controller has been studied.

At present, the failsafe mechanism design for AAR is seldom investigated. Related applications like rotorcrafts mainly count on engineering experience and manual calculation to design the control logic, like DJI autopilot and ArduPilot autopilot. Man-made mistakes, logical bugs or an incomplete treatment are hard to avoid in this approach. And when it comes to complex systems, this approach is very time-consuming. Therefore, this paper aims to use a model-based method, namely supervisory control theory (SCT) of state tree structures (STS), to design a comprehensive failsafe mechanism.

SCT is a formal method for synthesizing supervisors of discrete-event systems. On observing event strings generated by the plant, at each state the SCT would disable a suitable subset of controllable events to satisfy the given control specifications [312]. First put forward by [313], the SCT has a sound theoretical foundation [314, 315], and numerous industrial applications such as testbed assembly process [316], telephone directory assistance call center [317] and magnetic resonance image (MRI) scanner [318]. Later, to solve the problem of exponential computational effort faced by finite state machine (FSM) used in original SCT, *state charts* [319] are adopted

and this new version of SCT is named STS [320]. The STS uses the AND (Cartesian product) and OR (disjoint union) operation to present system hierarchies and uses *binary decision diagrams* (BDD) [321] to manage the computational complexity.

Compared with current failsafe mechanisms based on engineering experience, the STS approach has three main advantages: 1) *Correct by design*: The restricted behaviors under the supervision of the STS ensure that requirements are satisfied. Therefore, the control logic is free from incomplete treatment and logical bugs in the design phase. 2) *Compact*: The resulting supervisor is presented in the simplest way, which means when making a decision, only necessary information instead of the whole system state would be required. Therefore, a minimal disabling action is made for the system to stay within safe states. 3) *Flexibility*: The STS allows the modular modeling method and ensures the system can be readily evolved. Different modules (subsystems, requirements, etc.) can be added easily when taking different control hierarchies (from high-level to low-level) into consideration. This has been well presented in the application of theme park vehicles [322].

The main contributions of this paper are the following:

- This paper investigates the failsafe logic design of autonomous receivers using a sound formal verification theory. A supervisor is synthesized to cover common system failures and interaction among receivers, tankers and pilots. This design framework can be easily adopted for different aerial refueling procedures and other similar control tasks.
- Tools for synthesizing, implementing and simulating supervisors gained through STS for aerial refueling have been developed and posted in Github. This may stimulate the similar failsafe mechanism design in related domains.

The remainder of this paper is organized as follows. Section 2 summarizes the basics of STS. Section 3 presents the discretization of AAR procedures and summary of common safety issues. In section 4, functional demands and safety requirements are provided, as well as the event definitions. On this basis, section 5 presents the STS design of AAR and the generated supervisor using related software. In section 6, the supervisor is implemented in a simulation environment for AAR and tested for correctness. Section 7 concludes this paper.

14.2 Preliminaries of STS

This section presents the basics of STS theory, while details can be found in textbooks [314, 315, 320].

14.2.1 State Tree Structure

The State tree structure is an extension of the finite state machine in SCT, which introduces natural hierarchical structures into the system model. It mainly consists of two parts: *state tree* and *holon*. These two parts depict the same system but focus on different aspects. State tree,



say **ST**, organizes the state space of an STS, while the holon, say **H**, organizes the transitions of an STS. The nodes on a state tree are called states. Every state tree has a unique root state. A state on a state tree is called an OR (resp. AND) *superstate* if it can be represented as the disjoint union U (resp. Cartesian product X) of its children. Each child state is called an OR (resp. AND) superstate. The lowest level states are called *simple states*, which are required to be OR superstates to avoid redundant information. In the following text, the states of STS including simple states and superstates, are written in italics and start with capitals like *Standby*. In most application scenarios, OR superstates work sequentially while AND superstates work concurrently.

Holon organizes the state transitions of STS, which can be regarded as an automaton with hierarchies. It depicts the boundary and local state transitions of the state tree. A holon **H** is a 5-tuple $\mathbf{H} := \{X, \Sigma, \delta, X_o, X_m\}$, where X is a finite set consisting of states in **ST**; Σ is the finite event set (also called an *alphabet*); δ is the (partial) transition function on the state set: $\delta : X \times \Sigma \rightarrow X$; $X_o \subseteq X$ is a subset of X consisting of *initial states*; $X_m \subseteq X$ is another subset of X consisting of *marker states* that the whole system desires to reach.

In SCT, the alphabet Σ is partitioned as $\Sigma = \Sigma_c \cup \Sigma_u$, where Σ_c is the subset of *controllable events* that can be disabled at will while Σ_u is the subset of *uncontrollable events* that cannot be disabled by the controller. In engineering practice, Σ_c usually represents relevant discrete commands to the low-level controller, while Σ_u usually represents messages sent to the supervisor such as system health information and sensor signals like the waiting time exceeding a pre-defined threshold.

14.2.2 Plant, Specification and Supervisor

SCT aims to synthesize the supremal non-blocking language (event sequences) of *Plant*, while satisfying the requirements of *Specification*. The generated language is called *Supervisor*; their detailed descriptions are given as follows.

- **Plant.** Plants are models of behaviors of physical systems and processes, which contain all the possible states and transitions.
- **Specification.** Specifications are models of control requirements, which point out the unwanted states and transitions in correspondence to forbidden states. It can be given as illegal state sets[323] or illegal event sequences[322]. The latter form is used in this paper.
- **Supervisor.** The supervisor is the minimally restrictive event sequence of plants under the restriction of specifications, and is implemented by state feedback control functions [320] for events. In every state of the plant, the supervisor will provide a subset of controllable events among which the plant can choose one to execute. By doing so, the specifications are always satisfied.

In the synchronization algorithm, namely *Supcon*, for supervisors [320], all uncontrollable event sequences leading to *blocking states*, namely states that cannot reach marker states by any



event transitions, are deleted iteratively. Therefore, to model the specifications, the undesired event sequence should be made to lead to blocking states.²

14.3 Mode Discretization and Safety Issues

This section describes the plant for aerial refueling. Related AAR procedures are discretized and common safety issues are summarized, according to which the STS plant will be modeled.

14.3.1 Area Definition

The procedure discretization is based on air space decomposition. The air space is divided into different areas according to their locations relative to the tanker.

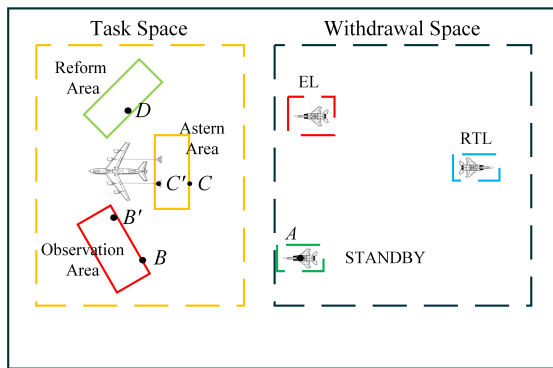


Figure 14.3: Top view of the air space division

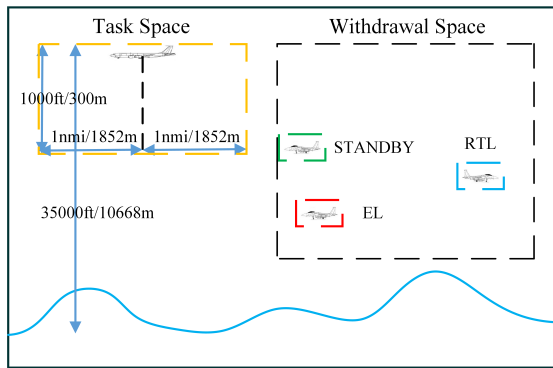


Figure 14.4: Top view of the air space division

As shown in Fig. 14.3 and 14.4, the air space is divided into two parts: *Task Space* and *Withdrawal Space*. The task space is the space where AAR tasks are carried out. It is assumed to be a box space centered at the tanker with 300m height(downward), 3704m length and an appropriate width.³ The task space contains three areas: observation area, astern area and reform

²Readers can find a similar example in Exercise 3 of Chapter 3.10 in the DES textbook [315] for a better understanding.

³These data are given according to [324, p. 54] that the refueling start point should be placed 1000ft(300m) below and 1nmi (1852m) behind the tanker.

area. The observation area at the left-hand side of the tanker is allocated for joining receivers. The astern area is the stabilized formation position behind the AAR equipment, approximately 100ft-aft of the drogue directly [324, p. 32]. The reform area is the area at the right and level or slightly above the tanker formation.

The withdrawal space is the airspace outside of the task space used for emergency and AAR preparation. When AAR is achieved or failed, the receiver will enter into the withdrawal space from the task space. On the other hand, when the receiver's health conditions allow a possible AAR, the receiver will enter the task space from the withdrawal space. The withdrawal space has three maneuver modes including STANDBY, RTL and EL, whose definitions are presented in section 14.3.2.1.

14.3.2 Mode Decomposition

Based on the air-to-air refueling demonstration of [170] and standard procedures for manned aircraft proposed by [324], the AAR work cycle is decomposed into the following distinct phases and modes. In the following text, the AAR mode will be presented in capitals like STANDBY MODE.⁴

14.3.2.1 Withdrawal Phase

The withdrawal phase is in correspondence to the withdrawal space. As mentioned before, there are three modes in this phase or space, namely STANDBY, RTL and EL.

- a) STANDBY MODE:** The receiver is waiting at point A (as shown in Fig. 14.3) for the next instruction. In this mode, the receiver has the ability to carry on AAR tasks.
- b) Return to Land (RTL) MODE:** The receiver returns to the nearest airbase to land, which may result from subsystem failures or pilot instructions. In this mode, the receiver may lose the ability to carry on AAR tasks but still keep the ability to return to base.
- c) Emergency Landing(EL) MODE:** The receiver makes an emergency landing, which may result from subsystem failures or pilot instructions. In this mode, the receiver may lose the ability to return to base and can only make an emergency landing.

14.3.2.2 Task Phase

The task phase contains all the AAR task procedures, mainly the joining, refueling and reforming sub-phases.

- a) Joining Sub-Phase:** Joining refers to the sub-phase where the receiver maneuvers from STANDBY MODE to the observation area. It has two modes:

⁴Standby can be a mode like STANDBY MODE or a simple state like *Standby*. They are two different concepts in this paper, but refer to the same thing in the physical world.

1. **JOINING-INIT MODE:** As shown in Fig. 14.5(a), the receiver flies to the observation area. The control objective is to control the receiver flying from STANDBY MODE to point B .
2. **JOINING-WAIT MODE:** As shown in Fig. 14.5(b), the receiver stays in the observation area and waits for the *connection clearance* from the tanker, namely the command given by the tanker to allow the receiver to fly to the astern area and connect its probe with the drogue. The control objective is to control the receiver flying to point B' and then keep the position.

b) Refueling Sub-Phase: Refueling refers to the sub-phase where the receiver connects to the tanker and transfers the fuel. It has three modes.

1. **REFUELING-INIT MODE:** As shown in Fig. 14.6(a), once the receiver is cleared for the connection it flies to the astern area. The control objective is to control the receiver flight to point C and then maintain the position.
2. **REFUELING-CAPTURE MODE:** The receiver initiates the connection between the probe and the tanker's drogue. As shown in Fig. 14.6(b), the control objective is to control the receiver flying to point C' , and then keep the position for connecting the probe with the drogue.
3. **REFUELING-TRANSFER MODE:** After a successful capture, the receiver and the tanker keep relatively stationary to transfer the fuel. When the fuel transfer is finished, the receiver should still keep connected with the tanker and wait for the *disconnection clearance*, namely the command given by the tanker to allow the receiver to disconnect from the drogue. As shown in Fig. 14.6(c), the control objective is to keep the receiver at the point C' and transfer the fuel.

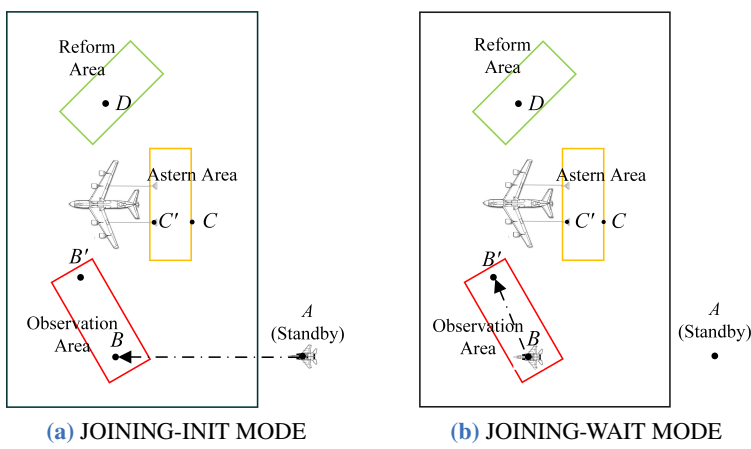
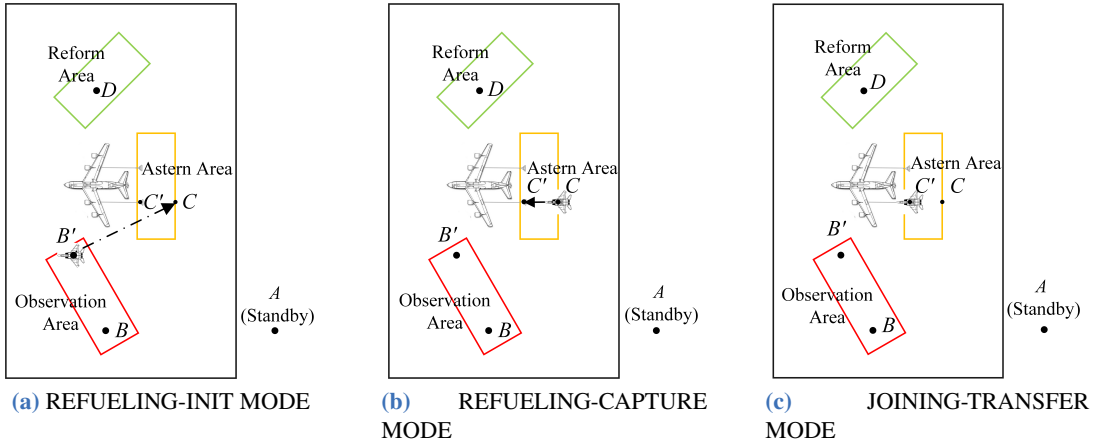
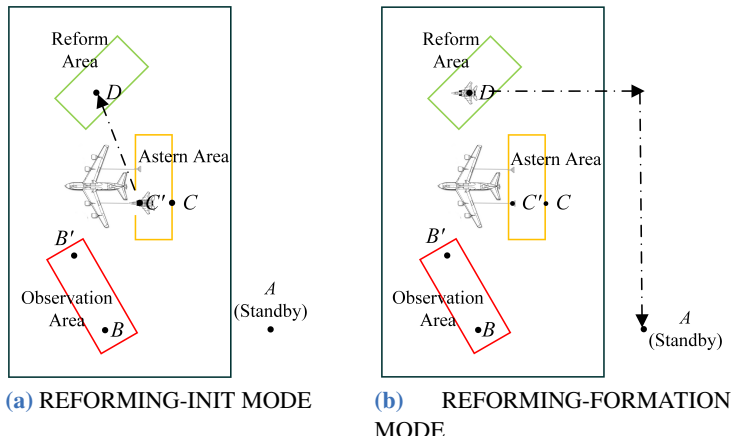


Figure 14.5: Joining sub-phase.

c) Reforming Sub-Phase: Reforming refers to the sub-phase where the receiver disconnects with the tanker, flies to the reform area and then leaves the formation. It has two modes.

1. **REFORMING-INIT MODE:** The receiver is cleared for disconnection and then flies to the reform area. As shown in Fig. 14.7(a), the control objective is to control the receiver

**Figure 14.6:** Refueling sub-phase.**Figure 14.7:** Reforming sub-phase.

flying to point D and then keep the position.

- REFORMING-FORMATION MODE:** The receiver rejoins the flight formation and then leaves the task space, which can be regarded as returning to the withdrawal space to form a circle in the model. As shown in Fig. 14.7(b), the control objective is to control the receiver to maneuver from point D to the withdrawal space.

14.3.3 Safety Issues

This subsection summarizes the common failure behaviors in aerial refueling. They are the health information that should be taken into consideration when making decisions. These failures mainly happen in those subsystems shown in Table 14.1.

Most of their failure behaviors can be depicted as the holon shown in Fig. 14.8. According to concrete requirements, a subsystem can have more states to describe the health, but only three different health states of each subsystem are considered here, namely *normal*, *minor damage* and *critical damage*. “Normal” state represents that the system satisfies the basic requirements with all components being healthy. “Minor damage” state represents that although there are some

Table 14.1: Subsystem Information

Category	Name	Basic Requirement
Receiver	Navigation	Provide data about the relative position and velocity between receivers and tankers to facilitate docking
	Control	Keep the receiver's position and velocity within an allowable range according to its current mode, to avoid collision with other aircraft and achieve successful docking
	Fuel	Provide the necessary fuel for flight
	Engine	Provide the necessary power and thrust for flight
Connection	Drogue&probe	Establish robust contact between the drogue and probe, and then transfer fuel from the tanker to the receiver
	Datalink	Exchange data for communication and high-accuracy computation of relative locations
Tanker	Tankersafety ¹	Facilitate the stable connection and transfer the fuel

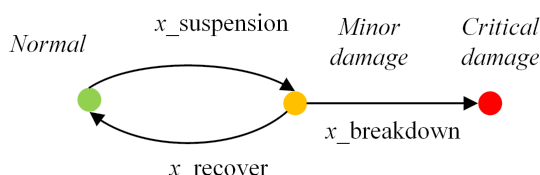
¹ To avoid redundancy, the tanker is modeled as a whole instead of with different subsystems like those of the receiver

failures in the system, the system can still satisfy the basic requirements. “Critical damage” state represents that the system can no longer satisfy the basic requirements.

Transitions among different states, namely $x_{\text{suspension}}$, x_{recover} and $x_{\text{break-down}}$ are detected by low-level modules, where x refers to an exact subsystem name as shown in Table 14.1, e.g., Navigation. They can be defined according to the specific designers’ purpose. For example, the transitions of the Navigation subsystem are given as follows:

- **Navigation_suspension:** The precision of navigation data has degraded to be lower than a specified threshold, but it can still satisfy the basic requirement of the navigation subsystem. Degradation reasons are multiple, such as bad weather for cameras, radars & lasers, multi-path effects, hostile jamming and spoofing for GPS [249].
- **Navigation_recover:** Precision quality exceeds a specified threshold, and the Navigation subsystem is healthy again.
- **Navigation_breakdown:** The *minor damage* state has lasted more than a given threshold time or the data provided do not fulfill the basic requirement of the navigation subsystem.

Owing to the special characteristics of the Fuel subsystem, there is no x_{recover} transition in this subsystem. Its holon can be seen in Fig. 14.9.

**Figure 14.8:** The general holon of subsystems.

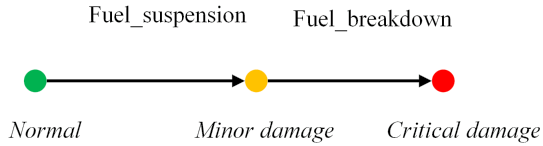


Figure 14.9: The holon of Fuel subsystem. To be consistent with other subsystems, the exhaustion of fuel is called *Fuel_breakdown* here.

14.4 User Requirements and Event Definitions

This section textually describes the requirements of aerial refueling. Functional demands and safety requirements are summarized from common user requirements of the logic control system; they will guide the design of plants and specifications, respectively. Event definitions are also provided here.

14.4.1 User Requirements

In engineering practice, aerial refueling systems have to satisfy multiple functional demands and safety requirements, as summarized in Table 14.2 and Table 14.3. Functional demands deal with what functions should exist in the system, like “the receiver can be forced by pilots to try connecting with the tanker even when the health conditions do not allow so”. They are used to guide the design of plants in STS. Safety requirements deal with what behaviors are illegal, e.g. “when control subsystem breaks down, the receiver cannot continue the current AAR task”. They are used to design the specifications in STS.

14.4.2 Event Definitions

Based on event characteristics of AAR tasks, four types of events are defined here, namely Mode Control Events (MCEs), Mode Input Events (MIEs), Automatic Triggered Events (ATEs) and Subsystem Failure Events (SFEs). MCEs and MIEs are controllable events, while ATEs and SFEs are uncontrollable events. Their detailed descriptions are given as follows.

Table 14.2: Functional Demands

Name	Definition
FD1	The receiver, which switches from the task phase to the withdrawal phase, should first try entering STANDBY. If not satisfying the safety requirement for STANDBY MODE (see SR1 in Table 14.3), the receiver should try entering RTL. If still not satisfying the safety requirement for RTL MODE (see SR2 in Table 14.3), the receiver should try entering EL.
FD2	In EL MODE, if health conditions satisfy the safety requirements (SR1 or SR2), the receiver can switch to STANDBY MODE or RTL MODE. Similarly, the receiver can switch to STANDBY from RTL.
FD3	If the receiver cannot carry on AAR tasks further, it should break away and switch to the withdrawal phase as soon as possible.
FD4	The receiver has to wait for the clearance commands from the tanker to connect or disconnect with the tanker.
FD5	Pilots can manually switch the receiver to the STANDBY, RTL or EL MODE from any state. When health conditions allow, such instructions should be executed as soon as possible and override any other automatic mode progression.
FD6	Pilots can force the enablement of the connection initiation and fuel transfer initiation (see MCE08 and MCE10 in Table 14.4), even though such maneuvers are forbidden by the autopilot due to severe health conditions.
FD7	Considering pilots may not know the real-time health information of receivers in timely fashion, when pilots ask the receiver to return to STANDBY MODE, the receiver can go to STANDBY, RTL and EL MODE. When asked to return to RTL MODE, the receiver can go to RTL and EL MODE. When asked to go to EL MODE, it can only switch to EL MODE.

1. **MCEs:** Commands generated by the autopilot to proceed automatically.
2. **MIEs:** Instructions sent from pilots to change the automatic AAR procedures.
3. **ATEs:** Detection results of AAR maneuvers. In most cases, an MCE has two possible ATEs, which mean success and failure. For example, the event MCE04 is to control the receiver to fly from the STANDBY position to the observation area, thus this command has two possible results: “arrived” (“ATE01: Join-Init-Succ”) and “not arrived” (“ATE02: Join-Init-Fail”).
4. **SFEs:** Failure related behaviors of subsystems. These events correspond to transitions including $x_{\text{suspension}}$, x_{recover} and $x_{\text{breakdown}}$, which are presented in Section 14.3.3.

The exact definition of every MCE is shown in Table 14.4. As for the MIEs, ATEs and SFEs, their meanings can be easily interpreted from their full names as shown in Fig. 14.12~14.23. Readers can refer to Appendix A.5 for their detailed definition tables.

14.5 State Tree Structure Design

Based on the preparation in section 14.3 and 14.4, this section shows the AAR failsafe design in the form of state tree structures, whose overall diagram is illustrated in Fig. 14.10.



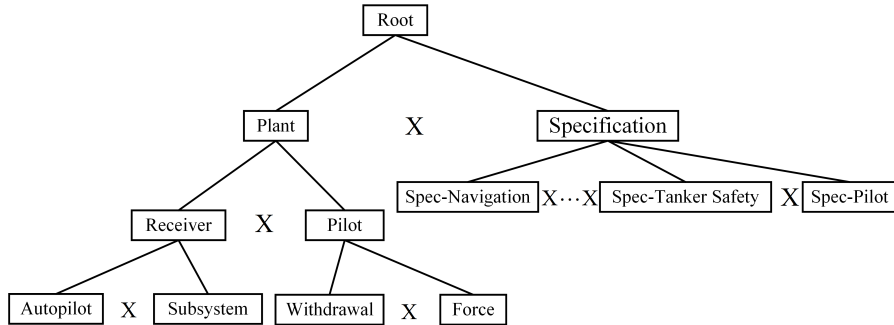
Table 14.3: Safety requirements in withdrawal phase

Name	Description
SR1	Entering and staying in STANDBY MODE are allowed when Navigation, Control, Engine, Drogue&probe, Datalink and Tankersafety subsystems are at <i>minor damage</i> or <i>normal</i> , and Fuel subsystem is at <i>normal</i> . If this requirement is not satisfied, transitions to STANDBY MODE are forbidden and transitions to RTL should be made.
SR2	Entering and staying in RTL MODE are allowed when Navigation, Fuel and Engine are at <i>minor damage</i> or <i>normal</i> . If not, transitions to RTL MODE are forbidden and transitions to EL MODE should be made.
SR3	The transition from STANDBY MODE to JOINING-INIT MODE is allowed when all the subsystems are at <i>normal</i> . If not, transitions to JOINING-INIT MODE are forbidden and the receiver should wait in STANDBY MODE.
SR4	Staying at JOINING-WAIT MODE is allowed when Fuel subsystem is at <i>normal</i> and other subsystems are at <i>minor damage</i> or <i>normal</i> . If not, transitions to JOINING-WAIT MODE are forbidden and transitions to the withdrawal phase should be made.
SR5	If the waiting time at JOINING-WAIT exceeds a specified threshold, then the receiver should make a transition to STANDBY MODE.
SR6	Entering REFUELING-INIT MODE is allowed when Navigation, Engine, Datalink and Tankersafety subsystems are at <i>minor damage</i> or <i>normal</i> , while Control, Fuel and Drogue&probe subsystems are at <i>normal</i> . If not, the receiver, even cleared for connection, should keep waiting at JOINING-WAIT MODE or make transitions to the withdrawal phase.
SR7	Staying at REFUELING-CAPTURE MODE or REFUELING-TRANSFER MODE (when the fuel transfer is not finished) is allowed when all the subsystems are at <i>normal</i> . If this requirement is not satisfied, the receiver is not allowed to stay at this mode. Under this situation, if Navigation, Engine, Datalink and Tankersafety subsystems are at <i>minor damage</i> or <i>normal</i> , while Control, Fuel and Drogue&probe subsystems are at <i>normal</i> , the receiver should retreat to REFUELING-INIT MODE. Otherwise, the receiver should make transitions to the withdrawal phase. (to be continued in Table ??)
SR8	When the fuel transfer is finished, staying at REFUELING-TRANSFER MODE is allowed when Navigation, Fuel, Engine, Datalink and Tankersafety are at <i>minor damage</i> or <i>normal</i> , while Control and Drogue&probe are at <i>normal</i> . If not, the receiver should make transitions to the withdrawal phase.
SR9	When the receiver is waiting for disconnection clearance at REFUELING-TRANSFER MODE after a successful fuel transfer, the receiver should disconnect from the drogue and switch to REFUELING-INIT MODE, if the waiting time exceeds a specified threshold.
SR10	Entering and Staying at REFORMING-INIT MODE or REFORMING-FORMATION MODE are allowed when Navigation, Control, Fuel and Engine subsystems are at <i>minor damage</i> or <i>normal</i> . If not, transitions to the withdrawal phase should be made.



Table 14.4: Mode Control Event Definitions

Name	Description
MCE01	Control the receiver to stay in EL MODE
MCE02	Control the receiver to stay in RTL MODE
MCE03	Control the receiver to stay in STANDBY MODE
MCE04	Control the receiver flying from STANDBY position to the observation area.
MCE05	Control the receiver to wait in the observation area while avoiding collision with other aircraft.
MCE06	Control the receiver flying to the astern area.
MCE07	Control the receiver to abandon the current connection initiation or fuel transfer initiation and fly to the astern area.
MCE08	Control the receiver to connect its probe with the tanker's drogue.
MCE09	The forced version of MCE08. It can only be activated by pilots, and cannot be forbidden by autopilots.
MCE10	Control the receiver to keep relatively stationary to the tanker, and open the valve to receive fuel
MCE11	The forced version of MCE10. It can only be activated by pilots, and cannot be forbidden by autopilots.
MCE12	Control the receiver to wait in the astern area while keeping connected with the tanker.
MCE13	Control the receiver flying to the reform area.
MCE14	Control the receiver to rejoin the formation.

**Figure 14.10:** The state tree of AAR with only AND superstates and their components displayed.

14.5.1 Plant design

In this subsection, the plant design is presented, which includes all the possible behaviors of the aerial refueling tasks.

14.5.1.1 (Receiver) Autopilot

Autopilot is the AND component of *Receiver*, which is responsible for recording the task procedures of AAR. It is an OR superstate with three simple states (*Standby*, *RTL* and *EL*) and three OR superstates (*Joining*, *Refueling* and *Reforming*), as shown in Fig. 14.11.

Fig. 14.12 shows the inner transitions of *Autopilot* (the detailed information of the three superstate is introduced later). In the normal work cycle, the *Autopilot* starts from *Standby* state, goes through the *Joining* superstate (MCE04), the *Refueling* superstate (MCE06), the *Reforming* superstate (MCE13) and finally returns to the *Standby* state (MCE03). In detail, taking event MCE04 as an example, it leads the receiver from *Standby* state to *Joining* superstate. When this

maneuver fails, namely “ATE01:Join-Init-Fail” happens, the receiver retreats to *Standby* state. Otherwise, “ATE02:Join-Init-Succ” happens, which leads the *Autopilot* to *Joining* superstate (shown in Fig. 14.13).

When failures happen, the *Autopilot* can retreat to *Standby*, *RTL* and *EL* states from *Joining*, *Refueling* and *Reforming* superstate through events MCE03, MCE02 and MCE01, respectively. Meanwhile, according to the real-time health conditions, the receiver can make transitions among states in the withdrawal phase like from *RTL* to *Standby*.

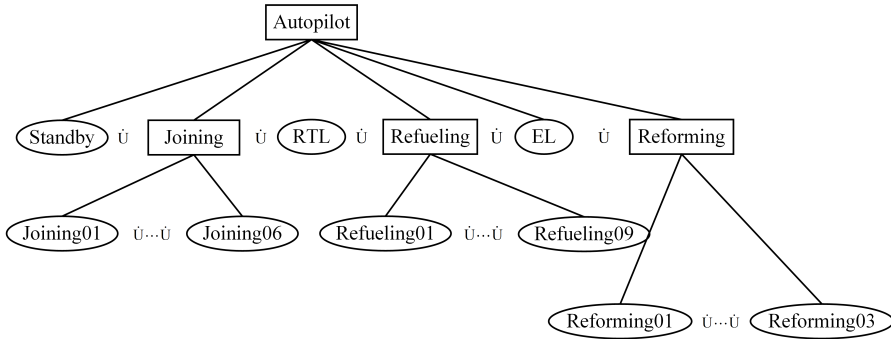


Figure 14.11: The state tree of *Autopilot*. *Joining01*...*Joining06* are children (OR components) of superstate *Joining*, whose detailed information is shown in Fig. 14.13. It is the same for *Refueling* and *Reforming*, whose information is shown in Fig. 14.14 and Fig. 14.15 respectively.

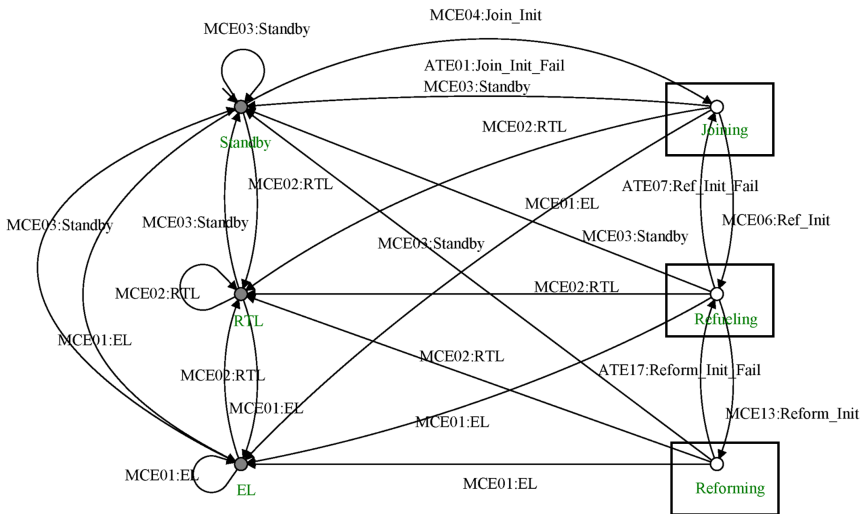


Figure 14.12: The holon of *Autopilot*. Figures are plotted through SUPREMICA [325]. Note that circles with arrow pointing to are initial states like *Standby*, and gray circles are marker states like *RTL*. The black squares indicate superstates.

a) *Joining* superstate: This is an OR superstate as shown in Fig. 14.13. It corresponds to the joining sub-phase presented in section 14.3.2, and contains six simple states.

When MCE04 happens, the *Autopilot* enters *Joining* superstate from *Standby*, and stays in *Joining01* state (belonging to JOINING-INIT MODE). When this maneuver succeeds (“ATE02:Join-Init-Succ”), it enters *Joining02* state (belonging to JOINING-WAIT MODE), where the receiver has to wait for the connection clearance from the tanker (FD4, see Table 14.2). When it is

not cleared ("ATE03:Join-Connection-no"), the receiver has to check whether the waiting time exceeds the specified threshold (SR5, see Table 14.3). If so, it has to abandon the current AAR task and return to the withdrawal phase. Otherwise, it can keep waiting (MCE05) or retreat to the withdrawal phase according to its health conditions. Once the receiver is cleared for connection ("ATE04:Join-Connection-yes"), it has to check whether it satisfies the safety requirement for MCE06 (SR6, see Table 14.3). If satisfied, the receiver can execute the event MCE06. Otherwise, it has to wait or withdraw.

b) *Refueling* superstate: This is an OR superstate as shown in Fig. 14.14. It corresponds to the Refueling sub-phase, and contains nine simple states.

Event MCE06 brings the *Autopilot* from *Joining* to *Refueling* superstate. In the *Refueling02* state (belonging to REFUELING-CAPTURE MODE), according to the safety requirement (SR7), the receiver can choose to initiate a connection (MCE08), back to *Refueling01* state (MCE07) or back to the withdrawal phase. MCE09 is the substitute for MCE08, so that the pilot can use it to force the connection action when MCE08 is forbidden by the generated supervisor (FD6). The connection action has two results: "ATE09:Ref-Cap-Fail" and "ATE10:Ref-Cap-Succ". Failure brings the receiver back to the *Refueling02* state while success leads the receiver to the *Refueling04* state (belonging to REFUELING-TRANSFER MODE), whose transitions are similar to those of *Refueling02* state.

Success of fuel transfer leads the receiver to *Refueling06* state, where it has to wait for the disconnection clearance (FD4). If not cleared, the receiver has to check the waiting time (SR9), similar to *Joining02* state. But if the time runs out, the receiver will directly disconnect with the tanker instead of returning to the withdrawal phase. If cleared, the receiver can initiate the event MCE13 or return to the withdrawal phase.

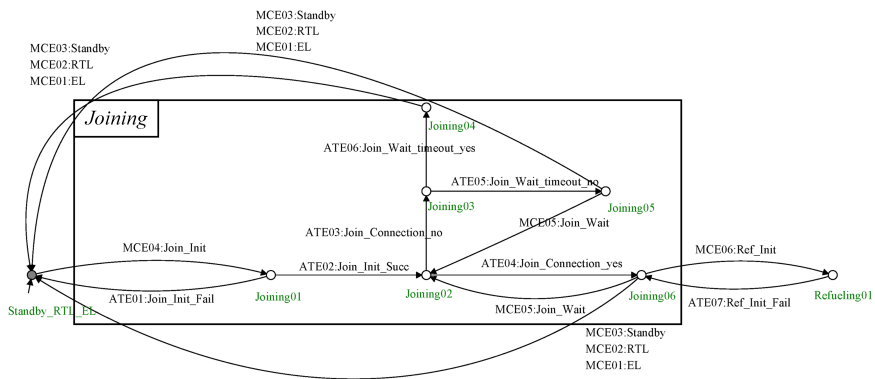
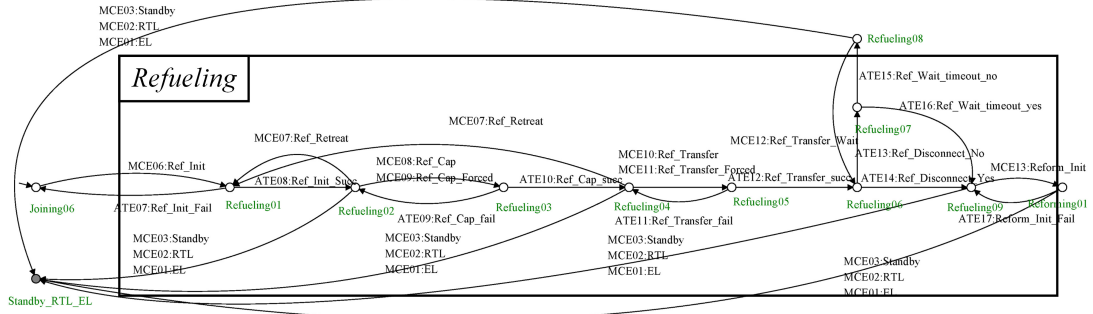
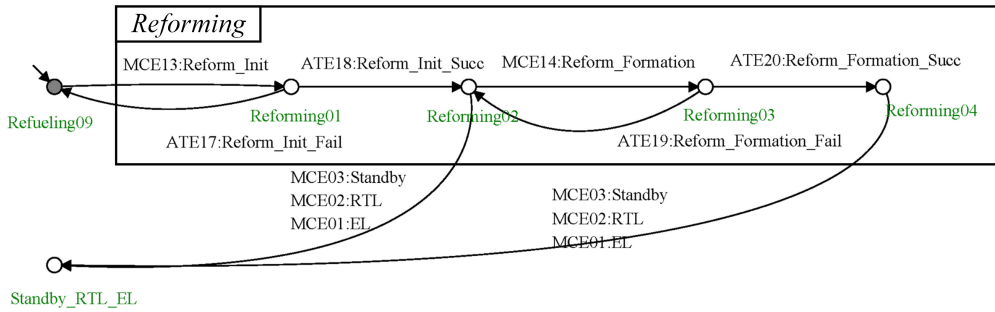


Figure 14.13: The holon of *Joining*. The simple states and transitions inside superstate *Joining* are enclosed by the black square. To avoid messy transition lines, this diagram has been simplified by using node *Standby_RTL_EL* to represent three separate nodes including *Standby*, *RTL* and *EL*, which have the same transition lines from node *Joining04*, *Joining05*, and *Joining06*. The following two diagrams have been simplified as well.

c) *Reforming* superstate: This is an OR superstate as shown in Fig. 14.15. It corresponds to the Reforming sub-phase, and contains three simple states. MCE13 will bring the receiver

Figure 14.14: The holon of *Refueling*.Figure 14.15: The holon of *Reforming*.

from *Refueling* to the *Reforming* superstate. Its success will lead to the *Reforming02* state, where the receiver can return to the withdrawal phase due to health conditions or form the formation (MCE14). Event “ATE20:Reform-Formation-Succ” implies the completion of a work cycle of AAR, and then the receiver should return to the withdrawal phase.

14.5.1.2 (Receiver) Subsystem

Subsystem is another AND component of Receiver, working in parallel with *Autopilot*. This superstate is responsible for recording the health information of different subsystems, namely Navigation, Control, Fuel, Engine, Drogue&probe, Datalink and Tanker safety subsystems. Their state trees are shown in Fig. 14.16. Their holon structures are similar to Fig. 14.8 and 14.9. The holons for *Navigation* and *Fuel* superstates are shown in Fig. 14.17 and 14.18 as an example.

14.5.1.3 (Pilot) Withdrawal

Withdrawal is an AND component of *Pilot*, which is responsible for implementing the FD7 in Table 14.2. Its holon is shown in Fig. 14.19. As shown in this figure, when “MIE02:RTL” happens, i.e., the pilot requires the receiver retreat to RTL MODE, both MCE02 and MCE01 are allowed to happen. This means the receiver can also switch to EL MODE besides RTL MODE

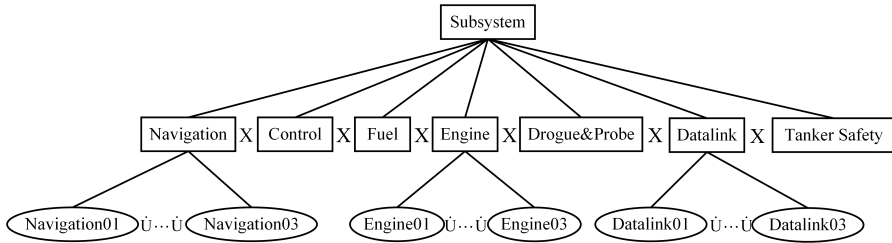


Figure 14.16: The state tree of *Subsystem*. Only part of the simple states are presented here owing to limited pages. These simple states represent different health conditions. For example, *Navigation01* means *normal*, *Navigation02* means *minor damage*, and *Navigation03* means *critical damage*.

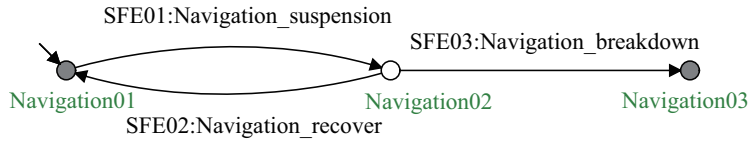


Figure 14.17: The holon of *Navigation* superstate.

in case the receiver is unhealthy and cannot return to base.

14.5.1.4 (Pilot) Force

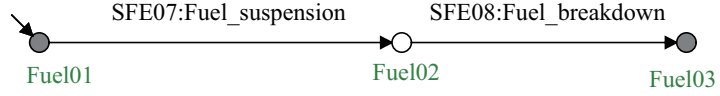
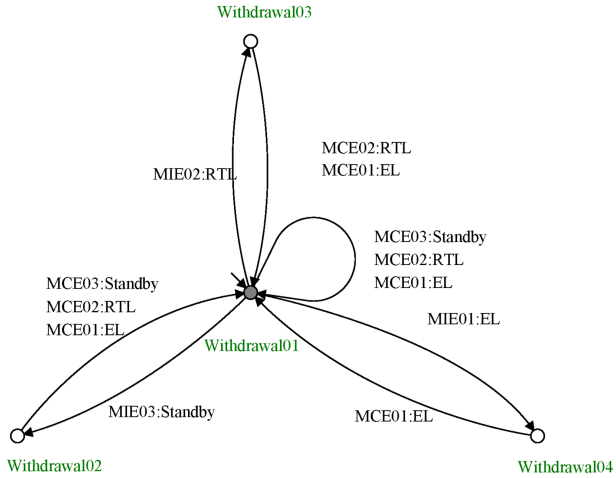
Force is another AND component of *Pilot* and implements the FD6 (in Table 14.2). As shown in Fig. 14.20, MCE09, a substitute of MCE08, can only be enabled when “MIE04:Force-Ref-Cap” happens, i.e., the pilot gives the corresponding command. After MCE09 or MCE08, this holon will return to the original state *Force01*. MCE03 is similar to MCE09.

14.5.1.5 Plant summary

So far, all the superstates and simple states of the *Plant* have been introduced, as shown in Fig. 14.21. Recall that the state of superstate depends on states of its children. Therefore the state of *Plant*, namely *Plant State*, can be represented as a 10-tuple

$$PS = (x_1, x_2, \dots, x_{10})$$

where x_i is the state of the ten superstates in the sequence of *Autopilot*, *Navigation*, *Control*, *Fuel*, *Engine*, *Drogue&probe*, *Datalink*, *Tankersafety*, *Withdrawal* and *Force*. An example of plant state is $PS = (RTL, Navigation01, Control01, Fuel01, Engine01, Drogue&probe01, Datalink01, Tankersafety02, Withdrawal03, Force03)$, where the meaning of *Control01*, *Fuel01*, ..., *Tankersafety02* is displayed in Fig. 14.16.

**Figure 14.18:** The holon of *Fuel* superstate.**Figure 14.19:** The holon of *Withdrawal* superstate.

14.5.2 Specification design

Specifications are mainly used to implement the safety requirements, restricting the undesired and unsafe behaviors of the system. As stated in section 14.2.2, these parallel specifications eliminate, in a minimally restrictive fashion, all behaviors leading to blocking states. They can be divided into two categories, including subsystem-related and pilot-related, as introduced in the following.

14.5.2.1 Subsystem-related specifications

These specifications, including *Spec-Navigation*, *Spec-Control*, *Spec-Fuel*, *Spec-Engine*, *Spec-Drogue&probe*, *Spec-Datalink* and *Spec-Tankersafety?* are used to restrict system behaviors when certain subsystems are damaged or break down according to the requirements presented in Table 14.3.

Take the *Spec-Navigation* as example. According to SR3 and SR7, when “SFE01:Navigation-suspension” happens, MCE04, MCE08 and MCE10 should be disabled. Therefore, as shown in Fig. 14.22, event sequences including (SFE01, MCE04), (SFE01, MCE08) and (SFE01, MCE10) will lead *Spec-Navigation* into blocking state *SpecNavi99*. And according to all safety requirements, when “SFE03:Navigation-breakdown” happens, all MCEs except for MCE01 should be forbidden. This means that when the Navigation subsystem breaks down, the receiver should

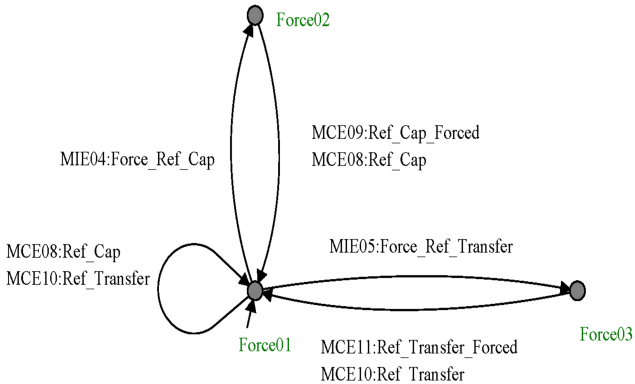
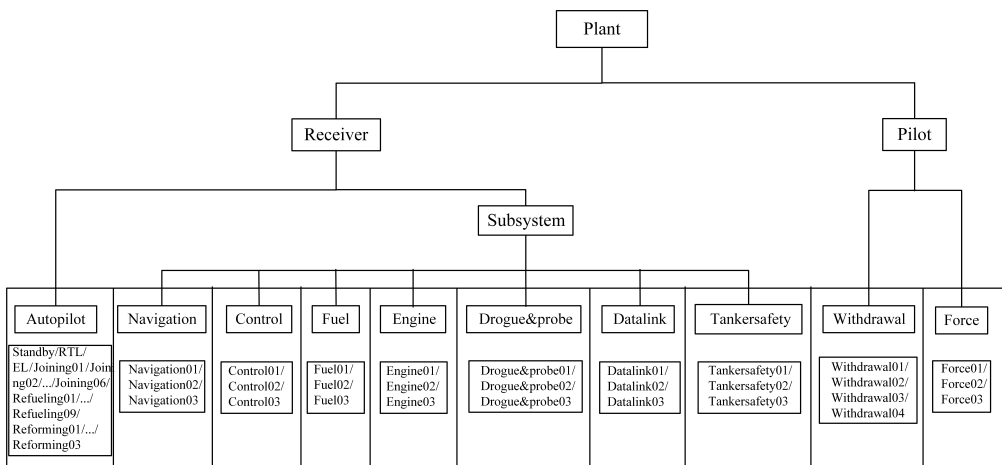
Figure 14.20: The holon of *Force* superstate.

Figure 14.21: Plant overview.

make an emergency landing.

14.5.2.2 Pilot-related specifications

This part refers to the specification *Spec-pilot*, which is used to implement the priority of pilot commands (MIEs) over the autopilot commands (MCEs), as stated in FD5. That is to say, when MIEs happen, except for MCE01, MCE02 and MCE03, other MCEs should be forbidden. As shown in the Fig. 14.23, when “MIE02: RTL” happens, events such as MCE04 and MCE05 are forbidden. Under this situation, the receiver has to perform corresponding mode transitions MCE02 or MCE01.

14.5.3 Supervisor

The *Plant* provides the plant state, a 10-tuple representing the state of the whole system, while the *Specification* points out the forbidden plant states. The supervisor is responsible for disabling certain controllable events (or enabling the rest) at certain plant states to guarantee that the *Plant* never reaches those forbidden plant states. The STSLib developed by [326] is used

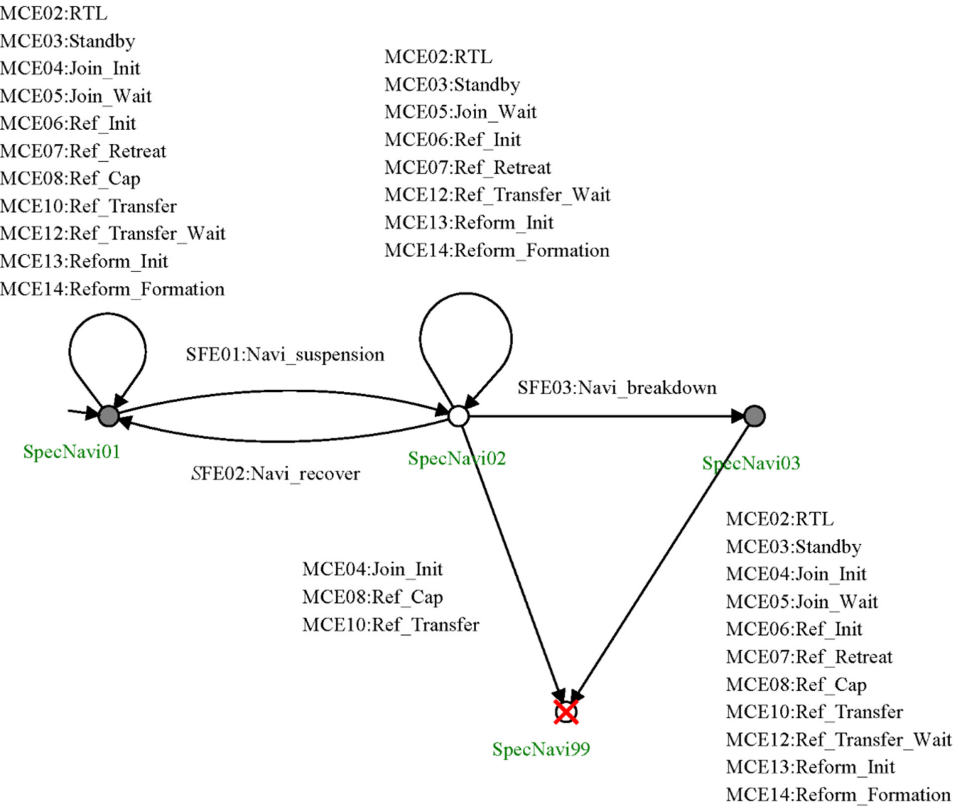


Figure 14.22: The holon of *Spec-Navigation*.

to compute the supervisor of AAR, which finishes within 2 seconds on a personal laptop with 3.2GHZ I5 CPU and 8GB RAM. The supervisor is implemented in binary decision diagrams (BDD) for every MCE, and is converted into a lookup table including all plant states where the MCEs are allowed to happen. The converting program can be found in the supporting material.

Take the resulting supervisor for MCE02 as an example. Its supervisor is shown in Table 14.5, which shows eight different plant states where MCE02 is allowed to happen. That only *Navigation*, *Fuel* and *Engine* are presented means that other superstates in the 10-tuple (such as *Control*, *Datalink*) have no influence on the enablement of MCE02 and no need for checking as well. For example, plant state (*Standby*, *Navigation01*, *Control01*, *Fuel01*, *Engine02*, *Drogue & probe01*, *Datalink01*, *Tankersafety01*, *Withdrawal01*, *Force01*) satisfies the 2nd scenario in Table 14.5 and MCE02 is allowed to happen at this state.

Putting all these different lookup tables together and taking the union of related superstates, the supervisor for the whole system can be presented in Table 14.6. Although the whole system has 413343 states in total, this table has only 235 rows, which shows the power of STS. Note that only 8 superstates need to be checked in the supervisor, fewer than the 10 superstates of plant states. The *Autopilot* and *Force* are ignored since there are no specific requirements about them in the specifications.

Table 14.5: Supervisor for MCE02 in the form of a lookup table

Scenarios	Navigation	Fuel	Engine
1	1	1	1
2	1	1	2
3	1	2	1
4	1	2	2
5	2	1	1
6	2	1	2
7	2	2	1
8	2	2	2

Table 14.6: Supervisor in the form of a lookup table. Only part of the table is shown.

Event	Navigation	Control ²	Fuel	Engine	Drogue Probe	Datalink	Tanker Safety	Withdrawal
MCE02	1	1~3	1	1	1~3	1~3	1~3	1~4
MCE02	1	1~3	1	3	1~3	1~3	1~3	1~4
.....								
MCE07	1	1	1	1	1	1	1	1
MCE07	1	1	1	1	1	1	3	1
MCE07	1	1	1	1	1	3	1	1
MCE07	1	1	1	1	1	3	3	1
.....								
MCE12	3	1	1	1	1	1	1	1
MCE12	3	1	1	1	1	1	3	1
MCE12	3	1	1	1	1	3	1	1
MCE12	3	1	1	1	1	3	3	1
.....								
MCE14	3	3	1	3	1~3	1~3	1~3	1
MCE14	3	3	3	1	1~3	1~3	1~3	1
MCE14	3	3	3	3	1~3	1~3	1~3	1

¹ In the implementation, states are represented by binary bits instead of decimal digits to improve program searching performance.

² Here 1 ~ 3 means that *Control* could be at *Control01*, *Control02* or *Control03*. It is similar for other superstates.

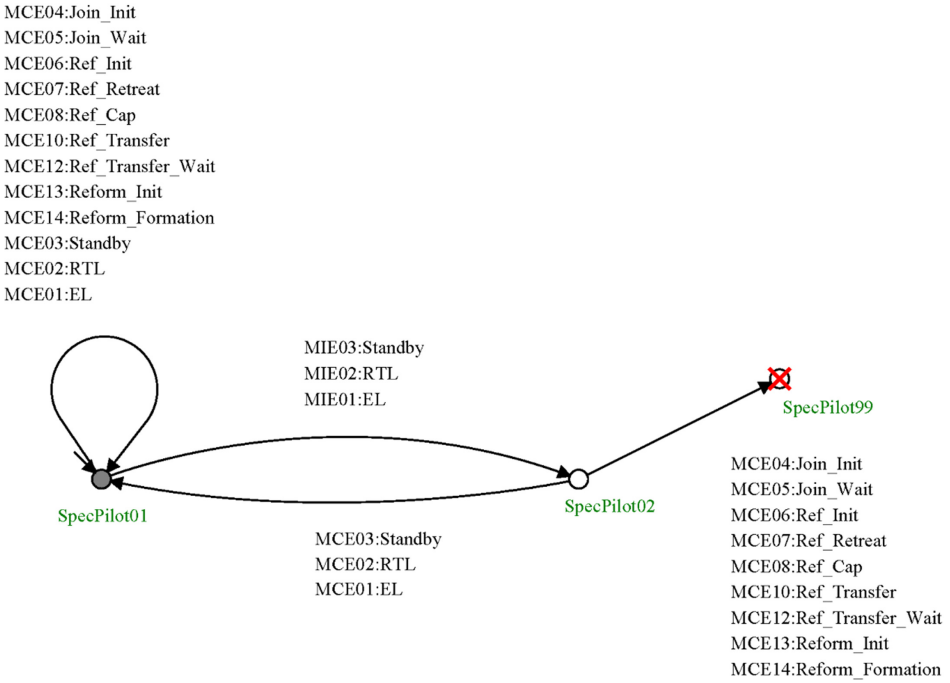


Figure 14.23: The holon of *Spec-Pilot*.

14.6 Implementation and Simulation

With the well-designed *Plant* and obtained supervisor, this section presents the implementation architecture of applying such a logic controller to the autonomous receiver control system. Based on this, a simulation platform of AAR is built using MATLAB2016b to test the logical correctness.

14.6.1 Implementation architecture

As shown in Fig. 14.24, the logic controller should be put between low-level controllers and information sources including *Sensor management*, *Prognostics and Health Management* (PHM) [327] and *Communication management*. The sensor management module is used to estimate the state of receivers such as location, velocity and altitude, determine what mode the receiver is currently in and then output the ATEs. For example, if this module confirms that the receiver has not arrived at the astern area (point C in Fig. 14.3), then “ATE07:Ref-Init-Fail” is generated and output. The PHM module is used to detect subsystem failures and generate SFEs. The communication management is responsible for receiving pilot instructions and generating MIEs, e.g., when the pilot requires the receiver to return to land then "MIE02:RTL" is generated. The low-level controller is used to generate the direct control command for the receiver’s velocity, acceleration, angular velocity, etc. There are 14 low-level controllers in correspondence to those 14 target modes such as STANDBY, JOINING-WAIT, and REFUELING-CAPTURE. At run time, the logic controller will choose one and only one low-level controller at the same time, i.e.,

Table 14.7: Pseudo-code for on-line logic controller

On-line logic controller

Input: the holon *Plant*, the lookup table *Supervisor*, initial *Plant State S = S₀*, Δ is a positive integer representing a mode decision period, and a time counter $k \in N$ and starts at 0, namely $k = 0$.

Step 1: $k = k + 1$

Step 2: The sensor management, PHM and communication management detect the occurrence of ATEs, SFEs and MIEs. if $k \bmod \Delta = 0$, go to Step 3; Otherwise, go to step 1.

Step 3: Collect events occurring in the mode decision period Δ .

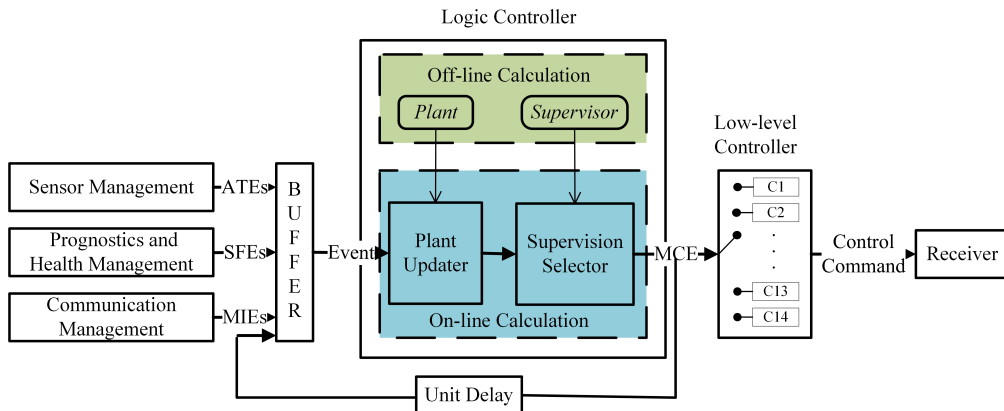
Step 4: Update the plant state *S* to *S₁* with events according to their occurrence sequence one by one.

Step 5: Enable certain MCEs according to *Supervisor* and current state *S₁*. Compare the priority of enabled MCEs and select one MCE with the highest priority.

Step 6: Update the plant state *S₁* to *S₂* with the selected MCE.

Step 7: *S = S₂*, go to step 1.

only one MCE would be enabled.

**Figure 14.24:** The implementation Architecture.

The logic controller is divided into two parts: off-line and on-line. The *Plant* (a holon or automaton with hierarchy structures) and *Supervisor* (a look-up table) can be computed off-line in advance and used as the input of on-line calculation. As for the on-line part, the *Plant Updater* module receives events including ATEs, SFEs and MIEs from the corresponding source and then updates the current plant state according to the pre-defined *Plant* holon. Note that the high-level decision-making is relatively slow in practice, but the low-level detection is fast. For example, the event ATEs, SFEs may be generated every 0.01s, but the decision period may be 1s. Thus a buffer is added to store those events according their occurrence sequence, and then to feed them all into the updater in every decision period. The *Supervision Selector* would enable certain MCEs according to the current plant state and the pre-defined *Supervisor*. The pseudo-code for the procedure is shown in Table 14.7 (The priority comparison presented in this algorithm is explained in the following Section 14.6.2).

14.6.2 MCE Priority

As mentioned before, the supervisor enforces the minimally restrictive behavior (set of generated event sequence) of plants under the restriction of specifications. Therefore, it will happen that several MCEs may be enabled at the same time and the same plant state. However, the aircraft can only be at one state, i.e., only one MCE can be picked and executed. Thus, the priority comparison among different MCEs is necessary for engineering practice. In this paper, the priority of MCEs is given according to their nodal distance to the success of AAR as defined in the flowchart shown in Fig. 14.25. And the priority is reflected by their indexes. That is to say, MCE01 possesses the least priority while MCE14 enjoys the highest priority.

For example, when the *Plant* is at state (*Refueling02, Navigation01, Control01, Fuel01, Engine01, Drogue & probe01, Datalink01, Tanker safety01, Withdrawal01, Force01*), MCE01, MCE02, MCE03, and MCE08 are all enabled. But since REFUELING-CAPTURE MODE is proceeding to the success of AAR but STANDBY, RTL and EL are proceeding to the failure of AAR. Therefore the event transiting to REFUELING-CAPTURE MODE is assigned with a higher priority than events transiting to STANDBY, RTL and EL, and would be chosen in this state.

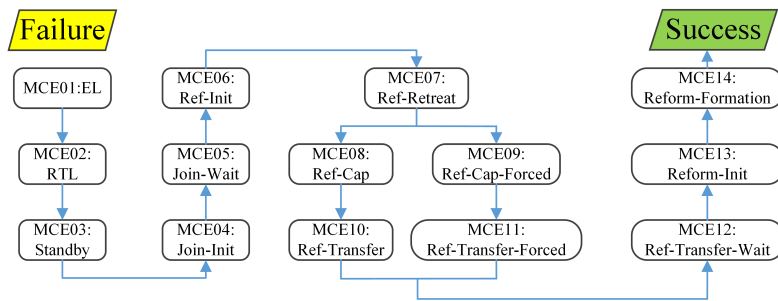


Figure 14.25: The flowchart of all MCEs in the AAR task. The distance of MCE is the nodal distance between the MCE node and the "Success" node along the line.

14.6.3 Simulation

The simulation platform is built within MATLAB2016b according to the implementation architecture shown in Fig. 14.24. This platform mainly consists of three parts: a Graphical User Interface (GUI), processing programs and a 3D visualization environment, as shown in Fig. 14.26 and 14.27. The GUI enables the user to start, pause and terminate the simulation, input pilot commands (MIEs) and subsystem failures (SFEs)⁵, and check the plant state and current MCE. The processing programs are the MATLAB functions used to implement the logic controller and low-level controller illustrated in Fig. 14.24. In detail, the embedded dynamic models of

⁵The ATEs can be detected and generated automatically by the processing programs.

Fighter-16 and Boeing-727 in MATLAB2016b are used to work as the receiver and the tanker.⁶ Each low-level controller (in correspondence to each MCE) would give commands such as engine thrust, pitch angle, yaw angle to control the movement of the receiver. The 3D visualization environment presents the real-time state of the receiver, tanker, and the drogue-probe for a more direct observation.

Within this simulation platform, the user can add subsystem failures and pilot commands at any time. The failsafe mechanism or on-line logic controller will select out the best MCE according to the receiver's current health conditions and pre-defined safety requirements. The corresponding low-level controller will then control the movement of the receiver, which will be shown in the 3D simulation environment. This can enable the user to test the receiver's behavior under different possible situations. Three different testing scenarios are presented as follows, which cover the typical functional and safety requirements of AAR. Their textual descriptions are in Appendix A.6, while videos can be found in Youku and YouTube⁷.

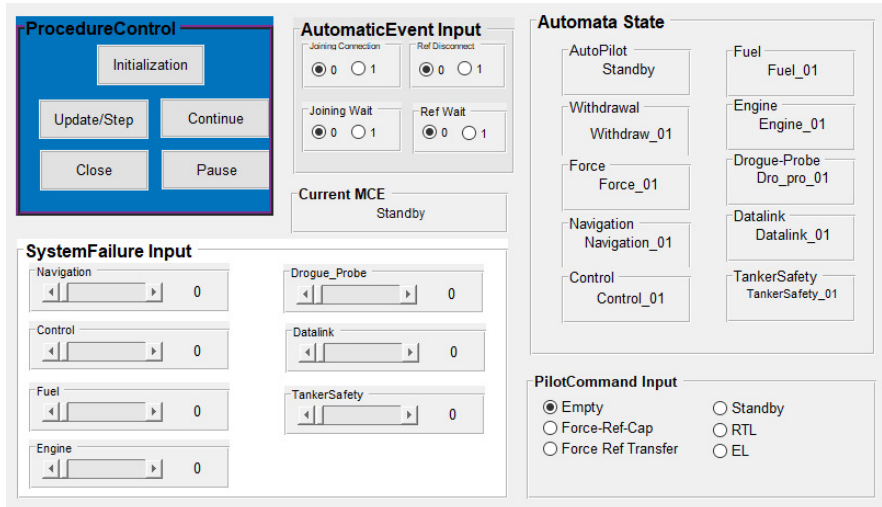


Figure 14.26: Graphical user interface.

14.7 Chapter Summary

This paper presents a new way to synthesize the failsafe mechanism of autonomous aerial refueling, namely the State Tree Structure. This formal method helps the system designer clarify all aspects of customer's requirements at the early stage of product development. It can precisely define every detail of the logic control system, and thus achieve less ambiguity and more consistency compared with traditional document-based methods.

To apply this method to AAR, the continuous AAR procedure is first decomposed into

⁶For more detailed information about dynamic models and controller designs, please refer to <https://www.youtube.com/watch?v=spuXvSr31D8&feature=youtu.be>

⁷For Youku, <https://youtu.be/R4-eMR9zqr0>. For Youtube, https://v.youku.com/v_show/id_XMzgwMTgwODU0OA==.html

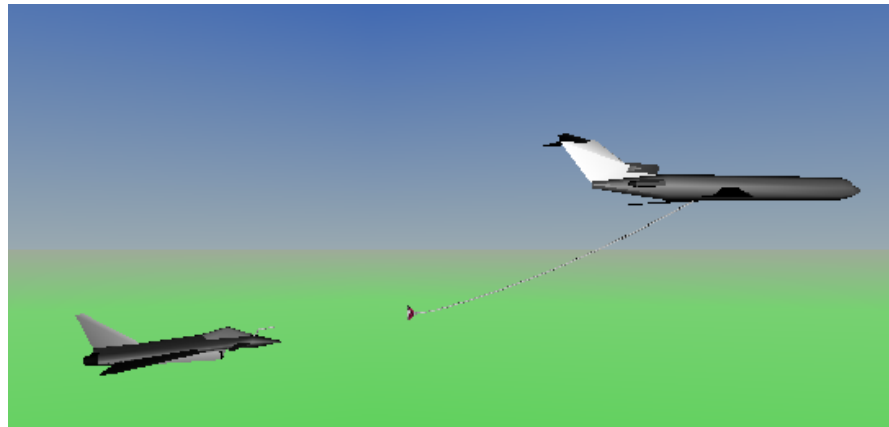


Figure 14.27: 3D simulation environment.

ten discrete flight modes such as STANDBY, JOINING-INIT and REFUELING-CAPTURE MODE, and common safety issues of seven important subsystems like Navigation and Drogue & Probe are collected. These describe the unrestricted behaviors of AAR, and thus define the plants of STS. Then, common user requirements including seven functional demands and ten safety requirements are summarized. The functional demands emphasize what behaviors must be included in the system, so they are used to guide the design of plants. Since the safety requirements point out what behaviors are illegal, they define the specifications of STS. Finally, the software package STSLib is used to compute the supervisor. This final logic controller only has 235 rows, but controls a system with 413343 states.

Based on this, an implementation scheme is proposed and tested in a simulation environment built within MATLAB2016b. Three test cases are presented, recorded and proven to be error-free. Related tools and programs have been uploaded onto [Github](#). The compact form of supervisor and the success of implementation reveals the power and great potential of supervisory control theory in the field of AAR.

Chapter 15 Autonomous Aerial Refueling of Multiple Receivers: An Efficient Rendezvous Scheduling Approach

Autonomous aerial refueling (AAR) is an important capability for the future successful deployment and operation of unmanned aerial vehicles (UAVs), so it is necessary to design an efficient rendezvous scheduling approach. In this paper, a general strategy for refueling missions is proposed for intensive refueling firstly, and then the tanker flight path and virtual queue sequence points are designed. Secondly, to obtain the optimal refueling time under the strategy, an integer linear programming (ILP) algorithm based on the branch-and-bound method is proposed, and some planning is further made for the waiting queue adjustment. Finally, the effectiveness of the proposed approach is demonstrated by simulation via two indexes, namely, the minimum oil volume and average volume of the receivers at the start of the refueling.

15.1 Introduction

UAVs have been widely used in recent years, however, their navigation time is limited by the rate of fuel consumption, so they mainly perform limited search and reconnaissance missions, which makes the study of autonomous aerial refueling technology for UAVs an urgent need, as recently verified by the first successful U.S. refueling mission of the MQ-25 Stingray unmanned refueling aircraft as shown in Fig. 1. Besides, UAVs have developed toward fleeting and clustering, relying on effective collaboration to solve complex missions, which requires autonomous aerial refueling technology for multiple UAVs [328].



Figure 15.1: Drone refuels U.S. Navy fighter jet in midair for the first time.

The rendezvous is a prerequisite for aerial refueling; much research has focused on the one-to-one rendezvous between a single receiver and a single tanker [329–332]. The main rendezvous strategies currently include on-course, point parallel, and en-path rendezvous [333]. Point parallel requires the receiver to be at the refueling control point in advance, and en-path

strategy requires that the tanker and receiver arrive at the rendezvous point simultaneously, forming a co-linear formation. A rendezvous path between a tanker and a receiver on the intended path to achieve rendezvous in the shortest time [329, 330]. A vector field-based 3D convergent path design method was proposed based on the Dubins model [331]. A heuristic search algorithm was designed based on a tanker flight path [332]. The problem of one-to-one rendezvous between a single tanker and a single receiver lacks the adaptability to the complex air traffic environment in the future. In [334], virtual points and tanker's path are designed to achieve multiple receiver refueling and saving fuel by preventing the receiver from hovering in the air.

However, there still exist some challenges in the path planning for aerial refueling of multiple receivers. First of all, the influence of the complexity of the UAV missions on the refueling task is not considered. For example, the refueling order of the UAVs who perform reconnaissance missions may be higher than that who execute the attacking missions. On the other hand, it is now mainly considered to expand the path of the tanker to complete the refueling of multiple UAVs, the safety of the refueling aircraft is difficult to ensure. Last but not least, the refueling interval between UAVs is considered relatively large for UAV formation. In the case of UAVs departing in formation for an assignment, which means that the refueling interval of the receiver is relatively small, how to complete refueling safely and efficiently has not been considered.

To solve the mentioned problems, this study proposes a novel path design for both tankers and receivers. The proposed strategy limits the fly range of the tanker and design a waiting queue for receivers. This is suitable for solving the intensive time refueling problem under a specific refueling sequence and guarantees the aircraft safety. Besides, based on the path, to get the minimum time consumption, a target point assignment algorithm for each receiver is proposed and some rules are made when the receivers are waiting in the queue.

This paper is organized as follows. The designed tanker's path and the whole refueling task procedures are introduced in Sec. II. In Sec. III, the problem is analyzed. Then, in Sec. IV, the main algorithm used in this paper is presented. Then, in Sec. V, the details and results of the simulation are presented. Finally, in Sec. VI, the conclusions are drawn.

15.2 Refueling Task Strategy and Problem Formulation

The tanker's path and virtual queue sequence points for receivers are specially designed and introduced in this part. Based on the path, the whole procedure of the refueling task in this paper is introduced and the problem is formulated.

15.2.1 Tanker's Path and Virtual Queue Sequence Points Design

The design of the tanker's path is shown in Fig. 1, which contains two parts, the straight line refueling section (AC and BD in Fig. 1) and the semi-circular arc section (\widehat{AD} and \widehat{BC} in Fig.

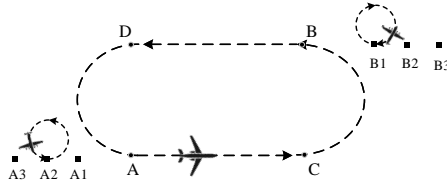


Figure 15.2: Tanker's path and virtual queue sequence points.

1). Besides, the points A and B are called “rendezvous point”, at which the tanker and receiver rendezvous, the points C and D are called “separation point”, at which the receiver finishes the refueling task and separate from the tanker.

The length and time of the two parts can be determined based on the following three guidelines.

- The length of the straight line refueling section is sufficient for one receiver to complete the refueling mission.
- Since the semi-circular arc section is not suitable for refueling, it is hoped that the tanker can fly through this section in the shortest time.
- The tanker flies horizontally in a straight line at a constant velocity v_t during the refueling section.

So the time of the refueling section is

$$t_{\text{internal}} = (t_{\text{refueling}} + t_{\text{operation}}) \times \gamma \quad (15.1)$$

where $t_{\text{refueling}}$ is the time that the receiver's fuel from empty to full, $t_{\text{operation}}$ is the time for the docking and separation of the receiver and the tanker in the refueling process and the item γ is a margin. And the length is

$$L = v_t \times t_{\text{internal}} \quad (15.2)$$

For the semi-circle arc section, since it is not suitable for refueling, we want the tanker to fly over in the shortest time, so the radius at maximum hovering angular rate is

$$R = \frac{v_t^2}{g\sqrt{2K_T - 2}} \quad (15.3)$$

where g is the gravitational acceleration and K_T denotes dimensionless thrust factor. Then we can obtain the time of the second part

$$t_{\text{arc}} = \frac{\pi \times v_t}{g\sqrt{2K_T - 2}}. \quad (15.4)$$

This paper considers the refueling situation when a group of receivers arrive at the refueling area with a small time interval, i.e., the receivers need a specific area to wait for other receivers to finish refueling. For such a purpose, we design virtual queue sequence points (A1,A2,A3... and B1,B2,B3...) near rendezvous points A and B as shown in Fig. 1. The distance between virtual queue sequence points is determined by the specific parameters of the receiver, which can be represented by

$$l = 2 \times r + l_{\text{offset}} \quad (15.5)$$

where r is the minimum turning radius of the receiver and l_{offset} is a compensation term to ensure safety.

15.2.2 Refueling Task Procedures

The procedure of the refueling task described in this paper can be divided into the following steps:

1. At the beginning of the refueling task, each receiver is assigned a refueling sequence value according to its operational mission or its own status.
2. The first receiver in the refueling sequence meets the tanker directly, other receivers are assigned virtual queue sequence points, and then fly to these points.
3. The receivers refuel in sequence, and when the previous receiver begins to rendezvous with the tanker, the sequence waiting for refueling moves into position in turn to form a new queue as shown in Fig. 3.
4. The receiver rendezvous with the tanker at point A or point B, and finish refueling and fly back to the task region at point C or point D.

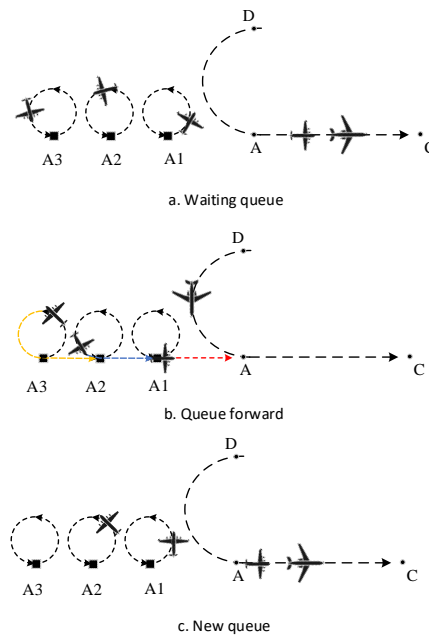


Figure 15.3: Queue adjustment

According to the steps above, the refueling mission of a single receiver can be divided into five phases: "mission", "cruise", "waiting", "rendezvous", "refueling".

- *Mission phase:* The receiver performs task.
- *Cruise phase:* The receiver flies to the assigned virtual point.
- *Waiting phase:* The receiver is staying in the waiting queue.
- *Rendezvous phase:* The receiver rendezvouses with the tanker from the waiting point.
- *Refueling phase:* The receiver docks with the tanker and refuels.

15.3 Problem Analysis

To achieve the minimum time consumption, in the five phases, the time of the “refueling phase” cannot be changed. The time of the rest four phases is related to the assigned virtual points. In this study, the assignment strategy can be described as the following {0, 1} matrix form:

$$\mathbf{S} = \begin{bmatrix} s_{11} & \cdots & s_{1m} \\ \vdots & \cdots & \vdots \\ s_{n1} & \cdots & s_{nm} \end{bmatrix} \quad (15.6)$$

where $s_{ij} = 1$ means the j th virtual point is assigned to the i th receiver, otherwise it is equal to 0 and n is the amount of the receivers and m is the amount of the virtual queue sequence points. And any receiver is uniquely assigned to one point, i.e.,

$$\sum_i s_{i,j} = 1. \quad (15.7)$$

Obviously, the assignment strategy depends on the shortest travel time or shortest travel distance for each receiver to reach the virtual queue sequence point. Because of the presence of the refueling sequence and the constraints of the tanker’s path, the shortest travel time or shortest travel distance is related to the following constraints.

1. **Tanker’s Path Constraints:** The design of the tanker’s path require the receiver should rendezvous with the tanker at point A or point B, and leave at point C or point D. If the receiver misses the timing, it should wait until the next time the tanker pass the points.
2. **Task Constraints:** The range of time intervals $\Delta t_{\text{internal}}$ between two adjacent receivers arriving at the refueling area is relative small, which is $T_{\text{tanker}} = 2 \times (t_{\text{internal}} + t_{\text{arc}}) \geq \Delta t_{\text{internal}} \geq 0$. Besides, the receivers need to be refueled in sequence, which is determined at the beginning of the refueling task based on the tasks performed by each receiver and its own status. The receiver of the first order is supposed to rendezvous with the tanker directly at point A.

By calculating the minimum time t_{ij} for each UAV i to navigate to the assigned virtual point of the refueling j , the shortest rendezvous matrix for the planned path of the tanker and the receiver can be obtained

$$\mathbf{T} = \begin{bmatrix} t_{11} & \cdots & t_{1m} \\ \vdots & \cdots & \vdots \\ t_{n1} & \cdots & t_{nm} \end{bmatrix}. \quad (15.8)$$

Given a strategy \mathbf{S} , the overall time for the refueling task can be obtained as

$$T_{\text{total}} = \text{vec}(\mathbf{T})^T \text{vec}(\mathbf{S}). \quad (15.9)$$

where vec represents . The problem of optimal aerial refueling time assignment can be described

as an Integer Linear Programming (ILP) problem

$$\min_{s_{ij}} \text{vec}(\mathbf{T})^T \text{vec}(\mathbf{S}) \quad (15.10)$$

subject to:

$$\begin{cases} \text{Avec}(\mathbf{S}) = \mathbf{b} \\ s_{ij} \in \{0, 1\} \end{cases} \quad (15.11)$$

where $\mathbf{S} = [s_{ij}] \in \mathbb{Z}^{n \times m}$ represents the assignment strategy, $\mathbf{b} = [1 \ 2 \ \dots \ n]^T$, $\mathbf{A} = (\mathbf{I}_{n \times n} \otimes [1 \ 2 \ \dots \ m]^T)$ and \otimes is the Kronecker product. Eq. (11) comes from Eqs. (6) and (7).

The ILP is widely used to solve Traveling salesman problem (TSP), Petri net analysis problem, and project scheduling problem [335], etc. The solution methods for the ILP problem include branch and bound, heuristic search and tangent plane method. Among them, the branch and bound algorithm is simple, straightforward, and fast on average [335], and a lot of commercial software has been developed. Therefore, this algorithm is used in this paper. The essence of the branch and bound method is to solve the value of the objective function of each node while enumerating the nodes, and stop the enumeration of this branch if the value can be determined to be the optimal solution on that branch. So it is necessary to find when to bound. The problem of the refueling task in this paper can be divided into two sub problems:

1. **Task Assignment.** Design appropriate bound criteria to solve the ILP problem (10),(11) using the branch and bound method.
2. **Velocity Planning.** Design velocity controller for each receiver to allow the receiver to move safely and orderly through the designed waiting queue and rendezvous with the tanker.

15.4 Virtual target points assignment and Queue Waiting Strategy Design

In this section, a bound criterion is proposed to solve the ILP problem. The choice can be considered as the overall optimal solution under the condition of having refueling aircraft path restrictions.

15.4.1 Priority initialization

The priority initialization function contains two parts, the one is determined by human-specified task priorities, the other is the receiver's states. So the function can be represented as

$$pri(i) = \begin{cases} h(i) \\ val_{i,\text{initial}} + d_{i,A}/k \end{cases} \quad (15.12)$$

where $h(i)$ is artificially established, and $val_{i,\text{initial}}$ is the initial fuel of the receiver at the beginning of the task, $d_{i,A}$ is the distance between the receiver and point A, k is the fuel efficiency of the receiver per kilometer, so the second part is the receiver's fuel when it arrives point A.

15.4.2 Virtual Target Point Assignment

Because of the existence of the refueling sequence, the branching order of the branch and bound method is already known, and at the same time, due to the design of the tanker path, as long as the refueling time at each branch node is guaranteed to be the shortest, then the total refueling time should be the least.

The virtual target point available to the current receiver is determined by the distribution of receivers ahead in the refueling order. Because the first receiver will directly merge with the tanker at point A at the beginning of the refueling mission, its situation is rather special, so we will first discuss the target point assignment of the first two receivers.

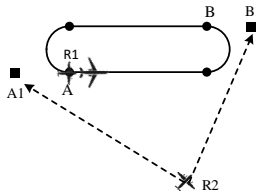


Figure 15.4: Target point option for the first two receivers

As shown in Fig. 4, R2 (the 2nd receiver) has two optional virtual target points A1 and B1 due to the task constraints. Nowadays, studies generally consider calculating the paths to reach A1, B1, and which one is shorter will be used as the target point. However, for the context of this thesis, when R2 reaches point B1, although the path is shorter, the tanker may have already flown past point B. Then R2 needs to wait for the next time that the tanker passes point B. At this time, although it takes longer to reach point A, it can arrive before the tanker reaches point A. R2 obviously chooses target point A1. Since the coordinates of the virtual point and the position of R2 are known, the arrival time of R1 (the 1st receiver) to point A and the arrival time of R2 to B1 can be calculated and the time interval can be obtained, i.e.,

$$\Delta t_{1,2}^B = t_{2,B1} - t_{1,A} \quad (15.13)$$

where $t_{2,B1}$ is the arrival time of R2 to B1 and $t_{1,A}$ is the arrival time of R1 to point A. So we first compare $\Delta t_{1,2}^B$ with $T_{\text{tanker}}/2$, if $\Delta t_{1,2}^B < T_{\text{tanker}}/2$, the target point of R2 is B1. Otherwise, the target point of R2 is A1.

For more general situations, the judgment conditions are more complex. As shown in Fig. 5, for a receiver R_i (the i th receiver), it has four optional virtual target points A2, A3, B1, B2, the reason can be found in Fig. 6. In Fig. 6(a), if the previous receiver is assigned to refuel at point B, R_i should take the assignment to A3 into account, but also the case of A2. It happens when R_i arrives at A2, the previous aircraft has already left for refueling or moved forward as

seen in Fig. 6(b). This situation is usually caused by the relatively large time interval between the arrival times of the receivers. When the receiver arrives at the target point, the receiver at the head of the same queue have already flown from the waiting area to the rendezvous point, so the queue will move forward one step as a whole.

First, R_i needs to consider whether the previous receiver is assigned to queue A or queue B. If it is queue A, R_i should consider B_1, B_2 first, otherwise it should give priority to A_2, A_3 in Fig. 5. Then check if there is a queue forward for those assigned in the same queue, finally select the target point.

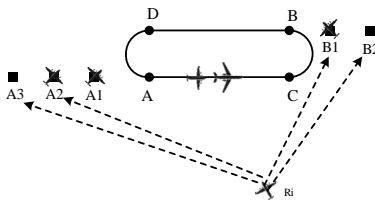


Figure 15.5: Target points options for formal receivers

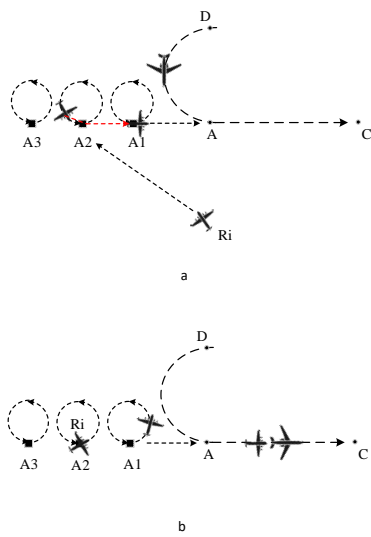


Figure 15.6: R_i considers the case of A2

15.4.3 Design of the Velocity Controller

In order to ensure safe and efficient refueling, the following specifications should be followed when receivers are in the queue:

1. The decision whether to move forward or not when a receiver begins to rendezvous with the tanker.

The corresponding reasons are as follows:

For rules 1 and 2 mentioned above, in actual combat, to avoid danger, the planned paths are often required to cross as few or even no crossings as possible. So each aircraft has to ensure that it flies a full circle before any other action is taken as shown in Fig. 6.

Algorithm 1 Assignment

Require: T_{tanker} , coordinates of virtual target points near point A in set \mathcal{A} , coordinates of virtual target points near point B in set \mathcal{B} , and \mathcal{A}_i and \mathcal{B}_j represent the i th and j th element in set \mathcal{A} and \mathcal{B} .

Ensure: \mathbf{S}

Let set C to record the receivers that will rendezvous with the tanker at point A, set \mathcal{D} at point B. Let numA to record number of occurrences of situation shown in Fig. 6 at point A, and numB at point B.

```

1: for  $i = 3$  to  $n$  do
2:   if  $i - 1 \in C$  then
3:      $j = \max(\mathcal{D})$ 
4:     calculate  $\Delta t_{i,j}^B = t_{i,Bj} - t_{i-1,A}$ 
5:      $k = \min(\mathcal{D}) + \text{numB}$ 
6:     compare  $k$ th receiver's beginning refueling time  $t_{B\text{queuehead}}$  with  $t_{i,Bj}$ 
7:     if  $\Delta t_{i,j}^B < T_{\text{tanker}}/2$  and  $t_{i,Bj} > t_{B\text{queuehead}}$  then
8:       add  $i$  to  $\mathcal{D}$  and  $i$ th receiver is assigned to  $\mathcal{B}_j$ 
9:     else if  $\Delta t_{i,j}^B < T_{\text{tanker}}/2$  and  $t_{i,Bj} < t_{B\text{queuehead}}$  then
10:      add  $i$  to  $\mathcal{D}$  and  $i$ th receiver is assigned to  $\mathcal{B}_{j+1}$ 
11:    else if  $\Delta t_{i,j}^B > T_{\text{tanker}}/2$  then
12:       $l = \max(C)$ 
13:       $m = \min(C) + \text{numA}$ 
14:      compare  $m$ th receiver's beginning refueling time  $t_{A\text{queuehead}}$  with  $t_{i,A_l}$ 
15:      if  $t_{i,A_l} > t_{A\text{queuehead}}$  then
16:        add  $i$  to  $C$  and  $i$ th receiver is assigned to  $\mathcal{A}_{l+1}$ 
17:      else if  $t_{i,A_k} < t_{A\text{queuehead}}$  then
18:        add  $i$  to  $C$  and  $i$ th receiver is assigned to  $\mathcal{A}_l$ 
19:      end if
20:    end if
21:  end if
22: end for

```

On the other hand, there is a limit to the velocity of the receiver, and we cannot guarantee that each receiver will move forward one step every time when a receiver begins refueling under the above-mentioned path-free condition, which means that the receiver needs to make a decision whether to move forward or not every time to decide its velocity. So the velocity limit may lead to a situation as shown in Fig. 7. It can be seen that due to the velocity limitation, the receiver at point A2 will not be able to fly to point A and fly another full circle before next time tanker arrives at point A. This scenario has an impact on the previous algorithm, and the target points available to each receiver change accordingly, as the queue may not move or move two points when the receiver at the front of the queue starts refueling. When the receiver on A2 starts refueling, the receiver on A3 will first consider flying to A1 instead of A2. For the example of the previous assignment point in queue A, the corresponding assignment logic is shown in **algorithm 1**.

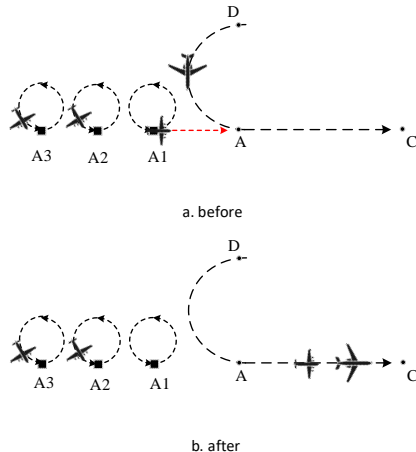


Figure 15.7: Queue position change considering velocity limit

15.5 Simulation and Results

To verify the efficiency of the designed algorithm, a simulation model is build in MATLAB/Simulink using the “Stateflow” toolbox. The state of each of receivers and the corresponding transition conditions are the same as those discussed above as seen in Fig. 8. In Fig. 8, for example, the “TC1” condition means that the receiver’s fuel has been in an unhealthy state.

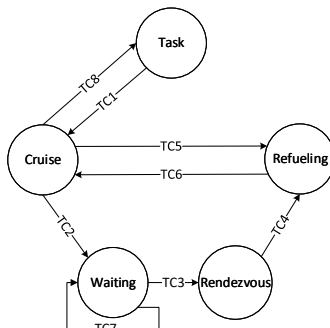


Figure 15.8: Finite state machine for receivers

Here, two indexes are defined, namely, the minimum oil volume of the receivers and the average oil volume of the receivers at the start of refueling. Due to different assignment strategies under the same initial conditions, each UAV starts refueling with a different amount of fuel. The initial fuel volumes of 11 receivers are set between 1400 and 1600 randomly. Simulations are performed and the values of the two indexes are recorded according to different allocation strategies, and the results are shown in Fig. 9. The first seven simulations are randomly assigned waiting points according to the refueling order, and the eighth simulation is a refueling task according to the assignment strategy proposed in this paper. It can be observed that, under the same starting conditions, the assignment strategy proposed in this paper can ensure the highest oil volume when the receiver starts refueling. Besides, the trajectory of UAVs can be found in Fig. 10, here, we assume that during the “mission” phase the UAV takes a roundabout way, under the velocity designed before. It can be observed that the trajectories of each UAVs are not

repeated, and all flying complete circles in the waiting area.

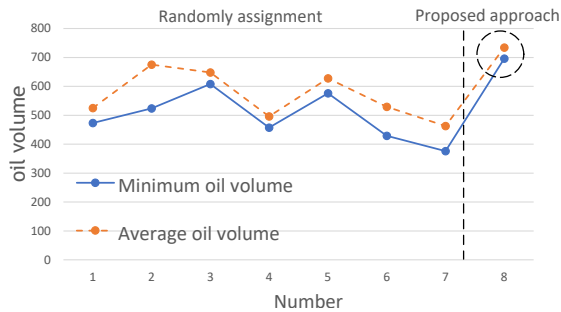


Figure 15.9: Comparison with Random assignments

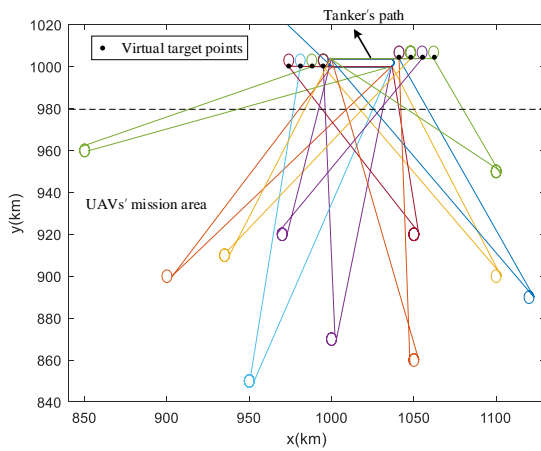


Figure 15.10: UAVs trajectory

15.6 Chapter Summary

This paper proposed a novel whole strategy for intensive refueling task of multiple receivers, which contains the design of the tanker's path and virtual queue sequence points. Based on the strategy, an target points assignment algorithm based on the branch and bound method are proposed and velocity planning is designed when the receivers waiting in the queue to get the minimum refueling time. Simulations results show that the proposed method ensures efficient refueling for multiple receivers. In future studies, consider abnormal situations, such as refueling docking failure, decide whether to continue refueling or go back to the waiting area. Furthermore, more accurate path planning will be considered, including dynamics constraints and obstacle avoidance.

Chapter 16 Aerial Refueling Scheduling of Multi-Receiver and Multi-Tanker under Spatial-Temporal Constraints

Given the constrained load capacities of these aircraft, aerial refueling becomes crucial to extend their operational time and range. Firstly, a fuel consumption calculation model for aerial refueling scheduling is established based on the receiver path. Then, two distinct methods, including an integrated one and a decomposed one, are designed to address the challenges of establishing refueling airspace and allocating tasks for tankers. Both methods aim to optimize total fuel consumption of the receivers and tankers within the aerial refueling scheduling framework. The optimization problem is established as nonlinear optimization models along with restrictions. The integrated method seamlessly combines refueling rendezvous point scheduling and tanker task allocation into unified process. It has a complete solution space and excels in optimizing total fuel consumption. The decomposed method, through the separation of rendezvous point scheduling and task allocation, achieves a reduced computational complexity. However, this comes at the cost of sacrificing optimality by excluding specific feasible solutions. Finally, numerical simulations are carried out to verify the feasibility and effectiveness of the proposed methods. These simulations yield insights crucial for the practical engineering application of both the integrated and decomposed methods in real-world scenarios.

16.1 Introduction

Recently, aerial refueling, particularly Autonomous Aerial Refueling (AAR), has drawn increasing attention from academia and industry, significantly impacting civil and military aviation. [11, 31, 44, 72, 151] Thomas et al. conducted a comprehensive review of the present and future aspects of aerial refueling, including modeling, sensors, control strategies, as well as simulation and test. [151] Aerial refueling research refers to many aviation techniques, such as dynamic, modeling, and simulation, [11, 31, 44, 72] path scheduling, [336, 337] docking control, [3, 68, 79, 88] drogue detection, [174, 290] mission scheduling, [337, 338] etc. However, few pieces of research concentrate on scheduling problems, [125] despite the crucial role they play in aerial refueling. In detail, aerial refueling scheduling is a decision-making problem of coordinating tankers and receivers according to the demand of the receivers subject to limited resources. In general, scheduling technology can significantly enhance aerial refueling efficiency, such as saving time for the key mission, reducing fuel consumption, ensuring refueling safety, increasing resource utilization, etc.

Since the 1880s, with the extensive deployment of aerial refueling capability in U.S. military aircraft, American scholars took the lead in the Aerial Refueling Scheduling Problem (ARSP) research. Bordelon proposed the determinants of the optimal aerial refueling rendezvous point, optimal takeoff fuel load, and minimum fuel carrying capacity. [339] This supported the mathematical modeling method to solve the optimization problem for aerial refueling. Many research endeavors have been devoted to improving the ARSP model with larger scales and more practical hypotheses, such as a mathematical model for multi-receiver and single tanker scenario, [340] scheduling solutions for a fleet of airplanes, [341, 342] parallel machine scheduling by heuristic algorithms[343] and a Deep Reinforcement Learning (DRL) based method for multi-receiver and multi-tanker. [344] These studies assume that the rendezvous points or the tanker's trajectory are known in advance and focus on refueling task allocation only. Additionally, some researches concentrated only on path planning for the aerial refueling problem, such as an adapted labeling algorithm for multi-tanker, [337] and an approximated fast heuristics algorithm for a single Unmanned Aerial Vehicle (UAV). [338]

Many mature algorithms have been developed for task allocation of different vehicles.[345, 346] Some optimization problems are similar to aerial refueling scheduling, such as refueling path scheduling for the UAVs by the mobile Ground Vehicle (GV), [347] or the mobile charging vehicles. [348, 349] In Ref. [347], the GV can act as the mobile refueling station for the UAVs. Then, a two-stage method by Mixed-Integer Linear Programming (MILP) was designed for Coverage Path Planning (CPP) missions for coupled UAV-GV. Spatial-temporal networks[348] and Mixed-Integer Nonlinear Programming (MINLP)[349] were adopted to solve the scheduling problem of mobile charging vehicles.

The aerial refueling scheduling result requires a balance between safety and efficiency. The drawbacks of the existing research can be summarized as follows. (A) There is a lack of studies that specifically focus on the problem of multiple tankers for multiple receivers, which is crucial in meeting today's extensive aerial refueling requirements. (B) Most studies used the total operating time as the optimization index,[343] but in forest fire-fighting practice, economics, such as the fuel consumption, is of great importance as well. (C) Almost all of the current studies concentrated on only one aspect of aerial refueling scheduling problem like mathematical modeling,[340] path planning,[337, 338] rendezvous point scheduling[339] or task allocation.[343, 344] Multi-receiver and multi-tanker studies generally only focused on the task allocation of tankers and assumed that the refueling missions are known in advance. However, receiver's path, rendezvous points, and task allocation are coupled with the total fuel consumption in aerial refueling. Therefore, a mere combination of the existing studies cannot lead to the optimal solution for the multi-receiver and multi-tanker aerial refueling scheduling problem, specifically aiming to minimize fuel consumption.

In this paper, multiple support tankers from the multiple takeoff and landing airports. Many challenges are involved, such as minimum and maximum fuel load constraints, threat areas, etc.

The aerial refueling scheduling problem is cast into a task allocating model with spatial-temporal constraints. Because the functions of fuel consumption and spatial-temporal constraints in the problem are nonlinear, the optimization for the rendezvous points and initial fuel load is a nonlinear programming problem which is difficult to solve. Thus, in the simulations, the Genetic Algorithm (GA) is employed to obtain the approximate optimal solution to such a nonlinear NP-hard problem. The main contributions of this work can be outlined as follows:

(1) For large-scale AAR requirements, the aerial refueling scheduling problem is studied in the scenario of multiple receivers and tankers, multiple airports, and long-range operations of receivers.

(2) Mathematical modeling, rendezvous points scheduling, path planning and task allocation are integrated, and the total fuel consumption is employed as the optimization index.

(3) Two aerial refueling scheduling methods with multiple receivers and tankers are proposed. In the integrated method, the rendezvous points and task allocation are scheduled simultaneously. A decomposed scheduling method is further designed for less calculation time by decoupling the whole optimization process into two independent processes: rendezvous point scheduling and task allocation. Simulation tests are carried out to compare the efficiency of the developed methods.

The remainder of this paper is organized as follows. Section 16.2 generalizes the aerial refueling mission for multi-receiver and multi-tanker and formulates scheduling models and fuel consumption models for the aircraft. Section 16.3 gives the scheduling flow and the path planning algorithm based on A* algorithm. In Section 16.4, the integrated and decomposed scheduling methods are proposed to obtain the optimal refueling solution. In Section 16.5, the proposed methods are testified by the simulation of aerial refueling scheduling problems with several receivers and tankers.

The notations used in this paper are summarized in Table 16.1.

16.2 Problem formulation

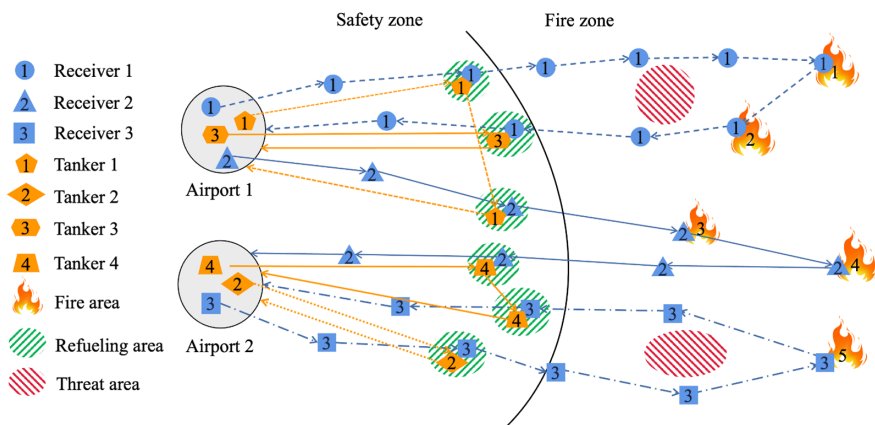
16.2.1 Aerial refueling mission

Fig. 16.1 is a schematic diagram of the aerial refueling scheduling problem by multiple receivers and tankers. In an aerial refueling problem, there are two different kinds of controlled objects: tankers and receivers. The optimization objective is to minimize the overall fuel consumption of receivers and tankers under the prerequisite that the receivers fly to and from the task area safely and accurately. As shown in Fig. 16.1, the whole airspace is divided into two by a black solid line. The left area is the safety zone, while the right area represents the task zone, which is deemed unsafe for tankers due to complex updraft. Aerial refueling can only be performed in the safety zone to guarantee safety. The left slash and right slash ellipses are the refueling and threat areas, respectively. The round, triangle, square nodes and pentagon,



Table 16.1: Definition of main notations

Notation	Meaning
N_r, N_t	Receiver number, tanker number
$\{\mathbf{p}_{r,i_r,i}\}_{i=0}^{N_{ir}}, \{\mathbf{p}_{r',i_r,i}\}_{i=0}^{N_{ir}}$	Departure path, return path of the i_r^{th} receiver
$\{\mathbf{p}_{t,i_t,0}, \mathbf{p}_{t,i_t,1}, \dots, \mathbf{p}_{t,i_t,k_{it}}, \mathbf{p}_{t,i_t,0}\}$	Path of the i_t^{th} tanker
F_{r,i_r}, F_{t,i_t}	Total fuel consumption mass of the i_r^{th} receiver, the i_t^{th} tanker
$F_{r,\text{tk}}, F_{r,\text{ld}}, F_{r,\text{rfl}}, F_{r,i_r,\text{tsk}}$	Fuel consumption mass during the takeoff, landing, refueling, task procedure
$F_{r,d_{i_r},i}$	Fuel consumption mass during the i^{th} flight segment of the i_r^{th} tanker
$F_{r,i_r,\text{rfl},1}, F_{t,i_t,\text{rfl},2}$	Received fuel mass during the first refueling, second refueling of the i_r^{th} tanker
$F_{t,\text{tk}}, F_{t,\text{ld}}, F_{t,\text{rfl}}$	Fuel consumption mass during the takeoff, landing, refueling procedure
$F_{t,d_{i_t},i}, F_{t,i_t,i,\text{wt}}$	Fuel consumption mass during the i^{th} flight segment, hovering and waiting procedure
$F_{t,i_t,i,\text{rfl}}$	Served fuel mass during the i^{th} refueling of the i_t^{th} tanker
$F_{r,\min}, F_{r,\max}, F_{t,\min}, F_{t,\max}$	Minimum and maximum safe fuel load mass of receiver and tanker
$\mathbf{P}_{\text{ob}}, \mathbf{P}_{\text{s}}$	Obstacle airspace set, safe airspace set
$\mathbf{k}_1, \mathbf{k}_2$	Waypoint serial numbers of the first and second aerial refueling route
$\mathbf{n}_1, \mathbf{n}_2$	Tankers' serial numbers allocated to the first and second refueling mission
$\mathbf{X}, \mathbf{Y}, K$	Refueling mission grouping matrix, refueling mission allocation matrix, number of missions

**Figure 16.1:** Schematic diagram of aerial refueling scheduling problem by multiple receivers and tankers.

rhombus, hexagon, trapezoid with different numbers represent the waypoints of different receivers and tankers. Correspondingly, the different kinds of lines passing through them are the flight paths of different tankers and receivers. The solid circles are airports located in the safety zone. The whole flight process of the receiver' operation is presented as follows: several receivers take off from the airports and perform the first aerial refueling operations when reaching the corresponding aerial refueling points. Then, they fly to the task areas and perform task. After that, they return to refueling points by following the planned path for the second aerial refueling operation. Finally, they return to the landing airports. Accordingly, the complete flight process of the tankers is given as follows: departing from the airport, flying through all aerial refueling mission points following the order of the sorted aerial refueling missions, completing each refueling, and finally, returning to the landing airport.

16.2.2 Basic assumptions

According to various complex factors of aerial refueling mission requirements, the aerial refueling mission model established in this paper is based on the following assumptions:

Assumption 1. Only fuel can be transferred by aerial refueling.

Assumption 2. Each receiver will be refueled twice in the whole round trip: the first one is on its departure path to guarantee enough fuel from the takeoff airport to reach the task area, and the second one is on its returning path to ensure enough fuel from the task area to the landing airport. One-to-one rendezvous approach is employed for the refueling between the tanker and the receiver.

Assumption 3. Since the refueling areas are set in the safe zone, all the flight paths of tankers will not be ex-posed to threats. Therefore, the tankers will fly according to the great circle paths between airports and each aerial refueling mission point.

Assumption 4. The fuel consumption of each aircraft in the takeoff and landing phases is taken into account according to the average fuel consumption.

Assumption 5. The aircraft flies at cruise speed during the whole operating process, and the altitude and speed of the aircraft are unchanged. The earth is an ideal sphere with a radius $R = 6371\text{km}$. The tanker and the receiver fly at a fixed cruising speed between the two waypoints with a fixed altitude $H = 5\text{km}$. Aircraft fly between two path points in the air according to the great circle paths.

Assumption 6. Tankers and receivers fly in the stratosphere, ignoring the influence of weather, wind direction, and wind speed.

The coordinate position is expressed by latitude and longitude. The equation for calculating the distance of the great circular arc between the starting point and the ending point is given as follows:

$$d(\mathbf{p}_1, \mathbf{p}_2) = (R + H) \cos^{-1} (\sin \beta_1 \sin \beta_2 + \cos \beta_1 \cos \beta_2) \cos (\alpha_2 - \alpha_1) \quad (16.1)$$

where $\mathbf{p}_1, \mathbf{p}_2 \in \mathbb{R}^2$ are the coordinates of starting and ending points on the path, $\alpha_1, \beta_1 \in \mathbb{R}$ are the latitude and longitude coordinates of the starting point, and $\alpha_2, \beta_2 \in \mathbb{R}$ are the latitude and longitude coordinates of the ending point.

The coordinates of the starting point and the ending point are given as follows:

$$\begin{cases} \mathbf{p}_1 = [\alpha_1 \beta_1]^T \\ \mathbf{p}_2 = [\alpha_2 \beta_2]^T \end{cases} \quad (16.2)$$

16.2.3 Scheduling models

16.2.3.1 Fuel consumption model

In this paper, the fuel consumption models of receivers and tankers adopt the nonlinear fuel consumption calculation equation to increase the model's authenticity. Because the fuel consumption of various aircraft is very complex and the parameter selection should be adjusted according to the specific situation, to simplify the calculation, a simplified model of the aerial refueling fuel consumption is employed in this paper.

The fuel consumption mass per unit distance of an aircraft at a specific flight altitude is given as follows:

$$f(G) = \frac{q}{G} \quad (16.3)$$

where $G \in \mathbb{R}$ represents the total weight of the aircraft, and $q \in \mathbb{R}$ represents the fuel coefficient of aircraft. The total weight of the aircraft includes the empty weight and carried load weight as follows:

$$G = (m_0 + m_c)g \quad (16.4)$$

where $m_0 \in \mathbb{R}$ is the empty mass of the aircraft, $m_c \in \mathbb{R}$ is the carried load mass which is variable during flight, and $g \in \mathbb{R}$ is the acceleration of gravity. The fuel consumption mass function concerning the remaining fuel mass is given as follows:[350]

$$F'(m_{rl}, d) = (m_0 + m_{rl}) \left(e^{\frac{d}{q}} - 1 \right) \quad (16.5)$$

where $m_{rl} \in \mathbb{R}$ is the remaining carried load.

Assuming that the carried load of the aircraft is only fuel, $m_{f,max} \in \mathbb{R}$ is the maximum carried fuel mass when it takes off, and $d_{max} \in \mathbb{R}$ is the maximum flight distance. Substituting $F'(m_{rl}, d) = m_{f,max}$, $m_{rl} = 0 \text{ kg}$ and $d = d_{max}$ into Eq.16.5, we can obtain the fuel coefficient calculating formula as follows:

$$q = \frac{d_{max}}{\ln(m_{f,max} + m_0) - \ln m_0} \quad (16.6)$$

The carried loads of a tanker in the aerial refueling mission are all fuel, while the carried loads of a receiver are composed of two parts: fuel and ammunition. The fuel consumption mass

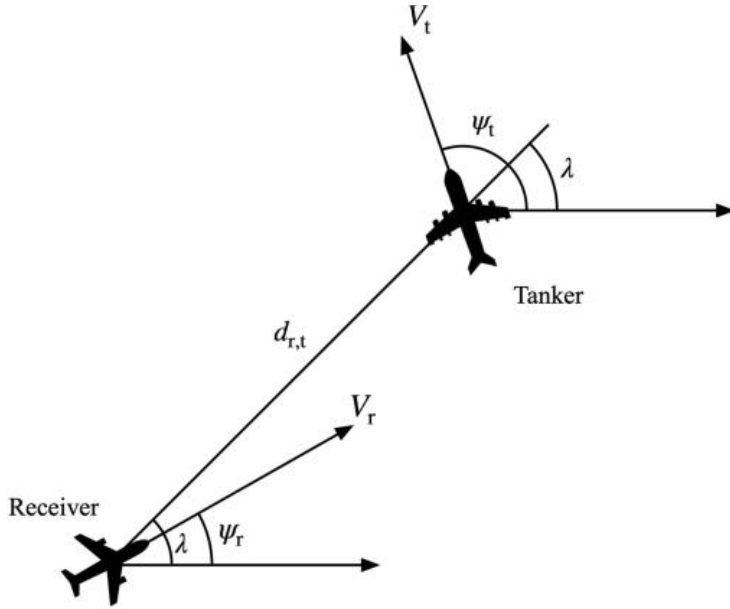


Figure 16.2: Relative geometry between a receiver and a tanker.[351]

equations of receivers and tankers concerning the remaining fuel mass are given as follows:

$$F'_r(m_1, m_{rf}, d) = e^{\ln(m_{r0} + m_1 + m_{rf}) + d/q_r} - (m_{r0} + m_1 + m_{rf}) \quad (16.7)$$

$$F'_t(m_{rf}, d) = e^{\ln(m_{t0} + m_{rf}) + d/q_t} - (m_{t0} + m_{rf}) \quad (16.8)$$

where $m_1 \in \mathbb{R}$ is the carried load mass of ammunition, $m_{r0}, m_{t0} \in \mathbb{R}$ are the empty mass of the receiver and the tanker, respectively, and $q_r, q_t \in \mathbb{R}$ are the fuel coefficient of the receiver and the tanker, respectively.

16.2.3.2 Dynamic model

Fig. 16.2 depicts the relative geometry between a receiver and a tanker. In Fig. 16.2, $\psi_r, \psi_t \in \mathbb{R}$ are the heading angles of the receiver and the tanker, respectively, $V_r, V_t \in \mathbb{R}$ are the speed of the receiver and the tanker, respectively, $\lambda \in \mathbb{R}$ denotes the Line-of-Sight (LOS) angle of the aircraft, and $d_{rt} \in \mathbb{R}$ denotes the distance between a receiver and a tanker.

The dynamics of the receiver and the tanker are represented as follows:[351]

$$\begin{cases} \dot{d}_{r,t} = -V_r \cos(\psi_r - \lambda) + V_t \cos(\psi_t - \lambda) \\ \dot{\lambda} = -\left(\frac{V_r}{d_{r,t}}\right) \sin(\psi_r - \lambda) + \left(\frac{V_t}{d_{r,t}}\right) \sin(\psi_t - \lambda) \end{cases} \quad (16.9)$$

16.2.3.3 Obstacle model

Receivers take off from the takeoff airports according to the schedule, arriving at the mission point safely and timely with aerial refueling support of tankers, and the same for the returning path. Receivers need to avoid threat areas distributed near the task areas during the flight paths. Therefore, refueling rendezvous points are constrained spatially by the threat areas.

The point set of obstacle airspace is given as follows:

$$\mathbf{P}_{\text{ob}} = \left\{ \mathbf{p} \in \mathbb{R}^2 \mid d(\mathbf{p}, \mathbf{p}_{ci}) < r_i, i = 1, 2, \dots, N_{\text{ob}} \right\} \quad (16.10)$$

where $\mathbf{p}_{ci} \in \mathbb{R}^2$ is the center coordinates of the i^{th} round obstacle area, $r_i \in \mathbb{R}$ is the radius of the round obstacle area, and $N_{\text{ob}} \in \mathbb{N}$ represents the number of obstacles.

16.2.3.4 Path model

The flight path in this paper is given in the form of the following sequential coordinate points set:

$$\{\mathbf{p}_i\}_{i=0}^{N_p} = \{\mathbf{p}_0, \mathbf{p}_1, \dots, \mathbf{p}_{N_p-1}, \mathbf{p}_{N_p}\} \quad (16.11)$$

where $\mathbf{p}_i, i = 0, 1, \dots, N_p$ represent the i^{th} point coordinates in the flight path, $\mathbf{p}_0, \mathbf{p}_{N_p}$ represent the coordinates of the starting point and the ending point, respectively, and $N_p \in \mathbb{N}$ represents the number of waypoints in the path.

The flight path of a receiver from its takeoff airport to its landing airport is separated into two parts: the flight path of the receiver from its takeoff airport to the target point, and the flight path of receiver from the target point to the landing airport. According to the notations above, where $\{\mathbf{p}_{r,i_r,i}\}_{i=0}^{N_{i_r}}, i_r = 1, 2, \dots, N_r$ represents the departure path of the i_r^{th} receiver, $\{\mathbf{p}'_{r,i_r,i}\}_{i=0}^{N'_{i_r}}, i_r = 1, 2, \dots, N_r$ represents the returning path of the i_r^{th} receiver, N_{i_r} and N'_{i_r} represent the total waypoint number of the departure and returning flight path of the i_r^{th} receiver, respectively, and $N_r \in \mathbb{N}$ is the number of receivers. The flight path of a tanker depends on the coordinates of its takeoff airport. The path $\{\mathbf{p}_{t,i_t,0}, \mathbf{p}_{t,i_t,1}, \dots, \mathbf{p}_{t,i_t,k_{i_t}}, \mathbf{p}_{t,i_t,0}\}, i_t = 1, 2, \dots, N_t$ is selected as the flight path of the i_t^{th} tanker, where $N_t \in \mathbb{N}$ is the number of tankers, $k_{i_t} \in \mathbb{N}$ is the number of refueling missions allocated to the i_t^{th} tanker, and $\mathbf{p}_{t,i_t,0} \in \mathbb{R}^2$ is the location coordinates of the takeoff and landing airport of the i_t^{th} tanker.

16.2.4 Fuel consumption calculation

The goal of refueling scheduling is to minimize the total fuel consumption of receivers and tankers under the premise that all aircraft are safe. The calculation methods of the fuel consumption of each receiver and tanker are given in this section. Since the missions and the flight paths of receivers and tankers in the problem are different, the fuel consumption mass of the two objects needs to be modeled separately for calculation.

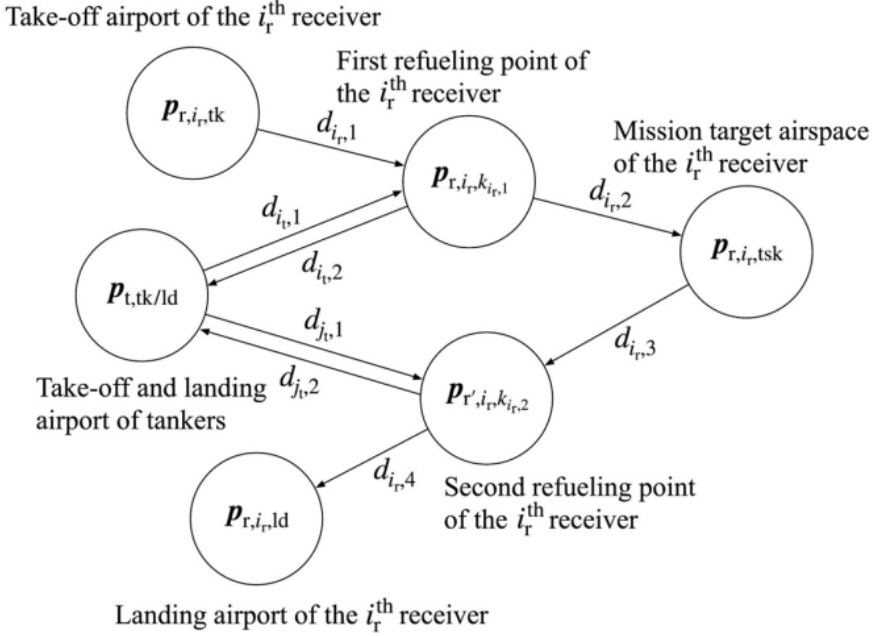


Figure 16.3: Aerial refueling point scheduling with a single receiver.

16.2.4.1 Receiver fuel consumption calculation

Fig. 16.3 depicts the flight path of a single receiver and two tankers in the aerial refueling scheduling problem. In Fig. 16.3, $i_r \in \{1, 2, \dots, N_r\}$ represents the serial number of the receiver, and N_r is the total number of receivers; $\mathbf{p}_{r,i_r,tk}, \mathbf{p}_{r,i_r,ld} \in \mathbb{R}^2$ represent the coordinates of takeoff and landing airport of the i_r^{th} receiver, respectively; $\mathbf{p}_{r,i_r,tsk} \in \mathbb{R}^2$ represents the coordinate of the target point of the i_r^{th} receiver; $\mathbf{p}_{t,tk/ld} \in \mathbb{R}^2$ represents the takeoff and landing airport of tankers; $\mathbf{p}_{r,i_r,k_{i_r},1}, \mathbf{p}_{r,i_r,k_{i_r},2} \in \mathbb{R}^2$ represent the coordinates of the first and second aerial refueling rendezvous points of the i_r^{th} receiver, respectively, where the number $k_{i_r,1} \in \{1, 2, \dots, N_{i_r}\}$ is the waypoint serial number of the first aerial refueling airspace on the departure path of the i_r^{th} receiver, and $k_{i_r,2} \in \{1, 2, \dots, N'_{i_r}\}$ is the waypoint serial number of the second aerial refueling airspace on the returning path of the i_r^{th} receiver.

In Fig. 16.3, $d_{i_r,1}, d_{j_r,1} \in \mathbb{R}$ represent the flight distances of tankers from the takeoff and landing airport $\mathbf{p}_{t,tk/ld}$ to the first and second refueling points of the receiver, respectively, and $d_{i_r,2}, d_{j_r,2} \in \mathbb{R}$ represent the flight distances of tankers from the first and second refueling points of the i_r^{th} receiver to the airport $\mathbf{p}_{t,tk/ld}$, respectively. The overall flight history of the i_r^{th} receiver includes five nodes and four flight paths. The lengths of the four paths of the i_r^{th} receiver are denoted by $d_{i_r,1}, d_{i_r,2}, d_{i_r,3}, d_{i_r,4} \in \mathbb{R}$, respectively. The length $d_{i_r,1}$ is the path length of the receiver from the takeoff airport to the first aerial refueling point, $d_{i_r,2}$ is the path length of the receiver from the first refueling rendezvous point to the target point, $d_{i_r,3}$ is the path length of the receiver returning from the target point to the second aerial refueling rendezvous point, and $d_{i_r,4}$ is the path length of the receiver from the second aerial refueling rendezvous point to the landing airport. The total fuel consumption of the i_r^{th} receiver is the sum of takeoff and landing

fuel consumption, fuel consumption of four cruise sections, and fuel consumption of the first and second aerial refueling as follows:

$$F_{r,i_r} = F_{r,tk} + F_{r,d_{i_r,1}} + F_{r,d_{i_r,2}} + F_{r,i_r,tsk} + F_{r,d_{i_r,3}} + F_{r,d_{i_r,4}} + 2F_{r,rfl} + F_{r,ld} \quad (16.12)$$

Here,

- (1) $F_{r,tk}, F_{r,ld} \in \mathbb{R}$ are the average fuel consumption mass of a receiver during takeoff and landing, respectively.
- (2) $F_{r,d_{i_r,1}}, F_{r,d_{i_r,2}}, F_{r,d_{i_r,3}}, F_{r,d_{i_r,4}} \in \mathbb{R}$ correspond to the fuel consumption mass of four flight segments $d_{i_r,1}, d_{i_r,2}, d_{i_r,3}, d_{i_r,4}$ of the i_r^{th} receiver, respectively.
- (3) $F_{r,rfl} \in \mathbb{R}$ is the expected fuel consumption mass of the i_r^{th} receiver.
- (4) $F_{r,ld} \in \mathbb{R}$ is the fuel consumption mass of the receiver during one aerial refueling.

According to the waypoint serial numbers of refueling rendezvous airspaces corresponding to the i_r^{th} receiver's flight paths $k_{i_r,1}$ and $k_{i_r,2}$, the path length of each flight segment is calculated by summing the distances between the consecutive path points on the segment as follows:

$$\left\{ \begin{array}{l} d_{i_r,1} = \sum_{i=1}^{k_{i_r,1}-1} d(\mathbf{p}_{r,i_r,i}, \mathbf{p}_{r,i_r,i+1}) \\ d_{i_r,2} = \sum_{i=k_{i_r,1}}^{N_{i_r}-1} d(\mathbf{p}_{r,i_r,i}, \mathbf{p}_{r,i_r,i+1}) \\ d_{i_r,3} = \sum_{i=1}^{k_{i_r,2}-1} d(\mathbf{p}_{r',i_r,i}, \mathbf{p}_{r',i_r,i+1}) \\ d_{i_r,4} = \sum_{i=k_{i_r,2}}^{N'_{i_r}-1} d(\mathbf{p}_{r',i_r,i}, \mathbf{p}_{r',i_r,i+1}) \end{array} \right. \quad (16.13)$$

where $\mathbf{p}_{r,i_r,i}, \mathbf{p}_{r',i_r,i} \in \mathbb{R}^2$ represent the coordinates of the i^{th} waypoint coordinates on the departure and returning paths of the i_r^{th} receiver, respectively. Fig. 16.4 is the carried fuel amount trend changes diagram of the i_r^{th} receiver in the whole flight. As shown in Fig. 16.4, the fuel load mass of a receiver is between the minimum and maximum safe fuel load mass $F_{r,\min}, F_{r,\max} \in \mathbb{R}$ of the receiver. The aircraft fuel consumption mass rate is positively correlated with the aircraft's total weight. The flight distance of each receiver's flight segment is fixed, and its load mass remains the same on each flight segment. As a result, in each flight segment, the smaller the initial or remaining fuel load mass of the receiver is, the smaller its fuel consumption mass is. To ensure that the receiver is safe, the amount of fuel carried by the receiver should not be less than $F_{r,\min}$ during the flight. Thus, for a purely fuel-consuming phase, the receiver consumes the least fuel when the remaining fuel is equal to $F_{r,\min}$ at the end of the phase.

When the amount of the carried fuel mass for the receiver is equal to $F_{r,\min}$ when it lands and before refueling, according to Eq. 16.7, the minimum aerial refueling mass required at two aerial refueling points and fuel consumption for each path section are derived as follows:



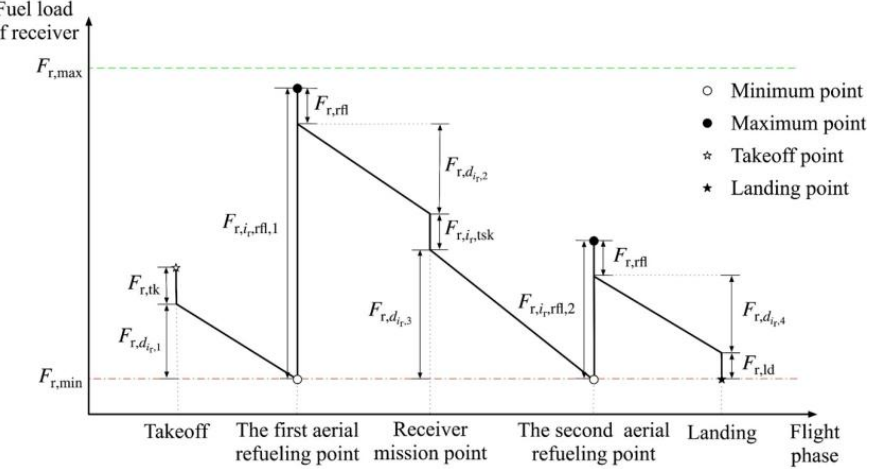


Figure 16.4: Carried fuel amount trend changes of the i_r^{th} receiver in whole flight phase.

$$\begin{cases} F_{r,d_{i_r,4}} = F'_r(0, F_{r,\min} + F_{r,\text{id}}, d_{i_r,4}) \\ F_{r,i_r,\text{rfl},2} = F_{r,\text{id}} + F_{r,d_{i_r,4}} + F_{r,\text{rfl}} \\ F_{r,d_{i_r,3}} = F'_r(0, F_{r,\min}, d_{i_r,3}) \\ F_{r,d_{i_r,2}} = F'_r(m_{r,i_r,1}, F_{r,\min} + F_{r,d_{i_r,3}} + F_{r,\text{tsk}}, d_{i_r,2}) \\ F_{r,i_r,\text{rfl},1} = F_{r,d_{i_r,2}} + F_{r,\text{tsk}} + F_{r,d_{i_r,3}} + F_{r,\text{rfl}} \\ F_{r,d_{i_r,1}} = F'_r(m_{r,i_r,1}, F_{r,\min}, d_{i_r,1}) \end{cases} \quad (16.14)$$

where $F_{r,i_r,\text{rfl},1}, F_{r,i_r,\text{rfl},2} \in \mathbb{R}$ represent the refueling mass of the i_r^{th} receiver for two aerial refueling operations, and $m_{r,i_r,1} \in \mathbb{R}$ represents the load mass of extinguishment retardant carried by the i_r^{th} receiver.

When the fuel load mass of a receiver is equal to $F_{r,\min}$ before the first aerial refueling operation, the takeoff fuel load mass of the i_r^{th} receiver is derived as follows:

$$F_{r,i_r,0} = F_{r,\min} + F_{r,d_{i_r,1}} + F_{r,\text{tk}} \quad (16.15)$$

In each node of the whole flight for the receiver, the task starting time $t_{r,i_r,\text{tsk}}$ is the only node with a known time, so the time of other nodes can be derived by $t_{r,i_r,\text{tsk}}$. The time spent on the path between the nodes is calculated by the path length and cruise speed of the receiver. The takeoff time of the i_r^{th} receiver is given as follows:

$$t_{r,i_r,0} = t_{r,i_r,\text{tsk}} - \frac{d_{i_r,1} + d_{i_r,2}}{V_r} - T_{\text{rfl}} \quad (16.16)$$

where $T_{\text{rfl}} \in \mathbb{R}$ is the time spent on aerial refueling for one flight.

The first aerial refueling rendezvous time of the i_r^{th} receiver is given as follows:

$$t_{r,i_r,\text{rfl},1} = t_{r,i_r,\text{tsk}} - \frac{d_{i_r,2}}{V_r} - T_{\text{rfl}} \quad (16.17)$$

The second aerial refueling rendezvous time of the receiver is given as follows:

$$t_{r,i_r,rfl,2} = t_{r,i_r,tsk} + T_{r,i_r,tsk} + \frac{d_{i_r,3}}{V_r} \quad (16.18)$$

where $T_{r,i_r,tsk} \in \mathbb{R}$ is the time spent on the i_r^{th} receiver to complete its task.

If the task zone is close to the airport, the aircraft can carry enough fuel before takeoff to complete the task, and it is unnecessary to be refueled again. For a receiver with a known route, the method of determining the number of in-flight refueling required is presented below.

Remark 1. If the receiver is not refueled during the entire flight, the fuel consumption from takeoff airport to landing airport should be less than its maximum amount of the carried fuel as follows:

$$F_{r,tk} + F_{r,dpt} + F_{r,i_r,tsk} + F_{r,rt} + F_{r,ld} < F_{r,max} \quad (16.19)$$

where $F_{r,dpt} \in \mathbb{R}$ is the fuel consumption without refueling on receiver's departure path that covers $d_{i_r,1}$ and $d_{i_r,2}$, and $F_{r,rt}$ is the fuel consumption without refueling on receiver's return path that covers $d_{i_r,3}$ and $d_{i_r,4}$ in Fig.16.3.

Remark 2. When the receiver needs to be refueled at least once, it is supposed that the only refueling is on its departure path, and the fuel consumption from the rendezvous point to the landing airport should be less than its maximum amount of the carried fuel. Similarly, if the only refueling is on its return path, the fuel consumption from the takeoff airport to the rendezvous point should be less than the maximum carried fuel amount. When the receiver meets one of the conditions, only one refueling is required, so the following inequations can be obtained:

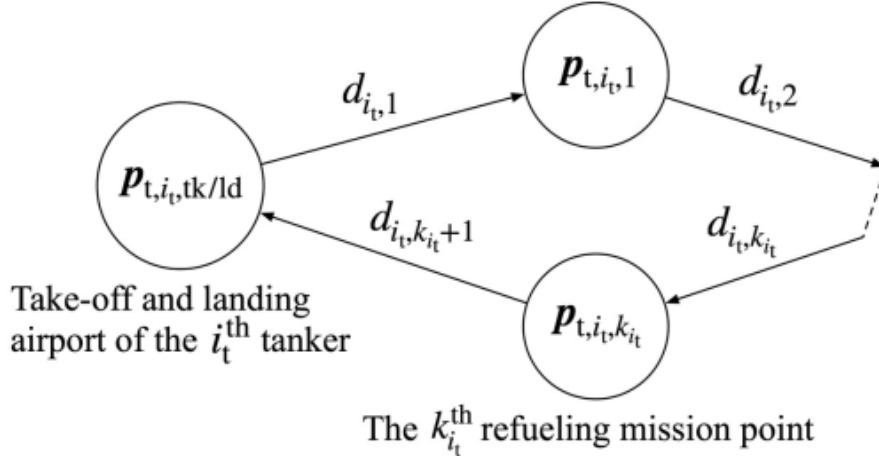
$$(F_{r,d_{i_r,2}} + F_{r,i_r,tsk} + F_{r,rt} + F_{r,ld} < F_{r,max}) \mid\mid (F_{r,tk} + F_{r,dpt} + F_{r,i_r,tsk} + F_{r,d_{i_r,3}} < F_{r,max}) \quad (16.20)$$

Remark 3. When the task area is far from the airport, the receiver does not satisfy Remark 2, and the receiver needs to be refueled twice. In keeping with the larger distance problem, proposed models are built in scenarios where the receivers need to be refueled twice. The constraint is that the fuel consumption of the receiver between refueling is less than the maximum carried fuel amount as follows:

$$F_{r,d_{i_r,2}} + F_{r,i_r,tsk} + F_{r,rt} + F_{r,d_{i_r,3}} < F_{r,max} \quad (16.21)$$

16.2.4.2 Tanker fuel consumption calculation

In the multi-receiver and multi-tanker aerial refueling problem, a tanker might be allocated with more than one refueling mission. Let the number of refueling missions allocated to the i_t^{th} tanker denoted as $k_{i_t} \in \mathbb{N}$, and its i^{th} refueling task be $T_{i_t,i}$. $\mathbf{p}_{t,i_t,i} \in \mathbb{R}^2$ corresponds to the rendezvous airspace coordinates of the i^{th} refueling task for the i_t^{th} tanker, $F_{t,i_t,i,rfl}$, $t_{t,i_t,i} \in \mathbb{R}$, $i = 1, 2, \dots, k_{i_t}$ are the refueling fuel mass and rendezvous time of the i^{th} refueling task of the i_t^{th}

Figure 16.5: Overall flight phase of the i_t^{th} tanker.

tanker, respectively. The task set of the i_t^{th} tanker ordered by time is $S_{i_t} = \{T_{i_t,1}, T_{i_t,2}, \dots, T_{i_t,k_{i_t}}\}$, $t_{t,i_t,1} < t_{t,i_t,2} < \dots < t_{t,i_t,k_{i_t}}$.

Since each refueling task should be allocated to one tanker, the total number of refueling tasks allocated for all the tankers is equal to the number of refueling required by receivers $2N_r$, ensuring that all refueling tasks are 100% covered. The following equality can be obtained:

$$\sum_{i_t=1}^{N_t} k_{i_t} = 2N_r \quad (16.22)$$

The mission of a single tanker is to complete all the aerial refueling tasks successively according to its task set S_{i_t} . The operational process for the i_t^{th} tanker is given as follows: the tanker takes off from the airport, traverses the assigned k_{i_t} aerial refueling task points in sequence, and finally lands at the airport. The overall flight path of the i_t^{th} tanker is shown in Fig. 16.5, where $i_t \in \{1, 2, \dots, N_t\}$ is the serial number of the tanker, N_t is the total number of tankers in the mission, $\mathbf{p}_{t,i_t,tk/ld} \in \mathbb{R}^2$ represents the coordinates of the takeoff and landing airport of the i_t^{th} tanker, respectively, $\mathbf{p}_{t,i_t,i} \in \mathbb{R}^2, i = 1, 2, \dots, k_{i_t}$ represents the rendezvous point coordinates of the i^{th} aerial refueling task of the i_t^{th} tanker, and $d_{i_t,i} \in \mathbb{R}, i = 1, 2, \dots, k_{i_t} + 1$ represents the i^{th} path length of the i_t^{th} tanker.

The overall flight of the i_t^{th} tanker consists of $(k_{i_t} + 2)$ nodes and $(k_{i_t} + 1)$ path segments. The first segment is the path from the takeoff airport $\mathbf{p}_{t,i_t,tk/ld}$ to the first refueling task point $\mathbf{p}_{t,i_t,1} \in \mathbb{R}^2$, the last segment is the $(k_{i_t} + 1)^{\text{th}}$ path from the $k_{i_t}^{\text{th}}$ refueling task point back $\mathbf{p}_{t,i_t,k_{i_t}} \in \mathbb{R}^2$ to the landing airport $\mathbf{p}_{t,i_t,tk/ld}$, and the rest are middle segments between each two successive aerial refueling tasks. The overall fuel consumption of the i_t^{th} tanker is the sum of the fuel consumption on $(k_{i_t} + 1)$ cruising path segments, fuel consumption for takeoff and landing, motions of aerial refueling operation, hovering and waiting, and fuel supply for refueling task at each refueling task node as follows:

$$F_{t,i_t} = F_{t,tk} + \sum_{i=1}^{k_{i_t}+1} F_{t,d_{i_t,i}} + k_{i_t} F_{t,rfl} + \sum_{i=1}^{k_{i_t}} F_{t,i_t,i,wt} + \sum_{i=1}^{k_{i_t}} F_{t,i_t,i,rfl} + F_{t,ld} \quad (16.23)$$

Here,

- (1) $F_{t,tk}, F_{t,ld} \in \mathbb{R}$ are the average fuel consumption mass during the takeoff and landing process of a tanker, respectively.
- (2) $F_{t,d_{i_t,i}} \in \mathbb{R}$ is the fuel consumption mass for the i^{th} flight path of the i_t^{th} tanker.
- (3) $F_{t,rfl} \in \mathbb{R}$ is the fuel consumption mass of a tanker in an aerial refueling.
- (4) $F_{t,i_t,i,wt}, F_{t,i_t,i,rfl} \in \mathbb{R}$ are the hovering and waiting fuel consumption mass, and fuel supply mass for the i^{th} refueling task of the i_t^{th} tanker, respectively.

The path length of each section is calculated as the great circle path distance between its start and end point as follows:

$$d_{i_t,i} = \begin{cases} d(\mathbf{p}_{t,i_t,tk/ld}, \mathbf{p}_{t,i_t,1}) & i = 1 \\ d(\mathbf{p}_{t,i_t,i-1}, \mathbf{p}_{t,i_t,i}) & i = 2, 3, \dots, k_{i_t} \\ d(\mathbf{p}_{t,i_t,k_{i_t}}, \mathbf{p}_{t,i_t,tk/ld}) & i = k_{i_t} + 1 \end{cases} \quad (16.24)$$

Since only fuel consumption processes exist in the flight of the tanker, the carried fuel mass of a tanker is continuously decreased, and the only minimal carried fuel mass is the remaining fuel mass when the tanker lands. Thus, similar to the analysis of the receiver, if the remaining carried fuel mass when the tanker lands is equal to the minimum safe load fuel mass of the tanker $F_{t,min}$, its overall fuel consumption mass during the flight is minimum.

Taking the landing carried fuel mass of the tanker equal to $F_{t,min}$, the corresponding fuel consumption mass of each flight segment can be derived from the fuel consumption function of tanker as follows:

$$F_{t,d_{i_t,i}} = \begin{cases} F'_t(F_{t,min} + F_{t,ld}, d_{i_t,i}) & i = k_{i_t} + 1 \\ F'_t\left(F_{t,min} + F_{t,ld} + \sum_{j=i+1}^{k_{i_t}+1} F_{t,d_{i_t,j}} + \sum_{j=i}^{k_{i_t}} F_{t,i_t,j,wt} + \sum_{j=i}^{k_{i_t}} F_{t,i_t,j,rfl} + (k_{i_t} + 1 - i) F_{t,rfl}, d_{i_t,i}\right) & i = 1, 2, \dots, k_{i_t} \end{cases} \quad (16.25)$$

Between two refueling tasks, the tanker needs to reach the rendezvous point of the next task at cruising speed, and then it hovers and waits for the arrival of the receiver for the subsequent refueling task. The time difference between the time of the i^{th} task $t_{t,i_t,i} \in \mathbb{R}$ and the time of the $(i-1)^{\text{th}}$ task $t_{t,i_t,i-1} \in \mathbb{R}$ of the i_t^{th} tanker is given as follows:

$$\Delta T_{t,i_t,i} = t_{t,i_t,i} - t_{t,i_t,i-1}, i = 2, 3, \dots, k_{i_t} \quad (16.26)$$

The time needed for hovering and waiting between the i^{th} mission and the $(i-1)^{\text{th}}$ mission of the i_t^{th} tanker is given as follows:



$$T_{t,i_t,i,wt} = \Delta T_{t,i_t,i} - T_{rlf} - \frac{d_{i_t,i}}{V_t}, i = 2, 3, \dots, k_{i_t} \quad (16.27)$$

During the hovering and waiting process, the tanker must also consume a certain amount of fuel. The fuel mass consumed by the hovering and waiting process between the i^{th} mission and the $(i-1)^{\text{th}}$ mission of the i_t^{th} tanker is defined as follows:

$$F_{t,i_t,i,wt} = T_{t,i_t,i,wt} C_{t,wt}, i = 2, 3, \dots, k_{i_t} \quad (16.28)$$

where $C_{t,wt} \in \mathbb{R}$ is the fuel consumption mass per unit time by the hovering and waiting process of a tanker. Then, the takeoff fuel load mass of the i_t^{th} tanker is calculated as follows:

$$F_{t,i_t,0} = \sum_{i=1}^{k_{i_t}+1} F_{t,d_{i_t,i}} + F_{t,tk} + F_{t,ld} + k_{i_t} F_{t,rfl} + \sum_{i=1}^{k_{i_t}} F_{t,k_{i_t},i,wt} + \sum_{i=1}^{k_{i_t}} F_{t,i_t,i,rfl} + F_{t,min} \quad (16.29)$$

The takeoff time calculation equation is derived from the first aerial refueling task of the i_t^{th} tanker as follows:

$$t_{t,i_t,0} = t_{t,i_t,1} - \frac{d_{i_t,1}}{V_t} \quad (16.30)$$

where $t_{t,i_t,1} \in \mathbb{R}$ denotes the rendezvous time of the first task of the i_t^{th} tanker.

16.3 Path planning

16.3.1 Scheduling flow

The objective in the aerial refueling scheduling of multi-receiver and multi-tanker consists of four parts: the flight path of each receiver, the rendezvous point and refueling mass of each aerial refueling mission, the refueling task allocation, and the flight path of each tanker. Due to the high computational complexity of refueling mission scheduling and path planning simultaneously, the method used in this paper is to separate the path scheduling of receivers from the scheduling objectives, and form a sequential structure to simplify the computational complexity. The detailed steps of aerial refueling scheduling are shown as follows and the comprehensive flow diagram is listed in Table 2.

- (1) Planning a path for each receiver considering aerial refueling cost.
- (2) Scheduling refueling rendezvous points and allocating tankers based on the receiver paths.
- (3) Obtaining the whole scheduling information for each receiver and tanker.

The primary purpose of the scheduling problem is to minimize the total fuel consumption of receivers and tankers by appropriate optimization algorithms. Two algorithms based on the established models are introduced in this paper: an integrated method and a decomposed method.



Table 16.2: Comprehensive flow of aerial refueling scheduling when the path of receiver is unknown.

Step	Flow diagram	Content
Operational information acquisition	<p>Airport 1: Icons 1, 2, 3, 4 Airport 2: Icons 3, 2, 4, 1</p>	<p>Input scheduling mission information, including:</p> <ul style="list-style-type: none"> (A) The mission information of receivers; (B) The threat information of airspace; (C) The technical specifications of receivers and tankers.
The path planning the receivers		<p>Obtain the path information by path planning algorithm introduced with aerial refueling cost for all the N_r receivers.</p>
Aerial refueling rendezvous point scheduling and the task allocation of tankers		<p>Perform path-based aerial refueling rendezvous scheduling, and allocate the refueling missions to the tanker at each point. In Section 4, an integrated method and a decomposed method are designed for optimization.</p>
Form a coordinate command result		<p>Obtain the mission information of each receiver and tanker based on the scheduling results, including takeoff time, takeoff fuel load, and aerial refueling information.</p>

The subsequent sections will provide detailed descriptions of each algorithm.

In the following Section 16.3.2 , we mainly describe the algorithm used for path planning which generates the receiver's path before scheduling.

16.3.2 A* algorithm

There have been various algorithms studied and applied in path planning, ranging from the classic A* search algorithm to advanced techniques such as Particle Swarm Optimization (PSO), Ant Colony Optimization (ACO), and Genetic Algorithm (GA). Among these path optimization algorithms, A* search algorithm is simple and widely used in many fields. A* search algorithm is an effective direct search method for solving the shortest paths in static road networks, which extends the search range from the starting node and decides which nodes should be extended by using a pre-determined cost function.[352] A* algorithm calculates the cost of each possible node that can be extended at the present time, and then selects the one with the smallest cost to be added to the search space, and then it is used to generate more possible nodes to be extended until the target point is added to the search space. Compared with Dijkstra's algorithm, A* algorithm only finds the shortest path from a specified source to a specified goal, and not the shortest-path tree from a specified source to all possible goals. This is a necessary trade-off for using a specific-goal-directed heuristic. The key in A* search algorithm is that it uses an estimation function $H(x)$ to inspire the search, and its core cost function is designed in the following form:

$$F(x) = G(x) + H(x) \quad (16.31)$$

where $G(x) \in \mathbb{R}$ is the true cost from the origin to the current node x , $H(x) \in \mathbb{R}$ is the estimated cost from the current node x to the goal, and the optimal path is to choose the smallest $F(x)$ from the origin to the end. In this paper, A* algorithm is selected to generate the receiver's path.

Because the refueling rendezvous points are selected from receiver's waypoints, the optimality of solution is related to waypoint accuracy. For this question, the required precision or waypoint number of the path can be simplified by interpolation. Thus, after interpolation using A* algorithm, interpolation is selectively adopted to reprocess the generated path to improve waypoint accuracy according to optimality need.

16.4 Scheduling methods

16.4.1 Integrated method

16.4.1.1 Scheduling flow

The integrated method establishes the optimization problem as a nonlinear optimization model along with restrictions. Fig. 16.6 depicts the algorithm flowchart of the integrated method. GA is employed to solve the optimization problem by the integrated method. Specifically, GA



begins with an initialization. It generates a random population with n_c chromosomes and computes the fitness value of each chromosome. Then, the algorithm enters a program loop. As long as the number of iterations does not exceed the maximum, the crossover operation and mutation are applied. The old population is then replaced with the newly generated population. Finally, we testify whether the optimal solution is obtained. If not, we return to the beginning, and repeat the program loop. The program loop will stop until the final optimal solution is acquired.

In the integrated method, refueling rendezvous point scheduling and tanker task allocation are integrated into one process to model the multi-receiver and multi-tanker aerial refueling scheduling problem. The advantages of the integrated method to solve the problem are given as follows: first, all aerial refueling rendezvous points are guaranteed to be traversed to ensure the completion of the task; second, this method maps the task requirements to $4M$ variables perfectly without simplifying the solution space, and the obtained mathematical model is accurate.

In this section, an integrated method based on the path of the receiver is established by taking the complete target variables as decision variables for aerial refueling scheduling. The modeling design for integrated aerial refueling airspace scheduling and task allocation of tankers has the following advantages: first, it is unnecessary to reduce the scheduling space, which can ensure that the two refueling demands of each receiver can be finished; second, the mathematical model obtained is accurate. In theory, if the computing power is enough, the optimal solution to the scheduling problem can be obtained.

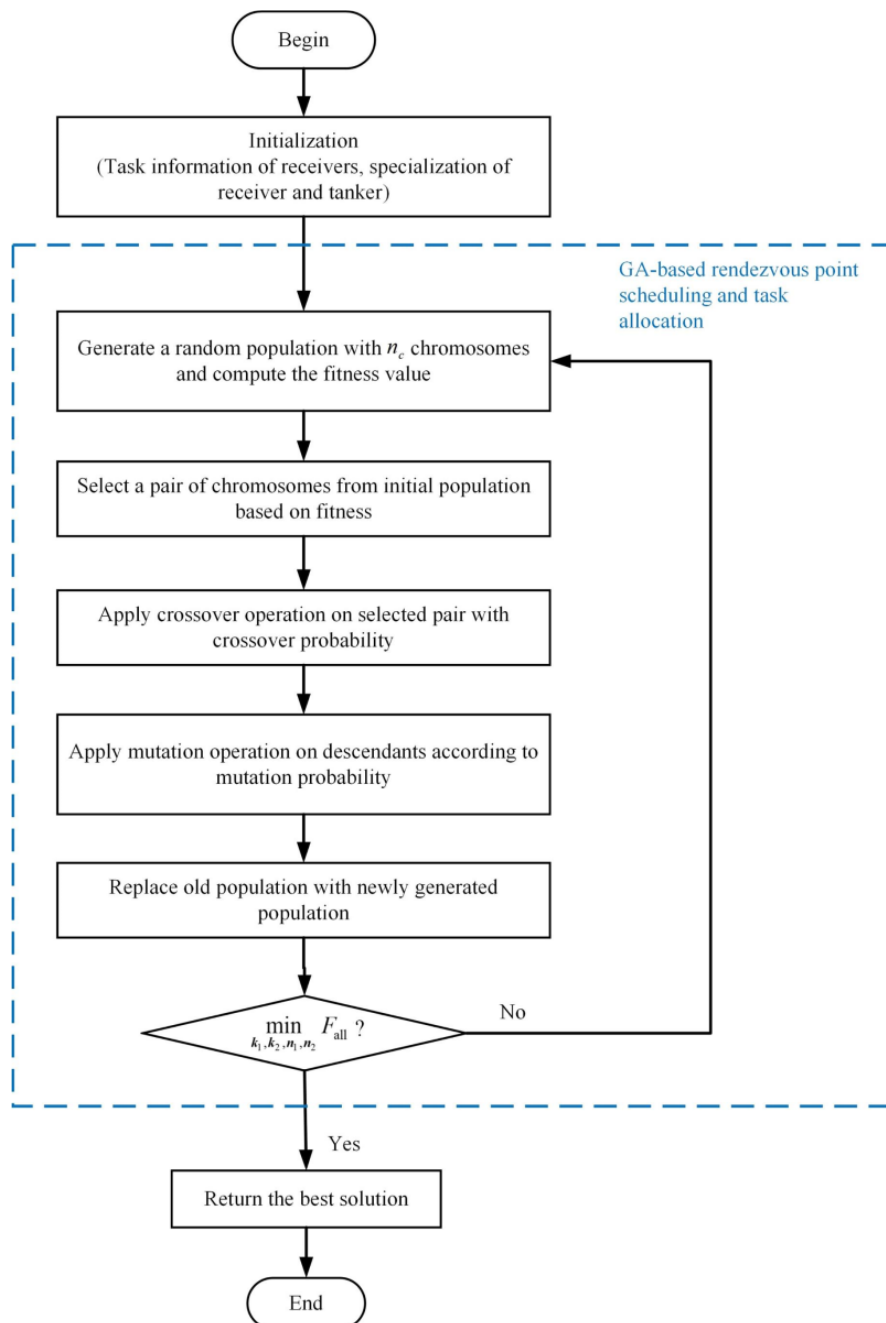
16.4.1.2 Optimization model

According to the long-range forest mission assumptions, since each receiver on the mission requires two aerial refueling, N_r receivers correspond to a total of $2N_r$ aerial refueling. For each refueling, the scheduling objective includes two parameters: the aerial refueling rendezvous point and the refueling tanker number. Thus, taking them as decision variables, the number of variables for this problem is $4N_r$, including $2N_r$ aerial refueling airspace coordinates and $2N_r$ refueling tanker numbers.

In this paper, the aerial refueling scheduling is based on the flight path, i.e., the aerial refueling point is set on the flight path of receivers. The path points on the flight path can be directly utilized as feasible points for aerial refueling rendezvous points to simplify the constraints. By utilizing the waypoint serial numbers on paths as the decision variables, the model built by this method is more concise, and the refueling points are directly guaranteed to be on the flight paths of receivers.

The decision variables for the multi-receiver and multi-tanker aerial refueling scheduling based on paths of receivers are categorized into four groups, which are represented by four vectors as follows:



**Figure 16.6:** Flowchart of integrated scheduling method.

$$\mathbf{k}_1 = \left[k_{1,1}, k_{2,1}, \dots, k_{i_r,1}, \dots, k_{N_r,1} \right], \mathbf{k}_2 = \left[k_{1,2}, k_{2,2}, \dots, k_{i_r,2}, \dots, k_{N_r,2} \right]$$

$$\mathbf{n}_1 = \left[n_{1,1}, n_{2,1}, \dots, n_{i_r,1}, \dots, n_{N_r,1} \right], \mathbf{n}_2 = \left[n_{1,2}, n_{2,2}, \dots, n_{i_r,2}, \dots, n_{N_r,2} \right]$$

Here,

(1) Vectors $\mathbf{k}_1, \mathbf{k}_2$ are the vectors of waypoint serial numbers of the first aerial refueling rendezvous points on the departure path, and the second aerial refueling rendezvous points on the returning path of the N_r receivers, respectively.

(2) Vectors $\mathbf{n}_1, \mathbf{n}_2$ are the vectors of the tankers' serial numbers assigned to the first and second refueling missions of overall N_r receivers, respectively.

Aerial refueling scheduling aims to minimize the total fuel consumption of receivers and tankers. The total fuel consumption in the objective function consists of the fuel consumption mass of N_r receivers and N_t tankers. The ultimate optimization model for the aerial refueling scheduling of multi-receiver and multi-tanker, including the refueling rendezvous point scheduling, along with the task allocation of tankers based on the receiver's path, can be expressed as follows:

$$\min_{\mathbf{k}_1, \mathbf{k}_2, \mathbf{n}_1, \mathbf{n}_2} F_{\text{all}} = \min_{\mathbf{k}_1, \mathbf{k}_2, \mathbf{n}_1, \mathbf{n}_2} \left(\sum_{i_r=1}^{N_r} F_{r,i_r} + \sum_{i_t=1}^{N_t} F_{t,i_t} \right) \quad (16.32)$$

subject to

$$\mathbf{p}_{r,i_r,k_{i_r,1}}, \mathbf{p}_{r',i_r,k_{i_r,2}} \in \mathbf{P}_s \quad (16.33a)$$

$$0 < T_{t,i_t,w} < T_{w,max} \quad (16.33b)$$

$$F_{r,i_r,0} \leq F_{r,max} \quad (16.33c)$$

$$F_{r,i_r,0} - F_{r,tk} - F_{r,d_{i_r,1}} + F_{r,rfl,i_r,1} - F_{r,rfl} \leq F_{r,max} \quad (16.33d)$$

$$F_{r,i_r,0} - F_{r,tk} - \sum_{i=1}^3 F_{r,d_{i_r,i}} + F_{r,rfl,i_r,1} + F_{r,rfl,i_r,2} - F_{r,tsk} - 2F_{r,rfl} \leq F_{r,max} \quad (16.33e)$$

$$F_{t,i_t,0} \leq F_{t,max} \quad (16.33f)$$

where $F_{r,i_r}, F_{t,i_t} \in \mathbb{R}$ denote the fuel consumption mass of the i_r^{th} receiver and the i_t^{th} tanker, respectively.

Based on the requirements of the mission, the aerial refueling scheduling is subject to a range of spatial and temporal constraints. Specifically, spatial constraints include airport distribution, receiver path, mission area, threat areas, refueling paths, etc.; temporal constraints include aerial refueling time interval, task time of receivers, refueling time, etc. Furthermore, aerial refueling scheduling is also limited by indirect factors such as aircraft specifications and alternate landing requirements.

For the multi-receiver and multi-tanker aerial refueling scheduling problem, the constraints



are made from the perspective of time, space, and technical limitations. The details of the constraints in Eq. 16.33 are given as follows: (1) Eq. 16.33a is a spatial constraint on tankers and receivers, which requires the aerial refueling rendezvous point to be within the safety area, where \mathbf{P}_s denotes the waypoints collection in the safety airspace for tankers.

(2) Eq. 16.33b is a temporal constraint on the tanker, where $T_{wt,max} \in \mathbb{R}$ denotes the maximum hovering and waiting time of tankers. This constraint guarantees that the tanker can reach the next refueling mission point at cruising speed without the receiver's waiting. In addition, if the tanker needs to wait, the waiting time does not exceed $T_{wt,max}$.

(3) Eq. 16.33c to Eq. 16.33e is the fuel mass constraint for the receiver, which requires that the fuel amount carried by the receiver after takeoff, the first or second aerial refueling does not exceed its maximum fuel amount $F_{r,max}$.

(4) Eq. 16.33f is the fuel mass constraint for the tanker, which requires that the fuel mass carried by the tanker after takeoff does not exceed its maximum value $F_{t,max}$.

16.4.2 Decomposed method

16.4.2.1 Scheduling flow

In the above section, the integrated method can basically meet the task demands for the aerial refueling scheduling task of multi-receiver and multi-tanker in the mission. However, when many refueling rendezvous points are covered, the computational complexity could be relatively high due to the simultaneous optimization of the aerial refueling rendezvous point scheduling and the task scheduling of tankers. Moreover, the optimization result will become less accurate because the optimization algorithm often falls into a local optimum instead of a global optimum. The enormous search space and strict constraints make the optimal result for reducing fuel consumption cannot be obtained. Thus, the integrated method can be improved in terms of computing complexity and optimizing accuracy. For such a purpose, an alternative method is proposed with better computational efficiency in the following section.

The integrated method becomes an inspiration for the following decomposed strategy, and then, a stepwise decoupled model, separating the refueling rendezvous airspace scheduling from the task allocation of tankers, is developed in this section. The basic idea is to, first, obtain the aerial refueling points with the least fuel consumption based on the path for each receiver, to obtain the aerial refueling mission information of all $2N_r$ aerial refueling, and then perform the task allocation optimization to allocate the aerial refueling missions to the tankers. In the task allocation process, the nested structure is adopted by splitting the refueling task allocation into two nested optimization loops. Specifically, the outer loop is mainly responsible for the grouping and clustering of refueling tasks, while the inner loop completes the scheduling for the allocation of tankers based on the optimization results obtained from the outer loop. Finally, the optimal result of refueling rendezvous point scheduling and task allocation is obtained.



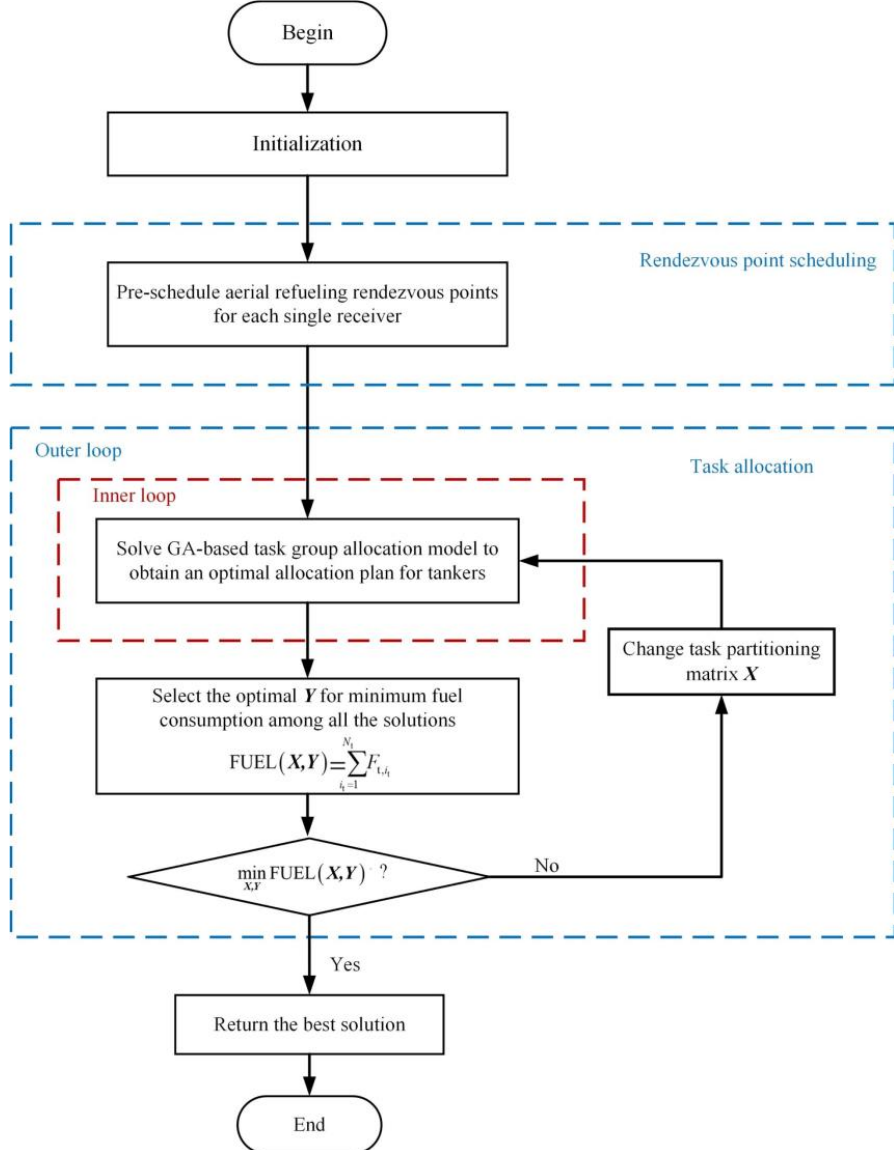


Figure 16.7: Flowchart of decomposed scheduling method.

Fig. 16.7 depicts the flowchart of the decomposed method. First, we carry out refueling rendezvous point scheduling for each receiver according to the fuel consumption model of a single receiver. The obtained feasible rendezvous points would be optimal for the fuel consumption of receivers. On this basis, an inner-and-outer loop structure is designed for the process of refueling task allocation. The external optimization loop is primarily to optimize the division of task groups, while the internal optimization loop focuses on the task group allocation for available tankers based on the outer grouping. After the nested optimization process is finished, the optimum task allocation result is obtained. By this method, we can efficiently accelerate the convergence speed and maintain high optimization accuracy.

16.4.2.2 Rendezvous point scheduling for a single receiver

As shown in Fig. 16.3, the fuel consumption in the aerial refueling scheduling to support two times of aerial refueling for a single receiver is the sum of fuel consumption for a single receiver and multiple tankers. In this case, there are usually multiple tankers available for deployment and located at different bases. Different from fuel consumption calculation in the scenario of multiple receivers, the average round flight distance of all the N_t tankers to the aerial refueling rendezvous point is selected as the flight distance of tankers in this model, and four flight path distances $d_{i_t,i}, d_{j_t,i}, i = 1, 2$ of tankers are calculated as follows:

$$\begin{cases} d_{i_t,i} = \frac{1}{N_t} \sum_{i=1}^{N_t} d(\mathbf{p}_{t,tk/ld}, \mathbf{p}_{r,i_r,k_{i_r,1}}) & i = 1, 2 \\ d_{j_t,i} = \frac{1}{N_t} \sum_{i=1}^{N_t} d(\mathbf{p}_{t,tk/ld}, \mathbf{p}_{r',i_r,k_{i_r,2}}) & i = 1, 2 \end{cases} \quad (16.34)$$

In the path-based aerial refueling scheduling model, rendezvous time $(t_{r,i_r,rfl,1}, t_{r,i_r,rfl,2})$, initial takeoff fuel load and takeoff time $(F_{r,i_r,0}, t_{r,i_r,0})$ of the receiver can be obtained.

The landing remaining fuel amount of a tanker is restricted to the minimum safe remaining fuel amount $F_{t,min}$. The fuel consumption of four flight paths of two tankers is calculated according to Eq. 16.8 in Section 16.2.3.1 as follows:

$$\begin{cases} F_{t,d_{i_t,1}} = F'_t(F_{t,min} + F_{t,ld}, d_{i_t,1}) \\ F_{t,d_{i_t,2}} = F'_t(F_{t,min} + F_{t,ld} + F_{t,d_{i_t,1}} + F_{r,i_r,rfl,1} + F_{t,rfl}, d_{i_t,2}) \\ F_{t,d_{j_t,1}} = F'_t(F_{t,min} + F_{t,ld}, d_{j_t,1}) \\ F_{t,d_{j_t,2}} = F'_t(F_{t,min} + F_{t,ld} + F_{t,d_{j_t,1}} + F_{r,i_r,rfl,2} + F_{t,rfl}, d_{j_t,2}) \end{cases} \quad (16.35)$$

The scheduling objective is to minimize the fuel consumption sum of a single receiver and multiple tankers supporting its two aerial refueling operations. The decision variables of the aerial refueling scheduling model for a single receiver are only locations of two waypoints $k_{i_r,1}$ and $k_{i_r,2}$. Therefore, the objective function is an airspace position function of two aerial refueling operations as follows:

$$\min_{k_{i_r,1}, k_{i_r,2}} \left(\sum_{i_r=1}^4 F_{r,d_{i_r,i}} + \sum_{i_t=1}^4 F_{t,d_{i_t,i}} \right) \quad (16.36)$$

subject to

$$\mathbf{p}_{r,i_r,k_{i_r},1}, \mathbf{p}_{r',i_r,k_{i_r},1} \in \mathbf{P}_s \quad (16.37a)$$

$$F_{r,i_r,0} \leq F_{r,\max} \quad (16.37b)$$

$$F_{r,i_r,0} - F_{r,\text{tk}} - F_{r,d_{i_r},1} + F_{r,\text{rfl},i_r,1} - F_{r,\text{rfl}} \leq F_{r,\max} \quad (16.37c)$$

$$F_{r,i_r,0} - F_{r,\text{tk}} - \sum_{i=1}^3 F_{r,d_{i_r},i} + F_{r,\text{rfl},i_r,1} + F_{r,\text{rfl},i_r,2} - F_{r,\text{tsk}} - 2F_{r,\text{rfl}} \leq F_{r,\max} \quad (16.37d)$$

In the scheduling problem of rendezvous point scheduling for a single receiver, the constraints are made from the perspective of time, space, and technical limitations. The details of the constraints in Eq. 16.37 are given as follows:

- (1) Eq. 16.37a is a spatial constraint that requires the aerial refueling point to be within the aerial refueling safety region.
- (2) Eq. 16.37b to Eq. 16.37d are the fuel amount constraints that restrict the fuel amount carried by the receiver not to exceed its maximum fuel amount $F_{r,\max}$.

Since the tanker only completes one aerial refueling mission in this model, the fuel tank capacity of an available tanker is much larger than the fuel amount required to complete one aerial refueling, so no relevant restriction for the tanker is proposed.

16.4.2.3 Mission scheduling method for multiple tankers

In the second step of the decomposed method, a mission scheduling method is proposed in a nested structure. In the nested structure, the outer loop optimization organizes refueling tasks into groups, and the inner loop optimization focuses on the task allocation of each group based on the outer loop grouping. The outer-loop employs a nonlinear optimization model subject to linear constraints, while the inner-loop adopts a linear model subject to linear constraints.

- (1) The outer loop of task allocation: Task grouping

The outer loop of task allocation aims to optimize the task grouping. After obtaining the $2N_r$ aerial refueling tasks from the scheduling of the single aircraft, the outer loop of the following nested task allocation method categorizes all the tasks into several task groups. Define V as all the $2N_r$ individual tasks set to be assigned, and A as all the internode arcs set. Then, define the grouping model of the outer loop on a directed graph $G = (V, A)$. The optimization variable matrix $\mathbf{X} = [x_{ij}] \in \mathbb{R}^{2N_r \times 2N_r}$ of variable is derived as follows:

$$x_{ij} = \begin{cases} 1, & \text{The tanker passes through the arc } (i, j) \\ 0, & \text{The tanker does not pass through the arc } (i, j) \end{cases} \quad (16.38)$$

where $x_{ij} = 1$ denotes that the i^{th} and j^{th} aerial refueling missions are collected into a group, and the tanker completes the i^{th} mission and then flies to the j^{th} mission point to achieve the task in sequence. The de-manded hovering and waiting time between the i^{th} and j^{th} refueling mission



point is given as follows:

$$T_{\text{wt},ij} = \Delta T_{ij} - T_{\text{rf}} - \frac{d_{ij}}{V_t} \quad (16.39)$$

where ΔT_{ij} and d_{ij} are the time difference and spatial distance between two mission nodes.

When performing grouping tasks, the i^{th} refueling task needs to be restricted before performing the j^{th} refueling task. In addition, to ensure that the tanker can reach the next mission point at cruising speed, its hovering and waiting time should not exceed the maximum hovering and waiting time $T_{\text{wt},ij}$. Therefore, the value range of each decision variable in the matrix \mathbf{X} is constrained by the hovering and waiting time of the tanker as follows:

$$x_{ij} = \begin{cases} 0 \text{ or } 1, & 0 \leq T_{\text{wt},ij} \leq T_{\text{wt,max}} \\ 0, & T_{\text{wt},ij} < 0 \text{ or } T_{\text{wt},ij} \geq T_{\text{wt,max}} \end{cases} \quad (16.40)$$

The task grouping results can be obtained by traversing the consecutive line segments on the directed graph \mathbf{G} , and the number of task groups is denoted as $K \in \mathbb{N}$.

(2) The inner loop of task allocation: Task group allocation

The inner loop of the task allocation is served as the task group allocation, i.e., the utilization of the available K tankers to complete the obtained K groups of aerial refueling tasks. In the inner loop, define the matrix $\mathbf{Y} = [y_{i_t,k}] \in \mathbb{R}^{N_t \times K}$ as the optimization variable matrix to represent the allocation of task groups. Hence, each decision variable in the matrix \mathbf{Y} is constrained as follows:

$$y_{i_t,k} = \begin{cases} 1, & \text{the } i_t^{\text{th}} \text{ tanker completes the } k^{\text{th}} \text{ group mission} \\ 0, & \text{the } i_t^{\text{th}} \text{ tanker does not complete the } k^{\text{th}} \text{ group mission} \end{cases} \quad (16.41)$$

The optimization objective of the problem is to minimize the total amount of fuel consumption of the N_t tankers as follows:

$$\min_{\mathbf{X}, \mathbf{Y}} \sum_{i_t=1}^{N_t} F_{t,i_t} \quad (16.42)$$

subject to

$$F_{t,i_t,0} \leq F_{t,\max} \quad i_t = 1, 2, \dots, N_t \quad (16.43a)$$

$$\sum_{i=1}^{2N_r} x_{ij} \leq 1 \quad i = 1, 2, \dots, 2N_r \quad (16.43b)$$

$$\sum_{j=1}^{2N_r} x_{ij} \leq 1 \quad j = 1, 2, \dots, 2N_r \quad (16.43c)$$

$$\sum_{k=1}^K y_{i_t,k} \leq 1 \quad i_t = 1, 2, \dots, N_t \quad (16.43d)$$

$$\sum_{i_t=1}^{N_t} y_{i_t,k} = 1 \quad k = 1, 2, \dots, K \quad (16.43e)$$

Both nonlinear and linear constraints on the optimization variables in this optimization model are required in Eq. 16.43. The details of the constraints are given as follows:

- (1) Eq. 16.43a ensures that the takeoff fuel load of each tanker is not greater than its maximum fuel load.
- (2) Eqs. 16.43b and 16.43c ensure that each task group has at most one predecessor task and one successor task.
- (3) Eq. 16.43d ensures that each tanker is assigned to at most one group of tasks.
- (4) Eq. 16.43e ensures that all the tasks are traversed and each group of tasks is assigned to one tanker.

The outer loop focuses on optimizing the variable matrix \mathbf{X} . For task allocation problems, the Hungarian algorithm is a widely adopted combinatorial optimization technique known for its efficiency, solving such problems in polynomial time.[353] The inner loop is solved by the Hungarian algorithm to obtain the maximum matching \mathbf{y} based on the outer loop grouping \mathbf{X} . Finally, the optimization results of \mathbf{X} and \mathbf{Y} are transformed into specific scheduling parameters \mathbf{n}_1 and \mathbf{n}_2 . This process yields the desired aerial refueling scheduling results.

16.5 Simulation results

16.5.1 Simulation setting

According to the proposed aerial refueling scheduling problem description, simulations are conducted for verification optimization algorithms. The simulation parameters are selected referring to the actual technical parameters of receivers and tankers. The main simulation parameters used in all subsequent experiments are set according to the requirements as follows:

- (1) The interested simulation area is $5000 \text{ km} \times 2500 \text{ km}$ approximately.
- (2) The cruise speed of a receiver and a tanker are 900 km/h and 800 km/h , respectively.



Table 16.3: Fuel consumption model parameters of tanker and receiver ^{a,b}.

Type	Receiver	Tanker
Maximum fuel load (kg)	15921	118100
Maximum range (km)	5745	4000
Bare weight (kg)	12973	134717
Jet fuel coefficient	7174	6354

Table 16.4: Mission parameters for aerial refueling scheduling simulation with $N^r = 5$.

Receiver number	Takeoff airport coordinate	Landing airport coordinate	task area coordinate	Task start time (h)	Task fuel consumption (kg)	Retardant load (kg)	Task time consumption
1	(3.2,7.3)	(3.2,3.3)	(28.5,11.1)	0	1500	2000	0.2
2	(3.2,3.3)	(3.2,7.3)	(25.5,4.1)	0.5	1500	2000	0.2
3	(3.2,3.3)	(1.2,13.3)	(22.5,12.1)	1.0	1500	2000	0.2
4	(3.2,3.3)	(1.2,13.3)	(27.5,8.1)	0.7	1500	2000	0.2
5	(3.2,7.3)	(3.2,13.3)	(20.5,2.1)	0.2	1500	2000	0.2

(3) The maximum fuel capacity of a receiver and a tanker are 11000 L and 118100 L, respectively.

(4) The safe remaining fuel amount for a receiver and a tanker are 300 L and 1000 L, respectively.

The fuel coefficients of the receiver and tanker are listed in Table 16.3, while the mission parameters for five receivers are listed in Table 16.4. There are three tanker airports whose coordinates and available tanker number are (1.0, 14.2) for 3 tankers, (1.0, 8.2) for 3 tankers and (1.0, 2.2) for 4 tankers. The maximum hovering and waiting time of a tanker is selected to be 1.0 hour.

GA ToolBox based on MATLAB is employed to solve the formulated nonlinear optimization problem. Some of the selected parameters and options are given as follows: PopulationSize = 200, CrossoverFraction = 0.8, MigrationFraction = 0.2, Max Generations = 100× numberOfVariables. MutationFunc randomly generates directions that are adaptive with respect to the last successful or unsuccessful generation.

16.5.2 Comparative method

As our method is proposed for the first time, it lacks the existing corresponding advanced solutions as a comparison. In this section, a fixed strategy is employed to compare the two proposed methods in the same scenario to verify the feasibility and efficiency of the proposed methods. In Section 16.5.3, experiments by the integrated method and the decomposed method were also carried out to verify the efficacies and deficiencies of the two methods qualitatively and quantitatively.

The parameters of the comparative experiment are based on the mission information in Section 16.5.3, and the additional settings of receiver number $N_r = 5$, available tanker number $N_t = 10$ and the number of receiver's path points $N_{i_r} = N'_{i_r} = 200$. Fig. 16.8 depicts the

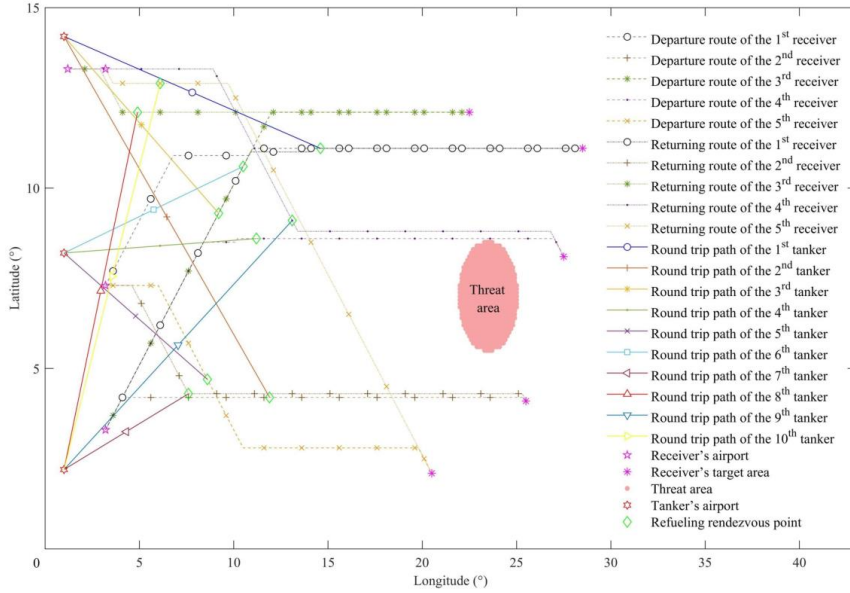


Figure 16.8: Optimization results with a comparative method.

Table 16.5: Mission scheduling results of fixed scheduling.

Receiver number	First aerial refueling			Second aerial refueling		
	Tanker number	Refueling volume (kg)	Refueling airspace coordinate(°)	Tanker number	Refueling volume (kg)	Refueling airspace coordinate(°)
1	1	11692	(14.6, 11.1)	6	3882	(10.5, 10.6)
2	2	11698	(11.9, 4.2)	7	2755	(7.6, 4.3)
3	3	11692	(9.2, 9.3)	8	2407	(4.9, 12.1)
4	4	11696	(11.2, 8.6)	9	4676	(13.1, 9.1)
5	5	11699	(8.6, 4.7)	10	2455	(6.1, 12.9)
Total fuel consumption (kg)		852608				

simulation result based on the comparative fixed strategy scheduling method, and more detailed information is shown in Table 16.5. In Fig. 16.8, the flight paths of receivers are drawn as marked dotted lines between the takeoff and landing airport and the task point, the scheduling aerial refueling rendezvous points are represented by green rhombus, and the execution path of each tanker is drawn as marked solid lines. The method can get a feasible plan for the mission, but its fuel consumption is high. Compared with the corresponding results of the integrated and decomposed scheduling methods in Fig. 16.9 and Fig. 16.10, the two proposed methods mainly improve the tanker task allocation strategy for better scheduling results.

16.5.3 Results analysis

16.5.3.1 Integrated method

The flight path diagram of the aerial refueling scheduling result for the integrated method is shown in Fig. 16.9. In Fig. 16.9, 6 tanker sorties are used to complete 10 aerial refueling missions, and the tanker on the 2nd to 5th sorties are assigned two aerial refueling missions. Unlike other tanker sorties, they do not return to the airport immediately after completing the

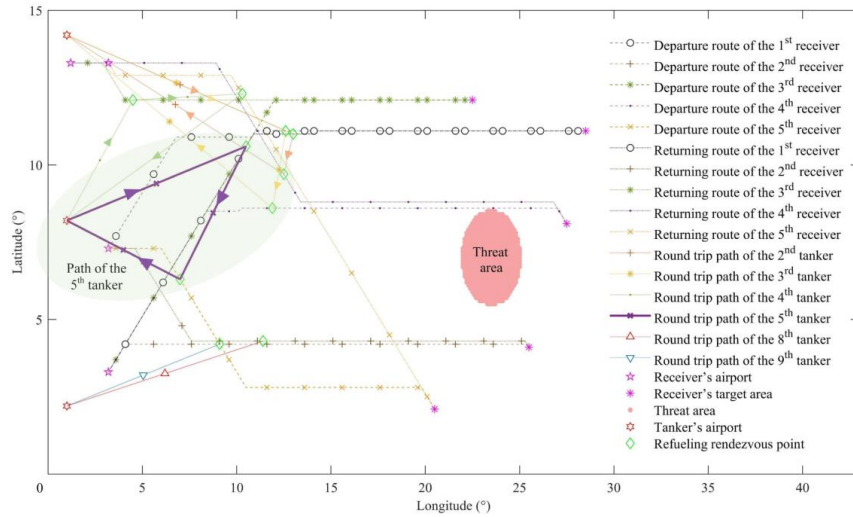


Figure 16.9: Optimization results with integrated method.

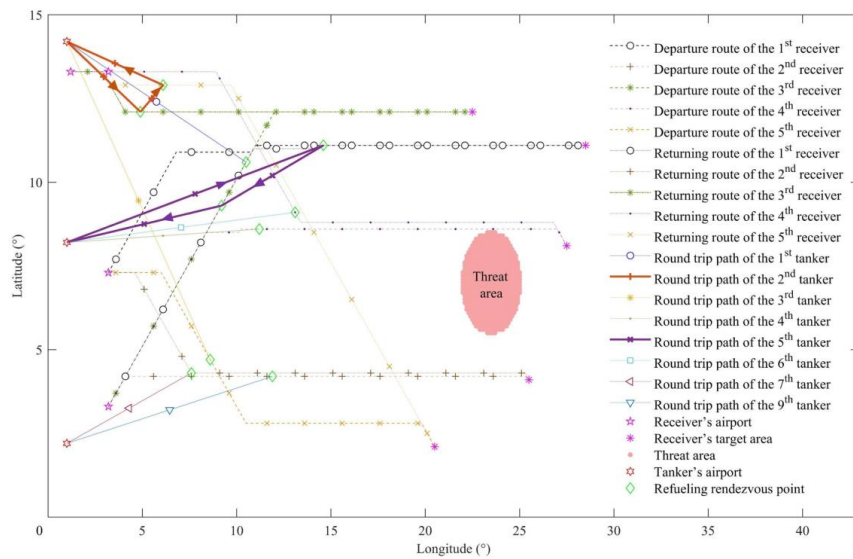


Figure 16.10: Optimization result with decomposed method.

Table 16.6: Mission scheduling results of integrated method.

Receiver number	First aerial refueling			Second aerial refueling		
	Tanker sortie number	Refueling volume (kg)	Refueling airspace coordinate(°)	Tanker sortie number	Refueling volume (kg)	Refueling a coordinate(
1	3	11606	(12.6, 11.1)	2	4552	(13.0, 11.0)
2	9	11557	(9.1, 4.2)	8	4664	(11.4, 4.3)
3	5	11095	(10.5,10.6)	4	2318	(4.5, 12.1)
4	3	11698	(11.9, 8.6)	2	4456	(12.5, 9.7)
5	3	11160	(7.0, 6.3)	4	3162	(10.3, 12.3)
Optimization time (s)	264					
Total fuel consumption (kg)	594978					

first refueling mission. Taking the scheduling result of the tanker on the 5th sortie as an instance, its path is shown by the cross marked solid purple line with arrows covered by a green circle, and the tanker takes off from the airport to its first refueling mission rendezvous point, refueling the 3rd receiver. Then, it moves to its second refueling mission rendezvous point at cruising speed, which is on the departure path of the 5th receiver, hovers for approximately 14 mins waiting for the receiver to arrive, finally fuels the 5th receiver, completes the second refueling mission and goes back to the airport for landing. This indicates that the optimization process by this method successfully schedules the aerial refueling rendezvous points into a relatively nearby spatial-temporal area. Therefore, the tanker can continuously complete the next aerial refueling mission after completing the prior task instead of directly returning to the airport. Due to the enormous weight of the tanker, the fuel consumption during the flight as well as for takeoff and landing are very large, so reducing the number of takeoff-and-landing times of tankers can significantly reduce the total fuel consumption. For the tanker sorties from the same airports, when their flight time does not overlap, they can be combined and assigned to the same one tanker. In this experiment, the landing time of the 9th tanker sortie is 0.52 h and the takeoff time of the 8th tanker sortie is 0.97 h. Thus, the 9th and the 8th sortie can be assigned to the same tanker in the airport at (1.0, 2.2). Similarly, the 5th and the 4th sortie, the 3rd and the 2nd sortie can also be combined because of non-overlap of time. Therefore, for this scheduling result, there are only 3 tankers needed to complete the refueling missions in practice. The degree to which tanker sorties can be combined depends on the time interval between refueling tasks.

According to the simulation results in Table 16.6, the integrated method for aerial refueling scheduling and task allocation can produce satisfactory optimization results to meet the mission requirements. Compared with the fixed scheduling strategy, the number of the required tanker sorties is reduced from 10 to 6, and meanwhile, the total fuel consumption is reduced by 30% from 852608 kg to 594978 kg. The refueling missions are planned by the optimization results to concentrate in a nearby spatial-temporal range as much as possible, which reduces the number of tanker sorties, thus reducing the overall fuel consumption.

In the integrated multi-receiver and multi-tanker aerial refueling model, the $2N_r$ decision variables correspond to a dimensional scheduling space of $2N_r$ sizes, and the overall number of

different solutions is $N_t^{2N_r} \prod_{i_r=1}^{N_r} N_{i_r} \prod_{i_r=1}^{N_r} N'_{i_r}$. The solution space grows exponentially as the number of receivers and tankers increases or as the number of the receiver's path waypoints increases. Besides, because the nonlinear temporal constraints in Eq. 16.33 of the integrated method are harsh to the refueling task allocation, it is not easy to find solutions. Thus, searching for the initial feasible solution using the GA in MATLAB is challenging and time-consuming. The optimization process may even be terminated prematurely because no feasible or better solution can be found for a long time, and the optimization result will be less effective. Therefore, an alternative method with less space complexity is expected to be established.

16.5.3.2 Decomposed method

As shown in Fig. 16.10, the decomposed method employs 8 tanker sorties and needs 4 tankers in practice after combination. This method can also meet the scheduling mission requirement and obtain more satisfactory optimization results than the fixed scheduling method. Although the overall fuel consumption cost obtained by the decomposed method is more than that by the integrated method, this model has a lower space complexity and optimization time.

According to the experimental results in Fig. 16.10 and Table 16.7, the 10 refueling missions are allocated into 8 groups, reducing the number of tanker sorties to 8, thus reducing the overall fuel consumption. As shown in Fig. 16.10, the tanker on the 2nd and 5th sorties are assigned two aerial refueling missions, represented by cross marked solid lines with arrows, and their flight path is similar to the tanker on the 1st sortie described in Section 16.5.3.1. Compared with the fixed scheduling strategy, the total fuel consumption is reduced by 20% to 682885 kg.

In the first step of the decomposed method, the aerial refueling rendezvous points scheduling is optimized separately for the individual receivers. The planning space size for the individual refueling point scheduling of each receiver is the product of the receiver's round-trip path points number $N_{i_r} \times N'_{i_r}$. In the nested task allocation model of the second step for tankers, the decision variable dimension of the outer loop is $4N_r^2$, while the dimension of the inner loop is $N_t \times K$. However, since the decision variables of both the outer and inner loops are variables of 0/1, the actual planning space is significantly reduced compared to the integrated method, although the number of decision space dimensions is extensive. Moreover, since the linear constraints of the inner and outer loops directly reduce most of the search area, they significantly reduce the difficulty to search for initial feasible points and therefore reduce the optimization time.

16.5.3.3 Comparative analysis

To compare the efficacies and deficiencies of the two improved methods qualitatively and quantitatively, the following simulation experiments were performed. Different receivers' path points number and receivers' number are selected to test the efficiency of the methods on different calculation complexity and scenario scale. To facilitate the path setting under different

Table 16.7: Mission scheduling results of decomposed method.

Receiver number	First aerial refueling			Second aerial refueling		
	Tanker sortie number	Refueling volume (kg)	Refueling airspace coordinate(°)	Tanker sortie number	Refueling volume (kg)	Refueling a coordinate(
1	5	11692	(12.6, 11.1)	1	3882	(13.0, 11.0)
2	9	11698	(9.1, 4.2)	7	2755	(11.4, 4.3)
3	5	11692	(10.5,10.6)	2	2407	(4.5, 12.1)
4	4	11696	(11.9, 8.6)	6	4676	(12.5, 9.7)
5	3	11699	(7.0, 6.3)	4	2455	(10.3, 12.3)
Optimization time (s)	42					
Total fuel consumption (kg)	682885					

conditions, the threat area was ignored in these experiments, and a straight line was used as the path of receivers.

(1) The optimization results of different receiver's path point number $N_{i_r} = N'_{i_r} = 100, 200, 300$, under the condition that receiver number $N_r = 5$, are listed in Table 16.8.

(2) The optimization results of different receiver number $N_r = 2, 5, 10, 20$, with a given specific number of receiver's path points $N_{i_r} = N'_{i_r} = 200$, are presented in Table 16.9. Each value listed in the table represents the average value of 5 independent runs for a particular configuration of $N_r = 2, 5, 10, 20$. In these configurations, the task time of each case is randomly generated within a range from 0 to 3 hours, and the coordinates are randomly generated within the task zone.

In Table 16.8, we consider the impact of waypoint number on the optimality of rendezvous points. The receiver's path generated by the A* algorithm can be interpolated to expand the range of available rendezvous point selections, according to precision requirements. The greater the number of waypoints along the same path is, the more accurate the rendezvous points can be selected. However, a larger selection of waypoints also entails a corresponding expansion of the optimization search space. Therefore, the receiver's waypoint count is chosen as a variable to assess the impact of increasing the waypoint count for the two developed methods. In this paper, the Inverse Distance Weighted (IDW) interpolation method is adopted in the following experiments. The new waypoints are calculated by taking a weighted average of the values at the original points.

As listed in Table 16.8, the three results are obtained from the same task, and only the number of waypoints is different through interpolation. In general, when the number of waypoints increases, the result of overall fuel consumption is lower. When the number of path points increases from 100 to 200, the computational complexity of the optimization by the integrated method increases, and its optimization time increases significantly; when the number of path points increases to 300, the optimization result of total fuel consumption in the integrated method increases greatly. The reduction of optimization time indicates that the GA converges faster, but at the cost of local optimum. Due to the large solving space, the global convergence of the algorithm is insufficient and it terminates early at the locally optimal solution. In contrast, the

Table 16.8: Mission scheduling results of decomposed method.

Number of path points	Integrated method			Decomposed method		
	Overall fuel consumption (kg)	Optimization time (s)	Tanker sorties	Overall fuel consumption (kg)	Optimization time (s)	Tanker sorties
100	604512	131	7	658174	31	8
200	557969	340	6	654874	48	8
300	674074	72	8	652565	62	8

decomposed method increases relatively less optimization time when the number of path points increases. Its optimization results are not insensitive to the rise of path points.

In Table 16.9, since this paper aims to schedule the aerial refueling problem for multi-receiver and multi-tanker, the simulations are performed to compare and analyze the effects on optimization results of two methods when the number of receivers increases. As listed in Table 16.9, in terms of the total fuel consumption, the optimization results by the integrated method have better results and better global optimality when the receiver number is only 2. Regarding the task allocation results by the tankers, the accumulation of aerial refueling tasks by the decomposed method depends mainly on the proximity of the paths of receivers in time and space. In the outer loop grouping model of task allocation by the decomposed method, the linear constraints delete infeasible aggregation solutions, making task combination much easier. However, the decomposed method cuts a large part of the feasible area in its first-step modeling. On the other hand, the integrated method can better account for the globality of the problem through the optimization search. The obtained solutions are with lower total fuel consumption through many generations of optimization. Regarding optimization time, the decomposed method for aerial refueling rendezvous point scheduling and task allocation of the tanker is better because of lower computational complexity. Its advantage is more apparent when the number of receivers is more, due to its better ability to aggregate tasks.

As the number of receivers N_r increases to 20, the problem model encounters a challenge due to numerous and stringent constraints. This results in a low success rate for solutions that satisfy all the specified conditions, subsequently reducing the algorithm's efficiency. The experiment demonstrated that it failed to find a solution meeting the constraints. The decomposed method addresses this issue, by partitioning the entire process of rendezvous point scheduling and refueling task allocation into two parts, thereby reducing the search space. This adjustment effectively resolves the problem, yielding a solution within a reasonable calculation time of 297 s.

Overall, the integrated method can obtain a better result in reducing fuel consumption. Still, the optimization time is increased significantly with increasing scenario size, and the difficulty of finding the initial feasible solution increases when using the GA to optimize the solution. Since the aerial refueling scheduling problem is decoupled into two independent processes by the decomposed method: aerial refueling rendezvous scheduling and task allocation for the tankers, it offers more advantages with lower computational complexity and less optimization time. Its

Table 16.9: Mission scheduling results of decomposed method.

Number of path points	Integrated method			Decomposed method		
	Overall fuel consumption (kg)	Optimization time (s)	Tanker sorties	Overall fuel consumption (kg)	Optimization time (s)	Tanker sorties
2	355240	24	3.4	365008	16	3.6
5	606016	205	6.2	592104	46	7.2
10	1575969	338	14.8	1078725	95	10.6
20		N/A		2572973	297	32

optimization results are relatively conservative but can meet the scheduling requirements. In practical applications, the advantages and disadvantages of the two methods can be combined and chosen according to the scenario requirements. In fact, both the integrated and decomposed methods proposed in this paper require tens of seconds for optimization calculations, so these two methods are currently unsuitable for fast scheduling so far. The overall refueling scheduling task is allocated based on these well-known conditions. Once the refueling plan is established, tankers execute the refueling process according to the plan, with realtime path planning and obstacle avoidance algorithms governing their movements.

16.6 Chapter Summary

Considering the aerial refueling mission of multi-receiver and multi-tanker with multiple takeoff and landing airports, an aerial refueling mission model and a fuel consumption model of the aircraft are established. Furthermore, an integrated method and a decomposed method of aerial refueling are designed to address the problem of refueling airspace scheduling and task allocation for tankers. Overall, the integrated method performs better in optimizing the total fuel consumption, but it can be prone to local optima and exhibits higher computational complexity. On the other hand, the decomposed method has the advantage of lower computational complexity, since it separates the refueling rendezvous point planning from the task planning and decouples the task grouping and task assignment in the task planning. It cuts out part of the feasible solutions, and therefore has a sub-optimal solution with lower computational complexity. Finally, the simulation results demonstrate that the proposed methods are feasible and effective. The integrated method can be selected when the planning accuracy is required, while the decomposed method can be selected when the computing resources are limited, or the planning time is confined. In practical applications, users can choose one according to the engineering requirements.

To get a better solution close to practical application, in the future, more spatial-temporal constraints should be taken into consideration. Also, the state information of the aircraft can be added to the model, so that the model can plan for aircraft that have already taken off. More detailed fuel calculation formulas will also be built according to different states to meet the needs of online planning. Meanwhile, there are many effective optimization algorithms that



can be adopted to improve the optimization result and realize online optimization, such as GA, PSO, ACO, Simulated Annealing (SA), Tabu Search (TS), Swarm Intelligence (SI), etc. These advanced optimization algorithms have great potential to improve the efficiency and optimality of the solution.

(1) The optimization problem is solved by learning methods. The learning method for solving the problem in combinatorial optimization is to train a neural network with different scenarios in advance. Thus, we can directly put the conditions of the actual scenarios into the trained neural network to quickly obtain the output solution. Many neural network methods can be introduced to solve combinatorial optimization problems, including the Hopfield neural network, the graph neural network, and the neural network with reinforcement learning. [354]

(2) The current path model is built in a discrete space. By changing the path model to a continuous space, transforming the model to a continuous optimization problem can also accelerate the solution.

(3) The computing time can be reduced by using a higher-performance computer. Computing time is related to hardware and software configurations, such as programming language, compiler, hardware configuration, etc. The simulations in this paper are programmed with MATLAB and run on a personal computer. In practical applications, changing the code to C, parallelizing the program, and running the program on a computer with better hardware configuration can decrease the solving time.



Bibliography

- [1] R. Jinrui and Q. Quan, “Progress in modeling and control of probe-and-drogue autonomous aerial refueling,” *Chinese Journal of Aeronautics*, vol. 37, no. 5, pp. 6–26, 2024.
- [2] P. R. Thomas, U. Bhandari, S. Bullock, T. S. Richardson, and J. L. Du Bois, “Advances in air to air refuelling,” *Progress in Aerospace Sciences*, vol. 71, pp. 14–35, 2014.
- [3] Q. Quan, Z. Wei, J. Gao, R. Zhang, and K. Cai, “A survey on modeling and control problems for probe and drogue autonomous aerial refueling at docking stage,” *Acta Aeronautica et Astronautica Sinica*, vol. 35, no. 9, pp. 2390–2410, 2014.
- [4] J. P. Nalepka and J. L. Hinchman, “Automated aerial refueling: extending the effectiveness of unmanned air vehicles,” in *AIAA Modeling and Simulation Technologies Conference and Exhibit*, ser. AIAA 2005-6005, Aug. 2005.
- [5] D. B. Wilson, A. Göktogan, and S. Sukkarieh, “Guidance and navigation for UAV airborne docking,” in *Proc. Robotics: Science and Systems*, 2015, pp. 1–9.
- [6] M. A. Bennington and K. D. Visser, “Aerial refueling implications for commercial aviation,” *Journal of Aircraft*, vol. 42, no. 2, pp. 366–375, 2005.
- [7] S. A. Cambone, K. J. Krieg, P. Pace, and W. Linton, “Unmanned aircraft systems roadmap 2005-2030,” *Office of the Secretary of Defense*, vol. 8, pp. 4–15, 2005.
- [8] A. Dogan, W. Blake, and C. Haag, “Bow wave effect in aerial refueling: Computational analysis and modeling,” *Journal of Aircraft*, vol. 50, no. 6, pp. 1856–1868, 2013.
- [9] U. Bhandari, P. R. Thomas, and T. S. Richardson, “Bow wave effect in probe and drogue aerial refuelling,” in *AIAA Guidance, Navigation, and Control (GNC) Conference*, 2013, p. 4695.
- [10] R. P. Dibley, M. J. Allen, and N. Nabaa, “Autonomous airborne refueling demonstration phase I flight-test results,” in *AIAA Atmospheric Flight Mechanics Conference and Exhibit*, ser. AIAA 2007-6639, Aug. 2007.
- [11] K. Ro, T. Kuk, and J. W. Kamman, “Dynamics and control of hose-drogue refueling systems during coupling,” *Journal of Guidance, Control, and Dynamics*, vol. 34, no. 6, pp. 1694–1708, 2011.
- [12] ———, “Active control of aerial refueling hose-drogue systems,” in *AIAA Guidance, Navigation, and Control Conference*, ser. AIAA 2010-8400, Aug. 2010.

- [13] J. B. Hoagg and D. S. Bernstein, “Nonminimum-phase zeros-much to do about nothing-classical control-revisited part II,” *IEEE control Systems*, vol. 27, no. 3, pp. 45–57, 2007.
- [14] L. Benvenuti, M. D. Di Benedetto, and J. W. Grizzle, “Approximate output tracking for nonlinear non-minimum phase systems with an application to flight control,” *International Journal of Robust and Nonlinear Control*, vol. 4, no. 3, pp. 397–414, 1994.
- [15] J. Doeblblier, T. Spaeth, J. Valasek, M. J. Monda, and H. Schaub, “Boom and receptacle autonomous air refueling using visual snake optical sensor,” *Journal of Guidance, Control, and Dynamics*, vol. 30, no. 6, pp. 1753–1769, 2007.
- [16] N. Fezans and T. Jann, “Towards automation of aerial refuelling manoeuvres with the probe-and-drogue system: modelling and simulation,” *Transportation Research Procedia*, vol. 29, pp. 116–134, 2018.
- [17] Z. Su, H. Wang, X. Shao, and Y. Huang, “A robust back-stepping based trajectory tracking controller for the tanker with strict posture constraints under unknown flow perturbations,” *Aerospace Science and Technology*, vol. 56, pp. 34–45, 2016.
- [18] L. S. Brian and L. L. Frank, *Aircraft control and simulation*. John Wiley & Sons, Inc., Hoboken, New Jersey, 2003.
- [19] A. Bloy and M. Khan, “Modeling of the receiver aircraft in air-to-air refueling,” *Journal of aircraft*, vol. 38, no. 2, pp. 393–396, 2001.
- [20] A. Barfield and J. Hinchman, “An equivalent model for UAV automated aerial refueling research,” in *AIAA Modeling and Simulation Technologies Conference and Exhibit*, ser. AIAA 2005-6006, 2005.
- [21] J. Guo, X.-M. Dong, L. Wang, and H.-B. Li, “Modeling and control of uavc with varying mass in autonomous aerial refueling,” *Flight Dynamics*, vol. 29, no. 6, pp. 36–40, 2011.
- [22] S. An and S. Yuan, “Relative position control design of receiver UAV in flying-boom aerial refueling phase,” *ISA transactions*, vol. 73, pp. 40–53, 2018.
- [23] C. Wu, J. Hui, J. Yan, Y. Guo, and B. Xiao, “Dynamic modeling and faster finite-time attitude stabilization of receiver aircraft for aerial refueling,” *Nonlinear Dynamics*, vol. 104, no. 1, pp. 467–481, 2021.
- [24] Z. Su, H. Wang, N. Li, Y. Yu, and J. Wu, “Exact docking flight controller for autonomous aerial refueling with back-stepping based high order sliding mode,” *Mechanical Systems and Signal Processing*, vol. 101, pp. 338–360, 2018.
- [25] A. Bloy and M. Khan, “Modelling of the hose and drogue in air-to-air refuelling,” *The Aeronautical Journal*, vol. 106, no. 1055, pp. 17–26, 2002.

- [26] Z.-B. Wei, Q. Quan, and K.-Y. Cai, “Research on relationship between drogue position and interference force for probe-drogue aerial refueling system based on link-connected model [In Chinese],” in *Control Conference (CCC), 2012 31st Chinese*. IEEE, 2012, pp. 1777–1782.
- [27] K. Ro and J. W. Kamman, “Modeling and simulation of hose-paradrogue aerial refueling systems,” *Journal of Guidance, Control, and Dynamics*, vol. 33, no. 1, pp. 53–63, 2010.
- [28] W. R. Williamson, E. Reed, G. J. Glenn, S. M. Stecko, J. Musgrave, and J. M. Takacs, “Controllable drogue for automated aerial refueling,” *Journal of Aircraft*, vol. 47, no. 2, pp. 515–527, 2010.
- [29] X. Dai, Q. Quan, J. Ren, and K.-Y. Cai, “Iterative learning control and initial value estimation for probe–drogue autonomous aerial refueling of UAVs,” *Aerospace Science and Technology*, vol. 82, pp. 583–593, 2018.
- [30] J. Vassberg, D. Yeh, A. Blair, and J. Evert, “Dynamic characteristics of a KC-10 wing-pod refueling hose by numerical simulation,” in *20th AIAA Applied Aerodynamics Conference*, ser. AIAA 2002-2712, 2002.
- [31] S. Yin, Y. Song, J. Yu, and F. Chen, “Hose–drogue motion estimation for aerial refueling using fluid and rigid dynamics,” *Journal of Aerospace Information Systems*, vol. 19, no. 11, pp. 705–716, 2022.
- [32] W. Ribbens, F. Saggio, R. Wierenga, and M. Feldmann, “Dynamic modeling of an aerial refueling hose & drogue system,” in *25th AIAA Applied Aerodynamics Conference*, ser. AIAA 2007-3802, Jun. 2007.
- [33] J. Vassberg, D. Yeh, A. Blair, and J. Evert, “Numerical simulations of kc-10 wing-mount aerial refueling hose-drogue dynamics with a reel take-up system,” in *21st AIAA Applied Aerodynamics Conference*, 2003, p. 3508.
- [34] H. Wang, X. Dong, J. Xue, and J. Liu, “Dynamic modeling of a hose-drogue aerial refueling system and integral sliding mode backstepping control for the hose whipping phenomenon,” *Chinese journal of aeronautics*, vol. 27, no. 4, pp. 930–946, 2014.
- [35] X. Dai, Z.-B. Wei, Q. Quan, and K.-Y. Cai, “Hose-drum-unit modeling and control for probe-and-drogue autonomous aerial refueling,” *IEEE Transactions on Aerospace and Electronic Systems*, vol. 56, no. 4, pp. 2779–2791, 2019.
- [36] Z. Zhu and S. Meguid, “Elastodynamic analysis of low tension cables using a new curved beam element,” *International journal of solids and structures*, vol. 43, no. 6, pp. 1490–1504, 2006.

- [37] ——, “Modeling and simulation of aerial refueling by finite element method,” *International Journal of Solids and Structures*, vol. 44, no. 24, pp. 8057–8073, 2007.
- [38] K. S. Paniagua, P. García-Fogeda, F. Arévalo, and J. B. Rodriguez, “Aeroelastic analysis of an air-to-air refueling hose–drogue system through an efficient novel mathematical model,” *Journal of Fluids and Structures*, vol. 100, p. 103164, 2021.
- [39] Z. Liu, X. He, Z. Zhao, C. K. Ahn, and H.-X. Li, “Vibration control for spatial aerial refueling hoses with bounded actuators,” *IEEE Transactions on Industrial Electronics*, vol. 68, no. 5, pp. 4209–4217, 2020.
- [40] Z.-B. Wei, X. Dai, Q. Quan, and K.-Y. Cai, “Drogue dynamic model under bow wave in probe-and-drogue refueling,” *IEEE Transactions on Aerospace and Electronic Systems*, vol. 52, no. 4, pp. 1728–1742, 2016.
- [41] X. Dai, Q. Quan, J. Ren, Z. Xi, and K.-Y. Cai, “Terminal iterative learning control for autonomous aerial refueling under aerodynamic disturbances,” *Journal of Guidance, Control, and Dynamics*, vol. 41, no. 7, pp. 1577–1584, 2018.
- [42] M. Vachon, R. Ray, and C. Calianno, “Calculated drag of an aerial refueling assembly through airplane performance analysis,” in *42nd AIAA aerospace sciences meeting and exhibit*, 2004, p. 381.
- [43] J. L. Hansen, J. E. Murray, and N. V. Campos, “The NASA dryden AAR project: a flight test approach to an aerial refueling system,” in *AIAA Atmospheric Flight Mechanics Conference and Exhibit*, ser. AIAA 2004-4939, Aug. 2004.
- [44] X. Dai, Z.-B. Wei, and Q. Quan, “Modeling and simulation of bow wave effect in probe and drogue aerial refueling,” *Chinese Journal of Aeronautics*, vol. 29, no. 2, pp. 448–461, 2016.
- [45] Y. Liu, H. Wang, Z. Su, and J. Fan, “Deep learning based trajectory optimization for uav aerial refueling docking under bow wave,” *Aerospace Science and Technology*, vol. 80, pp. 392–402, 2018.
- [46] R. Burns, C. Clark, and R. Ewart, “The automated aerial refueling simulation at the avtas laboratory,” in *AIAA Modeling and Simulation Technologies Conference and Exhibit*, 2005, p. 6008.
- [47] M. Specification, “Mil-hdbk-1797 flying qualities of piloted aircraft,” *United States Department of Defense*, 1997.
- [48] ——, “Mil-f-8785c flying qualities of piloted airplanes,” *United States Department of Defense*, 1980.

- [49] S. Venkataraman, A. Dogan, and W. Blake, “Vortex effect modelling in aircraft formation flight,” in *AIAA Atmospheric Flight Mechanics Conference and Exhibit*, 2003, p. 5385.
- [50] W. Blake, E. Dickes, and D. Gingras, “UAV aerial refueling-wind tunnel results and comparison with analytical predictions,” in *AIAA Atmospheric Flight Mechanics Conference and Exhibit*, ser. AIAA 2004-4820, 2004.
- [51] A. Dogan, T. Lewis, and W. Blake, “Wake-vortex induced wind with turbulence in aerial refueling-part b: Model and simulation validation,” in *AIAA Atmospheric Flight Mechanics Conference and Exhibit*, 2008, p. 6697.
- [52] ———, “Wake-vortex induced wind with turbulence in aerial refueling-part a: flight data analysis,” in *AIAA Atmospheric Flight Mechanics Conference and Exhibit*, 2008, p. 6696.
- [53] T. Gerz, F. Holzapfel, and D. Darracq, “Commercial aircraft wake vortices,” *Progress in Aerospace Sciences*, vol. 38, no. 3, pp. 181–208, 2002.
- [54] A. Dogan, T. A. Lewis, and W. Blake, “Flight data analysis and simulation of wind effects during aerial refueling,” *Journal of Aircraft*, vol. 45, no. 6, pp. 2036–2048, 2008.
- [55] D. Zhang, Y. Chen, and X. Fu, “Tanker wake effects on the trailing uav in autonomous aerial refueling,” *Journal of Applied Fluid Mechanics*, vol. 13, no. 2, pp. 629–637, 2020.
- [56] P. A. Cavallo, M. R. O’Gara, and J. D. Shipman, “Low-order response surface model for simulating wake interference in aerial refueling,” *Journal of Aircraft*, vol. 56, no. 5, pp. 1783–1793, 2019.
- [57] K. Yue, L. Cheng, T. Zhang, J. Ji, and D. Yu, “Numerical simulation of the aerodynamic influence of an aircraft on the hose-refueling system during aerial refueling operations,” *Aerospace Science and Technology*, vol. 49, pp. 34–40, 2016.
- [58] J. Katz, “Aerodynamic aspects of unmanned aerial vehicle aerial refueling,” *Journal of Aircraft*, vol. 54, no. 6, pp. 2311–2316, 2017.
- [59] K. Ro and E. Basaran, “Aerodynamic investigations of paratrooper assembly in aerial refueling system,” in *44th AIAA Aerospace Sciences Meeting and Exhibit*, 2006, p. 855.
- [60] J. Valasek, K. Gunnam, J. Kimmett, J. L. Junkins, and D. Hughes, “Vision based sensor and navigation system for autonomous aerial refueling,” 2002.
- [61] J. Kimmett, J. Valasek, and J. L. Junkins, “Vision based controller for autonomous aerial refueling,” in *Control Applications, 2002. Proceedings of the 2002 International Conference on*, vol. 2. IEEE, 2002, pp. 1138–1143.

- [62] J. Kimmett, J. Valasek, and J. Junkins, “Autonomous aerial refueling utilizing a vision based navigation system,” in *AIAA Guidance, Navigation, and Control Conference and Exhibit*, 2002, p. 4469.
- [63] J. Wang, N. Hovakimyan, and C. Cao, “Verifiable adaptive flight control: unmanned combat aerial vehicle and aerial refueling,” *Journal of guidance, control, and dynamics*, vol. 33, no. 1, pp. 75–87, 2010.
- [64] J. Wang, V. V. Patel, C. Cao, N. Hovakimyan, and E. Lavretsky, “Novel L1 adaptive control methodology for aerial refueling with guaranteed transient performance,” *Journal of guidance, control, and dynamics*, vol. 31, no. 1, pp. 182–193, 2008.
- [65] M. Fravolini, A. Ficola, M. Napolitano, G. Campa, and M. Perhinschi, “Development of modelling and control tools for aerial refueling for uavs,” in *AIAA Guidance, Navigation, and Control Conference and Exhibit*, 2003, p. 5798.
- [66] M. L. Fravolini, A. Ficola, G. Campa, M. R. Napolitano, and B. Seanor, “Modeling and control issues for autonomous aerial refueling for uavs using a probe-drogue refueling system,” *Aerospace science and technology*, vol. 8, no. 7, pp. 611–618, 2004.
- [67] M. D. Tandale, R. Bowers, and J. Valasek, “Trajectory tracking controller for vision-based probe and drogue autonomous aerial refueling,” *Journal of Guidance, Control, and Dynamics*, vol. 29, no. 4, pp. 846–857, 2006.
- [68] J. Valasek, D. Famularo, and M. Marwaha, “Fault-tolerant adaptive model inversion control for vision-based autonomous air refueling,” *Journal of Guidance, Control, and Dynamics*, vol. 40, no. 6, pp. 1336–1347, 2017.
- [69] Z. C. H. Liu Z, Yuan S Z, “Flight control of receiver aircraft in probe-and-drogue aerial refueling,” *Science Technology and Engineering*, vol. 11, no. 8, pp. 1755–1761, 2011.
- [70] Y. Ochi and T. Kominami, “Flight control for automatic aerial refueling via png and los angle control,” in *AIAA Guidance, Navigation, and Control Conference and Exhibit*, 2005, p. 6268.
- [71] D. Luo, R. Xie, and H. Duan, “A guidance law for uav autonomous aerial refueling based on the iterative computation method,” *Chinese Journal of Aeronautics*, vol. 27, no. 4, pp. 875–883, 2014.
- [72] A. Tsukerman, M. Weiss, T. Shima, D. Löbl, and F. Holzapfel, “Optimal rendezvous guidance laws with application to civil autonomous aerial refueling,” *Journal of Guidance, Control, and Dynamics*, vol. 41, no. 5, pp. 1167–1174, 2018.

- [73] Y. Liu, H. Wang, and J. Fan, “Docking safety assessment and optimization for autonomous aerial refueling: A data-driven method,” *IEEE Systems Journal*, vol. 15, no. 3, pp. 4057–4068, 2020.
- [74] Z. Su, H. Wang, P. Yao, Y. Huang, and Y. Qin, “Back-stepping based anti-disturbance flight controller with preview methodology for autonomous aerial refueling,” *Aerospace Science and Technology*, vol. 61, pp. 95–108, 2017.
- [75] Y. Liu, H. Wang, and J. Fan, “Novel docking controller for autonomous aerial refueling with probe direct control and learning-based preview method,” *Aerospace Science and Technology*, vol. 94, p. 105403, 2019.
- [76] L. Z., “Research on flight control technology of the receiver aircraft in probe-and-drogue autonomous aerial refueling,” Master’s thesis, Nanjing: College of Automation Engineering, Nanjing University of Aeronautics and Astronautics, 2012.
- [77] A. Dogan, C. Elliott, F. Riley, and W. Blake, “Effects of mass and size on control of large receiver in aerial refueling,” in *AIAA Atmospheric Flight Mechanics Conference*, 2009, p. 5927.
- [78] O. Murillo and P. Lu, “Comparison of autonomous aerial refueling controllers using reduced order models,” in *AIAA Guidance, Navigation and Control Conference and Exhibit*, 2008, p. 6790.
- [79] H. Duan, Y. Sun, and Y. Shi, “Bionic visual control for probe-and-drogue autonomous aerial refueling,” *IEEE Transactions on Aerospace and Electronic Systems*, vol. 57, no. 2, pp. 848–865, 2020.
- [80] Z. Yu, Y. Qu, Y. Zhang, C.-Y. Su, and Y. Zhang, “Wake vortex attenuation control of receiver uav in autonomous aerial refueling,” in *2018 IEEE CSAA Guidance, Navigation and Control Conference (CGNCC)*. IEEE, 2018, pp. 1–6.
- [81] Z. Yu, Y. Zhang, and Y. Qu, “Fault-tolerant control for autonomous aerial refueling against actuator fault in receiver uav,” *IFAC-PapersOnLine*, vol. 51, no. 24, pp. 274–279, 2018.
- [82] H. E. Sevil and A. Dogan, “Fault diagnosis in air data sensors for receiver aircraft in aerial refueling,” *Journal of Guidance, Control, and Dynamics*, vol. 38, no. 10, pp. 1959–1975, 2015.
- [83] L. Chang and Y. Jia, “Robust adaptive control of air-to-air refueling boom with state-dependent output constraints,” in *The 2019 International Conference on Artificial Life and Robotics (ICAROB2019)*, 2019, pp. 419–422.
- [84] Z. Su and H. Wang, “Probe motion compound control for autonomous aerial refueling docking,” *Aerospace Science and Technology*, vol. 72, pp. 1–13, 2018.

- [85] W. L. Lin H, *Iterative learning control theory*. Xi'an: Northwestern Polytechnical University Press, 1998.
- [86] H. B. J. Sun M X, *Iterative learning control*. Beijing: National Defense Industry Press, 1999.
- [87] J. Ren, X. Dai, Q. Quan, Z.-B. Wei, and K.-Y. Cai, “Reliable docking control scheme for probe-drogue refueling,” *Journal of Guidance, Control, and Dynamics*, vol. 42, no. 11, pp. 2511–2520, 2019.
- [88] R. Jinrui, Q. Quan, L. Cunjia, and C. Kai-Yuan, “Docking control for probe-drogue refueling: An additive-state-decomposition-based output feedback iterative learning control method,” *Chinese Journal of Aeronautics*, vol. 33, no. 3, pp. 1016–1025, 2020.
- [89] D.-w. Li and H.-l. Wang, “Uav flight control in automated aerial refueling,” *Journal of System Simulation*, vol. 22, no. 1, pp. 126–130, 2010.
- [90] M. Rehan and Z. H. Khan, “Robust formation control for aerial refueling,” in *Robotics and Artificial Intelligence (ICRAI), 2012 International Conference on*. IEEE, 2012, pp. 11–18.
- [91] H. Wang, Y. Du, and W. Gai, “Precise docking control in unmanned aircraft vehicle automated aerial refueling,” *Journal of Beijing University of Aeronautics and Astronautics*, vol. 37, no. 7, pp. 822–826, 2011.
- [92] W. Gai, H. Wang, and D. Li, “Trajectory tracking for automated aerial refueling based on adaptive dynamic inversion,” *Journal of Beijing University of Aeronautics and Astronautics*, vol. 38, no. 5, pp. 585–590, 2012.
- [93] V. Stepanyan, E. Lavretsky, and N. Hovakimyan, “Aerial refueling autopilot design methodology: application to f-16 aircraft model,” in *AIAA Guidance, Navigation, and Control Conference and Exhibit*, 2004, p. 5321.
- [94] C. Elliott and A. Dogan, “Investigating nonlinear control architecture options for aerial refueling,” in *AIAA Atmospheric Flight Mechanics Conference*, 2010, p. 7927.
- [95] ——, “Improving receiver station-keeping in aerial refueling by formulating tanker motion as disturbance,” in *AIAA Atmospheric Flight Mechanics Conference*, 2009, p. 5602.
- [96] J. H. Lee, H. E. Sevil, A. Dogan, and D. Hullender, “Estimation of receiver aircraft states and wind vectors in aerial refueling,” *Journal of Guidance, Control, and Dynamics*, vol. 37, no. 1, pp. 265–276, 2013.

- [97] S. M. Ross, M. Pachter, D. R. Jacques, B. A. Kish, and D. R. Millman, “Autonomous aerial refueling based on the tanker reference frame,” in *Aerospace Conference, 2006 IEEE*. IEEE, 2006, pp. 22–pp.
- [98] J. Waishek, A. Dogan, and W. Blake, “Derivation of the dynamics equations of receiver aircraft in aerial refueling,” *Journal of Guidance, Control, and Dynamics*, vol. 32, no. 2, pp. 586–598, 2009.
- [99] S. Kriel, J. Engelbrecht, and T. Jones, “Receptacle normal position control for automated aerial refueling,” *Aerospace Science and Technology*, vol. 29, no. 1, pp. 296–304, 2013.
- [100] X. Sun and X. G. Zhang, “The uav autonomous aerial refueling controller based on predictor auto disturbances rejection method,” in *Applied Mechanics and Materials*, vol. 380. Trans Tech Publ, 2013, pp. 347–352.
- [101] M. Pachter, C. Houpis, and D. Trosen, “Design of an air-to-air automatic refueling flight control system using quantitative feedback theory,” *International Journal of Robust and Nonlinear Control: IFAC-Affiliated Journal*, vol. 7, no. 6, pp. 561–580, 1997.
- [102] J. Guo, X.-M. Dong, K.-J. Liao, and H.-B. Li, “Design of uav autonomous controller for formation in aerial refueling,” *Flight Dynamics*, vol. 28, no. 6, pp. 36–40, 2010.
- [103] J. Ren, Q. Quan, H. Ma, and K.-Y. Cai, “Additive-state-decomposition-based station-keeping control for autonomous aerial refueling,” *Science China Information Sciences*, vol. 64, no. 11, pp. 1–3, 2021.
- [104] C. Wu, J. Yan, J. Shen, X. Wu, and B. Xiao, “Predefined-time attitude stabilization of receiver aircraft in aerial refueling,” *IEEE Transactions on Circuits and Systems II: Express Briefs*, vol. 68, no. 10, pp. 3321–3325, 2021.
- [105] C. Wu, J. Yan, X. Wu, Y. Guo, P. Mou, and B. Xiao, “Predefined-time sliding manifold-based fixed-time attitude stabilization control of receiver aircraft with measurement noises,” *Transactions of the Institute of Measurement and Control*, vol. 44, no. 11, pp. 2193–2203, 2022.
- [106] Q. He, H. Wang, Y. Chen, M. Xu, and W. Jin, “Command filtered backstepping sliding mode control for the hose whipping phenomenon in aerial refueling,” *Aerospace Science and Technology*, vol. 67, pp. 495–505, 2017.
- [107] T. Kuk and K. Ro, “Design, test and evaluation of an actively stabilised drogue refuelling system,” *The Aeronautical Journal*, vol. 117, no. 1197, pp. 1103–1118, 2013.
- [108] D. Yuan, T. Zhao, X. Hou, X. Cheng, Y. Qu, J. Yan, and X. Xing, “Study on the controllability of a drogue for hose-drogue aerial refueling system,” in *2017 11th Asian Control Conference (ASCC)*. IEEE, 2017, pp. 2592–2595.

- [109] P. García-Fogeda, J. Esteban Molina, and F. Arévalo, “Dynamic response of aerial refueling hose-drogue system with automated control surfaces,” *Journal of Aerospace Engineering*, vol. 31, no. 6, p. 04018110, 2018.
- [110] Y. Sun, H. Duan, and N. Xian, “Fractional-order controllers optimized via heterogeneous comprehensive learning pigeon-inspired optimization for autonomous aerial refueling hose–drogue system,” *Aerospace Science and Technology*, vol. 81, pp. 1–13, 2018.
- [111] Y. Sun, Z. Liu, Y. Zou, and X. He, “Active disturbance rejection controllers optimized via adaptive granularity learning distributed pigeon-inspired optimization for autonomous aerial refueling hose-drogue system,” *Aerospace Science and Technology*, vol. 124, p. 107528, 2022.
- [112] L. Chang and Y. Jia, “Adaptive control of a hose and drogue system with input nonlinearities and partial state constraints,” *International Journal of Control, Automation and Systems*, vol. 17, no. 10, pp. 2508–2520, 2019.
- [113] Z. Liu, J. Liang, Z. Zhao, M. Ö. Efe, and K.-S. Hong, “Adaptive fault-tolerant control of a probe-and-drogue refueling hose under varying length and constrained output,” *IEEE Transactions on Control Systems Technology*, vol. 30, no. 2, pp. 869–876, 2021.
- [114] Z. Liu, Z. Han, and W. He, “Adaptive fault-tolerant boundary control of an autonomous aerial refueling hose system with prescribed constraints,” *IEEE Transactions on Automation Science and Engineering*, 2022.
- [115] J. Wang, N. Hovakimyan, and C. Cao, “L1 adaptive augmentation of gain-scheduled controller for racetrack maneuver in aerial refueling,” in *AIAA Guidance, Navigation, and Control Conference*, ser. AIAA 2009-5739, Aug. 2009.
- [116] X. Wang, J. Li, X. Kong, X. Dong, and B. Zhang, “An approach to mathematical modeling and estimation of probe-drogue docking success probability for uav autonomous aerial refueling,” *International Journal of Aerospace Engineering*, vol. 2017, 2017.
- [117] Y. Liu, Z. Zhao, H. Ma, and Q. Quan, “A stochastic approximation method for probability prediction of docking success for aerial refueling,” *Applied Soft Computing*, vol. 103, p. 107139, 2021.
- [118] X.-F. Wang, J.-M. Li, X.-W. Kong, X.-M. Dong, and B. Zhang, “Towards docking safety analysis for unmanned aerial vehicle probe-drogue autonomous aerial refueling based on docking success-probability and docking reachability,” *Proceedings of the Institution of Mechanical Engineers, Part G: Journal of Aerospace Engineering*, vol. 233, no. 11, pp. 3893–3905, 2019.

- [119] “J-10 fails in the first aerial refueling test with the probe being broken[z/ol],” July 2012, https://v.youku.com/v_show/id_XNDI0MDg3ODQw.html.
- [120] J. Ding, J. Sprinkle, C. J. Tomlin, S. S. Sastry, and J. L. Paunicka, “Reachability calculations for vehicle safety during manned/unmanned vehicle interaction,” *Journal of Guidance, Control, and Dynamics*, vol. 35, no. 1, pp. 138–152, 2012.
- [121] “A failed aerial refueling of a fighter[z/ol],” March 2008, http://v.youku.com/v_show/id_XMjE0Njk5ODA=.html.
- [122] Y. Liu, J. Wang, Q. Quan, G.-X. Du, and L. Yang, “Reachability analysis on optimal trim state for aerial docking,” *Aerospace Science and Technology*, vol. 110, p. 106471, 2021.
- [123] K. Dong, Q. Quan, and W. M. Wonham, “Failsafe mechanism design for autonomous aerial refueling using state tree structures,” *Unmanned Systems*, vol. 7, no. 04, pp. 261–279, 2019.
- [124] M. O’Connell, G. Shi, X. Shi, K. Azizzadenesheli, A. Anandkumar, Y. Yue, and S.-J. Chung, “Neural-fly enables rapid learning for agile flight in strong winds,” *Science Robotics*, vol. 7, no. 66, p. eabm6597, 2022.
- [125] L. Hao and Q. Quan, “Autonomous aerial refueling of multiple uavs: An efficient rendezvous scheduling approach,” in *2021 China Automation Congress (CAC)*. IEEE, 2021, pp. 7463–7468.
- [126] G. Yan, D. Xunhua, and Q. Quan, “Vision-based robust position estimation in probe-and-drogue autonomous aerial refueling,” in *2018 IEEE CSAA Guidance, Navigation and Control Conference (GNCC)*, 2018.
- [127] L. Ying, Z. Zhiyao, M. Haibiao, and Q. Quan, “A stochastic approximation method for probability prediction of docking success for aerial refueling,” *Applied Soft Computing*, vol. 103, no. 1, 2021.
- [128] J. HUANG, X. Jiaqi, R. Jinrui, Q. Quan, and Y. ZHANG, “Aerial refueling scheduling of multi-receiver and multi-tanker under spatial-temporal constraints for forest firefighting,” *Chinese Journal of Aeronautics*, vol. 37, no. 5, pp. 71–91, 2024.
- [129] B. L. Stevens and F. L. Lewis, *Aircraft Control and Simulation*. John Wiley & Sons, 2004.
- [130] G. J. Ducard, *Fault-tolerant flight control and guidance systems: Practical methods for small unmanned aerial vehicles*. Springer Science & Business Media, 2009.
- [131] R. M. Murray, *A mathematical introduction to robotic manipulation*. CRC press, 2017.

- [132] L. T. Nguyen, *Simulator study of stall/post-stall characteristics of a fighter airplane with relaxed longitudinal static stability.* National Aeronautics and Space Administration, 1979, vol. 12854.
- [133] F. R. Garza and E. A. Morelli, “A collection of nonlinear aircraft simulations in matlab,” Tech. Rep., 2003.
- [134] J. Waishek, A. Dogan, and W. Blake, “Derivation of the dynamics equations of receiver aircraft in aerial refueling,” *Journal of guidance, control, and dynamics*, vol. 32, no. 2, pp. 586–598, 2009.
- [135] B. L. Stevens, F. L. Lewis, and E. N. Johnson, *Aircraft control and simulation: dynamics, controls design, and autonomous systems.* John Wiley & Sons, 2015.
- [136] K. Ro and J. W. Kamman, “Modeling and simulation of hose-paradrogue aerial refueling systems,” *Journal of guidance, control, and dynamics*, vol. 33, no. 1, pp. 53–63, 2010.
- [137] J. Vassberg, D. Yeh, A. Blair, and J. Evert, “Numerical simulations of KC-10 wing-mount aerial refueling hose-drogue dynamics with a reel take-up system,” in *21st AIAA Applied Aerodynamics Conference*, 2003, p. 3508.
- [138] K. Ro, E. Basaran, and J. W. Kamman, “Aerodynamic characteristics of paradrogue assembly in an aerial refueling system,” *Journal of aircraft*, vol. 44, no. 3, pp. 963–970, 2007.
- [139] W. R. Moorhouse D, “Us military specification mil-f-8785c,” Technical report, US Department of Defense, Tech. Rep., 1980.
- [140] C. R. Chalk, T. Harris, T. Neal, and E. Prichard, *Background Information and User Guide for MIL-F-8785B (ASG) military Specification-Flying Qualities of Piloted Airplanes*. Wright-Patterson Air Force Base, 1969.
- [141] U. Ly and Y. Chan, “Time-domain computation of aircraft gust covariance matrices,” in *6th Atmospheric Flight Mechanics Conference*, 1980, p. 1615.
- [142] Y. Q. Feng, “Research on the application of wind shear and atmospheric turbulence models in flight simulation,” 2010.
- [143] P. Gipe, “Wind power for home and business,” *Renewable for the 1990s and Beyond*, 1993.
- [144] B. N. Pamadi, *Performance, Stability, Dynamics, and Control of Airplanes.* AIAA, 2004.
- [145] A. Dogan, T. A. Lewis, and W. Blake, “Flight data analysis and simulation of wind effects during aerial refueling,” *Journal of Aircraft*, vol. 45, no. 6, pp. 2036–2048, 2008.

- [146] M. Rauscher, *Introduction to aeronautical dynamics*. Wiley, 1953.
- [147] Z.-B. Wei, X. Dai, Q. Quan, and K.-Y. Cai, “Drogue dynamic model under bow wave in probe-and-drogue refueling,” *IEEE Transactions on Aerospace and Electronic Systems*, vol. 52, no. 4, pp. 1728–1742, 2016, publisher: IEEE.
- [148] S. Weisberg, *Applied linear regression*. John Wiley & Sons, 2005, vol. 528.
- [149] R. Dibley, M. Allen, and N. Nabaa, “Autonomous airborne refueling demonstration phase I flight-test results,” in *AIAA atmospheric flight mechanics conference and exhibit*, 2007, p. 6639.
- [150] “Drogue Dynamics under Receiver Wake Effects (Aerial Refueling with Hose Drogue Unit).” [Online]. Available: http://v.youku.com/v_show/id_XNzMzOTU1NDQ0.html?from=s1.8-1-1.2,2014-11-08/2016-04-17
- [151] P. R. Thomas, U. Bhandari, S. Bullock, T. S. Richardson, and J. L. Du Bois, “Advances in air to air refuelling,” *Progress in Aerospace sciences*, vol. 71, pp. 14–35, 2014.
- [152] J. Nalepka and J. Hinchman, “Automated aerial refueling: extending the effectiveness of uavs,” in *AIAA modeling and simulation technologies conference and exhibit*, 2005, p. 6005.
- [153] Navy on track to deploy MQ-25A carrier tanker in 2026 on USS theodore roosevelt. [Online]. Available: <https://news.usni.org/2022/04/06/navy-on-track-to-deploy-mq-25a-carrier-tanker-in-2026-on-uss-theodore-roosevelt>.
- [154] Airbus achieves in-flight autonomous guidance and control of a drone from a tanker aircraft. [Online]. Available: <https://www.airbus.com/en/newsroom/press-releases/2023-03-airbus-achieves-in-flight-autonomous-guidance-and-control-of-a>.
- [155] L. Pollini, G. Campa, F. Giulietti, and M. Innocenti, “Virtual simulation set-up for uavs aerial refuelling,” in *AIAA Modeling and Simulation Technologies Conference and Exhibit*, 2003, p. 5682.
- [156] N. Fezans and T. Jann, “Towards automation of aerial refuelling manoeuvres with the probe-and-drogue system: modelling and simulation,” *Transportation Research Procedia*, vol. 29, pp. 116–134, 2018, aerospace Europe CEAS 2017 Conference. [Online]. Available: <https://www.sciencedirect.com/science/article/pii/S2352146518300152>
- [157] H. Wang, X. Dong, J. Guo, J. Liu, and J. Wang, “Dynamics modeling and analysis of hose whipping phenomenon of aerial refueling hose-drogue assembly,” *Acta Aeronautica et Astronautica Sinica*, vol. 36, no. 9, pp. 3116–3127, 2015.

- [158] D. Moorhouse and R. Woodcock, “US military specification MIL-F-8785C,” *US Department of Defense*, p. 48, 1980.
- [159] H. Ma, “Formation flight control and safety assessment of aerial refueling,” Ph.D. dissertation, Beihang University, Beijing, 2018.
- [160] M. Y. Arafat, M. M. Alam, and S. Moh, “Vision-based navigation techniques for unmanned aerial vehicles: Review and challenges,” *Drones*, vol. 7, no. 2 , 89, 2023.
- [161] J. Parry and S. Hubbard, “Review of sensor technology to support automated air-to-air refueling of a probe configured uncrewed aircraft,” *Sensors*, vol. 23, no. 2, p. 995, 2023.
- [162] Y. Liu, H. Wang, and J. Fan, “Novel docking controller for autonomous aerial refueling with probe direct control and learning-based preview method,” *Aerospace Science and Technology*, vol. 94, p. 105403, 2019. [Online]. Available: <https://www.sciencedirect.com/science/article/pii/S1270963819311496>
- [163] X. Dai, C. Ke, Q. Quan, and K.-Y. Cai, “Rflysim: Automatic test platform for uav autopilot systems with fpga-based hardware-in-the-loop simulations,” *Aerospace Science and Technology*, vol. 114, p. 106727, 2021.
- [164] N. S. Agency, “Aerial refueling,” Tech. Rep. ATP-56(B), November 2013.
- [165] R. S. Russell, “Non-linear f-16 simulation using simulink and matlab,” *University of Minnesota, Tech. paper*, 2003.
- [166] K. Ro and J. W. Kamman, “Modeling and simulation of hose-parachute aerial refueling systems,” *Journal of guidance, control, and dynamics*, vol. 33, no. 1, pp. 53–63, 2010.
- [167] D. Moorhouse and R. Woodcock, “US military specification MIL-F-8785C,” 1980.Report.
- [168] A. Dogan, S. Venkataraman, and W. Blake, “Modeling of aerodynamic coupling between aircraft in close proximity,” *Journal of Aircraft*, vol. 42, no. 4, pp. 941–955, 2005.
- [169] A. Dogan, W. Blake, and C. Haag, “Bow wave effect in aerial refueling: Computational analysis and modeling,” *Journal of Aircraft*, vol. 50, no. 6, pp. 1856–1868, 2013.
- [170] R. Dibley, M. Allen, and N. Nabaa, “Autonomous airborne refueling demonstration phase I flight-test results,” in *AIAA atmospheric flight mechanics conference and exhibit*, 2007, p. 6639.
- [171] R. M. Murray, Z. Li, and S. S. Sastry, *A mathematical introduction to robotic manipulation*. CRC press, 1994.
- [172] R. W. Beard and T. W. McLain, *Small unmanned aircraft: Theory and practice*. Princeton university press, 2012.

- [173] F. R. Garza and E. A. Morelli, “A collection of nonlinear aircraft simulations in matlab,” Tech. Rep., 2003.
- [174] J. Rasol, X. Yuelei, Z. Qing, H. Tian, and Z. Zhang, “N-fold bernoulli probability based adaptive fast-tracking algorithm and its application to autonomous aerial refuelling,” *Chinese Journal of Aeronautics*, vol. 36, no. 1, pp. 356–368, 2023.
- [175] L. Bo, X. Xiaoyang, W. Xingxing, and T. Wenting, “Ship detection and classification from optical remote sensing images: A survey,” *Chinese Journal of Aeronautics*, vol. 34, no. 3, pp. 145–163, 2021.
- [176] H. Dayong, Z. Xiangtian, and S. Zhang, “Robust image-based coordinated control for spacecraft formation flying,” *Chinese Journal of Aeronautics*, vol. 35, no. 9, pp. 268–281, 2022.
- [177] D. H. Costello, M. Violet, and D. Miller, “Transference of training for a DNN to complete the aerial refueling task,” in *AIAA SCITECH 2023 Forum*, 2023, p. 0192.
- [178] G. Campa, M. Mammarella, M. R. Napolitano, M. L. Fravolini, L. Pollini, and B. Stolarik, “A comparison of pose estimation algorithms for machine vision based aerial refueling for uavs,” in *2006 14th Mediterranean Conference on Control and Automation*. IEEE, 2006, pp. 1–6.
- [179] S. M. Ross, M. D. Menza, E. T. Waddell Jr, A. P. Mainstone, J. Velez, and A. F. F. T. C. E. A. CA, “Demonstration of a control algorithm for autonomous aerial refueling (project “no gyro”),” Technical report, Air Force Flight Test Center, Tech. Rep., 2005.
- [180] J. Hansen, J. Murray, and N. Campos, “The nasa dryden aar project: a flight test approach to an aerial refueling system,” in *AIAA atmospheric flight mechanics conference and exhibit*, 2004, p. 4939.
- [181] W. R. Williamson, G. J. Glenn, V. T. Dang, J. L. Speyer, S. M. Stecko, and J. M. Takacs, “Sensor fusion applied to autonomous aerial refueling,” *Journal of Guidance, Control, and Dynamics*, vol. 32, no. 1, pp. 262–275, 2009.
- [182] F. Jia-Ning, F. Qiang, U. Arif, and Q. Quan, “A pose estimation method of a moving target based on off-board monocular vision,” in *2016 IEEE Chinese Guidance, Navigation and Control Conference (CGNCC)*. IEEE, 2016, pp. 2082–2087.
- [183] J. Kimmett, J. Valasek, and J. Junkins, “Autonomous aerial refueling utilizing a vision based navigation system,” in *AIAA Guidance, Navigation, and Control Conference and Exhibit*, 2002, p. 4469.
- [184] A. D. Weaver, “Using predictive rendering as a vision-aided technique for autonomous aerial refueling,” 2009.

- [185] Q. Fu, Q. Quan, and K.-Y. Cai, “Robust pose estimation for multirotor uavs using off-board monocular vision,” *IEEE Transactions on Industrial Electronics*, vol. 64, no. 10, pp. 7942–7951, 2017.
- [186] S. Chen, H. Duan, Y. Deng, C. Li, G. Zhao, and Y. Xu, “Drogue pose estimation for unmanned aerial vehicle autonomous aerial refueling system based on infrared vision sensor,” *Optical Engineering*, vol. 56, no. 12, pp. 124 105–124 105, 2017.
- [187] J. Valasek, K. Gunnam, J. Kimmett, M. D. Tandale, J. L. Junkins, and D. Hughes, “Vision-based sensor and navigation system for autonomous air refueling,” *Journal of guidance, control, and dynamics*, vol. 28, no. 5, pp. 979–989, 2005.
- [188] M. D. Tandale, R. Bowers, and J. Valasek, “Trajectory tracking controller for vision-based probe and drogue autonomous aerial refueling,” *Journal of guidance, control, and dynamics*, vol. 29, no. 4, pp. 846–857, 2006.
- [189] C.-P. Lu, G. D. Hager, and E. Mjolsness, “Fast and globally convergent pose estimation from video images,” *IEEE transactions on pattern analysis and machine intelligence*, vol. 22, no. 6, pp. 610–622, 2000.
- [190] Q. Quan, *Introduction to multicopter design and control*. Springer, 2017.
- [191] Z.-B. Wei, X. Dai, Q. Quan, and K.-Y. Cai, “Drogue dynamic model under bow wave in probe-and-drogue refueling,” *IEEE Transactions on Aerospace and Electronic Systems*, vol. 52, no. 4, pp. 1728–1742, 2016.
- [192] P. Sturm, *Pinhole Camera Model*. Boston, MA: Springer US, 2014, pp. 610–613.
[Online]. Available: https://doi.org/10.1007/978-0-387-31439-6_472
- [193] R. Girshick, J. Donahue, T. Darrell, and J. Malik, “Rich feature hierarchies for accurate object detection and semantic segmentation,” in *Proceedings of the IEEE conference on computer vision and pattern recognition*, 2014, pp. 580–587.
- [194] S. Ren, K. He, R. Girshick, and J. Sun, “Faster r-cnn: Towards real-time object detection with region proposal networks,” *Advances in neural information processing systems*, vol. 28, 2015.
- [195] T.-Y. Lin, P. Dollár, R. Girshick, K. He, B. Hariharan, and S. Belongie, “Feature pyramid networks for object detection,” in *Proceedings of the IEEE conference on computer vision and pattern recognition*, 2017, pp. 2117–2125.
- [196] J. Redmon, S. Divvala, R. Girshick, and A. Farhadi, “You only look once: Unified, real-time object detection,” in *Proceedings of the IEEE conference on computer vision and pattern recognition*, 2016, pp. 779–788.

- [197] C.-Y. Fu, W. Liu, A. Ranga, A. Tyagi, and A. C. Berg, “Dssd: Deconvolutional single shot detector,” *arXiv preprint arXiv:1701.06659*, 2017.
- [198] T.-Y. Lin, P. Goyal, R. Girshick, K. He, and P. Dollár, “Focal loss for dense object detection,” in *Proceedings of the IEEE international conference on computer vision*, 2017, pp. 2980–2988.
- [199] A. Bochkovskiy, C.-Y. Wang, and H.-Y. M. Liao, “Yolov4: Optimal speed and accuracy of object detection,” *arXiv preprint arXiv:2004.10934*, 2020.
- [200] C.-Y. Wang, H.-Y. M. Liao, Y.-H. Wu, P.-Y. Chen, J.-W. Hsieh, and I.-H. Yeh, “CspNet: A new backbone that can enhance learning capability of cnn,” in *Proceedings of the IEEE/CVF conference on computer vision and pattern recognition workshops*, 2020, pp. 390–391.
- [201] S. Liu, L. Qi, H. Qin, J. Shi, and J. Jia, “Path aggregation network for instance segmentation,” in *Proceedings of the IEEE conference on computer vision and pattern recognition*, 2018, pp. 8759–8768.
- [202] Z. Zheng, P. Wang, D. Ren, W. Liu, R. Ye, Q. Hu, and W. Zuo, “Enhancing geometric factors in model learning and inference for object detection and instance segmentation,” *IEEE transactions on cybernetics*, vol. 52, no. 8, pp. 8574–8586, 2021.
- [203] Z. Zheng, P. Wang, W. Liu, J. Li, R. Ye, and D. Ren, “Distance-iou loss: Faster and better learning for bounding box regression,” in *Proceedings of the AAAI conference on artificial intelligence*, vol. 34, no. 07, 2020, pp. 12 993–13 000.
- [204] Y. Yuan, L. Cheng, Z. Wang, and C. Sun, “Position tracking and attitude control for quadrotors via active disturbance rejection control method,” *Science China Information Sciences*, vol. 62, pp. 1–10, 2019.
- [205] Q. Quan, K.-Y. Cai, and H. Lin, “Additive-state-decomposition-based tracking control framework for a class of nonminimum phase systems with measurable nonlinearities and unknown disturbances,” *International Journal of Robust and Nonlinear Control*, vol. 25, no. 2, pp. 163–178, 2015.
- [206] Z. Su, H. Wang, X. Shao, and P. Yao, “Autonomous aerial refueling precise docking based on active disturbance rejection control,” in *IECON 2015-41st Annual Conference of the IEEE Industrial Electronics Society*. Yokohama, Japan: IEEE, Nov. 2015, pp. 4574–4578.
- [207] Z. Liu, J. Liu, and W. He, “Modeling and vibration control of a flexible aerial refueling hose with variable lengths and input constraint,” *Automatica*, vol. 77, pp. 302–310, 2017.

- [208] H. T. Wang, X. M. Dong, and J. P. Xue, “Modeling and simulation of a time-varying inertia aircraft in aerial refueling,” *Chinese Journal of Aeronautics*, vol. 29, no. 2, pp. 335–345, 2016.
- [209] K. Ogata and Y. Yang, *Modern control engineering*. Prentice hall India, 2002, vol. 5.
- [210] Q. Quan, G.-X. Du, and K.-Y. Cai, “Proportional-integral stabilizing control of a class of mimo systems subject to nonparametric uncertainties by additive-state-decomposition dynamic inversion design,” *IEEE/ASME Transactions on Mechatronics*, vol. 21, no. 2, pp. 1092–1101, 2015.
- [211] D. Luo, J. Shao, Y. Xu, and J. Zhang, “Docking navigation method for uav autonomous aerial refueling,” *Science China Information Sciences*, vol. 62, pp. 1–16, 2019.
- [212] J. S. Lee and K. H. Yu, “Optimal path planning of solar-powered UAV using gravitational potential energy,” *IEEE Transactions on Aerospace and Electronic Systems*, vol. 53, no. 3, pp. 1442–1451, 2017.
- [213] J. L. G. Olavo, G. D. Thums, T. A. Jesus, L. C. De Araujo Pimenta, L. A. B. Torres, and R. M. Palhares, “Robust guidance strategy for target circulation by controlled UAV,” *IEEE/CAA Journal of Automatica Sinica*, vol. 54, no. 3, pp. 1415–1431, 2018.
- [214] V. Roberge, M. Tarbouchi, and G. Labonté, “Fast genetic algorithm path planner for fixed-wing military UAV using GPU,” *IEEE Transactions on Aerospace and Electronic Systems*, vol. 54, no. 5, pp. 2105–2117, 2018.
- [215] P. R. Thomas, U. Bhandari, S. Bullock, T. S. Richardson, and J. L. Du Bois, “Advances in air to air refuelling,” *Progress in Aerospace Sciences*, vol. 71, pp. 14–35, 2014.
- [216] K. Ro, T. Kuk, and J. W. Kamman, “Dynamics and control of hose-drogue refueling systems during coupling,” *Journal of Guidance, Control and Dynamics*, vol. 34, no. 6, pp. 1694–1708, 2011.
- [217] J. Vassberg, D. Yeh, A. Blair, and J. M. Evert, “Numerical simulations of KC-10 wing-mount aerial refueling hose-drogue dynamics with a reel take-up system,” in *21st applied aerodynamics conference*, 2003, p. 3508.
- [218] J. Vassberg, D. Yeh, A. Blair, and J. Evert, “Numerical simulations of KC-10 in-flight refueling hose-drogue dynamics with an approaching F/A-18D receiver aircraft,” in *23rd AIAA Applied Aerodynamics Conference*, 2005, p. 4605.
- [219] H. Wang, X. Dong, J. Xue, and J. Liu, “Dynamic modeling of a hose-drogue aerial refueling system and integral sliding mode backstepping control for the hose whipping phenomenon,” *Chinese Journal of Aeronautics*, vol. 27, no. 4, pp. 930–946, 2014.

- [220] K. Ro, H. Ahmad, and J. Kamman, “Dynamic modeling and simulation of hose-paradrogue assembly for mid-air operations,” in *AIAA Infotech@Aerospace Conference, Seattle, Washington, USA*, 2009, p. 1849.
- [221] K. Yue, L. Cheng, T. Zhang, J. Ji, and D. Yu, “Numerical simulation of the aerodynamic influence of an aircraft on the hose-refueling system during aerial refueling operations,” *Aerospace Science and Technology*, vol. 49, pp. 34–40, 2016.
- [222] B. Chen, X. Dong, Y. Xu, and Q. Lin, “Disturbance analysis and flight control law design for aerial refueling,” in *Mechatronics and Automation, 2007. ICMA 2007. International Conference on*, 2007, pp. 2997–3002.
- [223] R. Dibley, M. Allen, and N. Nabaa, “Autonomous airborne refueling demonstration phase I flight-test results,” in *AIAA Atmospheric Flight Mechanics Conference and Exhibit*, 2007, p. 6639.
- [224] Z. B. Wei, X. Dai, Q. Quan, and K. Y. Cai, “Drogue dynamic model under bow wave in probe-and-drogue refueling,” *IEEE Transactions on Aerospace and Electronic Systems*, vol. 52, no. 4, pp. 1728–1742, 2016.
- [225] X. H. Dai, Z. B. Wei, and Q. Quan, “Modeling and simulation of bow wave effect in probe and drogue aerial refueling,” *Chinese Journal of Aeronautics*, vol. 29, no. 2, pp. 448–461, 2016.
- [226] W. R. Williamson, E. Reed, G. J. Glenn, S. M. Stecko, J. Musgrave, and J. M. Takacs, “Controllable drogue for automated aerial refueling,” *Journal of Aircraft*, vol. 47, no. 2, pp. 515–527, 2010.
- [227] J. Vassberg, D. Yeh, A. Blair, and J. Evert, “Numerical simulations of KC-10 centerline aerial refueling hose-drogue dynamics with a reel take-up system,” in *22nd Applied Aerodynamics Conference and Exhibit*, 2004, p. 4719.
- [228] U. Bhandari, P. R. Thomas, and T. S. Richardson, “Bow wave effect in probe-and-drogue aerial refuelling,” in *AIAA Guidance, Navigation, and Control Conference*, 2013, p. 4695.
- [229] L. Ljung, “System identification,” in *Signal analysis and prediction*. Springer, 1998, pp. 163–173.
- [230] G. F. Franklin, J. D. Powell, and A. Emami-Naeini, *Feedback control of dynamic systems*. Pearson London, 2015, vol. 33.
- [231] “Drogue Dynamics during the Contact Phase of Aerial Refueling with Hose Drogue Unit.” [Online]. Available: http://v.youku.com/v_show/id_XMTQ1OTMzMjk1Mg==.html?from=y1.7-2,2016-02-01/2016-04-17

- [232] M. D. Tandale, R. Bowers, and J. Valasek, “Trajectory tracking controller for vision-based probe and drogue autonomous aerial refueling,” *Journal of Guidance, Control, and Dynamics*, vol. 29, no. 4, pp. 846–857, 2008.
- [233] U. Bhandari, P. R. Thomas, S. Bullock, T. S. Richardson, and J. L. du Bois, “Bow wave effect in probe and drogue aerial refuelling,” in *AIAA Guidance, Navigation, and Control Conference*, ser. AIAA 2013-4695, Aug. 2013.
- [234] H. Zhu, S. Yuan, and Q. Shen, “Vision/GPS-based docking control for the UAV Autonomous Aerial Refueling,” in *Guidance, Navigation and Control Conference (CGNCC), 2016 IEEE Chinese*. IEEE, 2016, pp. 1211–1215.
- [235] O. Khan and J. Masud, “Trajectory analysis of basket engagement during aerial refueling,” in *AIAA Atmospheric Flight Mechanics Conference*, ser. AIAA 2014-0190, Jan. 2014.
- [236] D. A. Bristow, M. Tharayil, and A. G. Alleyne, “A survey of iterative learning control,” *IEEE Control Systems*, vol. 26, no. 3, pp. 96–114, 2006.
- [237] H.-S. Ahn, Y. Chen, and K. L. Moore, “Iterative learning control: Brief survey and categorization,” *IEEE Transactions on Systems, Man, and Cybernetics, Part C (Applications and Reviews)*, vol. 37, no. 6, pp. 1099–1121, 2007.
- [238] J. Valasek, K. Gunnam, J. Kimmett, J. L. Junkins, D. Hughes, and M. D. Tandale, “Vision-based sensor and navigation system for autonomous air refueling,” *Journal of Guidance, Control, and Dynamics*, vol. 28, no. 5, pp. 979–989, 2005.
- [239] Y. Chen and C. Wen, *Iterative learning control: convergence, robustness and applications*. Springer-Verlag, 1999.
- [240] R. Chi, Z. Hou, S. Jin, and D. Wang, “Improved data-driven optimal tilc using time-varying input signals,” *Journal of Process Control*, vol. 24, no. 12, pp. 78–85, 2014.
- [241] NATO, “Atp-56(b) air-to-air refuelling,” NATO, Tech. rep., 2010.
- [242] J. Wang, V. V. Patel, C. Cao, N. Hovakimyan, and E. Lavretsky, “Verifiable l1 adaptive controller for aerial refueling,” in *AIAA Guidance, Navigation and Control Conference and Exhibit*, ser. AIAA Paper 2007-6313, Hilton Head, South Carolina, Aug. 2007.
- [243] J. X. Xu, Y. Chen, H. L. Tong, and S. Yamamoto, “Terminal iterative learning control with an application to rtpcvd thickness control,” *Automatica*, vol. 35, no. 9, pp. 1535–1542, 1999.
- [244] Y. Q. Chen, K. L. Moore, and H. S. Ahn, *Iterative Learning Control*. Springer US, 2012.
- [245] B. L. Stevens and F. L. Lewis, *Aircraft Control and Simulation*. John Wiley & Sons, 2004.

- [246] Z.-B. Wei, Q. Quan, and K.-Y. Cai, “Output feedback ilc for a class of nonminimum phase nonlinear systems with input saturation: An additive-state-decomposition-based method,” *IEEE Transactions on Automatic Control*, vol. 62, no. 1, pp. 502–508, 2017.
- [247] D. Nesić and A. R. Teel, “Sampled-data control of nonlinear systems: an overview of recent results,” *Perspectives in robust control*, vol. 268, pp. 221–239, 2001.
- [248] “A reliable docking control scheme for probe-drogue refueling,” <https://youtu.be/gTqAhAPINvQ>, accessed June 10, 2019.
- [249] P. Thomas, U. Bhandari, S. Bullock, T. Richardson, and J. du Bois, “Advances in air to air refuelling,” *Progress in Aerospace Sciences*, vol. 71, pp. 14 – 35, 2014.
- [250] X. Dai, Z. Wei, and Q. Quan, “Modeling and simulation of bow wave effect in probe and drogue aerial refueling,” *Chinese Journal of Aeronautics*, vol. 29, no. 2, pp. 448 – 461, 2016.
- [251] Z. Wei, X. Dai, Q. Quan, and K.-Y. Cai, “Drogue dynamic model under bow wave in probe-and-drogue refueling,” *IEEE Transactions on Aerospace and Electronic Systems*, vol. 52, no. 4, pp. 1728–1742, 2016.
- [252] C. Martínez, T. Richardson, P. Thomas, J. du Bois, and P. Campoy, “A vision-based strategy for autonomous aerial refueling tasks,” *Robotics and Autonomous Systems*, vol. 61, no. 8, pp. 876–895, 2013.
- [253] X. Wang, X. Kong, J. Zhi, Y. Chen, and X. Dong, “Real-time drogue recognition and 3D locating for UAV autonomous aerial refueling based on monocular machine vision,” *Chinese Journal of Aeronautics*, vol. 28, no. 6, pp. 1667–1675, 2015.
- [254] G. Campa, M. Fravolini, A. Ficola, M. Napolitano, B. Seanor, and M. Perhinschi, “Autonomous aerial refueling for UAVs using a combined GPS-machine vision guidance,” in *AIAA Guidance, Navigation, and Control Conference and Exhibit*, Providence, Rhode Island, 2004. AIAA paper 2004-5350.
- [255] Y. Sun, Y. Deng, H. Duan, and X. Xu, “Bionic visual close-range navigation control system for the docking stage of probe-and-drogue autonomous aerial refueling,” *Aerospace Science and Technology*, vol. 91, pp. 136–149, 2019.
- [256] F. Chaumette and S. Hutchinson, “Visual servo control. I. basic approaches,” *IEEE Robotics & Automation Magazine*, vol. 13, no. 4, pp. 82–90, 2006.
- [257] ——, “Visual servo control. ii. advanced approaches,” *IEEE Robotics & Automation Magazine*, vol. 14, no. 1, pp. 109–118, 2007.

- [258] G. Campa, M. R. Napolitano, and M. L. Fravolini, “Simulation environment for machine vision based aerial refueling for UAVs,” *IEEE Transactions on Aerospace and Electronic Systems*, vol. 45, no. 1, pp. 138–151, 2009.
- [259] A. J. Choi, H.-H. Yang, and J.-H. Han, “Study on robust aerial docking mechanism with deep learning based drogue detection and docking,” *Mechanical Systems and Signal Processing*, vol. 154, p. 107579, 2021.
- [260] J. A. B. Garcia and A. B. Younes, “Real-time navigation for drogue-type autonomous aerial refueling using vision-based deep learning detection,” *IEEE Transactions on Aerospace and Electronic Systems*, vol. 57, no. 4, pp. 2225–2246, 2021.
- [261] B. L. Stevens, F. L. Lewis, and E. N. Johnson, *Aircraft control and simulation: dynamics, controls design, and autonomous systems*. John Wiley & Sons, 2015.
- [262] Y. Gao, X. Dai, and Q. Quan, “Vision-based robust position estimation in probe-and-drogue autonomous aerial refueling,” in *2018 IEEE CSAA Guidance, Navigation and Control Conference (CGNCC)*. Xiamen, China: IEEE, 2018, pp. 1–6.
- [263] W.-F. Xie, Z. Li, X.-W. Tu, and C. Perron, “Switching control of image-based visual servoing with laser pointer in robotic manufacturing systems,” *IEEE Transactions on Industrial Electronics*, vol. 56, no. 2, pp. 520–529, 2008.
- [264] J. Papayanopoulos, K. Webb, and J. Rogers, “An autonomous docking mechanism for vertical lift unmanned aircraft,” *Journal of Mechanisms and Robotics*, vol. 11, no. 6, p. 061009, 2019.
- [265] Y. H. Liu, H. L. Wang, Z. K. Su, and et al, “Deep learning based trajectory optimization for uav aerial refueling docking under bow wave,” *Aerospace Science and Technology*, vol. 80, pp. 392–402, 2018.
- [266] Z. K. Su, H. L. Wang, X. L. Shao, and et al, “Back-stepping based anti-disturbance flight controller with preview methodology for autonomous aerial refueling,” *Aerospace Science and Technology*, vol. 61, pp. 95–108, 2017.
- [267] J. Wang, V. V. Patel, C. Cao, and et al, “Novel L1 adaptive control methodology for aerial refueling with guaranteed transient performance,” *Journal of guidance, control, and dynamics*, vol. 31, no. 1, pp. 182–193, 2008.
- [268] Q. S. He, H. T. Wang, Y. F. Chen, and et al, “Command filtered backstepping sliding mode control for the hose whipping phenomenon in aerial refueling,” *Aerospace Science and Technology*, vol. 67, pp. 495–505, 2017.

- [269] K. Ro, T. Kuk, and J. W. Kamman, “Dynamics and control of hose-drogue refueling systems during coupling,” *Journal of guidance, control, and dynamics*, vol. 34, no. 6, pp. 1694–1708, 2011.
- [270] X. H. Dai, Z. Wei, and Q. Quan, “Modeling and simulation of bow wave effect in probe and drogue aerial refueling,” *Chinese Journal of Aeronautics*, vol. 29, no. 2, pp. 448–461, 2016.
- [271] Z. B. Wei, X. H. Dai, Q. Quan, and et al, “Drogue dynamic model under bow wave in probe-and-drogue refueling,” *IEEE Transactions on Aerospace and Electronic Systems*, vol. 52, no. 4, pp. 1728–1742, 2016.
- [272] H. T. Wang, X. M. Dong, J. P. Xue, and et al, “Dynamic modeling of a hose-drogue aerial refueling system and integral sliding mode backstepping control for the hose whipping phenomenon,” *Chinese Journal of Aeronautics*, vol. 29, no. 2, pp. 335–345, 2016.
- [273] J. H. Hensen, J. E. Murray, and N. V. Campos, “The nasa dryden aar project: a flight test approach to an aerial refueling system,” in *AIAA Atmospheric Flight Mechanics Conference & Exhibit*, 2004, p. 4939.
- [274] R. Dibley, M. Allen, and N. Nabaa, “Autonomous airborne refueling demonstration phase I flight-test results,” in *AIAA Atmospheric Flight Mechanics Conference and Exhibit*, 2007, pp. 20–23.
- [275] NATO, “Nato atp-56(B) air-to-air refuelling,” Tech. Rep., 2010.
- [276] I. M. Mitchell, A. M. Bayen, and C. J. Tomlin, “A time-dependent hamilton-jacobi formulation of reachable sets for continuous dynamic games,” *IEEE Transactions on Automatic Control*, vol. 50, no. 7, pp. 947–957, 2005.
- [277] J. H. Gillula and G. M. Hoffmann, “Applications of hybrid reachability analysis to robotic aerial vehicles,” *The International Journal of Robotics Research*, vol. 30, no. 3, pp. 335–354, 2011.
- [278] T. Lombaerts, S. R. Schuet, and K. R. Wheeler, “Safe maneuvering envelope estimation based on a physical approach,” in *AIAA Guidance, Navigation, and Control (GNC) Conference*, 2013, pp. 1–20.
- [279] A. M. Bayen and I. M. Mitchell, “Aircraft autolander safety analysis through optimal control based reachable set computation,” *Journal of guidance, control, and dynamics*, vol. 30, no. 1, pp. 68–77, 2007.
- [280] J. H. Gillulay and C. J. Tomlin, “Guaranteed safe online learning of a bounded system,” in *Intelligent Robots and Systems, IEEE/RSJ International Conference*, 2011, pp. 2979–2984.

- [281] J. Ding, J. Sprinkle, and C. J. Tomlin, “Reachability calculations for vehicle safety during manned/unmanned vehicle interaction,” *Journal of guidance, control, and dynamics*, vol. 35, no. 1, pp. 138–152, 2012.
- [282] I. M. Mitchell, “A toolbox of level set methods,” Dept. Comput. Sci., Univ. British Columbia, Vancouver, BC, Canada, Tech. Rep., 2004, tech. Rep. TR-2004-09, pp. 99–114. [Online]. Available: <http://www.cs.ubc.ca/mitchell/ToolboxLS/toolboxLS.pdf>
- [283] S. Osher, R. Fedkiw, and K. Piechor, *Level set methods and dynamic implicit surfaces*. Springer, 2003.
- [284] F. Gavilan, R. Vazquez, and J. Acosta, “Adaptive control for aircraft longitudinal dynamics with thrust saturation,” *Journal of guidance, control, and dynamics*, vol. 38, no. 4, pp. 651–661, 2014.
- [285] B. L. Stevens, *Aircraft control and simulation: dynamics, controls Design, and autonomous Systems*. John Wiley & Sons, 2003.
- [286] M. G. Goman, A. V. Khramtsovsky, and E. N. Kolesnikov, “Evaluation of aircraft performance and maneuverability by computation of attainable equilibrium sets,” *Journal of guidance, control, and dynamics*, vol. 31, no. 2, pp. 329–339, 2015.
- [287] G. Campa, M. R. Napolitano, and M. L. Fravolini, “Simulation environment for machine vision based aerial refueling for uavs,” *IEEE Transactions on Aerospace and Electronic Systems*, vol. 71, no. 1, pp. 138–151, 2009.
- [288] M. D. Tandale, R. Bowers, and J. Valasek, “Trajectory tracking controller for vision-based probe and drogue autonomous aerial refueling,” *Journal of guidance, control, and dynamics*, vol. 29, no. 4, pp. 846–857, 2012.
- [289] G. X. Du, Q. Quan, B. X. Yang, and et al, “Controllability analysis for multirotor helicopter rotor degradation and failure,” *Journal of guidance, control, and dynamics*, vol. 38, no. 5, pp. 978–985, 2015.
- [290] X. F. Wang, X. M. Dong, and X. W. Kong, “Drogue detection for autonomous aerial refueling based on convolutional neural networks,” *Chinese Journal of Aeronautics*, vol. 30, no. 1, pp. 380–390, 2017.
- [291] N. K. Sinha and M. P. Griscik, “A stochastic approximation method,” *IEEE Transactions on Systems, Man, and Cybernetics*, vol. SMC-1, no. 4, pp. 338–344, 1971.
- [292] Z. Y. Zhao, Q. Quan, and K. Y. Cai, “A health performance prediction method of large-scale stochastic linear hybrid systems with small failure probability,” *Reliability Engineering and System Safety*, pp. 74–88, 2017.

- [293] H. J. Kushner, “Numerical methods for stochastic control problems in continuous time,” *SIAM Journal on Control and Optimization*, vol. 28, no. 5, pp. 999–1048, 1990.
- [294] A. Chutinan and B. H. Krogh, “Computational techniques for hybrid system verification,” *IEEE Transactions on Automatic Control*, vol. 48, no. 1, pp. 64–75, 2003.
- [295] O. Stursberg and B. H. Krogh, “Efficient representation and computation of reachable sets for hybrid systems,” in *Proceedings of the 6th International Workshop*. Prague, Czech Republic: Springer, April 2003, pp. 3–5.
- [296] A. A. Kurzhanskiy and P. Varaiya, “Ellipsoidal techniques for reachability analysis of discrete-time linear systems,” *IEEE Transactions on Automatic Control*, vol. 52, no. 1, pp. 26–38, 2007.
- [297] P. Turati, N. Pedroni, and E. Zio, “Advanced restart method for the estimation of the probability of failure of highly reliable hybrid dynamic systems,” *Reliability Engineering & System Safety*, vol. 154, pp. 117–126, 2016.
- [298] K. Margellos and J. Lygeros, “Toward 4-d trajectory management in air traffic control: a study based on monte carlo simulation and reachability analysis,” *IEEE Transactions on Control Systems Technology*, vol. 21, no. 5, pp. 1820–1833, 2013.
- [299] M. Prandini and J. H. Hu, “A stochastic approximation method for reachability computations,” in *Stochastic hybrid systems*, H. Blom and J. Lygeros, Eds. Springer, 2006, pp. 107–139.
- [300] M. Althoff, “Reachability analysis and its application to the safety assessment of autonomous cars,” Ph.D. dissertation, Technische Universität München, München, 2010.
- [301] F. Liang, Y. Cheng, Q. Song, and et al, “A resampling-based stochastic approximation method for analysis of large geostatistical data,” *Journal of the American Statistical Association*, vol. 108, no. 501, pp. 325–339, 2013.
- [302] I. M. Mitchell, A. M. Bayen, and C. J. Tomlin, “A time-dependent hamilton-jacobi formulation of reachable sets for continuous dynamic games,” *IEEE Transactions on Automatic Control*, vol. 50, no. 7, pp. 947–957, 2005.
- [303] J. H. Hu, M. Prandini, and S. Sastry, “Aircraft conflict detection in the presence of spatially correlated wind perturbations,” in *AIAA Guidance, Navigation, and Control Conference and Exhibit*. Austin, US: AIAA, Aug 2003, paper 2003-5339.
- [304] J. Hu, M. Prandini, and S. Sastry, “Aircraft conflict prediction in the presence of a spatially correlated wind field,” *IEEE Transactions on Intelligent Transportation Systems*, vol. 6, no. 3, pp. 326–340, 2005.

- [305] D. J. C. MacKay, “Introduction to monte carlo methods,” in *Learning in Graphical Models*, M. I. Jordan, Ed. Springer, 1998, pp. 175–204.
- [306] C. Bolkcom, “Air force aerial refueling methods: flying boom versus hose-and-drogue,” Library of Congress Washington DC Congressional Research Service, Tech. Rep., 2006.
- [307] A. Degani and M. Heymann, “Formal verification of human-automation interaction,” *Human Factors*, vol. 44, no. 1, pp. 28–43, 2002.
- [308] J. Ding, J. Sprinkle, C. J. Tomlin, S. S. Sastry, and J. L. Paunicka, “Reachability calculations for vehicle safety during manned/unmanned vehicle interaction,” *Journal of Guidance, Control, and Dynamics*, vol. 35, no. 1, pp. 138–152, 2012.
- [309] N. Meskin, K. Khorasani, and C. A. Rabbath, “A hybrid fault detection and isolation strategy for a network of unmanned vehicles in presence of large environmental disturbances,” *IEEE Transactions on Control Systems Technology*, vol. 18, no. 6, pp. 1422–1429, 2010.
- [310] Y. Zhang and J. Jiang, “Issues on integration of fault diagnosis and reconfigurable control in active fault-tolerant control systems,” in *Fault Detection, Supervision and Safety of Technical Processes 2006*. Elsevier, 2007, pp. 1437–1448.
- [311] G. P. Falconí and F. Holzapfel, “Adaptive fault tolerant control allocation for a hexacopter system,” in *American Control Conference (ACC), 2016*. IEEE, 2016, pp. 6760–6766.
- [312] W. Wonham, K. Cai, and K. Rudie, “Supervisory control of discrete-event systems: A brief history-1980-2015,” *IFAC-PapersOnLine*, vol. 50, no. 1, pp. 1791 – 1797, 2017, 20th IFAC World Congress.
- [313] P. J. G. Ramadge and W. M. Wonham, “The control of discrete event systems,” *Proceedings of the IEEE*, vol. 77, no. 1, pp. 81–98, Jan 1989.
- [314] K. Cai and W. M. Wonham, “Supervisor localization: a top-down approach to distributed control of discrete-event systems,” *IEEE Transactions on Automatic Control*, vol. 55, no. 3, pp. 605–618, 2010.
- [315] W. M. Wonham and K. Cai, *Supervisory control of discrete-event systems*. Springer, 2018.
- [316] B. A. Brandin and F. E. Charbonnier, “The supervisory control of the automated manufacturing system of the aip,” in *Proceedings of the Fourth International Conference on Computer Integrated Manufacturing and Automation Technology*, Oct 1994, pp. 319–324.
- [317] M. Seidl, “Systematic controller design to drive high-load call centers,” *IEEE transactions on control systems technology*, vol. 14, no. 2, pp. 216–223, 2006.

- [318] R. J. M. Theunissen, M. Petreczky, R. R. H. Schiffelers, D. A. van Beek, and J. E. Rooda, “Application of supervisory control synthesis to a patient support table of a magnetic resonance imaging scanner,” *IEEE Transactions on Automation Science and Engineering*, vol. 11, no. 1, pp. 20–32, 2014.
- [319] D. Harel, “Statecharts: a visual formalism for complex systems,” *Science of Computer Programming*, vol. 8, no. 3, pp. 231 – 274, 1987.
- [320] C. Ma and W. M. Wonham, “Nonblocking supervisory control of state tree structures,” *IEEE Transactions on Automatic Control*, vol. 51, no. 5, pp. 782–793, 2006.
- [321] R. E. Bryant, “Graph-based algorithms for boolean function manipulation,” *IEEE Transactions on Computers*, vol. C-35, no. 8, pp. 677–691, Aug 1986.
- [322] S. T. J. Forschelen, J. M. V. D. Mortel-Fronczak, R. Su, and J. E. Rooda, “Application of supervisory control theory to theme park vehicles,” *Discrete Event Dynamic Systems*, vol. 22, no. 4, pp. 511–540, Dec 2012.
- [323] J. Markovski, K. Jacobs, D. van Beek, L. Somers, and J. Rooda, “Coordination of resources using generalized state-based requirements,” *IFAC Proceedings Volumes*, vol. 43, no. 12, pp. 287 – 292, 2010, 10th IFAC Workshop on Discrete Event Systems.
- [324] N. S. Agency, “Air to air refuelling, ATP-56(B),” North Atlantic Treaty Organization, Tech. Rep., 2010.
- [325] R. Malik, K. Akesson, H. Flordal, and M. Fabian, “Supremica-an efficient tool for large-scale discrete event systems,” *IFAC-PapersOnLine*, vol. 50, no. 1, pp. 5794 – 5799, 2017, 20th IFAC World Congress.
- [326] C. Ma and W. M. Wonham, “Stslib and its application to two benchmarks,” in *The 9th International Workshop on Discrete Event Systems 2008*, May 2008, pp. 119–124.
- [327] P. W. Kalgren, C. S. Byington, M. J. Roemer, and M. J. Watson, “Defining phm, a lexical evolution of maintenance and logistics,” in *2006 IEEE Autotestcon*, Sept 2006, pp. 353–358.
- [328] J. Nalepka and J. Hinchman, “Automated aerial refueling: extending the effectiveness of uavs,” in *AIAA modeling and simulation technologies conference and exhibit*, 2005, p. 6005.
- [329] B. S. Burns, “Autonomous unmanned aerial vehicle rendezvous for automated aerial refueling,” Ph.D. dissertation, Air Force Institute of Technology, Graduate School of Engineering and Management, 2007.

- [330] B. Burns, P. Blue, and M. Zollars, “Autonomous control for automated aerial refueling with minimum-time rendezvous,” in *AIAA Guidance, Navigation and Control Conference and Exhibit*, 2007, p. 6739.
- [331] M. Owen, J. Nichols, and M. Colton, “Cooperative aerial tracking and rendezvous along time-optimal 3-dimensional curves,” in *AIAA Guidance, Navigation, and Control Conference*, 2011, p. 6546.
- [332] D. B. Wilson, M. A. T. Soto, A. H. Göktogan, and S. Sukkarieh, “Real-time rendezvous point selection for a nonholonomic vehicle,” in *2013 IEEE International Conference on Robotics and Automation*. IEEE, 2013, pp. 3941–3946.
- [333] J. L. Stephenson, *The air refueling receiver that does not complain*. Air University Press, 1999.
- [334] Y. Yoon, M. Kim, and Y. Kim, “Three-dimensional path planning for aerial refueling between one tanker and multiple uavs,” *International Journal of Aeronautical and Space Sciences*, vol. 19, pp. 1027–1040, 2018.
- [335] L. A. Wolsey, *Integer programming*. John Wiley & Sons, 2020.
- [336] H. Oh, S. Kim, H.-S. Shin, B. A. White, A. Tsourdos, and C. A. Rabbath, “Rendezvous and standoff target tracking guidance using differential geometry,” *Journal of Intelligent & Robotic Systems*, vol. 69, pp. 389–405, 2013.
- [337] C. Hansknecht, I. Joormann, B. Korn, F. Morscheck, and S. Stiller, “Feeder routing for air-to-air refueling operations,” *European Journal of Operational Research*, vol. 304, no. 2, pp. 779–796, 2023.
- [338] K. Sundar and S. Rathinam, “Algorithms for routing an unmanned aerial vehicle in the presence of refueling depots,” *IEEE Transactions on Automation Science and Engineering*, vol. 11, no. 1, pp. 287–294, 2013.
- [339] V. P. Bordelon and J. C. Marcotte, “Optimization of strategic airlift in-flight refueling,” Ph.D. dissertation, Air Force Institute of Technology, 1981.
- [340] Y. Liu, N. Qi, W. Yao, Y. Liu, and Y. Li, “Optimal scheduling for aerial recovery of multiple unmanned aerial vehicles using genetic algorithm,” *Proceedings of the Institution of Mechanical Engineers, Part G: Journal of Aerospace Engineering*, vol. 233, no. 14, pp. 5347–5359, 2019.
- [341] I. Gamzu and D. Segev, “A polynomial-time approximation scheme for the airplane refueling problem,” *Journal of Scheduling*, vol. 22, no. 1, pp. 119–135, 2019.

- [342] R. M. Entz, G. Scherer Schwening, and R. Fernandes de Oliveira, “Application of automatic algorithm generation to air-to-air refueling scheduling,” in *16th AIAA/ISSMO Multidisciplinary Analysis and Optimization Conference*, 2015, p. 2649.
- [343] S. Kaplan and G. Rabadi, “Exact and heuristic algorithms for the aerial refueling parallel machine scheduling problem with due date-to-deadline window and ready times,” *Computers & Industrial Engineering*, vol. 62, no. 1, pp. 276–285, 2012.
- [344] K. Zhu, J. Yang, Y. Zhang, J. Nie, W. Y. B. Lim, H. Zhang, and Z. Xiong, “Aerial refueling: Scheduling wireless energy charging for uav enabled data collection,” *IEEE Transactions on Green Communications and Networking*, vol. 6, no. 3, pp. 1494–1510, 2022.
- [345] S. Kim and I. Moon, “Traveling salesman problem with a drone station,” *IEEE Transactions on Systems, Man, and Cybernetics: Systems*, vol. 49, no. 1, pp. 42–52, 2018.
- [346] A. E. Carter and C. T. Ragsdale, “A new approach to solving the multiple traveling salesperson problem using genetic algorithms,” *European journal of operational research*, vol. 175, no. 1, pp. 246–257, 2006.
- [347] P. Maini, K. Sundar, M. Singh, S. Rathinam, and P. Sujit, “Cooperative aerial-ground vehicle route planning with fuel constraints for coverage applications,” *IEEE Transactions on Aerospace and Electronic Systems*, vol. 55, no. 6, pp. 3016–3028, 2019.
- [348] C. TT, “The vehicle routing problem of mobile charging vehicles and shared electric vehicles considering mobile charging service,” Master’s thesis, Beijing Jiaotong University, 2022.
- [349] K. Huang, K. An, and G. H. de Almeida Correia, “Planning station capacity and fleet size of one-way electric carsharing systems with continuous state of charge functions,” *European Journal of Operational Research*, vol. 287, no. 3, pp. 1075–1091, 2020.
- [350] J. F. Marchman, *Aerodynamics and Aircraft Performance*. James F. Marchman, 2004.
- [351] Y. Yoon, M. Kim, and Y. Kim, “Three-dimensional path planning for aerial refueling between one tanker and multiple uavs,” *International Journal of Aeronautical and Space Sciences*, vol. 19, pp. 1027–1040, 2018.
- [352] Y. Li and H. Cheng, “App: A* post-processing algorithm for robots with bidirectional shortcut and path perturbation,” *IEEE Robotics and Automation Letters*, 2023.
- [353] P. A. Lopes, S. S. Yadav, A. Ilic, and S. K. Patra, “Fast block distributed cuda implementation of the hungarian algorithm,” *Journal of Parallel and Distributed Computing*, vol. 130, pp. 50–62, 2019.

- [354] Y. Shi and Y. Zhang, “The neural network methods for solving traveling salesman problem,” *Procedia Computer Science*, vol. 199, pp. 681–686, 2022.



Appendix Proofs, Examples and Design

A.1 System Information about the Receiver Model

The aerodynamic forces of the receiver along the x -axis, the y -axis, and the z -axis are \bar{X} , \bar{Y} , \bar{Z} , which can be expressed as

$$\begin{aligned}\bar{X} &= \bar{q}SC_{X_T}(\alpha, \beta, p, q, r, \mathbf{u}_r) \\ \bar{Y} &= \bar{q}SC_{Y_T}(\alpha, \beta, p, q, r, \mathbf{u}_r) \\ \bar{Z} &= \bar{q}SC_{Z_T}(\alpha, \beta, p, q, r, \mathbf{u}_r)\end{aligned}$$

where \bar{q} is dynamic pressure, S is wing area, α is the angle of attack, β is the sideslip angle, aerodynamic parameters C_{X_T} , C_{Y_T} , C_{Z_T} can be obtained from wind tunnel tests or flight data. The aerodynamic moments of force of the receiver along the x -axis, the y -axis, and the z -axis are \bar{L} , \bar{M} , \bar{N} , which can be expressed as

$$\begin{aligned}\bar{L} &= \bar{q}SbC_{l_T}(\alpha, \beta, p, q, r, \mathbf{u}_r) \\ \bar{M} &= \bar{q}S\bar{c}C_{m_T}(\alpha, \beta, p, q, r, \mathbf{u}_r) \\ \bar{N} &= \bar{q}SbC_{n_T}(\alpha, \beta, p, q, r, \mathbf{u}_r)\end{aligned}$$

where b is the wing span, \bar{c} is the wing mean geometric chord, aerodynamic parameters C_{l_T} , C_{m_T} , C_{n_T} can be obtained from wind tunnel tests or flight data. Suppose that engine thrust F_T and its moment of momentum h_E are along the x -axis. Other parameters, which are related to the inertia moment and the change of the inertia moment, in Eq. (7.2) are

$$\begin{aligned}c_1 &= \frac{(J_y - J_z) J_z - J_{xz}^2}{\sum}, c_2 = \frac{(J_x - J_y + J_z) J_{xz}}{\sum}, \\ c_3 &= \frac{J_z}{\sum}, c_4 = \frac{J_{xz}}{\sum}, c_5 = c_6 = \frac{J_{xz}}{J_y} \\ c_7 &= \frac{1}{J_y}, c_8 = \frac{J_x (J_x - J_y) + J_{xz}^2}{\sum}, c_9 = \frac{J_x}{\sum} \\ \kappa_1 &= \frac{\dot{J}_{xz} J_{xz} - \dot{J}_{x1} J_z}{\sum}, \kappa_2 = \frac{\dot{J}_{xz} J_z - \dot{J}_{z1} J_{xz}}{\sum}, \kappa_3 = \frac{\dot{J}_{y1}}{J_y} \\ \kappa_4 &= \frac{\dot{J}_{x1} J_{xz} - \dot{J}_x J_{zx1}}{\sum}, \kappa_5 = \frac{\dot{J}_{x1} J_z - \dot{J}_{z1} J_{xz}}{\sum}, \sum = J_x J_z - J_{xz}^2\end{aligned}$$

with the solid part of the receiver has the inertia moment \mathbf{J}_0 , and fuel tanks have the inertia moment \mathbf{J}_f . Then, the total inertia moment of the receiver is $\mathbf{J} = \mathbf{J}_0 + \mathbf{J}_f$ as follows

$$\mathbf{J}_0 = \begin{bmatrix} J_{x0} & 0 & J_{xz0} \\ 0 & J_{y0} & 0 \\ -J_{xz0} & 0 & J_{z0} \end{bmatrix}, \mathbf{J}_f = \begin{bmatrix} J_{x1} & 0 & J_{xz1} \\ 0 & J_{y1} & 0 \\ -J_{xz1} & 0 & J_{z1} \end{bmatrix}, \mathbf{J} = \begin{bmatrix} J_x & 0 & J_{xz} \\ 0 & J_y & 0 \\ -J_{xz} & 0 & J_z \end{bmatrix}.$$

A.2 Proof of Theorem 9.1

First, define the $\mathbf{p}_{\text{pr}}^{(k)}(T^{(k)})$ as the probe terminal position in the k^{th} docking attempt. Then, according to Eq. (9.16), one has

$$\mathbf{p}_{\text{pr}}^{(k)}(T^{(k)}) = \hat{\mathbf{u}}_{\text{pr}}^{(k)} - \mathbf{v}_{\text{pr}}^{(k)} \quad (\text{A.1})$$

where, $\hat{\mathbf{u}}_{\text{pr}}^{(k)}$ can be further expressed by Eq. (9.19), which yields

$$\mathbf{p}_{\text{dr}}^{\text{e0},(k)} + \mathbf{u}_{\text{de,dr}}^{(k)} - \mathbf{p}_{\text{pr}}^{(k)}(T^{(k)}) = \mathbf{v}_{\text{pr}}^{(k)} - \mathbf{u}_{\text{e,pr}}^{(k)}. \quad (\text{A.2})$$

Meanwhile, according to the definition of $\mathbf{e}_{\text{pr}}^{(k)}$ in Eq. (9.23), one has

$$\mathbf{e}_{\text{pr}}^{(k)} = \mathbf{v}_{\text{pr}}^{(k)} - \mathbf{u}_{\text{e,pr}}^{(k)}. \quad (\text{A.3})$$

Thus, substituting Eq. (9.22) into Eq. (A.3) gives

$$\mathbf{e}_{\text{pr}}^{(k)} = (\mathbf{I} - \mathbf{K}_p) \cdot \mathbf{e}_{\text{pr}}^{(k-1)} + \tilde{\mathbf{v}}_{\text{pr}}^{(k-1)} \quad (\text{A.4})$$

where

$$\tilde{\mathbf{v}}_{\text{pr}}^{(k-1)} \triangleq \mathbf{v}_{\text{pr}}^{(k)} - \mathbf{v}_{\text{pr}}^{(k-1)}. \quad (\text{A.5})$$

Second, according to Eq. (9.5), the drogue terminal position $\mathbf{p}_{\text{dr}}^{(k)}(T^{(k)})$ in the k^{th} docking attempt is given by

$$\mathbf{p}_{\text{dr}}^{(k)}(T^{(k)}) = \mathbf{p}_{\text{dr}}^{\text{e0},(k)} + \Delta \mathbf{p}_{\text{dr}}^{\text{e},(k)} \quad (\text{A.6})$$

where $\mathbf{p}_{\text{dr}}^{\text{e0},(k)}$ is the drogue original equilibrium position, and $\Delta \mathbf{p}_{\text{dr}}^{\text{e},(k)}$ is the terminal position offset. According to Eq. (9.10), $\Delta \mathbf{p}_{\text{dr}}^{\text{e},(k)}$ comes from the bow wave effect and can be expressed

$$\Delta \mathbf{p}_{\text{dr}}^{\text{e},(k)} = \mathbf{m}_0 + \mathbf{M}_1 \cdot \Delta \mathbf{p}_{\text{dr/pr}}^{(k)}(T^{(k)}) + \mathbf{v}_{\text{dr}}^{(k)}. \quad (\text{A.7})$$

Thus, the docking error along the iteration axis is given by

$$\Delta \mathbf{p}_{\text{dr/pr}}^{(k)}(T^{(k)}) = \mathbf{p}_{\text{dr}}^{(k)}(T^{(k)}) - \mathbf{p}_{\text{pr}}^{(k)}(T^{(k)}). \quad (\text{A.8})$$

Substituting Eqs. (A.6)(A.7)(A.8) into Eqs. (9.20)(9.21) gives

$$\Delta \mathbf{p}_{\text{dr/pr}}^{(k)}(T^{(k)}) = \mathbf{A}_1 \cdot \Delta \mathbf{p}_{\text{dr/pr}}^{(k-1)}(T^{(k-1)}) + \mathbf{A}_2 \cdot \mathbf{e}_{\text{pr}}^{(k-1)} + \tilde{\mathbf{v}}_{\text{dr}}^{(k-1)} \quad (\text{A.9})$$

where

$$\mathbf{A}_1 \triangleq (\mathbf{M}_1 - \mathbf{I})^{-1} (\mathbf{M}_1 - \mathbf{K}_\alpha) = \mathbf{I} - (\mathbf{I} - \mathbf{M}_1)^{-1} (\mathbf{I} - \mathbf{K}_\alpha) \quad (\text{A.10})$$

$$\mathbf{A}_2 \triangleq (\mathbf{M}_1 - \mathbf{I})^{-1} (\mathbf{K}_p + \mathbf{K}_\alpha - \mathbf{I}) \quad (\text{A.11})$$

$$\tilde{\mathbf{v}}_{\text{dr}}^{(k-1)} \triangleq (\mathbf{M}_1 - \mathbf{I})^{-1} (\mathbf{v}_{\text{dr}}^{(k-1)} - \mathbf{v}_{\text{dr}}^{(k)}). \quad (\text{A.12})$$

For simplicity, an augmented system is defined as

$$\mathbf{X}^{(k)} = \mathbf{A} \cdot \mathbf{X}^{(k-1)} + \mathbf{v}^{(k-1)} \quad (\text{A.13})$$

where

$$\mathbf{X}^{(k)} \triangleq \begin{bmatrix} \Delta \mathbf{p}_{\text{dr/pr}}^{(k)}(T^{(k)}) \\ \mathbf{e}_{\text{pr}}^{(k)} \end{bmatrix}, \mathbf{v}^{(k)} \triangleq \begin{bmatrix} \tilde{\mathbf{v}}_{\text{dr}}^{(k)} \\ \tilde{\mathbf{v}}_{\text{pr}}^{(k)} \end{bmatrix} \quad (\text{A.14})$$

$$\mathbf{A} \triangleq \begin{bmatrix} \mathbf{A}_1 & \mathbf{A}_2 \\ \mathbf{0}_{3 \times 3} & \mathbf{A}_3 \end{bmatrix}, \mathbf{A}_3 \triangleq \mathbf{I} - \mathbf{K}_p. \quad (\text{A.15})$$

Furthermore, Eq. (A.14) can be written into the following form

$$\mathbf{X}^{(k)} = \mathbf{A}^k \cdot \mathbf{X}^{(0)} + \sum_{i=0}^{k-1} \mathbf{A}^i \mathbf{v}^{(k-i)}. \quad (\text{A.16})$$

Since \mathbf{M}_1 is a negative definite matrix, according to Eqs. (A.10)(A.10)(A.14), it is easy to verify that the spectral radius of \mathbf{A} is smaller than 1 ($\rho(\mathbf{A}) < 1$) when the following constraint is satisfied

$$0 \leq k_{\alpha_i} < 1, 0 < k_{p_i} \leq 1, i = 1, 2, 3. \quad (\text{A.17})$$

Moreover, since the disturbances $\mathbf{v}_{\text{pr}}^{(k)}$ and $\mathbf{v}_{\text{dr}}^{(k)}$ are both bounded with $\|\mathbf{v}_{\text{pr}}^{(k)}\| \leq B_{\text{pr}}$ and $\|\mathbf{v}_{\text{dr}}^{(k)}\| \leq B_{\text{dr}}$, it is easy to obtain from Eqs. (A.5)(A.10)(A.14) that $\mathbf{v}^{(k)}$ is also bounded with

$$\|\mathbf{v}^{(k)}\| \leq 2\sqrt{B_{\text{pr}}^2 + B_{\text{dr}}^2}. \quad (\text{A.18})$$

Then, substituting Eq. (A.18) into Eq. (A.16) gives

$$\begin{aligned} \|\mathbf{X}^{(k)}\| &\leq \|\mathbf{A}\|^k \|\mathbf{X}^{(0)}\| + \sum_{i=0}^{k-1} \|\mathbf{A}\|^i \|\mathbf{v}^{(k-i)}\| \\ &\leq \|\mathbf{A}\|^k \|\mathbf{X}^{(0)}\| + 2\sqrt{B_{\text{pr}}^2 + B_{\text{dr}}^2} \sum_{i=0}^{k-1} \|\mathbf{A}\|^i \\ &= \|\mathbf{A}\|^k \|\mathbf{X}^{(0)}\| + 2\sqrt{B_{\text{pr}}^2 + B_{\text{dr}}^2} \left(1 - \|\mathbf{A}\|^k\right). \end{aligned} \quad (\text{A.19})$$

When the constraint in Eq. (A.17) is satisfied, one has

$$\rho(\mathbf{A}) < 1 \Rightarrow \lim_{k \rightarrow \infty} \|\mathbf{A}\|^k = 0 \quad (\text{A.20})$$

which yields from Eq. (A.19) that

$$\lim_{k \rightarrow \infty} \|\mathbf{X}^{(k)}\| \leq 2\sqrt{B_{\text{pr}}^2 + B_{\text{dr}}^2}. \quad (\text{A.21})$$

According to the definition of $\mathbf{X}^{(k)}$ in Eq. (A.14), one has

$$\|\Delta \mathbf{p}_{\text{dr/pr}}^{(k)}(T^{(k)})\| \leq \|\mathbf{X}^{(k)}\|. \quad (\text{A.22})$$

Combining Eq. (A.21) and (A.22) gives

$$\lim_{k \rightarrow \infty} \|\Delta \mathbf{p}_{\text{dr/pr}}^{(k)}(T^{(k)})\| \leq 2\sqrt{B_{\text{pr}}^2 + B_{\text{dr}}^2} = B_{\text{dr/pr}}. \quad (\text{A.23})$$

Thus, the docking error $\Delta \mathbf{p}_{\text{dr/pr}}^{(k)}(T^{(k)})$ will converge to a bound $B_{\text{dr/pr}}$ as $k \rightarrow \infty$. In particular, by substituting $B_{\text{dr}} = 0, B_{\text{pr}} = 0$ into Eq. (A.23), one has $\lim_{k \rightarrow \infty} \|\Delta \mathbf{p}_{\text{dr/pr}}^{(k)}(T^{(k)})\| = 0$.

A.2.1 Proof of Theorem 10.1

First, define variables $\tilde{\mathbf{x}}_k(t) \triangleq \mathbf{x}_k(t) - \mathbf{x}_{k-1}(t)$, $\tilde{\mathbf{u}}_k(t) \triangleq \mathbf{u}_k(t) - \mathbf{u}_{k-1}(t)$, $\tilde{\mathbf{q}}_k \triangleq \mathbf{q}_k - \mathbf{q}_{k-1}$, $\tilde{\boldsymbol{\eta}}_k = \boldsymbol{\eta}_k - \boldsymbol{\eta}_{k-1}$. Starting from $\mathbf{e}_k(T)$, one has

$$\mathbf{e}_k(T) = \mathbf{e}_{k-1}(T) - \bar{\mathbf{C}} \tilde{\mathbf{x}}_k(T). \quad (\text{A.24})$$

The next step is to calculate $\tilde{\mathbf{x}}_k(t)$. Integrating both sides of equation $\mathbf{x}_k(t) = \mathbf{Ax}_k(t) + \mathbf{Bu}_k(t) + \boldsymbol{\phi}(\bar{\mathbf{y}}_k(t)) + \boldsymbol{\varphi}_k$ gives

$$\mathbf{x}_k(t) = \mathbf{x}_{0,k} + \int_0^t (\mathbf{Ax}_k(\tau) + \mathbf{Bu}_k(\tau) + \boldsymbol{\phi}(\bar{\mathbf{y}}_k(\tau)) + \boldsymbol{\varphi}_k) d\tau. \quad (\text{A.25})$$

Then,

$$\tilde{\mathbf{x}}_k(t) = \mathbf{M}_2 \tilde{\boldsymbol{\eta}}_k + \int_0^t (\mathbf{A}\tilde{\mathbf{x}}_k(\tau) + \mathbf{B}\tilde{\mathbf{u}}_k(\tau) + \boldsymbol{\phi}(\bar{\mathbf{y}}_k(\tau)) - \boldsymbol{\phi}(\bar{\mathbf{y}}_{k-1}(\tau)) + \boldsymbol{\varphi}_k - \boldsymbol{\varphi}_{k-1}) d\tau. \quad (\text{A.26})$$

According to the learning control law (10.17) and the learning update law (10.18), one has

$\tilde{\mathbf{u}}_k(t) = \mathbf{U}_b(t)\tilde{\mathbf{q}}_k = \mathbf{U}_b(t)\mathbf{L}_1\mathbf{e}_{k-1}(T)$ and $\tilde{\boldsymbol{\eta}}_k = \mathbf{L}_2\mathbf{e}_{k-1}(T)$. Then, Eq. (A.26) becomes

$$\tilde{\mathbf{x}}_k(t) = \mathbf{M}_2\mathbf{L}_2\mathbf{e}_{k-1}(T) + \int_0^t (\mathbf{A}\tilde{\mathbf{x}}_k(\tau) + \mathbf{B}\mathbf{U}_b(\tau)\mathbf{L}_1\mathbf{e}_{k-1}(T) + \boldsymbol{\phi}(\bar{\mathbf{y}}_k(\tau)) - \boldsymbol{\phi}(\bar{\mathbf{y}}_{k-1}(\tau)) + \boldsymbol{\varphi}_k - \boldsymbol{\varphi}_{k-1}) d\tau. \quad (\text{A.27})$$

Substituting $\tilde{\mathbf{x}}_k(T)$ into (A.24) gives

$$\mathbf{e}_k(T) = \left(\mathbf{I}_3 - \bar{\mathbf{C}}\mathbf{M}_2\mathbf{L}_2 - \int_0^T \bar{\mathbf{C}}\mathbf{B}\mathbf{U}_b(\tau)\mathbf{L}_1 d\tau \right) \mathbf{e}_{k-1}(T) - \bar{\mathbf{C}} \int_0^T (\mathbf{A}\tilde{\mathbf{x}}_k(\tau) + \boldsymbol{\phi}(\bar{\mathbf{y}}_k(\tau)) - \boldsymbol{\phi}(\bar{\mathbf{y}}_{k-1}(\tau)) + \boldsymbol{\varphi}_k - \boldsymbol{\varphi}_{k-1}) d\tau, \quad (\text{A.28})$$

where $\mathbf{I}_3 \in \mathbb{R}^{3 \times 3}$ is an identity matrix. According to Assumptions 2-3, taking the norm on both sides of Eq. (A.28) results in

$$\|\mathbf{e}_k(T)\| \leq \alpha \|\mathbf{e}_{k-1}(T)\| + \int_0^T \left(\|\bar{\mathbf{C}}\mathbf{A}\| + l_{\boldsymbol{\phi}} \|\bar{\mathbf{C}}\|^2 \right) \|\tilde{\mathbf{x}}_k(\tau)\| d\tau + DT \|\bar{\mathbf{C}}\|, \quad (\text{A.29})$$

where $\alpha = \left\| \mathbf{I}_3 - \bar{\mathbf{C}}\mathbf{M}_2\mathbf{L}_2 - \int_0^T \bar{\mathbf{C}}\mathbf{B}\mathbf{U}_b(\tau)\mathbf{L}_1 d\tau \right\|$. The next step is to calculate $\|\tilde{\mathbf{x}}_k(t)\|$. Taking norm on both sides of Eq. (A.27) yields

$$\|\tilde{\mathbf{x}}_k(t)\| \leq \|\mathbf{M}_2\mathbf{L}_2\mathbf{e}_{k-1}(T)\| + \int_0^t ((\|\mathbf{A}\| + l_{\boldsymbol{\phi}} \|\bar{\mathbf{C}}\|) \|\tilde{\mathbf{x}}_k(\tau)\| + \|\mathbf{B}\mathbf{U}_b(\tau)\mathbf{L}_1\| \|\mathbf{e}_{k-1}(T)\|) d\tau + DT. \quad (\text{A.30})$$

Applying the Gronwall-Bellman inequality [244] to Eq. (A.30) results in

$$\begin{aligned} \|\tilde{\mathbf{x}}_k(t)\| &\leq (\|\mathbf{M}_2\mathbf{L}_2\mathbf{e}_{k-1}(T)\| + DT) e^{(\|\mathbf{A}\| + l_{\boldsymbol{\phi}} \|\bar{\mathbf{C}}\|)t} + \int_0^t e^{(\|\mathbf{A}\| + l_{\boldsymbol{\phi}} \|\bar{\mathbf{C}}\|)(t-\tau)} \|\mathbf{B}\mathbf{U}_b(\tau)\mathbf{L}_1\| \|\mathbf{e}_{k-1}(T)\| d\tau \\ &\leq \beta(t) \|\mathbf{e}_{k-1}(T)\| + DT e^{(\|\mathbf{A}\| + l_{\boldsymbol{\phi}} \|\bar{\mathbf{C}}\|)t}, \end{aligned} \quad (\text{A.31})$$

where $\beta(t) = \|\mathbf{M}_2\mathbf{L}_2\| e^{(\|\mathbf{A}\| + l_{\boldsymbol{\phi}} \|\bar{\mathbf{C}}\|)t} + \int_0^t e^{(\|\mathbf{A}\| + l_{\boldsymbol{\phi}} \|\bar{\mathbf{C}}\|)(t-\tau)} \|\mathbf{B}\mathbf{U}_b(\tau)\mathbf{L}_1\| d\tau$. Substituting (A.31) into (A.29) gives

$$\|\mathbf{e}_k(T)\| \leq (\alpha + \gamma) \|\mathbf{e}_{k-1}(T)\| + \varepsilon, \quad (\text{A.32})$$

where $\gamma = \int_0^T \left(\|\bar{\mathbf{C}}\mathbf{A}\| + l_{\boldsymbol{\phi}} \|\bar{\mathbf{C}}\|^2 \right) \beta(\tau) d\tau$, $\varepsilon = DT \|\bar{\mathbf{C}}\| + \int_0^T \left(\|\bar{\mathbf{C}}\mathbf{A}\| + l_{\boldsymbol{\phi}} \|\bar{\mathbf{C}}\|^2 \right) DT e^{(\|\mathbf{A}\| + l_{\boldsymbol{\phi}} \|\bar{\mathbf{C}}\|)\tau} d\tau$.

When $\alpha + \gamma < 1$, compressed mapping holds for inequality (A.32), so $\|\mathbf{e}_k(T)\| \rightarrow \frac{\varepsilon}{1-\alpha-\gamma}$ as $k \rightarrow \infty$.

A.3 LQR controller design

The LQR controller is used to drive the state of each grid into the target set \mathcal{D}_{x_r} . The design process is summarized as follows. First, introduce an integral term $\Delta \mathbf{x}'_r = -\int \mathbf{C}^T \Delta \mathbf{x}_r$, where

$$\mathbf{C} = \begin{bmatrix} 0 & 0 & 1 & 0 \\ 0 & 0 & 0 & 1 \end{bmatrix}.$$

Let $\Delta \mathbf{x}_r^a = [\Delta \mathbf{x}_r^T \ \Delta \mathbf{x}'_r^T]^T$. Then

$$\Delta \mathbf{x}_r^a = \mathbf{A} \Delta \mathbf{x}_r^a + \mathbf{B} \mathbf{u} \quad (\text{A.33})$$

where

$$\mathbf{A} = \begin{bmatrix} \mathbf{A}_r & \mathbf{0}_{4 \times 2} \\ -\mathbf{C} & \mathbf{0}_{2 \times 2} \end{bmatrix}, \mathbf{B} = \begin{bmatrix} \mathbf{B}_r \\ \mathbf{0}_{2 \times 2} \end{bmatrix}.$$

The LQR controller is designed based on Eq.(A.33), where the matrixes \mathbf{Q} and \mathbf{R} are given in three cases: (i) $\mathbf{Q} = \text{diag}(10, 10, 10, 10, 10, 10)$, $\mathbf{R} = \text{diag}(1, 1)$; (ii) $\mathbf{Q} = \text{diag}(100, 10, 10, 10, 10, 10)$, $\mathbf{R} = \text{diag}(10, 1)$; (iii) $\mathbf{Q} = \text{diag}(100, 10, 10, 10, 100, 10)$, $\mathbf{R} = \text{diag}(10, 1)$.

A.4 Proof of ***

Since $z(t) = \mathbf{B}(\mathbf{x}_r, t) - \mathbf{B}(\mathbf{x}_t, t)$, one has

$$\begin{aligned} & E [(\mathbf{z}(t_2) - \mathbf{z}(t_1))(\mathbf{z}(t_2) - \mathbf{z}(t_1))^T] \\ &= E \left[(\mathbf{B}(\mathbf{x}_r, t_2) - \mathbf{B}(\mathbf{x}_t, t_2) - \mathbf{B}(\mathbf{x}_r, t_1) + \mathbf{B}(\mathbf{x}_t, t_1))^T \right. \\ & \quad \left. (\mathbf{B}(\mathbf{x}_r, t_2) - \mathbf{B}(\mathbf{x}_t, t_2) - \mathbf{B}(\mathbf{x}_r, t_1) + \mathbf{B}(\mathbf{x}_t, t_1)) \right] \\ &= E \left[((\mathbf{B}(\mathbf{x}_r, t_2) - \mathbf{B}(\mathbf{x}_r, t_1)) - (\mathbf{B}(\mathbf{x}_t, t_2) - \mathbf{B}(\mathbf{x}_t, t_1))) \right. \\ & \quad \left. ((\mathbf{B}(\mathbf{x}_r, t_2) - \mathbf{B}(\mathbf{x}_r, t_1)) - (\mathbf{B}(\mathbf{x}_t, t_2) - \mathbf{B}(\mathbf{x}_t, t_1)))^T \right] \end{aligned} \quad (\text{A.34})$$

Expanding the above equation results in

$$\begin{aligned} & E \left[\begin{array}{c} ((\mathbf{B}(\mathbf{x}_r, t_2) - \mathbf{B}(\mathbf{x}_r, t_1)) - (\mathbf{B}(\mathbf{x}_t, t_2) - \mathbf{B}(\mathbf{x}_t, t_1))) \\ ((\mathbf{B}(\mathbf{x}_r, t_2) - \mathbf{B}(\mathbf{x}_r, t_1)) - (\mathbf{B}(\mathbf{x}_t, t_2) - \mathbf{B}(\mathbf{x}_t, t_1)))^T \end{array} \right] \\ &= E [(\mathbf{B}(\mathbf{x}_r, t_2) - \mathbf{B}(\mathbf{x}_r, t_1))(\mathbf{B}(\mathbf{x}_r, t_2) - \mathbf{B}(\mathbf{x}_r, t_1))^T] - E [(\mathbf{B}(\mathbf{x}_t, t_2) - \mathbf{B}(\mathbf{x}_t, t_1))(\mathbf{B}(\mathbf{x}_r, t_2) - \mathbf{B}(\mathbf{x}_r, t_1))^T] \\ & \quad - E [(\mathbf{B}(\mathbf{x}_r, t_2) - \mathbf{B}(\mathbf{x}_r, t_1))(\mathbf{B}(\mathbf{x}_t, t_2) - \mathbf{B}(\mathbf{x}_t, t_1))^T] + E [(\mathbf{B}(\mathbf{x}_t, t_2) - \mathbf{B}(\mathbf{x}_t, t_1))(\mathbf{B}(\mathbf{x}_t, t_2) - \mathbf{B}(\mathbf{x}_t, t_1))^T] \end{aligned} \quad (\text{A.35})$$

Combined with Eq. (13.3), the equation (A.35) can be rewritten as

$$\begin{aligned} & E \left[\begin{array}{c} ((\mathbf{B}(\mathbf{x}_r, t_2) - \mathbf{B}(\mathbf{x}_r, t_1)) - (\mathbf{B}(\mathbf{x}_t, t_2) - \mathbf{B}(\mathbf{x}_t, t_1))) \\ ((\mathbf{B}(\mathbf{x}_r, t_2) - \mathbf{B}(\mathbf{x}_r, t_1)) - (\mathbf{B}(\mathbf{x}_t, t_2) - \mathbf{B}(\mathbf{x}_t, t_1)))^T \end{array} \right] \\ &= \rho(\mathbf{x}_r - \mathbf{x}_r)(t_2 - t_1)\mathbf{I}^3 - \rho(\mathbf{x}_t - \mathbf{x}_r)(t_2 - t_1)\mathbf{I}^3 - \rho(\mathbf{x}_r - \mathbf{x}_t)(t_2 - t_1)\mathbf{I}^3 + \rho(\mathbf{x}_t - \mathbf{x}_t)(t_2 - t_1)\mathbf{I}^3 \\ &= \rho(0)(t_2 - t_1)\mathbf{I}^3 - \rho(\mathbf{x}_t - \mathbf{x}_r)(t_2 - t_1)\mathbf{I}^3 - \rho(\mathbf{x}_r - \mathbf{x}_t)(t_2 - t_1)\mathbf{I}^3 + \rho(0)(t_2 - t_1)\mathbf{I}^3 \\ &= 2\rho(0)(t_2 - t_1)\mathbf{I}^3 - \rho(\mathbf{x}_t - \mathbf{x}_r)(t_2 - t_1)\mathbf{I}^3 - \rho(\mathbf{x}_r - \mathbf{x}_t)(t_2 - t_1)\mathbf{I}^3 \end{aligned} \quad (\text{A.36})$$

Table A1: Mode Input Event Definitions

Name	Description
MIE01	Require the receiver to return to STANDBY MODE as soon as possible
MIE02	Require the receiver to return to RTL MODE as soon as possible
MIE03	Require the receiver to return to EL MODE as soon as possible
MIE04	Activate MCE09
MIE05	Activate MCE11

Substituting $\rho(0) = 1$, $\tilde{\mathbf{x}}_{r/t} = \mathbf{x}_r - \mathbf{x}_t$ and $\rho(\mathbf{x}_r - \mathbf{x}_t) = \rho(\mathbf{x}_t - \mathbf{x}_r)$, equation A.36 reads

$$\begin{aligned}
& E \left[\begin{array}{l} ((\mathbf{B}(\mathbf{x}_r, t_2) - \mathbf{B}(\mathbf{x}_r, t_1)) - (\mathbf{B}(\mathbf{x}_t, t_2) - \mathbf{B}(\mathbf{x}_t, t_1))) \\ ((\mathbf{B}(\mathbf{x}_r, t_2) - \mathbf{B}(\mathbf{x}_r, t_1)) - (\mathbf{B}(\mathbf{x}_t, t_2) - \mathbf{B}(\mathbf{x}_t, t_1)))^\top \end{array} \right] \\
&= 2\rho(0)(t_2 - t_1)\mathbf{I}^3 - \rho(\mathbf{x}_t - \mathbf{x}_r)(t_2 - t_1)\mathbf{I}^3 - \rho(\mathbf{x}_r - \mathbf{x}_t)(t_2 - t_1)\mathbf{I}^3 \quad (\text{A.37}) \\
&= 2(t_2 - t_1)\mathbf{I}^3 - 2\rho(\mathbf{x}_r - \mathbf{x}_t)(t_2 - t_1)\mathbf{I}^3 \\
&= 2[1 - \rho(\mathbf{x}_r - \mathbf{x}_t)](t_2 - t_1)\mathbf{I}^3 \\
&= 2[1 - \rho(\tilde{\mathbf{x}}_{r/t})](t_2 - t_1)\mathbf{I}_3 \quad t_1 < t_2
\end{aligned}$$

According to A.34, one gets

$$\begin{aligned}
& E [\mathbf{z}(t_2) - \mathbf{z}(t_1)][\mathbf{z}(t_2) - \mathbf{z}(t_1)]^\top \\
&= 2[1 - \rho(\tilde{\mathbf{x}}_{r/t})](t_2 - t_1)\mathbf{I}_3 \quad t_1 < t_2 \quad (\text{A.38})
\end{aligned}$$

The proof is concluded.

A.5 Event Definitions

This appendix presents the complete definitions of MIEs, ATEs and SFEs in Table A1~A3. The definitions of MCEs have already been given in Table 14.4.

A.6 Testing Cases for the Simulation Platform

Case A: Transitions in withdrawal phase: According to the FD1 and FD5 shown in Table 14.2, the pilot can force the receiver to switch from the task phase to the withdrawal phase, and the receiver would choose the best mode according to its health conditions (related with SR1 and SR2 shown in Table 14.3). When the autopilot is at JOINING-WAIT MODE, namely *Joining05* state. When “MIE03:EL” happens, according to FD5 (implemented in *Spec-pilot* shown in Fig. 14.23), MCE05 is forbidden, and the *Autopilot* has to choose one routine from MCE01~MCE03.

Table A2: Automatic Triggered Event Definitions

Name	Description
ATE01	The event MCE04 fails, i.e., the receiver does not arrive at point B. ¹
ATE02	The event MCE04 succeeds, i.e., the receiver has arrived at point B.
ATE03	The receiver is not cleared for connection
ATE04	The receiver has been cleared for the connection
ATE05	The waiting time at the observation does not exceed the specified threshold
ATE06	The waiting time at the observation area exceeds the specified threshold
ATE07	The event MCE06 fails, i.e., the receiver has not arrived at point C.
ATE08	The event MCE06 succeeds, i.e., the receiver has arrived at point C.
ATE09	The event MCE08 fails, i.e., the receiver fails to connect its probe with the tanker's drogue
ATE10	The event MCE08 succeeds, i.e., the receiver successfully connects its probe with the tanker's drogue
ATE11	The event MCE10 fails, i.e., the tanker fails to transfer the fuel to the receiver.
ATE12	The event MCE10 succeeds, i.e. the tanker successfully transfers the fuel to the receiver.
ATE13	The receiver has not been cleared for disconnection
ATE14	The receiver has been cleared for disconnection
ATE15	The waiting time at the astern area does not exceed the specified threshold
ATE16	The waiting time at the astern area exceeds the specified threshold
ATE17	The event MCE13 fails, i.e., the receiver has not arrived at point D.
ATE18	The event MCE13 succeeds, i.e., the receiver arrives at point D.
ATE19	The event MCE14 fails, i.e., the receiver has not rejoined the receiver formation
ATE20	The event MCE14 succeeds, i.e., the receiver has successfully rejoined the receiver formation

¹ "has", "does", "has not", "does not" phases used here mean the estimated corresponding state is larger or smaller than a given threshold at the sample time of sensors. For example, ATE01 means that the estimated distance between the receiver and point *B* is larger than a given threshold.

Since its health conditions satisfy SR1, MCE03 is enabled and the *Autopilot* enters *Standby* state. But then if the Control subsystem is in *critical damage*, SR1 is not satisfied anymore. According to FD1 (implemented in *Spec-Control*), MCE03 is forbidden and the *Autopilot* executes the MCE02 instead.

Case B: Transitions in joining-refueling phases: According to SR1, SR2 and SR6 shown in Table 14.3, the transition to REFUELING-INIT MODE requires certain subsystems to be healthy. Otherwise, the receiver has to retreat to the joining phase or withdrawal phase. Say that the receiver is at *Joining06* state and REFUELING-INIT MODE, and flies from point *B* to point *C* as shown in Fig. 14.3. Then the Navigation subsystem is in *minor damage*, according to SR6, the receiver can still remain in REFUELING-INIT MODE. But then the Drogue&probe subsystem is in *minor damage*. According to SR6 the receiver has to retreat to JOINING-WAIT MODE. Otherwise, if the Navigation subsystem is in *critical damage*, then according to SR1 and SR2, the receiver should change to EL MODE right away.

Case C: Transitions in refueling phase: According to SR7 shown in Table 14.3 and FD6 in Table 14.2, in the REFUELING-CAPTURE MODE, if certain subsystems are in *minor damage*, the receiver abandons the current capture and retreats to the REFUELING-INIT MODE. But then the pilot can force the receiver to initiate the refueling capture even if the health conditions do not allow this decision. When the *Autopilot* is at *Refueling02* state and the Datalink subsystem is in *minor damage*, then MCE08 is forbidden (implemented in *Spec-Datalink*). Therefore, MCE07 is executed. Since the receiver does not satisfy SR7, it has to wait at the REFUELING-INIT MODE. But when “MIE04:Force-Ref-Cap” is given, the MCE09 is enabled (implemented in *Force* shown in Fig. 14.20). Thus the receiver is forced to initiate the refueling capture.

Table A3: Failure Related Event Definitions

Name	Description
SFE01: Navigation-suspension	
SFE02: Navigation-recover	The failure related behaviors of Navigation subsystem
SFE03: Navigation-breakdown	
SFE04:Control-suspension	
SFE05:Control-recover	The failure related behaviors of Control subsystem
SFE06:Control-breakdown	
SFE07:Fuel-suspension	
SFE08: Fuel-breakdown	The failure related behaviors of Fuel subsystem
SFE09:Engine-suspension	
SFE10:Engine-recover	The failure related behaviors of Engine subsystem
SFE11:Engine-breakdown	
SFE12:dro-pro-suspension	
SFE13:dro-pro-recover	The failure related behaviors of Drogue&probe subsystem
SFE14:dro-pro-breakdown	
SFE15:Datalink-suspension	
SFE16:Datalink-recover	The failure related behaviors of Datalink subsystem
SFE17:Datalink-breakdown	
SFE18: Tanker-suspension	
SFE19: Tanker-recover	The failure related behaviors of Tankersafety subsystem
SFE20: Tanker-breakdown	